

Applied Rare-Earth Spectroscopy for Fiber Laser Optimization

Von der Gemeinsamen Fakultät für Maschinenbau und Elektrotechnik
der Technischen Universität Carolo-Wilhelmina zu Braunschweig

zur Erlangung der Würde
eines Doktor-Ingenieurs (Dr.-Ing.)
genehmigte

Dissertation

von Dipl.-Phys. Reinhard Caspary
aus Roding

Eingereicht am: 27.06.2001
Mündliche Prüfung am: 17.07.2001
Berichterstatter: Prof. Dr.-Ing. W. Kowalsky
Prof. Dr. E. O. Göbel

Acknowledgements

This thesis is the result of my research work as a scientist at the *Institut für Hochfrequenztechnik* (IHF) of the Technical University at Braunschweig in the years 1995-2001. Of course, it would have been impossible without help of the staff at IHF and other people.

First of all I want to thank Prof. H.-G. Unger, the founder of the IHF and chairman of the examination committee as well as the co-examinators Prof. W. Kowalsky, director of the IHF, and Prof. E. O. Göbel, president of the *Physikalisch Technische Bundesanstalt* (PTB) at Braunschweig. Prof. Kowalsky was my academic supervisor and is responsible for the excellent working atmosphere in the institute. The head of my research group was Dr. U. Unrau. It was a pleasure to work with him and I am very thankful for his great support not only at work but also in personal matters. The co-operation with other colleagues in the group was also very pleasant: I wish to thank C. Carbonnier, who developed the fiber laser setup, which I used for the measurements in chapter 7, furthermore T. Baraniecki, M. Kozak, Dr. L. Anselm, Dr. A. Bahl, Dr. D. Goebel, E. Seiler, and (most important for me) K. Möhring. She prepared, poured, and polished in excellent quality all the ZBLAN glass samples on which this thesis is based.

The major part of the absorption measurements I carried out at the PTB. I am thankful to Dr. A. Schirmacher and his team who made their *Cary* spectrometer available for me and I wish to thank Prof. E. O. Göbel for critical proof reading of the manuscript.

As English is not my native language, I needed external help to eliminate at least the most serious linguistic mistakes in my manuscript. In this respect I am very grateful to my aunt W. Schuster. She spent several days of her summer holidays on this job, although the obscure physical content of the manuscript made it very hard for her. It is very likely that I did not interpret all her corrections in the right way, so I am to be blamed for the remaining mistakes.

My wife Kyungja Chu and my son Felix had some hard months when I finally wrote down the manuscript in winter and spring 2001. I did not spend much time for my family during this period of time. I am very thankful for all the support by my wife, which undoubtedly was a necessary pre-condition for the success of this work. I wish to thank also my parents who were always ready to provide us with help when needed.

Last not least I gratefully remember the inspiring correspondence with Prof. B. G. Judd, who saved me from a pitfall in the theory of mixed tensor operators and opened my eyes for some details of the configuration interactions.

Reinhard Caspary

Contents

Introduction	1
1 Energy levels of nl^N configurations	5
1.1 Characteristic properties of rare earth spectra	5
1.2 Central-field approximation	7
1.3 Perturbation theory	9
1.4 Classification of states	11
1.5 First order interactions	14
1.6 Configuration interactions	22
2 Radiative transitions	29
2.1 General properties	29
2.2 Electric dipole transitions (Judd-Ofelt theory)	34
2.3 Magnetic dipole transitions	39
3 Calculation of matrix elements	41
3.1 General m -electron operators	41
3.2 Matrix elements in N -electron systems	42
3.3 Transformation to LS -coupling	50
3.4 Calculation of reduced matrix elements	52
4 Absorption spectroscopy of rare earth ions	55
4.1 The glass samples	55
4.2 Measurement setup	59
4.3 Analysis of measured spectra	62
4.4 Ce:ZBLAN	70
4.5 Pr:ZBLAN	71
4.6 Er:ZBLAN	74
4.7 Tm:ZBLAN	78
4.8 Yb:ZBLAN	80
4.9 Comparison with the literature	82
5 Parameter fit to absorption properties	85
5.1 Fit of energy levels	85
5.2 Fit of oscillator strengths	89
5.3 Tm:ZBLAN	90
5.4 Pr:ZBLAN	95

5.5	Er:ZBLAN	98
5.6	Comparison with the literature	104
6	Emission spectroscopy of rare earth ions	109
6.1	Non-radiative transitions	109
6.2	Analysis of emission spectra	113
6.3	McCumber theory	117
6.4	Er:ZBLAN	119
6.5	Tm:ZBLAN	124
7	Rare earth doped fiber lasers	127
7.1	Fiber laser operation	127
7.2	Tm:ZBLAN fiber laser at $2.3\mu\text{m}$	130
7.3	Fiber laser simulation	138
7.4	Comparison of measurement and simulation	144
7.5	Optimization of parameters	148
	Conclusions	153
	References	155
	Appendix A: Racah's tensor operators	167
A.1	Algebra of tensor operators	167
A.2	Unit tensor operators	170
A.3	Angular momentum operators	173
	Appendix B: Properties of n-j symbols	174
B.1	The 3-j symbol	174
B.2	The 6-j symbol	176
	Appendix C: Alternative sets of radial parameters	179
	Appendix D: Calculated radiative properties	181
D.1	Pr:ZBLAN	181
D.2	Er:ZBLAN	187
D.3	Tm:ZBLAN	246
	Appendix E: Setup of the fluorescence spectrometer	253
E.1	General considerations	253
E.2	Calculations	255
E.3	Conclusions	256
E.4	The Setup	258

Introduction

Rare earth doped fiber lasers have interesting properties which make them attractive alternatives to other solid state lasers: One is the simple setup because of the waveguide structure of the fiber like in a diode laser, another the long interaction length of pump and laser field and the high surface to volume ratio for heat transfer, which result in very high efficiencies. Last but not least the inherent high beam quality of single-mode fiber lasers must be mentioned, which is more or less independent of the output power, in contrast to laser diodes. The simplest setup of a fiber laser consists of a rare earth doped fiber with fiber Bragg gratings written into the fiber at both ends as laser mirrors and a pigtailed pump diode spliced to one fiber end whereas the other end delivers the laser radiation. Such strikingly simple setups without any need of alignment are one reason for the fascination caused by these devices.

Deviations from this extremely simple setup are necessary if e.g. tunable or short-pulse fiber lasers [1] are built. Especially high power single-mode fiber lasers need a different pump configuration because laser diodes are not able to deliver high pump power in the fundamental mode of the doped fiber. The solution for this case are so-called double-clad fibers where the active single-mode core is surrounded by a multi-mode pump core which may be effectively coupled to multi-mode high power laser diodes. The drawback of this solution is that it is somewhat difficult to lead the pump power from the pump core to the doped fiber laser core. Nevertheless, this pump configuration is very successful and output powers above 100 W have already been achieved.

Instead of such high power fiber lasers our institute is specialized on fiber lasers in the mid-infrared. In that wavelength region of about $2 - 5 \mu\text{m}$ the silica fibers used for telecommunication systems and most fiber lasers are not useful since above about $2.3 \mu\text{m}$ electromagnetic radiation is absorbed by vibrations of the glass matrix, which means the fiber is not transparent any more. To shift this IR-edge to lower energies different glasses are used, which in general are called low-phonon-energy (LPE) glasses. In practice most LPE glasses are heavy-metal fluoride glasses of which the ZBLAN glass based on zirconium fluoride is the most famous type, followed by INDAT glasses based on indium fluoride. ZBLAN is used in this work. Fibers from such fluoride glasses may be used at wavelengths up to about $4 \mu\text{m}$ and, in the case of INDAT, even further. The fiber laser with the longest wavelength up to now of $3.9 \mu\text{m}$ was demonstrated at our institute [2].

If fiber transmissions at even longer wavelengths are needed chalcogenide glasses [3] are the solution, but these glasses are, in general, opaque in the visible range. The short wavelength edge of the transmission window is caused by electronic excitations of the glass matrix, and in case of the fluoride glasses, it is located in the near ultra-violet. Therefore, the chalcogenide glasses are no candidates for up-conversion fiber lasers in the visible range, which are of great

interest for many applications. Typical up-conversion fiber lasers are pumped in the near-infrared, but emit laser radiation in the visible range up to the blue by subsequent absorption of two or more pump photons. For this multi-stage process to be efficient, besides the large interaction length inherent to fiber lasers, long lifetimes of the respective energy levels are necessary, and therefore again LPE glasses are needed since the higher energy levels of dopant ions in silica glasses relax very fast by excitation of vibrations in the glass matrix.

Therefore, a wide range of applications is available for ZBLAN glasses. Experience shows that in the design of a rare earth doped ZBLAN fiber laser, suppressing competing laser transitions is as important as supporting the desired transitions. Furthermore, the tendency of lower energy levels to show higher intrinsic lifetimes, often makes it necessary to run several laser transitions in a cascade [4]. The complicated systems of interfering transitions make a simulation of such a fiber laser equally valuable and attractive.

Spectroscopic properties of the appropriate rare earth ion(s) play a major role in such a simulation, but not all of these properties may be measured directly or with reasonable effort and must therefore be calculated. When the author started with such laser simulations it turned out that nearly all spectroscopic data on rare earth ions in ZBLAN glass published until now rely on the fact that the spectra of rare earth ions do not depend very much on the host material. The usual way is to start with the Judd-Ofelt theory treating the positions of the spectral lines as being material-independent and use the three Judd-Ofelt parameters as a host-dependent description of the whole spectrum of absorption and emission transitions. Data from Carnall's investigations on rare earth ions in different host materials in the 60's and 70's of the last century are mainly used for the host-independent part of the Judd-Ofelt theory. Of particular interest to ZBLAN is [5], on which e.g. [6] is based, because the host material LaF_3 , although a crystal, is a fluoride and the publication contains detailed data for all rare earth ions.

Unfortunately, it was found that the spectroscopic data presented in the literature was of varying quality. That fact made it difficult to identify the origin of discrepancies between measurement and simulation when the simulations were used in the development of fiber lasers. Therefore the author decided to go deeper into the calculation process of the spectroscopic data and start with energy level calculations. His primary goal was not necessarily to achieve data of higher quality but first of all data of known quality and knowledge about the underlying basic principles and dependencies. The reasons for the fact that most scientists in this field avoid this step are, on the one hand, the complexity of energy level calculations compared with a Judd-Ofelt fit and, on the other hand, the success of the method, as long as one does not expect high accuracy. However, a personal computer today is able to diagonalize an energy matrix of the most complicated rare earth configuration $4f^7$ with 3432×3432 elements in a few hours, and therefore it seems to make sense nowadays to precede the Judd-Ofelt fit by an energy level fit as it is already been used in the case of crystal spectra. This work is intended to promote this step by giving free access to all developed computer programs.

The main part of this work consists of seven chapters. In the following a short description of their contents will be given.

Chapter 1. This chapter provides an introduction to the calculation of the energy level systems of rare earth ions. It is assumed that the reader has a basic knowledge of quantum mechanics. The most important mathematical tool needed in this chapter is the algebra of tensor operators from Racah which is not part of standard courses in quantum mechanics. A very brief and compact introduction is therefore given in appendix A together with an explanation of the tensor equations needed for this work. For a detailed overview, the reader is referred to [7] or the famous original papers of Racah [8, 9, 10, 11], which are somewhat more difficult to read as the nomenclature has changed in the meantime.

Chapter 2. In this chapter the calculation of the radiative emission and absorption parameters is explained. The major part of these calculations is the Judd-Ofelt theory. It allows a prediction of the radiative emission and absorption properties of a rare earth ion due to electric dipole radiation based on the results of the energy level calculations in the preceding chapter.

Chapter 3. While in the first two chapters tensor operator expressions of a lot of operators were given, here it is shown how these expressions are to be evaluated numerically and the matrix elements to be calculated. Part of this work was the development of a computer program which contains the basic rules from this chapter and the definitions of the higher level operators of the preceding two chapters to calculate and fit the energy level spectrum of nl^N configurations and the Judd-Ofelt parameters.

Chapter 4. Measurements of the absorption spectra and their analysis are explained in this chapter. Cerium, praseodymium, erbium, thulium, and ytterbium are picked as examples, and the results of a detailed analysis of their absorption spectrum in ZBLAN glass are given.

Chapter 5. In this chapter the mentioned computer program is used to fit the energy levels of thulium, praseodymium, and erbium to the appropriate measurement results evaluated in the preceding chapter. Results are the radial integrals defined in chapter 1 and the Judd-Ofelt parameters from chapter 2. Furthermore, a lot of related properties of the chosen rare earth ions are calculated. The large tables of calculated transition properties between all lower lying states are shifted to appendix D, because of their length.

Chapter 6. Here the measurement and analysis of emission spectra are explained, whereas some results of the preceding chapter are used for the evaluation of the spectra uses. The results of measurement and analysis for erbium and thulium are given.

Chapter 7. In this chapter fiber laser simulations are discussed as an application of rare earth spectroscopy. After an introduction to fiber laser operation in general, the theory for a computer program for fiber laser simulation is developed using the results from the previous

chapters. The results of this program are compared with measurements of the $2.3\,\mu\text{m}$ laser in a Tm:ZBLAN fiber and used to make predictions to optimize parameters of the laser setup.

Notation and dimensions. When writing a text with such a lot of formulae as it is done in this work, it is not easy, but of special importance, to use a nomenclature as consistent as possible on the one hand and close to the main stream of the literature on the other hand. Therefore it was decided to use a roman boldface font for general operators (e.g. \mathbf{H}), vector operators (e.g. \mathbf{L}), and tensor operators (e.g. $\mathbf{U}^{(k)}$). The last one is clearly distinguished from the others by its superscripted rank, and the meaning of the other two should normally be clear from the context. Vector operators and tensor operators have coordinates which are themselves operators but are written in a medium roman font, e.g. L_z or $U_q^{(k)}$. This decision makes obvious the difference between a tensor operator $\mathbf{U}_i^{(k)}$ of a particle i and the coordinate i of a tensor operator $U_i^{(k)}$, which is important since both cases appear quite often.

To be strict, special care should be taken of the position vector \mathbf{r} , which in quantum mechanics is an operator. But as soon as one switches to the spatial representation, i.e. when wave functions $\psi(\mathbf{r}) = \langle \mathbf{r} | \psi \rangle$ are used, the position is just a variable. The former is the case for example in the vector operator expressions of the interaction Hamiltonians, where a distance therefore should be written r , and the latter in the expressions of the radial integrals, where a distance should be r . The problem with the position vector is that quite often not the position itself is the operator but an inverse distance or the deviation to its coordinates. To make things not more difficult than necessary, and as the respective meaning of the distance is usually clear from the context, it was decided always to use r .

The unit system traditionally used in spectroscopy is the cgs system. Nevertheless it was decided to use only SI units here, which should be mentioned when comparing equations with the literature. The difference in most cases is a factor $4\pi\epsilon_0$. Furthermore, angular momenta have the dimension of Planck's constant \hbar , which results in the factor \hbar in certain equations, for example $\langle l | \mathbf{L}^2 | l \rangle = l(l+1) \hbar^2$.

Although the energy is undoubtedly the natural scale for absorption and emission spectra, in many cases the wavelength became the usual quantity to specify the lines itself. Using the wavelength also in the abscissa in a graphical representation is not very useful, as the spectra become heavily distorted. In this work spectra will always be given with wavenumbers in cm^{-1} as the x-axis, but the tabulated positions of lines will be given as a wavelength, too. The often used and simple conversion equation is

$$k/\text{cm}^{-1} = \frac{10^4}{\lambda/\mu\text{m}} ,$$

with the wavenumber k and the wavelength λ . The wavenumber thus is just the inverse wavelength.

1 Energy levels of nl^N configurations

1.1 Characteristic properties of rare earth spectra

Solutions and solid materials containing rare earth ions (also called lanthanides) from lanthanum (La) to lutetium (Lu) show a series of surprisingly sharp absorption and emission lines from the infrared up to the ultraviolet region. Furthermore, the spectra show only a minor dependence on the host material. These properties make the rare earth ions very attractive for laser applications. The rare earths which are of major economic importance today are neodymium (lasers around 1064 nm), holmium (lasers around $2\ \mu\text{m}$), and erbium (fiber amplifiers around 1550 nm).

A behavior similar to the lanthanides is also known of the actinide ions from actinium (Ac) to Lawrencium (Lr), but the fact that all actinides are radio-active and the actinides above plutonium (Pu) are artificial elements which do not appear in nature explains why spectroscopic investigations of the actinides are very rare. Therefore they will not be mentioned in this work any more, although most of what is said about lanthanides holds also for the actinides. Promethium (Pm) is the only rare earth metal which is radio-active and therefore investigated as rarely as the actinide ions.

The mentioned line spectra are related to transitions in the electronic system of the rare earth ions. Table 1.1 shows the electronic configurations of the lanthanide series. Besides the two 6s electrons, which are easily removed, the rare earth elements contain only an increasing number of 4f electrons. This rule is only violated by lanthanum, gadolinium, and lutetium, which contain a 5d instead of one 4f electron, because this results in an empty 4f shell for lanthanum, a half-filled 4f shell for gadolinium, and a completely filled 4f shell for lutetium, which are more stable than shells with one electron more or less. The appearance of these special configurations with a 5d electron leads to the suggestion that the ionization energy for the first 4f electron of the other lanthanides should be comparable with the ionization energy of the 5d electron of lanthanum, gadolinium, and lutetium and therefore be relatively small. Indeed the triply ionized rare earths turn out to be chemically most stable. Only europium shows a tendency to the di-ionized state, as this results in a half filled 4f shell. It is not easy therefore to get glasses or crystals containing pure Eu^{3+} .

Free atoms or ions generally show a discrete spectrum of electronic transitions. For energies up to the ultraviolet region, these transitions only involve partly filled shells above the core noble gas configuration. For most elements the orbitals of these partly filled shells are located in the outer region of the atoms or ions and are therefore strongly affected by the neighbor atoms if the free atom gas is condensed to solid state or liquid. What results from these interactions is the well-known band structure of non-localized electron states, exactly defined in crystals and less in glasses and liquids.

Table 1.1: Electronic configurations of the lanthanides (Ln) as elements and triply ionized. The basic closed shells of the nobel gas configuration [Xe] are skipped.

Z	element	symbol	Ln	Ln ³⁺
57	lanthanum	La	4f ⁰ 5d6s ²	4f ⁰
58	cerium	Ce	4f ² 6s ²	4f ¹
59	praseodymium	Pr	4f ³ 6s ²	4f ²
60	neodymium	Nd	4f ⁴ 6s ²	4f ³
61	promethium	Pm	4f ⁵ 6s ²	4f ⁴
62	samarium	Sm	4f ⁶ 6s ²	4f ⁵
63	europium	Eu	4f ⁷ 6s ²	4f ⁶
64	gadolinium	Gd	4f ⁷ 5d6s ²	4f ⁷
65	terbium	Tb	4f ⁹ 6s ²	4f ⁸
66	dysprosium	Dy	4f ¹⁰ 6s ²	4f ⁹
67	holmium	Ho	4f ¹¹ 6s ²	4f ¹⁰
68	erbium	Er	4f ¹² 6s ²	4f ¹¹
69	thulium	Tm	4f ¹³ 6s ²	4f ¹²
70	ytterbium	Yb	4f ¹⁴ 6s ²	4f ¹³
71	lutetium	Lu	4f ¹⁴ 5d6s ²	4f ¹⁴

In contrast to all other elements of the periodic table, the orbitals of the partly filled shell 4f^{*N*} of lanthanide ions (5f^{*N*} of actinides) are located mainly inside the spatial distribution of the nobel gas core. Therefore at least the lower levels of the ground configuration of the lanthanide ions do not build band structures and the appropriate electrons stay localized at the single atom for excitation energies up to the ultraviolet. Consequently, even in solid state materials or liquids, the lanthanide ions in principle behave like free ions and the discrete energy level structure is only moderately affected by the neighbor atoms.

The main influence of the host material is that the rotational invariance, and therefore the M_J degeneracy of the states with total angular momentum \mathbf{J} , is released. This leads to a splitting of every J state into $2J + 1$ so-called Stark levels which are sharp absorption lines in crystals and mix to absorption bands with bandwidths of $100 - 1000 \text{ cm}^{-1}$ in glasses and liquids. But it must be kept in mind that, in contrast to other solid state materials, these bands still belong to localized electron configurations. The broadening is just due to the random distribution of neighbors in glasses and liquids. Each single rare earth ion has a sharp line spectrum as in a crystal.

1.2 Central-field approximation

The energy levels of an ion with Hamilton operator \mathbf{H} are given by the eigenvalues E_k of \mathbf{H} . This eigenvalue equation is usually called the time-independent Schrödinger equation:

$$\mathbf{H}|\Psi_k\rangle = E_k|\Psi_k\rangle . \quad (1.1)$$

For an ion with a nucleus of charge number Z and N electrons in partly filled shells the electrostatic Hamiltonian is given by [12]:

$$\mathbf{H}' = - \sum_i \frac{\mathbf{p}_i^2}{2m_e} - \frac{1}{4\pi\epsilon_0} \sum_i \frac{Ze^2}{r_i} + \frac{1}{4\pi\epsilon_0} \sum_{i<j} \frac{e^2}{r_{ij}} \quad (1.2)$$

with the momentum operator \mathbf{p}_i of electron i , the electron mass m_e , the electron charge e , the dielectric constant ϵ_0 , the distance r_i of electron i from the nucleus, and the distance $r_{ij} = |\mathbf{r}_j - \mathbf{r}_i|$ between electrons i and j . The first term describes the kinetic energy of the electrons, the second term is the Coulomb energy of the electrons in the central field of the nucleus, and the third term takes into account the rejecting Coulomb forces between all electron pairs. The prime in \mathbf{H}' is a reminder that this is not the full Hamiltonian, it contains only the electrostatic interactions which usually are most important.

It is a well-known fact that exact solutions to a system with $N + 1$ particles (nucleus and electrons) only exist for $N = 1$, i.e. only for hydrogen-like systems. The usual way to solve the other cases starts with a central-field approximation, neglecting the interaction of the electrons in the third term of equation (1.2). Unfortunately, a rough evaluation of the order of magnitude of the second and the third terms shows that it is not sufficient just to skip the last term and treat it as a perturbation [12]. Instead, an unknown central potential $U(r)$ is assumed and the following equation taken as a zeroth order approximation to the more exact Hamiltonian in equation (1.2):

$$\mathbf{H}_0 = \sum_i \left[-\frac{\mathbf{p}_i^2}{2m_e} + U(r_i) \right] . \quad (1.3)$$

The Hamiltonian \mathbf{H}_0 is a sum of hydrogen-like one-electron operators, which may be solved separately. The eigenfunction of such a one-electron operator is [13]

$$\psi_\alpha(\mathbf{r}) = \frac{1}{r} R_{nl}(r) Y_{m_l}^l(\theta, \phi) \chi_{m_s} \quad (1.4)$$

with the radial function $R_{nl}(r)$, the spherical harmonic $Y_{m_l}^l(\theta, \phi)$, the spin function χ_{m_s} defined by $\chi_i \chi_j = \delta_{ij}$, the abbreviation $\alpha = nlm_l m_s$, and the usual quantum numbers of the shell (n), the orbital angular momentum (l and m_l) and the spin (m_s). The fundamental importance of equation (1.4) lies in the fact that the radial and angular parts are separated and only the radial part depends on the unknown potential $U(r)$, whereas the angular (and spin) part is

completely defined by the quantum numbers l , m_l , and m_s of the electron. Furthermore, the radial part depends only on the quantum numbers n , and l and is therefore fixed inside a given configuration $c = (nl)_1(nl)_2 \dots (nl)_N$.

From equation (1.4) we can easily construct a solution of the N -electron operator \mathbf{H}_0 by taking a product $\prod_i \psi_{\alpha_i}(\mathbf{r}_i)$ of one-electron wavefunctions. But such an eigenfunction does not reflect a physical state as inside the ion all N electrons are equivalent and a correct eigenfunction must be antisymmetric with respect to the interchange of the quantum numbers of any pair of electrons. The usual solution to that problem are the so-called determinantal product states or Slater determinants [12]

$$\Psi_{\alpha_1 \alpha_2 \dots \alpha_N}(\mathbf{r}_1, \mathbf{r}_2, \dots, \mathbf{r}_N) = \frac{1}{\sqrt{N!}} \begin{vmatrix} \psi_{\alpha_1}(\mathbf{r}_1) & \psi_{\alpha_2}(\mathbf{r}_1) & \cdots & \psi_{\alpha_N}(\mathbf{r}_1) \\ \psi_{\alpha_1}(\mathbf{r}_2) & \psi_{\alpha_2}(\mathbf{r}_2) & \cdots & \psi_{\alpha_N}(\mathbf{r}_2) \\ \vdots & \vdots & \ddots & \vdots \\ \psi_{\alpha_1}(\mathbf{r}_N) & \psi_{\alpha_2}(\mathbf{r}_N) & \cdots & \psi_{\alpha_N}(\mathbf{r}_N) \end{vmatrix}, \quad (1.5)$$

which obviously are eigenfunctions of \mathbf{H}_0 and satisfy the requirement to be antisymmetric. The fraction containing N is a normalization factor introduced for convenience. As equation (1.5) contains highly redundant information, an abbreviation for the determinant is usually used:

$$\Psi_{\alpha_1 \alpha_2 \dots \alpha_N} = \{\alpha_1 \alpha_2 \dots \alpha_N\}. \quad (1.6)$$

The detailed derivation of the eigenstates of the one-electron parts of the Hamiltonian \mathbf{H}_0 shows that their eigenvalues depend only on the quantum numbers n and l . Therefore all eigenstates of \mathbf{H}_0 within a configuration c , as defined by all possible sets $i = \alpha_1 \alpha_2 \dots \alpha_N$, are completely degenerated at the energy E_0^c :

$$\mathbf{H}_0 |\Psi_i^c\rangle = E_0^c |\Psi_i^c\rangle. \quad (1.7)$$

We will restrict ourselves to electronic transitions inside the ground configuration $4f^N$ of the rare earth ions, as the distance to the ground levels even of the first excited configurations is in the ultraviolet region [14, 15]. It should be noted that these excited configurations contain electrons like $5d$ and lead to broad absorption bands, which in principle should be easily distinguishable from the line spectra of the ground configuration. Since the UV-absorption edge of the glass matrix in the ZBLAN glasses used in this work is located in the same region, no clear evidence for these excited configurations was found inside the transparency region of the glasses.

To summarize this section: We defined \mathbf{H}_0 in equation (1.3) as a zeroth order approximation to the exact Hamiltonian \mathbf{H} of an ion with N electrons. The next section will show how all differences of \mathbf{H} to \mathbf{H}_0 can be treated as perturbations. In zeroth order, the energy levels of all states of a configuration are completely degenerated and the appropriate eigenfunctions are given by the determinantal product states in equation (1.5). Their angular part is completely defined by specification of the quantum numbers l , m_l , and m_s of all electrons,

whereas the radial part is unknown, as it depends on the unknown potential $U(r)$, but the radial function is the same for all states of a given configuration.

1.3 Perturbation theory

The zeroth order Hamiltonian \mathbf{H}_0 we used in the last section will need a couple of corrections \mathbf{H}_k ($k > 0$) to approach the real Hamiltonian

$$\mathbf{H} = \mathbf{H}_0 + \mathbf{W} \quad (1.8)$$

of a rare earth ion, with $\mathbf{W} = \sum_{k>0} \mathbf{H}_k$. An example, and indeed the most important one, are the remaining electrostatic interactions from the last section given by $\mathbf{H}_1 = \mathbf{H}' - \mathbf{H}_0$, whereas increasing values of k are usually used to reflect a decreasing magnitude of \mathbf{H}_k . As long as the matrix elements of \mathbf{W} are small compared with \mathbf{H}_0 the time-independent perturbation theory may be used to calculate the influence of \mathbf{W} on the energy level spectrum. In this section we will recall the perturbation theory with the equations needed in the following parts of this work.

Let us start with an eigenstate $|\varphi^c\rangle$ of \mathbf{H}_0 with the non-degenerated eigenvalue $E_0^c = \langle \varphi^c | \mathbf{H}_0 | \varphi^c \rangle$ in configuration c . The corrected eigenvalue E^c taking into account first and second order corrections is then given by the well-known equation [12]

$$E^c = E_0^c + \langle \varphi^c | \mathbf{W} | \varphi^c \rangle + \sum_{\substack{p,k \\ p \neq c}} \frac{|\langle \varphi_k^p | \mathbf{W} | \varphi^c \rangle|^2}{E_0^c - E_0^p}, \quad (1.9)$$

where k is an index labeling the eigenstates $|\varphi_k^p\rangle$ of the possibly degenerated eigenvalue E_0^p of \mathbf{H}_0 . It is important that equation (1.9), besides the perturbation operator \mathbf{W} , contains only eigenstates and eigenvalues of the zeroth order Hamiltonian \mathbf{H}_0 , which is our result from the last section. But we found that our \mathbf{H}_0 is completely degenerated inside a given electron configuration, and therefore equation (1.9) needs some modifications. The following generalization fits our needs:

$$E^c(i, j) = E_0^c \delta_{ij} + \langle \Psi_i^c | \mathbf{W} | \Psi_j^c \rangle + \sum_{\substack{p,k \\ p \neq c}} \frac{\langle \Psi_i^c | \mathbf{W} | \Psi_k^p \rangle \langle \Psi_k^p | \mathbf{W} | \Psi_j^c \rangle}{E_0^c - E_0^p}, \quad (1.10)$$

where $|\Psi_i^c\rangle$ is now a general state, for example a determinantal product state as defined in the last section, and E_0^c the degenerated eigenvalue of \mathbf{H}_0 in configuration c . Instead of a single energy as in equation (1.9), we get a matrix in the full state space of each configuration. In order to calculate the energy level spectrum one has to diagonalize all energy matrices $E^c(i, j)$ of interest, in our case only the matrix of the ground configuration $c = 4f^N$.

The three terms in equation (1.10) have an obvious physical meaning. The first term is the center of mass energy of configuration c . This energy is not of interest here, as we will

stay inside the ground configuration and therefore, from here on, we set E_0^c to zero for the sake of convenience. The second term is describing interactions inside configuration c , which will be discussed in detail in section 1.5. More complicated is the third term, which takes into account the interaction of configuration c with all other configurations p . Interactions of this type will be treated in section 1.6. We will see there that effective operators \mathbf{H}'_k can be found so that

$$\mathbf{H}'_k = \mathbf{H}_k \left(\sum_{\substack{p,k \\ p \neq n}} \frac{|\Psi_k^p\rangle \langle \Psi_k^p|}{E_0^c - E_0^p} \right) \mathbf{H}_k . \quad (1.11)$$

Instead of the prime in \mathbf{H}'_k , the inter-configuration interactions usually just get indices k different from their intra-configuration counterparts. Therefore, both types of interactions can be handled in the same way in numerical calculations, and equation (1.10) is reduced to

$$E^c(i, j) = \sum_k \langle \Psi_i^c | \mathbf{H}_k | \Psi_j^c \rangle . \quad (1.12)$$

The matrix elements of \mathbf{H}_k in equation (1.12) may be calculated from the determinantal product states as eigenstates of \mathbf{H}_0 given by equation (1.5), but these eigenstates still depend on the unknown potential $U(r)$. However, all of our perturbation operators will be rotational invariant and therefore it is possible to separate them into a product of two orthogonal operators, acting on the radial coordinates and the angular coordinates respectively $\mathbf{H}_k = \mathbf{H}_{k,r} \mathbf{H}_{k,\Omega}$. This allows us to express all matrix elements as products of a radial and an angular part. The radial part is a constant number (radial integral) inside a given configuration, as $\mathbf{H}_{k,r}$ depends only on the quantum numbers n and l and neither m_l nor m_s . Furthermore, it is this number which contains the full $U(r)$ -dependence of the matrix element. The general radial integral is

$$\langle \Psi_i^c | \mathbf{H}_{k,r} | \Psi_j^c \rangle = \int \cdots \int R_{nl}^N \mathbf{H}_{k,r} R_{nl}^N dr_1 \cdots dr_N \quad \text{for all } i \text{ and } j, \quad (1.13)$$

but as we will see in chapter 3, this N -fold integral actually reduces to an m -fold integral for \mathbf{H}_k being an m -body operator.

The problem to find the best potential $U(r)$ for the zeroth order approximation \mathbf{H}_0 and to calculate the radial integrals ab initio is usually very difficult. There are several step-by-step methods as, for example, the Hartree-Fock method to find a self-consistent solution. But such calculations are of limited value here, since the results are still approximations and besides, as we can never take into account all possible interaction operators, the angular part is not exact either. Therefore a fit to a measured energy spectrum is necessary anyway and the radial integrals themselves are normally used as fit parameters

$$X^k = \langle \Psi_i^c | \mathbf{H}_{k,r} | \Psi_j^c \rangle \quad \text{for all } i \text{ and } j \quad (1.14)$$

in a semiempirical fitting procedure. This treatment has the nice side effect that it automatically includes some higher order corrections. This happens due to the fact that it is not

unusual that perturbation operators of different interactions show the same angular dependence. The investigations of this “screening” effect have their roots in [16], and an up-to-date overview is found in [17]. If we set $x_k(i, j) = \langle \Psi_i^c | \mathbf{H}_{k, \Omega} | \Psi_j^c \rangle$, all energy levels of the configuration nl^N are found by diagonalizing a matrix given by the simple equation

$$E = \sum_k X^k x_k . \quad (1.15)$$

Because the matrix x_k depends only on the electron configuration and not on the host material, it must be calculated only once and may then be stored for further usage in the fitting loop. In the fitting loop, those values X^k are searched which fit a measured spectrum of energy levels best. This nonlinear fit leads, under certain conditions, to very large unrealistic values X^k , which are carefully balanced to cancel out each other. Direct calculations of the radial integrals may then serve as tests, whether the order of magnitude of the fit values is correct, or not.

1.4 Classification of states

On the way to break the general problem of the energy level calculation for rare earth ions down to smaller and even smaller pieces, we are now at a point where we have to make the important decision how to calculate the matrices x_k . They are completely defined, as we know the determinantal product states from equation (1.5), but because all states of a given configuration have the same eigenvalue E_c^0 from equation (1.7), all linear combinations of the determinantal product states must produce the same results. In other words: we are free to choose a coupling scheme which makes the calculations most simple.

The traditional treatment is based on the work of Racah [10]. He used Russell-Saunders coupling (also called LS -coupling) as a starting point. In this coupling scheme all orbital angular momenta \mathbf{l}_i are summed up to a total orbital angular momentum \mathbf{L} and all spins \mathbf{s}_i to a total spin \mathbf{S} , with the respective quantum numbers L and S . But in d^N and f^N configurations many of the states have the same pair of these quantum numbers. Racah therefore further classified the states by their properties under certain groups of symmetry transformations. The formal description of how a state transforms under the operations of a symmetry group is given by their irreducible representations, which act as quantum numbers here. For details of the group-theoretical methods see [7].

The classification scheme of Racah for l^N configurations consists of a chain of groups in which each group is a subgroup of all preceding ones as shown in table 1.2. We are interested here in the third chain for the f^N configuration, in which U_7 is the group of unitary transformations in the 7-dimensional space spanned by the orbital angular momentum of a f-electron: $m_l = -3, -2, -1, 0, +1, +2, +3$. The irreducible representation $[\lambda_1 \dots \lambda_7]$ of U_7 is equivalent to the specification of the quantum number S of the total spin. The next group R_7 is the group of rotations in seven dimensions with the irreducible representations $W = (w_1 w_2 w_3)$, where $2 \geq w_1 \geq w_2 \geq w_3 \geq 0$ and the group G_2 is a special group in

Table 1.2: Chains of symmetry groups for the classification of Racah for p^N -, d^N -, and f^N -states

l	groups	irreducible representations
1	$U_3 \supset R_3$	S, L
2	$U_5 \supset R_5 \supset R_3$	$S, W = (w_1 w_2), L$
3	$U_7 \supset R_7 \supset G_2 \supset R_3$	$S, W = (w_1 w_2 w_3), U = (u_1 u_2), L$

two dimensions with the irreducible representations $U = (u_1 u_2)$, where $2 \geq u_1 \geq u_2 \geq 0$. The final rotational group R_3 in three dimensions has an irreducible representation which is equivalent to the specification of quantum number L of the total orbital angular momentum. Unfortunately, in the configurations $f^5 - f^9$ some pairs of LS -states still remain unseparated and therefore an additional integer τ is introduced ad-hoc as a label.

For a full description of an LS -state, either the quantum numbers M_L and M_S of the z-components of \mathbf{L} and \mathbf{S} may be given, or the quantum numbers of the total angular momentum $\mathbf{J} = \mathbf{L} + \mathbf{S}$ and its z-component, J and M_J . The complete specification of a state is therefore

$$|f^N, \tau WUSLJM_J\rangle \quad \text{or} \quad |f^N, \tau WUSM_SLM_L\rangle, \quad (1.16)$$

whereas a determinantal product state is written as

$$|f^N, \{(m_l m_s)_1 (m_l m_s)_2 \dots (m_l m_s)_N\}\rangle. \quad (1.17)$$

In general, the physical states of the rare earth ions are neither pure LS -states nor determinantal product states. If the unitary matrix U diagonalizes the matrix E from equation (1.15), i.e. $U^T E U$ is diagonal, the columns of U contain the coefficients for the linear combination of base states which build the eigenstate of each energy level.

In our special case of rare earth ions in glasses we do not take into account interactions with neighbor atoms (crystal field interactions), as the individual Stark components of the absorption lines (see section 1.1) cannot be resolved anyway. Therefore we have a rotational invariant free-ion system and all interaction operators must be scalar operators. As a direct result from the Wigner-Eckart theorem (A.5), all matrix elements of scalar operators are diagonal in J and independent of M_J . Therefore J is a “good” quantum number and all states are $(2J + 1)$ -fold degenerated. The general state corresponding to energy level i is given by the so-called intermediate coupling

$$|f^N, \gamma_i J\rangle = \sum_j v_{ij} |f^N, (\tau WUSL)_j J\rangle. \quad (1.18)$$

The usual labeling scheme for electronic rare earth states is $^{2S+1}L_J$, i.e. the same nomenclature as for LS -terms. Since the rare earth states are in general mixed LS -states, normally

the dominating LS -component with the maximum value of $|v_{ij}|$ in equation (1.18) is used for the choice of L and S in the state label. States with the same S , L , and J numbers but different values of τ , W , or U are distinguished by an extra number. Nevertheless sometimes some higher energy levels share exactly the same dominating LS -component, in which case the label is also the same. Unfortunately, there is another labeling scheme in use, which takes the values of L and S from the LS -states which the appropriate rare earth states approach in the limit of a vanishing spin-orbit coupling. Both labeling schemes lead to the same labels in most cases at least for the lower lying energy levels, except for thulium, where the states 3H_4 and 3F_4 are exchanged. In general the labeling by LS -states is not really useful for higher energy levels which do not have dominating LS -components as the actual label then depends on the host material and details of the fitting procedure being used.

The main reasons for choosing the LS -classification scheme of Racah are, on the one hand, that the lowest energy levels of the rare earth ions are indeed often almost pure LS -states and, on the other hand, that the interaction operators \mathbf{H}_k may also be classified under the chain of symmetry groups from table 1.2. The latter reduces the interaction matrices to subspaces which can be diagonalized separately. For a theory developed in the 40's of the 20th century this is very important, as without powerful computers the diagonalization of large matrices was practically impossible. Furthermore, physicists always like symmetry classifications, as they give them insights into more basic laws.

The drawback of Racah's classification scheme is that the construction of states is much more difficult than for determinantal product states. He used the fractional parentage coefficients (cfp) as an elegant tool to construct the states of configuration $4f^N$ from the states of configuration $4f^{N-1}$ [10]. If just an $(N-1)$ -electron state and a one-electron state are multiplied, the result is obviously an eigenstate of \mathbf{H}_0 , but it is not antisymmetric, similar to the simple product states in section 1.2. To get correct antisymmetrized states, one has to build linear combinations of the product states again and the appropriate coefficients, apart from some factors, are the mentioned cfp's. Calculation of the cfp's as explained in detail in [7] is cumbersome, but it must be carried out only once and the result may then be tabulated. The most famous and complete collection is contained in a book from Nielson and Koster [18].

Nowadays even cheap desktop computers are much faster than supercomputers in the time when the theory of rare earth spectra was developed, and therefore it is not necessary any more to calculate the energy matrices in the LS -coupling. Together with the article [19], a program based on the B.Sc. thesis [20] was published to calculate the energy level system for a given l^N configuration and given radial integrals.

As we will see, we cannot entirely avoid the calculation of the cfp's in the end, nevertheless it was decided for this work to use also determinantal product states for matrix calculations, but we go far beyond [19]. All energy matrices in this work will be given in a form reduced to just two unit tensor operators, one acting in the orbital space and one in the spin space. Furthermore, we use the most complete set of six interaction operator types as published until now instead of only four sets in [19]. The computer program developed for this work

is able not only to calculate energy level systems, but also to fit the values of the radial integrals to given spectra, which needs completely different strategies to optimize the speed for recalculation of energy matrices in the fitting loop.

An important side effect when choosing plain determinantal product states as in [19] instead of the usual LS -states is that the labels of the calculated energy levels are not compatible to the literature any more. That is obviously a major deficiency, because of which the computer program used here was designed to be able to transform all matrices from the determinantal product state classification to the LS scheme by a unitary transformation which will be explained in section 3.3. It seems at first sight that nothing is gained now, because the calculation of this transformation matrix of course is more or less equivalent to a calculation of the cfp's, but the program does not calculate the cfp's explicitly and it uses a calculation method different from [7]. Besides the compatibility issue, another advantage results from using this back-transformation to the LS -scheme: As already explained, in our case each energy level will be $(2J + 1)$ -fold degenerate, therefore it is sufficient to use only one of these J -states in the calculations, which leads to a substantial decrease of computing time.

1.5 First order interactions

As we already discussed in section 1.1, the energy level system of triply ionized lanthanides in glasses may be calculated from a free ion Hamiltonian. The crystal field in first order just leads to broader absorption and emission lines by splitting the Stark levels. In section 1.3 we discussed the splitting of the completely degenerated states from section 1.2 inside a configuration in zeroth order. We found that first order perturbations take place inside the configuration itself, whereas second order perturbations are due to interactions with all other configurations (configuration interactions). In both cases two types of interactions are usually distinguished, which are called electrostatic and magnetic. The former are Coulomb interactions by electric charges and the latter are interactions by the angular momenta (orbital angular momentum and spin) of the electrons. Table 1.3 shows a collection of all free-ion interactions found in the literature, together with their radial integrals in configuration f^N .

Table 1.3: Free ion interaction operators and appropriate radial integrals in configuration f^N

	intra-configuration (1st order)	inter-configuration (2nd order)
electrostatic (Coulomb type)	$\mathbf{H}_1: F^2, F^4, F^6$	$\mathbf{H}_3: \alpha, \beta, \gamma$ $\mathbf{H}_4: T^2, T^3, T^4, T^6, T^7, T^8$
magnetic (spin-orbit type)	$\mathbf{H}_2: \zeta$ $\mathbf{H}_5: M^0, M^2, M^4$	$\mathbf{H}_6: P^2, P^4, P^6$

In this section we will develop the explicit expressions of the intra-configuration interactions, whereas the configuration interactions will be discussed in the following section.

Of the intra-configuration interactions, the largest one is the Coulomb interaction $\mathbf{H}_1 = \mathbf{H}' - \mathbf{H}_0$, already mentioned in section 1.3, with three radial parameters F^2 , F^4 , and F^6 in case of the configuration f^N . Taking \mathbf{H}_1 and the spin-orbit coupling \mathbf{H}_2 with its radial parameter ζ , one already gets roughly the structure of the energy level spectrum of the rare earth ions. All other interactions, including all inter-configuration interactions, only adjust the individual levels to fit reality somewhat better. The remaining intra-configuration interactions known from literature are the spin-spin interaction \mathbf{H}_{ss} and the spin-other-orbit interaction \mathbf{H}_{soo} , with the common radial parameters M^0 , M^2 , and M^4 . The appropriate perturbation Hamiltonian is named $\mathbf{H}_5 = \mathbf{H}_{ss} + \mathbf{H}_{soo}$.

Coulomb interaction. The Coulomb interaction $\mathbf{H}_1 = \mathbf{H}' - \mathbf{H}_0$ as calculated from equations (1.2) and (1.3) consists of two parts

$$\mathbf{H}_1 = \sum_i \left[-\frac{1}{4\pi\epsilon_0} \frac{Ze^2}{r_i} - U(r_i) \right] + \frac{1}{4\pi\epsilon_0} \sum_{i<j} \frac{e^2}{r_{ij}}. \quad (1.19)$$

Because the first term is purely radial and does not contain any interactions between the electrons, it causes an constant energy shift for all states of a given configuration. As long as we are only interested in the states of the ground configuration, we may ignore this term and write

$$\mathbf{H}'_1 = \frac{1}{4\pi\epsilon_0} \sum_{i<j} \frac{e^2}{r_{ij}}. \quad (1.20)$$

In order to transform this vector operator expression of the Coulomb interaction to a tensor operator equation, the inverse distance is expanded in terms of the spherical harmonics [17, 21]:

$$\frac{1}{r_{ij}} = \sum_{k=0}^{\infty} \frac{r_{<}^k}{r_{>}^{k+1}} \frac{4\pi}{2k+1} \sum_{q=-k}^k Y_q^{k*}(\theta_i, \phi_i) Y_q^k(\theta_j, \phi_j), \quad (1.21)$$

where $r_{<}$ is the smaller and $r_{>}$ the larger one of r_i and r_j . Inserting the definition of the element $c_q^{(k)} = \sqrt{4\pi/(2k+1)} Y_q^k$ of the tensor operator $\mathbf{c}^{(k)}$ from appendix A we get

$$\frac{1}{r_{ij}} = \sum_k \frac{r_{<}^k}{r_{>}^{k+1}} \sum_q (-1)^q (c_{-q}^{(k)})_i (c_q^{(k)})_j, \quad (1.22)$$

and as the sum over q in this equation is by definition a scalar product, the tensor operator expression of \mathbf{H}'_1 is given by [7, 17, 21]

$$\mathbf{H}'_1 = \frac{e^2}{4\pi\epsilon_0} \sum_k \sum_{i<j} \frac{r_{<}^k}{r_{>}^{k+1}} (\mathbf{c}_i^{(k)} \cdot \mathbf{c}_j^{(k)}). \quad (1.23)$$

The radial parameters F^k of the Coulomb interaction matrix $E'_1 = \sum_k F^k f_k$ are the Slater integrals defined by

$$F^k = \frac{e^2}{4\pi\epsilon_0} \iint \frac{r_{<}^k}{r_{>}^{k+1}} R_{nl}^2(r_i) R_{nl}^2(r_j) dr_i dr_j , \quad (1.24)$$

and the remaining angular operators \mathbf{f}_k with the matrix elements $f_k(i, j) = \langle \Psi_i | \mathbf{f}_k | \Psi_j \rangle$ are therefore

$$\mathbf{f}_k = \sum_{i < j} (\mathbf{c}_i^{(k)} \cdot \mathbf{c}_j^{(k)}) . \quad (1.25)$$

As long as we stay inside the configuration nl^N , the tensor $\mathbf{c}^{(k)}$ is proportional to $\mathbf{u}^{(k)}$, and we receive the final expression which is used for the calculations in this work as the angular part of the Coulomb interaction:

$$\mathbf{f}_k = \langle l || \mathbf{c}^{(k)} || l \rangle^2 \sum_{i < j} (\mathbf{u}_i^{(k)} \cdot \mathbf{u}_j^{(k)}) . \quad (1.26)$$

The 3-j symbol in the definition of $\langle l || \mathbf{c}^{(k)} || l \rangle$ (see appendix A) restricts k to even values from 0 to $2l$, but $k = 0$ is usually not of interest, since it results in a constant shift for all states inside a given configuration.

It can be shown that \mathbf{f}_k commutes with \mathbf{S}^2 , \mathbf{L}^2 , \mathbf{J} , and J_z . Furthermore it is diagonal in S and L and independent of J and M_J . The eigenstates of \mathbf{H}'_1 are therefore LS -terms.

Spin-orbit interaction. A second perturbation operator in the same order of magnitude as the Coulomb interaction comes from the relativistic Dirac equation. Assuming that the average speed of the electrons is much smaller than the speed of light, the spin-orbit interaction as the most important relativistic correction is given by the vector operator equation [7]

$$\mathbf{H}_2 = \frac{1}{2m_e^2 c^2} \sum_i (\mathbf{s}_i \cdot (\nabla_i U(r_i) \times \mathbf{p}_i)) , \quad (1.27)$$

where m_e is the electron mass, c the speed of light in vacuum and $\hbar = h/2\pi$ with Planck's constant h . Since $U(r)$ is a pure central potential, its gradient may be written as

$$\nabla U(r) = \frac{\mathbf{r}}{r} \frac{d}{dr} U(r) , \quad (1.28)$$

and the equation (1.27) becomes [7]

$$\mathbf{H}_2 = \frac{1}{2m_e^2 c^2} \sum_i \frac{1}{r_i} \frac{d}{dr_i} U(r_i) (\mathbf{s}_i \cdot \mathbf{l}_i) . \quad (1.29)$$

This equation can be transformed to a tensor operator expression quite easily if the correspondence between vector operators and tensor operators from appendix A is used, which keeps the scalar product

$$\mathbf{H}_2 = \frac{1}{2m_e^2 c^2} \sum_i \frac{1}{r_i} \frac{d}{dr_i} U(r_i) (\mathbf{s}^{(1)} \cdot \mathbf{l}^{(1)}) . \quad (1.30)$$

The radial parameter ζ of the spin-orbit interaction matrix $E_2 = \zeta z$ is defined by the equation

$$\zeta = \frac{\hbar^2}{2m_e^2 c^2} \int \frac{1}{r} \frac{d}{dr} U(r) R_{nl}^2(r) dr , \quad (1.31)$$

and the remaining angular operator \mathbf{z} with the matrix element $z(i, j) = \langle \Psi_i | \mathbf{z} | \Psi_j \rangle$ is

$$\mathbf{z} = \frac{1}{\hbar^2} \sum_i (\mathbf{s}^{(1)} \cdot \mathbf{l}^{(1)}) . \quad (1.32)$$

Since $\mathbf{s}^{(1)}$ and $\mathbf{l}^{(1)}$ are proportional to the unit tensor operators $\mathbf{t}^{(1)}$ and $\mathbf{u}^{(1)}$ respectively, this equation takes the following final form, which is used for the calculations in this work:

$$\mathbf{z} = \sqrt{3l(l+1)(2l+1)/2} \sum_i (\mathbf{t}^{(1)} \cdot \mathbf{u}^{(1)}) . \quad (1.33)$$

Spin-spin interaction. The remaining two interactions of an electron spin \mathbf{s}_i with the spin \mathbf{s}_j or the orbital momentum \mathbf{l}_j of another electron j are not as standard as the Coulomb and the spin-orbit interaction. There is much less literature about them, and they are often omitted in energy level calculations. A brief history of the investigation of the spin-spin interaction \mathbf{H}_{ss} and the spin-other-orbit interaction \mathbf{H}_{soo} is given by Goldschmidt in [17]. The publications found to be most useful for the investigations presented here are the following. Marvin gives in [22] the basic definitions and the radial integrals. It should be noted that his calculated results turned out to be incorrect for other cases than l^N (see [17]). Tensor-operator representations of \mathbf{H}_{ss} and \mathbf{H}_{soo} were calculated by Horie in [23], but the representations given by Judd [7] and Goldschmidt [17] seem to fit better in this work.

Systematic use of \mathbf{H}_{ss} and \mathbf{H}_{soo} in investigations of rare earth spectra starts with [24], which also gives both operators in a very compact form. It is almost exactly what we need here. Very helpful for testing the computer program were the calculated values of the angular matrix elements of the operators \mathbf{H}_{ss} and \mathbf{H}_{soo} given in [24] for the configuration f^2 and in [25] for the configuration f^{12} .

The vector operator expression of the spin-spin interaction is [7, 17]

$$\mathbf{H}_{ss} = \frac{1}{4\pi\epsilon_0} \frac{2\beta_m^2}{\hbar^2} \sum_{i \neq j} \left[\frac{(\mathbf{s}_i \cdot \mathbf{s}_i)}{r_{ij}^3} - \frac{3(\mathbf{r}_{ij} \cdot \mathbf{s}_i)(\mathbf{r}_{ij} \cdot \mathbf{s}_j)}{r_{ij}^5} \right] \quad (1.34)$$

with the Bohr magneton $\beta_m = e\hbar/2m_e c$. This equation may be transformed to a tensor operator form as shown in [7] and because of the symmetry of \mathbf{H}_{ss} in i and j , the sum needs to be carried out for $i < j$ only:

$$\mathbf{H}_{ss} = -\frac{1}{4\pi\epsilon_0} \frac{2\beta_m^2}{\sqrt{5}\hbar^2} \sum_k (-1)^k \sqrt{\frac{(2k+5)!}{(2k)!}} \sum_{i < j} \frac{r_{<}^k}{r_{>}^{k+3}} (\{\mathbf{c}_i^{(k)} \times \mathbf{c}_j^{(k+2)}\}^{(2)} \cdot \{\mathbf{s}_i^{(1)} \times \mathbf{s}_j^{(1)}\}^{(2)}) . \quad (1.35)$$

The radial parameters M^k of the spin-spin interaction matrix $E_{ss} = \sum_k M^k m_{k,ss}$ are integrals defined by Marvin in [22]. Inside a configuration nl^N these Marvin integrals are given by

$$M^k = \frac{1}{4\pi\epsilon_0} \frac{\beta_m^2}{2} \iint \frac{r_{<}^k}{r_{>}^{k+3}} R_{nl}^2(r_i) R_{nl}^2(r_j) dr_i dr_j , \quad (1.36)$$

and the remaining angular operators $\mathbf{m}_{k,ss}$ with the matrix elements $m_{k,ss}(i, j) = \langle \Psi_i | \mathbf{m}_{k,ss} | \Psi_j \rangle$ have the form

$$\mathbf{m}_{k,ss} = (-1)^{k+1} \frac{4}{\sqrt{5}\hbar^2} \sqrt{\frac{(2k+5)!}{(2k)!}} \sum_{i < j} (\{\mathbf{c}_i^{(k)} \times \mathbf{c}_j^{(k+2)}\}^{(2)} \cdot \{\mathbf{s}_i^{(1)} \times \mathbf{s}_j^{(1)}\}^{(2)}) . \quad (1.37)$$

Due to Judd [24], Hartree-Fock calculations give Marvin integrals for all rare earth ions with the approximate relations

$$M^2 = 0.56 M^0 \quad \text{and} \quad M^4 = 0.38 M^0 , \quad (1.38)$$

and therefore it became common practice to vary only M^0 in energy level calculations and fix the other two parameters to the given fractions. In general the influence of these integrals on the energy level fit is only moderate and therefore this assignment seems to be reasonable. For this reason it is used in the calculations of this work, too, although the computer program allows the variation of all three parameters.

As long as we stay inside the configuration nl^N , the operators $\mathbf{c}^{(k)}$ and $\mathbf{s}^{(1)}$ may be expressed in terms of the unit tensor operators $\mathbf{u}^{(k)}$ and $\mathbf{t}^{(1)}$ as given in the equations (A.22) and (A.24):

$$\begin{aligned} \mathbf{m}_{k,ss} = (-1)^{k+1} \frac{6}{\sqrt{5}} \sqrt{\frac{(2k+5)!}{(2k)!}} & \langle l || \mathbf{c}^{(k)} || l \rangle \langle l || \mathbf{c}^{(k+2)} || l \rangle \\ & \times \sum_{i < j} (\{\mathbf{u}_i^{(k)} \times \mathbf{u}_j^{(k+2)}\}^{(2)} \cdot \{\mathbf{t}_i^{(1)} \times \mathbf{t}_j^{(1)}\}^{(2)}) . \end{aligned} \quad (1.39)$$

The 3-j symbol in the definition of $\langle l || \mathbf{c}^{(k)} || l \rangle$ in equation (A.18) restricts k to even values from 0 up to $2l$ and, since $\langle l || \mathbf{c}^{(k+2)} || l \rangle$ arises in the above equation, actually up to $2l - 2$. Collecting all factors and expanding the factorials, we arrive at the equation which is used

for the calculations in this work:

$$\mathbf{m}_{k,ss} = -12\sqrt{(k+1)(k+2)(2k+1)(2k+3)(2k+5)/5} \\ \times \langle l||\mathbf{c}^{(k)}||l\rangle\langle l||\mathbf{c}^{(k+2)}||l\rangle \sum_{i<j} (\{\mathbf{u}_i^{(k)} \times \mathbf{u}_j^{(k+2)}\}^{(2)} \cdot \{\mathbf{t}_i^{(1)} \times \mathbf{t}_j^{(1)}\}^{(2)}) . \quad (1.40)$$

In order to compare this result with the representation given by Judd in [24], we first expand the scalar product to a tensor product by using equation (A.8):

$$\mathbf{m}_{k,ss} = -12\sqrt{(k+1)(k+2)(2k+1)(2k+3)(2k+5)} \\ \times \langle l||\mathbf{c}^{(k)}||l\rangle\langle l||\mathbf{c}^{(k+2)}||l\rangle \sum_{i<j} \{\{\mathbf{u}_i^{(k)} \times \mathbf{u}_j^{(k+2)}\}^{(2)} \times \{\mathbf{t}_i^{(1)} \times \mathbf{t}_j^{(1)}\}^{(2)}\}^{(0)} . \quad (1.41)$$

Dividing this equation by $3\sqrt{(2k+1)(2k+5)}$ in order to introduce the double tensor operator $\mathbf{w}^{(\kappa k)}$ from equation (A.37), and expanding the sum over i and j again, we get the angular part of equation (1) in [24]:

$$\mathbf{m}_{k,ss} = -2\sqrt{(k+1)(k+2)(2k+3)}\langle l||\mathbf{c}^{(k)}||l\rangle\langle l||\mathbf{c}^{(k+2)}||l\rangle \sum_{i \neq j} \{\mathbf{w}_i^{(1k)} \times \mathbf{w}_j^{(1k+2)}\}^{(22)0} . \quad (1.42)$$

In [24] all LS -matrix elements of $\mathbf{m}_{k,ss}$ in the configuration f^2 are printed and this table was used to test the computer program. The matrix elements in the configuration f^{12} were checked to be identical to f^2 [25].

Spin-other-orbit interaction. The interaction of the spin of one electron with the orbit of another electron is called spin-other-orbit interaction and its vector operator expression is [17]

$$\mathbf{H}_{soo} = \frac{1}{4\pi\epsilon_0} \frac{2\beta_m^2}{\hbar} \sum_{i \neq j} ([\nabla_i \frac{1}{r_{ij}} \times \mathbf{p}_i] \cdot [\mathbf{s}_i + 2\mathbf{s}_j]) . \quad (1.43)$$

This equation may be transformed to a lengthy tensor operator form given in [17], but if we stay inside the nl^N configuration, only the following terms do not vanish:

$$\mathbf{H}_{soo} = \frac{1}{4\pi\epsilon_0} \frac{\beta_m^2}{\sqrt{3}\hbar} \sum_k (-1)^k \sum_{i \neq j} ([\frac{r_{<}^{k-2}}{r_{>}^{k+1}} (2k+1) \sqrt{2k-1} \{\mathbf{c}_j^{(k)} \times \{\mathbf{c}_i^{(k)} \times \mathbf{l}_i^{(1)}\}^{(k-1)}\}^{(1)} \\ - \frac{r_{<}^k}{r_{>}^{k+3}} (2k+1) \sqrt{2k+3} \{\mathbf{c}_j^{(k)} \times \{\mathbf{c}_i^{(k)} \times \mathbf{l}_i^{(1)}\}^{(k+1)}\}^{(1)}] \cdot [\mathbf{s}_i^{(1)} + 2\mathbf{s}_j^{(1)}]) . \quad (1.44)$$

Substituting $k \rightarrow k+2$ in the first term of the sum over i and j yields

$$\mathbf{H}_{\text{soo}} = \frac{1}{4\pi\epsilon_0} \frac{\beta_m^2}{\sqrt{3}\hbar} \sum_k (-1)^k \sum_{i \neq j} \left(\left[\frac{r_{>}^k}{r_{<}^{k+3}} (2k+5) \sqrt{2k+3} \{ \mathbf{c}_j^{(k+2)} \times \{ \mathbf{c}_i^{(k+2)} \times \mathbf{l}_i^{(1)} \}^{(k+1)} \}^{(1)} \right. \right. \\ \left. \left. - \frac{r_{<}^k}{r_{>}^{k+3}} (2k+1) \sqrt{2k+3} \{ \mathbf{c}_j^{(k)} \times \{ \mathbf{c}_i^{(k)} \times \mathbf{l}_i^{(1)} \}^{(k+1)} \}^{(1)} \right] \cdot [\mathbf{s}_i^{(1)} + 2\mathbf{s}_j^{(1)}] \right) . \quad (1.45)$$

This makes clear that the radial part of this operator is the same as in \mathbf{H}_{ss} . Therefore the Marvin integrals are introduced by defining the spin-other-orbit interaction matrix in the form $E_{\text{soo}} = \sum_k M^k m_{k,\text{soo}}$. The remaining angular operators $\mathbf{m}_{k,\text{soo}}$ with the matrix elements $m_{k,\text{soo}}(i, j) = \langle \Psi_i | \mathbf{m}_{k,\text{soo}} | \Psi_j \rangle$ are then

$$\mathbf{m}_{k,\text{soo}} = 2 \frac{(-1)^k}{\hbar} \sqrt{\frac{2k+3}{3}} \sum_{i \neq j} \left(\left[(2k+5) \{ \mathbf{c}_j^{(k+2)} \times \{ \mathbf{c}_i^{(k+2)} \times \mathbf{l}_i^{(1)} \}^{(k+1)} \}^{(1)} \right. \right. \\ \left. \left. - (2k+1) \{ \mathbf{c}_j^{(k)} \times \{ \mathbf{c}_i^{(k)} \times \mathbf{l}_i^{(1)} \}^{(k+1)} \}^{(1)} \right] \cdot [\mathbf{s}_i^{(1)} + 2\mathbf{s}_j^{(1)}] \right) . \quad (1.46)$$

As we stay inside the configuration nl^N , the operators $\mathbf{c}^{(k)}$, $\mathbf{l}^{(1)}$, and $\mathbf{s}^{(1)}$ may be expressed by the equations (A.22) to (A.24) in terms of the unit tensor operators $\mathbf{u}^{(k)}$, $\mathbf{u}^{(1)}$, and $\mathbf{t}^{(1)}$ respectively

$$\mathbf{m}_{k,\text{soo}} = 2 (-1)^k \sqrt{\frac{2k+3}{3}} \sqrt{l(l+1)(2l+1)} \sqrt{3/2} \\ \times \sum_{i \neq j} \left(\left[(2k+5) \langle l || \mathbf{c}^{(k+2)} || l \rangle^2 \{ \mathbf{u}_j^{(k+2)} \times \{ \mathbf{u}_i^{(k+2)} \times \mathbf{u}_i^{(1)} \}^{(k+1)} \}^{(1)} \right. \right. \\ \left. \left. - (2k+1) \langle l || \mathbf{c}^{(k)} || l \rangle^2 \{ \mathbf{u}_j^{(k)} \times \{ \mathbf{u}_i^{(k)} \times \mathbf{u}_i^{(1)} \}^{(k+1)} \}^{(1)} \right] \cdot [\mathbf{t}_i^{(1)} + 2\mathbf{t}_j^{(1)}] \right) , \quad (1.47)$$

where again, as for the operator \mathbf{H}_{ss} , the 3-j symbol in the definition of $\langle l || \mathbf{c}^{(k)} || l \rangle$ in equation (A.18) restricts k to even values from 0 up to $2l-2$. Furthermore, the tensor product of two unit tensors of electron i may be reduced due to the equations (A.28) and (A.30), which leads to

$$\mathbf{m}_{k,\text{soo}} = -\sqrt{\frac{2k+3}{2}} \\ \times \sum_{i \neq j} \left(\left[(2k+5) \langle l || \mathbf{c}^{(k+2)} || l \rangle^2 \sqrt{\frac{(2l+k+3)(2l-k-1)(k+2)}{2k+5}} \{ \mathbf{u}_i^{(k+1)} \times \mathbf{u}_j^{(k+2)} \}^{(1)} \right. \right. \\ \left. \left. + (2k+1) \langle l || \mathbf{c}^{(k)} || l \rangle^2 \sqrt{\frac{(2l+k+2)(2l-k)(k+1)}{2k+1}} \{ \mathbf{u}_i^{(k+1)} \times \mathbf{u}_j^{(k)} \}^{(1)} \right] \cdot [\mathbf{t}_i^{(1)} + 2\mathbf{t}_j^{(1)}] \right) . \quad (1.48)$$

Finally, we evaluate the scalar product, introduce some factors $\sqrt{2}\mathbf{t}^{(0)}$ and change the order of the terms in the sum over i and j . (Thanks to B. R. Judd for his remarks on the

factor $\sqrt{2}$, which is necessary due to $\langle m_s | t_0^{(0)} | m'_s \rangle = \sqrt{1/2}$. That gives us the form of the angular part of \mathbf{H}_{soo} , as it is used for the calculations in this work:

$$\begin{aligned} \mathbf{m}_{k,\text{soo}} = & -\sqrt{2k+3} \sum_{i \neq j} \left[\langle l | \mathbf{c}^{(k)} | l \rangle^2 \sqrt{(2l+k+2)(2l-k)(k+1)(2k+1)} \right. \\ & \times [(\{\mathbf{u}_i^{(k+1)} \times \mathbf{u}_j^{(k)}\}^{(1)} \cdot \{\mathbf{t}_i^{(1)} \times \mathbf{t}_j^{(0)}\}^{(1)}) + 2(\{\mathbf{u}_i^{(k+1)} \times \mathbf{u}_j^{(k)}\}^{(1)} \cdot \{\mathbf{t}_i^{(0)} \times \mathbf{t}_j^{(1)}\}^{(1)})] \\ & + \langle l | \mathbf{c}^{(k+2)} | l \rangle^2 \sqrt{(2l+k+3)(2l-k-1)(k+2)(2k+5)} \\ & \left. \times [(\{\mathbf{u}_i^{(k+1)} \times \mathbf{u}_j^{(k+2)}\}^{(1)} \cdot \{\mathbf{t}_i^{(1)} \times \mathbf{t}_j^{(0)}\}^{(1)}) + 2(\{\mathbf{u}_i^{(k+1)} \times \mathbf{u}_j^{(k+2)}\}^{(1)} \cdot \{\mathbf{t}_i^{(0)} \times \mathbf{t}_j^{(1)}\}^{(1)})] \right]. \quad (1.49) \end{aligned}$$

In order to compare this result with the representation given by Judd in [24], we first expand the scalar products to tensor products by using equation (A.8):

$$\begin{aligned} \mathbf{m}_{k,\text{soo}} = & \sqrt{3(2k+3)} \sum_{i \neq j} \left[\langle l | \mathbf{c}^{(k)} | l \rangle^2 \sqrt{(2l+k+2)(2l-k)(k+1)(2k+1)} \right. \\ & \times [\{\{\mathbf{u}_i^{(k+1)} \times \mathbf{u}_j^{(k)}\}^{(1)} \times \{\mathbf{t}_i^{(1)} \times \mathbf{t}_j^{(0)}\}^{(1)}\}^{(0)} + 2\{\{\mathbf{u}_i^{(k+1)} \times \mathbf{u}_j^{(k)}\}^{(1)} \times \{\mathbf{t}_i^{(0)} \times \mathbf{t}_j^{(1)}\}^{(1)}\}^{(0)}] \\ & + \langle l | \mathbf{c}^{(k+2)} | l \rangle^2 \sqrt{(2l+k+3)(2l-k-1)(k+2)(2k+5)} \\ & \left. \times [\{\{\mathbf{u}_i^{(k+1)} \times \mathbf{u}_j^{(k+2)}\}^{(1)} \times \{\mathbf{t}_i^{(1)} \times \mathbf{t}_j^{(0)}\}^{(1)}\}^{(0)} + 2\{\{\mathbf{u}_i^{(k+1)} \times \mathbf{u}_j^{(k+2)}\}^{(1)} \times \{\mathbf{t}_i^{(0)} \times \mathbf{t}_j^{(1)}\}^{(1)}\}^{(0)}] \right]. \quad (1.50) \end{aligned}$$

The division of the first summand in the sum over i and j by $\sqrt{3(2k+1)(2k+3)}$ and the second by $\sqrt{3(2k+3)(2k+5)}$ in order to introduce the double tensor operator $\mathbf{w}^{(\kappa k)}$ from equation (A.37) results in the angular part of equation (2) in [24]:

$$\begin{aligned} \mathbf{m}_{k,\text{soo}} = & \sum_{i \neq j} \left[\langle l | \mathbf{c}^{(k)} | l \rangle^2 \sqrt{(2l+k+2)(2l-k)(k+1)} \right. \\ & \times [\{\mathbf{w}_i^{(1\ k+1)} \times \mathbf{w}_j^{(0\ k)}\}^{(11)0} + 2\{\mathbf{w}_i^{(0\ k+1)} \times \mathbf{w}_j^{(1\ k)}\}^{(11)0}] \\ & + \langle l | \mathbf{c}^{(k+2)} | l \rangle^2 \sqrt{(2l+k+3)(2l-k-1)(k+2)} \\ & \left. \times [\{\mathbf{w}_i^{(1\ k+1)} \times \mathbf{w}_j^{(0\ k+2)}\}^{(11)0} + 2\{\mathbf{w}_i^{(0\ k+1)} \times \mathbf{w}_j^{(1\ k+2)}\}^{(11)0}] \right]. \quad (1.51) \end{aligned}$$

In the same paper [24] a table of all LS -matrix elements of $\mathbf{m}_{k,\text{soo}}$ in the configuration f^2 has been published, which was used to test the results of the computer program. A similar table for the configuration f^{12} can be found in [25] and was used to check the computer program, too.

Table 1.4: All types of interactions which may interact with configuration l^N

(a)	$l'^{4l'+1}l^{N+1}$
(b)	$l'^{4l'+1}l^Nl''$
(c)	$l^{N-1}l'$
(d)	$l'^{4l'}l^{N+2}$ and $l'^{4l'+1}l''^{4l''+1}l^{N+2}$
(e)	$l^{N-2}l'^2$ and $l^{N-2}l'l''$.
(f)	$l'^{4l'}l^{N+1}l''$ and $l'^{4l'+1}l''^{4l''+1}l^{N+1}l''$
(g)	$l'^{4l'}l^Nl''^2$, $l'^{4l'+1}l''^{4l''+1}l^Nl''^2$, $l'^{4l'}l^Nl''l'''$, and $l'^{4l'+1}l''^{4l''+1}l^Nl''l'''$
(h)	$l'^{4l'+1}l^{N-1}l''^2$ and $l'^{4l'+1}l^{N-1}l''l'''$

1.6 Configuration interactions

As we found in section 1.3, the perturbation operators to correct the Hamiltonian in second order have their origin in interactions of the electronic configuration of interest with all other configurations. It stands to reason that it is impossible to calculate the sum in the last term of equation (1.10) without simplifications because of the high number of interaction states k in all the configurations p .

First of all we shall try to collect all the excited configurations which are indeed able to interact with the ground configuration nl^N . Since physical interactions always connect exactly two partners, in this case either two electrons or two properties of a single electron, non-vanishing matrix elements can only exist for excited configurations which differ from nl^N in the quantum numbers n or l of one or two electrons. Furthermore, the parity of the excited configuration must be the same as for nl^N , as the Hamiltonian is a scalar operator not affecting the parity. We will use the symbols l' , l'' , and l''' for electrons with either a quantum number n or l different from the electrons in the configuration nl^N and keep in mind that all the shells different from nl which contain electrons are full core shells in our case and therefore contain $4l + 2$ electrons. It is an easy task to verify that table 1.4 contains all configurations which are able to interact with nl^N .

The configurations (a)–(c) are single electron excitations, whereas the configurations (d)–(h) are reached by exciting two electrons, either from the closed core or from the nl -shell. The configurations (a)–(e) are discussed in detail by several authors [17, 26, 27], whereas (f) and (g) are said to be not of interest, because they result only in a shift of the whole energy level spectrum of configuration nl^N [26]. Unfortunately, no remark about the configurations (h) was found in the literature, but a short symbolic analysis by B. G. Judd showed that the interaction with this type of configuration also only shifts the center of mass energy of the configuration [28].

In the next step, typical matrix elements $\langle \Psi_i^c | \mathbf{H}_k | \Psi_k^p \rangle$ must be calculated with p being one of the above configurations. After inserting these matrix elements into the last term of

Table 1.5: Terms of the matrix E_3 for the two-body operators of the Coulomb configuration interaction

l	E_3
1	$\alpha L(L+1)$
2	$\alpha L(L+1) + \beta G(R_5)$
3	$\alpha L(L+1) + \beta G(G_2) + \gamma G(R_7)$

equation (1.10), an effective operator is looked for which acts inside the configuration nl^N only, instead of the full configuration space, and has the same matrix elements. The presentation of these calculations is beyond the scope of this work, in the next paragraphs we will just give the results. The formal expression for an effective operator has already been given in equation (1.11).

Coulomb configuration interaction. Since the Coulomb interaction is the largest part of the intra-configuration interactions, we expect the same to be the case here. It was found by Trees [29] that the introduction of an effective two-body operator proportional to \mathbf{L}^2 improved the accuracy of the calculated energy level spectrum for d^N configurations [29, 30, 31, 32]. A systematic investigation of the configurations (a)–(e) in table 1.4 was later done by Rajnak and Wybourne [26]. They inserted the operator \mathbf{H}'_1 into the last term of equation (1.10) and confirmed the results of Trees. But they also showed that, besides the two-body operators, some effective three-body operators are needed. Furthermore, for all configurations the full effective operator contains terms with the same angular dependence as the intra-configuration Coulomb interaction, thus “screening” the Slater integrals F^k . The appropriate two-body operators can be omitted in our semiempirical treatment since the fitting procedure automatically includes the change in the F^k ’s.

There are l two-body operators remaining and their sum is named \mathbf{H}_3 . The terms of the matrix E_3 of this operator are shown in table 1.5. The radial parameters are named α , β , and γ . $L(L+1)$ is the matrix of the angular operator \mathbf{L}^2/\hbar^2 and $G(S)$ the matrix of Casimir’s operator $\mathbf{G}(S)$ of the symmetry group S . If we take into account that \mathbf{L}^2 is proportional to Casimir’s operator $\mathbf{G}(R_3)$, it is obvious that the operators are reflecting the chain of symmetry groups from table 1.2.

For our energy level calculations we need the tensor operator expressions of the angular operators of all terms of \mathbf{H}_3 . With the use of the unit tensor operator of an N -electron system in the orbital space $\mathbf{U}^{(k)} = \sum_i \mathbf{u}^{(k)}$, the operator \mathbf{L}^2 is written as

$$(\mathbf{L}^{(1)} \cdot \mathbf{L}^{(1)}) = l(l+1)(2l+1)\hbar^2 (\mathbf{U}^{(1)} \cdot \mathbf{U}^{(1)}) . \quad (1.52)$$

Inserting the definition of $\mathbf{U}^{(1)}$ yields the equation which is used for the calculations in

this work (see also appendix A.3):

$$(\mathbf{L}^{(1)} \cdot \mathbf{L}^{(1)}) = l(l+1)(2l+1) \hbar^2 \left[\sum_i (\mathbf{u}_i^{(1)} \cdot \mathbf{u}_i^{(1)}) + 2 \sum_{i<j} (\mathbf{u}_i^{(1)} \cdot \mathbf{u}_j^{(1)}) \right]. \quad (1.53)$$

The first term in this equation is a one-body operator which could have been neglected as it just causes a shift of the energy level spectrum of the whole configuration. Nevertheless it was included in the calculations to enable us to calculate the quantum number L of all states in a straightforward way by diagonalizing the state matrix of this operator. This is necessary for example if the transformation matrix from the determinantal product states to Racah's classification scheme is calculated as described in section 3.3.

The next angular operator needed is Casimir's operator of the rotational group in d dimensions [7]:

$$\mathbf{G}(\mathbf{R}_d) = \frac{1}{d-2} \sum_{\substack{k=1 \\ k \text{ odd}}}^{d-2} (2k+1) (\mathbf{U}^{(k)} \cdot \mathbf{U}^{(k)}). \quad (1.54)$$

Inserting the definition of $\mathbf{U}^{(k)}$, we get the expression of this operator, which is used for the calculations in this work:

$$\mathbf{G}(\mathbf{R}_d) = \frac{1}{d-2} \sum_{\substack{k=1 \\ k \text{ odd}}}^{d-2} (2k+1) \left[\sum_i (\mathbf{u}_i^{(k)} \cdot \mathbf{u}_i^{(k)}) + 2 \sum_{i<j} (\mathbf{u}_i^{(k)} \cdot \mathbf{u}_j^{(k)}) \right]. \quad (1.55)$$

Again, the one-body term could have been neglected, but it was kept for the same reasons as in the case of the operator \mathbf{L}^2 .

The last operator is Casimir's operator of the special group G_2 [7]:

$$\mathbf{G}(G_2) = \frac{1}{4} \left[3(\mathbf{U}^{(1)} \cdot \mathbf{U}^{(1)}) + 11(\mathbf{U}^{(5)} \cdot \mathbf{U}^{(5)}) \right]. \quad (1.56)$$

If we again insert the definition of $\mathbf{U}^{(k)}$, we get the equation which is used for the calculations in this work, including the one-body term:

$$\mathbf{G}(G_2) = \frac{1}{4} \left[\sum_i (3(\mathbf{u}_i^{(1)} \cdot \mathbf{u}_i^{(1)}) + 11(\mathbf{u}_i^{(5)} \cdot \mathbf{u}_i^{(5)})) + 2 \sum_{i<j} (3(\mathbf{u}_i^{(1)} \cdot \mathbf{u}_j^{(1)}) + 11(\mathbf{u}_i^{(5)} \cdot \mathbf{u}_j^{(5)})) \right]. \quad (1.57)$$

The effective three-body operators arise from interactions with configurations of the types (a) and (c) in table 1.4. They are all proportional to operators $\mathbf{U}(kk'k'')$ containing a triple

Table 1.6: Possible values for the triplet $(kk'k'')$ in the three-body operators for the Coulomb configuration interaction

l	$(kk'k'')$
1	(222)
2	(222)(224)(244)(444)
3	(222)(224)(244)(246)(266)(444)(446)(466)(666)

scalar product, the definition of which is given in equation (A.9):

$$\mathbf{U}(kk'k'') = \sum_{h \neq i \neq j} (\mathbf{u}_h^{(k)} \cdot \mathbf{u}_i^{(k')} \cdot \mathbf{u}_j^{(k'')}) . \quad (1.58)$$

As usual, k , k' , and k'' are in general even integers in the range of zero up to $2l$, but zero must actually be excluded because such operators would be no three-body operators any more. Since all three unit tensor operators in equation (1.58) act on different electrons, they all commute and the order of the elements in the triplet $(kk'k'')$ is of no importance. It is a simple task therefore to show that table 1.6 contains all possible triplets. It should be noted that the triplet (226) is not possible for f^N configurations because it does not satisfy the triangle condition (each number is at least the absolute of the difference and at most the sum of the other two numbers) and therefore the 3-j symbol in the definition of the triple scalar product vanishes.

Feneuille [33] and Judd [34, 35] built linear combinations of the possible three-body operators in the d^N and f^N configuration respectively, which correspond to certain irreducible representations of the symmetry groups R_5 for d^N and R_7 and G_2 for f^N . It was found that some of the resulting operators actually were proportional to linear combinations of intra-configuration Coulomb operators or vanishing. For d^N configurations only two of four and for f^N configurations only six of nine three-body operators are linearly independent from the first order operators.

The energy matrix calculated from the three-body operators of Judd is $E_4 = \sum_c T^c t_c$ with the six radial parameters T^2 , T^3 , T^4 , T^6 , T^7 , and T^8 . The appropriate angular operators \mathbf{t}_c , with the matrix elements $t_c(i, j) = \langle \Psi_i | \mathbf{t}_c | \Psi_j \rangle$, already in the form used for the calculations in this work, are

$$\mathbf{t}_c = \sum_{h \neq i \neq j} \sum_{k, k', k''} \langle kk'k'' | c \rangle \sqrt{(2k+1)(2k'+1)(2k''+1)} (\mathbf{u}_h^{(k)} \cdot \mathbf{u}_i^{(k')} \cdot \mathbf{u}_j^{(k'')}) \quad (1.59)$$

with the coefficients $\langle kk'k'' | c \rangle$ as tabulated by Judd [34] and given here in table 1.7. Care must be taken when using equation (1.59) that the second sum runs over all permutations of

Table 1.7: The coefficients $\langle kk'k''|c\rangle$ from Judd for the three-body operators of the Coulomb configuration interaction [34]

$(kk'k'')$	c					
	2	3	4	6	7	8
(222)	$(\frac{605}{5292})^{\frac{1}{2}}$	$(\frac{32761}{889056})^{\frac{1}{2}}$	$(\frac{3575}{889056})^{\frac{1}{2}}$	$-(\frac{1573}{8232})^{\frac{1}{2}}$	$(\frac{264407}{823200})^{\frac{1}{2}}$	$(\frac{21879}{274400})^{\frac{1}{2}}$
(224)	$-(\frac{6760}{43659})^{\frac{1}{2}}$	$(\frac{33}{1372})^{\frac{1}{2}}$	$-(\frac{325}{37044})^{\frac{1}{2}}$	$-(\frac{15028}{305613})^{\frac{1}{2}}$	$(\frac{28717}{2778300})^{\frac{1}{2}}$	$-(\frac{37349}{926100})^{\frac{1}{2}}$
(244)	$-(\frac{1805}{391314})^{\frac{1}{2}}$	$-(\frac{4}{33957})^{\frac{1}{2}}$	$-(\frac{54925}{373527})^{\frac{1}{2}}$	$(\frac{4693}{12326391})^{\frac{1}{2}}$	$-(\frac{1273597}{28014525})^{\frac{1}{2}}$	$(\frac{849524}{9338175})^{\frac{1}{2}}$
(246)	$-(\frac{4160}{754677})^{\frac{1}{2}}$	$-(\frac{13}{264})^{\frac{1}{2}}$	$(\frac{625}{26136})^{\frac{1}{2}}$	$(\frac{1568}{107811})^{\frac{1}{2}}$	$(\frac{841}{1960200})^{\frac{1}{2}}$	$-(\frac{17}{653400})^{\frac{1}{2}}$
(444)	$(\frac{55016}{717409})^{\frac{1}{2}}$	$(\frac{49972}{622545})^{\frac{1}{2}}$	$(\frac{92480}{1369599})^{\frac{1}{2}}$	$-(\frac{297680}{5021863})^{\frac{1}{2}}$	$-(\frac{719104}{2282665})^{\frac{1}{2}}$	$-(\frac{73644}{2282665})^{\frac{1}{2}}$
(446)	$-(\frac{195}{204974})^{\frac{1}{2}}$	$(\frac{52}{1089})^{\frac{1}{2}}$	$(\frac{529}{11979})^{\frac{1}{2}}$	$-(\frac{49}{395307})^{\frac{1}{2}}$	$-(\frac{1369}{35937})^{\frac{1}{2}}$	$(\frac{68}{11979})^{\frac{1}{2}}$
(266)	$(\frac{1625}{143748})^{\frac{1}{2}}$	$(\frac{325}{199584})^{\frac{1}{2}}$	$(\frac{6889}{2195424})^{\frac{1}{2}}$	$-(\frac{1}{223608})^{\frac{1}{2}}$	$(\frac{625}{81312})^{\frac{1}{2}}$	$(\frac{1377}{27104})^{\frac{1}{2}}$
(466)	$(\frac{88400}{1185921})^{\frac{1}{2}}$	$-(\frac{442}{12705})^{\frac{1}{2}}$	$-(\frac{10880}{251559})^{\frac{1}{2}}$	$-(\frac{174080}{8301447})^{\frac{1}{2}}$	$-(\frac{8704}{3773385})^{\frac{1}{2}}$	$-(\frac{103058}{1257795})^{\frac{1}{2}}$
(666)	$(\frac{29393}{790614})^{\frac{1}{2}}$	$(\frac{205751}{784080})^{\frac{1}{2}}$	$-(\frac{79135}{1724976})^{\frac{1}{2}}$	$(\frac{79135}{175692})^{\frac{1}{2}}$	$(\frac{15827}{319440})^{\frac{1}{2}}$	$-(\frac{8379}{106480})^{\frac{1}{2}}$

the triplets $(kk'k'')$. It seems that this has been overlooked in [19] and [20]. In [34] the full LS -matrices for all six operators \mathbf{t}_c in the configuration f^3 have been tabulated, and it was assured that the computer program is able to reproduce the content of this table.

Spin-orbit configuration interaction. When the Coulomb interaction \mathbf{H}_1 and the spin-orbit interaction \mathbf{H}_2 as the two dominant interactions together are inserted in the second order term of equation (1.10), three interaction terms arise, which are in short form [17]:

$$E_A = \sum_{p \neq c} \frac{\langle c | \mathbf{H}_1 | p \rangle \langle p | \mathbf{H}_1 | c \rangle}{\Delta E} \quad (1.60)$$

$$E_B = \sum_{p \neq c} \frac{\langle c | \mathbf{H}_1 | p \rangle \langle p | \mathbf{H}_2 | c \rangle}{\Delta E} \quad (1.61)$$

$$E_C = \sum_{p \neq c} \frac{\langle c | \mathbf{H}_2 | p \rangle \langle p | \mathbf{H}_2 | c \rangle}{\Delta E} . \quad (1.62)$$

Obviously E_A is the energy matrix of the Coulomb configuration interaction we just discussed. The effective operators connected with the matrices E_B and E_C were investigated in detail by Rajnak and Wybourne [36]. Since the spin-orbit operator (1.29) is a one-body operator, only the configurations (a)–(c) in table 1.4, which are single electron excitations, have non-vanishing matrix elements in $c = f^N$. In [36] it was found that the effective operator of the energy matrix E_C has the same angular dependence as the usual spin-orbit operator

and is therefore “screened” by \mathbf{H}_2 in the semiempirical fitting procedure. Only the effective operator connected with the energy matrix E_B is new, as Judd found [24]. The authors of [36] themselves erroneously declared this operator to be equivalent to the spin-other-orbit operator \mathbf{H}_{soo} in its angular dependence.

The following equation is the tensor operator expression of this effective electrostatic spin-orbit interaction as given by Goldschmidt in [17], but with the usual radial parameters P^k from [24] instead of his Q^k (see appendix C for alternative parameter sets):

$$\mathbf{H}_6 = -\frac{1}{3\hbar} \sum_k \langle l || \mathbf{c}^{(k)} || l \rangle^2 P^k \sqrt{\frac{l(l+1)(2l+1)}{2k+1}} \times \sum_t (2t+1) \begin{Bmatrix} 1 & k & t \\ l & l & l \end{Bmatrix} \sum_{i \neq j} (\mathbf{u}_i^{(k)} \cdot \{\mathbf{s}_j^{(1)} \times \mathbf{u}_j^{(t)}\}^{(k)}) . \quad (1.63)$$

The radial parameters in the energy matrix $E_6 = \sum_k P^k p_k$ are defined by [24]

$$P^k = 6 \sum_{n'} \frac{R^k(nlnl, nln'l) \zeta(nl, n'l)}{|E(nl) - E(n'l)|} \quad (1.64)$$

with the Slater integrals R^k [17]

$$R^k(nlnl, nln'l) = \frac{e^2}{4\pi\epsilon_0} \iint \frac{r_{<}^k}{r_{>}^{k+1}} R_{nl}(r_i) R_{nl}(r_i) R_{nl}(r_j) R_{n'l}(r_j) dr_i dr_j \quad (1.65)$$

and the spin-orbit parameters ζ [17]

$$\zeta(nln'l) = \frac{\hbar^2}{2m_e^2 c^2} \int \frac{1}{r} \frac{d}{dr} U(r) R_{nl}(r) R_{n'l}(r) dr . \quad (1.66)$$

The 3-j symbol in the definition of $\langle l || \mathbf{c}^{(k)} || l \rangle$ in equation (A.18) restricts k in equation (1.63) to even values from 0 up to $2l$ and the mixed tensor operator limits t to values between $k-1$ and $k+1$. The case $t = k$ results in an operator which is antisymmetric in i and j and therefore vanishes by the sum over i and j . Furthermore, $k = 0$ obviously results in an operator proportional to the intra-configuration spin-orbit operator and is therefore omitted.

Similar to the Marvin integrals in section 1.5, in energy level fits of rare earth ions in the literature often only the parameter P^2 is varied and the other two are constrained to fixed fractions of P^2 . But in contrast to the Marvin integrals there are several different factors in use. In [5, 37, 38] the values $P^4 = 0.75 P^2$ and $P^6 = 0.50 P^2$ were used, while [39] uses $P^4 = 0.5 P^2$ and $P^6 = 0.1 P^2$, and in [25] the values $P^4 = 0.66 P^2$ and $P^6 = 0.48 P^2$ are calculated.

The remaining angular operator of the spin-orbit configuration interaction is \mathbf{p}_k , with the matrix elements $p_k(i, j) = \langle \Psi_i | \mathbf{p}_k | \Psi_j \rangle$. Expressing $\mathbf{s}^{(1)}$ in terms of the unit tensor operator $\mathbf{t}^{(1)}$ by equation (A.24) leads to the following expression:

$$\begin{aligned}
\mathbf{p}_k = & -\frac{1}{\sqrt{6}} \langle l || \mathbf{c}^{(k)} || l \rangle^2 \sqrt{\frac{l(l+1)(2l+1)}{2k+1}} \\
& \times \sum_{i \neq j} \left[(2k-1) \begin{Bmatrix} 1 & k & k-1 \\ l & l & l \end{Bmatrix} (\mathbf{u}_i^{(k)} \cdot \{\mathbf{t}_j^{(1)} \times \mathbf{u}_j^{(k-1)}\}^{(k)}) \right. \\
& \left. + (2k+3) \begin{Bmatrix} 1 & k & k+1 \\ l & l & l \end{Bmatrix} (\mathbf{u}_i^{(k)} \cdot \{\mathbf{t}_j^{(1)} \times \mathbf{u}_j^{(k+1)}\}^{(k)}) \right]. \quad (1.67)
\end{aligned}$$

The 6-j symbols are substituted by the algebraic expressions from equations (B.24) and (B.26), which leads to

$$\begin{aligned}
\mathbf{p}_k = & -\frac{1}{2\sqrt{6}} \langle l || \mathbf{c}^{(k)} || l \rangle^2 \\
& \times \sum_{i \neq j} \left[\frac{\sqrt{(2l+k+1)(2l-k+1)k(2k-1)}}{2k+1} (\mathbf{u}_i^{(k)} \cdot \{\mathbf{u}_j^{(k-1)} \times \mathbf{t}_j^{(1)}\}^{(k)}) \right. \\
& \left. - \frac{\sqrt{(2l+k+2)(2l-k)(k+1)(2k+3)}}{2k+1} (\mathbf{u}_i^{(k)} \cdot \{\mathbf{u}_j^{(k+1)} \times \mathbf{t}_j^{(1)}\}^{(k)}) \right]. \quad (1.68)
\end{aligned}$$

Finally, the tensors in the scalar product are recoupled, two factors $\sqrt{2} \mathbf{t}^{(0)}$ (see calculation of \mathbf{H}_{soo} in section 1.5) are introduced, and we end up with the equation which is used for the calculations in this work:

$$\begin{aligned}
\mathbf{p}_k = & \frac{1}{6} \langle l || \mathbf{c}^{(k)} || l \rangle^2 \\
& \times \sum_{i \neq j} \left[\sqrt{\frac{(2l+k+1)(2l-k+1)k(2k-1)}{2k+1}} (\{\mathbf{u}_i^{(k)} \times \mathbf{u}_j^{(k-1)}\}^{(1)} \cdot \{\mathbf{t}_i^{(0)} \times \mathbf{t}_j^{(1)}\}^{(1)}) \right. \\
& \left. - \sqrt{\frac{(2l+k+2)(2l-k)(k+1)(2k+3)}{2k+1}} (\{\mathbf{u}_i^{(k)} \times \mathbf{u}_j^{(k+1)}\}^{(1)} \cdot \{\mathbf{t}_i^{(0)} \times \mathbf{t}_j^{(1)}\}^{(1)}) \right]. \quad (1.69)
\end{aligned}$$

Judd in [35] published a table of all matrix elements of \mathbf{p}_k in the configuration f^2 and a similar table for the configuration f^{12} is found in [25]. The content of both tables was used to check the calculations of the computer program.

2 Radiative transitions

In the last chapter the origin of the energy level spectrum of triply ionized rare earths and a lot of detail corrections were discussed. Here we will recall the background of transitions between these energy levels.

Early in the 20th century van Vleck [40] was able to explain the nature of rare earth transitions by order of magnitude estimations. His conclusion was that only electric dipole, magnetic dipole and electric quadrupole transitions may be strong enough to account for the measured oscillator strengths with maximum values of some 10^{-6} . At that time not much more was known about the internal structure of the electronic energy levels of the rare earth ions than the quantum numbers of the ground states of nearly pure *LS*-character. Later Broer et al. [41] found a small error in the values of van Vleck's calculations and showed that electric quadrupole transitions would be too small to play a role in the rare earth spectra. Since that time only electric and magnetic dipole transitions are considered.

We shall start this chapter with a section recalling the general properties of the different types of transitions. In this section important quantities as the line strength, the oscillator strength, the cross section and their relations to the traditional Einstein coefficients will be introduced. The mathematical description of electric dipole transitions as the main contribution to the transitions in the electronic system of rare earth ions is named after Judd and Ofelt. In 1962 they both independently published a theory of these transitions in two different journals on the same day [42, 43]. Judd's starting point was the intensities of absorption lines, whereas Ofelt explained the intensity of emission lines, and in the end both got equivalent results. In the second section of this chapter we will follow the derivation of Judd, as it fits the mathematical concepts in this work better. The final section will give the analogous expressions for magnetic dipole transitions, which will turn out to be much simpler.

2.1 General properties

According to Einstein, there are three types of interactions of electro-magnetic radiation with matter: absorption, induced emission, and spontaneous emission of photons. To describe these processes he used the three coefficients B_{12} , B_{21} , and A_{21} respectively, in the equation [44]

$$N_1 B_{12} \varrho_\nu = N_2 (B_{21} \varrho_\nu + A_{21}) \quad (2.1)$$

which is valid in the equilibrium of absorption and emission. The background of this equation is a two-level system shown in figure 2.1 with the energy difference $h\nu$, where h is Planck's constant and ν the frequency. In equation (2.1) N_i is the occupation number of level i with $N_1 + N_2 = N$ as the total number of systems, and ϱ_ν the spectral energy density of the

radiation field at frequency ν . This energy density in thermal equilibrium is given by Planck's law

$$\varrho_\nu d\nu = \frac{8\pi\nu^2 n^3}{c^3} \frac{h\nu}{e^{h\nu/k_B T} - 1} d\nu \quad (2.2)$$

with the speed of light in vacuum c , the refractive index n of the host material, Boltzmann's constant k_B , and the temperature T . Furthermore, the distribution of the occupation numbers in the thermal equilibrium may be calculated by Boltzmann statistics

$$\frac{N_2}{N_1} = \frac{g_2}{g_1} e^{-h\nu/k_B T} , \quad (2.3)$$

where g_i is the degeneracy of state i . Inserting these two equations into equation (2.1), we receive the relations between the Einstein coefficients [44, 45, 46]

$$\frac{A_{21}}{B_{21}} = \frac{8\pi h\nu^3 n^3}{c^3} \quad (2.4)$$

and

$$\frac{B_{21}}{B_{12}} = \frac{g_1}{g_2} . \quad (2.5)$$

The Einstein coefficient A_{21} is the spontaneous emission rate of the excited state. In our case of the rare earth ions both energy levels consist of $g_i = 2J_i + 1$ Stark levels, where J_i is the quantum number of the total angular momentum of state i . Instead of the fundamental coefficient $A'_{21}(M_1, M_2, q)$ of the transition from Stark level M_2 of state 2 to Stark level M_1 of state 1 emitting radiation in the polarization mode q , the following mean value is usually taken [44]

$$A_{21} = \frac{1}{3(2J_2 + 1)} \sum_{M_1, M_2, q} A'_{21}(M_1, M_2, q) . \quad (2.6)$$

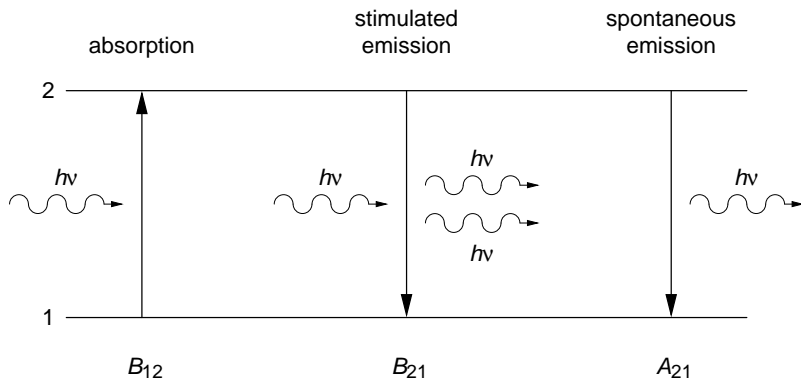


Figure 2.1: Basic two-level system illustrating the three types of interaction of electromagnetic radiation with matter

The sum over q together with the factor $1/3$ averages the polarization modes. In the same way the sum over M_2 together with the factor $1/(2J_2+1)$ gives the mean contribution from all Stark levels of the initial state. It is important to keep in mind that this treatment requires equally populated Stark levels. Therefore it is not valid for large Stark splittings and low temperatures. As an estimation we may take two Stark levels separated by 100 cm^{-1} , which is a usual value. In this case, according to Boltzmann's equation (2.3) at room temperature, the population density of the upper level is only around 60 % of the lower level. The remaining sum over M_1 in equation (2.6) is necessary to get the total rate to all destination levels in the lower set of Stark levels. Analogous definitions are used for the coefficients B_{12} and B_{21} .

The line strength is introduced in [44] to get a uniform description of all three types of interactions. It is defined as the squared matrix element of the dipole operator and, in case of an electric dipole transition, given by

$$S_{ed} = \frac{1}{4\pi\epsilon_0} \frac{1}{3(2J_i+1)} \sum_{M_i, M_j} |\langle \gamma_i J_i M_i | \mathbf{P} | \gamma_j J_j M_j \rangle|^2, \quad (2.7)$$

where the quantities belonging to the initial and the final states are marked by the indices i and j respectively. \mathbf{P} is the electric dipole operator, which will be given in section 2.2. To achieve the corresponding definition of the magnetic dipole linestrength S_{md} , \mathbf{P} must be replaced by the magnetic dipole operator \mathbf{M} from section 2.3. The summation of the polarization modes in equation (2.7) is contained in the scalar product.

Using the correspondence principle, the spontaneous emission rate A_{21} can be calculated by the classical Poynting vector, which is proportional to the squared multipole moment and therefore the classical equivalent to the line strength. The result of this calculation is [44]

$$A_{21} = \frac{64\pi^4 \bar{\nu}^3}{3hc^3(2J_2+1)} [\chi_{ed} S_{ed} + \chi_{md} S_{md}], \quad (2.8)$$

where $\bar{\nu}$ is the mean frequency of the transition taking into account the splitting of the Stark levels. There is some confusion in the literature about the dielectric correction factors χ_{ed} and χ_{md} which, in macroscopic equations as (2.8), take into account effects of the dielectricum. We use here the widely accepted factors [47]

$$\chi_{ed} = \frac{n(n^2+2)^2}{9} \quad \text{and} \quad \chi_{md} = n^3, \quad (2.9)$$

which include two different parts. One is the local field correction factor $(n^2+2)^2/9$ taking into account local changes to the external radiation field due to the electric field of the host lattice ions. This Lorentz factor is strictly valid only for an ion at a well-defined center of a tightly bound crystal matrix, but it is common practice to use it in general, as it is the best known approximation. Of course this factor is relevant only for electric dipole transitions. The remaining refractive index factors come from the formula $c' = c/n$ for the speed of light

in matter, whereas an n^2 in the magnetic dipole factor corrects c in the Bohr magneton β_m contained in the magnetic dipole operator (2.48). In the literature both of these factors and the two corresponding ones needed for absorption and stimulated emission are usually called local field correction factors, although the Lorentz factor is only one part of χ_{ed} .

Connected with the emission rate are two important quantities. One is the radiative lifetime τ_i of energy level i , which is given by

$$\tau_i = \frac{1}{\sum_j A_{ij}} , \quad (2.10)$$

where the sum runs over all levels j below i , and A_{ij} is the spontaneous emission rate of the transition $i \rightarrow j$. This lifetime is called radiative lifetime, because all non-radiative contributions to the real lifetime are neglected. They will be discussed in section 6.1. The other quantity is the branching ratio β_{ij} which is the statistical weight or probability of an excited system in state i to use the transition $i \rightarrow j$ for spontaneous relaxation:

$$\beta_{ij} = \tau_i A_{ij} , \quad (2.11)$$

whereas the sum over all possible channels must be $\sum_j \beta_{ij} = 1$.

In order to get a macroscopic expression for absorption or stimulated emission processes the polarizability of the quantum mechanical two-level system is compared with a classical oscillator. The quotient of both values is the dimensionless oscillator strength [44]:

$$f_{ij} = \frac{4\pi\epsilon_0}{e^2} \frac{8\pi^2 m_e \bar{\nu}}{3h(2J_i + 1)} [\chi'_{ed} S_{ed} + \chi'_{md} S_{md}] , \quad (2.12)$$

where m_e is the electron mass and χ'_{ed} and χ'_{md} are the dielectric correction factors already mentioned. They are obtained by dividing χ_{ed} and χ_{md} from equation (2.9) by n^2 [48]:

$$\chi'_{ed} = \frac{(n^2 + 2)^2}{9n} \quad \text{and} \quad \chi'_{md} = n . \quad (2.13)$$

The relation of the oscillator strengths to the appropriate Einstein coefficients is received by inserting equations (2.8) and (2.4) into (2.12):

$$f_{ij} = \frac{4\pi\epsilon_0}{e^2} \frac{m_e h \bar{\nu} n}{\pi} B_{ij} \quad (2.14)$$

and

$$\frac{f_{21}}{f_{12}} = \frac{2J_1 + 1}{2J_2 + 1} . \quad (2.15)$$

We should stress the fact that the equations (2.8) and (2.12) take into account the multiplet structure of the initial and the final levels by implicit summation in the line strength definition and the averaging quotient $2J_i + 1$. However, they are strictly valid only for sharp energy levels,

i.e. transitions with vanishing linewidth at frequency $\bar{\nu}$, and they are based on the assumption that all Stark levels are populated equally. To take into account the finite linewidth of the transitions we introduce the lineshape function $g_{ij}(\nu)$, normalized by the equation

$$\int g_{ij}(\nu) d\nu = 1 , \quad (2.16)$$

where the integral spans the full spectrum of the transition line. There are different opinions in the literature about the frequency $\bar{\nu}$ in equations (2.8), (2.12), and (2.14). Some authors write ν and keep it as a variable to carry it into the integrals over the transition line [49, 50]. But that leads to results which depend on the order in which the different equations are applied. In the opinion of the author of this work, this is just an academic discussion because, due to the implicit summation over the multiplets in the definition (2.6) of the line strengths contained in equations (2.8) and (2.12), $\bar{\nu}$ already is a mean value and, to be strict, it would be necessary to go back to the single-line line strengths and redo the summation with included ν . This does not seem to be worth the effort, especially since the equally populated Stark levels are an approximation anyway, and the additional error due to the fixed $\bar{\nu}$ is small, as long as the linewidth is small compared with the frequency.

Equation (2.1) may be interpreted as the steady state rate equation of the underlying two-level system by writing

$$-N_1 B_{12} \varrho_\nu + N_2 (B_{21} \varrho_\nu + A_{21}) = \frac{dN_1}{dt} = -\frac{dN_2}{dt} = 0 . \quad (2.17)$$

Taking into account only absorptions, the number of ions leaving state 1 per unit time interval by a transition to state 2 is equal to the number of absorbed photons from the radiation field. The coupling constant of this interaction process of radiation with matter is the cross section $\sigma_{12}(\nu)$ defined by the equation

$$\frac{dn_1}{dt} = -\sigma_{12}(\nu) n_1 \Phi_\nu = \frac{1}{n_I} \frac{d\Phi_\nu}{dx} \quad (2.18)$$

where $n_i = N_i/N$ is the relative occupation number, n_I the density of the dopant (ions per unit volume), and $\Phi_\nu = \varrho_\nu d\nu c / h\nu n$ the photon flux (number of photons per unit area and per unit time interval). The generalization of this equation to include the emission processes is straightforward, and a comparison with equation (2.17) yields the following equation where, furthermore, the lineshape was introduced [46]

$$\sigma_{ij}(\nu) d\nu = \frac{h\bar{\nu}n}{c} B_{ij} g_{ij}(\nu) d\nu . \quad (2.19)$$

Now we are able to connect the calculated oscillator strength from equation (2.12) to the measured cross section spectrum $\sigma(\nu)$:

$$f_{ij} = \frac{4\pi\epsilon_0}{e^2} \frac{m_e c}{\pi} \int \sigma(\nu) d\nu . \quad (2.20)$$

Furthermore, if we insert equation (2.4) into (2.19), we get a formula which is called the Fuchtbauer-Ladenburg equation [46]:

$$\sigma_{21}(\nu) = \frac{c^2}{8\pi\nu^2 n^2} A_{21} g_{21}(\nu) . \quad (2.21)$$

It allows to scale a normalized emission spectrum $g_{21}(\nu)$ to the spectral emission cross section by use of the calculated radiative emission rate A_{21} . This is very important, since absolute emission spectra are difficult to obtain. The analogue equation for the absorption cross section [46]

$$\sigma_{12}(\nu) = \frac{2J_2 + 1}{2J_1 + 1} \frac{c^2}{8\pi\nu^2 n^2} A_{21} g_{12}(\nu) \quad (2.22)$$

is less useful, since absorption spectra can usually be measured in absolute values, anyway. The lineshapes $g_{21}(\nu)$ and $g_{12}(\nu)$ of emission and of absorption are different, but linked by the Einstein coefficients. In section 6.3 we will discuss the McCumber theory which delivers an equation linking the absorption and emission cross sections of a transition.

2.2 Electric dipole transitions (Judd-Ofelt theory)

The transitions observed in triply ionized rare earth ions are mainly of electric dipole nature, only some contain significant magnetic dipole contributions. This observation is surprising at first, because the electric dipole operator

$$\mathbf{P} = -e \sum_i \mathbf{r}_i , \quad (2.23)$$

where e is the electrical charge of an electron and the sum runs over all electrons, has odd parity. Since all states inside a configuration possess the same parity, electric dipole transitions inside a configuration are forbidden, and with typical oscillator strengths around 10^{-6} the transitions are indeed relatively weak. The occurrence and weakness of these transitions is explained by small admixings of other configurations with opposite parity to the ground configuration $4f^N$ by the surrounding host material, i.e. the crystal field interaction. The methods to calculate the appropriate matrix elements use the perturbation theory in second order similar to the configuration interactions in section 1.6, but with the difference that there only configurations with the same parity as the ground configuration were relevant.

As mentioned in section 1.1, the crystal field interaction releases the J -degeneration of the free-ion states, because the external charge distribution is usually not invariant under rotations. The appropriate interaction operator is not used in the energy level calculations in this work, because in glasses the Stark levels with different values of M_J mix up to bands due to the random structure of glasses and are normally not separated. The interaction operator \mathbf{H}_{CF} we will develop here, is needed not only for the Judd-Ofelt theory, it is the same operator which is used to calculate the crystal field splitting of rare earth Stark levels in a crystalline host.

If the charge distribution of the host material is $e\rho(\mathbf{R})$, the electrostatic energy of all electrons with positions \mathbf{r}_i in the field of this charge is [51, 52]:

$$\mathbf{H}_{CF} = -\frac{e^2}{4\pi\epsilon_0} \sum_i \int \frac{\rho(\mathbf{R})}{|\mathbf{r}_i - \mathbf{R}|} dV . \quad (2.24)$$

The inverse distance may be expanded in spherical harmonics like in equation (1.21):

$$\frac{1}{|\mathbf{r}_i - \mathbf{R}|} = \sum_{k=0}^{\infty} \frac{r_i^k}{R^{k+1}} \frac{4\pi}{2k+1} \sum_{q=-k}^k Y_q^{k*}(\theta, \phi) Y_q^k(\theta_i, \phi_i) , \quad (2.25)$$

where the spherical coordinates of \mathbf{R} are (R, ϕ, θ) , and we use the fact that always $R > r_i$, as $\rho(\mathbf{R})$ is vanishing inside the lanthanide ion. If we insert the definition of $\mathbf{c}^{(k)}$ from equation (A.17) into equation (2.25), the crystal field Hamiltonian becomes

$$\mathbf{H}_{CF} = -\frac{e^2}{4\pi\epsilon_0} \sum_i \sum_{k,q} \sqrt{\frac{4\pi}{2k+1}} \int \frac{\rho(\mathbf{R})}{R^{k+1}} Y_q^{k*}(\theta, \phi) dV r_i^k (c_q^{(k)})_i . \quad (2.26)$$

The volume integral of \mathbf{R} usually is abbreviated

$$A_q^k = -\frac{e^2}{4\pi\epsilon_0} \sqrt{\frac{4\pi}{2k+1}} \int \frac{\rho(\mathbf{R})}{R^{k+1}} Y_q^k(\theta, \phi) dV \quad (2.27)$$

which leads to the following short form of the crystal field interaction [7, 52]:

$$\mathbf{H}_{CF} = \sum_{k,q} A_q^k \sum_i r_i^k (c_q^{(k)})_i . \quad (2.28)$$

If equation (2.28) is used to calculate energy level splittings in crystals, only matrix elements inside the ground configuration are of relevance. In that case the reduced matrix element of $\mathbf{c}^{(k)}$ limits k to even integers up to $2l$. For these energy level calculations the definition of a radial integral is necessary. Inside the configuration nl^N this radial integral is [52]

$$B_q^k = A_q^k \int r^k R_{nl}^2(r) dr , \quad (2.29)$$

and due to the properties of the spherical harmonics, it is not difficult to prove that the integer value of q must also always be even because of [7]

$$B_{-q}^k = (-1)^q B_q^k . \quad (2.30)$$

The second sum in equation (2.28) may be abbreviated as

$$D_q^{(k)} = \sum_i r_i^k (c_q^{(k)})_i \quad (2.31)$$

and this is essentially the q coordinate of the electric multipole (tensor) operator [42]

$$P_q^{(k)} = -eD_q^{(k)} , \quad (2.32)$$

where the coordinate q defines the polarization and $k = 1$ for the dipole moment. Inserting equation (2.31) into the crystal field interaction (2.28) and substituting (t, p) for (k, q) yields

$$\mathbf{H}_{CF} = \sum_{t,p} A_p^t D_p^{(t)} , \quad (2.33)$$

and since we are not limited to the nl^N configuration now, all integers between 0 and $2l$ are allowed for t , but only terms with odd values of t cause the required admixing of configurations with opposite parity, otherwise the matrix element of $D_q^{(1)}$ vanishes.

For the sake of simplicity we shall assume a well defined orientation of the rare earth ions and a corresponding q -polarisation of the radiation. This assumption, which we will release later, reduces equation (2.7) to

$$S_{ed} = \frac{e^2}{4\pi\epsilon_0} |\langle i | D_q^{(1)} | f \rangle|^2 . \quad (2.34)$$

The matrix element $\langle i | D_q^{(1)} | f \rangle$ is calculated by treating the crystal field interaction (2.33) with odd t as a small perturbation to the usual Hamiltonian. We already know that in first order this matrix element is zero and in second order the perturbation theory yields [42]

$$\langle \Phi_i^c | D_q^{(1)} | \Phi_f^c \rangle = \sum_{\substack{c',j \\ c' \neq c}} \sum_{\substack{t,p \\ t \text{ odd}}} A_q^t \left[\frac{\langle \Psi_i^c | D_q^{(1)} | \Psi_j^{c'} \rangle \langle \Psi_j^{c'} | D_p^{(t)} | \Psi_f^c \rangle}{E_f^c - E_j^{c'}} + \frac{\langle \Psi_i^c | D_p^{(t)} | \Psi_j^{c'} \rangle \langle \Psi_j^{c'} | D_q^{(1)} | \Psi_f^c \rangle}{E_i^c - E_j^{c'}} \right] . \quad (2.35)$$

In this equation $|\Psi_i^c\rangle$ is state i in the ground configuration c , whereas c' is any other configuration. E_i^c is the energy of $|\Psi_i^c\rangle$, and the symbol Φ instead of Ψ is used for states with a (small) admixing of c' -configurations to the respective Ψ state. The coupling scheme is of no importance here.

The following is strictly valid only for excited configurations c' of the most important type $l^{N-1}l'$, but Judd showed that the results are essentially the same for the other configurations [42]. The first approximation he made is that each excited configuration is assumed to be completely degenerated with energy $E_0^{c'}$. The validity of this assumption is certified if the distance to the ground configuration, namely $|E_{i/f}^c - E_j^{c'}|$, is large enough. But since the configurations $4f^N$ and $4f^{N-1}5d$ overlap in the ultraviolet [14, 15], transitions involving high energy levels should be treated with special care. The gain from this approximation is, however, essential since it allows application of the closure relation

$$\sum_j |\Psi_j^{c'}\rangle \langle \Psi_j^{c'}| = 1 , \quad (2.36)$$

and thus $D_q^{(1)}$ and $D_p^{(k)}$ can be united to a single operator by an equation like (A.26), but valid between different configurations. Disregarding a couple of factors, this results in a matrix element of the unit tensor operator $\mathbf{U}^{(\lambda)}$ and a sum over λ . The complete result is [42]:

$$\begin{aligned} \langle \Phi_i^c | D_q^{(1)} | \Phi_f^c \rangle &= \sum_{\substack{t,p,\lambda \\ t \text{ odd}}} (-1)^{p+q} A_q^t (2\lambda + 1) \langle \Psi_i^c | \mathbf{U}_{p+q}^{(\lambda)} | \Psi_f^c \rangle \\ &\times \frac{1}{2} \left[\Xi_f(t, \lambda) \begin{pmatrix} 1 & \lambda & t \\ q & -p-q & p \end{pmatrix} + \Xi_i(t, \lambda) \begin{pmatrix} t & \lambda & 1 \\ p & -p-q & q \end{pmatrix} \right], \quad (2.37) \end{aligned}$$

where

$$\Xi_{i/f}(t, \lambda) = 2 \sum_{c' \neq c} \left\{ \begin{matrix} 1 & \lambda & t \\ l & l' & l \end{matrix} \right\} \langle l || \mathbf{c}^{(1)} || l' \rangle \langle l' || \mathbf{c}^{(t)} || l \rangle \frac{\langle \Psi_i^c | r | \Psi_f^c \rangle \langle \Psi_i^c | r^k | \Psi_f^c \rangle}{E_{i/f}^c - E_0^{c'}} \quad (2.38)$$

and λ is a non-negative integer number up to $2l$. $\lambda = 0$ is useless since it leads to a vanishing matrix element for unequal initial and final states.

The two 3-j symbols in equation (2.37) are equal, except for a phase given by equation (B.5), thus [42]

$$\begin{aligned} \langle \Phi_i^c | D_q^{(1)} | \Phi_f^c \rangle &= \sum_{\substack{t,p,\lambda \\ t \text{ odd}}} (-1)^{p+q} A_q^t (2\lambda + 1) \begin{pmatrix} 1 & \lambda & t \\ q & -p-q & p \end{pmatrix} \langle \Psi_i^c | \mathbf{U}_{p+q}^{(\lambda)} | \Psi_f^c \rangle \\ &\times \frac{1}{2} \left[\Xi_f(t, \lambda) + (-1)^{1+\lambda+t} \Xi_i(t, \lambda) \right]. \quad (2.39) \end{aligned}$$

This equation already contains only matrix elements inside the ground configuration and is therefore ready for use with e. g. $\Xi_{i/f}$ as radial integrals. But Judd made a second approximation which simplifies equation (2.39) even further. This assumption is

$$E_i^c - E_0^{c'} = E_f^c - E_0^{c'} \quad (2.40)$$

and leads to $\Xi_i = \Xi_f$, and therefore the matrix element of $D_q^{(1)}$ is non-vanishing only if $1 + \lambda + t$ is even, meaning λ is even:

$$\langle \Phi_i^c | D_q^{(1)} | \Phi_f^c \rangle = \sum_{\substack{t,p,\lambda \\ t \text{ odd} \\ \lambda \text{ even}}} (-1)^{p+q} A_q^t \Xi(t, \lambda) (2\lambda + 1) \begin{pmatrix} 1 & \lambda & t \\ q & -p-q & p \end{pmatrix} \langle \Psi_i^c | \mathbf{U}_{p+q}^{(\lambda)} | \Psi_f^c \rangle. \quad (2.41)$$

This equation is now inserted into the electric dipole part of equation (2.12) and, after the already described averaging procedure over the polarisation modes (coordinate q) and the Stark levels, we get

$$f_{ed} = 4\pi\epsilon_0 \frac{8\pi^2 m_e \bar{\nu}}{3h(2J_i + 1)} \chi'_{ed} \sum_{M_i, M_j} |\langle \Phi_i^c | \mathbf{D}^{(1)} | \Phi_f^c \rangle|^2. \quad (2.42)$$

For rare earth doped crystals it is possible to measure the dependence of the oscillator strength on the relative orientation of the crystal to the well defined polarization of the radiation field of a laser beam. But in glasses the surroundings of individual rare earth ions are distributed randomly, and therefore usually only the averaged value from equation (2.42) can be measured.

Inserting equation (2.41) into (2.42) and using equation (3.51), which we will develop in the next chapter, we get the final result of Judd [42]:

$$f_{ed} = \sum_{\lambda \text{ even}} T_{\lambda} \bar{\nu} |\langle l^N, \gamma_i J_i || \mathbf{U}^{(\lambda)} || l^N, \gamma_j J_j \rangle|^2, \quad (2.43)$$

where

$$T_{\lambda} = \chi'_{ed} \frac{8\pi^2 m_e}{3h(2J_i + 1)} (2\lambda + 1) \sum_{\substack{t, p \\ t \text{ odd}}} \frac{|A_p^t|^2 \Xi^2(t, \lambda)}{2t + 1} \quad (2.44)$$

and the reduced matrix element is calculated in intermediate coupling (1.18).

In practice the definition of T_{λ} turned out to be hardly practicable because the factor $2J_i + 1$ makes T_{λ} level dependent. The formulation used today [48, 53] in case of the configuration f^N uses the three host dependent Judd-Ofelt parameters Ω_2 , Ω_4 , and Ω_6 in the line strength

$$S_{ed} = \frac{e^2}{4\pi\epsilon_0} \sum_{\lambda=2,4,6} \Omega_{\lambda} |\langle f^N, \gamma_i J_i || \mathbf{U}^{(\lambda)} || f^N, \gamma_j J_j \rangle|^2 \quad (2.45)$$

and the oscillator strength

$$f_{ed} = \frac{4\pi\epsilon_0}{e^2} \frac{8\pi^2 m_e \bar{\nu}}{3h(2J_i + 1)} \chi'_{ed} S_{ed} \quad (2.46)$$

with

$$\Omega_{\lambda} = (2\lambda + 1) \sum_{\substack{t, p \\ t \text{ odd}}} \frac{|A_p^t|^2 \Xi^2(t, \lambda)}{2t + 1}. \quad (2.47)$$

We should stress the fact that the electric dipole transitions calculated here only exist in presence of a crystal field and should therefore be absent in truly free ions. It can be expected, as it is actually the case, that the intensities of the transition spectrum show a substantial dependence on the host material. But in contrast, the relative intensities of the lines are host independent to a high degree. This is also not surprising, because on the one hand it cannot be expected that just three Judd-Ofelt parameters can adjust each transition, and on the other hand the energy levels are still dominated by the free-ion states and therefore the reduced matrix elements show only a minor host dependence. Consequently, the branching ratios and the relative absorption strengths are also only weakly host dependent [54].

In the Judd-Ofelt analysis of rare earth ions in glasses, the reduced matrix elements in equation (2.45) are usually treated as completely host independent and tables of these reduced

matrix elements from the literature for different host materials are used to fit measured absorption oscillator strengths using equation (2.20) to equation (2.45) via (2.46), taking the three Judd-Ofelt parameters as fit-parameters. Often used tables of reduced unit tensor matrix elements were published by Carnall et al. for rare earth ions in solutions [55, 56, 57, 58, 59, 60] and in LaF₃ [5, 39], but similar tables are available from other authors, too.

In chapter 5 we will see how to use equation (2.46) to fit the Judd-Ofelt parameters and calculate radiative emission properties for arbitrary transitions. But we will use reduced matrix elements calculated from the absorption spectra of the same glass samples. Nevertheless it is remarkable that just three parameters are sufficient to calculate the transition properties in the whole level spectrum of a rare earth ion with relatively high accuracy as numerous applications of the Judd-Ofelt theory in the literature show.

A more detailed calculation reveals some selection rules for the above transitions [43]. If J -mixing by the perturbing crystal field with odd t is neglected, which normally is a realistic approximation, then $\Delta J \leq 2l$. For pure LS -states $\Delta L \leq 2l$ holds in addition, and because the crystal field interaction (2.28) does not contain spin dependent terms, it must be $\Delta S = 0$.

2.3 Magnetic dipole transitions

Although most transitions between energy levels of rare earth ions are dominated by the electric dipole contribution, some also show a significant magnetic dipole character. Therefore we must also investigate the magnetic dipole operator

$$\mathbf{M} = -\frac{\beta_m}{\hbar}(\mathbf{L} + g_s\mathbf{S}) , \quad (2.48)$$

where $\beta_m = e\hbar/2m_e c$ is the Bohr magneton, e the electrical charge of an electron, $\hbar = h/2\pi$, h Planck's constant, m_e the electron mass, c the speed of light in vacuum, $\mathbf{L} = \sum_i \mathbf{l}_i$ the total orbital angular momentum, $\mathbf{S} = \sum_i \mathbf{s}_i$ the total spin and $g_s = 2.00231924$ the g -factor of the spin.

An external magnetic field \mathbf{B} couples to this dipole moment and splits the Stark levels due to the perturbing Hamilton operator

$$\mathbf{H}_B = c(\mathbf{B} \cdot \mathbf{M}) , \quad (2.49)$$

which is one of the simplest operators in the computer program developed for energy level calculations in this work.

Here we are interested in the matrix elements of \mathbf{M} . Fortunately, the magnetic dipole operator is of even parity so we can calculate the matrix elements directly and do not need a complicated theory as in case of the electric dipole moment. Expressions of \mathbf{L} and \mathbf{S} in terms of unit tensor operators can be found in section A.3 in the appendix.

As well as for the electric dipole transitions, selection rules can be found for magnetic dipole transitions. Due to equations (2.48) and (2.49), the rules $\Delta L = 0$ and $\Delta S = 0$ are obvious, and the matrix element in LS -representation furthermore yields $\Delta J \leq 1$ [61].

Analogous to equation (2.42) we have

$$f_{md} = \frac{4\pi\epsilon_0}{e^2} \frac{8\pi^2 m_e \bar{\nu}}{3h(2J_i + 1)} \chi'_{md} \sum_{M_i, M_j} |\langle \Phi_i^c | \mathbf{M} | \Phi_f^c \rangle|^2 . \quad (2.50)$$

Inserting equation (2.48) and using equation (3.51), we get the final expression [44, 53]

$$f_{md} = \frac{4\pi\epsilon_0}{e^2} \frac{8\pi^2 m_e \bar{\nu}}{3h(2J_i + 1)} \chi_{md} S_{md} , \quad (2.51)$$

with the line strength [44]

$$S_{md} = \frac{1}{4\pi\epsilon_0} \frac{\beta_m^2}{\hbar^2} |\langle f^N, \gamma_i J_i | | \mathbf{L} + g_s \mathbf{S} | | f^N, \gamma_j J_j \rangle|^2 . \quad (2.52)$$

Equations (2.52) and (2.51) are obviously the magnetic counterparts of equations (2.45) and (2.46).

3 Calculation of matrix elements

In the last two chapters a lot of tensor operator equations were derived to calculate the energy level spectra of rare earth ions and transitions inside these spectra. Here we will discuss how to evaluate the tensors in these equations numerically. The first section provides a systematic introduction of m -body operators in an N -particle system, which were already used ad-hoc in the preceding chapters. In the following section the actual rules to calculate numerical matrix elements are developed. These determinantal product state matrix elements may be transformed to LS -states using the transformation shown in the next section. The final section deals with the special problems connected with the calculation of reduced matrix elements.

The equations in this chapter are the core of the energy level computer program written and used for this work. They are coded in the language C so as to be calculated fast. In contrast, the equations in the preceding chapters only combine these basic matrices to the actual interaction matrices or reduced matrix elements in case of the Judd-Ofelt theory. Since this is much less time critical, the high level script language Python [62] was used, which results in a much more abstract and better maintainable code.

3.1 General m -electron operators

In an N -particle system, as e.g. the N electrons in our nl^N configuration, physical operators act on one particle i or two particles i and j . These one- and two-body operators may be denoted \mathbf{f}_i and \mathbf{g}_{ij} respectively. In section 1.6 we met effective three-body operators acting on three particles i , j , and k , which we may write \mathbf{h}_{ijk} . In this work we use lowercase letters for such elementary operators acting on just one, two, or three particles out of N in an N -body system. The elementary operators usually appear as parts of larger operators acting on the whole system of N particles

$$\mathbf{F} = \sum_i \mathbf{f}_i \quad \mathbf{G} = \sum_{i \neq j} \mathbf{g}_{ij} \quad \mathbf{H} = \sum_{i \neq j \neq k} \mathbf{h}_{ijk} . \quad (3.1)$$

These tensors are usually called one-body, two-body and three-body operators. To distinguish them from their elementary counterparts they get uppercase letters.

As a typical example of calculations with such tensors, we may build the scalar product of two one-electron tensor operators $\mathbf{U}^{(k)}$ and $\mathbf{T}^{(k)}$, which is the sum of a new one-electron and a two-electron operator:

$$(\mathbf{U}^{(k)} \cdot \mathbf{T}^{(k)}) = \sum_i (\mathbf{u}_i^{(k)} \cdot \mathbf{t}_i^{(k)}) + \sum_{i \neq j} (\mathbf{u}_i^{(k)} \cdot \mathbf{t}_j^{(k)}) . \quad (3.2)$$

In order to do numerical calculations we need some more rules. Let us first of all take the general determinantal product states $|\Psi\rangle = |\{\alpha_1\alpha_2\ldots\alpha_N\}\rangle$ from equation (1.6), where α is the set of quantum numbers of one electron, usually $nlm_l m_s$, but inside the nl^N configuration, $\alpha = m_l m_s$ is sufficient. Of course, the phase of the determinantal product states may be chosen arbitrarily, but for each state this phase can be chosen only once in a calculation, otherwise the diagonal matrix elements also get arbitrary phases. Therefore it is convenient to define phase rules, and we should choose the same rules as Condon and Shortley [44]. In their standard order, the α_i in the set $(\alpha_1\alpha_2\ldots\alpha_N)$ are sorted by the values of the single-electron quantum numbers α in decreasing order. If we use the nomenclature $m_l^\pm = (m_l, \pm\frac{1}{2})$, the standard order of all 14 single-electron states of the configuration $4f^N$ is

$$+3^+, +3^-, +2^+, +2^-, +1^+, +1^-, 0^+, 0^-, -1^+, -1^-, -2^+, -2^-, -3^+, -3^- . \quad (3.3)$$

All states in standard order get the phase +1. The definition of determinants consequently requires that $|\Psi\rangle$ has the phase +1 if, for its transformation to standard order, the number of exchanged pairs α_i and α_j is even, and -1 otherwise.

The first step of the computer program used for the calculations in this work is the preparation of all possible determinantal product states in standard order. Since the program is designed for nl^N -configurations, only the quantum number l and the number of electrons N are needed. Because m_l can take the $2l+1$ values $-l, \ldots, +l$ and m_s the two values $\pm\frac{1}{2}$, there are $4l+2$ possible single-electron states as the 14 states in (3.3) for $l=3$. The quantum numbers of the N -electron states are then derived by taking all combinations of N single-electron states out of $4l+2$. The number of states in the configuration nl^N is therefore

$$N_{\text{states}} = \binom{4l+2}{N} . \quad (3.4)$$

3.2 Matrix elements in N -electron systems

At this point in the computer program, all information necessary to define the determinantal product states is completed. In chapter 1 all interaction operators were given as one-, two-, or three-body operators built up by mixed tensor operators of elementary unit tensor operators $\mathbf{u}^{(k)}$ and $\mathbf{t}^{(k)}$ in the orbital and spin space respectively. Therefore the last item we need to know is how the matrix elements of these one-, two-, and three-body operators are actually calculated. The general matrix element of a one-electron operator \mathbf{F} in a two-electron system for example is

$$\langle\Psi'|\mathbf{F}|\Psi\rangle = \langle\{\alpha'_1\alpha'_2\}|\mathbf{f}_1 + \mathbf{f}_2|\{\alpha_1\alpha_2\}\rangle , \quad (3.5)$$

and the expansion of the determinants is

$$|\{\alpha_1\alpha_2\}\rangle = \frac{1}{\sqrt{2}}(|\alpha_1\alpha_2\rangle - |\alpha_2\alpha_1\rangle) . \quad (3.6)$$

Table 3.1: The basic mixed unit tensor operators in the computer program for energy level calculations

tensor	electrons	equation
$\mathbf{u}_q^{(k)}$	1	(3.11)
$\mathbf{t}_q^{(k)}$	1	(3.12)
$(\mathbf{u}_1^{(k)} \cdot \mathbf{u}_1^{(k)})$	1	(3.13)
$(\mathbf{t}_1^{(k)} \cdot \mathbf{t}_1^{(k)})$	1	(3.14)
$(\mathbf{u}_1^{(k)} \cdot \mathbf{t}_1^{(k)})$	1	(3.17)
$(\mathbf{u}_1^{(k)} \cdot \mathbf{u}_2^{(k)})$	2	(3.21)
$(\mathbf{t}_1^{(k)} \cdot \mathbf{t}_2^{(k)})$	2	(3.22)
$(\mathbf{u}_1^{(k)} \cdot \mathbf{t}_2^{(k)})$	2	(3.23)
$(\{\mathbf{u}_1^{(k_1)} \times \mathbf{u}_2^{(k_2)}\}^{(k)} \cdot \{\mathbf{t}_1^{(\kappa_1)} \times \mathbf{t}_2^{(\kappa_2)}\}^{(k)})$	2	(3.30)
$(\mathbf{u}_1^{(k_1)} \cdot \mathbf{u}_2^{(k_2)} \cdot \mathbf{u}_3^{(k_3)})$	3	(3.36)

This leads to the rather long expression

$$\begin{aligned} \langle \Psi' | \mathbf{F} | \Psi \rangle = \frac{1}{2} [& \langle \alpha'_1 \alpha'_2 | \mathbf{f}_1 | \alpha_1 \alpha_2 \rangle - \langle \alpha'_1 \alpha'_2 | \mathbf{f}_1 | \alpha_2 \alpha_1 \rangle - \langle \alpha'_2 \alpha'_1 | \mathbf{f}_1 | \alpha_1 \alpha_2 \rangle + \langle \alpha'_2 \alpha'_1 | \mathbf{f}_1 | \alpha_2 \alpha_1 \rangle \\ & + \langle \alpha'_1 \alpha'_2 | \mathbf{f}_2 | \alpha_1 \alpha_2 \rangle - \langle \alpha'_1 \alpha'_2 | \mathbf{f}_2 | \alpha_2 \alpha_1 \rangle - \langle \alpha'_2 \alpha'_1 | \mathbf{f}_2 | \alpha_1 \alpha_2 \rangle + \langle \alpha'_2 \alpha'_1 | \mathbf{f}_2 | \alpha_2 \alpha_1 \rangle] . \end{aligned} \quad (3.7)$$

Since \mathbf{f}_1 only acts on the first electron and \mathbf{f}_2 on the second one and since both operators are equivalent in all other respects, we get the final formula

$$\begin{aligned} \langle \Psi' | \mathbf{F} | \Psi \rangle = & \langle \alpha'_1 | \mathbf{f}_1 | \alpha_1 \rangle \delta(\alpha'_2, \alpha_2) - \langle \alpha'_1 | \mathbf{f}_1 | \alpha_2 \rangle \delta(\alpha'_2, \alpha_1) \\ & - \langle \alpha'_2 | \mathbf{f}_1 | \alpha_1 \rangle \delta(\alpha'_1, \alpha_2) + \langle \alpha'_2 | \mathbf{f}_1 | \alpha_2 \rangle \delta(\alpha'_1, \alpha_1) . \end{aligned} \quad (3.8)$$

Obviously, for larger numbers of N and especially for two- and three-electron operators much more complex sums appear. But fortunately it is not necessary to evaluate these sums completely, as the delta symbols assure that non-zero matrix elements exist only under certain conditions. A systematic study leads to certain rules, which will be given in the following paragraphs. Furthermore, we will develop expressions for all ten basic operators contained in the kernel of the computer program and used for the calculations in this work. Some of these mixed unit tensor operators have similar properties, so they can be grouped into five basic types, as shown in table 3.1. The tensors of the first group in this table are coordinates of rank- k tensors, all others are scalar products. Therefore the representations of all operators, except the first group, are symmetric matrices.

Matrix elements of one-electron operators. To calculate the matrix element $\langle \Psi' | \mathbf{F} | \Psi \rangle$ between the states $|\Psi\rangle = |\{\alpha_1 \alpha_2 \dots \alpha_N\}\rangle$ and $|\Psi'\rangle = |\{\alpha'_1 \alpha'_2 \dots \alpha'_N\}\rangle$ the sets $(\alpha_1 \alpha_2 \dots \alpha_N)$ and $(\alpha'_1 \alpha'_2 \dots \alpha'_N)$ are reordered so that all single-electron states equal in both states appear at the same position at the beginning of both sets. The matrix element may then be calculated by application of the following rules [7, 17, 44]: If after the mentioned reordering there is $\alpha'_i = \alpha_i$

- for all i , then

$$\langle \Psi' | \mathbf{F} | \Psi \rangle = \sum_i \langle \alpha_i | \mathbf{f}_1 | \alpha_i \rangle \quad (3.9)$$

- for all i except $i = N$, then

$$\langle \Psi' | \mathbf{F} | \Psi \rangle = \langle \alpha'_N | \mathbf{f}_1 | \alpha_N \rangle \quad (3.10)$$

and in all other cases the matrix element is zero. The matrix element is therefore at most a sum of single-electron matrix elements and no determinant has to be calculated. It is an easy task to check the validity of these rules in the special case of a two-electron system by comparison with equation (3.8). In the computer program the mentioned rules are used by a general subroutine for all one-electron operators.

In the following the expressions for all basic one-electron matrix elements contained in the core of the computer program for this work will be given. The first and most basic one is the matrix element of the q -coordinate of the elementary unit tensor operator $\mathbf{u}^{(k)}$. The value of this element is given by equation (A.20):

$$\langle m_{l_a} m_{s_a} | \mathbf{u}_q^{(k)} | m_{l_b} m_{s_b} \rangle = (-1)^{l-m_{l_a}} \delta(m_{s_a}, m_{s_b}) \begin{pmatrix} l & k & l \\ -m_{l_a} & q & m_{l_b} \end{pmatrix}. \quad (3.11)$$

Because of the 3-j symbol, this matrix element is non-vanishing only for $q = m_{l_a} - m_{l_b}$. The matrix element of the q -coordinate of the elementary unit tensor operator $\mathbf{t}^{(k)}$ is given by the similar expression

$$\langle m_{l_a} m_{s_a} | \mathbf{t}_q^{(k)} | m_{l_b} m_{s_b} \rangle = (-1)^{\frac{1}{2}-m_{s_a}} \delta(m_{l_a}, m_{l_b}) \begin{pmatrix} \frac{1}{2} & k & \frac{1}{2} \\ -m_{s_a} & q & m_{s_b} \end{pmatrix}, \quad (3.12)$$

and again this matrix element is non-vanishing only for $q = m_{s_a} - m_{s_b}$.

All other matrix elements defined in the core of the computer program, including all two- and three-electron operators, are scalar products of elementary unit tensor operators. The matrix element of the scalar product $(\mathbf{u}^{(k)} \cdot \mathbf{u}^{(k)})$ is given by the reduction equation (A.27) followed by (3.11):

$$\langle m_{l_a} m_{s_a} | (\mathbf{u}^{(k)} \cdot \mathbf{u}^{(k)}) | m_{l_b} m_{s_b} \rangle = \frac{1}{2l+1} \delta(m_{l_a}, m_{l_b}) \delta(m_{s_a}, m_{s_b}) \quad (3.13)$$

and in the same way

$$\langle m_{l_a} m_{s_a} | (\mathbf{t}^{(k)} \cdot \mathbf{t}^{(k)}) | m_{l_b} m_{s_b} \rangle = \frac{1}{2} \delta(m_{l_a}, m_{l_b}) \delta(m_{s_a}, m_{s_b}) . \quad (3.14)$$

The last matrix element of a one electron operator is the matrix element of the scalar product $(\mathbf{u}^{(k)} \cdot \mathbf{t}^{(k)})$, which is more complicated. First of all we expand the scalar product by its definition in equation (A.4)

$$\langle m_{l_a} m_{s_a} | (\mathbf{u}^{(k)} \cdot \mathbf{t}^{(k)}) | m_{l_b} m_{s_b} \rangle = \sum_q (-1)^q \langle m_{l_a} | u_q^{(k)} | m_{l_b} \rangle \langle m_{s_a} | t_{-q}^{(k)} | m_{s_b} \rangle . \quad (3.15)$$

We already know the values of the two matrix elements in this expression and, inserting the appropriate parts of the equations (3.11) and (3.12), we get

$$\begin{aligned} \langle m_{l_a} m_{s_a} | (\mathbf{u}^{(k)} \cdot \mathbf{t}^{(k)}) | m_{l_b} m_{s_b} \rangle = \\ \sum_q (-1)^{q+l+\frac{1}{2}-m_{l_a}-m_{s_a}} \begin{pmatrix} l & k & l \\ -m_{l_a} & q & m_{l_b} \end{pmatrix} \begin{pmatrix} \frac{1}{2} & k & \frac{1}{2} \\ -m_{s_a} & -q & m_{s_b} \end{pmatrix} , \end{aligned} \quad (3.16)$$

where the first 3-j symbol assures that $q = m_{l_a} - m_{l_b}$ and the second that $-q = m_{s_a} - m_{s_b}$. Therefore $\delta(m_{l_a} + m_{s_a}, m_{l_b} + m_{s_b})$ can be introduced instead of the sum to achieve the final expression

$$\begin{aligned} \langle m_{l_a} m_{s_a} | (\mathbf{u}^{(k)} \cdot \mathbf{t}^{(k)}) | m_{l_b} m_{s_b} \rangle = (-1)^{l+\frac{1}{2}-m_{l_b}-m_{s_a}} \delta(m_{l_a} + m_{s_a}, m_{l_b} + m_{s_b}) \\ \times \begin{pmatrix} l & k & l \\ -m_{l_a} & m_{l_a} - m_{l_b} & m_{l_b} \end{pmatrix} \begin{pmatrix} \frac{1}{2} & k & \frac{1}{2} \\ -m_{s_a} & m_{s_a} - m_{s_b} & m_{s_b} \end{pmatrix} . \end{aligned} \quad (3.17)$$

Matrix elements of two-electron operators. In order to calculate the matrix element $\langle \Psi' | \mathbf{G} | \Psi \rangle$ of a two-electron operator \mathbf{G} , first of all the single-electron states in $|\Psi\rangle$ and $|\Psi'\rangle$ are reordered in the same way as already described for the matrix element of a one-electron operator. The calculation of the matrix element is then greatly simplified by application of the following rules [7, 17]: If after the mentioned reordering there is $\alpha'_i = \alpha_i$

- for all i , then

$$\langle \Psi' | \mathbf{G} | \Psi \rangle = \sum_{i < j} \langle \{\alpha_i \alpha_j\} | \mathbf{g}_{12} | \{\alpha_i \alpha_j\} \rangle \quad (3.18)$$

- for all i except $i = N$, then

$$\langle \Psi' | \mathbf{G} | \Psi \rangle = \sum_i \langle \{\alpha_i \alpha'_N\} | \mathbf{g}_{12} | \{\alpha_i \alpha_N\} \rangle \quad (3.19)$$

- for all i except $i = N - 1, N$, then

$$\langle \Psi' | \mathbf{G} | \Psi \rangle = \langle \{ \alpha'_{N-1} \alpha'_N \} | \mathbf{g}_{12} | \{ \alpha_{N-1} \alpha_N \} \rangle \quad (3.20)$$

and in all other cases the matrix element is zero. Therefore only determinantal states of the type $|\{ \alpha_i \alpha_j \} \rangle = |\alpha_i \alpha_j \rangle - |\alpha_j \alpha_i \rangle$ have to be calculated, which is done by a general subroutine for all two-electron operators.

In the following the expressions for all basic two-electron matrix elements, which are included in the core of the computer program for this work, will be given. The matrix element of the operator $(\mathbf{u}_1^{(k)} \cdot \mathbf{u}_2^{(k)})$ is derived in the same way as equation (3.17). The main difference is that here the two operators act on different electrons and there on different spaces of one electron. We get

$$\begin{aligned} \langle m_{l_a} m_{s_a} m_{l_b} m_{s_b} | (\mathbf{u}_1^{(k)} \cdot \mathbf{u}_2^{(k)}) | m_{l_c} m_{s_c} m_{l_d} m_{s_d} \rangle = \\ (-1)^{2l-m_{l_b}-m_{l_c}} \delta(m_{l_a} + m_{l_b}, m_{l_c} + m_{l_d}) \delta(m_{s_a}, m_{s_c}) \delta(m_{s_b}, m_{s_d}) \\ \times \begin{pmatrix} l & k & l \\ -m_{l_a} & m_{l_a} - m_{l_c} & m_{l_c} \end{pmatrix} \begin{pmatrix} l & k & l \\ -m_{l_b} & m_{l_b} - m_{l_d} & m_{l_d} \end{pmatrix}, \quad (3.21) \end{aligned}$$

and substituting the quantum number l by s , we obtain the matrix element of the operator $(\mathbf{t}_1^{(k)} \cdot \mathbf{t}_2^{(k)})$

$$\begin{aligned} \langle m_{l_a} m_{s_a} m_{l_b} m_{s_b} | (\mathbf{t}_1^{(k)} \cdot \mathbf{t}_2^{(k)}) | m_{l_c} m_{s_c} m_{l_d} m_{s_d} \rangle = \\ (-1)^{1-m_{s_b}-m_{s_c}} \delta(m_{s_a} + m_{s_b}, m_{s_c} + m_{s_d}) \delta(m_{l_a}, m_{l_c}) \delta(m_{l_b}, m_{l_d}) \\ \times \begin{pmatrix} \frac{1}{2} & k & \frac{1}{2} \\ -m_{s_a} & m_{s_a} - m_{s_c} & m_{s_c} \end{pmatrix} \begin{pmatrix} \frac{1}{2} & k & \frac{1}{2} \\ -m_{s_b} & m_{s_b} - m_{s_d} & m_{s_d} \end{pmatrix}. \quad (3.22) \end{aligned}$$

The matrix element of the operator $(\mathbf{u}_1^{(k)} \cdot \mathbf{t}_2^{(k)})$ is also derived without difficulties:

$$\begin{aligned} \langle m_{l_a} m_{s_a} m_{l_b} m_{s_b} | (\mathbf{u}_1^{(k)} \cdot \mathbf{t}_2^{(k)}) | m_{l_c} m_{s_c} m_{l_d} m_{s_d} \rangle = \\ (-1)^{l+\frac{1}{2}-m_{s_b}-m_{l_c}} \delta(m_{l_a} + m_{s_b}, m_{l_c} + m_{s_d}) \delta(m_{l_b}, m_{l_d}) \delta(m_{s_a}, m_{s_c}) \\ \times \begin{pmatrix} l & k & l \\ -m_{l_a} & m_{l_a} - m_{l_c} & m_{l_c} \end{pmatrix} \begin{pmatrix} \frac{1}{2} & k & \frac{1}{2} \\ -m_{s_b} & m_{s_b} - m_{s_d} & m_{s_d} \end{pmatrix}. \quad (3.23) \end{aligned}$$

Much more complicated is the following matrix element of the scalar product of two mixed tensor operators, which appears e.g. in the spin-spin or spin-other-orbit interaction in section 1.5:

$$\langle m_{l_a} m_{s_a} m_{l_b} m_{s_b} | (\{\mathbf{u}_1^{(k_1)} \times \mathbf{u}_2^{(k_2)}\}^{(k)} \cdot \{\mathbf{t}_1^{(\kappa_1)} \times \mathbf{t}_2^{(\kappa_2)}\}^{(k)}) | m_{l_c} m_{s_c} m_{l_d} m_{s_d} \rangle = \sum_q (-1)^q \langle m_{l_a} m_{l_b} | \{\mathbf{u}_1^{(k_1)} \times \mathbf{u}_2^{(k_2)}\}_q^{(k)} | m_{l_c} m_{l_d} \rangle \langle m_{s_a} m_{s_b} | \{\mathbf{t}_1^{(\kappa_1)} \times \mathbf{t}_2^{(\kappa_2)}\}_{-q}^{(k)} | m_{s_c} m_{s_d} \rangle . \quad (3.24)$$

We should at first evaluate one of the two matrix elements in the sum using the definition of the q -coordinate of a mixed tensor operator from equation (A.7):

$$\langle m_{l_a} m_{l_b} | \{\mathbf{u}_1^{(k_1)} \times \mathbf{u}_2^{(k_2)}\}_q^{(k)} | m_{l_c} m_{l_d} \rangle = \sum_{q_1 q_2} (-1)^{k_1 - k_2 + q} \sqrt{2k + 1} \begin{pmatrix} k_1 & k_2 & k \\ q_1 & q_2 & -q \end{pmatrix} \langle m_{l_a} | u_{q_1}^{(k_1)} | m_{l_c} \rangle \langle m_{l_b} | u_{q_2}^{(k_2)} | m_{l_d} \rangle . \quad (3.25)$$

The second and third columns of the 3-j symbol are exchanged with use of equation (B.5), and the two matrix elements are evaluated by inserting equation (3.11), resulting in

$$\langle m_{l_a} m_{l_b} | \{\mathbf{u}_1^{(k_1)} \times \mathbf{u}_2^{(k_2)}\}_q^{(k)} | m_{l_c} m_{l_d} \rangle = \sum_{q_1 q_2} (-1)^{k+q+2l-m_{l_a}-m_{l_b}} \sqrt{2k+1} \times \begin{pmatrix} k_1 & k & k_2 \\ q_1 & -q & q_2 \end{pmatrix} \begin{pmatrix} l & k_1 & l \\ -m_{l_a} & q_1 & m_{l_c} \end{pmatrix} \begin{pmatrix} l & k_2 & l \\ -m_{l_b} & q_2 & m_{l_d} \end{pmatrix} . \quad (3.26)$$

The last two 3-j symbols fix $q_1 = m_{l_a} - m_{l_c}$ and $q_2 = m_{l_b} - m_{l_d}$ respectively, and the first 3-j symbol assures $q = q_1 + q_2$, therefore

$$\langle m_{l_a} m_{l_b} | \{\mathbf{u}_1^{(k_1)} \times \mathbf{u}_2^{(k_2)}\}_q^{(k)} | m_{l_c} m_{l_d} \rangle = (-1)^{2l+k-m_{l_c}-m_{l_d}} \sqrt{2k+1} \begin{pmatrix} k_1 & k & k_2 \\ m_{l_a} - m_{l_c} & -q & m_{l_b} - m_{l_d} \end{pmatrix} \times \begin{pmatrix} l & k_1 & l \\ -m_{l_a} & m_{l_a} - m_{l_c} & m_{l_c} \end{pmatrix} \begin{pmatrix} l & k_2 & l \\ -m_{l_b} & m_{l_b} - m_{l_d} & m_{l_d} \end{pmatrix} . \quad (3.27)$$

Evaluating the second matrix element in the sum in equation (3.24) in the same way yields the expression

$$\langle m_{s_a} m_{s_b} | \{\mathbf{t}_1^{(\kappa_1)} \times \mathbf{t}_2^{(\kappa_2)}\}_{-q}^{(k)} | m_{s_c} m_{s_d} \rangle = (-1)^{1+k-m_{s_c}-m_{s_d}} \sqrt{2k+1} \begin{pmatrix} \kappa_1 & k & \kappa_2 \\ m_{s_a} - m_{s_c} & q & m_{s_b} - m_{s_d} \end{pmatrix} \times \begin{pmatrix} l & \kappa_1 & l \\ -m_{s_a} & m_{s_a} - m_{s_c} & m_{s_c} \end{pmatrix} \begin{pmatrix} l & \kappa_2 & l \\ -m_{s_b} & m_{s_b} - m_{s_d} & m_{s_d} \end{pmatrix} . \quad (3.28)$$

Inserting the equations (3.27) and (3.28) into (3.24) results in the following expression:

$$\begin{aligned}
\langle m_{l_a} m_{s_a} m_{l_b} m_{s_b} | (\{ \mathbf{u}_1^{(k_1)} \times \mathbf{u}_2^{(k_2)} \}^{(k)} \cdot \{ \mathbf{t}_1^{(\kappa_1)} \times \mathbf{t}_2^{(\kappa_2)} \}^{(k)}) | m_{l_c} m_{s_c} m_{l_d} m_{s_d} \rangle = \\
(2k+1) \sum_q (-1)^{q+2l+1-m_{l_c}-m_{l_d}-m_{s_c}-m_{s_d}} \\
\times \begin{pmatrix} k_1 & k & k_2 \\ m_{l_a}-m_{l_c} & -q & m_{l_b}-m_{l_d} \end{pmatrix} \begin{pmatrix} \kappa_1 & k & \kappa_2 \\ m_{s_a}-m_{s_c} & q & m_{s_b}-m_{s_d} \end{pmatrix} \\
\times \begin{pmatrix} l & k_1 & l \\ -m_{l_a} & m_{l_a}-m_{l_c} & m_{l_c} \end{pmatrix} \begin{pmatrix} l & k_2 & l \\ -m_{l_b} & m_{l_b}-m_{l_d} & m_{l_d} \end{pmatrix} \\
\times \begin{pmatrix} l & \kappa_1 & l \\ -m_{s_a} & m_{s_a}-m_{s_c} & m_{s_c} \end{pmatrix} \begin{pmatrix} l & \kappa_2 & l \\ -m_{s_b} & m_{s_b}-m_{s_d} & m_{s_d} \end{pmatrix}. \quad (3.29)
\end{aligned}$$

The first two 3-j symbols fix $q = m_{l_a} + m_{l_b} - m_{l_c} - m_{l_d}$ and $-q = m_{s_a} + m_{s_b} - m_{s_c} - m_{s_d}$ respectively, therefore we can write finally

$$\begin{aligned}
\langle m_{l_a} m_{s_a} m_{l_b} m_{s_b} | (\{ \mathbf{u}_1^{(k_1)} \times \mathbf{u}_2^{(k_2)} \}^{(k)} \cdot \{ \mathbf{t}_1^{(\kappa_1)} \times \mathbf{t}_2^{(\kappa_2)} \}^{(k)}) | m_{l_c} m_{s_c} m_{l_d} m_{s_d} \rangle = (2k+1) \\
\times (-1)^{2l+1-m_{s_a}-m_{s_b}-m_{l_c}-m_{l_d}} \delta(m_{l_a} + m_{s_a} + m_{l_b} + m_{s_b}, m_{l_c} + m_{s_c} + m_{l_d} + m_{s_d}) \\
\times \begin{pmatrix} k_1 & k & k_2 \\ m_{l_a}-m_{l_c} & m_{l_c}+m_{l_d}-m_{l_a}-m_{l_b} & m_{l_b}-m_{l_d} \end{pmatrix} \\
\times \begin{pmatrix} \kappa_1 & k & \kappa_2 \\ m_{s_a}-m_{s_c} & m_{s_c}+m_{s_d}-m_{s_a}-m_{s_b} & m_{s_b}-m_{s_d} \end{pmatrix} \\
\times \begin{pmatrix} l & k_1 & l \\ -m_{l_a} & m_{l_a}-m_{l_c} & m_{l_c} \end{pmatrix} \begin{pmatrix} l & k_2 & l \\ -m_{l_b} & m_{l_b}-m_{l_d} & m_{l_d} \end{pmatrix} \\
\times \begin{pmatrix} l & \kappa_1 & l \\ -m_{s_a} & m_{s_a}-m_{s_c} & m_{s_c} \end{pmatrix} \begin{pmatrix} l & \kappa_2 & l \\ -m_{s_b} & m_{s_b}-m_{s_d} & m_{s_d} \end{pmatrix}. \quad (3.30)
\end{aligned}$$

Matrix elements of three-electron operators. As in the case of the one- and two-electron operators, the single-electron states in $|\Psi\rangle$ and $|\Psi'\rangle$ are first reordered. This simplifies the calculation of the matrix element $\langle \Psi' | \mathbf{H} | \Psi \rangle$ of a three-electron operator \mathbf{H} by application of the following rules [20], which are straightforward expansions of the appropriate rules for one- and two-electron operators: If after the reordering there is $\alpha'_i = \alpha_i$

- for all i , then

$$\langle \Psi' | \mathbf{H} | \Psi \rangle = \sum_{i < j < k} \langle \{ \alpha_i \alpha_j \alpha_k \} | \mathbf{h}_{123} | \{ \alpha_i \alpha_j \alpha_k \} \rangle \quad (3.31)$$

- for all i except $i = N$, then

$$\langle \Psi' | \mathbf{H} | \Psi \rangle = \sum_{i < j} \langle \{ \alpha_i \alpha_j \alpha'_N \} | \mathbf{h}_{123} | \{ \alpha_i \alpha_j \alpha_N \} \rangle \quad (3.32)$$

- for all i except $i = N - 1, N$, then

$$\langle \Psi' | \mathbf{H} | \Psi \rangle = \sum_i \langle \{ \alpha_i \alpha'_{N-1} \alpha'_N \} | \mathbf{h}_{123} | \{ \alpha_i \alpha_{N-1} \alpha_N \} \rangle \quad (3.33)$$

- for all i except $i = N - 2, N - 1, N$, then

$$\langle \Psi' | \mathbf{H} | \Psi \rangle = \langle \alpha'_{N-2} \alpha'_{N-1} \alpha'_N | \mathbf{h}_{123} | \alpha_{N-2} \alpha_{N-1} \alpha_N \rangle \quad (3.34)$$

and in all other cases the matrix element is zero. The general subroutine for three-electron operators in the computer program therefore has to calculate only three-dimensional determinants of single electron states.

The only three-electron interaction arising in chapter 1 is part of the Coulomb configuration interaction. Therefore only the matrix element of a triple scalar product of elementary unit tensor operators is included in the program core:

$$\begin{aligned} \langle m_{l_a} m_{s_a} m_{l_b} m_{s_b} m_{l_c} m_{s_c} | (\mathbf{u}_1^{(k_1)} \cdot \mathbf{u}_2^{(k_2)} \cdot \mathbf{u}_3^{(k_3)}) | m_{l_d} m_{s_d} m_{l_e} m_{s_e} m_{l_f} m_{s_f} \rangle = \\ \sum_{q_1 q_2 q_3} \begin{pmatrix} k_1 & k_2 & k_3 \\ q_1 & q_2 & q_3 \end{pmatrix} \langle m_{l_a} m_{s_a} | u_{q_1}^{(k_1)} | m_{l_d} m_{s_d} \rangle \\ \times \langle m_{l_b} m_{s_b} | u_{q_2}^{(k_2)} | m_{l_e} m_{s_e} \rangle \langle m_{l_c} m_{s_c} | u_{q_3}^{(k_3)} | m_{l_f} m_{s_f} \rangle . \end{aligned} \quad (3.35)$$

Fortunately, the sum does not have to be carried out at all, because the 3-j symbols in the evaluated three matrix elements in the sum, given by equation (3.11), fix all q_i :

$$\begin{aligned} \langle m_{l_a} m_{s_a} m_{l_b} m_{s_b} m_{l_c} m_{s_c} | (\mathbf{u}_1^{(k_1)} \cdot \mathbf{u}_2^{(k_2)} \cdot \mathbf{u}_3^{(k_3)}) | m_{l_d} m_{s_d} m_{l_e} m_{s_e} m_{l_f} m_{s_f} \rangle = \\ (-1)^{3l - m_{l_a} - m_{l_b} - m_{l_c}} \delta(m_{s_a}, m_{s_d}) \delta(m_{s_b}, m_{s_e}) \delta(m_{s_c}, m_{s_f}) \\ \times \begin{pmatrix} k_1 & k_2 & k_3 \\ m_{l_a} - m_{l_d} & m_{l_b} - m_{l_e} & m_{l_c} - m_{l_f} \end{pmatrix} \begin{pmatrix} l & k_1 & l \\ -m_{l_a} & m_{l_a} - m_{l_d} & m_{l_d} \end{pmatrix} \\ \times \begin{pmatrix} l & k_2 & l \\ -m_{l_b} & m_{l_b} - m_{l_e} & m_{l_e} \end{pmatrix} \begin{pmatrix} l & k_3 & l \\ -m_{l_c} & m_{l_c} - m_{l_f} & m_{l_f} \end{pmatrix} . \end{aligned} \quad (3.36)$$

3.3 Transformation to LS -coupling

The importance of a backtransformation of matrix elements and states to the LS -coupling scheme was already discussed in section 1.4. Both the determinantal product states and the LS -states of Racah form a complete set of normalized and orthogonal base states spanning the whole state space of a given N -electron configuration. Therefore there must be a unitary transformation connecting both bases:

$$|\tau WUSLJM_J\rangle = \sum_{\alpha_1 \alpha_2 \dots \alpha_N} |\{\alpha_1 \alpha_2 \dots \alpha_N\}\rangle \langle \alpha_1 \alpha_2 \dots \alpha_N | \tau WUSLJM_J\rangle \quad (3.37)$$

or, in short,

$$|\Phi_j\rangle = \sum_i |\Psi_i\rangle \langle \Psi_i | \Phi_j\rangle . \quad (3.38)$$

The method used here to calculate the transformation matrix $U_{ij} = \langle \Psi_i | \Phi_j\rangle$ strictly follows the chain of symmetry groups from table 1.2. Starting with U_7 , the operator \mathbf{S}^2 must be diagonal in LS -coupling. Therefore as the first step the matrix

$$M_1(i, j) = \langle \Psi_i | (\mathbf{S}^{(1)} \cdot \mathbf{S}^{(1)}) | \Psi_j\rangle \quad (3.39)$$

as the representation of \mathbf{S}^2 in the base of the determinantal product states is calculated and diagonalized:

$$M'_1 = V_1^T M_1 V_1 , \quad (3.40)$$

where the (diagonal) elements of M'_1 are the eigenvalues $S(S+1)\hbar^2$ of \mathbf{S}^2 in increasing order.

The next group in the chain is R_7 , therefore Casimir's operator of R_7 (see section 1.5) must also be diagonal in Racah's LS -coupling. We take the matrix

$$M_2(i, j) = \langle \Psi_i | \mathbf{G}(R_7) | \Psi_j\rangle \quad (3.41)$$

and calculate

$$M'_2 = V_1^T M_2 V_1 . \quad (3.42)$$

The important point is that, as R_7 is a subgroup of U_7 , we know that M'_2 must be diagonal with respect to subspaces with different eigenvalues of \mathbf{S}^2 . In other words, M'_2 contains non-zero matrix elements only in submatrices along the diagonal axis and each submatrix corresponds to a different eigenvalue S of \mathbf{S}^2 at the same rows and columns in M'_1 . An example of the shape of M'_2 is

$$M'_2 = \begin{pmatrix} \boxed{} & 0 & 0 \\ 0 & \boxed{} & 0 \\ 0 & 0 & \boxed{} \end{pmatrix} . \quad (3.43)$$

Table 3.2: Chain of operators which have to be diagonalized to get the transformation matrix from the determinantal product states to Racah's LS classification

operator	eigenvalue	group
\mathbf{S}^2/\hbar^2	$S(S+1)$	U_7
$\mathbf{G}(\mathbf{R}_7)$	W	R_7
$\mathbf{G}(\mathbf{G}_2)$	U	G_2
\mathbf{L}^2/\hbar^2	$L(L+1)$	R_3
\mathbf{J}^2/\hbar^2	$J(J+1)$	
J_z/\hbar	M_J	

In the next step each of these submatrices is diagonalized separately and the appropriate transformation matrices are combined to a matrix V_2 with the same shape as M'_2 . The matrix elements of the resulting diagonal matrix

$$M''_2 = V_2^T V_1^T M_2 V_1 V_2 \quad (3.44)$$

are the eigenvalues of $\mathbf{G}(\mathbf{R}_7)$. Groups of equal eigenvalues of $\mathbf{G}(\mathbf{R}_7)$ split the S -subspaces again to even smaller sub-subspaces, and inside these spaces the matrix

$$M''_3 = V_2^T V_1^T M_3 V_1 V_2, \quad (3.45)$$

with

$$M_3(i, j) = \langle \Psi_i | \mathbf{G}(\mathbf{G}_2) | \Psi_j \rangle \quad (3.46)$$

is diagonalized next.

In that way a unitary matrix $U = V_1 \dots V_6$ is built up, which diagonalizes the determinantal product state representations of all operators in table 3.2 simultaneously. Obviously this matrix also transforms the determinantal product states to Racah's LS -classification.

As already mentioned in section 1.4, Racah's classification by symmetry groups is not sufficient for the configurations $f^5 - f^9$. In these configurations even after the last step of diagonalizing J_z not all remaining subspaces are one-dimensional. Therefore an additional quantum number τ is introduced. The accidental states inside the remaining degenerated actually two-dimensional subspaces get the values $\tau = 1$ and 2 , whereas for all nondegenerate states $\tau = 1$ holds. Of course the arbitrarily labeled states are in general not identical to the states which result from Racah's cfp-treatment but the states in both schemes are linked by linear transformations inside the two-dimensional degenerated subspaces.

Of course all Hamilton operators are scalar operators since the energy is a scalar. Furthermore, in our special case of a practically free ion the Hamiltonians must be invariant under rotations. For the interaction operators discussed in chapter 1 this is obviously the

case as all these operators are scalar products. The crystal field interaction (2.28) in contrast is based on a sum of coordinates of tensor operators of higher rank and therefore also a scalar, but direction dependent. Consequently, in a crystal field in general all electronic states are non-degenerated except the two-fold so-called Kramers degeneracy of electron systems with an odd number of electrons, whereas in our case of the free ion all states are $(2J + 1)$ -fold degenerated with respect to the quantum number M_J . To save computing time, the program therefore reduces the matrix U to U_r by taking only the columns corresponding to states with $M_J = J$.

All energy matrices x_k in the computer program are immediately transformed to the LS -representation by

$$x'_k = U_r^T x_k U_r, \quad (3.47)$$

which reduces their size drastically. In the next step, these LS -matrices, together with the values X^k of the corresponding radial integrals, are used to build the full energy matrix

$$E' = \sum_k X^k x'_k \quad (3.48)$$

from equation (1.15). The diagonalization of E' by a unitary matrix V

$$\begin{pmatrix} e_1 & 0 & \cdots \\ 0 & e_2 & \cdots \\ \vdots & \vdots & \ddots \end{pmatrix} = V^T E' V \quad (3.49)$$

results in the spectrum of energy levels e_i as elements of the diagonal matrix. Furthermore, since E' is a LS -matrix, V is exactly the transformation matrix to the intermediate coupling scheme from equation (1.18). But care must be taken, when comparing the elements of V with the coefficients of intermediate coupling in the literature. The sign of the coefficients depends on the phase of the LS -states, i.e. the column vectors of U , which is arbitrarily chosen in the diagonalization process and is in general different from Racah's choice. Of course, in cases where pairs of τ -states appear, the coefficients of these states will be completely different.

3.4 Calculation of reduced matrix elements

The transformation matrices from the last section work perfectly for expectation values of many physical observables, but in the Judd-Ofelt theory reduced matrix elements appear which need special consideration. In fact equation (2.45) contains the reduced matrix elements of the operator $\mathbf{U}^{(k)}$ squared. To calculate these squared matrices, we take the Wigner-Eckart theorem from equation (A.5):

$$\langle J' M' | \mathbf{U}_q^{(k)} | J M \rangle = (-1)^{J' - M'} \begin{pmatrix} J' & k & J \\ -M' & q & M \end{pmatrix} \langle J' || \mathbf{U}^{(k)} || J \rangle \quad (3.50)$$

with the shortcut $M = M_J$. If we square this equation and sum over all possible values of M' and M , we get

$$\sum_{M',M} |\langle J'M' | \mathbf{U}_q^{(k)} | JM \rangle|^2 = \sum_{M',M} \begin{pmatrix} J' & k & J \\ -M' & q & M \end{pmatrix} \begin{pmatrix} J' & k & J \\ -M' & q & M \end{pmatrix} |\langle J' || \mathbf{U}^{(k)} || J \rangle|^2, \quad (3.51)$$

where the sum of the squared 3-j symbols is just $(2k+1)^{-1}$, according to equation (B.15). The squared reduced matrix element may therefore be calculated using the formula

$$|\langle J' || \mathbf{U}^{(k)} || J \rangle|^2 = (2k+1) \sum_{M',M} |\langle J'M' | \mathbf{U}_q^{(k)} | JM \rangle|^2, \quad (3.52)$$

and this equation obviously is equally valid in pure LS - and intermediate coupling. In case of the Judd-Ofelt theory the matrix elements on the right side are taken in intermediate coupling.

But unfortunately equation (3.52) has two disadvantages, first it gives only absolute values of reduced matrix elements, second all M_J -states are needed to use it. Instead of using the small U_r matrix containing only states with $M_J = J$, the full matrix U must be used in equation (3.47), which makes computation relatively slow.

The more elegant solution is to use the Wigner-Eckart theorem in equation (3.50) directly. To do that, values of M_J and M'_J must be picked, which always lead to a non-zero 3-j symbol on the right side. This 3-j symbol also requires $q = M'_J - M_J$ to be non-vanishing. Fortunately, it can be shown by inserting into the definition (B.3) that the choice $M'_J = J'$ and $M_J = J$ fulfils the requirement. Therefore we can calculate all reduced matrix elements with the reduced set of LS -states in U_r by application of the equation

$$\langle J' || \mathbf{U}^{(k)} || J \rangle = \frac{\langle J'J' | \mathbf{U}_{J'-J}^{(k)} | JJ \rangle}{\begin{pmatrix} J' & k & J \\ -J' & J' - J & J \end{pmatrix}}. \quad (3.53)$$

In contrast to equation (3.52), equation (3.53) depends on the phases of the LS -states in a more subtle way than it may seem at first. If the matrix element of $\mathbf{U}^{(k)}$ is taken in the LS -base, it is just the sign of the reduced matrix element which is undefined. But in intermediate coupling this non-diagonal matrix element is completely wrong here, as it is calculated from several terms with arbitrary phases.

The solution is to adjust the phases of the LS -states, i.e. the column vectors of the matrix U , properly. Therefore, if U was calculated as described in the last section, the submatrices $\langle JM'_J | \mathbf{U}^{(k)} | JM_J \rangle$ along the diagonal of the full JM_J -matrix are calculated. In all cases where the 3-j symbol in the Wigner-Eckart theorem (3.50) is non-zero, the reduced matrix element with undefined phase is calculated. Only in case of the diagonal elements, where $M'_J = M_J$, the arbitrary phases of the LS -states cancel out each other. These elements

therefore contain the correct value of the reduced matrix element, and the other states with $M'_J \neq M_J$ can be adjusted by changing the sign of the corresponding column vectors of U .

If this small modification is included in the calculation method described in the last section, the resulting LS -matrices can be directly used to calculate reduced matrix elements by the application of equation (3.53) even in intermediate coupling.

4 Absorption spectroscopy of rare earth ions

After three chapters of theory, we now come to practical tasks. In the first section of this chapter we will give some data on the ZBLAN glass samples used for the measurements in this work. This data is necessary to evaluate the absorption measurements which are described in the second section. In the third section the evaluation methods will be presented and the results for each measured rare earth ion are discussed in the remaining sections. Special care is taken to get realistic estimations of the accuracy of measured and calculated values. In figure 4.1 the measured energy levels of all investigated rare earth ions are shown.

4.1 The glass samples

The rare earth doped glass samples used in this work are heavy metal fluoride glasses (HMFG) of the ZBLAN type. This glass was invented in 1975 [63] and today it is the most widely used HMFG in several variations. It is named after its major components as can be seen from table 4.1 where the molar composition of the glass samples used in this work is given. To dope a ZBLAN glass some part of the lanthanum is usually substituted by the rare earth ion of interest. All samples contain approximately 2.5 mol% of PbF_2 which raises the refractive index by about 0.008. Used in the core of a glass fiber without lead in the cladding, this results in a numerical aperture NA of approximately 0.16.

The actual values differ somewhat from the nominal values because the raw materials are weighted and combined by hand. Therefore it is necessary to use the actual *measured* mass of each glass component to calculate the dopant concentration in a specific piece of glass and get an idea of the accuracy of this value. For each sample about 25 g of glass were used and the actual amount of each fluoride was measured with an uncertainty of $\Delta m = 0.5$ mg. It is an easy task to calculate the molar concentration of the dopant

$$p = \frac{m_d/M_d}{\sum_i m_i/M_i} = \frac{N_d}{\sum_i N_i} \quad (4.1)$$

with the mass m_i , the molar mass M_i , and the amount of substance N_i of component i , where $i = d$ for the dopant. Since all m_i were measured independently, we can use the Gauss formula

$$\Delta p = \sqrt{\sum_i \left(\frac{\partial p}{\partial m_i} \Delta m \right)^2} \quad (4.2)$$

to calculate the relative uncertainty of p

$$\frac{\Delta p}{p} = \frac{\Delta m}{N^2} \sqrt{N_d^2 \sum_i \left(\frac{1}{M_i} \right)^2 + \frac{N^2 + 2NN_d}{M_k^2}} \quad (4.3)$$

with $N = \sum_i N_i$.

Table 4.2 shows the molar concentration of the dopant ions in all glass samples. It turns out that the relative uncertainty resulting from the weighting process is only around 10^{-5} . Another source of errors is the fact that during the melting process some glass components are escaping vaporized, and therefore the glass composition changes. The magnitude of this effect is unknown, but it is expected to be negligible in the calculations. All glasses were poured to pieces of typically $8 \times 12 \times 18 \text{ mm}^3$, and all surfaces polished to optical quality. Opposite

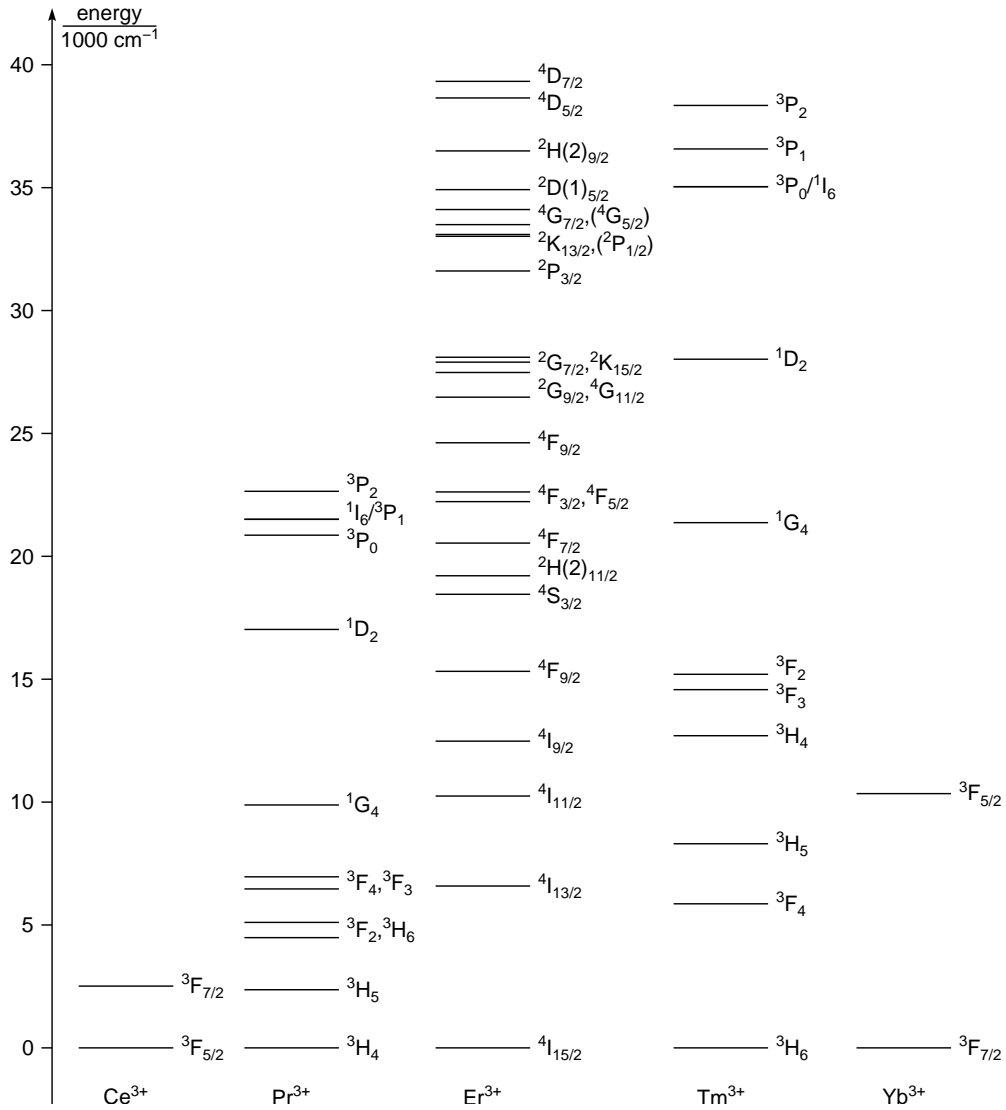


Figure 4.1: All energy levels in the transmission window of ZBLAN of the evaluated rare earth ions. States in parantheses were not observed, the calculated position is used instead.

Table 4.1: Molar composition of all glass samples

glass no.	Ln	ZrF ₄ mol%	BaF ₂ mol%	(La+Ln)F ₃ mol%	AlF ₃ mol%	NaF mol%	InF ₃ mol%	PbF ₂ mol%
1012	Ce	52.958	19.991	3.896	3.007	17.503	0.154	2.491
1118	Pr	52.745	19.925	3.893	3.067	17.744	0.133	2.493
1107	Pr	52.901	19.963	3.957	3.042	17.508	0.128	2.502
1159	Pr	52.440	19.776	3.765	2.987	18.371	0.176	2.485
958	Pr	52.959	20.001	3.839	3.058	17.497	0.132	2.513
1109	Pr	52.962	19.991	3.894	3.008	17.519	0.126	2.500
1095	Er	52.677	19.878	3.866	3.173	17.766	0.143	2.498
1100	Er	52.766	19.911	3.865	3.023	17.805	0.128	2.503
1032	Er	52.628	19.895	3.857	2.996	17.404	0.139	3.082
1110	Er	52.882	19.958	3.871	3.004	17.606	0.127	2.552
1104	Tm	52.916	19.941	3.897	3.038	17.519	0.189	2.500
1142	Tm	52.905	19.960	3.876	3.026	17.517	0.135	2.582
1030	Tm	52.782	19.886	3.945	3.091	17.630	0.149	2.517
881	Tm	52.834	19.928	3.871	3.009	17.733	0.129	2.495
1031	Yb	52.922	19.985	3.927	3.044	17.455	0.143	2.525
1176	Yb	52.925	20.009	3.874	3.005	17.541	0.139	2.507
1011	–	52.712	19.873	3.846	2.983	17.933	0.170	2.482
nominal		53	20	3.875	3	17	0.125	2.5

surfaces are not exactly parallel, to avoid interference effects.

In order to transform the molar concentration used in glass technology to the ion density n_I , which is the quantity of physical relevance and allows the comparison of different glasses, the mass density $\varrho = m/V$ of the glass is required:

$$n_I = \frac{\varrho N_A}{m} p, \quad (4.4)$$

where N_A is Avogadro's constant. Some time ago large series of density measurements were carried out at our institute and the conversion factor

$$\gamma = \frac{\varrho N_A}{m} = (1.84 \pm 0.02) \cdot 10^{20} \text{ cm}^{-3}/\text{mol\%} \quad (4.5)$$

for ZBLAN glass was found. Different dopants and small variations of the glass composition are covered by the specified uncertainty. Our value of $4.33 \pm 0.05 \text{ g/cm}^3$ for the density of the

Table 4.2: Dopant concentration and dimensions of all glass samples. The dimensions are mean values from measurements at two positions with an uncertainty of ± 0.10 mm.

glass no.	Ln	p mol%	Δp mol%	A mm	B mm	C mm
1012	Ce	1.005	$15 \cdot 10^{-6}$	7.15	14.23	18.38
1118	Pr	0.112	$1.7 \cdot 10^{-6}$	8.20	15.15	18.63
1107	Pr	0.191	$2.8 \cdot 10^{-6}$	7.93	14.18	18.78
1159	Pr	0.220	$3.2 \cdot 10^{-6}$	8.80	14.30	16.75
958	Pr	1.052	$13 \cdot 10^{-6}$	8.30	11.70	19.28
1109	Pr	3.003	$47 \cdot 10^{-6}$	7.98	14.08	18.80
1095	Er	0.103	$1.4 \cdot 10^{-6}$	8.48	12.03	17.38
1100	Er	0.304	$4.0 \cdot 10^{-6}$	8.35	11.28	17.55
1032	Er	0.996	$13 \cdot 10^{-6}$	6.68	16.38	19.98
1110	Er	2.993	$41 \cdot 10^{-6}$	8.05	14.38	18.98
1104	Tm	0.107	$1.4 \cdot 10^{-6}$	8.45	14.70	17.80
1142	Tm	0.300	$3.9 \cdot 10^{-6}$	8.70	15.35	17.25
1030	Tm	1.074	$14 \cdot 10^{-6}$	8.08	11.98	12.83
881	Tm	2.992	$29 \cdot 10^{-6}$	9.88	13.33	22.23
1031	Yb	1.021	$13 \cdot 10^{-6}$	8.35	11.50	20.30
1176	Yb	2.999	$41 \cdot 10^{-6}$	8.53	14.93	18.80
1011	—	—	—	8.30	15.33	18.98

ZBLAN glass is comparable with the values 4.37 ± 0.05 g/cm³ [64] and 4.30 ± 0.15 g/cm³ [65] found in the literature for only slightly different ZBLAN compositions.

Another important quantity is the spectral behavior of the refractive index. In [6] it was reported that the usual Cauchy formula

$$n(\lambda) = A\lambda^{-4} + B\lambda^{-2} + C + D\lambda^2 + E\lambda^4 \quad (4.6)$$

may be used with the values

$$\begin{aligned}
 A &= 1.35123 \cdot 10^{-5} \mu\text{m}^4 \\
 B &= 2.94780 \cdot 10^{-3} \mu\text{m}^2 \\
 C &= 1.48965 \\
 D &= -1.30933 \cdot 10^{-3} \mu\text{m}^{-2} \\
 E &= -3.23335 \cdot 10^{-6} \mu\text{m}^{-4}
 \end{aligned} \quad (4.7)$$

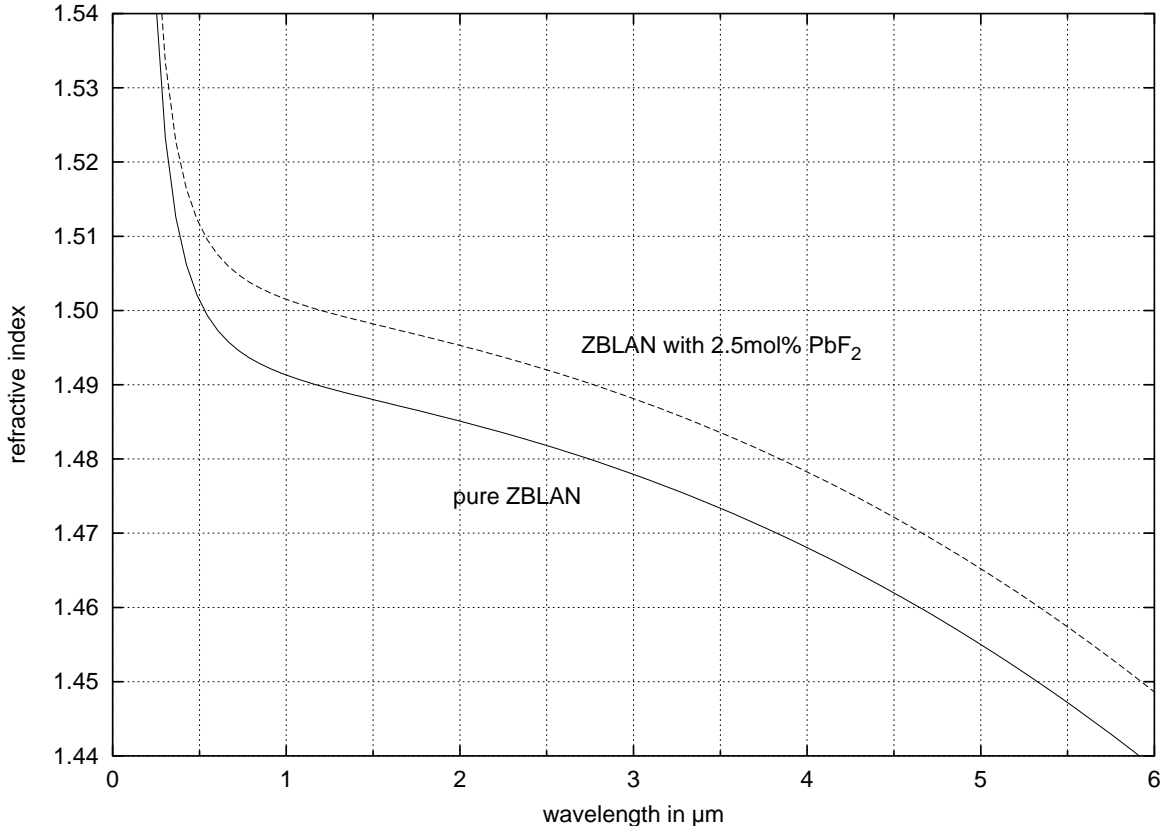


Figure 4.2: Refractive index spectrum of ZBLAN glass, according to equation (4.6)

for ZBLAN glasses without lead doping. Moderate changes of the refractive index by PbF_2 just raise the full spectrum. For a concentration of 2.5 mol%, the value $C = 1.49985$ was measured. In figure 4.2 the resulting spectrum of the refractive index is given.

4.2 Measurement setup

There are essentially two different methods to measure the absorption spectrum of rare earth doped glass samples. The first is to let tunable monochromatic radiation pass through the sample, the other uses a broad band source and the spectrum is calculated by a Fourier transformation. The general setup of a spectrometer of the first type is shown in figure 4.3. For such a spectrometer usually a high temperature source with a broad and smooth spectrum is used, as for example a halogen lamp. The radiation at the wavelength of interest is then taken from the emission spectrum of the source by using the monochromator as a narrow band filter. With an increasing resolution, i.e. a decreasing bandwidth of the monochromator, the

intensity of the usable radiation is decreasing. Of course in principle it is also possible to use tunable lasers as sources, but to achieve a broad spectrum, several lasers are necessary and therefore such a setup is rarely used.

The second method also uses a broad band high temperature source. As figure 4.4 shows, the radiation from this source is brought to interference with itself in a Michelson interferometer and the interference signal is detected. The intensity of the signal is recorded with respect to the position of the oscillating mirror and therefore the intensity spectrum of the source can be calculated via a Fourier transformation. The sample is placed in the beam before or after the interferometer. Of course in practice both setups, instead of lenses, use mirrors to avoid dispersion effects.

Compared with the monochromator setup, the Fourier method has the big advantage that the full spectrum of the source is always used, limited only by the bandwidth of the optical components in the light path and the detector. This is especially important in the infrared region where the spectral intensity of usable temperature sources and the detectivity of available detectors is low. But the drawback of high sensitivity is a rather low dynamic range compared with the monochromator setup. Another advantage of the Fourier transformation method is that the oscillation frequency of the moving mirror in the Michelson interferometer may be high even at high spectral resolution and complete spectra are usually measured with repetition rates in the Hz up to the kHz range compared with measurement durations of tens of minutes with a monochromator. In practice, the Fourier method is standard in the infrared, then called FT-IR spectrometer, but for shorter wavelengths the Michelson setup is used only in cases where fast measurements with low spectral resolution are needed.

The absorption spectra presented in this work were measured with two spectrometers. One was a monochromator spectrometer *Cary 5 G* from Varian for the range 175 – 3300 nm. To obtain an energy level spectrum, the wavelength scale of a monochromator obviously does not fit well, therefore it was necessary to split the spectral range into several pieces measured with different resolutions to keep the variation of the wavenumber resolution small. The second instrument was a FT-IR spectrometer *IFS 25* from Bruker. It contained a Si-detector for the

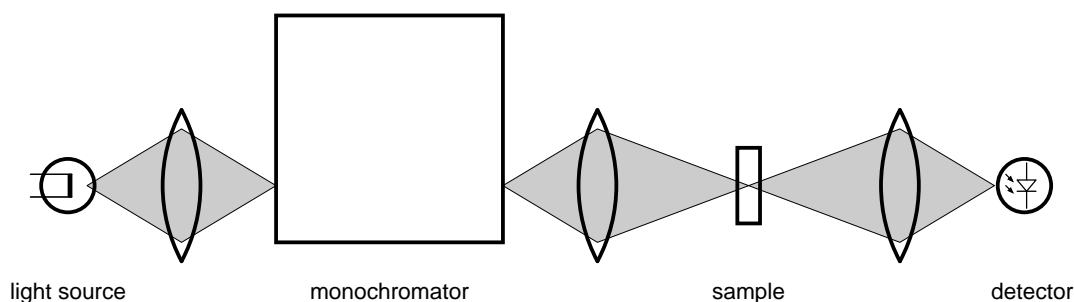


Figure 4.3: General setup of an absorption spectrometer with monochromator

range 633 – 1200 nm and a MCT-detector (HgCdTe) for the range 0.9 – 8 μm . The intrinsic scale of a Fourier spectrometer is the frequency, therefore no splitting of the spectral ranges was necessary. The better signal to noise ratio of one of the measured spectra suggested a crossover wavelength of roughly 2 μm . Features at shorter wavelengths were mainly extracted from the Varian spectra and those at longer wavelengths from the Bruker measurements.

Both types of spectrometers measure attenuation spectra in at least two steps. First a spectrum $I_0(k)$ without a sample is measured containing the spectral characteristic of the whole setup, e. g. the light source, optical components, and the detector. The second spectrum $I(k)$ is obtained with a sample inserted, and therefore the sample transmission is

$$T(k) = \frac{I(k)}{I_0(k)} \quad (4.8)$$

with the wavenumber k . Alternatively an absolute attenuation spectrum containing also reflection losses may be calculated by

$$\alpha^{abs}(k) = \ln \left(\frac{I_0(k)}{I(k)} \right) . \quad (4.9)$$

Spectrometers like the *Cary 5 G* use two measurement paths, one with sample and the other without, to pre-correct each data point in the spectrum and therefore achieve more accurate results. This keeps the influence of variable parameters as e.g. the CO_2 concentration

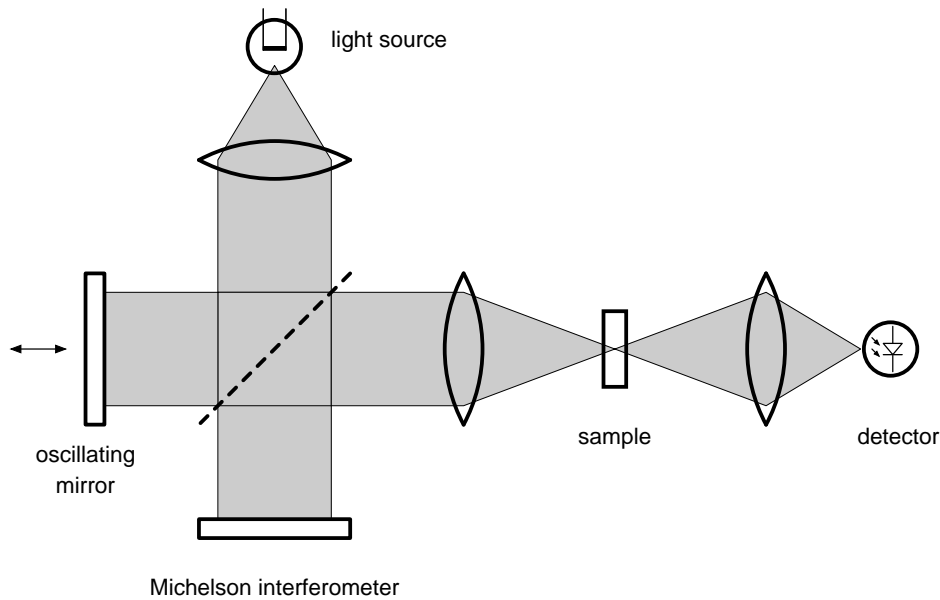


Figure 4.4: General setup of a Fourier transform spectrometer

in the air and temperature fluctuations smaller. Furthermore a spectrum obtained with a blocked sample path allows to correct for the dark current of the detector.

4.3 Analysis of measured spectra

To extract all necessary data from the raw absorption spectra received from the spectrometers, each spectrum was evaluated in a three-step process. At first the baseline of each spectrum had to be corrected, since we are only interested in rare earth dopants here and not in the properties of the glass host. The result of the first step is a spectrum of the absorption cross section of the dopant, used in the remaining evaluation steps and for laser simulations. In the next step the wavelengths and wavenumbers of the absorption peaks and the respective peak cross sections are estimated. These numbers are of limited value for energy level calculations and laser simulations, but important quantities to compare different rare earths and different host materials. In the final step the absorption lines are being integrated to get wavelength and wavenumber of the center of mass and the oscillator strength of each line. Each of these three steps will be discussed in more detail in the following paragraphs.

An important question is the accuracy of the extracted quantities. Starting with the estimated spectral uncertainty of the raw spectra, an appropriate error calculation is carried out for every step in the evaluation process. Therefore all numerical results can be given with a specified uncertainty. Nevertheless this uncertainty should not be interpreted as a σ -interval, because several error estimations are necessary on the way to the end results, and the actual error distribution is unknown. But these values are valuable to get an idea of individual uncertainties and especially to compare the accuracy of properties of different absorption lines.

All absorption lines were taken from at least two spectra with different dopant concentration and/or glass length. The lines from different spectra were evaluated separately and only the mean values of the results are presented in the tables of this chapter. Since for every value x_i an uncertainty Δx_i was available, the weighted mean

$$\bar{x} = \frac{\sum_i x_i / \Delta x_i}{\sum_i 1 / \Delta x_i} \quad (4.10)$$

was taken and the uncertainty of this mean value was calculated, using the equation

$$\Delta \bar{x} = \frac{1}{n} \sqrt{\sum_i [(x_i - \bar{x})^2 + \Delta x_i^2]} \quad (4.11)$$

where n is the number of x_i values.

Baseline correction. Figure 4.5 shows the uncorrected attenuation spectrum of the undoped glass sample 1011. It is obvious that the two spectrometers mentioned in the last

section cover the whole transmission window of ZBLAN glass. The window opens with the infrared (IR) edge at about 2000 cm^{-1} ($5\text{ }\mu\text{m}$). Radiation with lower energy is absorbed by vibrations of the glass matrix. Around 45000 cm^{-1} (220 nm) the window is closed at the ultraviolet (UV) edge, since radiation with higher energy is exciting electrons to the conducting band in the glass matrix. The level of the baseline at low energies in figure 4.5 is due to Fresnel reflections of approximately 4 % on each side, i.e. $T \sim 92\%$. Towards higher energies the wing of the UV edge leads to a slightly rising baseline. Rayleigh scattering should *not* be visible in such a thin glass, since in the attenuation equation

$$\alpha_R = \frac{A}{\lambda^4}, \quad (4.12)$$

the order of magnitude of the constant A is typically $1\text{ dB km}^{-1}\text{ }\mu\text{m}^4$ [66]. In case of the 8.3 mm thick sample in figure 4.5, the attenuation due to Rayleigh scattering should be about 0.005 dB at 50000 cm^{-1} .

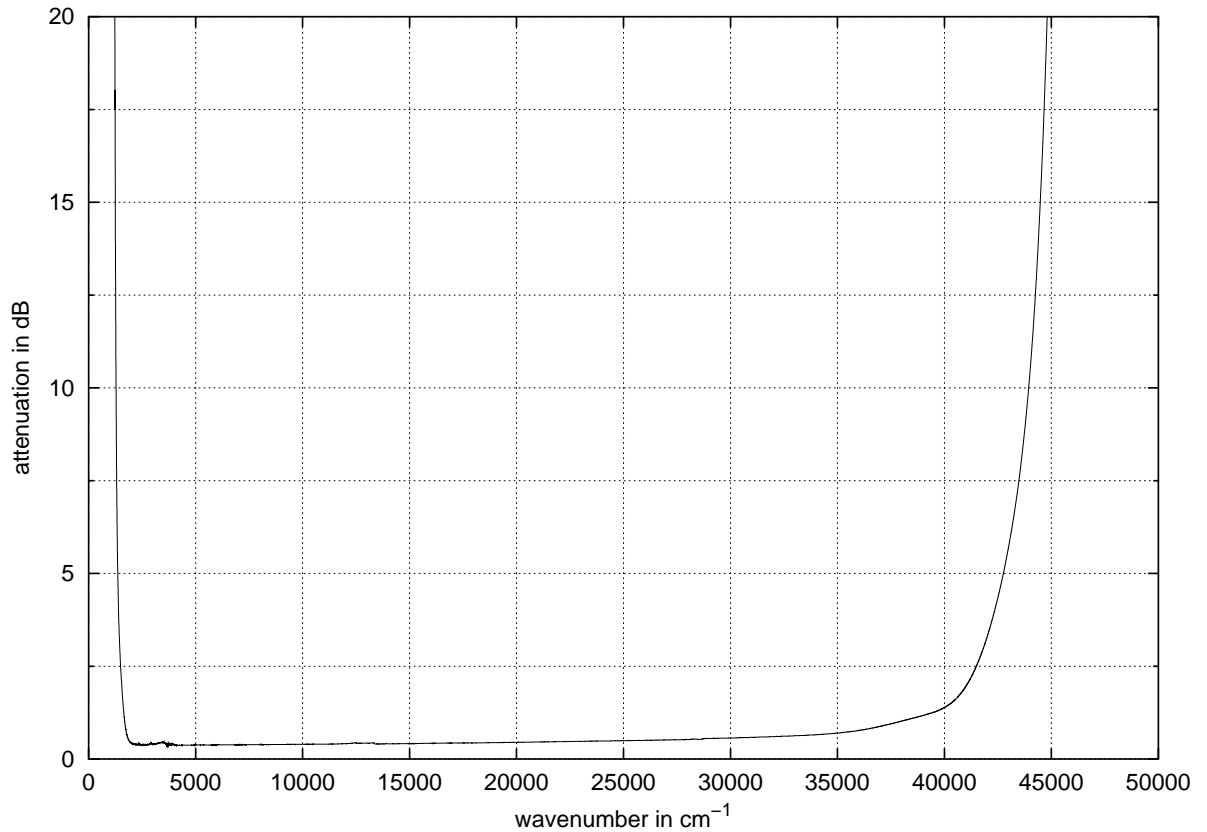


Figure 4.5: Transmission window of ZBLAN glass. Sample 1011, length $8.30 \pm 0.10\text{ mm}$

The Fresnel reflection at the refractive index step of a glass surface for an incident beam perpendicular to the surface is

$$R(\lambda) = \left(\frac{n(\lambda) - n_0}{n(\lambda) + n_0} \right)^2, \quad (4.13)$$

with the refractive index of the glass $n(\lambda)$ from equation (4.6) and the refractive index $n_0 = 1$ of the air. This reflection occurs on both surfaces of the glass and the resulting attenuation

$$\alpha_F^{abs}(\lambda) = \ln \left(\frac{1}{(1 - R(\lambda))^2} \right) \quad (4.14)$$

should simply be subtracted from all measurements. However, this method does not work well since the surfaces are never placed strictly perpendicular to the beam, otherwise unwanted interference effects would occur. This, on the one hand, changes equation (4.13) and, on the other hand, leads to a small vertical offset of the beam. In case of the *IFS 25* the offset causes significant variations in the detector signal because of its small detecting area. When the spectrometer was not well adjusted, even transmissions nominally above 100 % were observed when the offset accidentally shifted the beam to the center of the detector.

The dependence of the IR and UV absorption on the thickness l of the glass sample should follow the usual absorption law

$$I = I_0 \exp(\alpha l), \quad (4.15)$$

with the material specific and wavelength dependent parameter $\alpha(\lambda)$, extractable in principle from figure 4.5. However, it was observed that this equation can indeed be used only at the IR edge since the UV absorption besides equation (4.15) in addition depends strongly on the individual glass sample. The origin may be a varying content of microscopic crystals or bubbles in the samples or the influence of higher rare earth configurations.

But as a general method was needed to extract the rare earth absorption lines from the raw spectra, each spectrum was first split into pieces, each containing an individual absorption line or a group of overlapping lines and a certain part of baseline on both sides. Then a new spectrum with ten times reduced resolution was calculated from each piece. Because the monochromator spectrometer delivered spectra on a wavelength scale, these spectra were not equidistant when using wavenumbers. To avoid additional errors from the interpolation to a equidistant grid, the following trick was used to reduce the resolution without changing the original non-equidistant wavenumber grid: The spectrum was transformed to the time domain by a Fourier transformation, then apodised by half of a Gaussian function with a suitably chosen width, and transformed back to the wavenumber domain. The difference of the original and the smoothed spectra is more or less the noise contained in the measurement data, and the absolute value of this difference is used as the estimated uncertainty of the spectrum. Next a “rubber band” was constructed for the smoothed spectrum, consisting of a sequence of straight lines with increasing slope as close as possible but always below the

spectrum at every data point. This “rubber band” was taken as the baseline and subtracted from the original measurement as shown in figure 4.6.

The rubber band method fails if the real baseline changes its slope significantly below the absorption line. This is important especially at the sharp IR edge in contrast to the somewhat smoother UV edge (see figure 4.5). Fortunately in case of the IR edge, the absorption law in equation (4.15) can be used. Figure 4.7 shows an example where the baseline was taken from the undoped ZBLAN sample 1011 and then transformed to the length of the cerium sample using equation (4.15). This method is expected to be accurate as long as measurements with different sample lengths or different dopant concentrations result in the same cross section spectra.

The resulting absorption line of the rare earth dopant depends on the thickness of the glass sample and the concentration n_I of the dopant from equation (4.4). Therefore the attenuation spectrum is converted to a cross section spectrum, which is a material constant. The cross section $\sigma(k)$ is defined as the coefficient in the differential equation for the attenuation (see

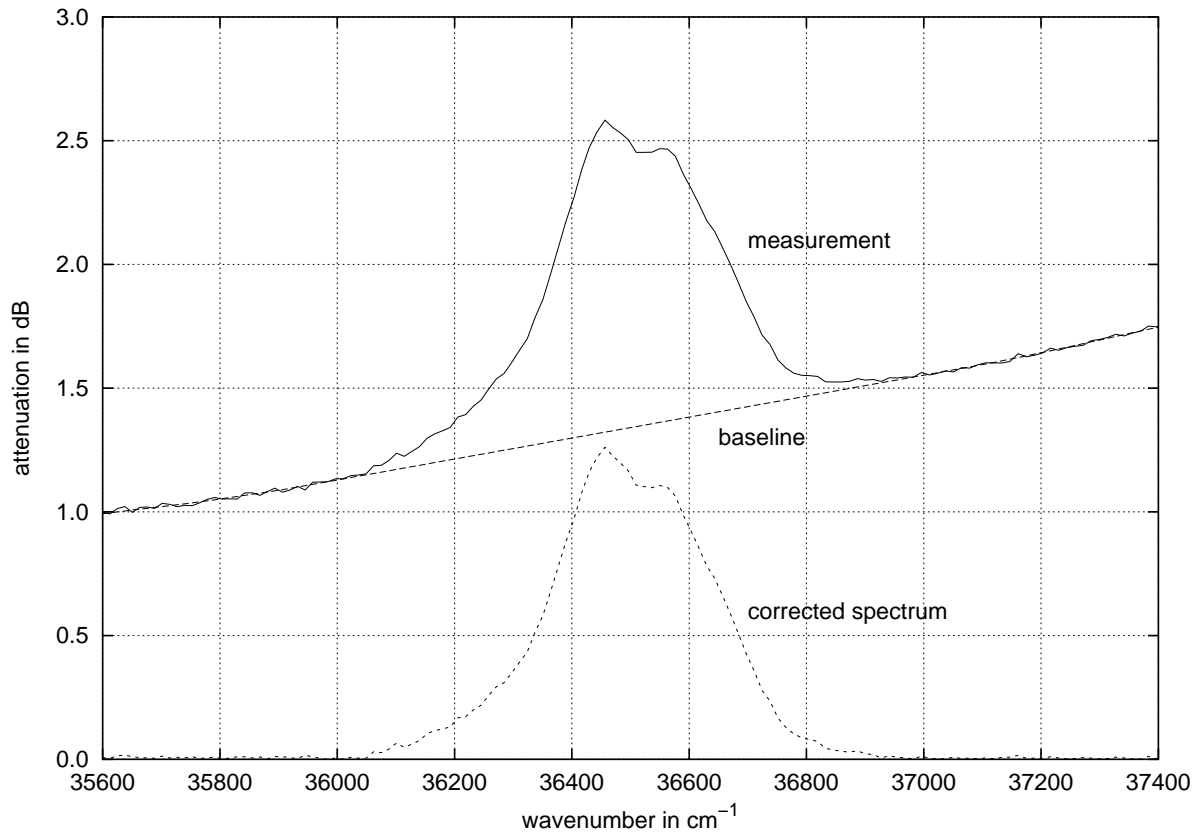


Figure 4.6: Baseline correction of the erbium line ${}^2\text{H}_{9/2}^{(2)}$. Sample 1032, length 16.38 ± 0.10 mm

also (2.18))

$$\frac{dI(k)}{dx} = -\sigma(k) n_I I(k) \quad (4.16)$$

and is therefore characteristic of a specific rare earth ion in a certain host material. The attenuation spectrum is converted using the equation

$$\sigma(k) = \frac{\alpha^{abs}(k)}{l\gamma p} \quad (4.17)$$

where l is the length of the sample, p the molar concentration as defined in equation (4.1), and γ the conversion factor from equation (4.5). Since all quantities in this equation are independent, the corresponding relative uncertainty may be calculated by the Gaussian error distribution

$$\frac{\Delta\sigma}{\sigma} = \sqrt{\left(\frac{\Delta\alpha}{\alpha}\right)^2 + \left(\frac{\Delta\gamma}{\gamma}\right)^2 + \left(\frac{\Delta p}{p}\right)^2 + \left(\frac{\Delta l}{l}\right)^2}. \quad (4.18)$$

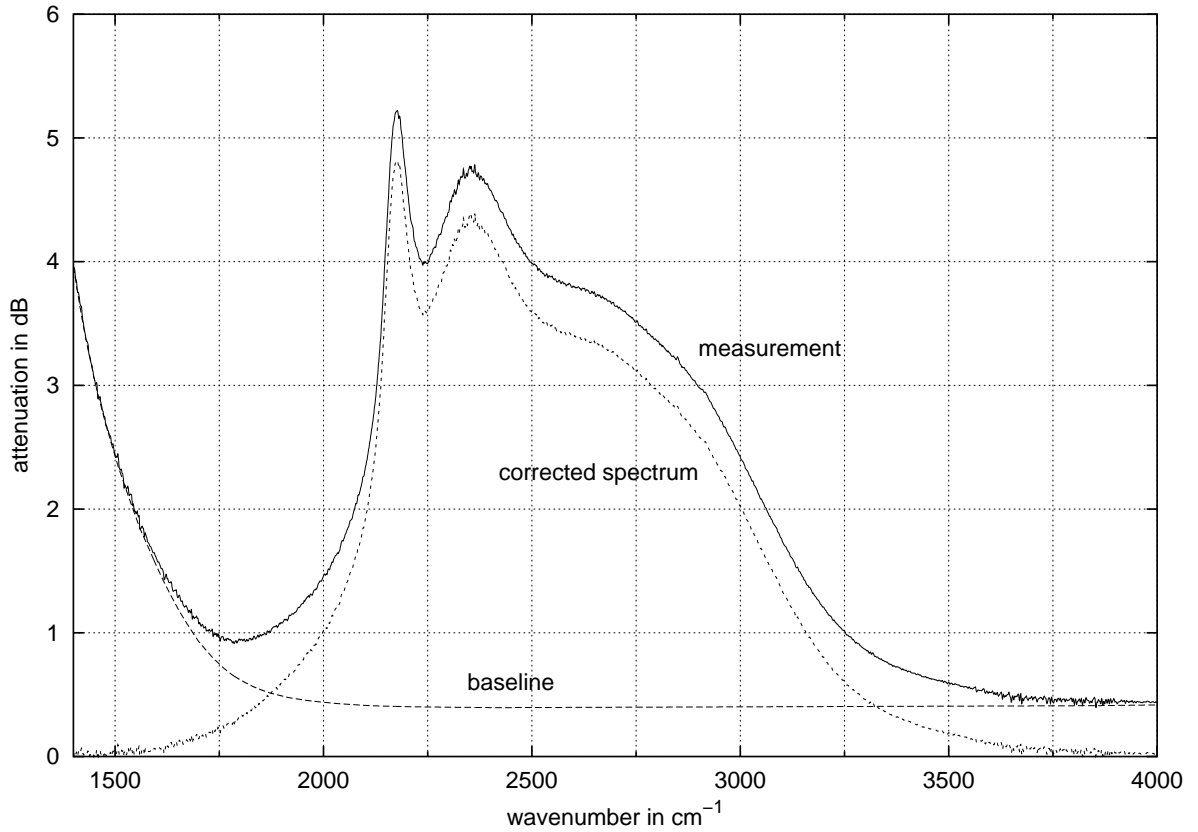


Figure 4.7: Baseline correction of the cerium line $^2F_{7/2}$. Sample 1012, length 7.15 ± 0.10 mm

The variation of the cross section spectra obtained by different absorption lengths and different glass samples usually stayed inside the range given by this uncertainty. This certifies the estimated uncertainty of the raw spectra, as this is often the dominant term in equation (4.18).

Peak search. Searching a peak position is a standard process which could also be done manually. But in order to find not only the peak position, but also an estimation of the accuracy of this position, the following algorithm was used: An interval bracketing the peak is set manually. Inside this interval, the first derivative of the curve was calculated several times with decreasing resolution until the resolution spanned the whole interval. Especially at a high resolution the first derivative changes the sign several times near the maximum and the uncertainty interval is given by the interval between the first and the last sign changes plus half of the inverse resolution on both sides. With decreasing resolution the curve becomes smoother and, as a consequence, the length of the sign changing interval decreases, while the value of the inverse resolution increases. From all these uncertainty intervals the smallest one is picked as $2\Delta k_p$ with the peak position k_p in the center. The peak cross section and its uncertainty are taken from the cross section spectrum calculated in the first evaluation step as explained in the last paragraph.

In the literature together with the peak cross section σ_p the effective linewidth $\Delta\lambda_{eff}$ is usually specified, which is defined as

$$\Delta\lambda_{eff} = \frac{\int I(\lambda)d\lambda}{I(\lambda_p)}, \quad (4.19)$$

where the integral spans the full absorption (or emission) line, and instead of the intensity I the cross section can be used as well. Equivalent to this definition is the statement that the product of the peak cross section and the effective linewidth is the area below the cross section spectrum of the appropriate line. The spectral uncertainty of the cross section may also be integrated and gives the uncertainty of the effective linewidth. The effective linewidth expressed in wavenumbers is given analogously by

$$\Delta k_{eff} = \frac{\int I(k)dk}{I(k_p)}, \quad (4.20)$$

and both quantities are connected by

$$\Delta\lambda_{eff} = \frac{\Delta k_{eff}}{k_p^2} \quad \text{and} \quad \Delta k_{eff} = \frac{\Delta\lambda_{eff}}{\lambda_p^2}. \quad (4.21)$$

Overlap of absorption lines. Difficulties with the evaluation of the effective linewidth arise if several absorption lines overlap. In these cases attempts were made to split the lines by a special technique. These separated lines were also necessary to calculate the oscillator

strength as described in the next paragraph. First of all, a fit with several Gauss functions was applied to the spectrum of the group of absorption lines, one or more Gauss functions for each line. The sum of the fitted functions is usually different from the actual cross section spectrum because the real shape of the individual lines is normally not just a Gauss function. But because the sum of all lines must be the measured cross section spectrum, the fit functions in the next step were only used as weight functions. At each wavelength the measured cross section was distributed among all lines according to the value of their respective Gauss function(s) at that wavenumber. Therefore, it was assured that at each wavenumber the sum of all lines was exactly the measured cross section. Figure 4.8 shows an example of the results from this procedure.

Of course the fact that the sum of all separated lines resembles the measured spectrum is no guarantee for the accuracy of the line shapes. It seems reasonable to expect that the uncertainty is at maximum around the crossover of two lines. Therefore an additional uncertainty $\Delta\sigma_{a,i}$

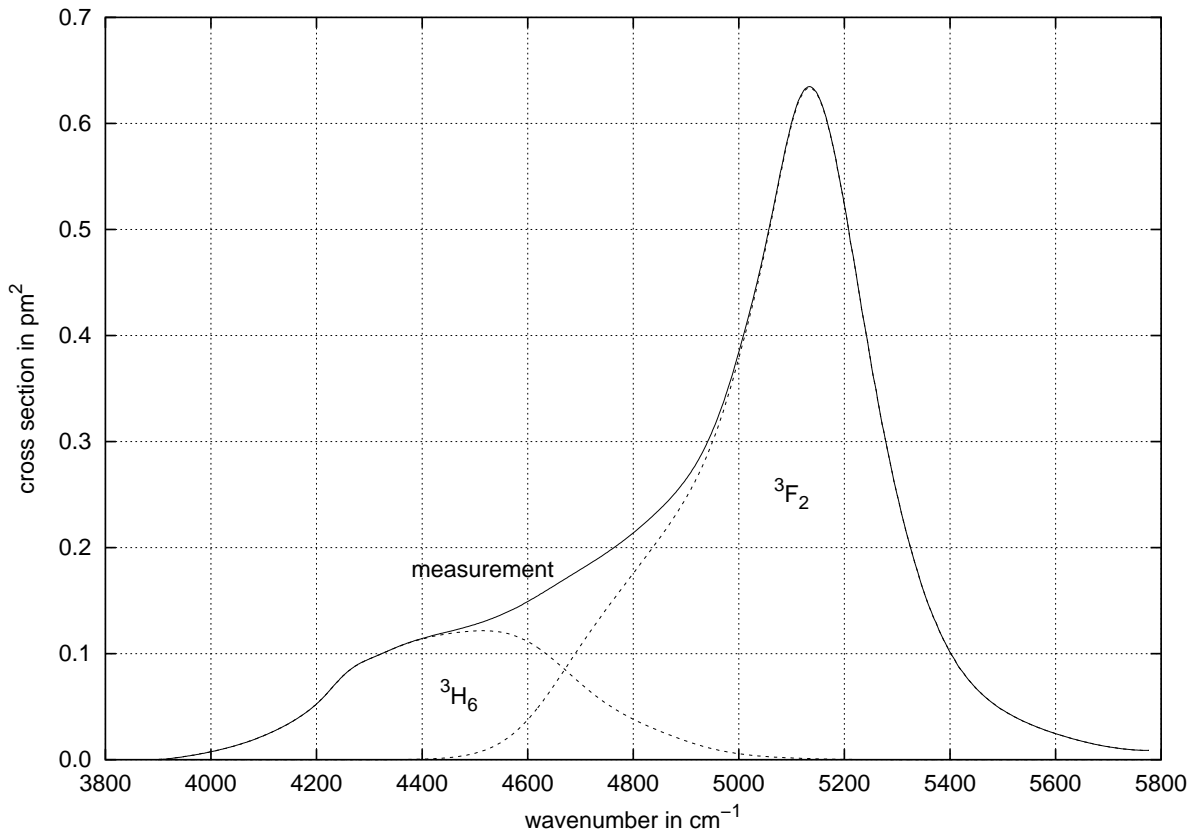


Figure 4.8: Separation of the absorption lines corresponding to the praseodymium levels ³H₆ and ³F₂.
Sample 958

was estimated with a maximum of $\sigma_i(k)/4$ if the weight factor $w_i(k)$ of the appropriate line i reaches 0.5:

$$\Delta\sigma_{a,i}(k) = \begin{cases} \frac{w_i(k)}{2} \sigma_i(k) & \text{for } 0 \leq w_i(k) < 0.5, \\ \frac{1 - w_i(k)}{2} \sigma_i(k) & \text{for } 0.5 \leq w_i(k) \leq 1. \end{cases} \quad (4.22)$$

The total spectral uncertainty of line i is then given by the Gaussian sum of the estimated additional uncertainty due to the split process and the uncertainty of the measured total cross section which should be independent of each other:

$$\Delta\sigma_i = \sqrt{\Delta\sigma_{a,i}^2 + \Delta\sigma^2}. \quad (4.23)$$

Peak positions of overlapping lines were determined after separating them.

Oscillator strength. The oscillator strength of a transition is proportional to the area below the appropriate absorption line as given by equation (2.20):

$$f = \frac{4\pi\epsilon_0 m_e c^2}{e^2 \pi} \int \sigma(k) dk \quad (4.24)$$

with the dielectric constant ϵ_0 , the mass of an electron m_e , the speed of light in vacuum c , and the charge of an electron e . Unfortunately, there is some confusion in the literature about this equation which appears in several forms. Some authors (e. g. [50]) erroneously include the dielectric correction in this equation. It seems that the origin of this error is one of Carnall's articles [55], which he corrected later [61].

The accuracy of the calculated oscillator strength is given by the integral of the spectral uncertainty of the cross section like for the effective linewidth in the last paragraph. In case of groups of overlapping lines, the oscillator strengths and their uncertainties are calculated for each separated line as well as for the group as a whole. The latter value can be given with much higher accuracy since the additional uncertainty due to the split process is not included in this case.

Connected with the area below the absorption line is the center of mass wavenumber k_{cm} , which divides the area into two equal parts. With the definition of the wavenumbers k_{\pm}

$$\int_{-\infty}^{k_{\pm}} [\sigma(k) \mp \Delta\sigma(k)] dk = \int_{k_{\pm}}^{\infty} [\sigma(k) \pm \Delta\sigma(k)] dk, \quad (4.25)$$

the value

$$\Delta k_{cm} = \frac{k_+ - k_-}{2} \quad (4.26)$$

was taken as the specified uncertainty of the center of mass position.

In the same way as the center of mass, the two wavenumbers $k_{-\sigma}$ and $k_{+\sigma}$ were calculated, which divide the area in the ratio 15:85 and 85:15 like the σ -interval of a Gaussian function.

They describe the extension of the absorption line like the effective linewidth, and their values are usually asymmetric to k_{cm} . The uncertainties of $k_{-\sigma}$ and $k_{+\sigma}$ were also calculated by equation (4.26), but with the definition of k_{\pm} changed in a straightforward manner. In case of $k_{-\sigma}$ in equation (4.25) a factor 15/85 must be applied to the right side, in case of $k_{+\sigma}$ it is a factor 85/15.

4.4 Ce:ZBLAN

The electronic configuration of triply ionized cerium is $[\text{Xe}]4f^1$ and the single f-electron results in just two LSJ -levels and a total of 14 Stark states. The ground level is $^2F_{5/2}$ and the excited level is $^2F_{7/2}$. Figure 4.9 shows the spectrum of the absorption cross section based on four measured attenuation spectra. The spectrum shows a broad absorption line with two peaks and a broad shoulder. They are related to three groups of Stark levels, a phenomenon which is well-known in rare earth absorption spectra, for example also for holmium [54]. The position

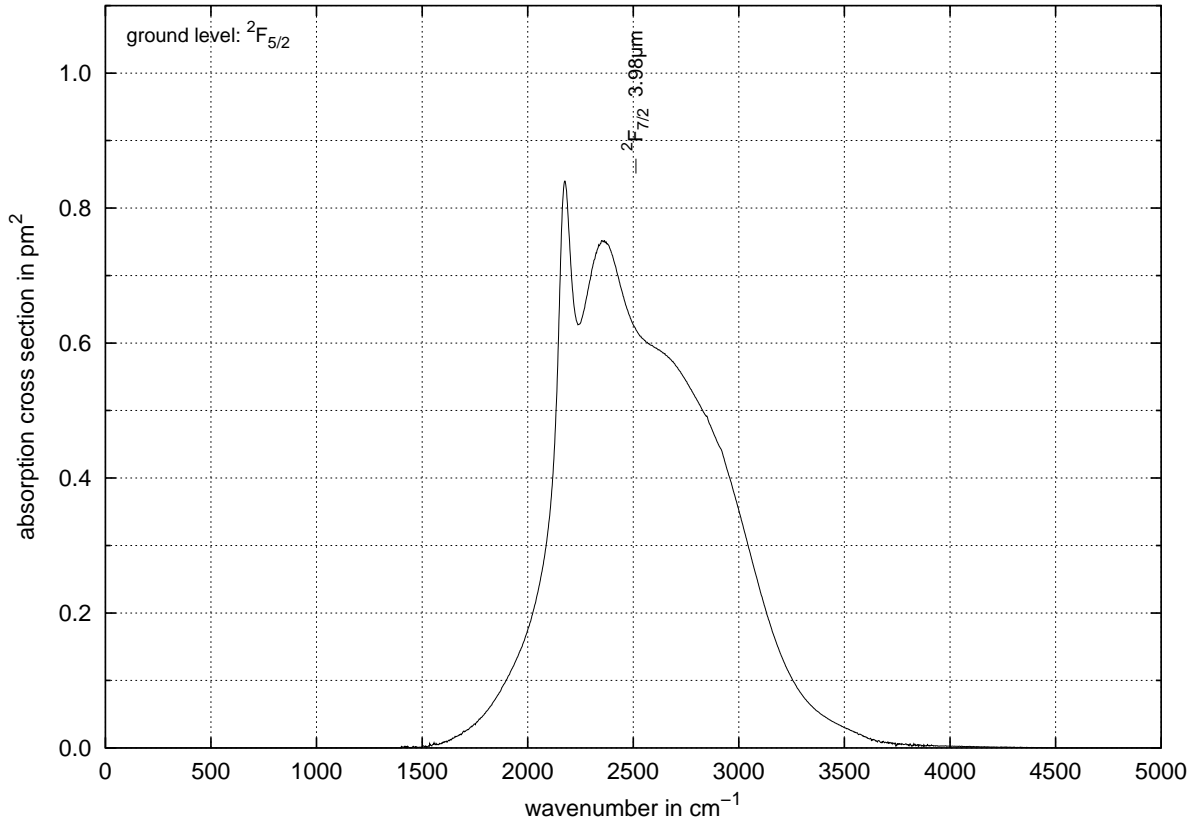


Figure 4.9: Spectrum of the absorption cross section of Ce:ZBLAN with center of mass position

Table 4.3: Peak positions and effective linewidth of Ce:ZBLAN (* relative uncertainty)

level	k_p cm^{-1}	λ_p nm	σ_p pm^2	rel.*	Δk_{eff} cm^{-1}	$\Delta \lambda_{eff}$ nm	rel.*
$^2F_{7/2}$	2176.0 ± 1.0	4595.5 ± 2.0	0.840 ± 0.008	0.9 %	780 ± 10	1650 ± 25	1.4 %
	2354 ± 7	4250 ± 15	0.751 ± 0.009	1.3 %			

Table 4.4: Oscillator strength and center of mass position of Ce:ZBLAN (* relative uncertainty)

level	f_{meas} 10^{-8}	rel.*	k_{cm} cm^{-1}	λ_{cm} nm	$\Delta k_{-\sigma}$ cm^{-1}	$\Delta k_{+\sigma}$ cm^{-1}
$^2F_{7/2}$	741 ± 8	1.0 %	2513 ± 5	3980 ± 9	-331.0 ± 2.5	$+423 \pm 4$

of the two peaks is given in table 4.3.

The oscillator strength of the single absorption transition in table 4.4 is relatively high. However, the wavelength of the transition with approximately $4 \mu\text{m}$ is so large that use of this transition is very uncommon and data are scarcely found in the literature. Carnall [39] found four Stark level transitions in $\text{Ce}^{3+}:\text{LaF}_3$ with the center of mass wavenumber $k_{cm} = 2470 \text{ cm}^{-1}$, which is comparable with the value in ZBLAN from table 4.4.

On the other hand, the transitions to the first excited configuration $[\text{Xe}]5d^1$ in the ultra-violet are of some interest. An overview of the work in this field is given in [3]. Of particular interest in our case is the photoinduced change of the refractive index in cerium doped fluoride glasses. An attractive application of this sensitivity are fiber Bragg gratings in fluoride fibers [67].

4.5 Pr:ZBLAN

Triply ionized praseodymium has the electronic configuration $[\text{Xe}]4f^2$. Due to equation (3.4) these two electrons can combine to a total of 91 different states, which build 13 energy levels in LS - or intermediate coupling. Figure 4.10 shows the absorptions to higher levels starting from the ground level 3H_4 . For each line or group of lines 2 – 6 measured spectra were evaluated. All levels were found except 1S_0 , which is located around 47000 cm^{-1} , i.e. outside the transmission window of ZBLAN glass. Furthermore, in section 5.4 we will see that the ground state absorption to 1S_0 is a very weak transition. One of the scarce measurement reports of this level is [68], where it was found at 46986 cm^{-1} in LaF_3 and its weakness was confirmed. Another report of this level is found in [69] where it was located at about 46500 cm^{-1} in a LaB_3O_6 crystal.

The transition to level 3H_5 again shows two peaks as in the cerium spectrum. The positions

of all peaks are collected in table 4.5 and only the (slightly) higher of the two peaks of $^3\text{H}_5$ was used to calculate the effective linewidth. The level $^3\text{H}_6$ shows no separate peak in the spectrum. With an approximate range of $200 - 650\text{ cm}^{-1}$, the effective linewidths are all smaller than the value of cerium.

Table 4.6 shows the appropriate oscillator strengths and center of mass positions. Three groups of energy levels had to be separated. In the pair $^3\text{H}_6/^3\text{F}_2$ the first line is well defined, even though no peak can be observed, because the second line is very narrow and high. The third group on the other hand shows three quite distinct lines in the spectrum, one of which corresponds to the pair $^3\text{P}_1/^1\text{I}_6$, but it was impossible to split these two levels. The weakest of all absorption lines corresponds to the transition to $^1\text{G}_4$ at 1010 nm . This is the pump level of the praseodymium doped fiber amplifier at $1.3\text{ }\mu\text{m}$, and this weak absorption is one of the major problems of this amplifier [70]. The broad and strong absorption band from $^3\text{P}_0$ to $^3\text{P}_2$ absorbs the blue part of the visible spectrum and leads to the dark green color of the praseodymium doped glass samples.

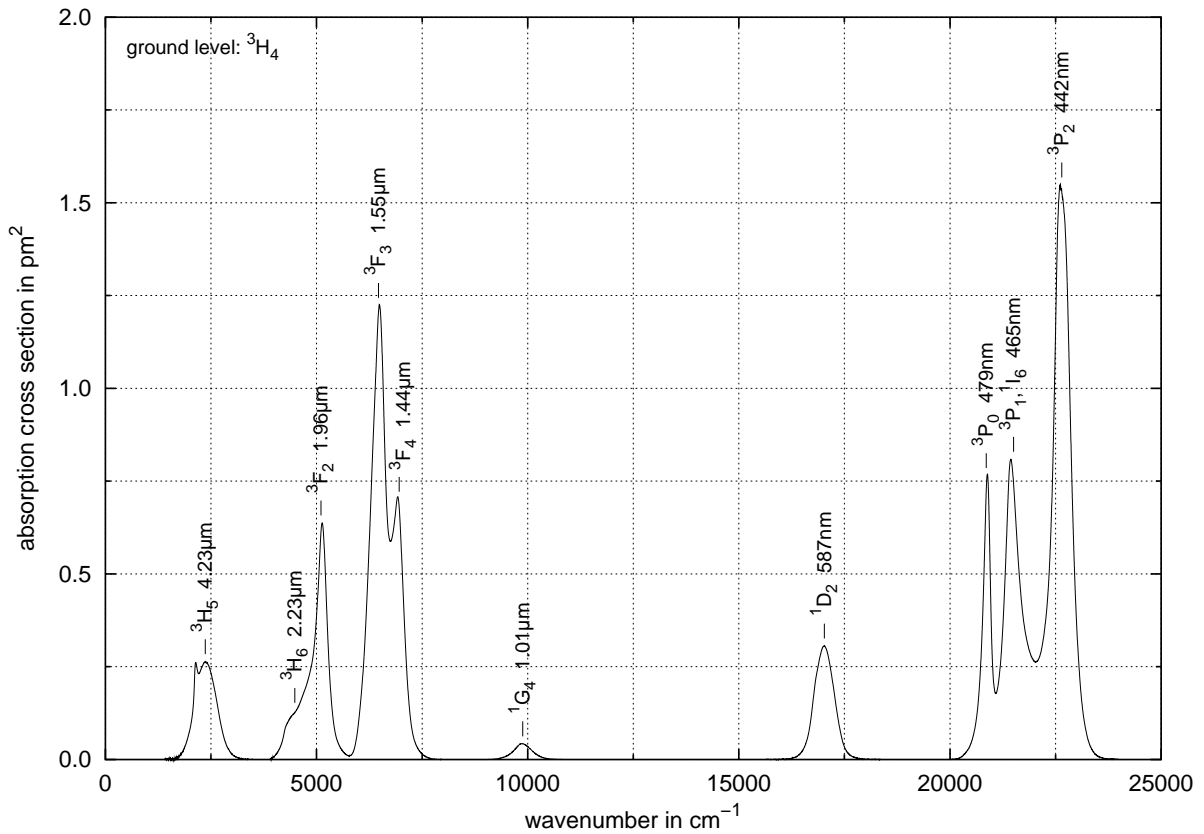


Figure 4.10: Spectrum of the absorption cross section of Pr:ZBLAN with center of mass positions

Table 4.5: Peak positions and effective linewidths of Pr:ZBLAN (* relative uncertainty)

level	k_p cm^{-1}	λ_p nm	σ_p pm^2	rel.*	Δk_{eff} cm^{-1}	$\Delta \lambda_{eff}$ nm	rel.*
$^3\text{H}_5$	2138 ± 3	4677 ± 7	0.262 ± 0.003	1.2 %	660 ± 15	1180 ± 25	1.9 %
	2364 ± 3	4230 ± 5	0.264 ± 0.003	1.2 %			
$^3\text{H}_6$	4523 ± 3	2211.0 ± 1.5	0.1240 ± 0.0025	2.0 %	550 ± 40	270 ± 20	7.4 %
$^3\text{F}_2$	5133.0 ± 1.0	1948.1 ± 0.4	0.636 ± 0.004	0.7 %	395 ± 10	150 ± 4	2.7 %
$^3\text{F}_3$	6489 ± 3	1541.2 ± 0.7	1.222 ± 0.009	0.7 %	460 ± 15	110 ± 3	2.8 %
$^3\text{F}_4$	6938.5 ± 1.0	1441.20 ± 0.20	0.640 ± 0.015	2.2 %	340 ± 20	70 ± 4	5.8 %
$^1\text{G}_4$	9857.5 ± 1.0	1014.45 ± 0.10	0.0427 ± 0.0005	1.2 %	548 ± 9	56.4 ± 0.9	1.6 %
$^1\text{D}_2$	17021 ± 5	587.50 ± 0.15	0.306 ± 0.010	3.2 %	575 ± 25	19.9 ± 0.8	4.1 %
$^3\text{P}_0$	20879 ± 3	478.94 ± 0.07	0.710 ± 0.025	3.9 %	225 ± 20	5.1 ± 0.5	9.1 %
$^3\text{P}_1, ^1\text{I}_6$	21440.5 ± 1.0	466.405 ± 0.020	0.810 ± 0.010	1.4 %	590 ± 30	12.9 ± 0.7	5.4 %
$^3\text{P}_2$	22606 ± 9	442.35 ± 0.20	1.545 ± 0.020	1.4 %	530 ± 15	10.40 ± 0.30	2.8 %

Table 4.6: Oscillator strengths and center of mass positions of Pr:ZBLAN (* relative uncertainty)

level	f_{meas} 10^{-8}	rel.*	k_{cm} cm^{-1}	λ_{cm} nm	$\Delta k_{-\sigma}$ cm^{-1}	$\Delta k_{+\sigma}$ cm^{-1}
$^3\text{H}_5$	196.0 ± 3.0	1.4 %	2365 ± 4	4229 ± 8	-245.0 ± 3.0	$+270 \pm 4$
$^3\text{H}_6$	77 ± 5	6.6 %	4485 ± 20	2230 ± 9	-220 ± 9	$+220 \pm 30$
$^3\text{F}_2$	283 ± 6	2.2 %	5105 ± 5	1959.0 ± 2.0	-230 ± 15	$+168 \pm 4$
group:	361 ± 3	0.9 %	5041 ± 3	1983.5 ± 1.0	-458 ± 5	$+202.0 \pm 2.5$
$^3\text{F}_3$	635 ± 15	2.5 %	6467 ± 7	1546.0 ± 1.5	-217 ± 5	$+200 \pm 15$
$^3\text{F}_4$	245 ± 15	5.4 %	6958 ± 10	1437.5 ± 2.0	-140 ± 15	$+164 \pm 8$
group:	881 ± 8	0.9 %	6558 ± 4	1524.9 ± 0.9	-258 ± 3	$+391 \pm 4$
$^1\text{G}_4$	26.4 ± 0.5	1.8 %	9883 ± 7	1011.9 ± 0.7	-234 ± 7	$+246 \pm 9$
$^1\text{D}_2$	200 ± 10	5.3 %	17025 ± 20	587.3 ± 0.7	-240 ± 20	$+240 \pm 25$
$^3\text{P}_0$	180 ± 15	9.7 %	20860 ± 10	479.40 ± 0.30	-120 ± 15	$+85 \pm 20$
$^3\text{P}_1, ^1\text{I}_6$	540 ± 30	5.6 %	21505 ± 20	465.0 ± 0.4	-260 ± 40	$+360 \pm 40$
$^3\text{P}_2$	925 ± 30	3.1 %	22645 ± 10	441.60 ± 0.20	-225 ± 20	$+228 \pm 9$
group:	1650 ± 30	2.0 %	22365 ± 30	447.1 ± 0.6	-1160 ± 30	$+413 \pm 9$

4.6 Er : ZBLAN

In triply ionized erbium there are 11 electrons in the 4f shell, it has the configuration $[\text{Xe}]4f^{11}$. Such a three-hole system, according to equation (3.4), has 364 Stark states in total and 41 levels in LS - or intermediate coupling. Figures 4.11 and 4.12 show the measured absorption spectrum containing all absorption transitions starting from the ground level $^4I_{15/2}$ found in the transmission window of the ZBLAN glass. For each line or group of lines 2 – 7 spectra were evaluated. The main transmission windows of Er : ZBLAN in the visible range are below the $^4F_{9/2}$ in the dark red region and above this line in the orange and yellow. Together with a small window in the blue region between $^4F_{7/2}$ and $^4F_{5/2}$, this results in a pink color of the erbium doped glass samples.

With the help of the calculations in section 5.5 it was possible to assign the appropriate states to all of these lines up to 40000 cm^{-1} . Only the two levels $^2P_{1/2}$ and $^4G_{5/2}$ are missing in the spectrum. Due to the energy level calculations they are expected at 33020 cm^{-1} and

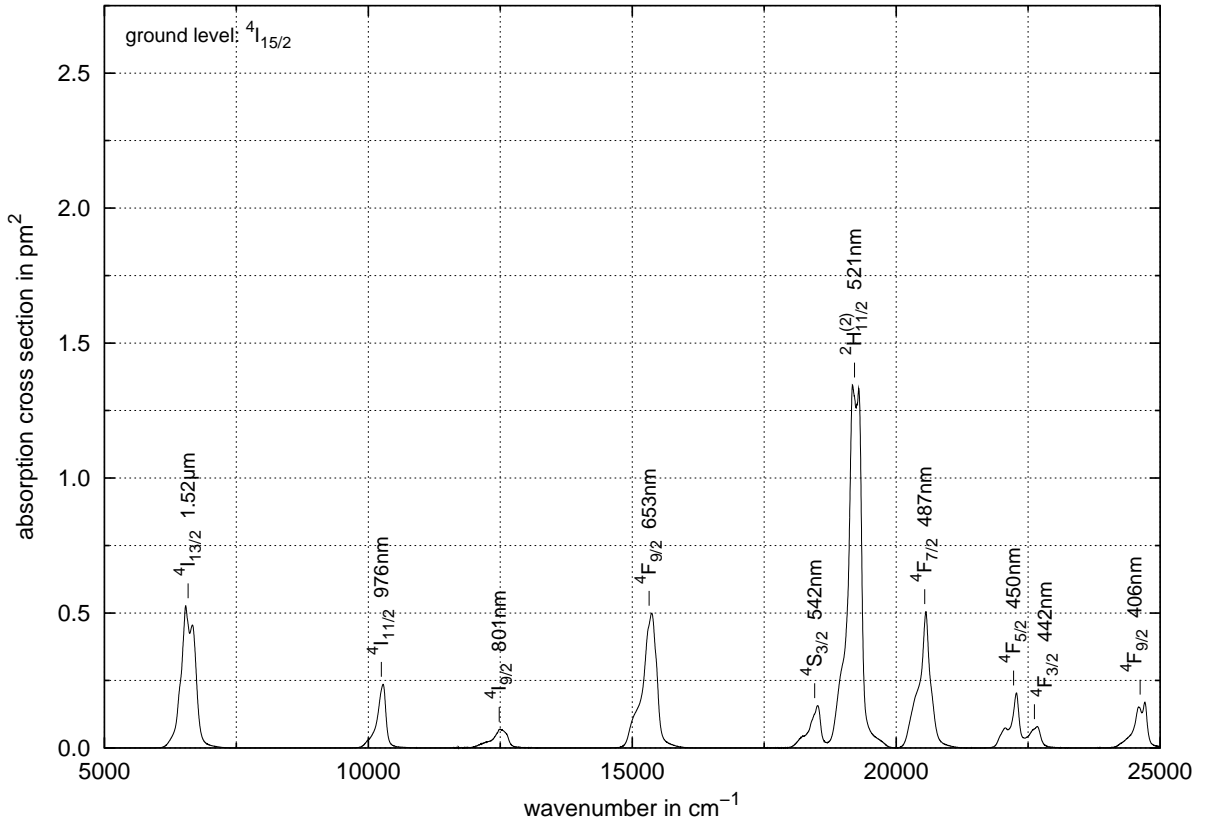


Figure 4.11: Spectrum of the absorption cross section of Er : ZBLAN below 25000 cm^{-1} with center of mass positions

33496 cm^{-1} respectively. But since the calculated oscillator strengths of ≈ 0 and $0.9 \cdot 10^{-8}$ are extremely small, their detection is indeed very unlikely. The oscillator strength of the transition ${}^4\text{I}_{15/2} \rightarrow {}^2\text{P}_{1/2}$ is vanishing due to the fact that this transition with $\Delta J = 7$ is forbidden by the selection rules given in chapter 2.

The position of the energy levels of triply ionized erbium is quite at optimum for pumping. Usual laser diodes available with high output power can be used around 980 nm and 800 nm. The level ${}^4\text{F}_{9/2}$ fits to the optimum wavelength of DCM dye, and the position of ${}^2\text{H}_{11/2}^{(2)}$ is nearly the first harmonic of Nd:YAG and not far from the 514 nm-line of an argon ion laser. Finally, the strong blue line of the argon ion laser at 488 nm can also be used.

In table 4.7 all peaks found in the erbium spectrum are listed. In cases where a line showed two peaks the effective linewidth was calculated for the higher peak only. The absorption line of ${}^4\text{G}_{11/2}$ in figure 4.12 has a somewhat unusual structure at its top. This structure was the same for all measurements and therefore an artefact due to low detector signal can be

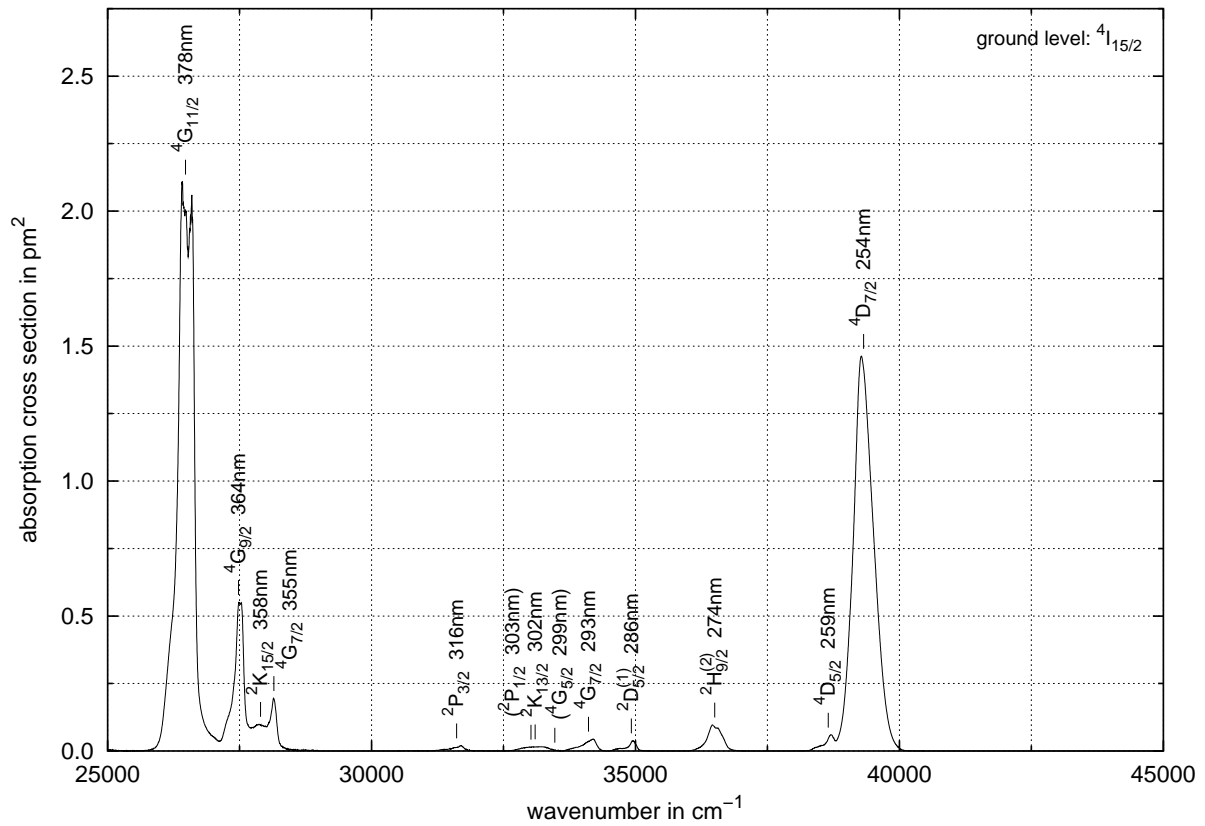


Figure 4.12: Spectrum of the absorption cross section of Er:ZBLAN above 25000 cm^{-1} with center of mass positions. The levels in parantheses were not measured and therefore their calculated position is shown.

excluded. Furthermore its calculated oscillator strength from section 5.5 fits the measured value. The range of the effective linewidths with approximately $200 - 600 \text{ cm}^{-1}$ is similar to praseodymium and the same is true for the span of peak cross sections.

The measured oscillator strengths and center of mass positions of all absorption lines are shown in table 4.8. The values of the oscillator strengths cover a range of $7 - 900 \cdot 10^{-8}$. Four groups of levels had to be split to individual lines, which was no problem for the pairs $^4\text{S}_{3/2}/^2\text{H}_{11/2}^{(2)}$ and $^4\text{F}_{5/2}/^4\text{F}_{3/2}$. In the group from $^4\text{G}_{11/2}$ up to $^4\text{G}_{7/2}$ separation of the dominating $^4\text{G}_{11/2}$ is also easy, but the three other lines overlap so strongly that in case of $^4\text{G}_{7/2}$ the estimated uncertainty of the oscillator strength is larger than the value itself. This effect is even stronger for $^4\text{D}_{5/2}$, where the 50 times larger neighbor $^4\text{D}_{7/2}$ leads to an uncertainty 1.5 times larger than the oscillator strength.

Table 4.7: Peak positions and effective linewidths of Er:ZBLAN (* relative uncertainty)

level	k_p cm^{-1}	λ_p nm	σ_p pm^2	rel.*	Δk_{eff} cm^{-1}	$\Delta \lambda_{eff}$ nm	rel.*
$^4\text{I}_{13/2}$	6539.0 ± 1.0	1529.30 ± 0.25	0.527 ± 0.009	1.8 %	313 ± 6	73.5 ± 1.5	1.8 %
	6668 ± 3	1499.7 ± 0.7	0.455 ± 0.005	1.1 %			
$^4\text{I}_{11/2}$	10280.0 ± 1.0	972.77 ± 0.09	0.235 ± 0.015	6.1 %	210 ± 10	19.5 ± 1.0	5.3 %
$^4\text{I}_{9/2}$	12487 ± 7	800.8 ± 0.4	0.0690 ± 0.0010	1.7 %	365 ± 10	23.5 ± 0.8	3.4 %
$^4\text{F}_{9/2}$	15369.0 ± 1.0	650.66 ± 0.04	0.50 ± 0.03	6.2 %	330 ± 20	13.9 ± 0.8	5.9 %
$^4\text{S}_{3/2}$ $^2\text{H}_{11/2}^{(2)}$	18513 ± 3	540.15 ± 0.09	0.157 ± 0.004	2.5 %	280 ± 30	8.1 ± 0.9	11.2 %
	19171 ± 3	521.62 ± 0.08	1.34 ± 0.04	2.8 %			
	19290.5 ± 1.0	518.395 ± 0.025	1.33 ± 0.03	2.5 %			
$^4\text{F}_{7/2}$	20563.5 ± 1.0	486.300 ± 0.025	0.505 ± 0.020	3.6 %	272 ± 6	6.45 ± 0.15	2.4 %
$^4\text{F}_{5/2}$ $^4\text{F}_{3/2}$	22068 ± 7	453.15 ± 0.15	0.0745 ± 0.0015	2.2 %	215 ± 10	4.35 ± 0.20	5.0 %
	22278.0 ± 1.0	448.870 ± 0.020	0.200 ± 0.010	5.9 %			
	22673.5 ± 1.0	441.040 ± 0.020	0.0795 ± 0.0025	3.4 %			
$^4\text{F}_{9/2}$	24591 ± 9	406.65 ± 0.15	0.150 ± 0.006	4.1 %	295 ± 15	4.85 ± 0.25	5.3 %
	24710.0 ± 1.0	404.695 ± 0.015	0.170 ± 0.015	8.0 %			
$^4\text{G}_{11/2}$	26412 ± 7	378.60 ± 0.10	2.10 ± 0.15	6.0 %	375 ± 20	5.4 ± 0.3	5.7 %
	26594 ± 7	376.03 ± 0.10	2.05 ± 0.15	7.9 %			
$^4\text{G}_{9/2}$	27515 ± 25	363.5 ± 0.3	0.55 ± 0.05	8.6 %	240 ± 50	3.2 ± 0.7	21.2 %
$^2\text{K}_{15/2}$	27870 ± 15	358.80 ± 0.20	0.0975 ± 0.0030	2.9 %	350 ± 250	5 ± 3	71.9 %
$^4\text{G}_{7/2}$	28146.0 ± 1.0	355.285 ± 0.015	0.185 ± 0.025	12.7 %	150 ± 150	2.0 ± 1.5	90.9 %
$^2\text{P}_{3/2}$	31695 ± 15	315.50 ± 0.15	0.0190 ± 0.0020	10.1 %	320 ± 50	3.2 ± 0.5	17.1 %

Table 4.7: Peak positions and effective linewidths of Er:ZBLAN (* relative uncertainty) (*continued*)

level	k_p cm^{-1}	λ_p nm	σ_p pm^2	rel.*	Δk_{eff} cm^{-1}	$\Delta \lambda_{\text{eff}}$ nm	rel.*
$^2\text{K}_{13/2}$	33210 ± 70	301.2 ± 0.6	0.0152 ± 0.0009	5.8 %	610 ± 50	5.5 ± 0.5	8.2 %
$^4\text{G}_{7/2}$	34189.0 ± 1.0	292.492 ± 0.009	0.0440 ± 0.0030	6.3 %	320 ± 15	2.70 ± 0.15	5.4 %
$^2\text{D}_{5/2}^{(1)}$	34950.0 ± 1.0	286.124 ± 0.008	0.038 ± 0.005	12.3 %	210 ± 25	1.70 ± 0.20	10.9 %
$^2\text{H}_{9/2}^{(2)}$	36457.5 ± 1.0	274.291 ± 0.008	0.097 ± 0.008	8.4 %	335 ± 25	2.50 ± 0.20	7.1 %
$^4\text{D}_{5/2}$	38691.5 ± 1.0	258.454 ± 0.007	0.053 ± 0.008	14.2 %	200 ± 300	1.5 ± 2.0	131.7 %
$^4\text{D}_{7/2}$	39277.5 ± 1.0	254.598 ± 0.006	1.46 ± 0.10	6.6 %	455 ± 25	2.95 ± 0.15	5.3 %

Table 4.8: Oscillator strengths and center of mass positions of Er:ZBLAN (* relative uncertainty)

level	f_{meas} 10^{-8}	rel.*	k_{cm} cm^{-1}	λ_{cm} nm	$\Delta k_{-\sigma}$ cm^{-1}	$\Delta k_{+\sigma}$ cm^{-1}
$^4\text{I}_{13/2}$	186.5 ± 3.0	1.5 %	6585 ± 3	1518.5 ± 0.7	-134 ± 4	$+134 \pm 3$
$^4\text{I}_{11/2}$	56 ± 3	5.8 %	10246 ± 8	976.0 ± 0.7	-135 ± 10	$+81 \pm 9$
$^4\text{I}_{9/2}$	28.7 ± 0.8	2.9 %	12480 ± 6	801.3 ± 0.4	-235 ± 15	$+141 \pm 6$
$^4\text{F}_{9/2}$	185 ± 15	7.3 %	15320 ± 15	652.7 ± 0.7	-195 ± 20	$+130 \pm 15$
$^4\text{S}_{3/2}$	49 ± 6	11.6 %	18455 ± 20	541.9 ± 0.6	-195 ± 20	$+100 \pm 200$
$^2\text{H}_{11/2}^{(2)}$	475 ± 15	3.0 %	19209 ± 7	520.60 ± 0.20	-150 ± 8	$+115 \pm 5$
group:	525 ± 15	2.9 %	19194 ± 6	521.00 ± 0.15	-245 ± 15	$+126 \pm 5$
$^4\text{F}_{7/2}$	155 ± 4	2.5 %	20538 ± 5	486.90 ± 0.10	-180 ± 6	$+123 \pm 6$
$^4\text{F}_{5/2}$	49.0 ± 2.5	5.4 %	22225 ± 10	449.95 ± 0.20	-189 ± 9	$+88 \pm 8$
$^4\text{F}_{3/2}$	25.5 ± 2.0	7.8 %	22620 ± 15	442.10 ± 0.30	-140 ± 30	$+110 \pm 10$
group:	74.5 ± 3.0	3.9 %	22287 ± 8	448.70 ± 0.15	-205 ± 10	$+350 \pm 10$
$^4\text{F}_{9/2}$	57 ± 3	5.6 %	24620 ± 10	406.20 ± 0.20	-170 ± 15	$+120 \pm 10$
$^4\text{G}_{11/2}$	900 ± 60	6.6 %	26475 ± 15	377.70 ± 0.25	-160 ± 15	$+140 \pm 15$
$^4\text{G}_{9/2}$	150 ± 40	23.9 %	27480 ± 40	363.9 ± 0.5	-200 ± 300	$+90 \pm 30$
$^2\text{K}_{15/2}$	40 ± 30	77.2 %	27900 ± 500	359 ± 6	-100 ± 500	$+150 \pm 150$
$^4\text{G}_{7/2}$	30 ± 30	100.1 %	28100 ± 600	355 ± 7	-100 ± 600	$+70 \pm 50$
group:	1120 ± 70	6.2 %	26525 ± 20	377.00 ± 0.30	-180 ± 15	$+910 \pm 60$
$^2\text{P}_{3/2}$	7.0 ± 1.5	18.1 %	31610 ± 50	316.4 ± 0.5	-250 ± 150	$+130 \pm 40$
$^2\text{K}_{13/2}$	10.5 ± 0.9	8.8 %	33095 ± 25	302.15 ± 0.20	-240 ± 40	$+215 \pm 20$

Table 4.8: Oscillator strengths and center of mass positions of Er:ZBLAN (* relative uncertainty)
(continued)

level	f_{meas} 10^{-8}	rel.*	k_{cm} cm^{-1}	λ_{cm} nm	$\Delta k_{-\sigma}$ cm^{-1}	$\Delta k_{+\sigma}$ cm^{-1}
$^4G_{7/2}$	16.0 ± 1.0	6.6 %	34110 ± 15	293.15 ± 0.15	-210 ± 20	$+125 \pm 15$
$^2D_{5/2}^{(1)}$	9.0 ± 1.0	12.8 %	34920 ± 20	286.35 ± 0.15	-195 ± 30	$+85 \pm 20$
$^2H_{9/2}^{(2)}$	37 ± 3	8.7 %	36495 ± 20	274.00 ± 0.15	-140 ± 25	$+145 \pm 20$
$^4D_{5/2}$	15 ± 20	139.0 %	38650 ± 300	258.5 ± 2.0	-150 ± 100	$+100 \pm 400$
$^4D_{7/2}$	750 ± 50	7.2 %	39325 ± 25	254.30 ± 0.15	-185 ± 25	$+210 \pm 25$
group:	770 ± 50	7.1 %	39315 ± 25	254.35 ± 0.15	-190 ± 30	$+220 \pm 20$

4.7 Tm:ZBLAN

The 12-electron configuration $[Xe]4f^{12}$ of triply ionized thulium can also be treated as a two-hole system. The states are therefore the same as in praseodymium, i.e. 91 in total and 13 states in LS - or intermediate coupling. Figure 4.13 shows the cross section spectrum due to absorption from the ground level 3H_6 . For each absorption line or group of lines 2 – 5 spectra were evaluated. As in the case of praseodymium, all levels were detected except 1S_0 , which is expected at around 75000 cm^{-1} . This value is obviously too large to be detected and anyway the calculations show that the ground state absorption to this level would be extremely weak.

Table 4.9 contains all peaks observed in the thulium spectrum. Energy level 1G_4 has two peaks, the higher one was used to calculate the effective linewidth. The levels 1I_6 and 3P_0 are overlapping and not separable. Energy level calculations showed that the two-fold structure of the according line is not related to the energy difference of these two levels. On the one hand, the peak cross sections in the thulium spectrum are relatively low and, on the other hand, the effective linewidths in the approximate range $300 - 850\text{ cm}^{-1}$ are relatively large.

The absorption spectrum of triply ionized thulium does not fit the wavelengths of available pump lasers as well as erbium, but especially the level 3H_4 is very attractive, since laser diodes around 790 nm are available with high output power. Furthermore, laser diodes around 680 nm can be used as pump sources.

The values of the measured oscillator strengths and center of mass positions are listed in table 4.10. Two groups of absorption lines had to be splitted. In case of 3F_2 the much larger neighbor level 3F_3 results in a high uncertainty. In the group from 1I_6 to 3P_1 , the latter was separated without difficulties, but the remaining two levels were not separated for the reasons mentioned above. The relatively low accuracy for a non-overlapping absorption line in case of 1D_2 is due to the fact that this part of the spectrum accidentally was not measured with same high resolution as the other parts. From the visible spectrum 1G_4 absorbs a part of blue and the levels from 3H_4 to 3F_2 absorb large parts of red, which results in a yellow-brown color of the thulium doped glass samples.

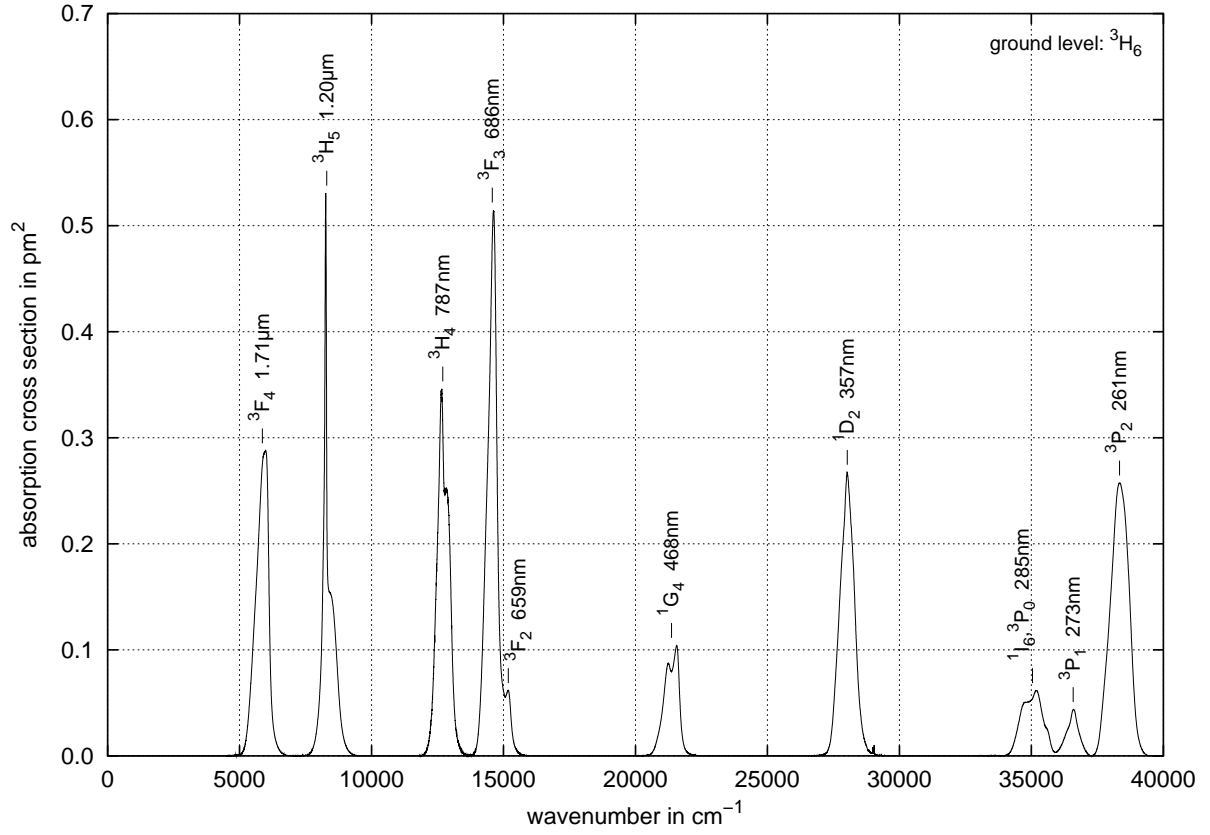


Figure 4.13: Spectrum of the absorption cross section of Tm:ZBLAN with center of mass positions

Table 4.9: Peak positions and effective linewidths of Tm:ZBLAN (* relative uncertainty)

level	k_p cm^{-1}	λ_p nm	σ_p pm^2	rel.*	Δk_{eff} cm^{-1}	$\Delta \lambda_{\text{eff}}$ nm	rel.*
$^3\text{F}_4$	5984 ± 7	1671.0 ± 2.0	0.2875 ± 0.0025	0.8 %	575 ± 9	160.5 ± 2.5	1.6 %
$^3\text{H}_5$	8262.0 ± 1.0	1210.35 ± 0.15	0.53 ± 0.05	10.3 %	260 ± 10	38.0 ± 2.0	4.7 %
$^3\text{H}_4$	12652 ± 5	790.4 ± 0.3	0.344 ± 0.005	1.6 %	515 ± 15	32.2 ± 0.8	2.5 %
$^3\text{F}_3$	14619 ± 5	684.05 ± 0.25	0.515 ± 0.030	5.5 %	435 ± 20	20.5 ± 1.0	4.9 %
$^3\text{F}_2$	15187 ± 3	658.45 ± 0.15	0.060 ± 0.004	6.4 %	300 ± 100	13 ± 4	34.0 %
$^1\text{G}_4$	21243 ± 7	470.75 ± 0.15	0.087 ± 0.004	4.5 %	630 ± 50	13.5 ± 1.0	7.6 %
	21558.5 ± 1.0	463.855 ± 0.020	0.105 ± 0.010	10.0 %			
$^1\text{D}_2$	28018 ± 3	356.92 ± 0.04	0.270 ± 0.030	10.9 %	650 ± 80	8.0 ± 1.0	12.3 %

Table 4.9: Peak positions and effective linewidths of Tm:ZBLAN (* relative uncertainty) (*continued*)

level	k_p cm^{-1}	λ_p nm	σ_p pm^2	rel.*	Δk_{eff} cm^{-1}	$\Delta \lambda_{\text{eff}}$ nm	rel.*
$^1\text{I}_6, ^3\text{P}_0$	34810 ± 40	287.3 ± 0.3	0.0506 ± 0.0007	1.4 %	980 ± 30	7.95 ± 0.25	3.2 %
	35185 ± 20	284.20 ± 0.15	0.0615 ± 0.0015	2.5 %			
$^3\text{P}_1$	36602.0 ± 1.0	273.210 ± 0.007	0.0440 ± 0.0025	5.3 %	530 ± 30	3.95 ± 0.25	6.0 %
$^3\text{P}_2$	38333.5 ± 1.0	260.870 ± 0.007	0.257 ± 0.004	1.7 %	845 ± 20	5.75 ± 0.15	2.3 %

Table 4.10: Oscillator strengths and center of mass positions of Tm:ZBLAN (* relative uncertainty)

level	f_{meas} 10^{-8}	rel.*	k_{cm} cm^{-1}	λ_{cm} nm	$\Delta k_{-\sigma}$ cm^{-1}	$\Delta k_{+\sigma}$ cm^{-1}
$^3\text{F}_4$	187.0 ± 2.5	1.2 %	5862 ± 4	1706.0 ± 1.0	-280 ± 5	$+207 \pm 3$
$^3\text{H}_5$	156 ± 7	4.7 %	8305 ± 15	1204.5 ± 2.0	-140 ± 10	$+315 \pm 10$
$^3\text{H}_4$	201 ± 4	1.9 %	12702 ± 5	787.3 ± 0.3	-216 ± 7	$+251 \pm 5$
$^3\text{F}_3$	255 ± 15	6.5 %	14575 ± 20	686.1 ± 0.9	-230 ± 20	$+170 \pm 25$
$^3\text{F}_2$	20 ± 8	37.6 %	15200 ± 100	659 ± 5	-100 ± 200	$+140 \pm 50$
group:	275 ± 15	6.0 %	14595 ± 20	685.2 ± 0.9	-240 ± 20	$+220 \pm 30$
$^1\text{G}_4$	75 ± 7	9.5 %	21370 ± 40	468.0 ± 0.9	-300 ± 40	$+250 \pm 40$
$^1\text{D}_2$	195 ± 30	15.3 %	28020 ± 70	356.9 ± 0.9	-290 ± 70	$+280 \pm 80$
$^1\text{I}_6, ^3\text{P}_0$	68.5 ± 2.5	3.9 %	35040 ± 25	285.40 ± 0.20	-425 ± 20	$+380 \pm 30$
$^3\text{P}_1$	26.0 ± 2.0	7.5 %	36575 ± 25	273.40 ± 0.20	-270 ± 50	$+230 \pm 25$
group:	95 ± 3	3.5 %	35240 ± 30	283.80 ± 0.25	-545 ± 25	$+1315 \pm 25$
$^3\text{P}_2$	246 ± 8	3.3 %	38345 ± 15	260.80 ± 0.10	-350 ± 20	$+340 \pm 20$

4.8 Yb:ZBLAN

With the configuration $[\text{Xe}]4f^{13}$, triply ionized ytterbium is a one-hole system with the same states as the one-electron system of triply ionized cerium. The two LSJ -states split into 14 Stark levels and, compared with cerium, the two LSJ -states are exchanged, which means $^2\text{F}_{7/2}$ is the ground state and $^2\text{F}_{5/2}$ the excited state. The absorption spectrum in figure 4.14, based on four measured spectra, shows a sharp peak at 975 nm with a broad foot part. Table 4.11 gives the exact peak position and the effective linewidth. The cross section at the maximum is comparable with cerium, but the width of the ytterbium absorption is much smaller. Table 4.12 shows that the oscillator strength, like the linewidth, is also less than half

of the cerium value. For different barium-thorium-fluoride glasses in [71] peak wavelengths in the range 992 – 994 nm are reported and oscillator strengths in the range $200 - 249 \cdot 10^{-8}$. A detailed analysis of the dependence of the ytterbium spectrum on the glass composition is found in [72] for borate, phosphate, oxide, fluoride, and oxyfluoride glasses.

Ytterbium like cerium is not very attractive for itself with its two energy levels although it is used in fiber lasers at 1020 nm to pump praseodymium doped fiber amplifiers (PDFAs) for signals at $1.3 \mu\text{m}$. In contrast to cerium, the wavelength of the ytterbium transition fits perfectly to the usual laser diodes used to pump erbium doped fiber amplifiers (EDFA) at 980 nm. Used as a co-dopant to another rare earth ion, the existence of just two energy levels is an important advantage, because the ytterbium concentration may be quite high without disturbing the transitions of the other rare earth ion at different wavelengths. On the other hand, this high concentration ensures effective energy transfer to appropriate states of the second dopant.

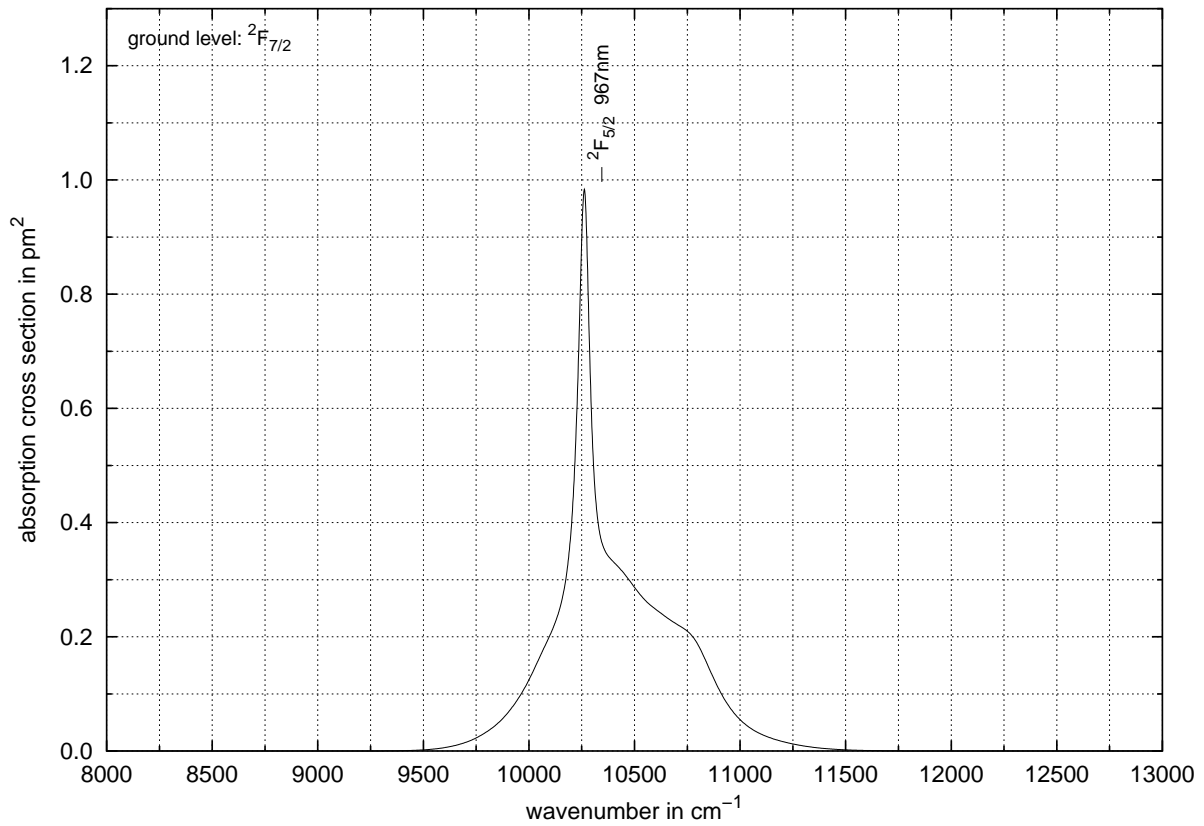


Figure 4.14: Spectrum of the absorption cross section of Yb:ZBLAN with center of mass position

Table 4.11: Peak position and effective linewidth of Yb:ZBLAN (* relative uncertainty)

level	k_p cm^{-1}	λ_p nm	σ_p pm^2	rel.*	Δk_{eff} cm^{-1}	$\Delta \lambda_{eff}$ nm	rel.*
$^2F_{5/2}$	10262.5 ± 1.0	974.43 ± 0.09	1.00 ± 0.10	12.5 %	310 ± 15	29.5 ± 1.5	4.6 %

Table 4.12: Oscillator strength and center of mass position of Yb:ZBLAN (* relative uncertainty)

level	f_{meas} 10^{-8}	rel.*	k_{cm} cm^{-1}	λ_{cm} nm	$\Delta k_{-\sigma}$ cm^{-1}	$\Delta k_{+\sigma}$ cm^{-1}
$^2F_{5/2}$	345 ± 15	4.9 %	10345 ± 20	966.5 ± 2.0	-195 ± 15	$+385 \pm 15$

4.9 Comparison with the literature

In this section some tables will be given so that the measured oscillator strengths of ground state absorptions of triply ionized rare earth ions in ZBLAN glass from this work can be compared with respective values found in the literature. We start with praseodymium in table 4.13, where the results obtained from several ZBLAN glasses and the related ZBLA are listed together with an INDAT and a tellurite glass. INDAT is the name of a class of fluoride glasses based on indium fluoride. Tellurite glasses are oxide glasses with a high refractive index of $n \approx 2$, which show some special properties like broader emission lines, which make them interesting alternatives to the silica glasses usually used for erbium doped fiber amplifiers in optical telecommunication. In [73] a couple of different ZBLA compositions were investigated and table 4.13 gives the range of obtained values. The table shows only insignificant variations of the oscillator strengths in ZBLAN and ZBLA glasses whereas the respective values in INDAT are generally smaller. In case of the lower energy levels they reach only half of the ZBLA(N) values. The oscillator strengths in the tellurite glass are, on the other hand, in most cases larger by about a factor of two.

Table 4.14 contains the oscillator strengths of ground state absorptions of triply ionized erbium in several glass hosts. In addition to the praseodymium table, a zinc-cadmium fluoride glass is contained in this table. The authors of [64] and [74] investigated some different compositions of ZBLAN and INDAT glasses respectively and the ranges of values obtained are given in the table. It can be seen that our results are only slightly different from the values reported in [6] at the same institute whereas the values in [64] are all somewhat smaller. This may be explained by the fact that the compositional variations of the glasses used in [64] are small compared with the broad range of values obtained. Therefore, the difference to the values from this work may also be addressed to differences in the glass composition. In contrast to the case of praseodymium, the oscillator strengths in the INDAT glasses as

Table 4.13: Oscillator strengths in 10^{-8} of ground state absorption transitions of triply ionized praseodymium in several glasses. Ellipses mark levels contained in the level above due to overlapping lines.

level	ZBLAN	ZBLAN	ZBLAN	ZBLAN	ZBLA	INDAT	tellurite
3H_5	196 ± 3		166.6		168		
3H_6	77 ± 5		348	50	$336 - 370$	31	206
3F_2	283 ± 6	312	...	293	...	125	636
3F_3	635 ± 15	548	865	601	$800 - 914$	383	1106
3F_4	245 ± 15	289	...	251	...	138	341
1G_4	26.4 ± 0.5	29.1	25	25	$31 - 39$	12	51
1D_2	200 ± 10	185	196	233	$182 - 201$	150	328
3P_0	180 ± 15	216	215	296	$213 - 247$	129	598
3P_1	540 ± 30		470	601	$413 - 485$	443	875
1I_6
3P_2	925 ± 30		920	1031	$863 - 876$	686	1560
ref.	here	[75]	[76]	[77]	[73]	[77]	[78]

investigated in [74] are comparable with ZBLAN in general but contain some significantly smaller or larger values. The tellurite glass again shows stronger absorptions than ZBLAN.

In table 4.15 the oscillator strengths of $Tm:ZBLAN$ as measured in this work are listed together with appropriate values from the literature. Besides an INDAT and an zinc-cadmium fluoride glass, the values of a chalcogenide glass are given whereas GAS serves as a shortcut for germanium-arsene sulphide. Similar to the case of praseodymium, the values obtained from different ZBLAN glasses show only minor differences. Compared with ZBLAN, the INDAT glass in most cases shows larger, and ZnCd similar oscillator strengths. The respective values obtained from the chalcogenide glass in contrast are much larger than in all fluoride glasses.

Table 4.14: Oscillator strengths in 10^{-8} of ground state absorption transitions of triply ionized erbium in several glasses. Ellipses mark levels contained in the level above due to overlapping lines.

level	ZBLAN	ZBLAN	ZBLAN	INDAT	ZnCd	tellurite
$^4I_{13/2}$	186.5 ± 3		$134.27 - 156.92$	$100 - 117$	117	208.87
$^4I_{11/2}$	56 ± 3	56.1	$41.19 - 46.66$	$40 - 55$		73.43
$^4I_{9/2}$	28.7 ± 0.8		$17.24 - 28.06$	$26 - 34$	19	34.46
$^4F_{9/2}$	185 ± 15	188.8	$136.50 - 170.49$	$191 - 205$	195	251.64
ref.	here	[6]	[64]	[74]	[79]	[80]

Oscillator strengths in 10^{-8} of triply ionized erbium (*continued*)

level	ZBLAN	ZBLAN	ZBLAN	INDAT	ZnCd	tellurite
$^4S_{3/2}$	49 ± 6	38.3	$30.12 - 34.19$	$23.4 - 40$	37	
$^2H_{11/2}^{(2)}$	475 ± 15	510.5	$337.02 - 431.77$	$358 - 415$	294	1192.46
$^4F_{7/2}$	155 ± 4	159.6	$117.32 - 140.95$	$156 - 195$	167	191.45
$^4F_{5/2}$	49 ± 2.5	50.3	$61.77 - 73.78$	$76 - 105$	78	79.86
$^4F_{3/2}$	25.5 ± 2	28.9
$^4F_{9/2}$	57 ± 3	57.4	$38.75 - 50.71$	$56 - 64$	55	60.66
$^4G_{11/2}$	900 ± 60	902.6	$560.17 - 786.55$	$752 - 814$	525	1837.13
$^4G_{9/2}$	150 ± 40	158.9		$113 - 213$	160	
ref.	here	[6]	[64]	[74]	[79]	[80]

Table 4.15: Oscillator strengths in 10^{-8} of ground state absorption transitions of triply ionized thulium in several glasses. Ellipses mark levels contained in the level above due to overlapping lines.

level	ZBLAN	ZBLAN	ZBLAN	INDAT	ZnCd	GAS
3F_4	187 ± 2.5	190.5	$155.99 - 169.08$	165	182	666
3H_5	156 ± 7	173.3	$132.30 - 152.58$	144	164	432
3H_4	201 ± 4	194.8	$173.02 - 190.21$	261	195	748
3F_3	255 ± 15	229.5	$234.40 - 256.29$	359	300	730
3F_2	20 ± 8	42.0	...	41	...	
1G_4	75 ± 7	73.2	$66.43 - 72.44$	123	64	
1D_2	195 ± 30	190.2	$144.04 - 180.4$	278	191	
1I_6	68.5 ± 2.5		$40.05 - 56.18$			
3P_0			
3P_1	26 ± 2		$13.77 - 19.53$			
3P_2	246 ± 8		$90.22 - 236.91$			
ref.	here	[6]	[81]	[82]	[79]	[83]

5 Parameter fit to absorption properties

On the way to calculating the radiative spectroscopic properties of rare earth ions for use in fiber laser simulations, we are arriving at the final and central step, namely the fitting procedures. In figure 5.1 a flow chart of the whole procedure is given as a summary of the preceding chapters. In the first section of this chapter the fit of the radial parameters to the measured energy levels will be explained. One result is the transformation matrix V defining the intermediate coupling which is needed to calculate the reduced matrix elements as already described in section 3.4. In the second section of this chapter these reduced matrix elements are being used to fit the Judd-Ofelt parameters to the measured oscillator strengths. In the remaining sections the fitting procedures will be applied to the results of the last chapter for thulium, praseodymium, and erbium and finally compared with values from the literature.

5.1 Fit of energy levels

The goal of the energy level fit is to find values of the radial integrals which lead to a calculated energy level spectrum resembling the center of mass positions of the measured absorption lines as closely as possible. The central equation of this procedure is equation (3.48), which we shall recall here:

$$E' = \sum_k X^k x'_k, \quad (5.1)$$

where k runs over the sub-terms of all interactions of interest, X^k is a radial integral, x'_k the corresponding angular interaction matrix, and E' the total energy matrix. The prime was introduced in chapter 3 to express the fact that we use matrices in LS -coupling. But the equation is valid in general, not depending on the used coupling scheme, as its derivation in section 1.3 shows.

The determinantal product state matrices of the basic mixed unit tensor operators given in chapter 3 are immediately transformed to LS -coupling to get rid of the unnecessary, since degenerated, M_J states. The resulting matrices are stored for further use in different energy interaction matrices x'_k , the expressions of which are given in chapter 1. These matrices are again stored, as they are needed several times in the fitting procedure.

Suppose we already know the values X^k of the radial integrals, then the positions of all energy levels are the diagonal elements of E' after diagonalization as already given in equation (3.49)

$$\begin{pmatrix} k_1 & 0 & \cdots \\ 0 & k_2 & \cdots \\ \vdots & \vdots & \ddots \end{pmatrix} = V^T \frac{E'}{hc} V, \quad (5.2)$$

where the column vectors of the unitary matrix V contain the coefficients of the intermediate coupling states in equation (1.18). The elements of the diagonalized matrix in equation (5.2)

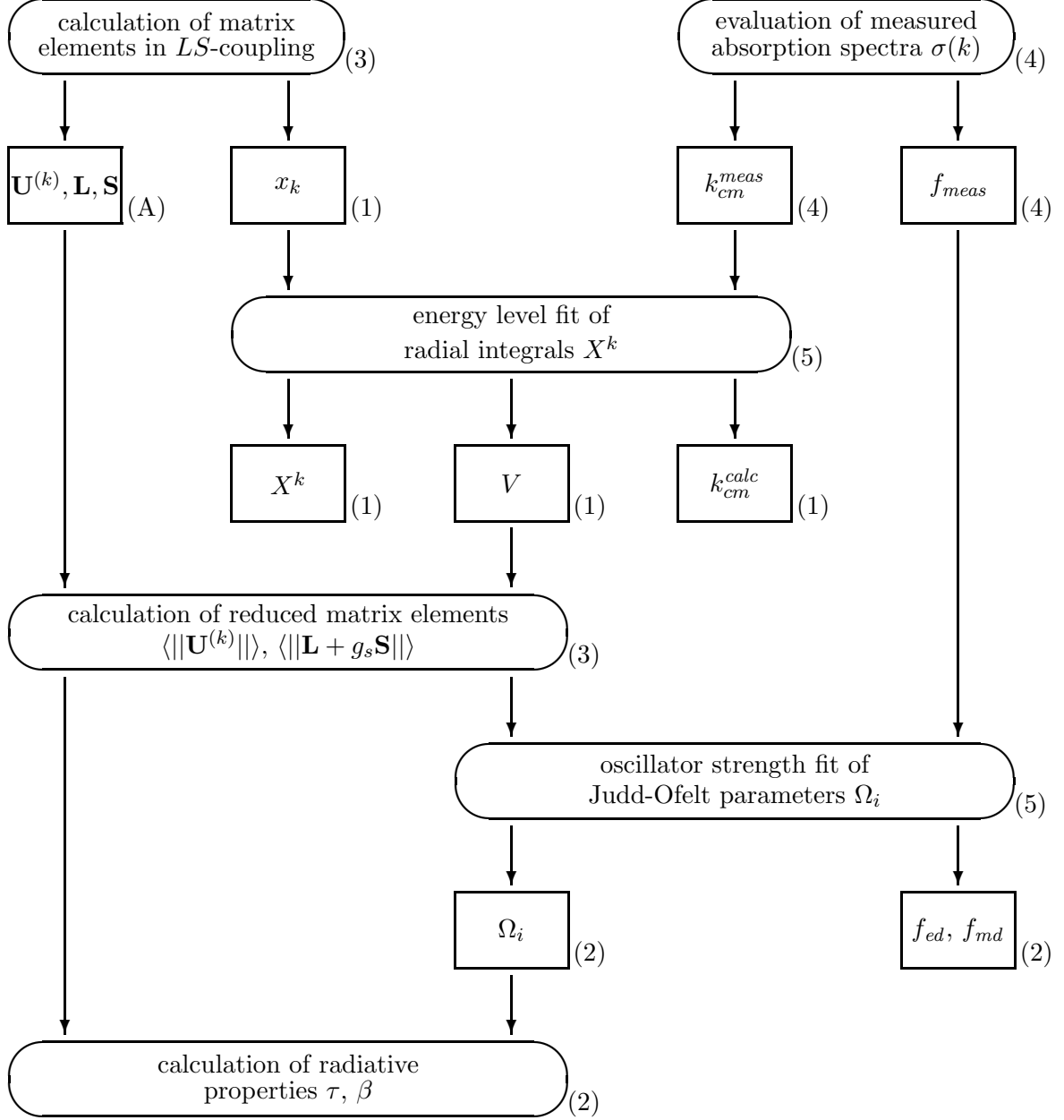


Figure 5.1: Flow chart of the procedure to extract the radiative properties of a rare earth ion from its absorption spectrum. The numbers in parantheses outside the boxes refer to the appropriate chapters.

are given as wavenumbers since in practice the radial integrals are usually used in the form

$$\hat{X}^k = \frac{X^k}{hc} , \quad (5.3)$$

and therefore have the dimension cm^{-1} of the wavenumbers. Of course, V depends on \hat{X}^k and therefore the dependence of the energy level positions k_i on \hat{X}^k

$$k_i = \sum_{k,j,l} \hat{X}^k v_{ij}^T(\hat{X}^k) x_{k,jl} v_{li}(\hat{X}^k) \quad (5.4)$$

is nonlinear, in contrast to the non-diagonal energy matrix E' in the linear equation (5.1).

One parameter needs special treatment in the nonlinear fitting procedure: It is usual to set the energy of the ground level of the ground configuration to zero, because the measured wavenumbers are always differences. In equation (5.2), however, the zero level is the center of mass of the configuration, because in chapter 1 we discarded all interaction terms which only shift the configuration as a whole. The most prominent of these terms is $F^0 \mathbf{f}_0$ from the Coulomb interaction. To adjust the offset of the energy levels we thus take the mean difference between the measured and calculated energy levels

$$k_0 = \frac{1}{n} \sum_{i=1}^n (k_i^{\text{meas}} - k_i^{\text{calc}}) , \quad (5.5)$$

and add it to the calculated wavenumbers k^{calc} . The least squares parameter to be minimized in the fitting procedure is then given by

$$\chi^2 = \sum_{i=1}^n \left(\frac{k_i^{\text{meas}} - (k_i^{\text{calc}} + k_0)}{\Delta k_i^{\text{meas}}} \right)^2 . \quad (5.6)$$

Several different fitting procedures were tested, but not much time was spent on doing that, because it turned out soon that the simplex method [84] is working satisfactorily. In this method $n + 1$ points are spread in the n -dimensional parameter space, if the number of parameters is n . One point is the initial guess, the others here were derived from that initial guess by multiplying one coordinate for each point with a certain factor, which was 2 at the beginning of the fitting procedure. The simplex, defined by the $n + 1$ points, is moving through the $n + 1$ -dimensional χ^2 -mountains by reflecting one point through the n -dimensional area spanned by the other points. It is shrinks when arriving in a valley and expands in flat areas. For the break condition the parameter

$$\tau = \sqrt{\frac{\sum_{i=1}^n (\chi_i^2 - \bar{\chi}^2)^2}{n}} \quad (5.7)$$

was chosen, with the χ^2 -value χ_i^2 of point i and the mean value of all points $\bar{\chi}^2$. The movement of the simplex is stopped when either the number of steps reaches 1000 or $\tau < 0.001$ holds.

All nonlinear fitting methods suffer from the risk that they may find only a local minimum of χ^2 instead of the global one which is usually of interest. To lower this risk, the point with minimum χ^2 from the fitting run is taken several times as a guess value for a new run. The factor used to spread the initial points with is 2 in the first run, is lowered by 0.2 each time until it reaches 0.2. The loop of simplex runs is stopped when either the minimum χ^2 or its relative difference to the last run

$$\Delta_r = \frac{\chi_{last}^2 - \chi^2}{\frac{1}{2}(\chi_{last}^2 + \chi^2)} \quad (5.8)$$

reaches a value smaller than 0.001.

The interesting simplex method is explained in some more detail in [85]. Compared with other methods, it needs more frequent evaluations of χ^2 , which might be a problem for large state spaces. In such cases it would probably make sense to investigate different fitting procedures. But for the configurations of the rare earth ions in this work the simplex method was satisfying.

Although χ^2 is very useful as the parameter to be minimized in the fitting procedure, it is not well suited for comparisons with other calculations, since it is squared and its value depends on the number of fitted levels. Therefore we define the parameter

$$\overline{\Delta k} = \frac{\sqrt{\chi^2 \sum_{i=1}^n \Delta k_i^{meas}}}{n}, \quad (5.9)$$

which can be interpreted as the mean deviation of measured and calculated values, weighted by the uncertainty of the measured values. This parameter has the same dimension as k .

Fortunately, it is nowadays not necessary any more to carry out the energy level calculations for rare earth ions from scratch. There are a lot of published radial integrals and the lower energy levels have already been assigned. This assignment is not host dependent since the lower energy levels often have dominant *LS*-components. But for higher levels the *LS*-label changes from host to host and states with similar energies may change their positions. Therefore an energy level calculation is usually carried out in several steps. At first only Coulomb and spin-orbit interactions are taken into account and only low energy levels with well-defined quantum numbers are used. The calculated positions of all other energy levels allow some more assignments then. This step is much simplified by a Judd-Ofelt fit using the states from the first step, because in many cases closely located levels have sufficiently different oscillator strengths to distinguish them, even if they are in the wrong order after the first and rough step of the energy level calculation.

Now more levels are usable and in the next step an energy level fit with some more interactions will be performed, usually the Coulomb configuration interactions since they come next in the order of magnitude. After this step some more, or even all absorption lines may be assigned, and in the last step all interactions will be taken into account. As initial values of the radial integrals either suitable values from the literature are taken or the results from the preceding step. For the rare earth ions used in this work, the described method allowed an assignment of all absorption lines without doubt.

5.2 Fit of oscillator strengths

The so-called Judd-Ofelt fit is indeed not really a fit, but a linear optimization problem with a well-defined solution. The goal is to find values for the three Judd-Ofelt parameters Ω_λ , $\lambda = 2, 4, 6$, which minimize the difference between the calculated oscillator strength given by equation (2.12) and the measured value from equation (4.24). Splitting the electric dipole oscillator strength to be $f_{ed} = \sum_\lambda f_{ed,\lambda} \Omega_\lambda$, the basic equation is given by

$$f_{meas} - f_{md} = f_{ed,\lambda} \Omega_\lambda, \quad (5.10)$$

which in case of n absorption transitions is a system of n linear equations and three free parameters. For such an overdetermined linear system

$$\mathbf{b} = \mathbf{A} \mathbf{x}, \quad (5.11)$$

the well-known solution which minimizes $\chi^2 = |\mathbf{A} \mathbf{x} - \mathbf{b}|^2$, is the solution of the square system

$$\mathbf{A}^T \mathbf{b} = \mathbf{A}^T \mathbf{A} \mathbf{x}, \quad (5.12)$$

which is

$$\mathbf{x} = (\mathbf{A}^T \mathbf{A})^{-1} \mathbf{A}^T \mathbf{b}. \quad (5.13)$$

In this equation in our case \mathbf{x} is obviously the three-dimensional vector Ω_λ , but what about \mathbf{A} and \mathbf{b} ? Unfortunately, it has become a tradition to use the straightforward assignment $\mathbf{b} = f_{meas} - f_{md}$ and $\mathbf{A} = f_{ed,\lambda}$. In this case the minimized quantity is

$$\chi^2 = \sum_i \left(f_{meas}^{(i)} - f_{ed}^{(i)} - f_{md}^{(i)} \right)^2, \quad (5.14)$$

where i labels the different absorption transitions. But this may be considered the optimum solution only in the special case that all oscillator strengths were measured with the same absolute accuracy, which is very unlikely. The origin of this situation could be an early application of Judd's formula by Carnall in [55]. He wrote that "the statistical significance of the parameters was gauged by computing their standard errors in the usual manner" and this means minimizing the quantity

$$\chi^2 = \sum_i \left(\frac{f_{meas}^{(i)} - f_{ed}^{(i)} - f_{md}^{(i)}}{\Delta f_{meas}^{(i)}} \right)^2 \quad (5.15)$$

by the correct assignment

$$\begin{aligned} \mathbf{b} &= \frac{f_{meas} - f_{md}}{\Delta f_{meas}} \\ \mathbf{A} &= \frac{f_{ed,\lambda}}{\Delta f_{meas}}. \end{aligned} \quad (5.16)$$

But then he defined the root mean square deviation

$$\sigma_{rms} = \sqrt{\frac{\sum_i \left(f_{meas}^{(i)} - f_{ed}^{(i)} - f_{md}^{(i)} \right)^2}{n - 3}}, \quad (5.17)$$

where 3 is the number of Judd-Ofelt parameters, and of course this parameter is not minimized by the use of (5.16). This led to a situation where people get better values of σ_{rms} if they use the wrong optimization method. The conclusion drawn by the author is not to use the parameter σ_{rms} at all and instead, analogous to equation (5.9), define the parameter

$$\overline{\Delta f} = \frac{\sqrt{\chi^2 \sum_{i=1}^n \Delta f_{meas}^{(i)}}}{n}. \quad (5.18)$$

In order to show that the choice of the proper least squares parameter is not just an academic one the following must be stated: For a long time it was common sense that the Judd-Ofelt theory fails in case of praseodymium, because it was not unusual to get negative values for Ω_2 , in contradiction to the definition of the Judd-Ofelt parameters. The reason was attributed to the small distance to the first excited configuration, which conflicts with Judd's second approximation (2.40). This led to the logical solution of taking equation (2.39) instead of (2.41). The so-called modified Judd-Ofelt theories [77, 86, 87] therefore contain Ω_λ with odd λ . These additional parameters must be very small to agree with the theory, but this was not the case. In [76] as a different solution it was supposed to omit certain transitions in the optimization procedure, especially $^3H_4 \rightarrow ^3P_2$. All in all, the modifications were not very successful and satisfying, and finally it was found [88] that the assignment (5.16) produces better results than all modifications, without negative Judd-Ofelt parameters. Nevertheless, the odd order Judd-Ofelt parameters with their unrealistic large values are still in use [82, 89].

To summarize this section: The whole secret of the Judd-Ofelt fit is to take the assignment (5.16) and calculate (5.13). The most complicated thing is the inversion of the 3×3 matrix $\mathbf{A}^T \mathbf{A}$. Obviously, this is some orders of magnitude less difficult than calculating the reduced matrix elements with an energy level fit, and this is one reason why most people just use tabulated reduced matrix elements from the literature.

5.3 Tm : ZBLAN

We start with the results of the energy level fit for thulium, because of the three ions which will be presented this is most simple. The configuration [Xe]4f¹² produces the *LS*-terms ¹S, ¹D, ¹G, ¹I and ³P, ³F, ³H. Due to spin-orbit coupling these terms split to 13 *LSJ*-states with a total of 91 Stark sub-states.

The calculations were carried out in three steps as described in section 5.1. At first only Coulomb and spin-orbit interactions with the radial integrals F^2 , F^4 , F^6 , and ζ were considered, as shown in table 5.1. In the next run, the Coulomb configuration interaction

Table 5.1: Results of the energy level and Judd-Ofelt fits for Tm:ZBLAN to 11 absorption lines. The constraints $M^2 = 0.56 M^0$, $M^4 = 0.38 M^0$, $P^4 = 0.75 P^2$, and $P^6 = 0.50 P^2$ were made.

parameter	initial	step 1	step 2	step 3	unit
base	250.00	190.16	121.47	149.80	cm^{-1}
F^2	100134.00	103486.85	102418.36	102403.01	cm^{-1}
F^4	69613.00	77972.00	73215.09	73241.80	cm^{-1}
F^6	55975.00	57838.06	51087.23	50320.22	cm^{-1}
ζ	2636.00	2617.39	2628.98	2583.47	cm^{-1}
α	17.26		14.56	17.43	cm^{-1}
β	-624.50		-759.42	-841.95	cm^{-1}
γ	1820.00		(1820)	(1820)	cm^{-1}
M^0	3.81			-2.35	cm^{-1}
P^2	695.00			12.78	cm^{-1}
$\overline{\Delta k}$		237.3	44.3	22.5	cm^{-1}
Ω_2		2.847	2.862	2.920	pm^2
Ω_4		1.830	1.861	1.856	pm^2
Ω_6		0.733	0.687	0.670	pm^2
$\overline{\Delta f}$		43.4	33.3	30.1	10^{-8}

with the integrals α , β , and γ was included and finally the spin-spin and spin-other-orbit interaction and the spin-orbit configuration interaction with the parameters M^0 and P^2 . It is known that due to the symmetry properties of the according angular operator the parameter γ is correlated strongly to the energy level $^1\text{S}_0$ [56] and because the position of this level was not measured γ was fixed to its initial value. When γ was allowed to vary in the fitting procedure this led to unrealistic high values of this parameter compensated by a drastically reduced F^6 . Together with the obligatory center of the ground state (“base” in table 5.1) a total of nine parameters were used to fit the ten absorption lines of table 4.10. Due to the low number of available energy levels it was necessary to fix the remaining integrals M^2 , M^4 , P^4 , and P^6 as indicated in the headline of table 5.1. The initial guess for the radial integrals was taken from [39] where energy level calculations for LaF_3 were published, but it should be noted that the fractions $M^4/M^0 = 0.31$, $P^4/P^2 = 0.5$, and $P^6/P^2 = 0.1$ were taken different from our choice. After each energy level fit, the obtained states in intermediate coupling were used to calculate the Judd-Ofelt parameters Ω_2 , Ω_4 , and Ω_6 , which are also given in the table.

As explained in section 4.7, it was impossible to separate the absorption lines corresponding to the states $^1\text{I}_6$ and $^3\text{P}_0$. In order to perform the energy level fit the calculated values for

Table 5.2: Optimum energy level and Judd-Ofelt fits for Tm:ZBLAN

no.	level	k_{meas} cm ⁻¹	Δk_{meas} cm ⁻¹	k_{calc} cm ⁻¹	Δ cm ⁻¹	f_{meas} 10 ⁻⁸	Δf_{meas} 10 ⁻⁸	f_{ed} 10 ⁻⁸	f_{md} 10 ⁻⁸	Δ 10 ⁻⁸
0	³ H ₆			150				0.0	0.0	
1	³ F ₄	5862	(4)	5861	-0.1	186.9	(2.3)	193.2	0.0	6.3
2	³ H ₅	8303	(14)	8310	7.4	156.0	(7.3)	106.7	40.9	-8.5
3	³ H ₄	12702	(5)	12700	-1.9	201.3	(3.8)	185.9	0.0	-15.4
4	³ F ₃	14574	(18)	14583	8.1	253.9	(16.4)	186.2	0.0	-67.7
5	³ F ₂	15180	(119)	15088	-92.3	20.4	(7.7)	28.9	0.0	8.5
6	¹ G ₄	21366	(42)	21395	29.7	74.7	(7.1)	71.4	0.0	-3.3
7	¹ D ₂	28018	(68)	28068	49.6	195.1	(29.8)	196.5	0.0	1.4
8	¹ I ₆	35039	(26)	34992	0.0	68.3	(2.7)	45.0	2.2	-0.4
9	³ P ₀	...		35643		20.7	0.0	...
10	³ P ₁	36576	(24)	36577	0.8	26.2	(2.0)	34.8	0.0	8.6
11	³ P ₂	38344	(16)	38342	-1.4	245.8	(8.1)	236.2	0.0	-9.5
12	¹ S ₀			75006				0.0	0.0	
		$\overline{\Delta k}$:			22.5	$\overline{\Delta f}$:			30.1	

these two levels had to be weighted by $2J + 1$:

$$k_{cm}({}^1\text{I}_6/{}^3\text{P}_0) = \frac{13 k({}^1\text{I}_6) + k({}^3\text{P}_0)}{14}, \quad (5.19)$$

while the calculated oscillator strengths as integral values were just summed up.

It can be seen from table 5.1 that the first step with just Coulomb and spin-orbit interactions already gave useful results, as it was proposed in section 1.5. The average deviation from the measured energy levels is around 240 cm⁻¹. Inclusion of the Coulomb configuration interaction in the next step drastically increased the quality of the energy level fit, whereas the impact of the inclusion of M^0 and P^2 in the third step is much less significant and the parameters behave somewhat arbitrarily. It is interesting to see that the influence of the fitting steps on the quality of the Judd-Ofelt fit is limited. Furthermore, the Judd-Ofelt parameters themselves show only minor variations, in other words they are insensitive to the detailed composition of the states in intermediate coupling. This was a constant observation during extensive fit calculations, the end results of which are only presented here, but that was not a surprising investigation, as this fact has already been known for a long time and is indeed the main reason for the success of the Judd-Ofelt theory. The energy level of ¹S₀ due to the chosen value of the parameter γ is far in the ultraviolet region, well separated from all

other energy levels and shows an extremely weak oscillator strength which in contrast to the position should not be linked to γ .

In table 5.2 details of the final results are given. The deviations of the calculated energy levels from measurements are all smaller than the accuracy of the measured values, while this is not the case for the oscillator strengths. This is not surprising because there are only three parameters to fit the oscillator strengths, whereas ten were used for the energy levels. Since both sides are connected by the reduced matrix elements, the attempt has been made to perform an overall fitting procedure of all twelve parameters to eleven energy levels plus eleven oscillator strengths. But the results were never satisfying, neither for thulium nor for the other ions. Normally this overall procedure led to somewhat worse results concerning the energy levels and slightly better results for the oscillator strengths. But often the fitting process ran out of control resulting in extremely large and carefully balanced radial integrals which usually is an indicator for certain dependencies between the fitting parameters.

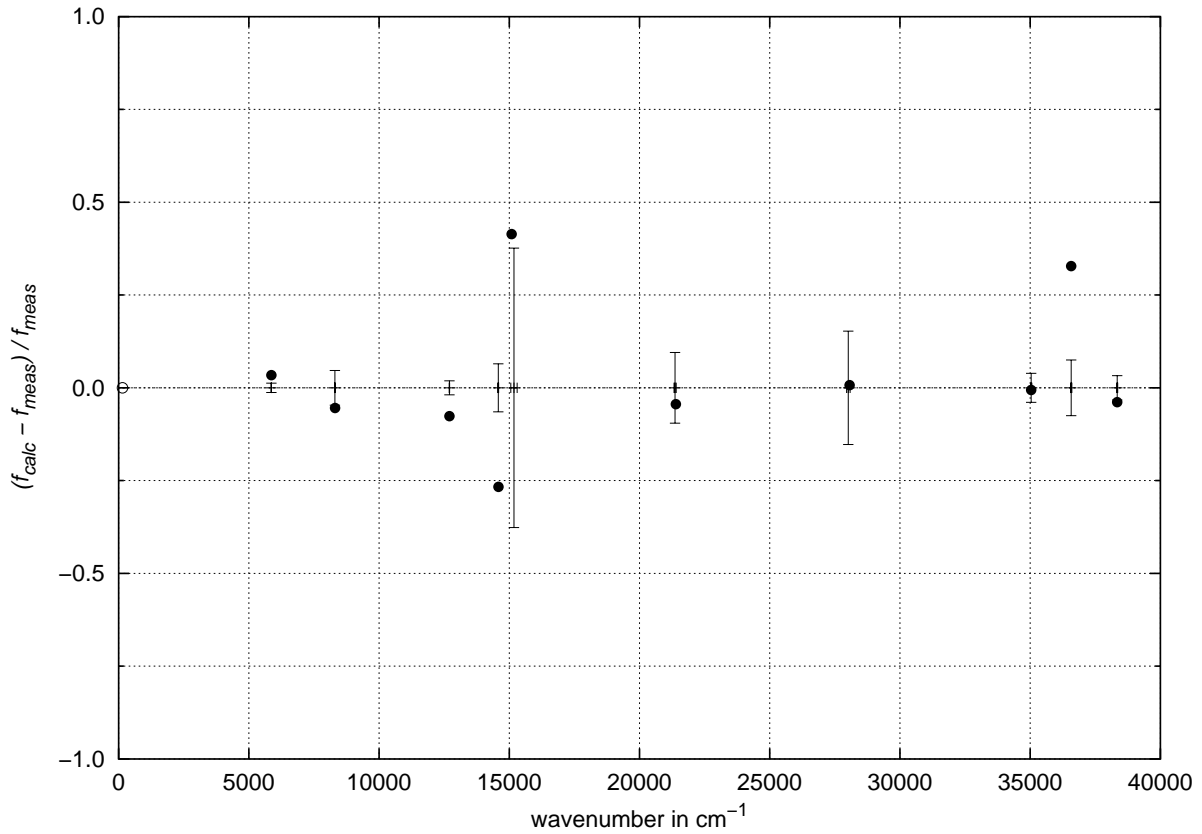


Figure 5.2: Comparison of calculated (dots) and measured (errorbars) oscillator strengths for Tm:ZBLAN. The circle indicates the calculated center of mass position of the ground state.

Table 5.3: Intermediate coupling in Tm:ZBLAN: Squared coefficients of LS -components for the energy levels in the first column. Overlines indicate a negative sign of the appropriate unsquared coefficient.

3P_0		1S_0	
9	$\overline{0.9428}$	0.0572	
12	$\overline{0.0572}$	$\overline{0.9428}$	
3P_1			
10	$\overline{1.0000}$		
3F_2		1D_2	3P_2
5	$\overline{0.7665}$	$\overline{0.2148}$	$\overline{0.0187}$
7	$\overline{0.1956}$	$\overline{0.4284}$	$\overline{0.3760}$
11	$\overline{0.0379}$	$\overline{0.3569}$	0.6053
3F_3			
4	$\overline{1.0000}$		
3F_4		3H_4	1G_4
1	$\overline{0.6175}$	0.0850	0.2975
3	0.2799	0.5985	0.1215
6	0.1026	$\overline{0.3164}$	0.5810
3H_5			
2	$\overline{1.0000}$		
3H_6		1I_6	
0	0.9913	$\overline{0.0087}$	
8	0.0087	0.9913	

In figure 5.2 the ratio of calculated and measured oscillator strengths is plotted, together with bars indicating the relative uncertainty of the measured values. From this graph the high accuracy of the energy level fit becomes obvious. The measurement errors and deviations of the calculations are distributed homogeneously.

Important results are the coefficients of the LS -states in intermediate coupling, given in table 5.3. A somewhat compact notation was used in this table, since in the full matrix V most elements are zero. The left column contains the number of the energy level, starting with zero for the ground level, and above each square sub-matrix the appropriate LS -components are mentioned. All coefficients are listed squared, therefore the sum of the elements in a row or column of a sub-matrix is 1. A negative sign of a non-squared coefficient is indicated by an overline. As an example, the state of energy level 6, i.e. 1G_4 in intermediate coupling is:

$$|(^1G) 4\rangle = 0.32 |^3F_4\rangle - 0.56 |^3H_4\rangle + 0.76 |^1G_4\rangle , \quad (5.20)$$

where the parantheses in the left state symbol indicate that 1G is the main component of this state, but only J is a good quantum number and S and L are not.

It is interesting that, besides the states 2, 4, and 10, with unique quantum number J , only the energy level pairs 0/8 and 9/12 show a dominant LS -character. All others, including the lowest levels, are heavily mixed states. The coupling matrix from table 5.3 was used to calculate the radiative emission and absorption properties of Tm:ZBLAN as mentioned in section 2.1. The results are lengthy tables which therefore had to be shifted to section D.3 in the appendix.

5.4 Pr:ZBLAN

With the configuration [Xe]4f², triply ionized praseodymium shows some similarities to the two-hole system of thulium. In LS -coupling the states are the same, but the intermediate coupling states will found to be different.

Analogous to thulium, the energy level fit was performed in three steps, and the values for the initial guess were taken from [39]. The general trend is similar to that of thulium: The first step with Coulomb and spin-orbit interaction already gives good results, but the

Table 5.4: Results of the energy level and Judd-Ofelt fits for Pr:ZBLAN to 10 absorption lines. The constraints $M^2 = 0.56 M^0$, $M^4 = 0.38 M^0$, $P^4 = 0.75 P^2$, and $P^6 = 0.50 P^2$ were made.

parameter	initial	step 1	step 2	step 3	unit
base	205.00	337.72	329.13	327.39	cm ⁻¹
F^2	68878.00	68902.18	68571.99	68576.05	cm ⁻¹
F^4	50347.00	52456.72	49991.40	49972.76	cm ⁻¹
F^6	32901.00	36731.00	32412.18	32415.29	cm ⁻¹
ζ	751.70	722.94	727.03	728.18	cm ⁻¹
α	16.23		17.00	16.99	cm ⁻¹
β	-566.60		-417.96	-417.98	cm ⁻¹
γ	1371.00		(1371)	(1371)	cm ⁻¹
M^0	2.08			0.19	cm ⁻¹
P^2	88.60			1.67	cm ⁻¹
$\overline{\Delta k}$		99.3	5.3	4.8	cm ⁻¹
Ω_2		1.864	1.982	1.981	pm ²
Ω_4		4.684	4.647	4.645	pm ²
Ω_6		7.213	6.969	6.972	pm ²
$\overline{\Delta f}$		123.8	124.1	124.0	10 ⁻⁸

Table 5.5: Optimum energy level and Judd-Ofelt fits for Pr:ZBLAN

no.	level	k_{meas} cm ⁻¹	Δk_{meas} cm ⁻¹	k_{calc} cm ⁻¹	Δ cm ⁻¹	f_{meas} 10 ⁻⁸	Δf_{meas} 10 ⁻⁸	f_{ed} 10 ⁻⁸	f_{md} 10 ⁻⁸	Δ 10 ⁻⁸
0	³ H ₄			327				0.0	0.0	
1	³ H ₅	2365	(4)	2364	-1.0	196.2	(2.8)	173.5	14.1	-8.6
2	³ H ₆	4485	(18)	4498	13.3	77.4	(5.1)	75.3	0.0	-2.1
3	³ F ₂	5105	(5)	5107	2.3	283.3	(6.2)	284.9	0.0	1.6
4	³ F ₃	6467	(7)	6463	-4.2	637.0	(16.2)	653.4	0.0	16.4
5	³ F ₄	6958	(10)	6954	-3.3	244.2	(13.1)	392.5	0.7	149.0
6	¹ G ₄	9883	(7)	9883	0.3	26.4	(0.5)	27.0	0.4	1.0
7	¹ D ₂	17026	(20)	17023	-3.7	199.2	(10.7)	117.4	0.0	-81.8
8	³ P ₀	20859	(12)	20856	-3.0	180.0	(17.4)	267.9	0.0	87.9
9	³ P ₁	21505	(20)	21472	-1.9	542.6	(30.5)	273.4	0.0	-127.6
10	¹ I ₆	...		21511		141.5	0.0	...
11	³ P ₂	22645	(10)	22646	1.2	926.8	(28.7)	407.1	0.0	-519.7
12	¹ S ₀			46461				24.1	0.0	
		$\overline{\Delta k}$:			4.8	$\overline{\Delta f}$:			124.0	

third does not improve the fit significantly compared with the second step with the Coulomb configuration interaction. Furthermore, the oscillator strength fit is insensitive to the number of included interactions, and so are the Judd-Ofelt parameters. But in detail there are significant differences to the case of thulium. The energy level fit produces much better results, while the Judd-Ofelt fit is worse. Nevertheless, negative Ω_2 values, which led to the modified Judd-Ofelt theories, did not arise as long as the definition (5.15) for χ^2 was used. Some experiments with the definition (5.14) were carried out, and indeed usually resulted in negative values of Ω_2 , which confirms the results in [88]. The differences between radial integrals achieved for ZBLAN and the LaF₃ values are moderate and stay in the usual range, except for the parameters M^0 and P^2 which again show a somewhat arbitrary behavior.

The strikingly good correspondence between the calculated and measured energy levels may be studied in detail in table 5.5. All deviations stay well below the specified uncertainty of the measurement. Equally to the case of thulium it was impossible to separate the absorption line overlapping with ¹I₆. In case of praseodymium this is the level ³P₁ and therefore, in order to perform an energy level fit the calculated values had to be weighted by $2J + 1$, which here gives

$$k_{cm}({}^3P_1/{}^1I_6) = \frac{3k({}^3P_1) + 13k({}^1I_6)}{16}, \quad (5.21)$$

while the calculated oscillator strengths were just summed up again. As known from the literature, the lower success of the Judd-Ofelt theory for praseodymium is mainly caused by the three 3P levels [76]. Comparing figure 5.3 with figure 5.2 for thulium the higher accuracy of the thulium fit becomes apparent. The level 1S_0 of praseodymium is located in the ultraviolet, but not as far as in the case of thulium, and the oscillator strength is much larger.

Although triply ionized thulium and praseodymium share the same LS -states, they are remarkable different in intermediate coupling. The non-zero coefficients of the transformation matrix V are listed in table 5.6. While the states of thulium are highly mixed, the praseodymium states are nearly pure LS -states. Only the energy levels 5 and 6 contain a significant part of a second LS -state. As in case of thulium, the coupling matrix is used to calculate the radiative emission and absorption properties of Pr:ZBLAN from section 2.1. The resulting tables may be found in section D.1 in the appendix.

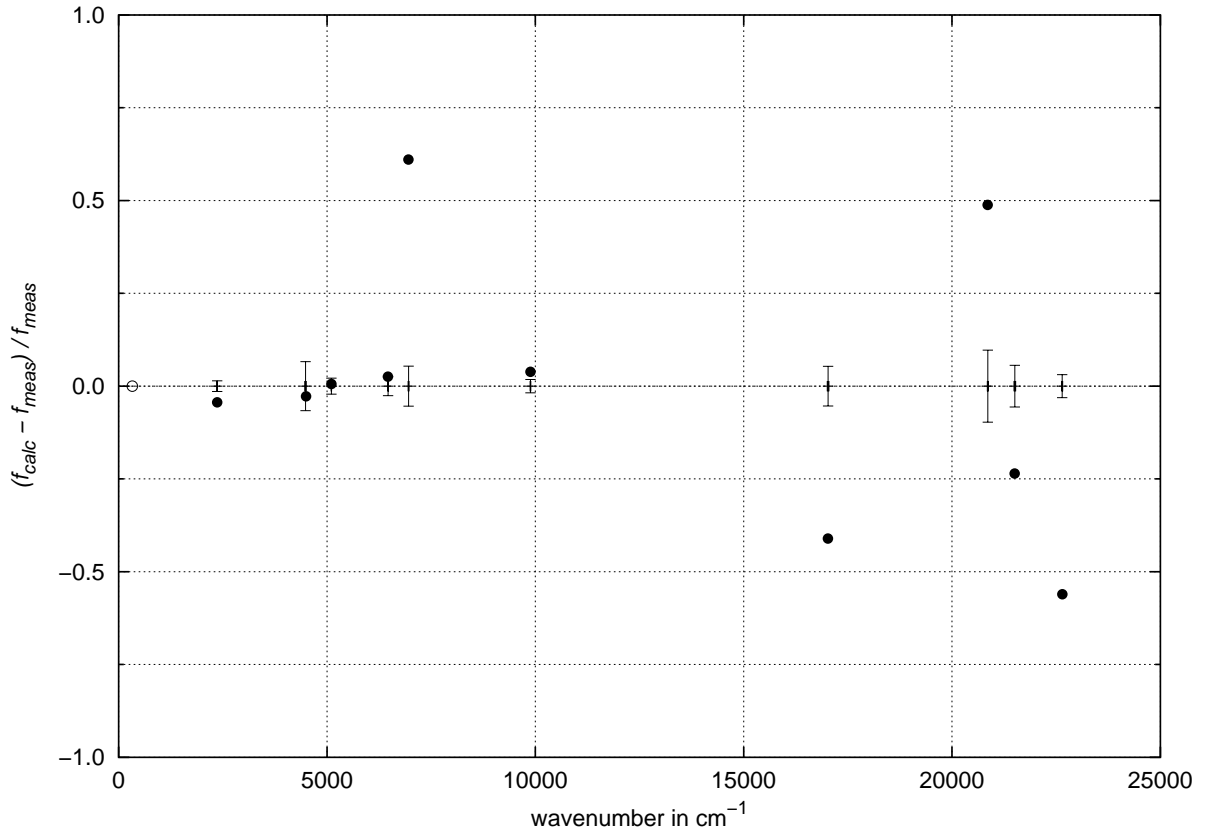


Figure 5.3: Comparison of calculated (dots) and measured (errorbars) oscillator strengths for Pr:ZBLAN. The circle indicates the calculated center of mass position of the ground state.

Table 5.6: Intermediate coupling in Pr:ZBLAN: Squared coefficients of LS -components for the energy levels in the first column. Overlines indicate a negative sign of the appropriate unsquared coefficient.

	3P_0	1S_0	
8	$\overline{0.9902}$	0.0098	
12	0.0098	0.9902	
	3P_1		
9	1.0000		
	3F_2	1D_2	3P_2
3	$\overline{0.9781}$	0.0218	0.0002
7	0.0211	0.8986	0.0803
11	0.0008	0.0797	$\overline{0.9195}$
	3F_3		
4	1.0000		
	3H_4	3F_4	1G_4
0	$\overline{0.9730}$	0.0009	$\overline{0.0261}$
5	0.0137	0.6690	$\overline{0.3173}$
6	0.0133	$\overline{0.3301}$	$\overline{0.6566}$
	3H_5		
1	1.0000		
	3H_6	1I_6	
2	0.9972	$\overline{0.0028}$	
10	$\overline{0.0028}$	0.9972	

5.5 Er:ZBLAN

Triply ionized erbium has the electronic configuration $[\text{Xe}]4f^{11}$ and is therefore a three-hole system with a more complex set of states than praseodymium and thulium. Like in a three-electron system, there are 17 LS -terms:

$$\begin{aligned}
 &^2S, ^2D^{(1/2)}, ^2F^{(1/2)}, ^2G^{(1/2)}, ^2H^{(1/2)}, ^2I, ^2K, ^2L \\
 &^4S, ^4D, ^4F, ^4G, ^4I,
 \end{aligned} \tag{5.22}$$

where the terms 2D , 2F , 2G , and 2H appear twice with different properties in Racah's group theoretical classification. Normally they are distinguished in short by adding the numbers 1 or 2 in parantheses. The spin-orbit interaction splits the LS -states to 41 LSJ -states consisting of 364 Stark levels in total.

The energy level calculations were performed in the same three steps as in the cases of thulium and praseodymium with the difference that for the three-hole system erbium, the

Table 5.7: Results of the energy level and Judd-Ofelt fits for Er:ZBLAN to 21 absorption lines. The constraints $M^2 = 0.56 M^0$, $M^4 = 0.38 M^0$, $P^4 = 0.75 P^2$, and $P^6 = 0.50 P^2$ were made.

parameter	initial	step 1	step 2	step 3	unit
base	219.00	80.87	171.02	50.99	cm^{-1}
F^2	97483.00	97981.89	96524.60	97088.92	cm^{-1}
F^4	67904.00	73240.32	69795.97	68587.69	cm^{-1}
F^6	54010.00	53172.31	54060.53	55006.43	cm^{-1}
ζ	2376.00	2383.96	2355.08	2369.69	cm^{-1}
α	17.79		19.33	17.81	cm^{-1}
β	-582.10		-646.19	-559.04	cm^{-1}
γ	1800.00		1721.75	1603.10	cm^{-1}
T^2	400.00		436.44	471.61	cm^{-1}
T^3	43.00		26.93	20.39	cm^{-1}
T^4	73.00		98.35	18.81	cm^{-1}
T^6	-271.00		-562.79	-398.11	cm^{-1}
T^7	308.00		39.88	199.03	cm^{-1}
T^8	299.00		338.92	449.82	cm^{-1}
M^0	3.86			4.66	cm^{-1}
P^2	594.00			475.64	cm^{-1}
$\overline{\Delta k}$		1475.3	480.3	93.3	cm^{-1}
Ω_2		2.931	2.822	2.915	pm^2
Ω_4		1.476	1.670	1.464	pm^2
Ω_6		1.184	1.172	1.184	pm^2
$\overline{\Delta f}$		65.4	67.4	64.9	10^{-8}

Coulomb configuration interaction, besides the three two-electron operators, consists of six three-electron operators with the radial integrals T^2 , T^3 , T^4 , T^6 , T^7 , and T^8 . The values for the initial guess were again taken from [39], whereas it should be noted that the parameters γ and T^2 were not fitted in this publication and different factors connecting the M^k and P^k integrals were used (see section 5.3).

In table 5.7 the values of the radial integrals during the three-step fitting procedure are given. All parameters stay in the usual range, and in contrast to praseodymium and thulium, the inclusion of the parameters M^0 and P^2 results in a significantly improved energy level system. Perhaps in these cases the number of measured energy levels was too small. Taking only Coulomb and spin-orbit interaction in the first fitting step, however, gives much worse

values compared with the other two ions. The large value of $\overline{\Delta k}$ is mainly due to ${}^2K_{15/2}$ and ${}^2K_{13/2}$ with deviations of about 600 cm^{-1} and 500 cm^{-1} respectively. Again, like in case of the other ions, the Judd-Ofelt parameters from the first step on show only minor changes.

The results of the last step in the fitting process, together with the measured values, are listed in table 5.8. The correspondence is very good, and larger deviations are only found for some energy levels with large uncertainty in the measurement. In some cases the deviation of the calculated values exceeds the specified uncertainty a little, but in most cases it is much smaller. Compared with thulium and praseodymium the oscillator strengths in case of erbium match better, the deviation is usually similar to the uncertainty of the measurement. An exception is level ${}^4D_{7/2}$ with a rather large difference to the measurement. Figure 5.4 shows the relation between calculated and measured oscillator strengths in a graphical form and also illustrates the high accuracy of the erbium fit. The large uncertainties around 28000 cm^{-1} and 39000 cm^{-1} are due to peak splitting procedures. From table 5.8 it can be

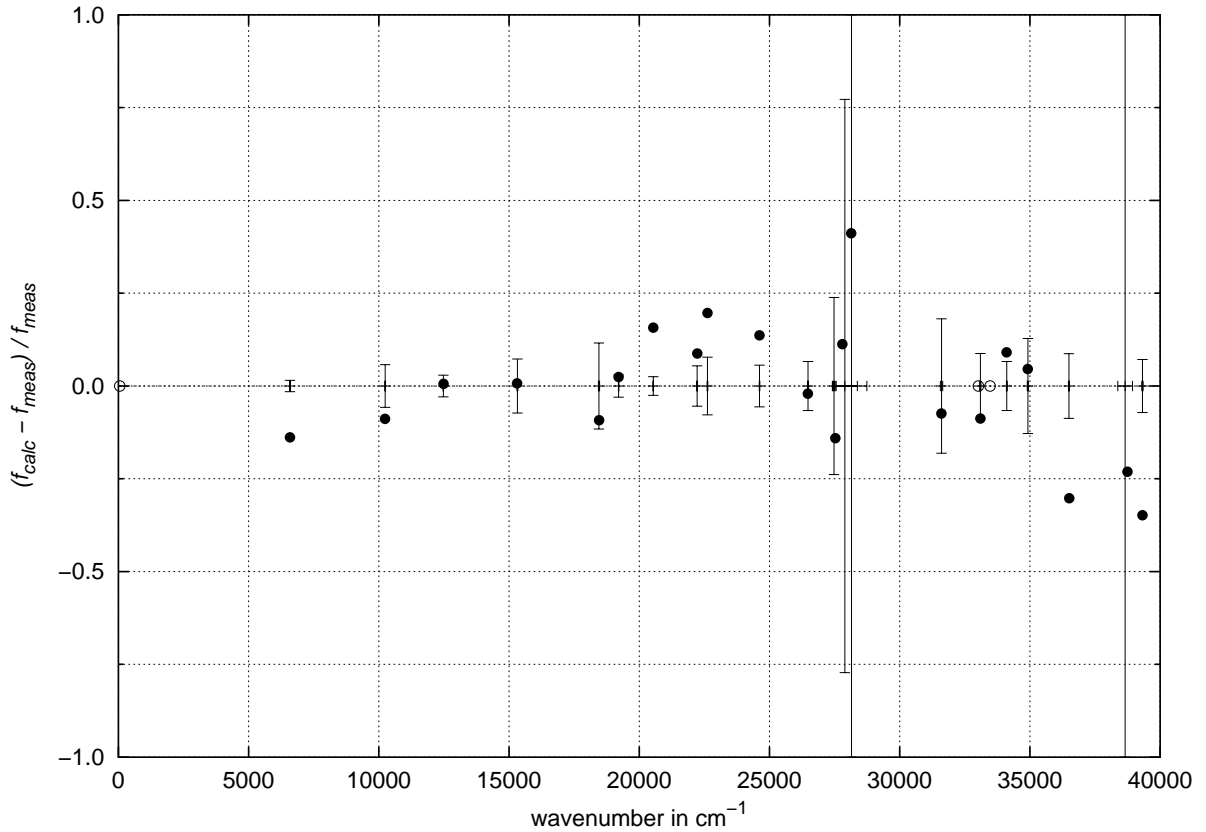


Figure 5.4: Comparison of calculated (dots) and measured (errorbars) oscillator strengths for Er:ZBLAN. The circles indicate calculated levels which were not measured.

seen that the energy level spectrum of erbium exceeds the transmission window of ZBLAN and reaches nearly 100000 cm^{-1} . Levels $^2\text{P}_{1/2}$ and $^4\text{G}_{5/2}$ were not observed, and the calculation reveals that this is due to extremely small oscillator strengths. The ground state absorption $^4\text{I}_{15/2} \rightarrow ^2\text{P}_{1/2}$ is discriminated by the selection rule $\Delta J \leq 6$ of electric dipole transitions, as given in section 2.2.

Table 5.9 provides a listing of the non-zero coefficients of all states in intermediate coupling. It is only the first three and some higher energy levels that correspond to states with a dominating LS -component above 75 %. The smallest maximum coefficient is 24 % in case of energy level 10. Such states are very likely to have different names in different host materials, since small variations may change the maximum coefficient. The transformation matrix to intermediate coupling again was used to calculate the radiative emission and absorption properties of Er:ZBLAN. For obvious reasons these tables were limited to transitions between states with energy levels below 45000 cm^{-1} and may be found in section D.2 in the appendix.

Table 5.8: Optimum energy level and Judd-Ofelt fits for Er:ZBLAN

no.	level	k_{meas} cm^{-1}	Δk_{meas} cm^{-1}	k_{calc} cm^{-1}	Δ cm^{-1}	f_{meas} 10^{-8}	Δf_{meas} 10^{-8}	f_{ed} 10^{-8}	f_{md} 10^{-8}	Δ 10^{-8}
0	$^4\text{I}_{15/2}$			51				0.0	0.0	
1	$^4\text{I}_{13/2}$	6585	(3)	6586	0.9	186.3	(2.9)	113.9	46.6	-25.8
2	$^4\text{I}_{11/2}$	10246	(8)	10237	-8.5	55.6	(3.2)	50.7	0.0	-4.9
3	$^4\text{I}_{9/2}$	12480	(6)	12483	3.3	28.7	(0.8)	28.9	0.0	0.2
4	$^4\text{F}_{9/2}$	15322	(17)	15306	-15.7	185.6	(13.5)	186.9	0.0	1.3
5	$^4\text{S}_{3/2}$	18454	(21)	18455	1.2	49.0	(5.7)	44.5	0.0	-4.5
6	$^2\text{H}_{11/2}^{(2)}$	19209	(7)	19209	-0.1	475.2	(14.3)	486.7	0.0	11.6
7	$^4\text{F}_{7/2}$	20538	(5)	20538	0.0	155.3	(3.9)	179.7	0.0	24.4
8	$^4\text{F}_{5/2}$	22224	(11)	22228	4.4	49.1	(2.7)	53.5	0.0	4.3
9	$^4\text{F}_{3/2}$	22619	(14)	22617	-2.3	25.4	(2.0)	30.4	0.0	5.0
10	$^4\text{F}_{9/2}$	24618	(11)	24613	-5.2	56.8	(3.2)	64.5	0.0	7.7
11	$^4\text{G}_{11/2}$	26476	(16)	26471	-5.4	895.3	(59.0)	876.9	0.0	-18.4
12	$^4\text{G}_{9/2}$	27480	(39)	27531	50.8	148.8	(35.5)	127.8	0.0	-20.9
13	$^2\text{K}_{15/2}$	27894	(478)	27797	-96.7	40.5	(31.3)	39.6	5.5	4.6
14	$^4\text{G}_{7/2}$	28149	(588)	28134	-15.3	30.5	(30.5)	43.0	0.0	12.5
15	$^2\text{P}_{3/2}$	31608	(46)	31601	-6.7	6.9	(1.3)	6.4	0.0	-0.5
16	$^2\text{P}_{1/2}$			33021				0.0	0.0	
17	$^2\text{K}_{13/2}$	33096	(24)	33096	-0.1	10.5	(0.9)	9.4	0.2	-0.9
18	$^4\text{G}_{5/2}$			33473				0.9	0.0	

Table 5.8: Optimum energy level and Judd-Ofelt fits for Er:ZBLAN (*continued*)

no.	level	k_{meas} cm ⁻¹	Δk_{meas} cm ⁻¹	k_{calc} cm ⁻¹	Δ cm ⁻¹	f_{meas} 10 ⁻⁸	Δf_{meas} 10 ⁻⁸	f_{ed} 10 ⁻⁸	f_{md} 10 ⁻⁸	Δ 10 ⁻⁸
19	⁴ G _{7/2}	34111	(15)	34104	-6.6	15.8	(1.0)	17.2	0.0	1.4
20	² D _{5/2} ⁽¹⁾	34920	(20)	34918	-1.9	9.0	(1.2)	9.4	0.0	0.4
21	² H _{9/2} ⁽²⁾	36496	(19)	36512	15.7	36.5	(3.2)	25.5	0.0	-11.0
22	⁴ D _{5/2}	38655	(279)	38744	89.1	14.3	(19.9)	11.0	0.0	-3.3
23	⁴ D _{7/2}	39324	(25)	39323	-0.8	753.7	(53.9)	491.3	0.0	-262.4
24	² I _{11/2}			41168				17.0	0.0	
25	² L _{17/2}			41632				57.0	0.0	
26	⁴ D _{3/2}			42344				5.8	0.0	
27	² P _{3/2}			42891				0.2	0.0	
28	² I _{13/2}			43601				18.9	0.2	
29	⁴ D _{1/2}			47085				0.0	0.0	
30	² L _{15/2}			47860				3.1	0.0	
31	² H _{9/2} ⁽¹⁾			48184				2.5	0.0	
32	² D _{5/2} ⁽²⁾			49005				5.5	0.0	
33	² H _{11/2} ⁽¹⁾			51183				6.3	0.0	
34	² F _{7/2} ⁽²⁾			54537				11.0	0.0	
35	² D _{3/2} ⁽²⁾			55119				0.5	0.0	
36	² F _{5/2} ⁽²⁾			63208				0.0	0.0	
37	² G _{7/2} ⁽²⁾			66325				0.8	0.0	
38	² G _{9/2} ⁽²⁾			70311				1.5	0.0	
39	² F _{5/2} ⁽¹⁾			93316				0.0	0.0	
40	² F _{7/2} ⁽¹⁾			97811				8.8	0.0	
		$\overline{\Delta k}$:		93.3		$\overline{\Delta f}$:		64.9		

Table 5.9: Intermediate coupling in Er:ZBLAN: Squared coefficients of *LS*-components for the energy levels in the first column. Overlines indicate a negative sign of the appropriate unsquared coefficient.

	² P _{1/2}	⁴ D _{1/2}
16	0.9218	$\overline{0.0782}$
29	$\overline{0.0782}$	0.9218

Table 5.9: Intermediate coupling in Er:ZBLAN (*continued*)

	$^4S_{3/2}$	$^4F_{3/2}$	$^2P_{3/2}$	$^4D_{3/2}$	$^2D_{3/2}^{(2)}$	$^2D_{3/2}^{(1)}$	
5	0.6845	0.0488	0.1902	0.0019	0.0005	0.0741	
9	0.1600	0.6297	0.0056	0.0000	0.0000	0.2048	
15	0.1245	0.2379	0.3740	0.0327	0.0337	0.1972	
26	0.0060	0.0603	0.0786	0.5350	0.0259	0.2942	
27	0.0243	0.0096	0.3294	0.2132	0.2559	0.1675	
35	0.0007	0.0137	0.0223	0.2172	0.6840	0.0621	
	$^4F_{5/2}$	$^4G_{5/2}$	$^2D_{5/2}^{(1)}$	$^4D_{5/2}$	$^2D_{5/2}^{(2)}$	$^2F_{5/2}^{(2)}$	$^2F_{5/2}^{(1)}$
8	0.8468	0.0013	0.1247	0.0023	0.0181	0.0050	0.0019
18	0.0010	0.9143	0.0123	0.0003	0.0096	0.0351	0.0274
20	0.1344	0.0006	0.5554	0.1472	0.1613	0.0007	0.0004
22	0.0104	0.0210	0.2973	0.4285	0.2345	0.0071	0.0013
32	0.0041	0.0249	0.0049	0.3937	0.4510	0.0789	0.0425
36	0.0032	0.0363	0.0049	0.0263	0.1253	0.5985	0.2054
39	0.0001	0.0017	0.0006	0.0017	0.0001	0.2746	0.7212
	$^4F_{7/2}$	$^4G_{7/2}$	$^2G_{7/2}^{(1)}$	$^4D_{7/2}$	$^2F_{7/2}^{(2)}$	$^2G_{7/2}^{(2)}$	$^2F_{7/2}^{(1)}$
7	0.9256	0.0011	0.0437	0.0001	0.0030	0.0242	0.0023
14	0.0376	0.4176	0.2589	0.0042	0.0227	0.2357	0.0234
19	0.0251	0.5374	0.2757	0.0018	0.0014	0.1562	0.0025
23	0.0016	0.0128	0.0013	0.9443	0.0103	0.0001	0.0296
34	0.0101	0.0298	0.0181	0.0452	0.5234	0.0005	0.3728
37	0.0000	0.0013	0.3947	0.0000	0.0314	0.5716	0.0009
40	0.0000	0.0001	0.0076	0.0044	0.4078	0.0117	0.5685
	$^4I_{9/2}$	$^4F_{9/2}$	$^2H_{9/2}^{(1)}$	$^4G_{9/2}$	$^2H_{9/2}^{(2)}$	$^2G_{9/2}^{(2)}$	$^2G_{9/2}^{(1)}$
3	0.5167	0.1406	0.0372	0.0002	0.1732	0.0521	0.0800
4	0.2731	0.5845	0.0000	0.0085	0.0090	0.0455	0.0793
10	0.1265	0.2379	0.0690	0.0515	0.1700	0.1548	0.1903
12	0.0455	0.0012	0.0082	0.8016	0.1393	0.0036	0.0005
21	0.0374	0.0351	0.0805	0.1285	0.3247	0.1573	0.2365
31	0.0008	0.0000	0.7811	0.0071	0.1779	0.0266	0.0065
38	0.0000	0.0007	0.0240	0.0025	0.0058	0.5600	0.4069
	$^4I_{11/2}$	$^2H_{11/2}^{(2)}$	$^4G_{11/2}$	$^2I_{11/2}$	$^2H_{11/2}^{(1)}$		
2	0.8235	0.1477	0.0132	0.0038	0.0118		

Table 5.9: Intermediate coupling in Er:ZBLAN (*continued*)

6	0.1500	$\overline{0.4708}$	0.3549	$\overline{0.0030}$	0.0213
11	0.0255	$\overline{0.2658}$	$\overline{0.6055}$	$\overline{0.0005}$	0.1027
24	$\overline{0.0010}$	0.0162	0.0120	0.6746	0.2962
33	0.0001	0.0995	0.0144	$\overline{0.3180}$	0.5680
${}^4I_{13/2}$ ${}^2K_{13/2}$ ${}^2I_{13/2}$					
1	0.9913	$\overline{0.0077}$	0.0009		
17	0.0055	0.8977	0.0968		
28	$\overline{0.0032}$	$\overline{0.0946}$	0.9022		
${}^4I_{15/2}$ ${}^2K_{15/2}$ ${}^2L_{15/2}$					
0	0.9716	$\overline{0.0281}$	0.0003		
13	$\overline{0.0278}$	$\overline{0.9162}$	0.0560		
30	0.0006	0.0557	0.9437		
${}^2L_{17/2}$					
25	1.0000				

5.6 Comparison with the literature

Energy level fits are usually performed for rare earth ions in crystalline hosts since the large number of Stark levels observed in these materials is better suited to such a fitting procedure. Nevertheless, table 5.10 besides LaF_3 crystals also contains the radial parameters obtained for two more praseodymium doped glasses besides our ZBLAN and for water, which is somewhat similar to glasses. ZBS is a zinc borosulphate glass and SFSP a mixed fluoride-phosphate glass. The values of the parameters of Coulomb and spin-orbit interaction are similar in all hosts whereas the parameters α , β , and γ show some variations but in all cases are of the same order of magnitude. Much larger are the deviations in case of the magnetic interaction parameters M^0 and P^2 , but those are the smallest contributions to the total Hamiltonian. All in all it can be expected therefore that the transition matrix elements calculated from either set of radial parameters will be similar.

In table 5.11 a similar collection of radial parameters for erbium doped materials is shown. Besides our ZBLAN and a cadmium borosulphate glass the parameters obtained for water and LaF_3 and LaCl_3 as crystalline hosts are contained again. Due to the parameters T^i corresponding to effective three electron operators of the Coulomb configuration interaction the number of parameters is much larger than in case of praseodymium or thulium. However, there are a lot more energy levels available for the fitting procedure. The magnitude of the variations of the parameters corresponding to the Coulomb and spin-orbit interaction again is not large but in contrast to praseodymium this also holds for α and β . The other parameters

Table 5.10: Radial parameters of triply ionized praseodymium in several hosts. Numbers in parantheses were not varied in the fitting procedure. The following parameters were constrained to certain values: $M^2 = 0.56M^0$, $M^4 = 0.38M^0$, $P^4 = 0.75P^2$, and $P^6 = 0.50P^2$.

parameter	ZBLAN	ZBS	SFSP	H ₂ O	LaF ₃	LaF ₃	LaF ₃
F^2	68576	71354	70247 [†]	68674 [†]	68805 [†]	68878	69305
F^4	49973	54336	51534 [†]	50395 [†]	50575 [†]	50347	50675
F^6	32415	36426	35819 [†]	32648 [†]	32715 [†]	32901	32813
ζ	728	736	739.2	740.75	744.44	751.7	750.8
α	17	(31.60)	5.3	21.255	15.294	16.23	(21)
β	-418	(-1450)	-457.02	-799.94	-669.02	-566.6	-842
γ	(1371.00)	(1260)		1342.9	1411.8	1371	1625
M^0	0.2	(1.70)				2.08 [‡]	(1.99)
P^2	1.7	(255)				-88.6 [‡]	(200)
ref.	here	[37]	[90]	[56]	[68]	[39]	[5]

[†] Values calculated from given E^i parameters (see appendix C)

[‡] Special constraints: $M^2 = 0.56M^0$, $M^4 = 0.31M^0$, $P^4 = 0.50P^2$, and $P^6 = 0.10P^2$

are of the same order of magnitude in all materials except LaCl₃, which seems to be due to the small number of used parameters which are known to be not independent (see appendix C). The good correspondence of the M^0 and P^2 values is striking and may be addressed to the large number of observed absorption transitions.

Table 5.11: Radial parameters of triply ionized erbium in several hosts. Numbers in parantheses were not varied in the fitting procedure. The following parameters were constrained to certain values: $M^2 = 0.56M^0$, $M^4 = 0.38M^0$, $P^4 = 0.75P^2$, and $P^6 = 0.50P^2$.

parameter	ZBLAN	CdBS	H ₂ O	LaF ₃	LaF ₃	LaCl ₃
F^2	97150	100081	99183 [†]	97483	100274	99115
F^4	68917	71594	72778 [†]	67904	70555	73444
F^6	56692	50762	53812 [†]	54010	49900	50496
ζ	2360	2394	2380.7	2376	2381	2367
α	17.4	13.50	18.347	17.79	17.88	19.7
β	-553	-585	-509.28	-582.1	-599	-427
γ	1348	1675	649.71	(1800)	1719	(750)
ref.	here	[91]	[56]	[39]	[5]	[92]

Radial parameters of triply ionized erbium in several hosts (*continued*)

parameter	ZBLAN	CdBS	H ₂ O	LaF ₃	LaF ₃	LaCl ₃
T^2	551	(647)		(400)	441	(0)
T^3	20.7	(46)		43	42	(0)
T^4	11.4	(80)		73	64	455
T^6	-405	(-321)		-271	-314	-256
T^7	228	(462)		308	387	168
T^8	530	(451)		299	363	(0)
M^0	4.9	(3.95)		3.86 [†]	(4.58)	
P^2	556	(506)		594 [‡]	852	
ref.	here	[91]	[56]	[39]	[5]	[92]

[†] Values calculated from given E^i parameters (see appendix C)

[‡] Special constraints: $M^2 = 0.56M^0$, $M^4 = 0.31M^0$, $P^4 = 0.50P^2$, and $P^6 = 0.10P^2$

Table 5.12: Radial parameters of triply ionized thulium in several hosts. Numbers in parantheses were not varied in the fitting procedure. The following parameters were constrained to certain values: $M^2 = 0.56M^0$, $M^4 = 0.38M^0$, $P^4 = 0.75P^2$, and $P^6 = 0.50P^2$.

parameter	ZBLAN	ZBLAN	MKZ	H ₂ O	LaF ₃	LaF ₃
F^2	102403	104111 [†]	105707 [†]	103886 [†]	100134	102459
F^4	73242	77663 [†]	77402 [†]	77024 [†]	69613	72424
F^6	50320	59244 [†]	55762 [†]	57448 [†]	55975	51380
ζ	2583	2658.27	2655.4	2628.7	2636	2640
α	17.4	-3.75		14.677	17.26	(17)
β	-842	-241.80		-631.79	-624.5	-737
γ	(1820.00)				(1820)	(1700)
M^0	-2.4				3.81 [†]	(4.93)
P^2	12.8				695 [‡]	729.6
ref.	here	[93]	[94]	[56]	[39]	[5]

[†] Values calculated from given E^i parameters (see appendix C)

[‡] Special constraints: $M^2 = 0.56M^0$, $M^4 = 0.31M^0$, $P^4 = 0.50P^2$, and $P^6 = 0.10P^2$

Table 5.13: Judd-Ofelt parameters of triply ionized praseodymium in several glasses

glass	Ω_2	Ω_4	Ω_6	ref.
ZBLAN	1.730	4.970	6.885	here
ZBLAN	3.3	3.8	6.1	[75]
ZBLAN	0.84	4.79	9.14	[6]
ZBLA	-0.141	4.91	8.54	[95]
INDAT	-1.79	2.11	5.71	[89]
INDAT	-1.2	3.8	5.2	[77]
CdF ₂	-3.8	4.7	10.2	[77]
tellurite	0.86	6.36	8.01	[78]

The radial parameters of thulium doped in some hosts are listed in table 5.12 where MKZ is a sulphate glass. Again the parameters corresponding to Coulomb and spin-orbit interaction show only a minor and unspecific dependence on the host material. The largest variations are found in F^6 . This may be a result from the fact that in all hosts the parameter γ was fixed since in case of thulium the level 1S_0 is too far in the ultra-violet to be observed and γ is closely related to the position of this level as already mentioned. The energy level calculations performed for this work showed that F^6 is connected with γ to some degree, which may explain the larger deviation of this parameter in different hosts. In case of praseodymium the level 1S_0 is much less separated from the other levels of the ground configuration, and it turned out that the results of the fitting procedure are also less sensitive to the value of γ . Similar to praseodymium the variations of the other parameters are larger than those of the Slater and spin-orbit parameters. This is especially the case for the parameters M^0 and P^2 , which have only minor influence on the energy level structure, at least in glasses, where the Stark levels are not resolved.

Finally we shall give a collection of Judd-Ofelt parameters from the literature in tables 5.13 to 5.15 for praseodymium, erbium, and thulium doped glasses respectively. The Judd-Ofelt parameters of praseodymium in table 5.13 are of limited value since they strongly depend on the minimization method chosen as already explained in section 5.2. Therefore small or even negative value of Ω_2 are usually obtained. It seems that besides the values from this work only the parameters from [75] are based on the minimization method using measured values weighted by their uncertainty. The Judd-Ofelt parameters of the erbium doped ZBLAN glasses in table 5.14 are quite similar. The values of Ω_4 and Ω_6 in the other erbium doped glasses are comparable but Ω_2 is varies considerably. A similar behaviour can be observed from table 5.15 for thulium doped glasses.

To summarize this section: The radial parameters related to the energy level structure, which in case of the lanthanides is not very sensitive to the host material, show only a

Table 5.14: Judd-Ofelt parameters of triply ionized erbium in several glasses

glass	Ω_2	Ω_4	Ω_6	ref.
ZBLAN	2.912	1.464	1.184	here
ZBLAN	2.92	1.79	1.00	[6]
ZBLAN	2.91	1.27	1.11	[97]
ZBLAN	2.73	1.40	1.10	[65]
ZBLAN	1.83-2.70	0.96-1.40	0.81-0.91	[64]
HBLAC	3.20	1.65	1.23	[98]
INDAT	2.17-2.46	1.47-2.31	0.89-1.23	[74]
BZYTZ	1.89	1.54	0.95	[99]
ZnCd	1.3	1.6	0.9	[79]
ZnCl ₂	4.73	0.65	0.21	[100]
tellurite	2.60-5.41	0.93-1.33	0.70-1.04	[101]
silica	4.23	1.04	0.61	[97]

moderate host dependence which nevertheless is large enough to be not negligible. The main part of the host dependence is contained in the Judd-Ofelt parameters due to large variations in the intensities of the transitions. However, it should be kept in mind that the Judd-Ofelt parameters possess large uncertainties not only from the measurement but also due to the approximations made in the theory. In [96] it was reported that the statistical analysis of large sets of Judd-Ofelt parameters from the literature showed that the Judd-Ofelt parameters are not sensitive to small variations of glass compositions.

Table 5.15: Judd-Ofelt parameters of triply ionized thulium in several glasses

glass	Ω_2	Ω_4	Ω_6	ref.
ZBLAN	3.022	1.802	0.726	here
ZBLAN	2.70	1.59	1.09	[6]
ZBLAN	2.21-2.75	0.95-1.82	0.82-1.02	[81]
HBLAC	2.81	2.07	0.96	[98]
INDAT	1.77	2.30	1.69	[82]
ZnCd	2.1	1.5	1.3	[79]
GLS	5.7	1.7	1.4	[3]
tellurite	5.7	1.4	1.6	[102]

6 Emission spectroscopy of rare earth ions

In the last chapter we finished the extensive discussion of the radiative properties of triply ionized rare earth ions derived from absorption measurements. Before we finally begin with fiber laser simulations, we need to take care of two more aspects of rare earth spectroscopy. The theories did not allow the prediction of the lineshape of emission lines, therefore we need to measure these spectra. Furthermore we have to take non-radiative transitions into account.

6.1 Non-radiative transitions

For changing their electronic state, rare earth ions in solids do not necessarily absorb or emit photons, since they can undergo a variety of non-radiative transitions. The most important ones are multiphonon transitions affecting single ions and energy transfer processes between two ions. In principle both effects may be investigated separately, as energy transfer is negligible at low dopant concentrations and multiphonon transitions are vanishing at low temperatures and can be neglected for transitions with large energy gaps.

As for all excited states radiative transitions, multiphonon transitions, and energy transfers occur simultaneously, the lifetime τ consists of three terms according to

$$\tau = \frac{1}{A_{rad} + W_{mp} + W_{et}} , \quad (6.1)$$

where A_{rad} is the total radiative relaxation rate from equation (2.8), and W_{mp} and W_{et} are the rates of the multiphonon transitions and energy transfers respectively. The quantum yield η is defined as the radiative portion of the total relaxation rate of a given energy level, which is an important property for laser and amplifier applications:

$$\eta = \tau A_{rad} . \quad (6.2)$$

Multiphonon transitions. The interaction of f-electrons with vibration modes of the glass matrix allows excited electronic levels to relax by exciting vibrations of the glass network. Unlike the situation in crystals, these vibrations are spatially localized because of the absence of translational invariance in vitreous materials. Nevertheless, the quantized modes are commonly called phonons.

For small energy gaps in the order of $k_B T$, with Boltzmann's constant k_B and the temperature T , the transitions occur very fast in upward and downward directions leading to thermalization of the involved electronic levels. This happens especially for the Stark levels inside M_J -multiplets. In cases where some J -levels are closely located it is important to know

the relative occupation numbers of the corresponding states. The Boltzmann distribution yields, for the relative occupation number n_i of state i in the thermal equilibrium,

$$n_i = \frac{(2J_i + 1)e^{-E_i/k_B T}}{\sum_j (2J_j + 1)e^{-E_j/k_B T}} , \quad (6.3)$$

where E_i is the center of mass energy of state i , and the sum runs over all states in the neighborhood of i , including i . The common radiative lifetime of such a couple of energy levels is e.g.

$$\tau = \frac{1}{\sum_i n_i A_i} , \quad (6.4)$$

with the spontaneous radiative emission rate A_i from equation (2.8). For fast estimations the value

$$\frac{k_B T}{hc} \approx 200 \text{ cm}^{-1} \quad \text{for} \quad T = 293 \text{ K} \quad (6.5)$$

is often useful.

Energy gaps larger than the maximum phonon energy $E_{max} = h\nu_{max}$ must be bridged by more than one phonon, hence the name multiphonon transition. These transitions proceed predominantly in the downward direction and lead to high non-radiative relaxation rates for small energy gaps, which need only a couple of phonons for the transition.

Multiphonon relaxation rates increase with increasing temperature, and as it is expressed by equation (6.1), this leads to decreasing lifetimes of the electronic levels. This temperature dependence is strong in particular for levels which are closely spaced to the next lower lying energy level because of their low quantum yield. In the literature, two main theories describing the temperature and energy gap dependence of multiphonon transitions can be found: the Huang-Rhys theory [103] and the Riseberg-Moos theory [104].

Huang and Rhys [103] developed a single-configuration-coordinate model based on the Franck-Condon principle. This model was extended to arbitrary oscillator parabola and parabola offsets by Struck and Fonger [105, 106]. They derived an equation for the multiphonon relaxation rate which is given here in an approximation valid for transitions inside the $4f^N$ configuration of rare earth ions [106]:

$$W_{mp} = A \frac{[S_0 (n_B + 1)]^p}{p!} e^{-S_0(2n_B+1)} , \quad (6.6)$$

where A is an empirical factor in the order of 10^{13} s^{-1} , S_0 is the Huang-Rhys-Pekar number [106], which measures the parabola offset, n_B the Bose-Einstein occupation number of the effective phonon mode

$$n_B = \frac{1}{e^{h\nu/kT} - 1} , \quad (6.7)$$

Table 6.1: Multiphonon parameters of some fluoride glasses

glass	C s^{-1}	α cm	T K	ref.
BZYTZ	$4.5 \cdot 10^{10}$	$5.78 \cdot 10^{-3}$	300	[99]
HBLAC	$1.3 \cdot 10^9$	$5.0 \cdot 10^{-3}$	80	[98]
ZBLA	$1.88 \cdot 10^{10}$	$5.77 \cdot 10^{-3}$	80	[117, 118]
ZBLAN	$1.99 \cdot 10^5$	$2.11 \cdot 10^{-3}$	300	[6]
ZBLAN	$5.11 \cdot 10^{11}$	$6.65 \cdot 10^{-3}$		[65]
ZnCd	$8.4 \cdot 10^8$	$2.11 \cdot 10^{-3}$	300	[79]

and p the smallest number of phonons needed to bridge the energy gap ΔE . In principle, p should be an integer, but usually the expression $p = \Delta E/E_{max}$ is used.

In his approach, Kiel [107] examined the first-order term of the orbit-lattice interaction and carried it to high orders of time-dependent perturbation theory to describe the emission of many phonons. Based on this theoretically intractable approach, Riseberg and Moos [104] developed a phenomenological model for crystals, which was applied to glasses by Layne et al. [106, 108]. In this model, the multiphonon rate can be calculated by

$$W_{mp} = B (n_B + 1)^p e^{-\alpha \Delta E} , \quad (6.8)$$

where B and α are host dependent parameters, ΔE is the energy gap and n_B and p are denoted equivalent to equation (6.6). For the investigation of multiphonon relaxation rates as a function of the energy gap ΔE , equation (6.8) is often simplified to

$$W_{mp} = C e^{-\alpha \Delta E} . \quad (6.9)$$

However, it should be noted that the parameter C depends on temperature, as expressed by equation (6.8). While the maximum phonon energy is obtained from the Raman spectrum, the parameters C and α are calculated by a fit of the measured nonradiative emission rates for different ΔE to equation (6.9). For this procedure glasses with different dopant ions are necessary to obtain a variety of different ΔE 's. Furthermore, it is important to use low dopant concentrations to be able to neglect the energy transfer rates W_{et} in equation (6.1) when calculating W_{mp} from the measured lifetime. Tables of B or C and α for various glasses and other host materials can be found in many publications: [3, 6, 50, 79, 98, 99, 109, 110, 111, 112, 113, 114, 115, 116, 117, 118]. Table 6.1 is just a small collection of the values of some different fluoride glasses.

Equation (6.9) may be used to predict the multiphonon rate for given transitions, but because of the finite width of the levels of rare earth ions in glasses, the energy gaps are not

known exactly. This leads to significant errors for small gaps [99], which can be reduced with a numerical fit of the temperature dependence [98, 118].

It is worth noting that rare earth ions have typical Huang-Rhys-Pekar numbers $S_0 \ll 1$ [106], and it can be shown that in this case the temperature dependence of equations (6.6) and (6.8) is nearly the same from 0 K to temperatures well above room temperature [117, 118].

Both models predict a relaxation rate which is strongly decreasing with an increasing number of phonons p . Therefore, only the phonons with an energy near E_{max} are considered, as they lead to the smallest p . These highest energy phonons correspond to stretching vibrations of the network forming components of the glass, and their energy is a key parameter for the non-radiative properties of host materials. Typical maximum phonon energies are 1100 cm^{-1} for silica, 780 cm^{-1} for tellurite, 580 cm^{-1} for ZBLAN, 510 cm^{-1} for INDAT, and 350 cm^{-1} for GLS glasses.

Energy transfer. Energy transfer is caused by interactions between two dopant ions, e.g. via dipole-dipole coupling. These non-radiative interactions are discussed extensively in the literature, see e.g. [50, 114], so we need not go into detail here. But because of the fundamental importance of energy transfer processes in rare earth doped fiber lasers, we should give at least a rough sketch of the basic principles.

First of all we must distinguish between energy transfers between rare earth ions of the same species and between different ions in case of a co-doped material. The main consequence of the former is concentration quenching, i.e. the lifetime of energy levels decreases in most cases with increasing dopant concentration, but the reverse was also found [119]. If the distance between ions of the same type is small enough to transfer the excitation energy of

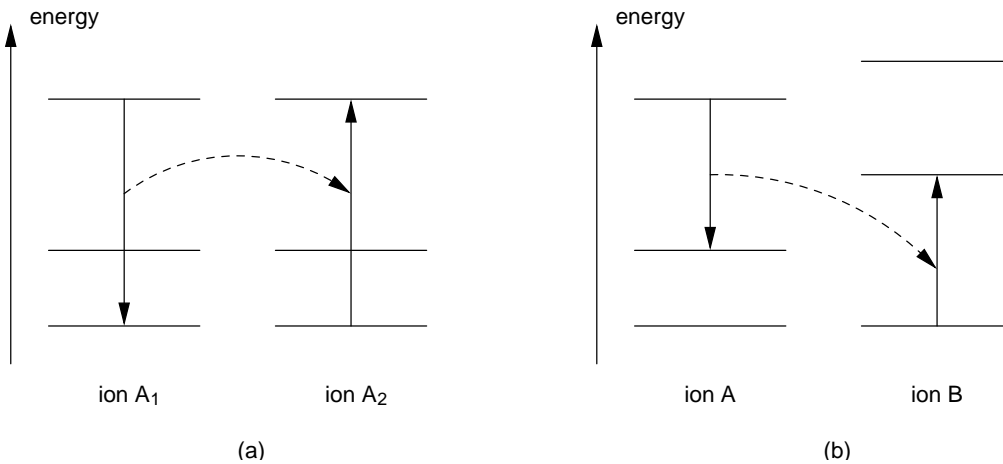


Figure 6.1: Two important energy transfer processes. (a) nearly resonant energy transfer between ions of the same species, (b) cross-relaxation between different ions.

ion A_1 to A_2 as figure 6.1(a) shows, a chain of energy transfers starts. This chain often ends at impurities of the glass matrix where the energy is absorbed by phonons and lost therefore for the laser process. Although the ions A_1 and A_2 are the same rare earths, the positions of their Stark levels are in general different because of their different neighborhoods. Therefore even this simple chain process is not completely energy resonant and needs interaction with absorbed and emitted phonons. An important parameter for the concentration quenching effect is the critical distance R_0 of the dopant ions. This distance is defined as the mean ion distance when the case

$$W_{et} = A_{rad} + W_{mp} \quad (6.10)$$

is reached and is different for different energy levels.

In contrast to the usually unwanted concentration quenching effect, energy transfer between different ions is often used for better performance of fiber lasers. A typical process of this kind is the cross-relaxation process in figure 6.1(b). As a co-dopant ytterbium is often used, because of its broad and strong absorption around $1\ \mu\text{m}$, where powerful laserdiodes are available as pump sources. The excitation of the ytterbium ions is then transferred to the actual laser ion, for which direct diode pumping is less efficient.

It is very difficult to classify all different types of energy transfers, since each pair of rare earth ions has its certain specialities. In the case of low phonon energy glasses, as for example ZBLAN, excited energy levels possess relatively large lifetimes in the millisecond range and therefore a lot of transitions may interact, because even processes where the acceptor ion is not in the ground state are important in these glasses.

6.2 Analysis of emission spectra

Emission spectroscopy is somewhat more difficult than absorption measurements. For this work a self-made fluorescence spectrometer was used, which is described in detail in appendix E. While large absorption spectra may be obtained as a whole, in emission each transition needs special treatment. The measured fluorescence spectra in general are evaluated using the same techniques as already described in case of the absorption spectra in section 4.3. The specialities in the evaluation of emission spectra are to be discussed in the following paragraphs.

Background losses. Instead of the transmission or absorption values obtained by absorption spectrometers, a fluorescence spectrometer delivers plain unscaled intensity spectra. Therefore the baseline correction does not play an important role, the dark current of the detectors is relatively small and simply subtracted from the measured spectra. The drawback of such a one-way measurement is the fact that the spectral response of the whole optical path is contained in the measurement results.

Figure 6.2 shows the transmission spectrum due to molecule absorptions in the free space and on the surfaces along the optical path. The strength of the liquid water absorption line

corresponds to a water film of about $20\text{ }\mu\text{m}$ thickness. The water film most probably occurred as condensed water on the surface of the detector window because the detector was cooled by liquid nitrogen in a dewar housing. To get this spectrum a SiC heating element from Kanthal with a power of 100 W was used instead of the fluorescence source. Such a heating element, which is also widely known under its product name *Globar*, has an operating temperature of $1000 - 1400\text{ }^\circ\text{C}$. It is used as a broadband graybody emitter instead of an expensive and complicated blackbody source. If the actual temperature T and emissivity $\epsilon(\nu)$ of the used heating element were known, the full spectral response $D(\nu)$ of the spectrometer including lenses, mirrors, the monochromator, detector, and a long-pass filter (see appendix E) could be obtained. This is due to the fact that the spectral intensity of such a radiation source is given by Planck's law

$$I_S(\nu)d\nu = \epsilon(\nu) \frac{8\pi\nu^2}{c^2} \frac{h\nu}{e^{h\nu/k_B T} - 1} d\nu, \quad (6.11)$$

where c is the speed of light in the medium (usually air), h Planck's constant, and k_B Boltz-

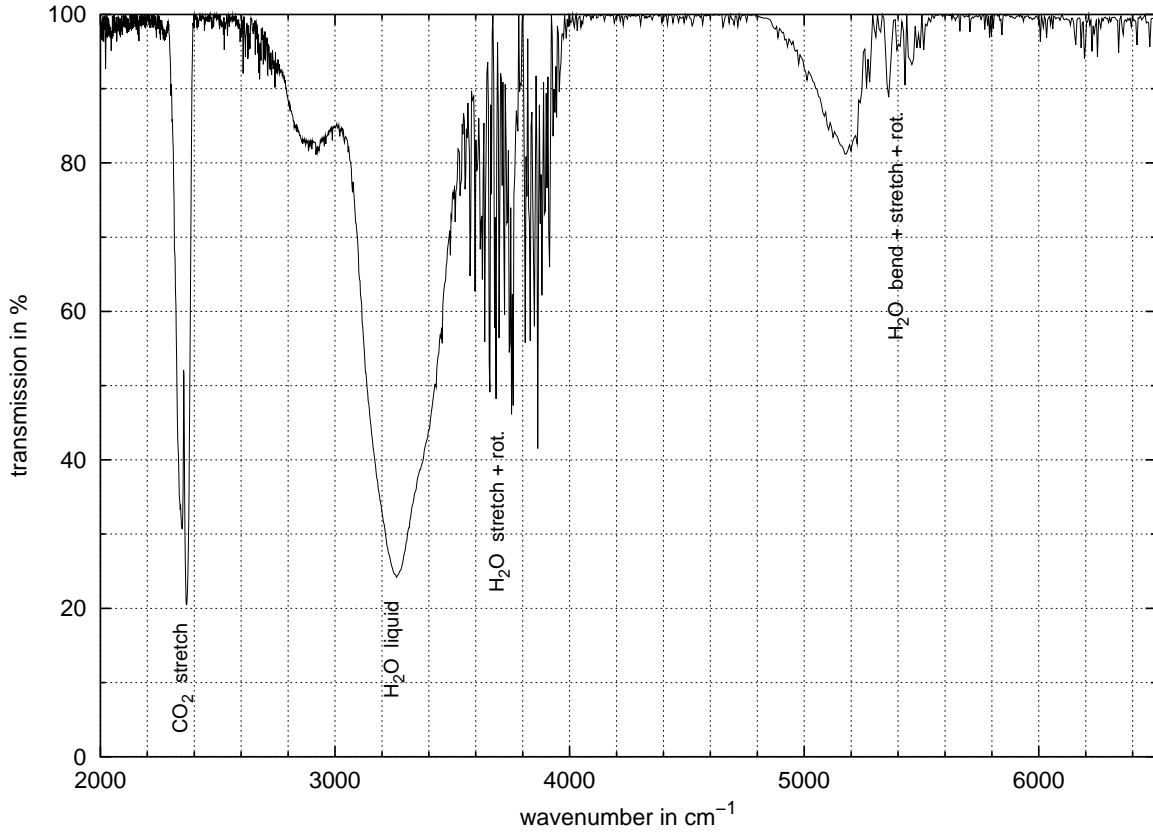


Figure 6.2: Background losses due to air absorption in the fluorescence spectrometer

mann's constant. The emissivity specifies the deviation from the blackbody radiation and should only be moderately wavelength dependent in the interesting spectral range. If $I_0(\nu)$ is the measured intensity spectrum, the spectral response may be calculated by

$$D(\nu) = \frac{I_0(\nu)}{I_S(\nu)} . \quad (6.12)$$

The quotient $I(\nu)/D(\nu)$, where $I(\nu)$ is a measured sample spectrum, is the pure fluorescence spectrum of the doped glass with accurate relative intensities of all detected fluorescence lines. However, in contrast to these theoretical considerations our graybody source had a temperature not known exactly and an unknown emissivity, but was used in the same manner by setting $\epsilon(\nu) = 1$. In the small spectral range spanned by an emission line, a constant emissivity should be a valid approximation, but information about the relative intensities is obviously lost. To get an idea of the errors caused by this treatment, equation (6.11) is eval-

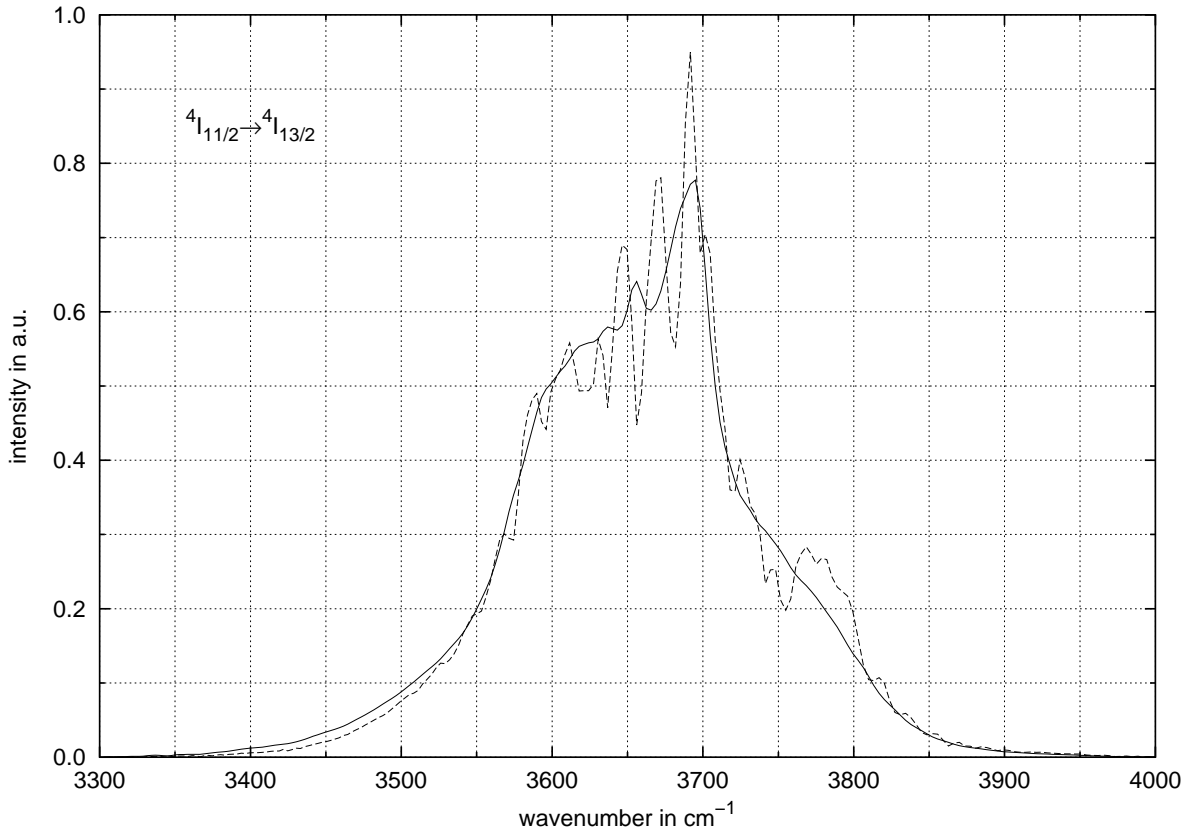


Figure 6.3: Corrected (smooth line) and measured (dashed line) spectrum of the $2.7\ \mu\text{m}$ fluorescence of Er:ZBLAN with superimposed absorption lines from gaseous water

uated for 1000 °C and 1400 °C resulting in a mean value $\overline{I_S(\nu)}$ and a respective uncertainty $\Delta\overline{I_S(\nu)}$.

The importance of the correction by the background spectrum $D(\nu)$, especially in the mid-infrared where a couple of molecule absorption lines are located, is demonstrated by figure 6.3. It shows the emission line of the transition $^4I_{11/2} \rightarrow ^4I_{13/2}$ in Er:ZBLAN, which is heavily distorted by the rotation spectrum of gaseous water combined with stretching vibrations of the water molecule. To get rid of the remaining artefacts due to different spectral resolutions of $I(\nu)$ and $I_0(\nu)$ the corrected spectrum $I(\nu)/D(\nu)$ must be slightly smoothed, which here was done by use of the Fourier technique described in section 4.3. The resolution of the corrected spectra was reduced by a factor of three.

Scaling to cross sections. Even corrected emission spectra as described in the preceding paragraph are still relative spectra because the fluorescence sample emits in all directions in contrast to absorption measurements where the intensity of a transmitted radiation beam is

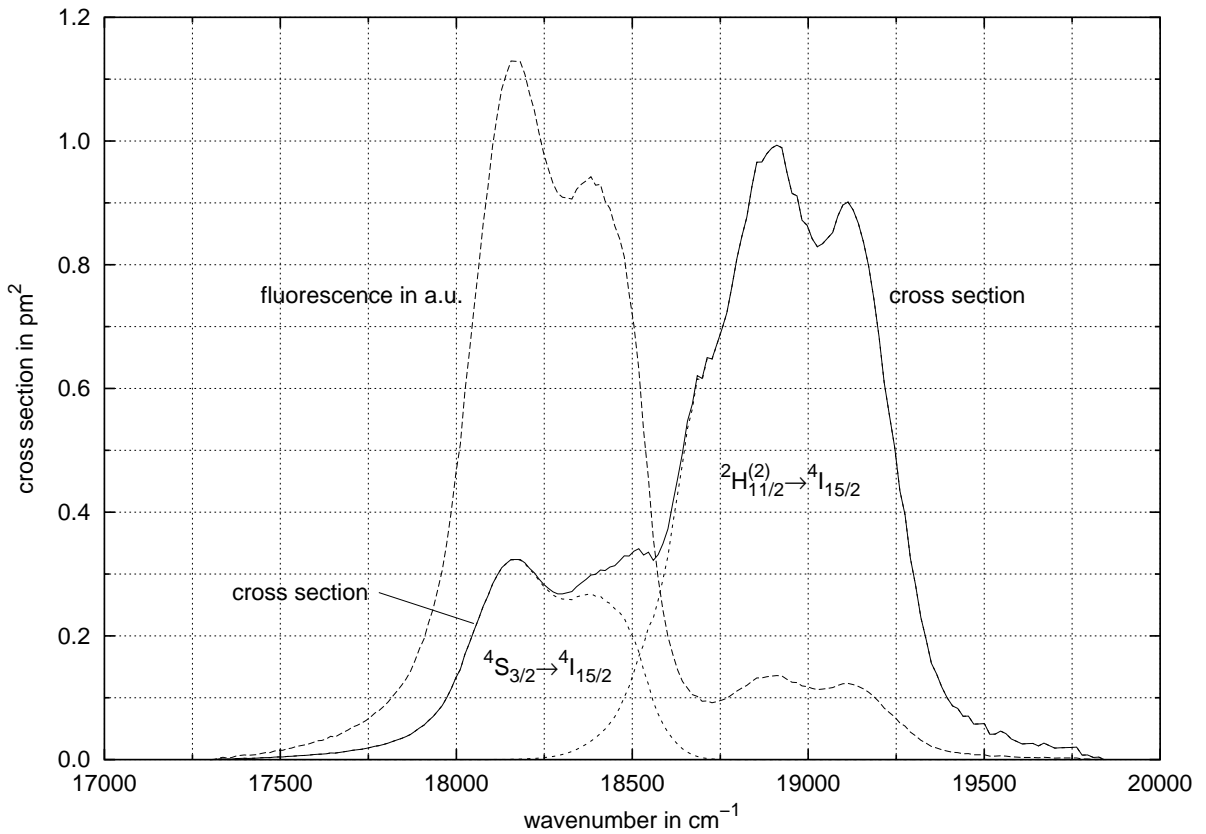


Figure 6.4: Separation of overlapping emission lines of two erbium transitions. Sample 1032

measured. However, for laser simulations the spectral cross section of stimulated emission is needed. Therefore we use the Fuchtbauer-Ladenburg equation (2.21) together with the calculated radiative spontaneous emission rate from equation (2.8) to scale the measured fluorescence lineshape $g_{21}(k)$ of a transition to a cross section spectrum

$$\sigma_{21}(k) = \frac{1}{8\pi c k_{cm}^2 n^2} A_{21} g_{21}(k) , \quad (6.13)$$

where the frequency ν was replaced by the wavenumber $k = \nu/c$ and the lineshape $g(k)$, due to the different normalization $\int g(k)dk = 1$, has the dimension of an inverse wavenumber in contrast to $g(\nu)$ and therefore a factor c is introduced.

Care must be taken in case of overlapping lines, which must be separated before equation (6.13) is applied to each component separately. Figure 6.4 shows that the application of equation (6.13) to the combined spectrum using the sum of the A_{21} 's of all lines contained in the spectrum would lead to completely wrong results. The initial levels of the two transitions in Er:ZBLAN shown in figure 6.4 are $^4S_{3/2}$ and $^2H_{11/2}^{(2)}$ respectively, which are separated by only about 750 cm^{-1} . Therefore they are thermally coupled by multiphonon transitions and the Boltzmann distribution (2.3) predicts a probability of only about 7 % for an excited ion in one of these two states to be actually in the higher state $^2H_{11/2}^{(2)}$. Therefore, in the fluorescence spectrum, the transition $^4S_{3/2} \rightarrow ^4I_{15/2}$ is dominating although $^2H_{11/2}^{(2)} \rightarrow ^4I_{15/2}$ turns out to have the larger emission cross section.

6.3 McCumber theory

In principle, emission spectra of most electronic transitions of a rare earth ion can be obtained if a suitable pump source is available. The usual type of absorption spectrometers, in contrast, deliver only the spectrum of transitions starting from the ground state because the intensity of the detection beam is too low to excite a significant part of the dopant ions. Measurement of excited state absorptions (ESA) is considerably more difficult even than obtaining emission cross sections [3]. Therefore, it would be a great help to be able to calculate ESA cross sections from the appropriate emission spectra. This does not seem to be impossible, since all three types of interactions of radiation and matter are linked by the equations (2.4) and (2.5).

Instead of averaging over virtually equally populated Stark levels as in the equations of chapter 2, McCumber calculated the cross sections taking into account for each Stark level the position and occupation probability due to Boltzmann statistics [120, 121]. His result for transitions between an upper level 2 and a lower level 1 was

$$\sigma_{12}(\nu) = \sigma_{21}(\nu) e^{(h\nu - \overline{\Delta E})/k_B T} , \quad (6.14)$$

where k_B is Boltzmann's constant, T the temperature, and $\overline{\Delta E}$ the free net energy required for an excitation from one Stark level of multiplet 1 to a Stark level in multiplet 2. According

to Boltzmann statistics this energy depends on the temperature by

$$e^{\overline{\Delta E}/k_B T} = \frac{n_1}{n_2}, \quad (6.15)$$

where n_i is the total probability of the electronic system of an ion to be in state i . If we denote by E_{is} the energy of Stark level i in multiplet s , the quotient on the right side of equation (6.15) can be written

$$\frac{n_1}{n_2} = \frac{\sum_{s=0}^{c_1-1} e^{-E_{1s}/k_B T}}{\sum_{s=0}^{c_2-1} e^{-E_{2s}/k_B T}}, \quad (6.16)$$

with c_s being the number of Stark levels in multiplet s . This number for an ion with an even number of f-electrons is $2J_s + 1$, and in case of an odd number of electrons $J + \frac{1}{2}$ due to Kramers degeneracy.

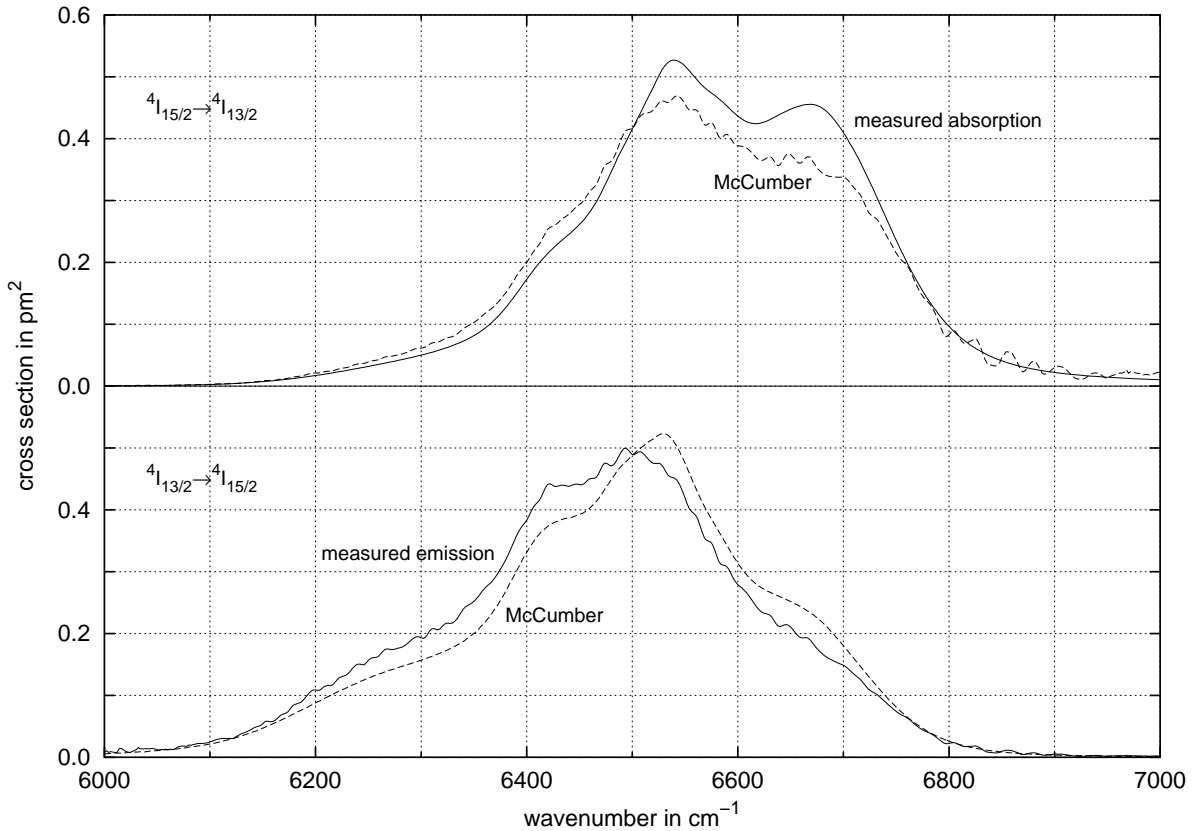


Figure 6.5: Application of the modified McCumber theory to Er:ZBLAN. Sample 1032

However, the positions of the Stark levels are not known in case of a rare earth ion in a glass host. Therefore, in [49] a modified McCumber theory was proposed. In this theory the Stark levels are assumed to be spaced equidistantly so that we can set

$$\begin{aligned} E_{1s} &= \frac{s}{c_1 - 1} \Delta E_1 \\ E_{2s} &= \frac{s}{c_2 - 1} \Delta E_2 + E_0, \end{aligned} \quad (6.17)$$

where ΔE_i is the difference between the highest and lowest Stark levels of multiplet i and E_0 the distance between the lowest Stark levels of both multiplets. All these values are not really well-defined and in [49] for E_0 the mean value of absorption and emission peak was used because both spectra were available, which is an unusual case. Furthermore it was reported that using the distance between the peak and the position where the line reaches 5 % of its peak value as ΔE_i produced satisfying results which were not very sensitive to this criterion. For level 1 the 5 % position at the low energy side of the emission spectrum was used and for level 2 the 5 % position at the high energy side of the absorption spectrum.

The McCumber theory is mainly used to calculate the emission cross section of the $1.55 \mu\text{m}$ transition ${}^4\text{I}_{13/2} \rightarrow {}^4\text{I}_{15/2}$ in erbium doped glasses for fiber amplifiers. When the modified McCumber theory was applied to all transitions in this work of which absorption *and* emission spectra were available, the best result was indeed received with this transition as shown in figure 6.5. The approximate lineshape of the respective transition on the one hand was usually achieved in the other cases, too, but in most cases not as well as in figure 6.5. On the other hand the relative magnitude of emission and absorption cross sections was often heavily over- or under-estimated.

Fiddling around with the three parameters E_0 , ΔE_1 , and ΔE_2 led to much better results but no rules applicable in general which would allow reasonable estimations of unknown cross section spectra were found. It turned out that the problem is not well suited to nonlinear fitting procedures, as $\chi^2(E_0, \Delta E_1, \Delta E_2)$ is quite flat in the optimum region and the three parameters are not completely independent. The parameter values resulting from the fitting procedure were strongly depending on the initial values used, whereas the calculated spectra were more or less independent of this choice. Using the k_{cm} , $\Delta k_{-\sigma}$ and $\Delta k_{+\sigma}$ values given in the tables of this work led to similar results compared with using peak and 5 % positions, sometimes the calculated spectra were better, sometimes worse than from the modified McCumber theory.

It should be noted that in contrast to these observations e.g. in [3] a strikingly good correspondence between measured and calculated line spectra using the modified McCumber theory was found for a couple of transitions.

6.4 Er : ZBLAN

Emission spectra of Er : ZBLAN were obtained using the setup described in appendix E with a titan-sapphire laser (TiSa) at about 800 nm as a pump source. The glass used is sample 1032

doped with about 1 mol% erbium (see tables 4.1 and 4.2), which was pumped with 1 – 4 W from the focussed TiSa laser beam. Figure 6.6 shows the relevant absorption transitions and all seven detected and evaluated emission transitions.

The ground state absorption (GSA) of the pump laser ends in level $^4I_{9/2}$, which preferably relaxes fast and non-radiatively to the next lower level $^4I_{11/2}$ since their energy difference can be bridged by less than four phonons. The $2.73\ \mu\text{m}$ transition to $^4I_{13/2}$ has already been the subject of extensive studies (e.g. [1, 4]) and is the strongest emission in the mid-infrared in ZBLAN glass. With moderate pump power applied to an erbium-doped ZBLAN fiber with bare fiber ends this transition is usually starting laser operation right from the Fresnel reflections at the fiber ends. This may be surprising at first, because the transition ends in the level from which the famous $1.54\ \mu\text{m}$ transition used by erbium doped fiber amplifiers (EDFA)

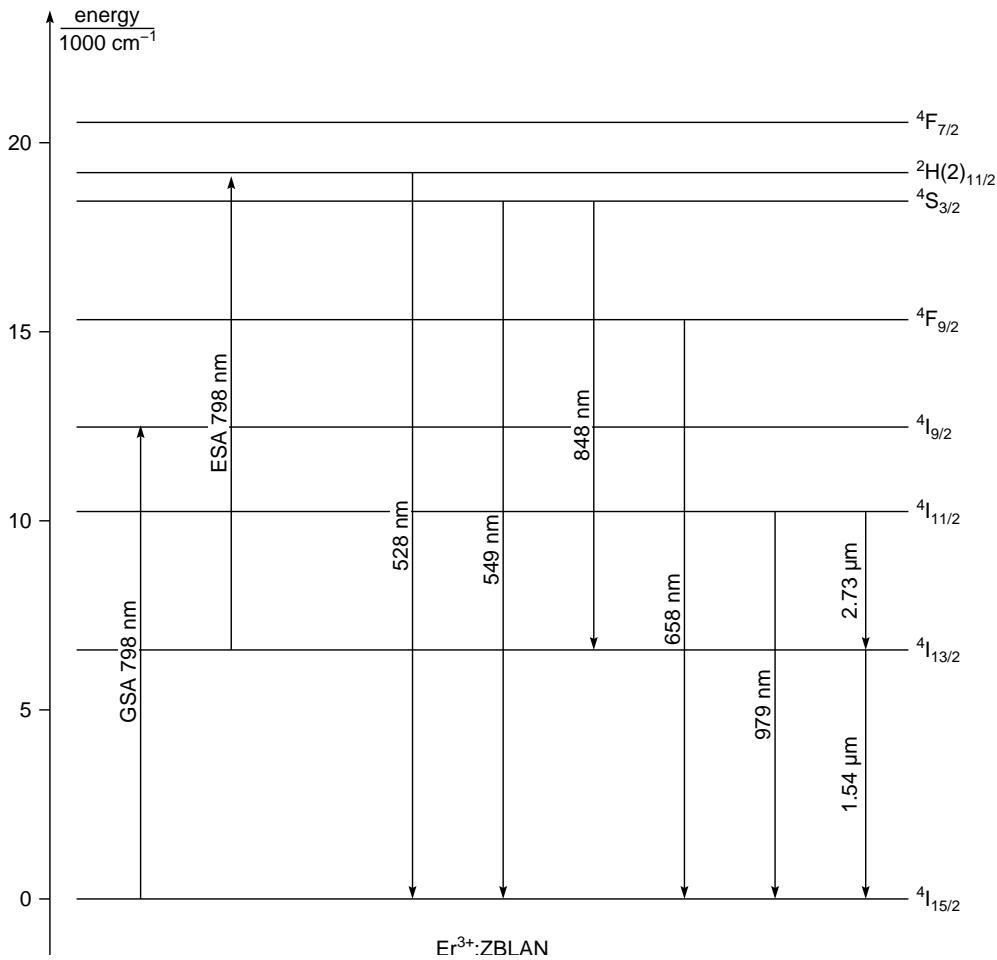


Figure 6.6: Energy levels of $\text{Er}:\text{ZBLAN}$ with pump transitions and evaluated emission lines

starts and which has a long lifetime of several milliseconds. The reason why the $2.73\ \mu\text{m}$ laser nevertheless runs effectively is due to the fact that the energy difference between $^4\text{I}_{13/2}$ and $^2\text{H}_{11/2}^{(2)}$ accidentally fits the GSA pumped with a wavelength of 800 nm. This results in an excited state absorption (ESA) of the pump radiation which continuously depletes the lower laser level.

The energy difference of the closely spaced level pair $^4\text{S}_{3/2}$ and $^2\text{H}_{11/2}^{(2)}$ is only about $750\ \text{cm}^{-1}$. Therefore these levels are thermally coupled by fast absorption and emission of phonons which, due to Boltzmann statistics, at room temperature leads to a relative occupation number of about 7 % for the upper level $^2\text{H}_{11/2}^{(2)}$. It may seem paradoxical but it is due to the short distance of these two levels that it is possible to observe the fluorescence from the relaxation of $^2\text{H}_{11/2}^{(2)}$ to the ground state. If the distance were somewhat larger, this level would relax very fast and non-radiative to $^4\text{S}_{3/2}$. Nevertheless, the small occupation number of the upper level results in a relatively small peak overlapping with the dominating peak

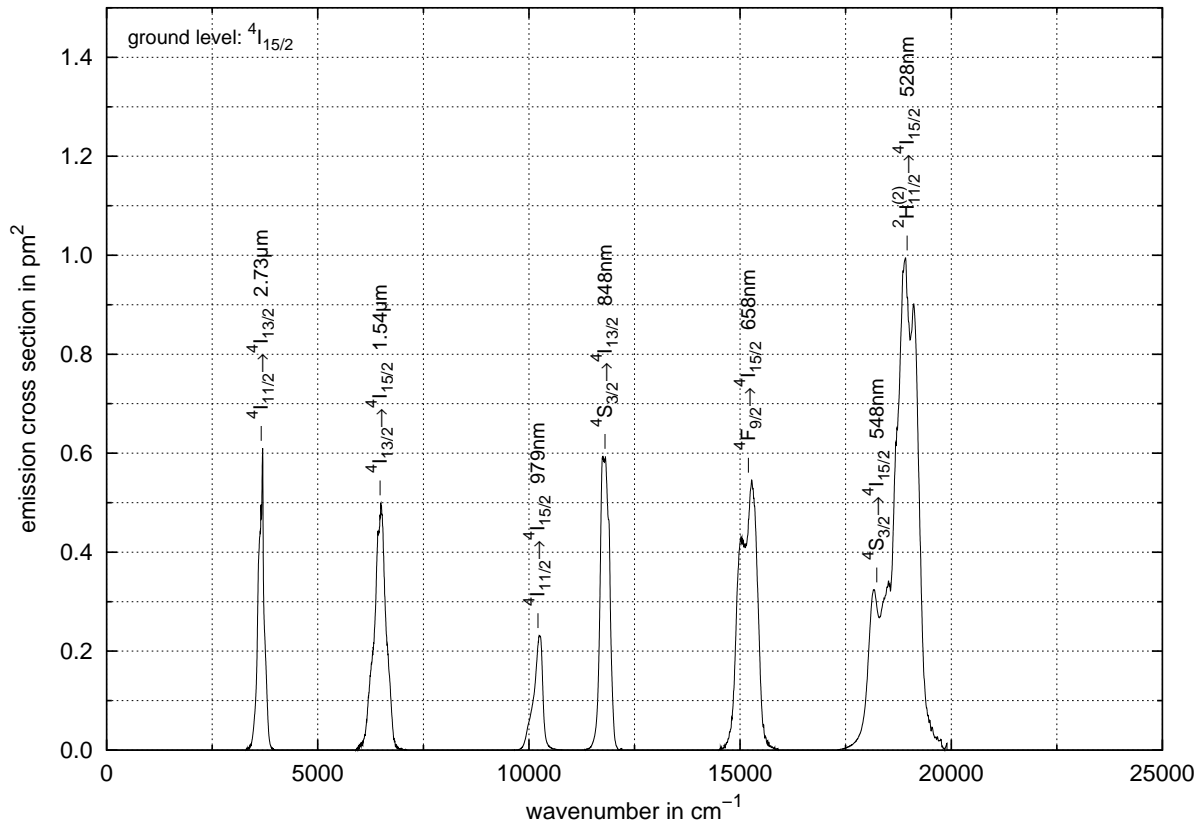


Figure 6.7: Spectrum of the emission cross section of Er:ZBLAN

Table 6.2: Peak positions and effective linewidths of Er:ZBLAN (* relative uncertainty)

transition	k_p cm^{-1}	λ_p nm	σ_p pm^2	rel.*	Δk_{eff} cm^{-1}	$\Delta \lambda_{eff}$ nm	rel.*
$^4I_{11/2} \rightarrow ^4I_{13/2}$	3694.0 ± 1.0	2707.2 ± 0.7	0.60 ± 0.15	21.2 %	160 ± 25	115 ± 20	16.3 %
$^4I_{13/2} \rightarrow ^4I_{15/2}$	6495 ± 15	1539 ± 3	0.50 ± 0.10	21.0 %	340 ± 70	80 ± 15	22.0 %
$^4I_{11/2} \rightarrow ^4I_{15/2}$	10252 ± 5	975.4 ± 0.5	0.230 ± 0.020	9.2 %	255 ± 20	24.5 ± 2.0	8.7 %
$^4S_{3/2} \rightarrow ^4I_{13/2}$	11770 ± 40	849.5 ± 2.5	0.59 ± 0.04	6.5 %	265 ± 15	19.1 ± 0.9	4.8 %
$^4F_{9/2} \rightarrow ^4I_{15/2}$	15030 ± 30	665.0 ± 1.5	0.425 ± 0.015	3.6 %	490 ± 20	21.0 ± 0.8	4.0 %
	15275 ± 7	654.7 ± 0.3	0.545 ± 0.020	3.8 %			
$^4S_{3/2} \rightarrow ^4I_{15/2}$	18170 ± 10	550.4 ± 0.3	0.325 ± 0.030	8.7 %	500 ± 40	15.0 ± 1.0	8.0 %
	18401 ± 6	543.45 ± 0.20	0.265 ± 0.015	5.6 %			
$^2H_{11/2}^{(2)} \rightarrow ^4I_{15/2}$	18915 ± 15	528.7 ± 0.4	0.99 ± 0.07	6.7 %	600 ± 200	17 ± 6	36.9 %
	19110 ± 3	523.29 ± 0.08	0.90 ± 0.05	6.1 %			

Table 6.3: Oscillator strengths and center of mass positions of Er:ZBLAN (* relative uncertainty)

transition	f_{meas} 10^{-8}	rel.*	k_{cm} cm^{-1}	λ_{cm} nm	$\Delta k_{-\sigma}$ cm^{-1}	$\Delta k_{+\sigma}$ cm^{-1}
$^4I_{11/2} \rightarrow ^4I_{13/2}$	110 ± 20	17.2 %	3660 ± 20	2730 ± 15	-80 ± 15	$+80 \pm 15$
$^4I_{13/2} \rightarrow ^4I_{15/2}$	190 ± 40	22.2 %	6480 ± 40	1544 ± 10	-170 ± 40	$+150 \pm 50$
$^4I_{11/2} \rightarrow ^4I_{15/2}$	67 ± 7	11.1 %	10215 ± 15	978.5 ± 1.5	-155 ± 25	$+90 \pm 20$
$^4S_{3/2} \rightarrow ^4I_{13/2}$	175 ± 10	6.3 %	11800 ± 10	847.6 ± 0.8	-100 ± 10	$+100 \pm 10$
$^4F_{9/2} \rightarrow ^4I_{15/2}$	300 ± 15	4.6 %	15195 ± 20	658.2 ± 0.8	-220 ± 15	$+185 \pm 10$
$^4S_{3/2} \rightarrow ^4I_{15/2}$	180 ± 20	10.5 %	18230 ± 40	548.5 ± 1.0	-180 ± 30	$+220 \pm 40$
$^2H_{11/2}^{(2)} \rightarrow ^4I_{15/2}$	650 ± 250	41.4 %	18950 ± 150	528 ± 4	-200 ± 400	$+230 \pm 70$
group:	800 ± 400	42.2 %	18850 ± 200	530 ± 6	-500 ± 400	$+290 \pm 70$

from the transition of $^4S_{3/2}$ to the ground state as it was already shown in figure 6.4. It is due to these two emission lines that even erbium doped silica fibers show a green fluorescence when pumped at 800 nm or 980 nm, although much less than ZBLAN fibers. This light in the laboratory is of great value when aligning free space fiber laser or fiber amplifier setups, although the process is an unwanted loss factor in many cases. The bright emission allows to build efficient up-conversion fiber lasers at 550 nm with erbium doped ZBLAN fibers.

One might expect to see a peak from the transition ${}^2\text{H}_{11/2}^{(2)} \rightarrow {}^4\text{I}_{13/2}$ in the wing of the peak from ${}^4\text{S}_{3/2} \rightarrow {}^4\text{I}_{13/2}$ for the same reason as in the case of the transitions to the ground state, but this is not the case. The reason is that here the radiative emission rate of the transition from ${}^4\text{S}_{3/2}$ is nearly five times larger than that of the transition from ${}^2\text{H}_{11/2}^{(2)}$ whereas in the former case of the transitions to the ground state the radiative emission rate of ${}^2\text{H}_{11/2}^{(2)}$ was four times larger than that of ${}^4\text{S}_{3/2}$. This shows that in the interpretation of emission spectra of rare earth ions a number of aspects needs to be considered.

In figure 6.7 the emission cross section spectrum of all evaluated transitions based on the fluorescence spectra scaled using the Fuchtbauer-Ladenburg equation (6.13) is given. Like in case of the absorption spectra each emission line was measured several times with different settings to prevent artefacts. The results were averaged and the differences were used to

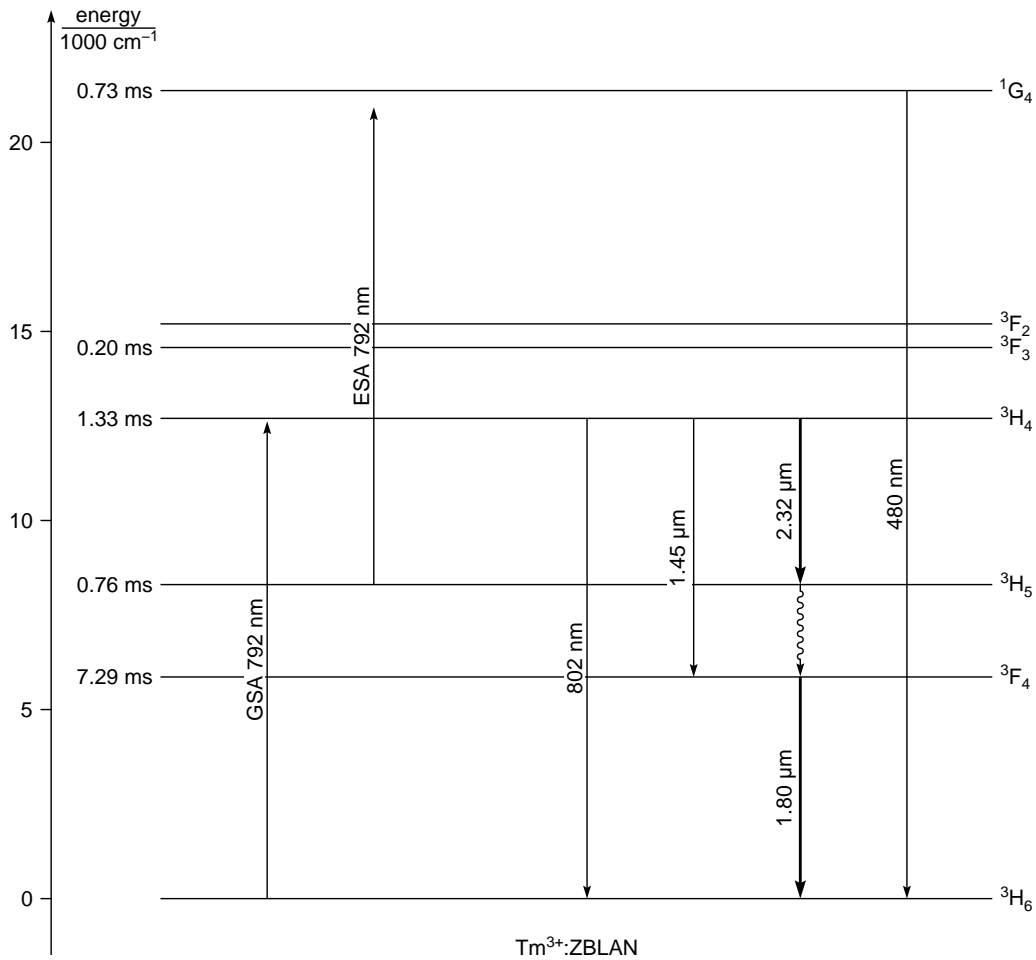


Figure 6.8: Energy levels of $\text{Tm}^{3+}:\text{ZBLAN}$ with pump transitions and some emission lines

estimate the uncertainty. In the spectral range of these lines, the only stronger line missing is the emission line corresponding to the GSA pump transition. The peak positions and effective line widths of all transitions were evaluated and are listed in table 6.2 with given accuracy. The width of the lines is comparable with the respective absorption lines except for $^4S_{3/2}$ and $^2H_{11/2}^{(2)}$, which are much broader. The center of mass wavenumber of every emission line was estimated in the same way as in case of the absorption spectra and is given in table 6.3. For completeness in this table the oscillator strength is also given but it should be remembered that this value due to use of the Fuchtbauer-Ladenburg equation is a direct result from the Judd-Ofelt calculations. However, the specified uncertainty has its origin in the measurement.

6.5 Tm:ZBLAN

The emission spectrum of Tm:ZBLAN is of some more importance in the context of this work since we will use the results in the next chapter to simulate a fiber laser. Figure 6.8

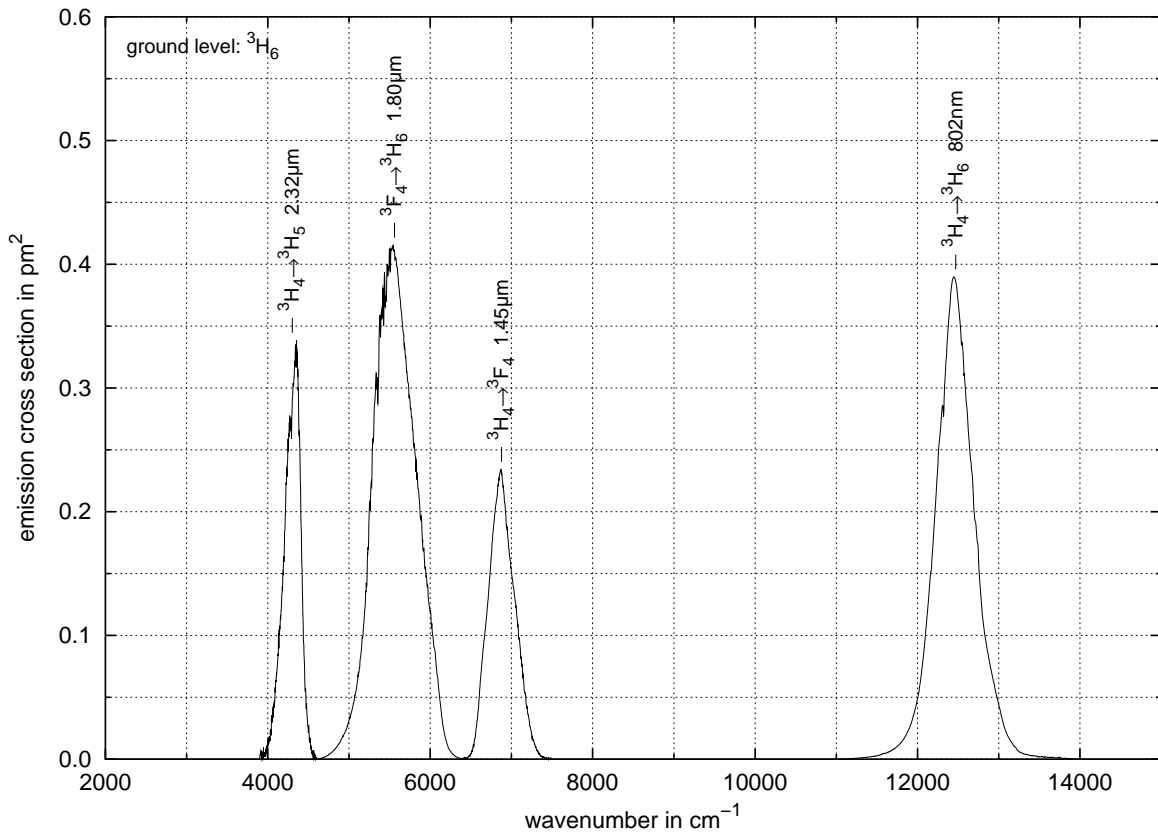


Figure 6.9: Spectrum of the emission cross section of Tm:ZBLAN

Table 6.4: Peak positions and effective linewidths of Tm:ZBLAN (* relative uncertainty)

transition	k_p cm ⁻¹	λ_p nm	σ_p pm ²	rel.*	Δk_{eff} cm ⁻¹	$\Delta \lambda_{eff}$ nm	rel.*
$^3H_4 \rightarrow ^3H_5$	4345 ± 15	2300 ± 7	0.330 ± 0.020	6.0 %	240 ± 20	128 ± 9	7.4 %
$^3F_4 \rightarrow ^3H_6$	5520 ± 50	1810 ± 15	0.405 ± 0.015	3.9 %	645 ± 15	213 ± 5	2.3 %
$^3H_4 \rightarrow ^3F_4$	6870 ± 5	1455.5 ± 1.0	0.233 ± 0.004	1.8 %	381 ± 8	80.5 ± 1.5	2.1 %
$^3H_4 \rightarrow ^3H_6$	12448 ± 7	803.3 ± 0.5	0.390 ± 0.015	4.1 %	550 ± 100	36 ± 7	19.6 %

Table 6.5: Oscillator strengths and center of mass positions of Tm:ZBLAN (* relative uncertainty)

transition	f_{meas} 10 ⁻⁸	rel.*	k_{cm} cm ⁻¹	λ_{cm} nm	$\Delta k_{-\sigma}$ cm ⁻¹	$\Delta k_{+\sigma}$ cm ⁻¹
$^3H_4 \rightarrow ^3H_5$	89 ± 5	5.3 %	4302 ± 9	2324 ± 5	-120 ± 10	$+89 \pm 6$
$^3F_4 \rightarrow ^3H_6$	295 ± 5	1.7 %	5560 ± 8	1798.5 ± 2.5	-250 ± 6	$+286 \pm 7$
$^3H_4 \rightarrow ^3F_4$	100.5 ± 2.0	2.1 %	6879 ± 5	1453.6 ± 1.0	-159 ± 5	$+181 \pm 7$
$^3H_4 \rightarrow ^3H_6$	270 ± 40	14.0 %	12470 ± 70	802 ± 4	-250 ± 50	$+290 \pm 70$

shows part of the energy level system of thulium with the absorption and emission transitions which are of relevance here. Except for the 480 nm fluorescence all other emission lines in this figure were measured and the results of the evaluation of these measurements will be given in the following.

Similar to the case of erbium in the preceding section, a TiSa laser was used as the pump source, but in this case at wavelengths around 790 nm. The glass was sample 1030 doped with about 1.1 mol% of thulium (see tables 4.1 and 4.2). The beam of the pump laser with a power of 3 W was focussed into the glass sample in the fluorescence spectrometer discussed in appendix E. In figure 6.9 the emission cross section spectrum of all four evaluated fluorescence lines is given. Again the spectra were scaled by use of the Fuchtbauer-Ladenburg equation (6.13) and several spectra with different settings were taken from every line.

The GSA pump transition at about 790 nm in thulium ends in level 3H_4 . In the literature sometimes the name of this level and 3F_4 is exchanged for reasons already mentioned in section 1.4. Therefore the actually used definition must always be made clear before speaking about thulium transitions. All fluorescence transitions starting at 3H_4 have been detected. The $2.32 \mu\text{m}$ transition to 3H_5 is the laser transition used for the fiber laser in the next chapter. This laser transition stands in competition with the $1.45 \mu\text{m}$ emission to 3F_4 , which must be suppressed to get the $2.3 \mu\text{m}$ laser running. It is this $1.45 \mu\text{m}$ transition, on which the upcoming S-band fiber amplifiers are based, which usually use fluoride fibers. This amplifier

transition opens a new optical telecommunication window at 1450 – 1530 nm in the existing transmission fibers subsequent to the usual gain band of conventional erbium doped fiber amplifiers (EDFA) at 1530 – 1610 nm. This is important as it can be foreseen that in the near future the EDFA's in backbone networks will be driven to the physical limit of their bandwidth.

The emission line corresponding to the GSA pump transition in Tm : ZBLAN was measured as its cross section is needed for the fiber laser simulations. It is not unlikely in fiber lasers that this emission line starts lasing if it is not suppressed because of its large cross section. To get the lineshape of this transition the wavelength of the pump laser was shifted to a flat part in one of both wings to be able to cut its narrow laser line out of the measured data from the much broader fluorescence afterwards. The last emission line measured here is the 1.80 μm fluorescence of the first excited level $^3\text{F}_4$. The 2.3 μm laser in the configuration used in the next chapter needs a cascade laser running on this transition to bring the excited ions accumulated in the long living level $^3\text{F}_4$ back to the ground state.

Similar to the case of erbium, there exists an up-conversion transition from $^3\text{H}_5$ to $^1\text{G}_4$ but it is not as effective here. One reason is that the energy difference of the ESA does not match the GSA transition as well as in erbium. The other reason is that the initial state of the ESA transition is separated from the next lower lying level $^3\text{F}_4$ by only about 2400 cm^{-1} , which in ZBLAN can be bridged by four phonons leading to a fast non-radiative decay, which lowers the chance of the up-conversion process to take place. Nevertheless, in thulium pumped at 790 nm, the bright blue emission at 480 nm from $^1\text{G}_4$ also serves as a nice alignment aid in the laboratory. Because of the mentioned disadvantages other pumping schemes are usually used to build efficient blue fiber lasers with thulium.

In table 6.4 the peak positions of all four emission lines are given and table 6.5 shows wavenumber and wavelength of the center of mass of all transitions together with the oscillator strength. It should be mentioned again that due to use of the Fuchtbauer-Ladenburg equation the values of these oscillator strengths are actually the calculated values from the Judd-Ofelt theory and only the specified uncertainty comes from the measurement.

7 Rare earth doped fiber lasers

In the preceding chapters we developed theories for the electronic system of triply ionized rare earth ions and used them to evaluate absorption and emission spectra. Now we have arrived at the final step of this work, which originally was the starting point, and use the results for the simulation of a fiber laser. We begin this chapter with a section about general fiber laser operation to make the practical and theoretical background clear. The following section will provide a description and some experimental results from Tm : ZBLAN fiber lasers at $2.3\,\mu\text{m}$. The simulation algorithm will be presented in the next section and its results compared with the measurements, and in the last section we will use the simulation to find the conditions at which the output power of the $2.3\,\mu\text{m}$ fiber laser is maximized.

7.1 Fiber laser operation

In the introduction of this work we mentioned the variety of different fiber laser setups, but we will concentrate here on the very simple setup shown in figure 7.1. It is the basic setup used in our laboratory for continuous wave (cw) fiber lasers. Like every laser it consists of three fundamental parts. The first part is the power source, which is a pump laser here since fiber lasers belong to the class of optically pumped solid state lasers. The type of the pump laser in principle is arbitrary as long as it delivers the right wavelength. For applications the goal is always to use laser diodes as pump lasers as they are small, electrically driven devices, but for laboratory setups it is often preferable to use large wavelength tunable high power lasers like the titan-sapphire (TiSa) laser, which are more flexible in experiments. The second

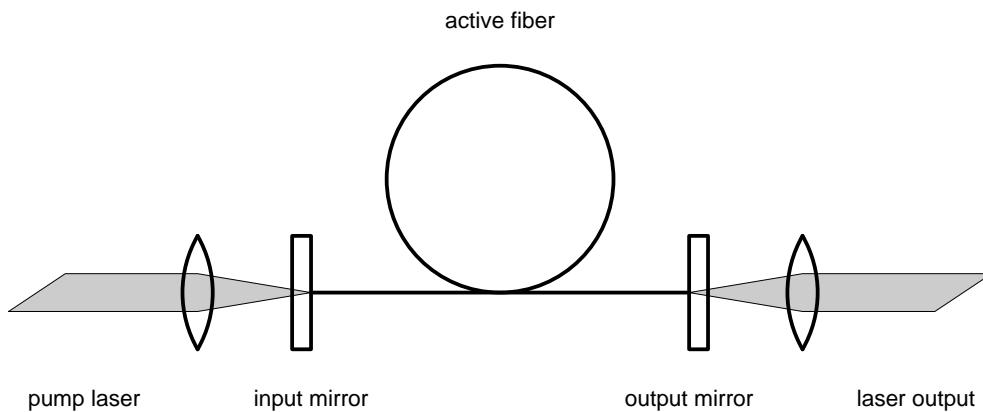


Figure 7.1: Basic free space setup of a cw fiber laser

part is the active medium storing pump energy in a metastable state, which may be used for stimulated emission. This part in case of a fiber laser is the core of the fiber, which in our case is doped with rare earth ions. In principle it is also possible to use other dopants, as e.g. transition metals, and Raman fiber lasers use the glass material of the undoped fiber core itself for the laser process. The remaining third part of a laser is the feedback mechanism to support the process of stimulated emission, for which two mirrors are used here as it is usual in most types of lasers. In the setup of figure 7.1 the mirrors must be dielectric mirrors whereas the input mirror should be highly transparent for the pump beam and the output mirror partly transparent for the laser beam. Since the laser resonator is a waveguide structure, the mirrors are just flat dielectric coatings placed at the fiber ends with physical contact to the fiber. Alternative setups use e.g. fiber Bragg gratings, which are fiber sections with periodic refractive index changes along the fiber which may be written into the fiber by UV laser radiation.

The laser process is based on stimulated emissions in the active material which provide gain at the laser wavelength. If the mirror feedback exceeds the losses inside the optical amplifier, it is immediately driven to the nonlinear large signal regime where the amplification process saturates at a level according to the pump power delivered. The part of this radiation which is exceeding the losses in the resonator may be coupled out as the laser beam, which due to the inherent coherence of the stimulated emission is also highly coherent. Corresponding to this simple principle of laser operation is a mathematical description which has already been given in equation (2.18) and shall be recalled here because of its fundamental importance:

$$\pm \frac{dn_i}{dt} = \sigma(\nu) n_i \Phi_\nu = \pm \frac{1}{n_I} \frac{d\Phi(\nu)}{dx} , \quad (7.1)$$

n_i being the relative occupation number of energy level i in the active material, n_I the density of dopant ions (in general: active systems), $\Phi(\nu)$ the photon flux at the frequency ν , and $\sigma(\nu)$ the emission or absorption cross section. Depending on the choice of the signs and the type of cross section used, this double equation describes the fundamental process of absorption and stimulated emission in laser materials where the cross section is the coupling constant of the interaction of radiation with matter. The left part (matter) can be expanded to a system of rate equations and the right part (radiation) to the gain equations.

As a more general expansion of the rate equation of level i in segment p for an unlimited system of states we use the following expression

$$\begin{aligned} \frac{dn_i}{dt} = & \sum_j \left[A_{ji} + W_{ji} + \int f(\nu) (\phi^+(\nu, x) + \phi^-(\nu, x)) \sigma_{ji}(\nu) d\nu \right] n_j(x) \\ & - \sum_j \left[A_{ij} + W_{ij} + \int f(\nu) (\phi^+(\nu, x) + \phi^-(\nu, x)) \sigma_{ij}(\nu) d\nu \right] n_i(x) , \end{aligned} \quad (7.2)$$

which is straightforward but needs some explanations. The equation is describing the temporal development of the relative occupation number n_i of level i and consists of two sums running

over all levels j of the dopant ion. The first sum contains all contributions from transitions ending in level i and the second sum the contributions from all transitions starting from level i . The only difference between both sums is the order of i and j . Since the terms of the first sum lead to an increasing occupation number whereas the terms of the second sum reduce it, the sums appear with a positive and a negative sign respectively. A_{ij} is the radiative emission rate of level i to j from equation (2.8) whereas W_{ij} denotes the nonradiative emissions mainly due to multiphonon emission and may be calculated directly or from the measured lifetime of level i using the appropriate equations in section 6.1. The integrals are the interaction terms due to absorption and stimulated emission from equation (7.1) with some modifications. The flux of photons is replaced by its spectral counterpart $\phi = d\Phi/d\nu$ and separated in two parts ϕ^+ and ϕ^- where the sign denotes the direction, e.g. the positive sign for the flux co-directional to the pump beam and the negative sign for the opposite direction. The position variable along the fiber is x and the integral over ν spans the full absorption or emission line.

Until now we have treated the field of electromagnetic radiation just like a swarm of floating photons but it is well-known that this description does not cover all of its properties. The Maxwell equations describe the wave character of this field and in this description the fundamental mode of electromagnetic radiation guided by the core of a single-mode fiber, which is a cylindric waveguide, is the so-called LP_{01} mode with a lateral intensity profile which in case of a weakly guiding fiber is well approximated by the Gauss function [122]. Part of this wave extends into the cladding of the fiber and is therefore not affected by the dopant ions in the core. The factor $f(\nu)$ in equation (7.2) contains the fraction of the total lateral intensity integral, which is interacting with the doped fiber core. In case of a single-mode fiber the intensity profile is fixed by the geometry of the fiber and not disturbed due to the partial interaction, but in the multi-mode regime the situation is much more difficult. However, the fraction of the guided radiation extending into the cladding can be expected to be relatively small in case of a multi-mode fiber.

For a system of N energy levels N rate equations (7.2) are in existence, one for each level, but they are not linearly independent as each equation is determined by all others, which can be seen immediately when writing down the equations in a concrete case. Mathematically speaking, the N -dimensional linear system of rate equations has rank $N-1$. To get a system of linear equations with full rank, which is solvable for n_i in the stationary case where $dn_i/dt = 0$ for all n_i , one of the equations is replaced by the following one, which obviously is a necessary condition fixing the relative occupation numbers:

$$\sum_i n_i(x) = 1 . \quad (7.3)$$

The right side of equation (7.1) is expanded to a second set of differential equations. There

exist two gain equations, one for each direction:

$$\begin{aligned} \pm \frac{d\phi^\pm(\nu, x)}{dx} = & w(\nu) \sum_{ij} A_{ij} g_{ij}(\nu) d\nu n_I n_i(x) \\ & + f(\nu) \sum_{ij} \text{sign}(i - j) \sigma_{ij}(\nu) n_I n_i(x) \phi^\pm(\nu, x) \\ & - \alpha(\nu) \phi^\pm(\nu, x) . \end{aligned} \quad (7.4)$$

The first term of equation (7.4) describes the contribution of the spontaneous emission to the radiation field. In that term $g_{ij}(\nu)$ is the lineshape function normalized according to equation (2.16) and $w(\nu)$ the fraction of the total spontaneous emission, which is guided by the fiber core. Spontaneous emission occurs in all directions with the same intensity, but if the angle between the direction of a photon and the fiber is too large, it will leave the core. The second term in equation (7.4) takes into account absorption and stimulated emission processes whereas the sign of the appropriate contribution is given by the sign of $i - j$. Finally the fiber always shows a certain amount of background losses summarized by $\alpha(\nu)$, defined by $\phi(x) = \phi_0 \exp(-\alpha x)$, where α is usually wavelength dependent.

At both fiber ends, i.e. $x = 0$ or $x = l$, the mirrors reflect the co- and counter-propagating photon fluxes into each other. If we denote the reflectivity of input and output mirror by $R^{in}(\nu)$ and $R^{out}(\nu)$ respectively, we get the boundary conditions

$$\begin{aligned} \phi^+(\nu, 0) &= R^{in}(\nu) \phi^-(\nu, 0) + T^{in}(\nu) \phi_p(\nu) \\ \phi^-(\nu, l) &= R^{out}(\nu) \phi^+(\nu, l) \end{aligned} , \quad (7.5)$$

where the flux of pump photons $\phi_p(\nu)$ through input mirror 1 with transmission factor $T^{in}(\nu)$ is already included.

The rate equations (7.2) and (7.3) together with the gain equations (7.4) and the boundary conditions (7.5) represent a complex system of coupled differential equations, which may only be solved numerically. In section 7.3 we will discuss an algorithm solving this set of equations in the stationary case, i.e. $dn_i/dt = 0$ for all i , to simulate cw fiber lasers.

7.2 Tm:ZBLAN fiber laser at 2.3 μm

The 2.3 μm fiber laser using Tm:ZBLAN fibers is well-known from the literature. Pulsed operation was shown in 1988 [123] and a year later also cw operation [124]. The breakthrough was achieved by the simultaneous operation of the 1.9 μm laser in a cascade, which drastically raised the maximum output power as demonstrated in a couple of publications [125, 126, 127, 128]. Furthermore, broadly tunable fiber lasers at 2.3 μm were developed [129, 130, 131].

The 2.3 μm fiber laser has the advantage that the number of four involved energy levels is relatively small as it can be seen in the energy level system of thulium, as shown in figure 6.8.

The upper laser level is reached directly by the pump absorption. The laser transition ends in the next lower energy level 3H_5 , which is located not far above the first excited state 3F_4 and therefore is expected to relax fast and non-radiatively to that state. The level 3F_4 has a long lifetime, which caused problems in the first experiments with this fiber laser [123], but a simultaneously running laser at $1.9\ \mu\text{m}$ can be used to depopulate it efficiently [125], a common trick for fluoride glass fiber lasers [4]. Care must be taken when designing the laser mirrors to prevent the $1.45\ \mu\text{m}$ transition from starting laser operation by a high transmission factor of the mirrors at this wavelength. At around $800\ \text{nm}$ the mirrors should be transparent to let the pump radiation pass and suppress the $802\ \text{nm}$ laser transition.

Figure 7.2 shows the laboratory setup used to measure the characteristics of a couple of these cascade lasers. As no suitable ZBLAN fiber from our institute was available at that time, a Tm:ZBLAN fiber F400-32-1 from Thorlabs was used. The thulium concentration of this fiber is 2000 ppm (weight), the core diameter $7.8\ \mu\text{m}$, and the $NA = 0.16$. The V -number of a fiber [122]

$$V = \frac{\pi d_{\text{core}}}{\lambda} NA, \quad (7.6)$$

where d_{core} is the core diameter and λ the wavelength, is a widely used parameter for single-mode fibers. The single-mode regime of a fiber ends at $V = 2.405$ since above this value the first higher modes are guided by the core. A fiber with small V -numbers is weakly guiding and more and more sensitive to bending, which is not surprising as with increasing wavelength of the radiation the small core finally becomes irrelevant. Sometimes the value $V = 1.6$

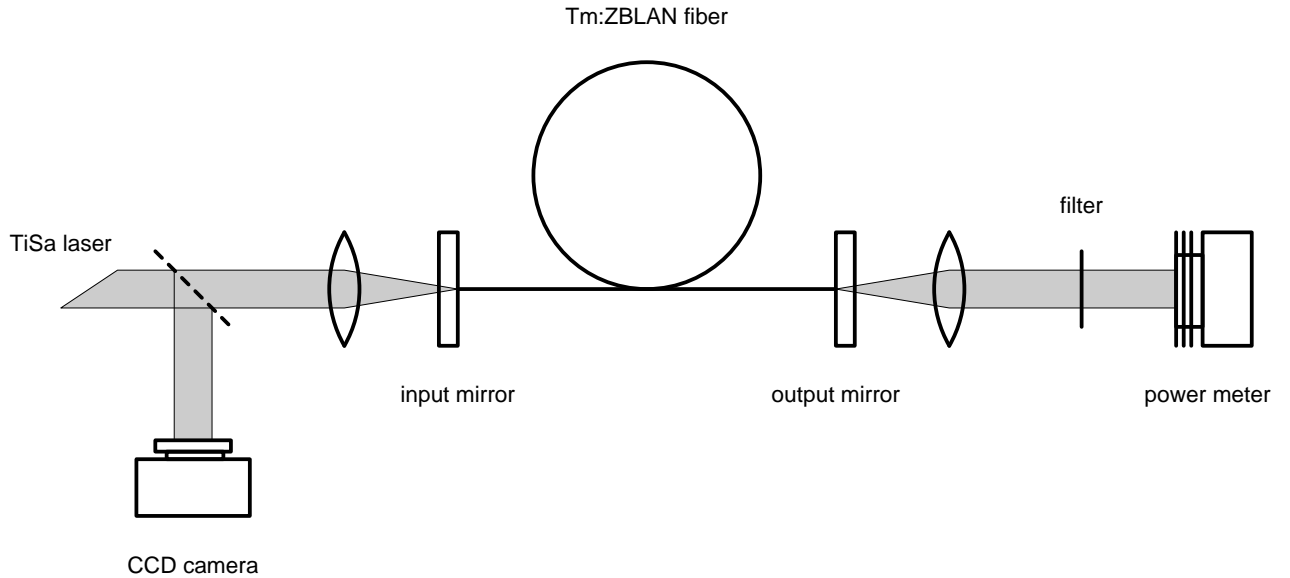


Figure 7.2: Measurement setup to measure the laser characteristics of the Tm:ZBLAN fiber laser

is mentioned as the “guiding limit” of a fiber, but this is a very soft criterion. According to equation (7.6), the fiber used here has the V -numbers 5.5 @ 790 nm, 2.1 @ 1890 nm, and 1.7 @ 2340 nm at the wavelengths of relevance here. The fiber therefore is single-mode at the two wavelengths of the laser cascade and slightly multi-mode at the pump wavelength.

Figure 7.3 shows the reflectivity of the available mirrors. Mirror 144 is highly reflecting at $2.3\ \mu\text{m}$ and was used as the input mirror, the others have different reflection factors at this wavelength. The substrates of the mirror coatings have a diameter of 1" and a thickness of some millimeters. The substrate material was BK7 for the input mirror and CaF_2 for the others to reduce attenuation of the infrared laser beam.

To transform the pump beam with a $1/e^2$ -diameter of about 2 mm down to match the mode field diameter (MFD) at the input end of the fiber, an objective 06 GLC 003 from Melles Griot was used. It has a focal length of 14.5 mm and a clear aperture of 8 mm. The same objective was used at the output side to collimate the laser beam. When the laser beam is approximated

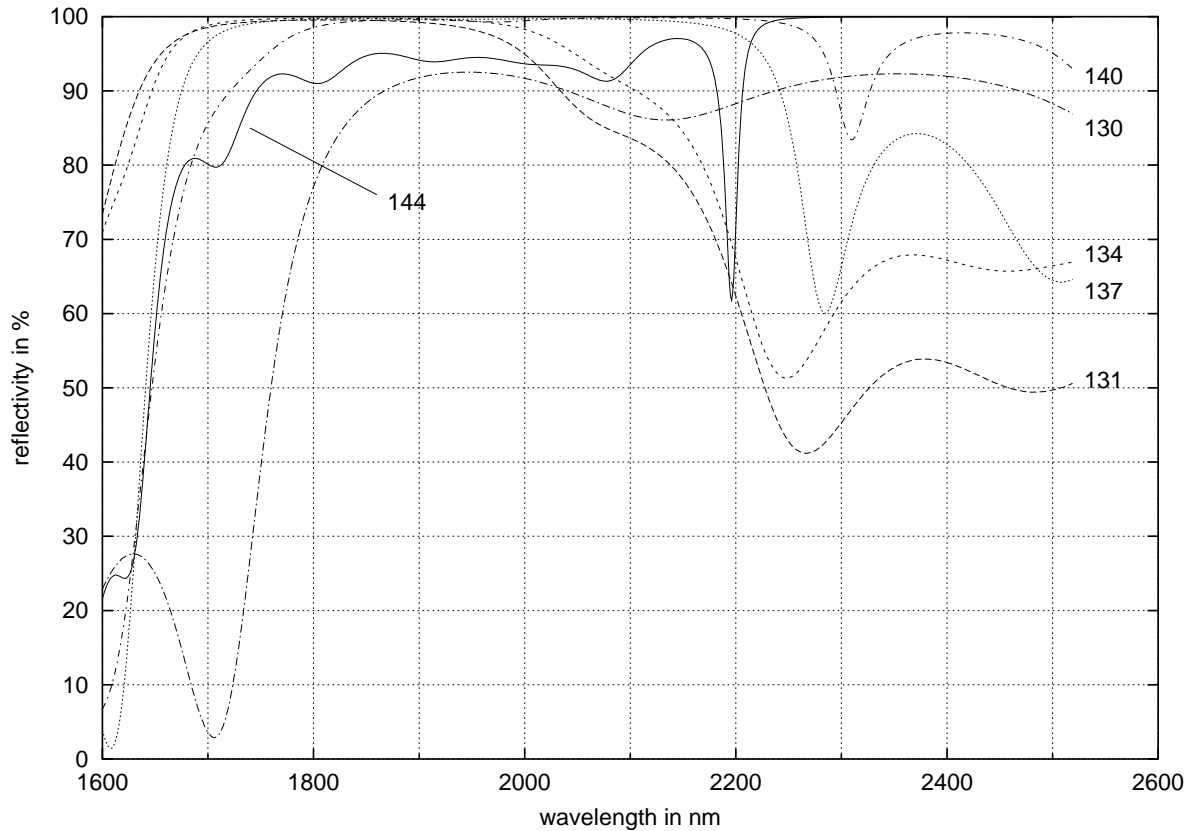


Figure 7.3: Reflectivity of different mirrors. Mirror 144 is an input mirror, the others were used as output mirrors with different reflection factors around $2.3\ \mu\text{m}$.

Table 7.1: Reflectivity of the laser mirrors at both wavelengths of the laser cascade. The span of each reflectivity in the measured range of wavelengths is given.

mirror	$R(1886 \pm 30 \text{ nm})$ %	$R(2343 \pm 35 \text{ nm})$ %
144	94.5 ± 0.6	100
131	99.3 ± 0.3	50.4 ± 3.6
134	99.8 ± 0.1	65.5 ± 2.4
137	99.7	77.6 ± 6.6
140	99.6 ± 0.1	90.4 ± 7.0
130	90.6 ± 1.6	92.2 ± 0.2

by a Gaussian beam with waist at the fiber end, its diameter at the position f_0 of the lenses may be calculated by the following equation for the diameter of Gaussian beams [122]

$$d(x) = d_0 \sqrt{1 + \left(\frac{x}{x_0}\right)^2}, \quad (7.7)$$

where $x = 0$ is the waist position, d_0 the waist diameter and $x_0 = \pi d_0^2 / 4\lambda$ the confocal parameter. Here we are in the far field and the equation may be reduced to

$$d(x) = d_0 \frac{x}{x_0}. \quad (7.8)$$

The waist diameter is the *MFD* of the fiber at the respective wavelength, which in the single-mode case is given by [132]

$$MFD = d_{core}(0.65 + 1.619/V^{1.5} + 2.879/V^6) \quad (7.9)$$

and where V is the V -number mentioned above. Inserting equation (7.9) into (7.8) we calculate a diameter of about 3.6 mm for the collimated laser beam at both wavelengths of the cascade. This value is much smaller than the clear aperture of the objective.

In the experiments a TiSa laser was serving as the pump source at 790 nm with output powers up to about 1.6 W with reasonable beam quality. This beam quality is very important for the measurements because only the lowest radiation modes of the pump laser beam are coupled into the slightly multi-mode fiber. Since on the one hand the output power of the fiber laser is related to the pump power *in* the fiber, but on the other hand we are only able to measure the power *from* the pump laser, we have to care about a constant incoupling factor. This factor strongly depends on the mixture of radiation modes in the pump beam. At low power the intensity profile of the beam had a Gaussian shape, indicating a TEM₀₀ mode but

at certain moderate power levels of the TiSa laser, and in general in high power operation the beam shape turned out to be heavily distorted. Therefore, a small fraction of the pump beam was directed to the CCD camera of a beam analyzer system to monitor the shape of the pump beam online.

The output power of the fiber laser was measured using a sensitive optical power meter with a detector independent of the wavelength in a broad wavelength range. Therefore, a filter is needed to get the output power of the $1.9\ \mu\text{m}$ laser and the $2.3\ \mu\text{m}$ separately. Moreover, at low output power levels care must be taken that the stray light of the pump beam emerging from the fiber cladding and the remaining pump power from the fiber core does not affect the results. In principle the solution is simple: Just measure the overall power P'_i behind as many different filters i (one may just be free space) as the beam contains wavelengths j . The transmission factor T_{ij} of filter i at wavelength j can then be seen as an element of a transmission matrix \mathbf{T} determining the measured power vector $\mathbf{P}' = \mathbf{TP}$ by the matrix

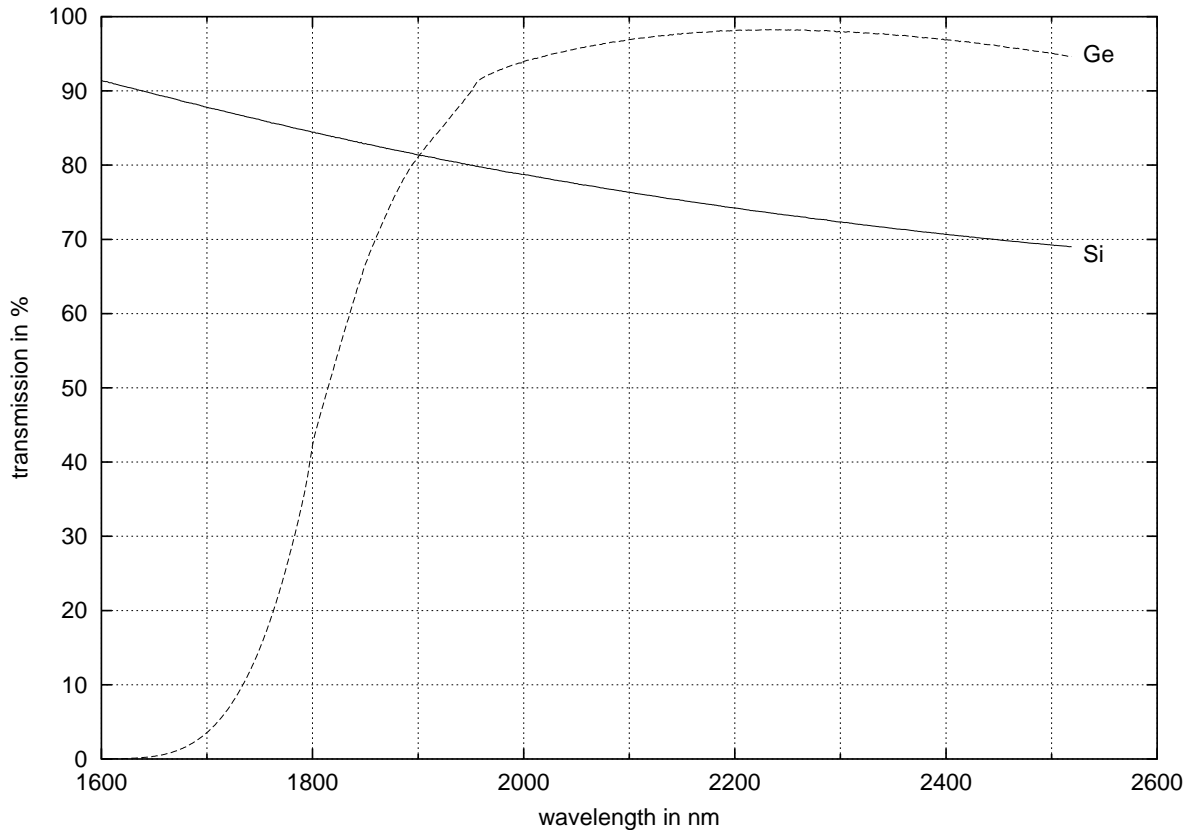


Figure 7.4: Transmission factor of the silicon and germanium filter used to separate the power of the 1.9 and $2.3\ \mu\text{m}$ laser

Table 7.2: Filter transmissions used in the transmission matrix to calculate the output power of the fiber laser at both wavelengths of the laser cascade. The span of each transmission factor in the measured range of wavelengths is given.

filter	$T(1886 \pm 30 \text{ nm})$ %	$T(2343 \pm 35 \text{ nm})$ %
Si	81.9 ± 0.9	71.6 ± 0.6
Ge	76.4 ± 7.6	97.6 ± 0.4

multiplication

$$P'_i = \sum_j T_{ij} P_j , \quad (7.10)$$

where P_j is the output power of the fiber laser at wavelength j . This output power may therefore be calculated from the measured values by the inverse transformation $\mathbf{P} = \mathbf{T}^{-1}\mathbf{P}'$

$$P_j = \sum_i T_{ji}^{-1} P'_i . \quad (7.11)$$

Of course, this implies that the filters were chosen to have suitably different transmission factors for \mathbf{T} to be not singular. But in practice this is not the only criterion since the output power levels from the fiber level at different wavelengths, i.e. the elements of vector \mathbf{P} may

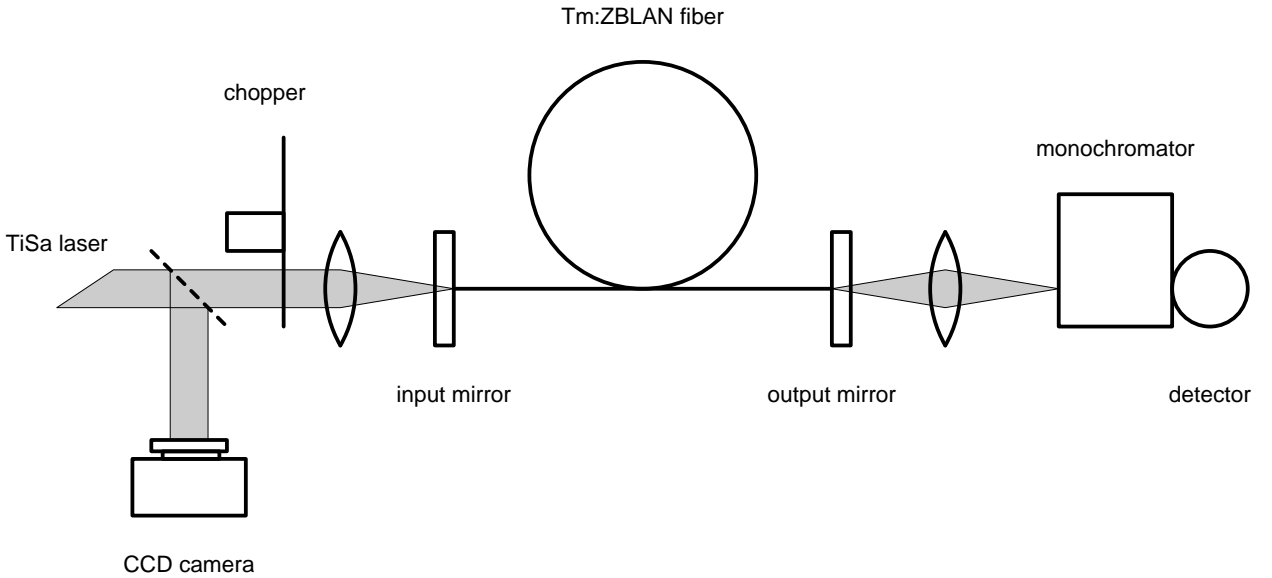


Figure 7.5: Modified setup to measure the laser wavelengths and threshold powers

Table 7.3: Measured laser wavelengths and threshold powers for fiber lasers with different fiber lengths and output mirrors. The lengths of fibers 1, 2, and 3 were 0.494 m, 0.995 m, and 1.596 m respectively.

	fiber			output mirror / reflectivity				wavelength		threshold	
meas.	1	2	3	131 50 %	134 66 %	140 90 %	130 92 %	$\lambda^{1.9}$ nm	$\lambda^{2.3}$ nm	$P_{in}^{1.9}$ mW	$P_{in}^{2.3}$ mW
1	×			×				1869	2342	35	72
2	×				×			1867	2320	7	24
3	×						×	1856	2378	35	42
4		×			×			1906	2312	3	18
5		×					×	1900	2352	2	2
6		×					×	1884	2330	23	16
7		×					×	1883	2330	62	58
8			×	×				1886	2341	100	120
9			×		×			1916	2308	46	35
10			×			×		1903	2357	26	18
11			×				×	1882	2316	64	76

be differing even in the order of magnitude, which leads to very large uncertainties in the results of equation (7.11). It is obvious that the optimum solution would be ideal bandpass filters at the respective wavelengths, in which case \mathbf{T} would be the unit matrix. Here it was decided to take two semiconductor filters, the spectral transmission factors of which are shown in figure 7.4. Both filters block the pump laser completely, and they have different ratios of the respective transmission factors at wavelengths around $1.9\ \mu\text{m}$ and $2.3\ \mu\text{m}$. The relevant ranges are summarized in table 7.2.

In order to obtain the right values of the filter transmission, the wavelength of both laser transitions was measured together with each laser characteristic by a small modification of the experimental setup according to figure 7.5. The monochromator, together with the semiconductor detector, was used to measure the wavelengths and with help of the chopper the laser threshold was detected. Therefore the pump power was increased until a spike was seen on an oscilloscope connected to the detector. The detector was an InSb-detector in a dewar housing cooled by liquid nitrogen.

Table 7.3 shows a compilation of results from the laser experiments which were carried out with three fibers of the approximate lengths 0.5 m, 1.0 m, and 1.6 m and four of the available output mirrors. As expected, it can be seen that the threshold power usually decreases with increasing reflectivity of the output mirror. Some measurements show deviations from this behaviour, which can be addressed to a worse incoupling factor since some time passed between the measurements, which were not performed in the order given in table 7.3. Moreover, it can

Table 7.4: Threshold powers and output power at an input power of 500 mW interpolated from the measured data

	threshold		$P_{in} = 500$ mW	
meas.	$P_{in}^{1.9}$ mW	$P_{in}^{2.3}$ mW	$P_{out}^{1.9}$ mW	$P_{out}^{2.3}$ mW
1		88		7.6 ± 1.3
2		36		12.0 ± 2.0
3	78	85	9.9 ± 1.6	2.4 ± 1.4
4		50		15.1 ± 3.4
5	2	33	7.8 ± 3.2	10.4 ± 3.2
6	30	40	15.2 ± 4.7	8.4 ± 4.4
7	77	72	5.4 ± 1.3	3.5 ± 1.2
8		115		8.3 ± 1.7
9		58		19.8 ± 4.8
10		54		2.1 ± 0.5
11	83	87	5.1 ± 1.2	2.5 ± 1.1

be seen that the wavelength of the $1.9\mu\text{m}$ laser increases with increasing fiber length. This is usual for such a three-level laser because with increasing fiber length the unpumped section of the fiber becomes longer and absorbs the emission from this transition. Since the absorption line of a transition is always shifted to shorter wavelengths, the ratio between emission and absorption cross section, and therefore the gain, gets larger for larger wavelengths. For that reason the laser wavelength will be shifted to larger wavelengths to compensate for the larger losses of a longer fiber. In a short fiber shorter wavelengths with larger emission cross sections are preferred. For the same reasons the wavelength of the $1.9\mu\text{m}$ laser in a certain fiber length decreases with increasing reflectivity of the output mirror since the higher reflectivity compensates for part of the losses.

Some graphical plots of the measured laser characteristics will be given in the next section when they are compared with the results of the simulation. In table 7.4 we give some values extracted from the measurement data. Supposing that the accuracy of the transmission factors of the filters is much higher than that of the measured power levels, the following equation was used to estimate the uncertainty of the calculated optical power at the two laser wavelengths:

$$\Delta P_j = \sqrt{\sum_i (T_{ji}^{-1} \Delta P_i)^2}, \quad (7.12)$$

which is valid only for independent errors. Although we expect some systematic errors which

couple the uncertainty of the measurements, the equation was used to give at least an estimation of the accuracy of the calculated values. A relative uncertainty of 5% was estimated for the measured power values. As table 7.2 shows, the ratio of the transmission factors at both wavelengths is not very large. Therefore the elements in the matrix \mathbf{T}^{-1} are of similar magnitude and opposite sign for both measurements which leads to large uncertainties, which in case of the $1.9\mu\text{m}$ laser are often larger than the value itself. Such values, where $\Delta P^{1.9}$ was larger than $P^{1.9}$, were omitted from table 7.4. It can be seen that the threshold powers in table 7.4 obtained by fitting the first data points are similar to the values from table 7.3, but in almost every case somewhat larger. This is explained by the fact that the threshold powers in table 7.3 were obtained by recording a laser peak when the pump power was switched on. This is obviously no criterion for a running cw laser but it can be expected to happen at power levels not far below the real threshold. Furthermore it should be noted that the threshold values in table 7.4 are very uncertain due to the large uncertainty of the power levels. The output power obtained with an input power of 500 mW is given in table 7.4 for comparison. However, it should be remembered that these values strongly depend on the incoupling and outcoupling factors, which are unknown, and not every laser was aligned to its overall optimum which is rather time consuming in such a free space setup. Therefore the values are no clear indicators of the efficiency of the laser, which can be seen from the measurements 5, 6, and 7, which used the same fiber length and mirrors and therefore should be equal, but actually show quite different results.

7.3 Fiber laser simulation

In this section we will develop a simulation model for a cw fiber laser based on the equations given in section 7.1. The model simulates the stationary case of an arbitrary laser system in a rare earth doped fiber. It will not take into account energy transfer processes in general, which are especially of interest when co-dopants are used. However, we will show a way to implement these features, too. Furthermore any spacial holeburning effects are ignored here, but it should be possible to include the appropriate modifications to the computer program without difficulties.

In order to simulate a fiber laser numerically we need to convert the equations of section 7.1 into a discrete form and find an algorithm to solve the resulting equations. The problem contains three dimensions, one of which is the energy level, which is already a discrete value. The other two are the frequency ν or wavelength λ of the radiation field and the position x along the fiber, which have to be split in certain pieces which not necessarily must be of equal length. We shall use the indices i and j for energy levels and k and p for wavelength and position respectively. Since we are only interested in cw fiber lasers here, we have to solve the rate equations (7.2) in the stationary state $dn_i/dt = 0$. When converting the integral to

a sum, it seems convenient to introduce the plain photon fluxes again

$$\Phi(\nu) = \int_{\nu}^{\nu+d\nu} \phi(\nu') d\nu' , \quad (7.13)$$

which leads to the following discrete form of the rate equation of level i in fiber segment p :

$$\begin{aligned} 0 = & \sum_j \left[A_{ji} + W_{ji} + \sum_k f_k (\Phi_{kp}^+ + \Phi_{kp+1}^-) \sigma_{jik} \right] n_{jp} \\ & - \sum_j \left[A_{ij} + W_{ij} + \sum_k f_k (\Phi_{kp}^+ + \Phi_{kp+1}^-) \sigma_{ijk} \right] n_{ip} , \end{aligned} \quad (7.14)$$

where the index $p + 1$ of Φ^- should be noted. It is necessary since by Φ_{kp}^{\pm} we denote the photon flux between the fiber segments $p - 1$ and p . Φ_{kp}^- therefore is the flux leaving the segment p towards segment $p - 1$ and not what we need in equation (7.14). To simplify the form of this equation further we introduce the matrix B_{ij}^{sp} by the definition

$$B_{ij}^{sp} = \begin{cases} -\sum_{j'} (A_{ij'} + W_{ij'}) & \text{if } j = i \text{ and} \\ A_{ji} + W_{ji} & \text{otherwise} \end{cases} \quad (7.15)$$

and the analogous definition of the matrix B_{ijk}^{st} for the terms of absorption and stimulated emission

$$B_{ijk}^{st} = \begin{cases} -f_k \sum_{j'} \sigma_{ij'k} & \text{if } j = i \text{ and} \\ f_k \sigma_{jik} & \text{otherwise} . \end{cases} \quad (7.16)$$

All elements of both matrices above are given before the actual simulation starts and are therefore calculated outside the simulation kernel. Let us assume now that we already know the value of the photon fluxes into segment p and define the matrix B_{ijp} by

$$B_{ijp} = \begin{cases} 1 & \text{for } i = 0 \text{ and} \\ B_{ij}^{sp} + \sum_k B_{ijk}^{st} (\Phi_{kp}^+ + \Phi_{kp+1}^-) & \text{otherwise} , \end{cases} \quad (7.17)$$

then the rate equations in the fiber segment p just build a set of linear equations, which is solved by inversion of the matrix to get the relative occupation numbers of all energy levels in that fiber segment. The appropriate equation for level i is

$$\sum_j B_{ijp} n_{jp} = \begin{cases} 1 & \text{for } i = 0 \text{ and} \\ 0 & \text{otherwise} , \end{cases} \quad (7.18)$$

and the special treatment of $i = 0$ includes equation (7.3).

The second part of the problem are the gain equations (7.2), which first of all shall also be given in a discrete form for the photon flux in the direction of the pump beam:

$$\frac{\Phi_{kp+1}^+ - \Phi_{kp}^+}{\Delta x_p} = w_k \sum_{ij} A_{ij} g_{ijk} n_I n_{ip} + f_k \sum_{ij} \text{sign}(i - j) \sigma_{ijk} n_I n_{ip} \Phi_{kp}^+ - \alpha_k \Phi_{kp}^+ \quad (7.19)$$

and in the opposite direction

$$\frac{\Phi_{kp}^- - \Phi_{kp+1}^-}{\Delta x_p} = w_k \sum_{ij} A_{ij} g_{ijk} n_I n_{ip} + f_k \sum_{ij} \text{sign}(i - j) \sigma_{ijk} n_I n_{ip} \Phi_{kp+1}^- - \alpha_k \Phi_{kp+1}^- . \quad (7.20)$$

Again we define some matrices containing all data known before the simulation starts. From the term of spontaneous emission we define

$$G_{kpi}^{sp} = n_I w_k \Delta x_p \sum_j A_{ij} g_{ijk} , \quad (7.21)$$

from the term of absorption and stimulated emission

$$G_{kpi}^{st} = n_I f_k \Delta x_p \sum_j \text{sign}(i - j) \sigma_{ijk} , \quad (7.22)$$

and from the term of the background losses

$$G_{kp}^{att} = \alpha_k \Delta x_p . \quad (7.23)$$

As soon as we know the values of the relative occupation numbers n_{ip} in segment p , we can calculate the two new matrices

$\begin{aligned} G_{kp}^{(1)} &= \sum_i G_{kpi}^{sp} n_{ip} & \text{and} \\ G_{kp}^{(2)} &= 1 + G_{kp}^{att} + \sum_i G_{kpi}^{st} n_{ip} , \end{aligned} \quad (7.24)$

which again simplify the expression of the gain equation. The photon flux leaving segment p in the direction of the pump beam and in the opposite direction can now be calculated by

$\begin{aligned} \Phi_{kp+1}^+ &= G_{kp}^{(1)} + G_{kp}^{(2)} \Phi_{kp}^+ & \text{and} \\ \Phi_{kp}^- &= G_{kp}^{(1)} + G_{kp}^{(2)} \Phi_{kp+1}^- \end{aligned} \quad (7.25)$
--

respectively. According to equation (7.5) the fluxes are partially reflected by the mirrors at the fiber ends and a flux Φ_k^p of pump photons is added, which leads to the equations

$$\begin{aligned}\Phi_{k0}^+ &= R_k^{in} \Phi_{k0}^- + T_k^{in} \Phi_k^p \quad \text{and} \\ \Phi_{km}^- &= R_k^{out} \Phi_{km}^+ ,\end{aligned}\tag{7.26}$$

if the number of fiber segments is m . The equation converting power values to photon fluxes and vice-versa is

$$\Phi = \frac{P}{h\nu A_{core}} ,\tag{7.27}$$

where h is Planck's constant and A_{core} is the area of the fiber core.

The boxed expressions above are all equations needed for the simulation kernel, what is still missing is only a suitable algorithm. However, the way in which we developed the equations already suggests the structure of the algorithm in figure 7.6, which we will use. It starts with the values of all fluxes set to zero except the pump flux entering the segment 0. This flux is used to calculate the values of the relative occupation numbers of all energy levels in fiber segment 0 by solving the linear set of rate equations (7.18). Taking these occupation numbers equation (7.25) gives the increased or decreased flux of photons to the next segment 1, where again at first the occupation numbers and then the new photon flux are calculated. In this way we proceed until the output end of the fiber is reached. At that point equation (7.26) gives the part of the photon flux reflected from the output mirror as the initial value of the backward flux. In the same way as before we now proceed in the opposite direction of the

```

 $\Phi_{kp}^\pm = 0$ 
 $\Phi_{k0}^+ = T_k^{in} \Phi_k^p$ 
repeat
  for  $p = 0$  to  $m - 1$ 
    calculate  $n_{ip}$  (7.17), (7.18)
    calculate  $\Phi_{kp+1}^+$  (7.24), (7.25)
     $\Phi_{km}^- = R_k^{out} \Phi_{km}^+$  (7.26)
  for  $p = m - 1$  to  $0$ 
    calculate  $n_{ip}$  (7.17), (7.18)
    calculate  $\Phi_{kp}^-$  (7.24), (7.25)
     $\Phi_{k0}^+ = R_k^{in} \Phi_{k0}^- + T_k^{in} \Phi_k^p$  (7.26)
until converged
 $\Phi_k^{out} = T_k^{out} \Phi_{km}^+$ 

```

Figure 7.6: Algorithm of the simulation kernel in pseudo-code with the appropriate equations indicated

fiber, from the last segment back to the first. Having arrived there, we use equation (7.26) again to calculate the reflected photon flux and add the flux from the pump laser. After the first loop the new values of Φ_{k0}^+ will be quite different from the initial ones, but after a couple of iterations these values usually converge to the stationary case. For the break criterion we define the value

$$Q = \max_k \left(\frac{2|\Phi_{k0}^+ - \Phi_k^0|}{\Phi_{k0}^+ + \Phi_k^0} \right), \quad (7.28)$$

where Φ_k^0 is the vector Φ_{k0}^+ from the last iteration. The iteration loop is left when Q falls below a certain value.

All operations in the simulation kernel are usual matrix operations such as multiplication, addition, and inversion, which are carried out at high speed by usual program libraries. Therefore the whole fiber laser simulation program including the kernel loop was again written in the high level language Python [62]. The small delay due to the Python interpreter compared with a compiled C program is not significant since most of the computing time is consumed by the matrix operations. Usual simulation runs need about 100 iterations if the pump power is well above the threshold power, and with 200 wavelengths, 10 fiber segments, and $Q = 10^{-3}$ this takes less than a minute even on low-end computers.

It is worth noting that the kernel acts on the wavelength grid without any reference to the wavelength values represented by k . In cases where the wavelength of a laser is already known, using just this single value increases the speed of computation significantly. On the other hand, when a fine grid of wavelengths is offered, the simulation automatically pins to the maximum gain position. However, it should be remembered that the model does not take into account the homogenous line width of a transition and the respective effects are not simulated. A number of 10 fiber segments turned out to be suitable in most cases but care must be taken that the pump power is not absorbed completely in the first segment, otherwise errors caused by the discrete treatment of the continuous fiber cause unrecoverable errors in the calculated photon flux which often lead to undamped oscillations in successive iterations. Even when the length of the fiber segments is chosen to be short enough, it happens that equation (7.25) gives negative values at certain wavelengths due to rounding errors. These negative values must be clipped to zero to avoid unstable behaviour.

Obviously, the term for spontaneous emission in the gain equations (7.25) is not really necessary above the laser threshold but it is still useful as it produces a constant seed of photon flux at all wavelengths at a resonable power level. If this term is omitted, these seed values must be given together with the pump flux before the beginning of the iteration loop, otherwise the laser will not start running. As a rough approximation of the factor w in this term, which is the probability for a spontaneously emitted photon to be guided by the fiber core, the value

$$w = \frac{1}{2}(1 - \cos(\arcsin(NA))) \quad (7.29)$$

is used, which is the value of the quotient $\Omega/4\pi$, where Ω is the solid angle spanned by the acceptance angle of the fiber with given NA and 4π the full solid angle. The concept of an

acceptance angle is normally used for multi-mode fibers only and does not really make sense in case of a single-mode fiber but an exact value is not needed anyway.

Of more importance is the confinement factor $f(\nu)$ in the terms of absorption and spontaneous emission, which is the fraction of the radiation field affected by the fiber core as explained in section 7.1. For the case of a single-mode fiber [132] gives the expression

$$f(\nu) = \left(\frac{W}{V}\right)^2 \left(1 + \left(\frac{J_0(U)}{J_1(U)}\right)^2\right) \quad (7.30)$$

with the V -number from equation (7.6), $W = 1.1428V - 0.9960$, $U = V^2 + W^2$, and the Bessel function $J_i(x)$ of order i . In the multi-mode regime with V -numbers above 2.405 this equation is not valid and quickly reaches unreasonable values above 1. A general calculation of $f(\nu)$ in the multi-mode case seems to be impossible or at least very cumbersome because it depends on the relative intensity carried in the different radiation modes, which depends on a variety of conditions. However, the value is expected to be relatively large in multi-mode

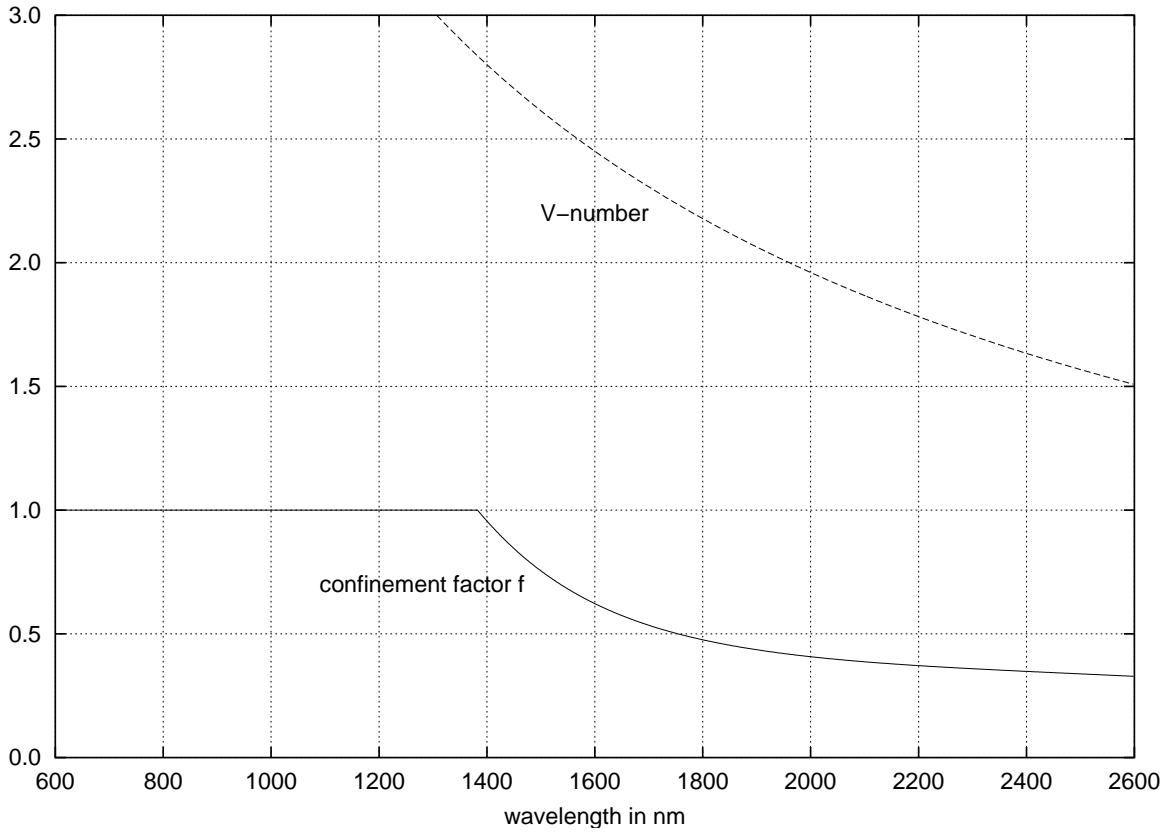


Figure 7.7: V -number and confinement factor f for the Tm:ZBLAN fiber used.

fibers and therefore equation (7.30) is used for all wavelengths, but all values exceeding 1 are clipped to $f(\nu) = 1$. Figure 7.7 shows the spectral dependence of this factor for the fiber used in the laser experiments in the last section together with the value of the V -number. It can be seen that for both lasers of the laser cascade at $1.9\ \mu\text{m}$ and $2.3\ \mu\text{m}$ the value of the confinement factor is below 0.5.

Extensive use of the simulation program showed no problems with the numerical stability of the algorithm as long as the fiber segments were chosen to be short enough as explained above and the background loss $\alpha(\nu)$ was set to a nonzero value. It turned out that this attenuation term in the gain equation (7.25) is effectively damping the small rounding errors occurring in every numerical calculation, which in certain cases led to photon fluxes slightly increasing in each iteration step without limits when $\alpha(\nu)$ was omitted. Even very small values of $\alpha(\nu)$ were found to assure the numerical stability of the algorithm in all simulations carried out.

As already mentioned, the model equations of the simulation developed here do not cover energy transfer processes. The transition rates of such processes are proportional to the occupation number of the initial levels of both interacting transitions. When such terms are inserted in the rate equations, they become non-linear, which makes the solution much more difficult. However, the kernel algorithm does not depend on the method used to solve the rate equations. A straightforward way to implement the important case of a co-dopant would be to fix, at first, the occupation numbers of dopant 2 and then solve the rate equations of dopant 1, which are now linear again. In the next step these results would be treated as fixed in the rate equations of dopant 2 to solve them. In the third step a better solution for the occupation numbers of dopant 1 could be calculated and so forth. This iteration, similar to the main loop of the laser simulation, should converge to an approximation of the correct values after some iteration steps. Of course, such an additional iteration process for each fiber segment would increase the simulation time drastically.

7.4 Comparison of measurement and simulation

The fiber laser simulation model developed in the last section is very useful for the development of such lasers. It allows unlimited variations of the parameters to investigate the dependencies between these parameters. Suppressing or increasing the cross section of a specific transition, for example, is an experiment which is impossible in reality but quite easy in a computer model. However, even when using parameters of highest quality, we never have the guarantee that the simulated values reflect reality. The first step with a simulation program therefore is to simulate a real setup and compare the calculated values with the measurements. This was done for the measurements from section 7.2 and excellent agreement was achieved under certain conditions, which will be discussed in the following. The figures 7.8 to 7.10 show three typical results. For these graphs measurements with different behaviour of the laser characteristics were chosen. The correspondence between measurement and calculation in all other cases was similar.

The parameters of the thulium-doped ZBLAN-fiber used were already given in section 7.2. The fiber core has a diameter of $7.8\ \mu\text{m}$ and the numerical aperture is $NA = 0.16$. The actual attenuation of the fiber is unknown, therefore a value of $0.1\ \text{dB/m}$ is used in the simulation since Thorlabs specifies the attenuation of these fibers to be smaller than this value, which in practice is rather low.

Only four energy levels and three transitions between these levels had to be used (see figure 6.8). The cross sections of the pump transition ${}^3\text{H}_6 \rightarrow {}^3\text{H}_4$ were measured in absorption and emission and the same was the case for the $1.9\ \mu\text{m}$ laser transition ${}^3\text{F}_4 \rightarrow {}^3\text{H}_6$. The third relevant transition is the $2.3\ \mu\text{m}$ laser transition ${}^3\text{H}_4 \rightarrow {}^3\text{H}_5$, which was measured only in emission. Therefore the cross section of the corresponding absorption was calculated using the McCumber theory as explained in section 6.3, although the result may be questionable. However the importance of this cross section is expected to be limited since the lower laser level has a relatively short lifetime. Two more transitions could have been of interest: the $1.45\ \mu\text{m}$ transition ${}^3\text{H}_4 \rightarrow {}^3\text{F}_4$ and the $1.2\ \mu\text{m}$ transition ${}^3\text{H}_5 \rightarrow {}^3\text{H}_6$. Both were included

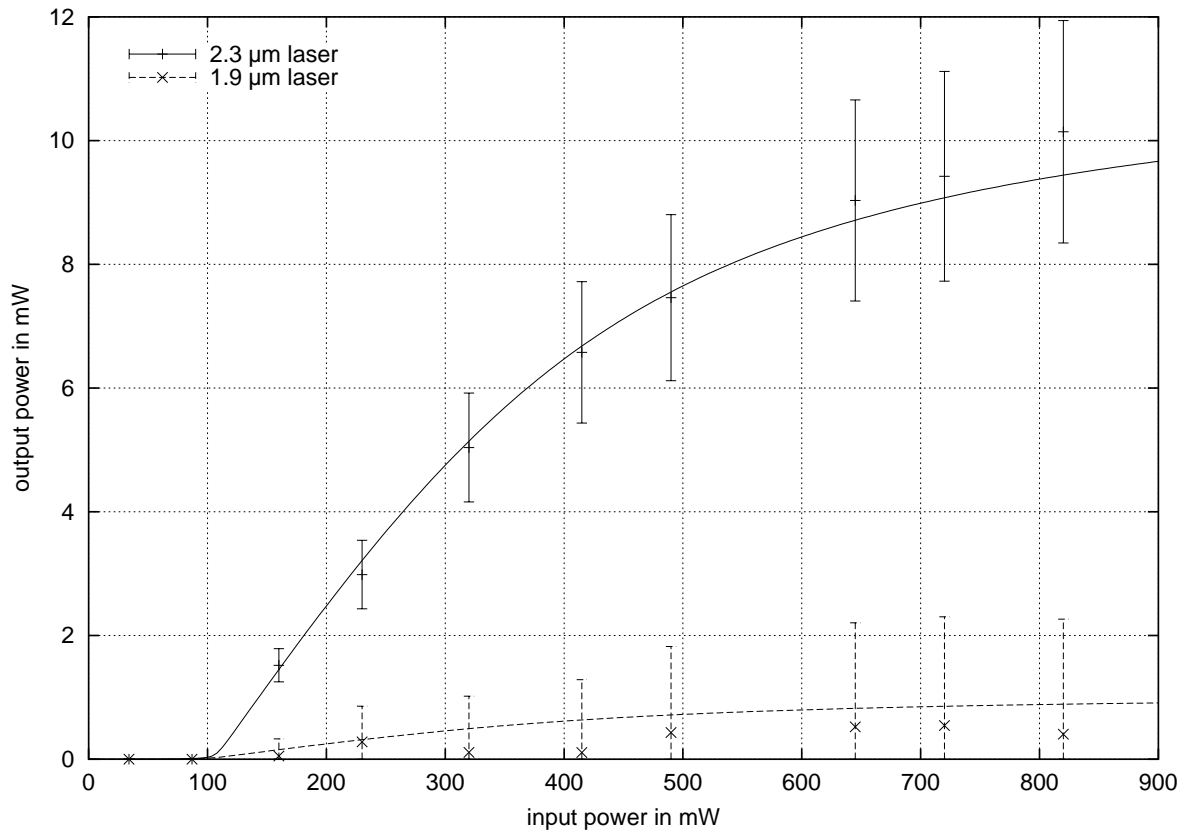


Figure 7.8: Comparison of measured and simulated laser characteristics (measurement 1)

in first simulations, but no evidence for beginning laser operation at these wavelengths was found just like in the laboratory experiments. Therefore, these wavelengths were omitted in further calculations to speed up the simulation. To take the spontaneous radiative emissions into account, in the rate and gain equations the transition rates A_{ij} calculated from the Judd-Ofelt theory were used. What is most uncertain of the spectroscopic parameters are the nonradiative transition rates. Measurements of the lifetime of the energy levels were not available and would have been of limited value anyway as the glass composition of the fiber from Thorlabs is unknown. Therefore equation (6.9) was used with the parameters from [6] given in table 6.1. This resulted in the estimated lifetimes $\tau(^3\text{H}_4) = 1.33$ ms, $\tau(^3\text{H}_5) = 0.76$ ms, and $\tau(^3\text{F}_4) = 7.29$ ms, which is comparable to literature values. Most important are the non-radiative transitions for the lifetime of $^3\text{H}_5$. Since this transition links the lower level of the $2.3\text{ }\mu\text{m}$ laser with the upper level of the $1.9\text{ }\mu\text{m}$ laser, it determines the saturation of the laser cascade, which is most effective when the lifetime of $^3\text{H}_5$ is low. The saturation effect can be seen in all three figures 7.8 to 7.10, especially in the first one. Simulations with different values

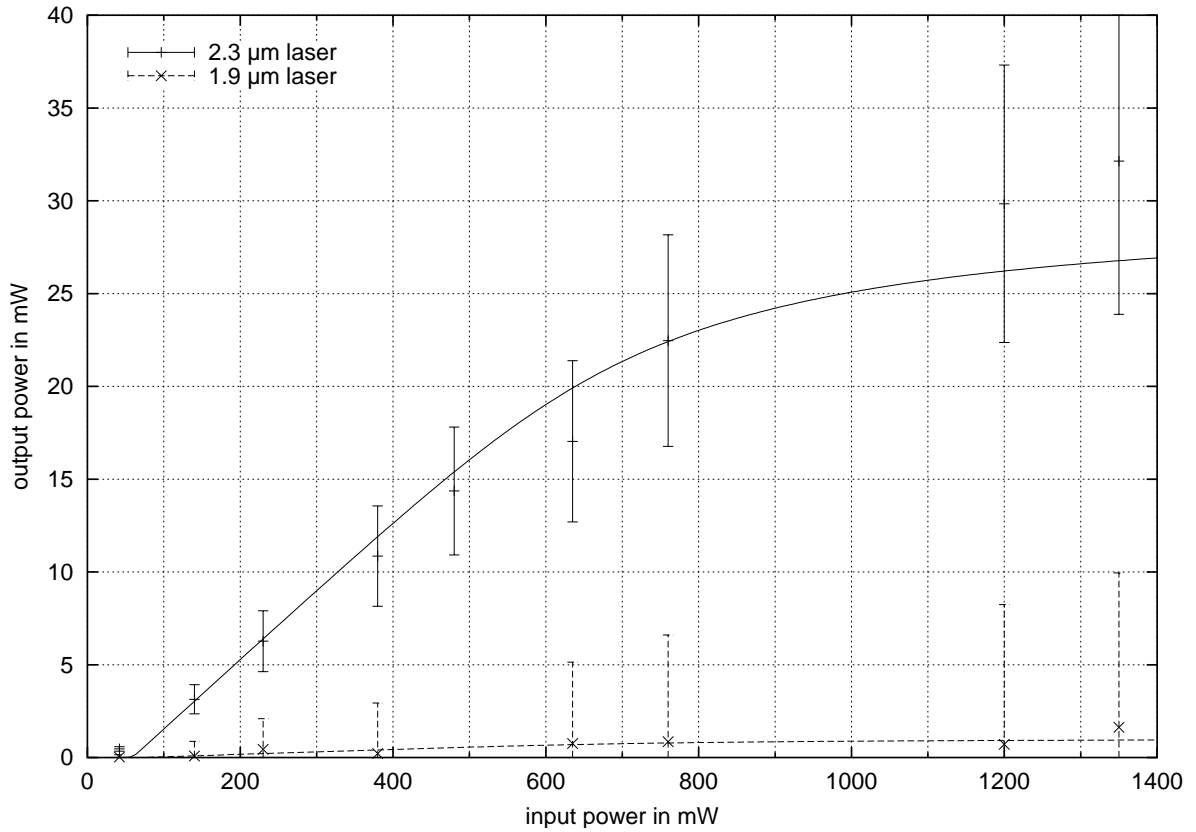


Figure 7.9: Comparison of measured and simulated laser characteristics (measurement 4)

of this lifetime indeed showed stronger saturation in case of a larger lifetime and vanishing saturation for a small lifetime. Since the lifetime of ${}^3\text{H}_5$ is not the only unknown parameter, as we will see, it is not possible to fix its value by such calculations, but it seems that the value above is reasonable.

The dominating uncertainty when comparing the measured laser characteristics with the simulation are the coupling factors on both sides of the fiber. The input power is measured in front of the incoupling optics. Before the pump beam enters the fiber, it passes the lenses of the focussing objective, which sums up to four Fresnel reflections at the surfaces of the lenses in case of the objective used here. An additional Fresnel reflection reduces the pump power when it enters the substrate of the input mirror. In the approximation of incident rays perpendicular to the surfaces these four Fresnel reflections reduce the pump power by a factor of about 0.8. The following partial reflection by the coating of the input mirror is already contained in the simulation model, but the final and completely unknown factor is the incoupling efficiency of the pump beam into the fiber core itself. Values above 0.5 are usually

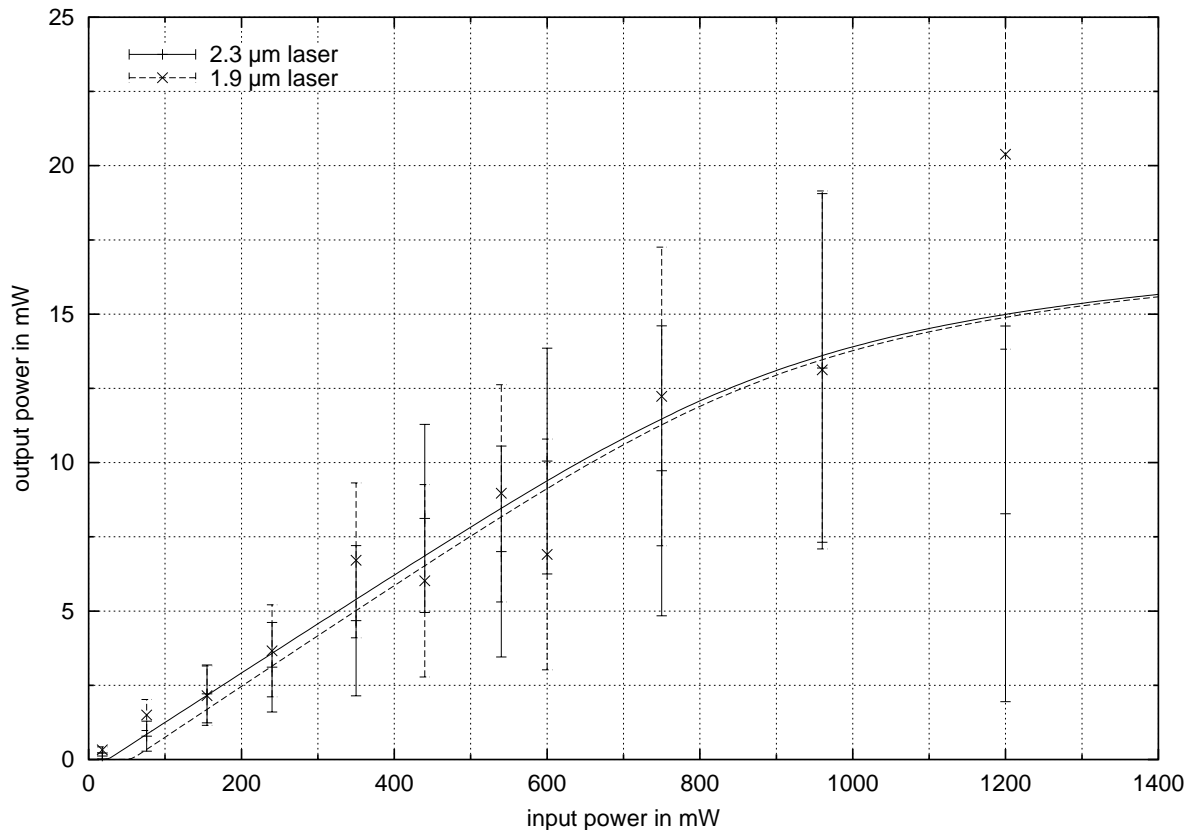


Figure 7.10: Comparison of measured and simulated laser characteristics (measurement 5).

considered as good for free space coupling into a single-mode fiber. Since the surface of the mirror coating was adapted to the refractive index of the fiber glass, no additional reflection occurs at the interface to the fiber. At the output side of the fiber laser the situation is the same concerning the Fresnel reflections, but the coupling efficiency in that case is 1, of course. Furthermore, we have to take into account losses due to absorption in the lens glasses, which is not negligible at the long laser wavelengths. Using all available data on the objectives, a total transmission factor of 0.7 was estimated at $2.3\ \mu\text{m}$ and 0.75 at $1.9\ \mu\text{m}$, including the Fresnel reflection at the mirror substrate. All these factors were included in the laser simulation as first approximations, but the coupling efficiencies are even worse in reality and different for each measurement. In the computer program the coupling factors V_{in} and V_{out} are used to take into account these unknown losses. The best coincidence between measurement and simulation in most cases was found when V_{in} was set to values in the range of 0.3 – 0.6 and V_{out} in the range 0.7 – 1.0. Values outside these ranges appeared only in bad measurements, which also were indicated e.g. by high values of the measured laser threshold.

During the period of time in which the laser simulation was used, it was possible in all cases to fit the measurements by variation of the unknown parameters. However, since there are always some of these values which are unknown or only approximately known, it is unlikely that the characteristics of a completely new laser setup may be predicted correctly. Nevertheless the simulation is of great value when measured values of a certain setup are available and the simulation is used to optimize certain values, usually the output power. Such calculations will be presented in the next section. Besides, the simulation turned out to be very successful in the interpretation of certain features in the laser characteristics as e.g. the order in which cascade laser transitions start lasing or the way in which they interact.

7.5 Optimization of parameters

The results from the last section ensured the validity of our laser simulation with the parameters used and so we are free now to play around with the design parameters of the fiber laser setup. In this final section we will discuss the results from two sets of simulations which were carried out to maximize the output power of the $2.3\ \mu\text{m}$ laser.

When using a laser diode for pumping the $2.3\ \mu\text{m}$ fiber laser at 790 nm, a maximum pump power of 50 mW should be reasonable. Figure 7.11 shows the output power which may be obtained when using such a pump diode for a fiber length up to 2 m and any of the available output mirrors. In the simulation coupling efficiencies of 100 % were assumed on both sides, the values therefore will be smaller in a real setup. The simulation shows that the threshold length increases with decreasing reflectivity of the output mirror, which obviously must be the case because higher gain is necessary to compensate for a lower reflectivity. The fiber length at which maximum gain is achieved also decreases with increasing fiber length from 0.6 m for $R = 50\%$ to 0.3 m for $R = 92\%$. The maximum output power of all setups is expected to be obtained with a fiber length of 0.35 m and mirror 140 ($R = 90\%$) with a value of about 5 mW. From zero towards larger fiber lengths all lasers show a steep increase of the output

power until the maximum value is reached but from the maximum to larger fiber lengths the output power decreases much more slowly. The slope of this falling edge is determined mainly by the background losses of the fiber, since the output power stays constant at the maximum value when the attenuation is set to zero. It follows that a fiber laser with a low loss fiber is less sensitive to the optimum fiber length than one with a fiber with higher background losses. This conclusion is in agreement with practical experience.

Figure 7.12 shows the photon fluxes along the fiber core in a near-optimum setup according to figure 7.11 using a fiber length of 0.5 m and output mirror 137. The fluxes in the figure are scaled to powers using equation (7.27) since the reader is probably more familiar with these values. The figure clearly shows why this is the optimum fiber length. The pump power is completely absorbed along the fiber, but there is still a small amount of remaining pump power at the fiber end necessary for the $1.9\ \mu\text{m}$ laser, which is attenuated by an unpumped fiber section, because it is a three-level laser. This laser holds the largest part of the radiation field in the fiber and it can be seen that after some gain in the first half of the fiber this

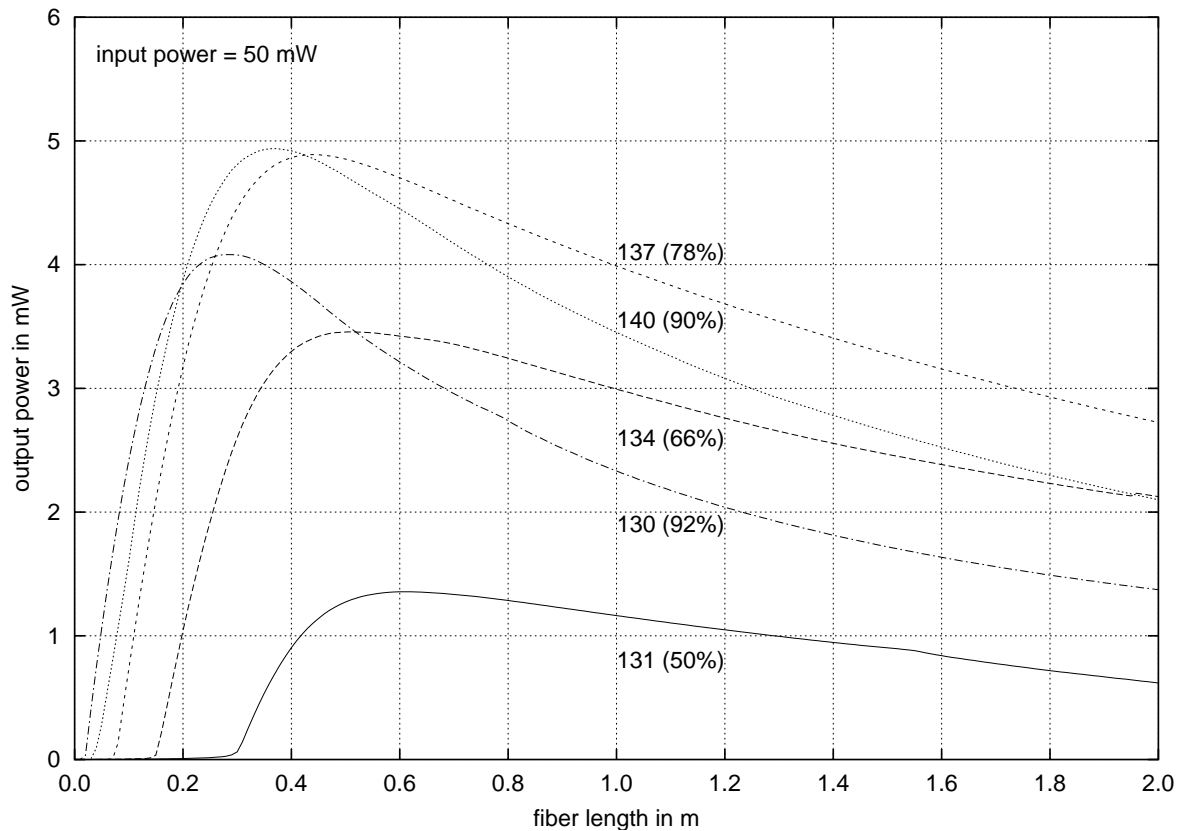


Figure 7.11: Output power of the $2.3\ \mu\text{m}$ laser using different output mirrors and fiber lengths

$1.9\,\mu\text{m}$ power flux is slightly attenuated. The fraction of power coupled out through the output mirror is given by the difference in the power levels of the fluxes in both directions and in case of $1.9\,\mu\text{m}$ is very small due to the high reflectivity of the output mirror at that wavelength. The main part of the $1.9\,\mu\text{m}$ laser beam leaves the resonator through the input mirror. The photon flux at $2.3\,\mu\text{m}$ also shows gain only in the first half of the fiber, but stays constant to the end of the fiber afterwards because the lower level of this four-level laser is rapidly depopulated by multiphonon emission.

While the data from figures 7.11 and 7.12 in principle could also be obtained by measurements, the distribution of the relative occupation numbers of all energy levels along the fiber core as shown in figure 7.13 are accessible only in the simulation. The calculations are based on the same setup and confirm the conclusions drawn from figure 7.12. The high pump power in the first part of the fiber strongly depletes the ground level $^3\text{H}_6$ so that nearly half of the dopant ions are excited. In this first section the occupation number of the upper laser level $^3\text{H}_4$ of the $2.3\,\mu\text{m}$ laser is the largest of the excited states. The lower level $^3\text{H}_5$ of this transi-

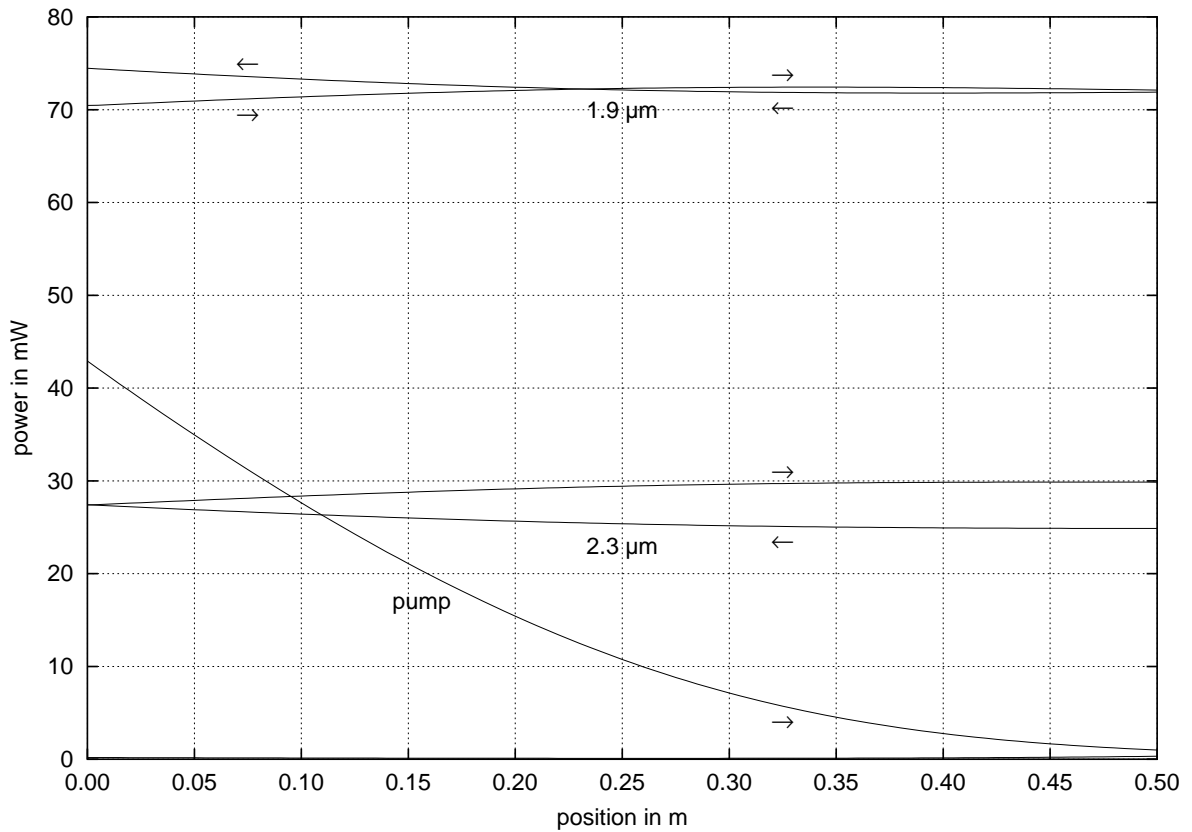


Figure 7.12: Calculated power of the radiation field in the fiber. Pump power: 50 mW, output mirror: 137

tion is always less populated and the ratio of the occupation numbers of lower and upper laser level is approximately one half and more or less constant along the fiber. In the middle of the fiber the decreasing occupation numbers of these levels cross the value of the first excited level 3F_4 , which stays nearly constant along the whole fiber. In the second half of the fiber this level is not filled effectively any more from the higher levels, but at the same time the weakly pumped fiber absorbs part of the $1.9\ \mu\text{m}$ flux which fills the level. Both processes compensate for each other to a high degree in this certain case. Furthermore, it can be seen in figure 7.13 that population inversion is never achieved for the $1.9\ \mu\text{m}$ transition along the whole fiber, although it is usually mentioned as the criterion for laser action. However, population inversion probably is reached if the spectrum of Stark levels is taken into account instead of the total occupation numbers in figure 7.13 because the wavelength of such a three-level laser is shifted towards long wavelengths in the emission lineshape and, strictly speaking, the product of occupation number and cross section should be taken as the laser criterion.

Besides the maximum output power which may be achieved by using the existing mirrors,

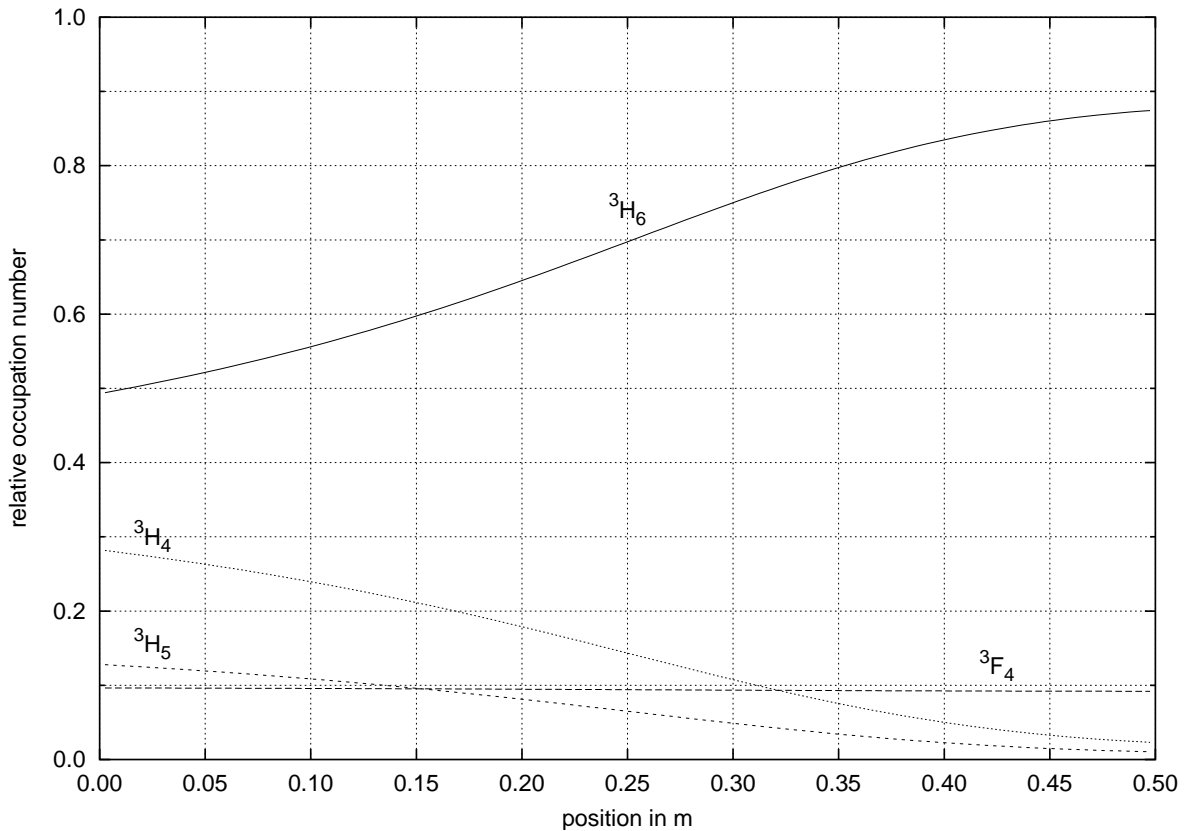


Figure 7.13: Relative occupation numbers along the fiber. Pump power: 50 mW, output mirror: 137

it is also interesting to find the maximum output power in case of arbitrary mirrors and fiber lengths. Therefore, the fiber laser was simulated with ideal mirrors with 100 % transmission for the pump laser and a reflectivity of 100 % in the $1.9\ \mu\text{m}$ region of both mirrors. Around $2.3\ \mu\text{m}$ a reflectivity of 100 % was assumed for the input mirror and the reflectivity of the output mirror was varied in the range of 50 – 100 %. Figure 7.14 shows the results obtained for fiber lengths up to 2 m. The pump power was set to 50 mW again. The maximum output power was found to be 6.2 mW obtained with fiber lengths around 0.5 m and about 87 % reflectivity of the output mirror. It turns out that the maximum output power expected from the existing mirrors according to figure 7.11 is not far from the global optimum. Of course, the optimum fiber length and mirror reflectivity also depends on the input power, and the two cases evaluated here are just examples of the large range of investigations possible with the simulation model at hand.

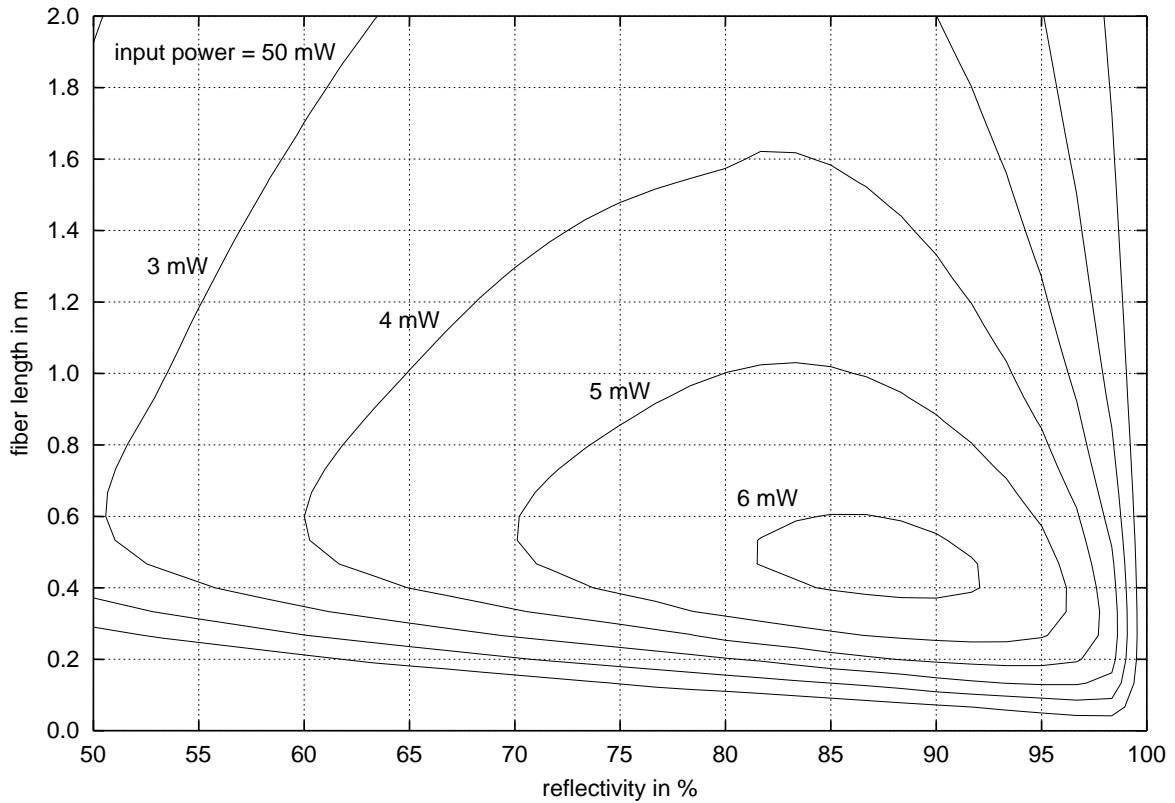


Figure 7.14: Search of the fiber length and reflectivity of the output mirror to maximize the output power of the $2.3\ \mu\text{m}$ laser. The contour lines mark 1 mW steps of the output power. Some values are given.

Conclusions

As explained in the introduction, this work was started with the goal of getting suitable spectroscopic parameters with known quality. Furthermore basic principles and dependencies were to be made clear. It should be obvious from the preceding chapters that both goals were attained. Good or even excellent agreement was achieved when measurements and calculations were compared. It was especially the work on the first chapters that gave the author deep insights into the physics of rare-earth ions. It is the hope of the author that this text provides its reader a useful introduction to this subject. Let us now recall the whole survey of this work in short and remind us important results and features.

We started with the theory of describing the structure of the energy level system of rare-earth ions. All six types of interaction operators, which were found in the literature and which are relevant in case of vitreous hosts, were collected and expressed in a certain form based on just the two unit tensor operators $\mathbf{u}^{(k)}$ and $\mathbf{t}^{(k)}$, in the orbital and the spin spaces respectively. For all combinations of these unit tensor operators occurring in the higher level interaction operators the equations to calculate the respective matrix elements in the base of determinantal product states were developed. This did not cause grave difficulties, a few exceptions excluded.

It was explained that the mathematical simplicity of these expressions is accompanied by certain disadvantages. First of all the results, besides the plain wavenumbers of the energy levels, are not compatible with the literature, which uses Racah's *LS*-classification scheme. Furthermore, it is not possible in the determinantal product state base to profit from the rotational invariance of all interaction operators used here. The solution was a straightforward transformation matrix from the determinantal product state base to a *LS*-representation, which is almost completely equivalent to the usual Racah-classification.

The kernel of the computer program developed for energy level calculations and calculation of the mentioned combinations of unit tensor operators therefore works with determinantal product states, but the resulting matrices are immediately transformed into the *LS*-representation. In that step, due to rotational invariance, the dimension of the matrices is greatly reduced by skipping all elements where $M_J \neq J$ holds. All higher level operators are calculated by simple combinations of these elementary matrices afterwards.

The next natural step are the radiative transitions between the energy levels of the ground configuration. Dominating in this field is the Judd-Ofelt theory for electric dipole transitions, but a couple of accompanying equations were also given and discussed in detail. Attempts were made to follow the history of most of these equations to their roots since in this field there is some confusion in the literature. In order to calculate the line strengths of any of these radiative transitions the calculation of reduced matrix elements is necessary. Unfortunately the usual method of calculating their values needs the full state space and does not profit from

the mentioned rotational invariance. Nevertheless, a phase convention for the transformation matrix to the LS -base was found, which allows us to use the same reduced space containing only states with $M_J = J$ as for the usual matrix elements. Computation times are thus reduced significantly.

At this point the theory was complete so that the fitting of calculated values to absorption measurements could be started. Therefore the absorption spectra of Ce^{3+} , Pr^{3+} , Er^{3+} , Tm^{3+} , and Yb^{3+} in ZBLAN glass were evaluated in detail with special focus on the error calculations. In case of Pr^{3+} , Er^{3+} , and Tm^{3+} the results obtained were used in energy level and Judd-Ofelt fits, which showed excellent agreement between measurement and calculation, namely in case of erbium. The results of the fitting procedures and a comparison of the radial and Judd-Ofelt parameters obtained with values from the literature confirmed the well-known fact that the line strengths of the transitions depend much more on the host material than the positions of the energy levels do. Nevertheless the influence of the host is strong enough so that energy level calculations seem to be worth the effort.

After an evaluation of the emission spectra of Er^{3+} and Tm^{3+} in order to receive spectral emission cross sections, we finally came to fiber laser simulation in the last chapter. A novel stationary simulation model for cw fiber lasers was developed, which allows for unlimited spectral resolution. The results obtained from this model for a $1.9/2.3\ \mu\text{m}$ cascade fiber laser in $\text{Tm}:\text{ZBLAN}$ were compared with a couple of measurements, and an excellent agreement was found. This allowed us to give some examples of fiber laser simulations performed to find the conditions for maximum output power at $2.3\ \mu\text{m}$ under certain constraints. In addition, the insights into the fiber obtained by the simulation model were demonstrated.

All in all, the way from the energy level calculations to the final fiber laser simulation turned out to be very successful and undoubtedly will continue to be used at our institute in the future. Moreover the computer programs developed for this work seem to be of some value for other people working in the fields of fiber lasers and rare-earth spectroscopy and therefore will soon be made available under the GNU General Public License [133] for free. The author has been using almost exclusively free software for many years now and therefore it seems to be a matter of fairness to make the results of his programming efforts available to the community which has been providing him with excellent free software all the time.

References

- [1] C. Frerichs. *Modulation von Erbium-dotierten Faserlasern im mittleren Infrarot (engl. Modulation of erbium doped fiber lasers in the mid-infrared)*. Dissertation (engl. doctoral dissertation), Fakultät für Maschinenbau und Elektrotechnik der Technischen Universität Braunschweig, Braunschweig, 1996.
- [2] J. Schneider, Carbonnier C., and U. B. Unrau. Characterization of a Ho^{3+} doped fluoride fiber laser with $3.9\,\mu\text{m}$ emission wavelength. *Applied Optics*, 36(33): 8595–8600, 1997.
- [3] T. Schweizer. *Rare-Earth-Doped Gallium Lanthanum Sulphide Glasses for Mid-Infrared Fibre Lasers*. Dissertation (engl. doctoral dissertation), Fachbereich Physik der Universität Hamburg, Hamburg / Southampton, 1998.
- [4] J. Schneider. *Kaskaden-Faserlaser im mittleren Infrarot (engl. Cascade fiber lasers in the mid-infrared)*. Dissertation (engl. doctoral dissertation), Fakultät für Maschinenbau und Elektrotechnik der Technischen Universität Braunschweig, Braunschweig, 1996.
- [5] W. T. Carnall, H. Crosswhite, and H. M. Crosswhite. Energy level structure and transition probabilities of the trivalent lanthanides in LaF_3 . Report ANL-78-XX-95, Argonne National Laboratory, Chemistry Division, Illinois, 1978.
- [6] L. Wetenkamp. *Charakterisierung von laseraktiv dotierten Schwermetallfluorid-Gläsern und Faserlasern (engl. Characterization of Laser-actively Doped Heavy-metal Fluoride Glasses and Fiber Lasers)*. Dissertation (engl. doctoral dissertation), Fakultät für Maschinenbau und Elektrotechnik der Technischen Universität Braunschweig, Braunschweig, 1991.
- [7] B. R. Judd. *Operator Techniques in Atomic Spectroscopy*. Advanced Physics Monograph Series. McGraw-Hill Company, New York, 1963.
- [8] G. Racah. Theory of complex spectra. I. *Physical Review*, 61: 186–197, February 1942.
- [9] G. Racah. Theory of complex spectra. II. *Physical Review*, 62: 438–462, November 1942.
- [10] G. Racah. Theory of complex spectra. III. *Physical Review*, 63(9-10): 367–382, May 1943.
- [11] G. Racah. Theory of complex spectra. IV. *Physical Review*, 76(9): 1352–1365, November 1949.

-
- [12] C. Cohen-Tannoudji, B. Diu, and F. Lalœ. *Quantum Mechanics*, volume 2. Wiley & Sons, New York, 2nd edition, 1977.
- [13] C. Cohen-Tannoudji, B. Diu, and F. Lalœ. *Quantum Mechanics*, volume 1. Wiley & Sons, New York, 2nd edition, 1977.
- [14] G. H. Dieke and H. M. Crosswhite. The spectra of the doubly and triply ionized rare earths. *Applied Optics*, 2(7): 675–686, July 1963.
- [15] G. H. Dieke. *Spectra and Energy Levels of Rare Earth Ions in Crystals*. Wiley & Sons, New York, 1968.
- [16] R. F. Bacher and S. Goudsmit. Atomic energy relations. I. *Physical Review*, 46: 948–969, December 1934.
- [17] Z. B. Goldschmidt. *Handbook on the Physics and Chemistry of Rare Earths*, volume 1, chapter 1: *Atomic Properties (Free Atom)*, pages 1–171. North-Holland Publishing Company, Amsterdam, 1978.
- [18] C. W. Nielson and G. F. Koster. *Spectroscopic Coefficients for the p^n , d^n , and f^n Configurations*. MIT Press, Cambridge, Massachusetts, 1963.
- [19] S. Edvardsson and D. Åberg. An atomic program for energy levels of equivalent electrons: lanthanides and actinides. *Computer Physics Communications*, 133: 396–406, 2001.
- [20] D. Åberg. *A Semi-empirical Study of Heavy Ions: Actinides and Rare-earths*. B. Sc. thesis, Mid Sweden University, Sundsvall, 1999.
- [21] B. G. Wybourne. *Spectroscopic Properties of Rare Earths*. Interscience Publishers, New York, 1965.
- [22] H. H. Marvin. Mutual magnetic interactions of electrons. *Physical Review*, 71(2): 102–110, January 1947.
- [23] H. Horie. Spin-spin and spin-other-orbit interactions. *Progress of Theoretical Physics*, 10(3): 296–308, September 1953.
- [24] B. R. Judd, H. M. Crosswhite, and H. Crosswhite. Intra-atomic magnetic interactions for f electrons. *Physical Review*, 169(1): 130–138, May 1968.
- [25] W. T. Carnall, P. R. Fields, J. Morrison, and R. Sarup. Absorption spectrum of $\text{Tm}^{3+}:\text{LaF}_3$. *Journal of Chemical Physics*, 52(8): 4054–4059, April 1970.
- [26] K. Rajnak and B. G. Wybourne. Configuration interaction effects in l^n configurations. *Physical Review*, 132(1): 280–290, October 1963.

-
- [27] G. Racah and J. Stein. Effective electrostatic interactions in l^n configurations. *Physical Review*, 156(1): 58–64, April 1967.
- [28] B. R. Judd. Private communication, May 2001.
- [29] R. E. Trees. Configuration interaction in Mn II. *Physical Review*, 83(4): 756–760, August 1951.
- [30] R. E. Trees. Term values in the $3d^54s$ configuration of Fe III. *Physical Review*, 84(6): 1089–1091, December 1951.
- [31] G. Racah. $L(L+1)$ correction in the spectra of the iron group. *Physical Review*, 85: 381–382, 1952.
- [32] R. E. Trees. The $L(L+1)$ correction to the Slater formulas for the energy levels. *Physical Review*, 85: 382, 1952.
- [33] S. Feneuille. Opérateurs à trois particules pour des électrons d équivalents (engl. Three-particle operators for equivalent d-electrons). *Comptes rendus des séances de l'Académie des Sciences, Série B*, 262: 23–26, January 1966.
- [34] B. R. Judd. Three-particle operators for equivalent electrons. *Physical Review*, 141(1): 4–14, January 1966.
- [35] B. R. Judd. Zeeman effect as a prototype for intra-atomic interactions. *Physica*, 33: 174–182, 1967.
- [36] K. Rajnak and B. G. Wybourne. Electrostatically correlated spin-orbit interactions in l^n -type configurations. *Physical Review*, 134(3A): A596–A600, May 1964.
- [37] V. V. Ravi Kanth Kumar and C. K. Jayasankar. Optical properties of Pr^{3+} in alkali zinc borosulphate glasses. *Journal of Alloys and Compounds*, 193: 189–191, 1993.
- [38] V. V. Ravi Kanth Kumar and C. K. Jayasankar. Spectroscopic investigations of Pr(III) ions in alkali cadmium borosulphate glasses. *Journal of Non-Crystalline Solids*, 163: 249–260, 1994.
- [39] W. T. Carnall, G. L. Goodman, K. Rajnak, and R. S. Rana. A systematic analysis of the spectra of the lanthanides doped into single crystal LaF_3 . *Journal of Chemical Physics*, 90(7): 3443–3457, April 1989.
Note: *Appendix I contains 63 pages of tables and may be ordered from the American Institute of Physics (AIP) by PAPS number JCPSA-90-3443-63.*
- [40] J. H. van Vleck. The puzzle of rare earth spectra in solids. *Journal of Physical Chemistry*, 41: 67–80, 1937.

-
- [41] L. J. F. Broer, C. J. Gorter, and J. Hoogschagen. On the intensities and the multipole character in the spectra of the rare earth ions. *Physica*, XI(4): 231–250, December 1945.
- [42] B. R. Judd. Optical absorption intensities of rare-earth ions. *Physical Review*, 127(3): 750–761, August 1962.
- [43] G. S. Ofelt. Intensities of crystal spectra of rare-earth ions. *Journal of Chemical Physics*, 37(3): 511–520, August 1962.
- [44] E. U. Condon and G. H. Shortley. *The Theory of Atomic Spectra*. Cambridge University Press, New York, 1935.
- [45] W. Koechner. *Solid-State Laser Engineering*. Springer-Verlag, Berlin, 4th edition, 1996.
- [46] W. L. Barnes, R. I. Laming, E. J. Tarbox, and P. R. Morkel. Absorption and emission cross section of Er^{3+} doped silica fibers. *IEEE Journal of Quantum Electronics*, 27(4): 1004–1010, April 1991.
Note: *Although the derivation of the Fuchtbauer-Ladenburg equations in this paper in general is correct, it contains a couple of printing errors.*
- [47] W. B. Fowler and D. L. Dexter. Relation between absorption and emission probabilities in luminescent centers in ionic solids. *Physical Review*, 128(5): 2154–2165, December 1962.
- [48] J. D. Axe. Radiative transition probabilities within f^n configurations: The fluorescence spectrum of europium ethylsulfate. *Journal of Chemical Physics*, 39(5): 1154–1160, September 1963.
- [49] W. J. Miniscalco and R. S. Quimby. General procedure for the analysis of Er^{3+} cross sections. *Optics Letters*, 16(4): 258–260, February 1991.
- [50] W. J. Miniscalco. *Rare Earth Doped Fibre Lasers and Amplifiers*, chapter 2: *Optical and Electronic Properties of Rare Earth Ions in Glasses*, pages 19–133. Marcel Dekker, New York, 1993.
- [51] S. H ufner. *Optical Spectra of Transparent Rare Earth Compounds*. Academic Press, New York, 1978.
- [52] C. A. Morrison and R. P. Leavitt. *Handbook on the Physics and Chemistry of Rare Earths*, volume 5, chapter 46: *Spectroscopic properties of triply ionized lanthanides in transparent host lattices*, pages 461–692. North-Holland Publishing Company, Amsterdam, 1982.

-
- [53] W. T. Carnall. *Handbook on the Physics and Chemistry of Rare Earths*, volume 3, chapter 24: *The Absorption and Fluorescence Spectra of Rare Earth Ions in Solution*, pages 171–208. North-Holland Publishing Company, Amsterdam, 1979.
- [54] R. Caspary and U. B. Unrau. *Glass and Rare-Earth Doped Glasses for Optical Fibres*, volume 22 of *IEE EMIS Datareviews Series*, chapter C3.3: Ho^{3+} -Doped Halide Glasses, pages 224–237. IEE, INSPEC, London, 1998.
- [55] W. T. Carnall, P. R. Fields, and B. G. Wybourne. Spectral intensities of the trivalent lanthanides and actinides in solution. I. Pr^{3+} , Nd^{3+} , Er^{3+} , Tm^{3+} , and Yb^{3+} . *Journal of Chemical Physics*, 42(11): 3797–3806, June 1965.
- [56] W. T. Carnall, P. R. Fields, and K. Rajnak. Electronic energy levels in the trivalent lanthanide aquo ions. I. Pr^{3+} , Nd^{3+} , Pm^{3+} , Sm^{3+} , Dy^{3+} , Ho^{3+} , Er^{3+} , and Tm^{3+} . *Journal of Chemical Physics*, 49(10): 4424–4442, November 1968.
- [57] W. T. Carnall, P. R. Fields, and K. Rajnak. Electronic energy levels of the trivalent lanthanide aquo ions. II. Gd^{3+} . *Journal of Chemical Physics*, 49(10): 4443–4446, November 1968.
- [58] W. T. Carnall, P. R. Fields, and K. Rajnak. Electronic energy levels of the trivalent lanthanide aquo ions. III. Tb^{3+} . *Journal of Chemical Physics*, 49(10): 4447–4449, November 1968.
- [59] W. T. Carnall, P. R. Fields, and K. Rajnak. Electronic energy levels of the trivalent lanthanide aquo ions. IV. Eu^{3+} . *Journal of Chemical Physics*, 49(10): 4450–4455, November 1968.
- [60] W. T. Carnall, Jan P. Hessler, and F. Wagner, Jr. Transition probabilities in the absorption and fluorescence spectra of lanthanides in molten lithium nitrate-potassium nitrate eutectic. *Journal of Physical Chemistry*, 82(20): 2152–2158, 1978.
- [61] W. T. Carnall, P. R. Fields, and K. Rajnak. Spectral intensities of the trivalent lanthanides and actinides in solution. II. Pm^{3+} , Sm^{3+} , Eu^{3+} , Gd^{3+} , Tb^{3+} , Dy^{3+} , and Ho^{3+} . *Journal of Chemical Physics*, 49(10): 4412–4423, November 1968.
- [62] <http://www.python.org>.
- [63] M. Poulain, M. Poulain, J. Lucas, and P. Brun. Verres fluorés au tétrafluore de zirconium; propriétés optiques d’un verre dopé au Nd^{3+} (engl. Fluoride fibers from zirconium fluoride; optical properties of a fiber doped with Nd^{3+}). *Materials Research Bulletin*, 10(3): 243–246, 1975.
- [64] J. McDougall, D. B. Hollis, and M. J. P. Payne. Spectroscopic properties of Er^{3+} in fluoride glass. *Physics and Chemistry of Glasses*, 37(6): 256–257, December 1996.

-
- [65] K. Soga, M. Tsuda, S. Sakuragi, H. Inoue, S. Inoue, and A. Makishima. Effects of chloride introduction on the optical properties and the upconversion emission with 980 nm excitation of Er^{3+} in zblan fluoride glasses. *Journal of Non-Crystalline Solids*, 222: 272–281, 1997.
- [66] J. L. Adam. *Glass and Rare-Earth Doped Glasses for Optical Fibres*, volume 22 of *IEE EMIS Datareviews Series*, chapter C1.2: *Intrinsic scattering losses of halide glasses*, pages 170–175. IEE, INSPEC, London, 1998.
- [67] H. Poignant, S. Boj, E. Delevaque, M. Monerie, T. Taunay, P. Niay, P. Bernage, and W. X. Xie. Efficiency and thermal behaviour of cerium-doped fluorozirconate glass fibre Bragg gratings. *Electronics Letters*, 30(16): 1339–1341, August 1994.
- [68] W. T. Carnall, P. R. Fields, and R. Sarup. $^1\text{S}_0$ level of Pr^{3+} in crystal matrices and energy-level parameters for the $4f^2$ configuration of Pr^{3+} in LaF_3 . *Journal of Chemical Physics*, 51(6): 2587–2591, September 1969.
- [69] A. M. Srivastava and D. A. Doughty. On the vacuum-ultraviolet excited luminescence of Pr^{3+} in LaB_3O_6 . *Journal of the Electrochemical Society*, 144(7): L190–L192, July 1997.
- [70] P. Krummrich. *Praseodym-dotierte Faserverstärker für den Wellenlängenbereich um $1,3\mu\text{m}$ (engl. Praseodymium doped fiber amplifiers in the wavelength range of $1.3\mu\text{m}$)*. Dissertation (engl. doctoral dissertation), Fakultät für Maschinenbau und Elektrotechnik der Technischen Universität Braunschweig, Braunschweig, 1995.
- [71] D. C. Yeh, W. A. Sibley, M. Suscavage, and M. G. Drexhage. Radiation effects and optical transitions in Yb^{3+} doped barium-thorium fluoride glass. *Journal of Non-Crystalline Solids*, 88: 66–82, 1986.
- [72] M. J. Weber, J. E. Lynch, D. H. Blackburn, and D. J. Cronin. Dependence of the stimulated emission cross section of Yb^{3+} on host glass composition. *IEEE Journal of Quantum Electronics*, QE-19(10): 1600–1608, October 1983.
- [73] J. L. Adam and W. A. Sibley. Optical transitions of Pr^{3+} ions in fluorozirconate glass. *Journal of Non-Crystalline Solids*, 76: 267–279, 1985.
- [74] A. Flórez, Y. Messaddeq, O. L. Malta, and M. A. Aegerter. Optical transition probabilities and compositional dependence of Judd-Ofelt parameters of Er^{3+} ions in fluoroindate glass. *Journal of Alloys and Compounds*, 227: 135–140, 1995.
- [75] P. Goldner and F. Auzel. Comparison between standard and modified Judd-Ofelt theories in a Pr^{3+} -doped fluoride glass. *Acta Physica Polonica A*, 90(1): 191–196, 1996.

-
- [76] R. S. Quimby and W. J. Miniscalco. Modified Judd-Ofelt technique and application to optical transitions in Pr^{3+} -doped glass. *Journal of Applied Physics*, 75(1): 613–615, January 1994.
- [77] J. A. Medeiros Neto, D. W. Hewak, and H. Tate. Application of a modified Judd-Ofelt theory to praseodymium-doped fluoride glasses. *Journal of Non-Crystalline Solids*, 183: 201–207, 1995.
- [78] J. Hormadaly and R. Reisfeld. Intensity parameters and laser analysis of Pr^{3+} and Dy^{3+} in oxide glasses. *Journal of Non-Crystalline Solids*, 30: 337–348, 1979.
- [79] B. Villacampa, V. M. Orera, R. I. Merino, R. Cases, P. J. Alonso, and R. Alcalá. Optical properties of $\text{ZnF}_2\text{-CdF}_2$ glasses doped with 4f ions. *Materials Research Bulletin*, 26(8): 741–748, 1991.
- [80] J. McDougall, D. B. Hollis, and M. J. P. Payne. Spectroscopic properties of Er^{3+} in fluorozirconate, germanate, tellurite and phosphate glasses. *Physics and Chemistry of Glasses*, 37(2): 73–75, April 1996.
- [81] J. McDougall, D. B. Hollis, and M. J. P. Payne. Spectroscopic properties of Tm^{3+} in ZBLAN fluoride glass. Part 2. Judd-Ofelt parameters. *Physics and Chemistry of Glasses*, 36(3): 139–140, June 1995.
- [82] A. Flórez, M. Flórez, S. A. López-Rivera, J. Martin, P. Porcher, O. L. Malta, Y. Mes-saddeq, and M. A. Aegerter. 4f–4f intensities of the Tm^{3+} ions in fluorindate glasses: the influence of third-order effects through odd intensity parameters. *Journal of Alloys and Compounds*, 277: 333–337, July 1998.
- [83] Y. B. Shin, W. Y. Cho, and J. Heo. Multiphonon and cross relaxation phenomena in Ge-As(or Ga)-S glasses doped with Tm^{3+} . *Journal of Non-Crystalline Solids*, 208: 29–35, 1996.
- [84] V. Gupta. <http://www.omniscia.org/~vivake/python/Simplex.py>, 2001.
- [85] W. H. Press, S. A. Teukolsky, W. T. Vetterling, and B. P. Flannery. *Numerical Recipes in Fortran 77 – The Art of Scientific Computing*, volume 1. Cambridge University Press, Cambridge, 2nd edition, 1996.
- [86] F. Auzel, S. Hubert, and P. Delamoye. Absolute oscillator strengths of 5f – 5f transitions of U^{4+} in ThBr_4 and in hydrobromic acid solutions. *Journal of Luminescence*, 26: 251–262, 1982.
- [87] A. A. Kornienko, A. A. Kaminskii, and E. B. Dunina. Dependence of the line strength of f – f transitions on the manifold energy. *Physica Status Solidi B*, 157: 267–273, 1990.

-
- [88] P. Goldner and F. Auzel. Application of standard and modified Judd-Ofelt theories to a praseodymium-doped fluorozirconate glass. *Journal of Applied Physics*, 79(10): 7972–7977, May 1996.
- [89] A. Flórez, O. L. Malta, Y. Messaddeq, and M. A. Aegerter. Judd-Ofelt analysis of Pr^{3+} ions in fluoroindate glasses: influence of odd third order intensity parameters. *Journal of Non-Crystalline Solids*, 213&214: 315–320, 1997.
- [90] A. Suresh Kumar and S. V. J. Lakshman. Spectroscopic studies on Pr(III) , Nd(III) , Er(III) and Tm(III) ions in fluoro-, boro- and acetophosphate glass environments. *Journal of the Less-Common Metals*, 148: 357–361, 1989.
- [91] C. K. Jayasankar and V. V. Ravi Kanth Kumar. Spectroscopic properties of Er^{3+} ions in cadmium and alkali cadmium borosulphate glasses. *Pramana – Journal of Physics*, 48(6): 1151–1160, June 1997.
- [92] H. Crosswhite, H. M. Crosswhite, and B. R. Judd. Magnetic parameters for the configuration f^3 . *Physical Review*, 174(1): 89–94, October 1968.
- [93] J. McDougall, D. B. Hollis, and M. J. P. Payne. Spectroscopic properties of Tm^{3+} in ZBLAN fluoride glass. Part 1. Reduced matrix elements. *Physics and Chemistry of Glasses*, 35(6): 229–230, December 1994.
- [94] Y. Subramanyam, L. R. Moorthy, and S. V. J. Lakshman. Judd-Ofelt intensity parameters and laser analysis of Tm^{3+} in certain sulphate glasses. *Journal of Non-Crystalline Solids*, 139: 67–73, 1992.
- [95] J. McDougall, D. B. Hollis, X. Liu, and M. J. P. Payne. Judd-Ofelt parameter of rare earth ions in ZBLA, fluoride glass. *Physics and Chemistry of Glasses*, 35(3): 145–146, June 1994.
- [96] K. Binnemans and C. Görller-Walrand. Are the Judd-Ofelt parameters sensitive enough to reflect small compositional changes in lanthanide-doped glasses? *Journal of Physics – Condensed Matter*, 10: L167–L170, 1998.
- [97] X. Zou and T. Izumitani. Spectroscopic properties and mechanisms of excited state absorption and energy transfer upconversion for Er^{3+} -doped glasses. *Journal of Non-Crystalline Solids*, 162: 68–80, 1993.
- [98] R. Cases and M. A. Chamarro. Judd-Ofelt analysis and multiphonon relaxations of rare earth ions in fluorohafnate glasses. *Journal of Solid State Chemistry*, 90(2): 313–319, 1991.

-
- [99] M. Eyal, R. Reisfeld, C. K. Jørgensen, and B. Bendow. Laser properties of holmium and erbium in thorium-, zinc- and yttrium-based fluoride glass. *Chemical Physics Letters*, 139(5): 395–400, September 1987.
- [100] M. Shojiya, M. Takahashi, R. Kanno, Y. Kawamoto, and K. Kadono. Optical transitions of Er^{3+} ions in ZnCl_2 -based glass. *Journal of Applied Physics*, 82(12): 6259–6266, December 1997.
- [101] J. McDougall, D. B. Hollis, and M. J. P. Payne. Spectroscopic properties of Er^{3+} and Tm^{3+} in tellurite glasses. *Physics and Chemistry of Glasses*, 37(6): 254–255, December 1996.
- [102] J. S. Wang, E. Snitzer, E. M. Vogel, and G. H. Sigel, Jr. 1.48, 1.88 and 2.8 μm emissions of Tm^{3+} and Tm^{3+} - Ho^{3+} -codoped tellurite glasses. *Journal of Luminescence*, 60&61: 145–149, 1994.
- [103] K. Huang and A. Rhys. Theory of light absorption and non-radiative transitions in f-centres. *Proceedings of the Royal Society of London, Series A*, 204: 406–423, 1951.
- [104] L. A. Riseberg and H. W. Moos. Multiphonon orbit-lattice relaxation of excited states of rare-earth ions in crystals. *Physical Review*, 174(2): 429–438, October 1968.
- [105] C. W. Struck and W. H. Fonger. Unified model of the temperature quenching of narrow-line and broad-band emissions. *Journal of Luminescence*, 10: 1–30, 1975.
- [106] W. H. Fonger and C. W. Struck. Unified model of energy transfer for arbitrary Franck-Condon offset and temperature. *Journal of Luminescence*, 17: 241–261, 1978.
- [107] A. Kiel. *Quantum electronics*, volume 1, chapter *Multi-Phonon Spontaneous Emission in Paramagnetic Crystals*, pages 765–772. Columbia University Press, New York, 1964.
- [108] C. B. Layne, W. H. Lowdermilk, and M. J. Weber. Multiphonon relaxation of rare-earth ions in oxide glasses. *Physical Review Letters*, 16(1): 10–20, July 1977.
- [109] B. Peng and T. Izumitani. Optical properties, fluorescence mechanisms and energy transfer in Tm^{3+} , Ho^{3+} and Tm^{3+} - Ho^{3+} doped near-infrared laser glasses, sensitized by Yb^{3+} . *Optical Materials*, 4(6): 797–810, October 1995.
- [110] B. Peng and T. Izumitani. Blue, green and 0.8 μm Tm^{3+} , Ho^{3+} doped upconversion laser glasses, sensitized by Yb^{3+} . *Optical Materials*, 4(6): 701–711, October 1995.
- [111] R. Reisfeld. *Radiationless Processes*, chapter *Multiphonon Relaxation in Glasses*, pages 489–498. Plenum Press, New York, 1980.

-
- [112] R. Reisfeld, M. Eyal, E. Greenberg, and C. K. Jørgensen. Luminescence of six J -levels of holmium(III) in barium zirconium fluoride glass at room temperature. *Chemical Physics Letters*, 118(1): 25–28, July 1985.
- [113] R. Reisfeld, M. Eyal, and C. K. Jørgensen. Comparison of laser properties of rare earths in oxide and fluoride glasses. *Journal of the Less-Common Metals*, 126: 187–194, 1986.
- [114] R. Reisfeld and C. K. Jørgensen. *Handbook on the Physics and Chemistry of Rare Earths*, volume 9, chapter 58: *Excited State Phenomena in Vitreous Materials*, pages 1–90. Elsevier Science Publishers B. V., Amsterdam, 1987.
- [115] R. Reisfeld. *Spectroscopy of Solid State Laser-Type Materials*, chapter *Glass Lasers and Solar Applications*, pages 343–396. Plenum Press, New York, 1987.
- [116] L. A. Riseberg and M. J. Weber. *Progress in Optics*, volume 14, chapter 3: *Relaxation Phenomena in Rare-Earth Luminescence*, pages 89–159. North-Holland Publishing Company, Amsterdam, 1976.
- [117] M. D. Shinn, W. A. Sibley, M. G. Drexhage, and R. N. Brown. Optical transitions of Er^{3+} ions in fluorozirconate glass. *Physical Review B*, 27(11): 6635–6648, June 1983.
- [118] K. Tanimura, M. D. Shinn, W. A. Sibley, M. G. Drexhage, and R. N. Brown. Optical transitions of Ho^{3+} ions in fluorozirconate glass. *Physical Review B*, 30(5): 2429–2437, September 1984.
- [119] X. Zou and H. Toratani. Blue and green upconversion fluorescences of Ho^{3+} in fluoride glasses. *Journal of Non-Crystalline Solids*, 201: 37–46, 1996.
- [120] D. E. McCumber. Einstein relations connecting broadband emission and absorption spectra. *Physical Review*, 136(4A): A954–A957, November 1964.
- [121] D. E. McCumber. Theory of phonon-terminated lasers. *Bulletin of the American Physical Society*, 9: 280, March 1964.
- [122] H. G. Unger. *Optische Nachrichtentechnik (engl. Optical telecommunication)*, volume 1. Hüthig, Heidelberg, 3. edition, 1993.
- [123] L. Esterowitz, R. Allen, and I. Aggarwa. Pulsed laser emission at $2.3\,\mu\text{m}$ in a thulium-doped fluorozirconate fibre. *Electronics Letters*, 24(17): 1104, August 1988.
- [124] R. Allen and Esterowitz L. cw diode pumped $2.3\,\mu\text{m}$ fiber laser. *Applied Physics Letters*, 55(8): 721–722, August 1989.
- [125] R. Smart, J. Carter, A. Tropper, and D. Hanna. Fluoride fiber lasers. In *Proceedings of the SPIE*, volume 1373, pages 158–165, 1990.

-
- [126] J. N. Carter, D. C. Hanna, R. G. Smart, and A. C. Tropper. Thulium-doped fluorozirconate fiber lasers operating at around 0.8, 1.47, 1.9, and 2.3 μm pumped at 790 nm. In *OSA Proceedings on Advanced Solid-State Lasers*, volume 10, pages 218–221, 1991.
- [127] R. G. Smart, J. N. Carter, A. C. Tropper, and D. C. Hanna. Continuous-wave oscillation of Tm^{3+} -doped fluorozirconate fibre lasers at around 1.47 μm , 1.9 μm and 2.3 μm when pumped at 790 nm. *Optics Communications*, 82(5+6): 563–570, May 1991.
- [128] J. N. Carter, R. G. Smart, A. C. Tropper, and D. C. Hanna. Thulium-doped fluorozirconate fibre lasers. *Journal of Non-Crystalline Solids*, 140: 10–15, 1992.
- [129] R. M. Percival, S. F. Carter, D. Szebesta, S. T. Davey, and Stallard W. A. Thulium-doped monomode fluoride fibre laser broadly tunable from 2.25 to 2.5 μm . *Electronics Letters*, 27(21): 1912–1913, October 1991.
- [130] R. M. Percival, D. Szebesta, and S. T. Davey. Highly efficient and tunable operation of the two colour Tm-doped fluoride fibre laser. *Electronics Letters*, 28(7): 671–673, March 1992.
- [131] F. J. McAleavey, J. O’Gorman, J. F. Donegan, B. D. MacCraith, J. Hegarty, and G. Mazé. Narrow linewidth, tunable Tm^{3+} -doped fluoride fiber laser for optical-based hydrocarbon gas sensing. *IEEE Selected Topics in Quantum Electronics*, 3(4): 1103–1111, August 1997.
- [132] E. G. Neumann. *Single-Mode Fibers*, volume 57 of *Springer Series in Optical Sciences*. Springer-Verlag, Berlin, 1988.
- [133] <http://www.gnu.org>.
- [134] J. C. Slater. The theory of complex spectra. *Physical Review*, 34(10): 1293–1322, November 1929.
- [135] J. C. Slater. *Quantum Theory of Atomic Structure*, volume 1. McGraw-Hill Book Company, New York, 1960.
- [136] J. C. Slater. *Quantum Theory of Atomic Structure*, volume 2. McGraw-Hill Book Company, New York, 1960.
- [137] B. R. Judd. Reduced matrix elements. *American Journal of Physics*, 49(4): 371–372, April 1981.
- [138] B. R. Judd and H. Crosswhite. Orthogonalized operators for the f shell. *Journal of the Optical Society of America B*, 1(2): 255–260, April 1984.

- [139] B. R. Judd and M. A. Suskin. Complete set of orthogonal scalar operators for the configuration f^3 . *Journal of the Optical Society of America B*, 1(2): 261–265, April 1984.
- [140] A. Pasternak and Z. B. Goldschmidt. Spin-dependent interactions in the 3d configurations of the third spectra of the ion group. *Physical Review A*, 6(1): 55–68, July 1972.

Appendix A

Racah's tensor operators

The theory of the spectra of many-electron atoms is based on a set of rules published by Slater in 1929 [134]. In their famous book *The Theory of Atomic Spectra* [44], Condon and Shortley 1935 developed the complete theory of many-electron spectra based on determinantal product states. Although many problems were too complex in that theory to carry out the calculations without the help of computers, major improvements of the theory seemed to be unlikely. But between 1942 and 1949, Racah published a set of four papers [8, 9, 10, 11], titled *Theory of Complex Spectra* which, besides others, introduced the new concept of a tensor operator to the energy level calculations. Especially the new classification scheme based on the theory of continuous symmetry groups made even calculations of the complex f^N configurations possible. The theory of many-electron spectra based on Racah's work and used until today was developed in the 50's and 60's of the last century. In 1963 Judd published the book *Operator Techniques in Atomic Spectroscopy* [7], which is still one of the standard textbooks in this field. Missing in this book are only the configuration interactions. Another publication giving a comprehensive overview of the topics established until 1960 are the two volumes *Quantum Theory of Atomic Structure* from Slater [135, 136].

We will not try to develop Racah's theory of tensor operators in detail here. Instead we will just give the equations which turned out to be of special interest throughout this work, together with some explanations. For detailed information, especially on the theory of finite and continuous groups, the reader is referred to Judd's book [7].

A.1 Algebra of tensor operators

A spherical tensor operator $\mathbf{T}^{(k)}$ of rank k with the elements $T_q^{(k)}$ and $q = -k, \dots, +k$ is defined by its commutation relations with an arbitrary angular momentum operator \mathbf{J} [9]:

$$\begin{aligned} [J_z, T_q^{(k)}] &= q T_q^{(k)} \\ [J_{\pm}, T_q^{(k)}] &= \sqrt{k(k+1) - q(q \pm 1)} T_{q \pm 1}^{(k)}, \end{aligned} \quad (\text{A.1})$$

where $J_{\pm} = J_x \pm iJ_y$. The theory of tensor operators may be seen as a generalisation of the theory of vector operators from Condon and Shortley [44]. Vector operators are linked to tensor operators of rank 1 by the equations [7]

$$\begin{aligned} T_x &= \frac{-1}{\sqrt{2}} (T_{-1}^{(1)} - T_{+1}^{(1)}) \\ T_y &= \frac{i}{\sqrt{2}} (T_{-1}^{(1)} + T_{+1}^{(1)}) \\ T_z &= T_0^{(1)}. \end{aligned} \quad (\text{A.2})$$

Of special importance for the transformation of vector operator equations to tensor operator expressions is the fact that equation (A.2) keeps the value of the scalar product

$$(\mathbf{T} \cdot \mathbf{U}) = (\mathbf{T}^{(1)} \cdot \mathbf{U}^{(1)}) . \quad (\text{A.3})$$

This is assured by the definition of the scalar product of tensor operators [7]:

$$(\mathbf{T}^{(k)} \cdot \mathbf{U}^{(k)}) = \sum_q (-1)^q T_q^{(k)} U_{-q}^{(k)} . \quad (\text{A.4})$$

The relation of the tensor operators to operators of angular moments as given in equation (A.1) allows a special formulation of the Wigner-Eckart theorem, which turns out to be one of the most important equations in the application of the theory of tensor operators to the spectroscopy of many-electron atoms [7]:

$$\langle j'm' | T_q^{(k)} | jm \rangle = (-1)^{j'-m'} \begin{pmatrix} j' & k & j \\ -m' & q & m \end{pmatrix} \langle j' || \mathbf{T}^{(k)} || j \rangle . \quad (\text{A.5})$$

In the matrix element of this equation $|jm\rangle$ is an eigenstate of any given angular momentum operator \mathbf{J} , for example spin or orbital angular momentum. The six numbers in parantheses on the right side are a 3-j symbol, the properties of which may be found in appendix B.1. It connects the angular dependence of the states $|jm\rangle$ and $|j'm'\rangle$ to the angular properties of the tensor operator. The symbol $\langle j' || \mathbf{T}^{(k)} || j \rangle$ is called a reduced matrix element, a very important and widely used subject in the theory of tensor operators. Equation (A.5) shows that the m dependence of any tensor operator is identical and thus a specific tensor operator is completely defined by its reduced matrix element.

It should be noted that the reduced matrix element is completely different from a matrix element in the usual sense. There is no bra and no ket in the reduced matrix element, on which the tensor could act, which is symbolized by double bars instead of the single bar in a bra or ket. To stress this fact even more, some authors use a medium italic font instead of the usual boldface roman font for the tensor symbol, for a discussion of this subject see [137]. In the opinion of the author of this work, the double bar should be sufficient, and as the tensor in the matrix element is still a tensor although there is no written state to act on, we should use the above form with a boldface roman symbol for the tensor.

Two tensor operators $\mathbf{T}^{(k_1)}$ and $\mathbf{U}^{(k_2)}$ may be combined to a mixed tensor operator $\mathbf{Q}^{(k)}$, written as [7]

$$\mathbf{Q}^{(k)} = \{\mathbf{T}^{(k_1)} \times \mathbf{U}^{(k_2)}\}^{(k)} \quad (\text{A.6})$$

and with the tensor elements

$$Q_q^{(k)} = \sum_{q_1, q_2} T_{q_1}^{(k_1)} U_{q_2}^{(k_2)} \langle k_1, q_1, k_2, q_2 | k_1, k_2, k, q \rangle . \quad (\text{A.7})$$

The coefficient $\langle k_1, q_1, k_2, q_2 | k_1, k_2, k, q \rangle$ is the well-known Clebsch-Gordan coupling coefficient for the coupling of two angular momenta \mathbf{j}_1 and \mathbf{j}_2 to the total momentum $\mathbf{j} = \mathbf{j}_1 + \mathbf{j}_2$, given in equation (B.2), if k and q are changed to j and m . A special case of a mixed tensor operator of rank 0 is the scalar product (A.4) of two tensor operators, which may be written [7]

$$(\mathbf{T}^{(k)} \cdot \mathbf{U}^{(k)}) = (-1)^k \sqrt{2k+1} \{ \mathbf{T}^{(k)} \times \mathbf{U}^{(k)} \}_0^{(0)}. \quad (\text{A.8})$$

The generalisation to a triple scalar product is useful for effective three-body operators in the theory of configuration interactions [26, 34]:

$$(\mathbf{T}^{(k)} \cdot \mathbf{U}^{(k')} \cdot \mathbf{V}^{(k'')}) = \sum_{q, q', q''} \begin{pmatrix} k & k' & k'' \\ q & q' & q'' \end{pmatrix} T_q^{(k)} U_{q'}^{(k')} V_{q''}^{(k'')}. \quad (\text{A.9})$$

Among many other properties of mixed tensor operators, [7] gives the general reduced matrix element

$$\langle j' || Q_q^{(k)} || j \rangle = (-1)^{j'+k+j} \sqrt{2k+1} \sum_{j''} \begin{Bmatrix} k_1 & k & k_2 \\ j & j'' & j' \end{Bmatrix} \langle j' || \mathbf{T}^{(k_1)} || j'' \rangle \langle j'' || \mathbf{U}^{(k_2)} || j \rangle. \quad (\text{A.10})$$

The six numbers in curly braces are a 6-j symbol, the properties of which may be found in appendix B.2. If the operators $\mathbf{T}^{(k_1)}$ and $\mathbf{U}^{(k_2)}$ act on different parts of the system, for example on different electrons or one in the spin space and the other in the orbital space, an even more compact form of this equation is possible, which is given in [7].

When handling expressions of tensor operators, it is often necessary to re-order the components of a mixed tensor operator. The general relationship may be obtained from equation (A.7):

$$\{ \mathbf{U}^{(k_2)} \times \mathbf{T}^{(k_1)} \}^{(k)} = (-1)^{k_1+k_2+k} \{ \mathbf{T}^{(k_1)} \times \mathbf{U}^{(k_2)} \}^{(k)}. \quad (\text{A.11})$$

Since two operators acting on different parts of a system always commute, this expression immediately allows the conclusion that the sum $k_1 + k_2 + k$ of a mixed tensor operator built from two operators acting on different parts of the system must be even, otherwise the operator vanishes.

Another important case is the re-coupling of a mixed tensor operator built by three tensor operators [7]:

$$\{ \{ \mathbf{T}^{(k_1)} \times \mathbf{U}^{(k_2)} \}^{(k_{12})} \times \mathbf{V}^{(k_3)} \}^{(k)} = \sum_{k_{23}} \langle (k_1 k_2) k_{12}, k_3, k | k_1, (k_2 k_3) k_{23}, k \rangle \{ \mathbf{T}^{(k_1)} \times \{ \mathbf{U}^{(k_2)} \times \mathbf{V}^{(k_3)} \}^{(k_{23})} \}^{(k)}. \quad (\text{A.12})$$

This expression again shows the close relationship to the theory of vector operators, as the coefficient $\langle (k_1 k_2) k_{12}, k_3, k | k_1, (k_2 k_3) k_{23}, k \rangle$ is the recoupling coefficient of three angular momenta \mathbf{j}_1 , \mathbf{j}_2 , and \mathbf{j}_3 to the total momentum $\mathbf{j} = \mathbf{j}_1 + \mathbf{j}_2 + \mathbf{j}_3$, given in equation (B.18), if

k is replaced by j . In the theory of vector operators this recoupling coefficient is necessary due to the fact that the set of eigenstates in the two cases $(\mathbf{j}_1 + \mathbf{j}_2) + \mathbf{j}_3$ and $\mathbf{j}_1 + (\mathbf{j}_2 + \mathbf{j}_3)$ is different.

Two useful special cases for mixed tensor operators of rank 0 may be easily derived from equation (A.12):

$$\{\{\mathbf{T}^{(k_1)} \times \mathbf{U}^{(k_2)}\}^{(k_3)} \times \mathbf{V}^{(k_3)}\}^{(0)} = \{\mathbf{T}^{(k_1)} \times \{\mathbf{U}^{(k_2)} \times \mathbf{V}^{(k_3)}\}^{(k_1)}\}^{(0)} \quad (\text{A.13})$$

and

$$(\{\mathbf{T}^{(k_1)} \times \mathbf{U}^{(k_2)}\}^{(k_3)} \cdot \mathbf{V}^{(k_3)}) = (-1)^{k_3 - k_1} \sqrt{\frac{2k_3 + 1}{2k_1 + 1}} (\mathbf{T}^{(k_1)} \cdot \{\mathbf{U}^{(k_2)} \times \mathbf{V}^{(k_3)}\}^{(k_1)}) . \quad (\text{A.14})$$

A.2 Unit tensor operators

In the theory of vector operators, there appear three basic operators connected with each electron: the coordinate vector \mathbf{r} with its derivatives, the orbital angular momentum \mathbf{l} , and the spin \mathbf{s} . The corresponding tensor operators are $\mathbf{c}^{(k)}$, $\mathbf{l}^{(1)}$, and $\mathbf{s}^{(1)}$. The definition for $\mathbf{l}^{(1)}$ and $\mathbf{s}^{(1)}$ is given by equation (A.2) and it is an easy task to show that [7]

$$\langle l' || \mathbf{l}^{(1)} || l \rangle = \delta(l', l) \sqrt{l(l+1)(2l+1)} . \quad (\text{A.15})$$

The reduced matrix element of $\mathbf{s}^{(1)}$ is given by the same equation, if we change l to s . But since s may have only one value $s = \frac{1}{2}$, we can write

$$\langle s || \mathbf{s}^{(1)} || s \rangle = \sqrt{3/2} . \quad (\text{A.16})$$

The tensor $\mathbf{c}^{(k)}$ is a little more difficult. It is defined to fit into equation (1.21) for the Coulomb interaction [7]:

$$\mathbf{c}_q^{(k)} = \sqrt{\frac{4\pi}{(2k+1)}} Y_q^k , \quad (\text{A.17})$$

and it may be shown [7] that this definition is equivalent to the specification

$$\langle l' || \mathbf{c}^{(k)} || l \rangle = (-1)^{l'} \sqrt{(2l'+1)(2l+1)} \begin{pmatrix} l' & k & l \\ 0 & 0 & 0 \end{pmatrix} . \quad (\text{A.18})$$

The introduction of a unit tensor operator $\mathbf{u}^{(k)}$ is often very useful. Its straightforward definition is

$$\langle l' || \mathbf{u}^{(k)} || l \rangle = \delta(l', l) . \quad (\text{A.19})$$

The action of such a tensor on a state $|lm\rangle$ is given by the Wigner-Eckart theorem (A.5):

$$\mathbf{u}_q^{(k)} |l, m\rangle = \sum_{m'} (-1)^{l-m'} \begin{pmatrix} l & k & l \\ -m' & q & m \end{pmatrix} |l, m'\rangle . \quad (\text{A.20})$$

The author thinks that it is also useful to define a unit tensor operator $\mathbf{t}^{(k)}$ in the spin space in the same way as $\mathbf{u}^{(k)}$ in the orbital space. But as s has only one possible value, the definition is reduced to

$$\langle s || \mathbf{t}^{(k)} || s \rangle = 1 . \quad (\text{A.21})$$

Since all calculations in this work stay inside the configuration nl^N , we can reduce the set of basic operators from $\mathbf{c}^{(k)}$, $\mathbf{l}^{(1)}$, and $\mathbf{s}^{(1)}$ to $\mathbf{u}^{(k)}$ and $\mathbf{t}^{(k)}$, and all other tensor operators can be expressed in terms of these two operators only. The transformation equations are:

$$\mathbf{c}^{(k)} = \langle l || \mathbf{c}^{(k)} || l \rangle \mathbf{u}^{(k)} \quad (\text{A.22})$$

$$\mathbf{l}^{(1)} = \sqrt{l(l+1)(2l+1)} \hbar \mathbf{u}^{(1)} \quad (\text{A.23})$$

$$\mathbf{s}^{(1)} = \sqrt{3/2} \hbar \mathbf{t}^{(1)} . \quad (\text{A.24})$$

Closely related to the unit tensor operator is the operator $\mathbf{v}^{(k)}$, which is widely used in the literature:

$$\langle l' || \mathbf{v}^{(k)} || l \rangle = \delta(l', l) \sqrt{2k+1} . \quad (\text{A.25})$$

In calculations with tensor operators it is not unusual that mixed unit tensor operators appear, the two components of which act in the same space and on the same particle. Such a mixed tensor operator may be reduced to a single unit tensor operator by the following equation:

$$\{\mathbf{u}^{(k_1)} \times \mathbf{u}^{(k_2)}\}^{(k)} = (-1)^{2l+k} \sqrt{2k+1} \begin{Bmatrix} k_1 & k & k_2 \\ l & l & l \end{Bmatrix} \mathbf{u}^{(k)} . \quad (\text{A.26})$$

A fast proof of this formula is received by calculating the reduced matrix element of the mixed tensor operator using equation (A.10). The straightforward way by calculating the action of the q -coordinate of the mixed tensor operator on a state $|l_a, m_{l_a}, l_b, m_{l_b}\rangle$ and using equation (B.28) is somewhat more difficult, but produces the same result.

If the mixed tensor operator is a scalar product, the expression is simplified to

$$(\mathbf{u}^{(k)} \cdot \mathbf{u}^{(k)}) = \frac{1}{\sqrt{2l+1}} \mathbf{u}^{(0)} , \quad (\text{A.27})$$

Some special cases arise quite often and therefore shall be given explicitly:

$$\{\mathbf{u}^{(1)} \times \mathbf{u}^{(k)}\}^{(k-1)} = -\frac{1}{2} \sqrt{\frac{(2l+k+1)(2l-k+1)k}{l(l+1)(2l+1)(2k+1)}} \mathbf{u}^{(k-1)} \quad (\text{A.28})$$

$$\{\mathbf{u}^{(1)} \times \mathbf{u}^{(k)}\}^{(k)} = -\frac{1}{2} \sqrt{\frac{k(k+1)}{l(l+1)(2l+1)}} \mathbf{u}^{(k)} \quad (\text{A.29})$$

$$\{\mathbf{u}^{(1)} \times \mathbf{u}^{(k)}\}^{(k+1)} = \frac{1}{2} \sqrt{\frac{(2l+k+2)(2l-k)(k+1)}{l(l+1)(2l+1)(2k+1)}} \mathbf{u}^{(k+1)} . \quad (\text{A.30})$$

In mixed tensor operators of two operators $\mathbf{c}^{(k_1)}$ and $\mathbf{c}^{(k_2)}$ acting on the same electron, similar reduction expressions can be derived [7]:

$$\{\mathbf{c}^{(k_1)} \times \mathbf{c}^{(k_2)}\}^{(k)} = (-1)^k \sqrt{2k+1} \begin{pmatrix} k_1 & k & k_2 \\ 0 & 0 & 0 \end{pmatrix} \mathbf{c}^{(k)} \quad (\text{A.31})$$

$$(\mathbf{c}^{(k)} \cdot \mathbf{c}^{(k)}) = (-1)^k \sqrt{2k+1} \mathbf{c}^{(0)} , \quad (\text{A.32})$$

which in contrast to equations (A.26) and (A.27) may have non-vanishing matrix elements between different configurations, too. As counterparts to the equations (A.28–A.30), we find [7]:

$$\{\mathbf{c}^{(1)} \times \mathbf{c}^{(k)}\}^{(k-1)} = -\sqrt{\frac{k}{2k+1}} \mathbf{c}^{(k-1)} \quad (\text{A.33})$$

$$\{\mathbf{c}^{(1)} \times \mathbf{c}^{(k)}\}^{(k)} = 0 \quad (\text{A.34})$$

$$\{\mathbf{c}^{(1)} \times \mathbf{c}^{(k)}\}^{(k+1)} = \sqrt{\frac{k+1}{2k+1}} \mathbf{c}^{(k+1)} . \quad (\text{A.35})$$

As a tensor operator acting in the spin space as well as in the orbital space the double tensor operator $\mathbf{w}^{(\kappa k)}$ with rank κ in the spin space and rank k in the orbital space is often introduced, which is defined by [7]

$$\langle sl' || \mathbf{w}^{(\kappa k)} || sl \rangle = \delta(l', l) \sqrt{(2\kappa+1)(2k+1)} \quad (\text{A.36})$$

and may also be written as

$$\mathbf{w}^{(\kappa k)} = \sqrt{(2\kappa+1)(2k+1)} \mathbf{t}^{(\kappa)} \mathbf{u}^{(k)} . \quad (\text{A.37})$$

The two components of this tensor are combined to a mixed tensor operator using the notation

$$\mathbf{w}^{(\kappa k)v} = \sqrt{(2\kappa+1)(2k+1)} \{\mathbf{t}^{(\kappa)} \times \mathbf{u}^{(k)}\}^{(v)} . \quad (\text{A.38})$$

A special case arising in some types of magnetic interactions is

$$\{\mathbf{w}^{(\kappa_1 k_1)} \times \mathbf{w}^{(\kappa_2 k_2)}\}^{(k)0} = \sqrt{(2\kappa_1+1)(2\kappa_2+1)(2k_1+1)(2k_2+1)} \{ \{ \mathbf{t}^{(\kappa_1)} \times \mathbf{t}^{(\kappa_2)} \}^{(k)} \times \{ \mathbf{u}^{(k_1)} \times \mathbf{u}^{(k_2)} \}^{(k)} \}^{(0)} . \quad (\text{A.39})$$

A.3 Angular momentum operators

The vector operators of the total orbital angular momentum, the total spin, and the total angular momentum are \mathbf{L} , \mathbf{S} , and \mathbf{J} , with $\mathbf{J} = \mathbf{L} + \mathbf{S}$. Their translation to the tensor operators $\mathbf{L}^{(1)}$, $\mathbf{S}^{(1)}$, and $\mathbf{J}^{(1)}$ is done by equation (A.2). Since $\mathbf{L}^{(1)} = \sum_i \mathbf{l}_i^{(1)}$, we may write immediately

$$\mathbf{L}^{(1)} = \sqrt{l(l+1)(2l+1)}\hbar \mathbf{U}^{(1)} \quad (\text{A.40})$$

with use of equation (A.23) and where $\mathbf{U}^{(1)} = \sum_i \mathbf{u}_i^{(1)}$. With the same methods we get expressions for $\mathbf{S}^{(1)}$ and $\mathbf{J}^{(1)}$, and by using the elementary unit tensor operators the following equations are derived, which are directly applicable to the computer program:

$$\mathbf{L}^{(1)} = \sqrt{l(l+1)(2l+1)}\hbar \sum_i \mathbf{u}_i^{(1)} \quad (\text{A.41})$$

$$\mathbf{S}^{(1)} = \sqrt{3/2}\hbar \sum_i \mathbf{t}_i^{(1)} \quad (\text{A.42})$$

$$\mathbf{J}^{(1)} = \sum_i [\sqrt{l(l+1)(2l+1)}\hbar \mathbf{u}_i^{(1)} + \sqrt{3/2}\hbar \mathbf{t}_i^{(1)}] . \quad (\text{A.43})$$

Operators also often used are the scalar products \mathbf{L}^2 , \mathbf{S}^2 , \mathbf{LS} , and \mathbf{J}^2 of the total angular momenta. The appropriate tensor operator expressions are easy to derive from equations (A.41) and (A.42) with use of equation (3.2):

$$(\mathbf{L}^{(1)} \cdot \mathbf{L}^{(1)}) = l(l+1)(2l+1)\hbar^2 \left[\sum_i (\mathbf{u}_i^{(1)} \cdot \mathbf{u}_i^{(1)}) + 2 \sum_{i<j} (\mathbf{u}_i^{(1)} \cdot \mathbf{u}_j^{(1)}) \right] \quad (\text{A.44})$$

$$(\mathbf{S}^{(1)} \cdot \mathbf{S}^{(1)}) = \frac{3}{2}\hbar^2 \left[\sum_i (\mathbf{t}_i^{(1)} \cdot \mathbf{t}_i^{(1)}) + 2 \sum_{i<j} (\mathbf{t}_i^{(1)} \cdot \mathbf{t}_j^{(1)}) \right] \quad (\text{A.45})$$

$$(\mathbf{L}^{(1)} \cdot \mathbf{S}^{(1)}) = \sqrt{3l(l+1)(2l+1)/2}\hbar^2 \left[\sum_i (\mathbf{u}_i^{(1)} \cdot \mathbf{t}_i^{(1)}) + \sum_{i \neq j} (\mathbf{u}_i^{(1)} \cdot \mathbf{t}_j^{(1)}) \right] \quad (\text{A.46})$$

$$(\mathbf{J}^{(1)} \cdot \mathbf{J}^{(1)}) = (\mathbf{L}^{(1)} \cdot \mathbf{L}^{(1)}) + (\mathbf{S}^{(1)} \cdot \mathbf{S}^{(1)}) + 2(\mathbf{L}^{(1)} \cdot \mathbf{S}^{(1)}) , \quad (\text{A.47})$$

where the first expression was already given in equation (1.53).

Appendix B

Properties of n -j symbols

B.1 The 3-j symbol

If two angular momentum operators \mathbf{j}_1 and \mathbf{j}_2 are coupled to the sum vector $\mathbf{j} = \mathbf{j}_1 + \mathbf{j}_2$, the new states $|j_1 j_2 j m\rangle$ are linear combinations of the product state $|j_1 m_1 j_2 m_2\rangle = |j_1 m_1\rangle |j_2 m_2\rangle$

$$|j_1 j_2 j m\rangle = \sum_{m_1 m_2} \langle j_1, m_1, j_2, m_2 | j_1, j_2, j, m \rangle |j_1 m_1 j_2 m_2\rangle. \quad (\text{B.1})$$

The coupling coefficient $\langle j_1, m_1, j_2, m_2 | j_1, j_2, j, m \rangle$ is called Clebsch-Gordan coefficient and is closely related to the 3-j symbol [7]:

$$\langle j_1, m_1, j_2, m_2 | j_1, j_2, j, m \rangle = (-1)^{j_1 - j_2 + m} \sqrt{2j + 1} \begin{pmatrix} j_1 & j_2 & j \\ m_1 & m_2 & -m \end{pmatrix}. \quad (\text{B.2})$$

The full algebraic expression for the 3-j symbol is quite large [9]:

$$\begin{aligned} \begin{pmatrix} j_1 & j_2 & j_3 \\ m_1 & m_2 & m_3 \end{pmatrix} &= \delta(m_1 + m_2 + m_3) (-1)^{j_1 - j_2 - m_3} \\ &\times \sqrt{\frac{(j_1 + j_2 - j_3)!(j_1 - j_2 + j_3)!(-j_1 + j_2 + j_3)!(j_1 - m_1)!}{(j_1 + m_1)!(j_2 - m_2)!(j_2 + m_2)!(j_3 - m_3)!(j_3 + m_3)!}} \\ &\times \sum_z \frac{(-1)^z}{\binom{z!(j_1 + j_2 - j_3 - z)!(j_1 - m_1 - z)!(j_2 + m_2 - z)!}{(j_3 - j_2 + m_1 + z)!(j_3 - j_1 - m_2 + z)!}}. \quad (\text{B.3}) \end{aligned}$$

The arguments of the 3-j symbol may either all have integral values or two columns may contain half-integral values. If the argument of any of the factorials is negative, the 3-j symbol is zero. The integer z in the sum is allowed to take all negative or positive values and zero as long as all arguments of the factorials in the sum are not negative.

To perform symbolic calculations with 3-j symbols, it is important to know their specific symmetry properties. The factorials in the first fraction assure that $m_i = -j_i, \dots, +j_i$ and j_1, j_2 , and j_3 fulfill the triangle condition, i.e. each of them is at least the absolute of the difference and at most the sum of the other two. Furthermore the 3-j symbol is zero if not $m_1 + m_2 + m_3 = 0$.

Even permutations of columns do not change the value of a 3-j symbol [7]

$$\begin{pmatrix} j_1 & j_2 & j_3 \\ m_1 & m_2 & m_3 \end{pmatrix} = \begin{pmatrix} j_2 & j_3 & j_1 \\ m_2 & m_3 & m_1 \end{pmatrix} = \begin{pmatrix} j_3 & j_1 & j_2 \\ m_3 & m_1 & m_2 \end{pmatrix}, \quad (\text{B.4})$$

whereas odd permutations of columns introduce a phase factor [7]

$$\begin{pmatrix} j_1 & j_2 & j_3 \\ m_1 & m_2 & m_3 \end{pmatrix} = (-1)^{j_1+j_2+j_3} \begin{pmatrix} j_2 & j_1 & j_3 \\ m_2 & m_1 & m_3 \end{pmatrix}. \quad (\text{B.5})$$

Multiplying the bottom line by -1 has the same effect [7]

$$\begin{pmatrix} j_1 & j_2 & j_3 \\ m_1 & m_2 & m_3 \end{pmatrix} = (-1)^{j_1+j_2+j_3} \begin{pmatrix} j_1 & j_2 & j_3 \\ -m_1 & -m_2 & -m_3 \end{pmatrix}. \quad (\text{B.6})$$

The following 3-j symbol is important because it appears in the reduced matrix element of the tensor operator $\mathbf{c}^{(k)}$ as given in equation (A.18) [7]:

$$\begin{pmatrix} j_1 & j_2 & j_3 \\ 0 & 0 & 0 \end{pmatrix} = (-1)^{\frac{1}{2}j} \sqrt{\frac{(j-2j_1)!(j-2j_2)!(j-2j_3)!}{(j+1)!}} \times \frac{(\frac{1}{2}j)!}{(\frac{1}{2}j-j_1)!(\frac{1}{2}j-j_2)!(\frac{1}{2}j-j_3)!}, \quad (\text{B.7})$$

where $j = j_1 + j_2 + j_3$ is even. If j is odd, the value of the 3-j symbol is zero. Inside the configuration nl^N , the 3-j symbol of equation (B.7) usually is needed in the following form:

$$\begin{pmatrix} l & k & l \\ 0 & 0 & 0 \end{pmatrix} = (-1)^{l+\frac{k}{2}} \sqrt{\frac{(2l-k)!}{(2l+k+1)!}} \frac{k!(l+\frac{k}{2})!}{(\frac{k}{2})^2(l-\frac{k}{2})!}. \quad (\text{B.8})$$

Another 3-j symbol, which arises, for example, in scalar mixed tensor operators, is the following:

$$\begin{pmatrix} j & j' & 0 \\ m & -m' & 0 \end{pmatrix} = \begin{pmatrix} j' & 0 & j \\ -m' & 0 & m \end{pmatrix} = \delta(j, j') \delta(m, m') \frac{(-1)^{j-m}}{\sqrt{2j+1}}. \quad (\text{B.9})$$

Especially 3-j symbols, many arguments of which are zero, usually have simple algebraic expressions, as e.g.

$$\begin{pmatrix} 0 & k & k \\ 0 & 0 & 0 \end{pmatrix} = \frac{(-1)^k}{\sqrt{2k+1}} \quad (\text{B.10})$$

or the following set:

$$\begin{pmatrix} 1 & k & k-1 \\ 0 & 0 & 0 \end{pmatrix} = (-1)^k \sqrt{\frac{k}{(2k+1)(2k-1)}} \quad (\text{B.11})$$

$$\begin{pmatrix} 1 & k & k \\ 0 & 0 & 0 \end{pmatrix} = 0 \quad (\text{B.12})$$

$$\begin{pmatrix} 1 & k & k+1 \\ 0 & 0 & 0 \end{pmatrix} = (-1)^{k+1} \sqrt{\frac{k+1}{(2k+3)(2k+1)}}. \quad (\text{B.13})$$

In larger calculations it is important to know equations which allow the reduction of products of 3-j symbols. The two expressions which turned out to be of most importance in the calculations for this work are given by Judd [7]

$$\sum_{j_3, m_3} (2j_3 + 1) \begin{pmatrix} j_1 & j_2 & j_3 \\ m_1 & m_2 & m_3 \end{pmatrix} \begin{pmatrix} j_1 & j_2 & j_3 \\ m'_1 & m'_2 & m_3 \end{pmatrix} = \delta(m_1, m'_1) \delta(m_2, m'_2) \quad (\text{B.14})$$

and

$$\sum_{m_1, m_2} \begin{pmatrix} j_1 & j_2 & j_3 \\ m_1 & m_2 & m_3 \end{pmatrix} \begin{pmatrix} j_1 & j_2 & j'_3 \\ m_1 & m_2 & m'_3 \end{pmatrix} = \frac{\delta(j_3, j'_3) \delta(m_3, m'_3)}{2j_3 + 1}. \quad (\text{B.15})$$

It should be noted that Racah [9] originally used a function V instead of 3-j symbols, which is given by

$$V(j_1 j_2 j; m_1 m_2 m) = (-1)^{j_1 - j_2 - j_3} \begin{pmatrix} j_1 & j_2 & j \\ m_1 & m_2 & m \end{pmatrix}. \quad (\text{B.16})$$

B.2 The 6-j symbol

When three angular momentum operators \mathbf{j}_1 , \mathbf{j}_2 , and \mathbf{j}_3 are coupled to their sum \mathbf{j} , there are two different solutions: $\mathbf{j} = \mathbf{j}_{12} + \mathbf{j}_3$ and $\mathbf{j} = \mathbf{j}_1 + \mathbf{j}_{23}$, where $\mathbf{j}_{12} = \mathbf{j}_1 + \mathbf{j}_2$ and $\mathbf{j}_{23} = \mathbf{j}_2 + \mathbf{j}_3$. The eigenstates of \mathbf{j} in these two coupling schemes are $|(j_1 j_2) j_{12}, j_3, j\rangle$ and $|j_1, (j_2 j_3) j_{23}, j\rangle$ respectively. Both sets of eigenstates represent the same system and must therefore be connected by a linear transformation, which we may write as [7, 10]

$$|j_1, (j_2 j_3) j_{23}, j\rangle = \sum_{j_{12}} \langle (j_1 j_2) j_{12}, j_3, j | j_1, (j_2 j_3) j_{23}, j \rangle |(j_1 j_2) j_{12}, j_3, j\rangle. \quad (\text{B.17})$$

The recoupling coefficient $\langle (j_1 j_2) j_{12}, j_3, j | j_1, (j_2 j_3) j_{23}, j \rangle$ in this equation is closely related to the 6-j symbol [7]:

$$\langle (j_1 j_2) j_{12}, j_3, j \mid j_1, (j_2 j_3) j_{23}, j \rangle = \sqrt{(2j_{12} + 1)(2j_{23} + 1)} (-1)^{j_1 + j_2 + j_3 + j} \begin{Bmatrix} j_1 & j_2 & j_{12} \\ j_3 & j & j_{23} \end{Bmatrix}. \quad (\text{B.18})$$

As in case of the 3-j symbol the full algebraic expression of the 6-j symbol appears to be rather large [7]

$$\begin{Bmatrix} j_1 & j_2 & j_3 \\ l_1 & l_2 & l_3 \end{Bmatrix} = \Delta(j_1 j_2 j_3) \Delta(j_1 l_2 l_3) \Delta(l_1 j_2 l_3) \Delta(l_1 l_2 j_3) \times \sum_z \frac{(-1)^z (z+1)!}{\left[\begin{aligned} &(z - j_1 - j_2 - j_3)!(z - j_1 - l_2 - l_3)!(z - l_1 - j_2 - l_3)! \\ &\times (z - l_1 - l_2 - j_3)!(j_1 + j_2 + l_1 + l_2 - z)! \\ &\times (j_2 + j_3 + l_2 + l_3 - z)!(j_3 + j_1 + l_3 + l_1 - z)! \end{aligned} \right]}}, \quad (\text{B.19})$$

where $\Delta(abc)$ is a function which is non-vanishing only if its arguments satisfy the triangle condition, i.e. each of them is at least the absolute of the difference and at most the sum of the other two. The definition for this function is

$$\Delta(abc) = \sqrt{\frac{(a+b-c)!(a-b+c)!(-a+b+c)!}{(a+b+c+1)!}}. \quad (\text{B.20})$$

The arguments of the 6-j symbol may either all have integral values or two columns may contain half-integral arguments. If the argument of any of the factorials is negative, the 6-j symbol is zero. The integer z in the sum is allowed to take all negative or positive values and zero as long as all arguments of the factorials in the sum are not negative.

Permutations of columns do not change the value of a 6-j symbol [7]

$$\begin{Bmatrix} j_1 & j_2 & j_3 \\ l_1 & l_2 & l_3 \end{Bmatrix} = \begin{Bmatrix} j_2 & j_1 & j_3 \\ l_2 & l_1 & l_3 \end{Bmatrix}, \quad (\text{B.21})$$

and the same holds for an exchange of the upper and lower arguments in each of any pair of columns [7]:

$$\begin{Bmatrix} j_1 & j_2 & j_3 \\ l_1 & l_2 & l_3 \end{Bmatrix} = \begin{Bmatrix} l_1 & l_2 & j_3 \\ j_1 & j_2 & l_3 \end{Bmatrix}. \quad (\text{B.22})$$

The following 6-j symbols appear quite often in tensor operator calculations and have relatively short algebraic expressions:

$$\begin{Bmatrix} 0 & k & k \\ l & l & l \end{Bmatrix} = \frac{(-1)^{2l+k}}{\sqrt{(2k+1)(2l+1)}} \quad (\text{B.23})$$

$$\left\{ \begin{matrix} 1 & k & k-1 \\ l & l & l \end{matrix} \right\} = \frac{(-1)^{2l+k}}{2} \sqrt{\frac{(2l+k+1)(2l-k+1)k}{l(l+1)(2l+1)(2k-1)(2k+1)}} \quad (\text{B.24})$$

$$\left\{ \begin{matrix} 1 & k & k \\ l & l & l \end{matrix} \right\} = \frac{(-1)^{2l+k+1}}{2} \sqrt{\frac{k(k+1)}{l(l+1)(2l+1)(2k+1)}} \quad (\text{B.25})$$

$$\left\{ \begin{matrix} 1 & k & k+1 \\ l & l & l \end{matrix} \right\} = \frac{(-1)^{2l+k+1}}{2} \sqrt{\frac{(2l+k+2)(2l-k)(k+1)}{l(l+1)(2l+1)(2k+1)(2k+3)}}. \quad (\text{B.26})$$

In the calculations for this work, the following two equations linking 6-j and 3-j symbols turned out to be of special importance [7]:

$$\begin{aligned} \left\{ \begin{matrix} j_1 & j_2 & j_3 \\ k_1 & k_2 & k_3 \end{matrix} \right\} \begin{pmatrix} j_1 & j_2 & j_3 \\ m_1 & m_2 & m_3 \end{pmatrix} &= \sum_{q_1, q_2, q_3} (-1)^{k_1+k_2+k_3+q_1+q_2+q_3} \\ &\times \begin{pmatrix} j_1 & k_2 & k_3 \\ m_1 & q_2 & -q_3 \end{pmatrix} \begin{pmatrix} k_1 & j_2 & k_3 \\ -q_1 & m_2 & q_3 \end{pmatrix} \begin{pmatrix} k_1 & k_2 & j_3 \\ q_1 & -q_2 & m_3 \end{pmatrix} \end{aligned} \quad (\text{B.27})$$

and

$$\begin{aligned} \sum_{m_3} \begin{pmatrix} j_1 & j_2 & j_3 \\ m_1 & m_2 & m_3 \end{pmatrix} \begin{pmatrix} k_1 & k_2 & j_3 \\ q_1 & -q_2 & m_3 \end{pmatrix} &= \sum_{k_3, q_3} (-1)^{k_1+k_2+k_3+q_1+q_2+q_3} \\ &\times (2k_3+1) \left\{ \begin{matrix} j_1 & j_2 & j_3 \\ k_1 & k_2 & k_3 \end{matrix} \right\} \begin{pmatrix} k_1 & j_2 & k_3 \\ -q_1 & m_2 & q_3 \end{pmatrix} \begin{pmatrix} j_1 & k_2 & k_3 \\ m_1 & q_2 & -q_3 \end{pmatrix}. \end{aligned} \quad (\text{B.28})$$

It should be noted that Racah [9, 10] originally used a function W instead of 6-j symbols, which is given by

$$W(j_1 j_2 j j_3; j_{12} j_{23}) = (-1)^{j_1+j_2+j_3+j} \left\{ \begin{matrix} j_1 & j_2 & j_{12} \\ j_3 & j & j_{23} \end{matrix} \right\}. \quad (\text{B.29})$$

Appendix C

Alternative sets of radial parameters

Besides the radial parameters and their corresponding matrices introduced in chapter 1, for historic reasons a couple of different definitions are in use. In the following some transformation equations will be given for the alternative parameters which in the opinion of the author are of most importance. In principle all definitions should be equivalent and lead to the same results, but especially at times when computers were not as widely available as today, it was preferable to use a set of parameters which made the calculations most easy.

Completely different is the background of an approach of Judd et al. in [138, 139] where the authors developed linear combinations of the usual operators resulting in new operators orthogonal to each other. Equivalent to the orthogonality is the condition that all operators correspond to different representations of the symmetry groups in the chain in table 1.2. Such a definition has the advantage that during the incremental improvement of an energy level fit by introducing more and more operators, the values of the radial parameters are independent of the additional parameters. The semiempirical fitting procedure is numerically somewhat more stable then. However, these new operators were not widely used afterwards, because of which we will not go into details here.

The first order Coulomb interaction matrix in section 1.5 was found to be $\sum_k F^k f_k$ with the Slater integrals F^k . To avoid fractional coefficients in their determinantal product state calculations Condon and Shortley introduced corresponding parameters F_i by using the definition [7, 44]

$$F_0 = F^0, \quad F_2 = \frac{1}{225}F^2, \quad F_4 = \frac{1}{1089}F^4, \quad \text{and} \quad F_6 = \frac{25}{184041}F^6 \quad (\text{C.1})$$

for f^N configurations. To assure $\sum_i F_i f^i = \sum_k F^k f_k$, the relations between the corresponding matrix elements must be

$$f^0 = f_0, \quad f^2 = 225f_2, \quad f^4 = 1089f_4, \quad \text{and} \quad f^6 = \frac{184041}{25}f_6. \quad (\text{C.2})$$

Racah [11] suggested a different set of parameters E^i instead of the Slater parameters since the corresponding operators possess certain symmetry properties and are therefore invariant under operations of the groups R_7 and G_2 . Using these operators utilizes calculations of the Coulomb interaction in f^N configurations in Racah's classification scheme and therefore the parameters E^i are used quite often. The set of equations transforming the Slater matrix elements to Racah's definition is [11]

$$\begin{pmatrix} e_0 \\ e_1 \\ e_2 \\ e_3 \end{pmatrix} = \begin{pmatrix} 1 & 0 & 0 & 0 \\ 9/7 & 1/42 & 1/77 & 1/462 \\ 0 & 143/42 & -130/77 & 5/66 \\ 0 & 11/42 & 4/77 & -1/66 \end{pmatrix} \begin{pmatrix} f^0 \\ f^2 \\ f^4 \\ f^6 \end{pmatrix}. \quad (\text{C.3})$$

The corresponding transformation of the radial parameters uses the inverse (and transposed) matrix [11]

$$\begin{pmatrix} E^0 \\ E^1 \\ E^2 \\ E^3 \end{pmatrix} = \begin{pmatrix} 1 & -10 & -33 & -286 \\ 0 & 70/9 & 77/3 & 2002/9 \\ 0 & 1/9 & -1/3 & 7/9 \\ 0 & 5/3 & 2 & -91/3 \end{pmatrix} \begin{pmatrix} F_0 \\ F_2 \\ F_4 \\ F_6 \end{pmatrix}. \quad (\text{C.4})$$

To convert Racah's E^i parameters to Slater parameters the inverse transformations have to be used, which shall also be given here for convenience:

$$\begin{pmatrix} f^0 \\ f^1 \\ f^2 \\ f^3 \end{pmatrix} = \begin{pmatrix} 1 & 0 & 0 & 0 \\ -10 & 70/9 & 1/9 & 5/3 \\ -33 & 77/3 & -1/3 & 2 \\ -286 & 2002/9 & 7/9 & -91/3 \end{pmatrix} \begin{pmatrix} e_0 \\ e_1 \\ e_2 \\ e_3 \end{pmatrix} \quad (\text{C.5})$$

and

$$\begin{pmatrix} F_0 \\ F_1 \\ F_2 \\ F_3 \end{pmatrix} = \begin{pmatrix} 1 & 9/7 & 0 & 0 \\ 0 & 1/42 & 143/42 & 11/42 \\ 0 & 1/77 & -130/77 & 4/77 \\ 0 & 1/462 & 5/66 & -1/66 \end{pmatrix} \begin{pmatrix} E^0 \\ E^2 \\ E^4 \\ E^6 \end{pmatrix}. \quad (\text{C.6})$$

Usually the version F^k of the Slater parameters is needed, in this case equation (C.6) is followed by the inverse of (C.1).

In [24] the use of definition (C.1) also for the parameters P^k of the spin-orbit configuration interaction was suggested, but it is still uncommon:

$$P_0 = P^0, \quad P_2 = \frac{1}{225}P^2, \quad P_4 = \frac{1}{1089}P^4, \quad \text{and} \quad P_6 = \frac{25}{184041}P^6. \quad (\text{C.7})$$

Finally, it shall be noted that some authors use another set of radial parameters Q^k for the spin-orbit configuration interaction, slightly different from the P^k 's [17, 140]. Their definition

$$Q^k = \frac{\langle l || \mathbf{c}^{(k)} || l \rangle^2}{6} P^k \quad (\text{C.8})$$

is somewhat unsatisfying from a theoretical point of view since it mixes radial and angular properties of the operator.

Appendix D

Calculated radiative properties

The three sections of this chapter contain a complete collection of the radiative properties defined in section 2.1 for the triply ionized rare earth ions praseodymium, erbium, and thulium doped into ZBLAN glass. All data in the tables were calculated with the radial integrals and Judd-Ofelt parameters obtained in chapter 5.

For each ion two tables are given, the first containing emission and the second absorption transitions. In case of praseodymium and thulium, all transitions were included, for erbium only the transitions between the 29 levels below 47000 cm^{-1} . Both tables are internally sorted to parts with different initial states. In the tables the final state, calculated wavenumber, and wavelength of the transition are given, but the wavelength only if it is smaller than $8 \mu\text{m}$. Furthermore, both tables contain the squared reduced matrix elements $|\langle ||\mathbf{U}^{(k)}|| \rangle|^2$ and $|\langle ||\mathbf{L} + g_s\mathbf{S}|| \rangle|^2/\hbar^2$ with the abbreviations $|\mathbf{U}^{(k)}|^2$ and $|\mathbf{M}/\beta_m|^2$ respectively. In the emission tables the spontaneous radiative emission rates A_{ed} and A_{md} with electric and magnetic dipole character, as defined in equation (2.8), together with the branching ratio β from equation (2.11) are given. The radiative lifetime from equation (2.10) is specified with each initial state. In the absorption tables the oscillator strengths as defined in equation (2.12) are contained instead of the emission rates and branching ratios. Equation (2.15) may be used to calculate the respective oscillator strengths for stimulated emission.

In the calculations the refractive index of ZBLAN glass at the wavelength of the transition was needed for the dielectric correction factors in equations (2.9) and (2.13). Therefore the Cauchy formula (4.6) and the parameters (4.7) were used with the adjusted parameter C as explained there, because the glass samples contained PbF_2 . For transitions with wavelengths below 200 nm and above $10 \mu\text{m}$ the refractive index was fixed to the value at 200 nm and $10 \mu\text{m}$ respectively since the Cauchy formula is not valid for such extreme wavelengths.

D.1 Pr : ZBLAN

Table D.1: Radiative emission properties of Pr : ZBLAN

final	k_{calc} cm^{-1}	λ_{calc} nm	$ \mathbf{U}^{(2)} ^2$	$ \mathbf{U}^{(4)} ^2$	$ \mathbf{U}^{(6)} ^2$	$ \mathbf{M}/\beta_m ^2$	A_{ed} s^{-1}	A_{md} s^{-1}	β
	initial: $^1\text{S}_0$						$\tau = 0.00 \text{ ms}$		
$^3\text{P}_2$	23815	420	0.0665	0.0000	0.0000	0.0000	4009	0	0.007
$^1\text{I}_6$	24951	401	0.0000	0.0000	0.5664	0.0000	138830	0	0.259
$^3\text{P}_1$	24990	400	0.0000	0.0000	0.0000	0.0196	0	29	0.000
$^3\text{P}_0$	25605	391	0.0000	0.0000	0.0000	0.0000	0	0	0.000

Table D.1: Radiative emission properties of Pr:ZBLAN (*continued*)

final	k_{calc} cm ⁻¹	λ_{calc} nm	$ \mathbf{U}^{(2)} ^2$	$ \mathbf{U}^{(4)} ^2$	$ \mathbf{U}^{(6)} ^2$	$ \mathbf{M}/\beta_m ^2$	A_{ed} s ⁻¹	A_{md} s ⁻¹	β
¹ D ₂	29439	340	0.5009	0.0000	0.0000	0.0000	58215	0	0.108
¹ G ₄	36578	273	0.0000	0.4069	0.0000	0.0000	219551	0	0.409
³ F ₄	39507	253	0.0000	0.1556	0.0000	0.0000	107440	0	0.200
³ F ₃	39998	250	0.0000	0.0000	0.0000	0.0000	0	0	0.000
³ F ₂	41354	242	0.0034	0.0000	0.0000	0.0000	1147	0	0.002
³ H ₆	41963	238	0.0000	0.0000	0.0002	0.0000	216	0	0.000
³ H ₅	44097	227	0.0000	0.0000	0.0000	0.0000	0	0	0.000
³ H ₄	46134	217	0.0000	0.0066	0.0000	0.0000	7583	0	0.014
	initial: ³ P ₂						$\tau = 0.03$ ms		
¹ I ₆	1135	—	0.0000	0.0255	0.1419	0.0000	1	0	0.000
³ P ₁	1175	—	0.4228	0.0000	0.0000	2.2987	0	0	0.000
³ P ₀	1790	5588	0.1902	0.0000	0.0000	0.0000	1	0	0.000
¹ D ₂	5623	1778	0.0011	0.0721	0.0000	0.5655	26	2	0.001
¹ G ₄	12763	784	0.6368	0.0432	0.0175	0.0000	1446	0	0.047
³ F ₄	15692	637	0.4504	0.1075	0.0093	0.0000	2485	0	0.081
³ F ₃	16183	618	0.2581	0.3081	0.0000	0.0057	3640	0	0.119
³ F ₂	17539	570	0.0322	0.2998	0.0000	0.0003	3485	0	0.114
³ H ₆	18148	551	0.0000	0.5009	0.0541	0.0000	7178	0	0.235
³ H ₅	20282	493	0.0000	0.1887	0.1316	0.0000	6685	0	0.219
³ H ₄	22319	448	0.0000	0.0364	0.1362	0.0000	5586	0	0.183
	initial: ¹ I ₆						$\tau = 0.14$ ms		
³ P ₁	39	—	0.0000	0.0000	0.0003	0.0000	0	0	0.000
³ P ₀	654	—	0.0000	0.0000	0.0037	0.0000	0	0	0.000
¹ D ₂	4488	2228	0.0000	0.1582	1.7174	0.0000	190	0	0.026
¹ G ₄	11628	860	0.2474	1.4256	0.6976	0.0000	3174	0	0.434
³ F ₄	14557	687	0.0827	0.5933	0.4025	0.0000	2993	0	0.409
³ F ₃	15048	665	0.0000	0.0009	0.0023	0.0000	12	0	0.002
³ F ₂	16404	610	0.0000	0.0050	0.0304	0.0000	176	0	0.024
³ H ₆	17013	588	0.0034	0.0124	0.0043	0.0418	79	1	0.011
³ H ₅	19147	522	0.0003	0.0006	0.0018	0.0299	19	2	0.003
³ H ₄	21183	472	0.0089	0.0499	0.0231	0.0000	671	0	0.092

Table D.1: Radiative emission properties of Pr:ZBLAN (*continued*)

final	k_{calc} cm ⁻¹	λ_{calc} nm	$ \mathbf{U}^{(2)} ^2$	$ \mathbf{U}^{(4)} ^2$	$ \mathbf{U}^{(6)} ^2$	$ \mathbf{M}/\beta_m ^2$	A_{ed} s ⁻¹	A_{md} s ⁻¹	β
	initial: ³ P ₁						$\tau = 0.03$ ms		
³ P ₀	615	–	0.0000	0.0000	0.0000	1.9804	0	0	0.000
¹ D ₂	4449	2248	0.0753	0.0000	0.0000	0.2008	9	1	0.000
¹ G ₄	11589	863	0.0000	0.0775	0.0000	0.0000	409	0	0.014
³ F ₄	14517	689	0.0000	0.2694	0.0000	0.0000	2811	0	0.097
³ F ₃	15008	666	0.5714	0.1964	0.0000	0.0000	5080	0	0.176
³ F ₂	16365	611	0.2697	0.0000	0.0000	0.0004	1726	0	0.060
³ H ₆	16974	589	0.0000	0.0000	0.1247	0.0000	3138	0	0.109
³ H ₅	19108	523	0.0000	0.2857	0.0893	0.0000	10091	0	0.350
³ H ₄	21144	473	0.0000	0.1710	0.0000	0.0000	5600	0	0.194
	initial: ³ P ₀						$\tau = 0.03$ ms		
¹ D ₂	3834	2608	0.0154	0.0000	0.0000	0.0000	4	0	0.000
¹ G ₄	10974	911	0.0000	0.0502	0.0000	0.0000	674	0	0.023
³ F ₄	13902	719	0.0000	0.1128	0.0000	0.0000	3099	0	0.106
³ F ₃	14393	695	0.0000	0.0000	0.0000	0.0000	0	0	0.000
³ F ₂	15750	635	0.2951	0.0000	0.0000	0.0000	5043	0	0.173
³ H ₆	16359	611	0.0000	0.0000	0.0726	0.0000	4903	0	0.168
³ H ₅	18493	541	0.0000	0.0000	0.0000	0.0000	0	0	0.000
³ H ₄	20529	487	0.0000	0.1726	0.0000	0.0000	15500	0	0.530
	initial: ¹ D ₂						$\tau = 0.42$ ms		
¹ G ₄	7140	1401	0.3267	0.0501	0.0786	0.0000	226	0	0.095
³ F ₄	10068	993	0.5736	0.0000	0.0192	0.0000	567	0	0.238
³ F ₃	10559	947	0.0302	0.0169	0.0000	0.1405	71	3	0.031
³ F ₂	11916	839	0.0132	0.0817	0.0000	0.0743	301	2	0.128
³ H ₆	12525	798	0.0000	0.0649	0.0062	0.0000	297	0	0.125
³ H ₅	14659	682	0.0000	0.0020	0.0003	0.0000	16	0	0.007
³ H ₄	16695	599	0.0028	0.0162	0.0506	0.0000	893	0	0.376
	initial: ¹ G ₄						$\tau = 1.93$ ms		
³ F ₄	2929	3415	0.0764	0.1389	0.3342	2.5998	18	1	0.037
³ F ₃	3420	2924	0.0036	0.0049	0.0501	2.2280	4	1	0.009
³ F ₂	4776	2094	0.0000	0.0155	0.0056	0.0000	3	0	0.006
³ H ₆	5385	1857	0.2416	0.2432	0.2257	0.0000	119	0	0.230

Table D.1: Radiative emission properties of Pr:ZBLAN (*continued*)

final	k_{calc} cm ⁻¹	λ_{calc} nm	$ \mathbf{U}^{(2)} ^2$	$ \mathbf{U}^{(4)} ^2$	$ \mathbf{U}^{(6)} ^2$	$ \mathbf{M}/\beta_m ^2$	A_{ed} s ⁻¹	A_{md} s ⁻¹	β
³ H ₅	7519	1330	0.0360	0.0916	0.3967	0.1439	335	1	0.647
³ H ₄	9556	1047	0.0015	0.0061	0.0207	0.0616	37	1	0.073
	initial: ³ F ₄						$\tau = 2.53$ ms		
³ F ₃	491	–	0.0255	0.0730	0.0067	4.5160	0	0	0.000
³ F ₂	1847	5413	0.0013	0.0016	0.0904	0.0000	1	0	0.002
³ H ₆	2456	4071	0.5842	0.6271	0.4784	0.0000	25	0	0.064
³ H ₅	4590	2178	0.0316	0.3184	0.4649	0.1476	111	0	0.280
³ H ₄	6627	1509	0.0180	0.0511	0.4884	0.1528	258	0	0.654
	initial: ³ F ₃						$\tau = 1.82$ ms		
³ F ₂	1356	7373	0.0212	0.0508	0.0000	6.5205	0	0	0.001
³ H ₆	1965	5088	0.0000	0.3183	0.8461	0.0000	16	0	0.029
³ H ₅	4099	2439	0.6286	0.3468	0.0000	0.0000	60	0	0.110
³ H ₄	6136	1630	0.0655	0.3473	0.6989	0.0060	473	0	0.860
	initial: ³ F ₂						$\tau = 4.41$ ms		
³ H ₆	609	–	0.0000	0.0167	0.3038	0.0000	0	0	0.001
³ H ₅	2743	3646	0.0000	0.2978	0.6597	0.0000	52	0	0.229
³ H ₄	4779	2092	0.5084	0.4042	0.1187	0.0000	175	0	0.771
	initial: ³ H ₆						$\tau = 43.50$ ms		
³ H ₅	2134	4686	0.1080	0.2328	0.6422	10.8034	9	1	0.414
³ H ₄	4171	2398	0.0001	0.0327	0.1396	0.0000	13	0	0.586
	initial: ³ H ₅						$\tau = 109.49$ ms		
³ H ₄	2036	4911	0.1095	0.2021	0.6111	10.5085	8	1	1.000

Table D.2: Radiative absorption properties of Pr:ZBLAN

final	k_{calc} cm ⁻¹	λ_{calc} nm	$ \mathbf{U}^{(2)} ^2$	$ \mathbf{U}^{(4)} ^2$	$ \mathbf{U}^{(6)} ^2$	$ \mathbf{M}/\beta_m ^2$	f_{ed} 10 ⁻⁸	f_{md} 10 ⁻⁸
	initial: ³ H ₄							
³ H ₅	2036	4911	0.1095	0.2021	0.6111	10.5085	173.5	14.1
³ H ₆	4171	2398	0.0001	0.0327	0.1396	0.0000	75.3	0.0
³ F ₂	4779	2092	0.5084	0.4042	0.1187	0.0000	284.9	0.0
³ F ₃	6136	1630	0.0655	0.3473	0.6989	0.0060	653.4	0.0

Table D.2: Radiative absorption properties of Pr:ZBLAN (*continued*)

final	k_{calc} cm ⁻¹	λ_{calc} nm	$ \mathbf{U}^{(2)} ^2$	$ \mathbf{U}^{(4)} ^2$	$ \mathbf{U}^{(6)} ^2$	$ \mathbf{M}/\beta_m ^2$	f_{ed} 10 ⁻⁸	f_{md} 10 ⁻⁸
³ F ₄	6627	1509	0.0180	0.0511	0.4884	0.1528	392.5	0.7
¹ G ₄	9556	1047	0.0015	0.0061	0.0207	0.0616	27.0	0.4
¹ D ₂	16695	599	0.0028	0.0162	0.0506	0.0000	117.4	0.0
³ P ₀	20529	487	0.0000	0.1726	0.0000	0.0000	267.9	0.0
³ P ₁	21144	473	0.0000	0.1710	0.0000	0.0000	273.4	0.0
¹ I ₆	21183	472	0.0089	0.0499	0.0231	0.0000	141.5	0.0
³ P ₂	22319	448	0.0000	0.0364	0.1362	0.0000	407.1	0.0
¹ S ₀	46134	217	0.0000	0.0066	0.0000	0.0000	24.1	0.0
initial: ³ H ₅								
³ H ₆	2134	4686	0.1080	0.2328	0.6422	10.8034	158.9	12.5
³ F ₂	2743	3646	0.0000	0.2978	0.6597	0.0000	213.7	0.0
³ F ₃	4099	2439	0.6286	0.3468	0.0000	0.0000	153.6	0.0
³ F ₄	4590	2178	0.0316	0.3184	0.4649	0.1476	288.4	0.4
¹ G ₄	7519	1330	0.0360	0.0916	0.3967	0.1439	323.5	0.6
¹ D ₂	14659	682	0.0000	0.0020	0.0003	0.0000	2.2	0.0
³ P ₀	18493	541	0.0000	0.0000	0.0000	0.0000	0.0	0.0
³ P ₁	19108	523	0.0000	0.2857	0.0893	0.0000	495.3	0.0
¹ I ₆	19147	522	0.0003	0.0006	0.0018	0.0299	4.1	0.3
³ P ₂	20282	493	0.0000	0.1887	0.1316	0.0000	484.5	0.0
¹ S ₀	44097	227	0.0000	0.0000	0.0000	0.0000	0.0	0.0
initial: ³ H ₆								
³ F ₂	609	—	0.0000	0.0167	0.3038	0.0000	13.3	0.0
³ F ₃	1965	5088	0.0000	0.3183	0.8461	0.0000	157.6	0.0
³ F ₄	2456	4071	0.5842	0.6271	0.4784	0.0000	199.7	0.0
¹ G ₄	5385	1857	0.2416	0.2432	0.2257	0.0000	190.8	0.0
¹ D ₂	12525	798	0.0000	0.0649	0.0062	0.0000	48.3	0.0
³ P ₀	16359	611	0.0000	0.0000	0.0726	0.0000	93.0	0.0
³ P ₁	16974	589	0.0000	0.0000	0.1247	0.0000	165.7	0.0
¹ I ₆	17013	588	0.0034	0.0124	0.0043	0.0418	18.0	0.3
³ P ₂	18148	551	0.0000	0.5009	0.0541	0.0000	551.6	0.0
¹ S ₀	41963	238	0.0000	0.0000	0.0002	0.0000	0.6	0.0

Table D.2: Radiative absorption properties of Pr:ZBLAN (*continued*)

final	k_{calc} cm ⁻¹	λ_{calc} nm	$ \mathbf{U}^{(2)} ^2$	$ \mathbf{U}^{(4)} ^2$	$ \mathbf{U}^{(6)} ^2$	$ \mathbf{M}/\beta_m ^2$	f_{ed} 10 ⁻⁸	f_{md} 10 ⁻⁸
	initial: 3F_2							
3F_3	1356	7373	0.0212	0.0508	0.0000	6.5205	10.3	10.2
3F_4	1847	5413	0.0013	0.0016	0.0904	0.0000	33.3	0.0
1G_4	4776	2094	0.0000	0.0155	0.0056	0.0000	15.3	0.0
1D_2	11916	839	0.0132	0.0817	0.0000	0.0743	140.7	1.1
3P_0	15750	635	0.2951	0.0000	0.0000	0.0000	268.5	0.0
3P_1	16365	611	0.2697	0.0000	0.0000	0.0004	255.2	0.0
1I_6	16404	610	0.0000	0.0050	0.0304	0.0000	112.5	0.0
3P_2	17539	570	0.0322	0.2998	0.0000	0.0003	746.1	0.0
1S_0	41354	242	0.0034	0.0000	0.0000	0.0000	8.3	0.0
	initial: 3F_3							
3F_4	491	—	0.0255	0.0730	0.0067	4.5160	4.0	1.7
1G_4	3420	2924	0.0036	0.0049	0.0501	2.2280	26.7	6.6
1D_2	10559	947	0.0302	0.0169	0.0000	0.1405	30.4	1.3
3P_0	14393	695	0.0000	0.0000	0.0000	0.0000	0.0	0.0
3P_1	15008	666	0.5714	0.1964	0.0000	0.0000	638.9	0.0
1I_6	15048	665	0.0000	0.0009	0.0023	0.0000	6.4	0.0
3P_2	16183	618	0.2581	0.3081	0.0000	0.0057	655.2	0.1
1S_0	39998	250	0.0000	0.0000	0.0000	0.0000	0.0	0.0
	initial: 3F_4							
1G_4	2929	3415	0.0764	0.1389	0.3342	2.5998	146.0	5.1
1D_2	10068	993	0.5736	0.0000	0.0192	0.0000	206.5	0.0
3P_0	13902	719	0.0000	0.1128	0.0000	0.0000	117.9	0.0
3P_1	14517	689	0.0000	0.2694	0.0000	0.0000	294.1	0.0
1I_6	14557	687	0.0827	0.5933	0.4025	0.0000	1349.6	0.0
3P_2	15692	637	0.4504	0.1075	0.0093	0.0000	370.3	0.0
1S_0	39507	253	0.0000	0.1556	0.0000	0.0000	477.8	0.0
	initial: 1G_4							
1D_2	7140	1401	0.3267	0.0501	0.0786	0.0000	164.2	0.0
3P_0	10974	911	0.0000	0.0502	0.0000	0.0000	41.3	0.0
3P_1	11589	863	0.0000	0.0775	0.0000	0.0000	67.4	0.0
1I_6	11628	860	0.2474	1.4256	0.6976	0.0000	2250.4	0.0

Table D.2: Radiative absorption properties of Pr : ZBLAN (*continued*)

final	k_{calc} cm ⁻¹	λ_{calc} nm	$ \mathbf{U}^{(2)} ^2$	$ \mathbf{U}^{(4)} ^2$	$ \mathbf{U}^{(6)} ^2$	$ \mathbf{M}/\beta_m ^2$	f_{ed} 10 ⁻⁸	f_{md} 10 ⁻⁸
³ P ₂	12763	784	0.6368	0.0432	0.0175	0.0000	326.9	0.0
¹ S ₀	36578	273	0.0000	0.4069	0.0000	0.0000	1150.1	0.0
	initial: ¹ D ₂							
³ P ₀	3834	2608	0.0154	0.0000	0.0000	0.0000	3.4	0.0
³ P ₁	4449	2248	0.0753	0.0000	0.0000	0.2008	19.2	1.1
¹ I ₆	4488	2228	0.0000	0.1582	1.7174	0.0000	1648.2	0.0
³ P ₂	5623	1778	0.0011	0.0721	0.0000	0.5655	54.9	3.8
¹ S ₀	29439	340	0.5009	0.0000	0.0000	0.0000	864.6	0.0
	initial: ³ P ₀							
³ P ₁	615	–	0.0000	0.0000	0.0000	1.9804	0.0	6.6
¹ I ₆	654	–	0.0000	0.0000	0.0037	0.0000	2.2	0.0
³ P ₂	1790	5588	0.1902	0.0000	0.0000	0.0000	94.7	0.0
¹ S ₀	25605	391	0.0000	0.0000	0.0000	0.0000	0.0	0.0
	initial: ³ P ₁							
¹ I ₆	39	–	0.0000	0.0000	0.0003	0.0000	0.0	0.0
³ P ₂	1175	–	0.4228	0.0000	0.0000	2.2987	43.9	5.1
¹ S ₀	24990	400	0.0000	0.0000	0.0000	0.0196	0.0	1.0
	initial: ¹ I ₆							
³ P ₂	1135	–	0.0000	0.0255	0.1419	0.0000	12.9	0.0
¹ S ₀	24951	401	0.0000	0.0000	0.5664	0.0000	1115.3	0.0
	initial: ³ P ₂							
¹ S ₀	23815	420	0.0665	0.0000	0.0000	0.0000	92.1	0.0

D.2 Er : ZBLAN

Table D.3: Radiative emission properties of Er : ZBLAN

final	k_{calc} cm ⁻¹	λ_{calc} nm	$ \mathbf{U}^{(2)} ^2$	$ \mathbf{U}^{(4)} ^2$	$ \mathbf{U}^{(6)} ^2$	$ \mathbf{M}/\beta_m ^2$	A_{ed} s ⁻¹	A_{md} s ⁻¹	β
	initial: ² F _{7/2} ⁽¹⁾						$\tau = 0.00$ ms		
² F _{5/2} ⁽¹⁾	4495	2225	0.1498	0.1273	0.0732	3.2904	17	3	0.000
² G _{9/2} ⁽²⁾	27500	364	2.1349	0.6503	0.1815	0.0815	43870	20	0.059

Table D.3: Radiative emission properties of Er:ZBLAN (*continued*)

final	k_{calc} cm ⁻¹	λ_{calc} nm	$ \mathbf{U}^{(2)} ^2$	$ \mathbf{U}^{(4)} ^2$	$ \mathbf{U}^{(6)} ^2$	$ \mathbf{M}/\beta_m ^2$	A_{ed} s ⁻¹	A_{md} s ⁻¹	β
² G _{7/2} ⁽²⁾	31486	318	0.0590	0.1874	0.4580	0.1519	8945	57	0.012
² F _{5/2} ⁽²⁾	34603	289	0.0017	0.1630	0.4579	0.0609	9568	31	0.013
² D _{3/2} ⁽²⁾	42692	234	0.0065	0.0792	0.0000	0.0000	3219	0	0.004
² F _{7/2} ⁽²⁾	43274	231	0.1953	0.0499	0.1060	0.0067	19166	7	0.026
² H _{11/2} ⁽¹⁾	46628	214	0.7869	0.5181	0.0017	0.0000	97456	0	0.131
² D _{5/2} ⁽²⁾	48806	205	0.1004	0.0886	0.0224	0.0216	16668	33	0.022
² H _{9/2} ⁽¹⁾	49627	202	0.0168	0.0172	0.0959	0.0031	7368	5	0.010
² L _{15/2}	49951	200	0.0000	0.1019	0.0610	0.0000	8891	0	0.012
⁴ D _{1/2}	50726	197	0.0000	0.0051	0.0000	0.0000	311	0	0.000
² I _{13/2}	54210	184	0.0000	0.7919	0.1580	0.0000	69139	0	0.093
² P _{3/2}	54920	182	0.1300	0.1192	0.0000	0.0000	29557	0	0.040
⁴ D _{3/2}	55467	180	0.0164	0.0244	0.0000	0.0000	4591	0	0.006
² L _{17/2}	56179	178	0.0000	0.0000	0.6325	0.0000	42781	0	0.058
² I _{11/2}	56643	177	0.1491	0.0103	0.1592	0.0000	37388	0	0.050
⁴ D _{7/2}	58488	171	0.0016	0.0055	0.0036	0.0408	1104	109	0.002
⁴ D _{5/2}	59067	169	0.0237	0.2363	0.0001	0.0048	27574	13	0.037
² H _{9/2} ⁽²⁾	61299	163	0.0634	0.0440	0.0444	0.0002	22401	1	0.030
² D _{5/2} ⁽¹⁾	62893	159	0.0287	0.0414	0.0007	0.0000	11631	0	0.016
⁴ G _{7/2}	63707	157	0.0091	0.0751	0.0056	0.0002	11920	1	0.016
⁴ G _{5/2}	64338	155	0.0018	0.0019	0.0108	0.0006	1778	2	0.002
² K _{13/2}	64715	155	0.0000	0.0002	0.0519	0.0000	5402	0	0.007
² P _{1/2}	64790	154	0.0000	0.0188	0.0000	0.0000	2411	0	0.003
² P _{3/2}	66210	151	0.0528	0.0659	0.0000	0.0000	23434	0	0.031
⁴ G _{7/2}	69677	144	0.0002	0.0632	0.0049	0.0005	10777	2	0.014
² K _{15/2}	70013	143	0.0000	0.5794	0.0211	0.0000	96597	0	0.130
⁴ G _{9/2}	70280	142	0.0003	0.0010	0.0107	0.0024	1685	11	0.002
⁴ G _{11/2}	71340	140	0.0028	0.0655	0.0120	0.0000	13832	0	0.019
⁴ F _{9/2}	73198	137	0.0340	0.1247	0.0002	0.0003	35624	2	0.048
⁴ F _{3/2}	75194	133	0.0005	0.0214	0.0000	0.0000	4508	0	0.006
⁴ F _{5/2}	75583	132	0.0021	0.0104	0.0014	0.0002	3216	1	0.004

Table D.3: Radiative emission properties of Er:ZBLAN (*continued*)

final	k_{calc} cm ⁻¹	λ_{calc} nm	$ \mathbf{U}^{(2)} ^2$	$ \mathbf{U}^{(4)} ^2$	$ \mathbf{U}^{(6)} ^2$	$ \mathbf{M}/\beta_m ^2$	A_{ed} s ⁻¹	A_{md} s ⁻¹	β
⁴ F _{7/2}	77273	129	0.0018	0.0064	0.0034	0.0000	2791	0	0.004
² H _{11/2} ⁽²⁾	78602	127	0.0333	0.0209	0.0111	0.0000	22052	0	0.030
⁴ S _{3/2}	79356	126	0.0175	0.0106	0.0000	0.0000	10731	0	0.014
⁴ F _{9/2}	82505	121	0.0106	0.0141	0.0030	0.0000	9971	0	0.013
⁴ I _{9/2}	85327	117	0.0121	0.0296	0.0009	0.0000	15958	0	0.021
⁴ I _{11/2}	87573	114	0.0061	0.0083	0.0014	0.0000	6858	0	0.009
⁴ I _{13/2}	91224	110	0.0000	0.0006	0.0003	0.0000	287	0	0.000
⁴ I _{15/2}	97760	102	0.0000	0.0049	0.0000	0.0000	2170	0	0.003
	initial: ² F _{5/2} ⁽¹⁾						$\tau = 0.00$ ms		
² G _{9/2} ⁽²⁾	23005	435	0.0227	0.1143	0.4126	0.0000	3295	0	0.005
² G _{7/2} ⁽²⁾	26991	370	1.5392	0.3735	0.0527	0.0507	38067	16	0.056
² F _{5/2} ⁽²⁾	30108	332	0.2855	0.0052	0.0000	0.0005	8812	0	0.013
² D _{3/2} ⁽²⁾	38197	262	0.1944	0.0226	0.0000	0.0033	13336	3	0.020
² F _{7/2} ⁽²⁾	38779	258	0.0014	0.0501	0.5088	0.0958	15861	93	0.023
² H _{11/2} ⁽¹⁾	42133	237	0.0000	0.0523	0.2248	0.0000	10454	0	0.015
² D _{5/2} ⁽²⁾	44311	226	0.0000	0.1689	0.0000	0.0173	8895	26	0.013
² H _{9/2} ⁽¹⁾	45132	222	0.9041	0.3173	0.0171	0.0000	119185	0	0.175
² L _{15/2}	45456	220	0.0000	0.0000	0.6402	0.0000	29635	0	0.044
⁴ D _{1/2}	46231	216	0.0118	0.0000	0.0000	0.0000	1426	0	0.002
² I _{13/2}	49715	201	0.0000	0.0006	0.1580	0.0000	9902	0	0.015
² P _{3/2}	50425	198	0.0002	0.1728	0.0000	0.0008	13974	2	0.021
⁴ D _{3/2}	50972	196	0.0288	0.0327	0.0000	0.0125	7503	29	0.011
² L _{17/2}	51684	193	0.0000	0.0000	0.0829	0.0000	5822	0	0.009
² I _{11/2}	52148	192	0.0000	0.5822	0.0496	0.0000	55533	0	0.082
⁴ D _{7/2}	53993	185	0.0004	0.0016	0.0106	0.0072	1079	20	0.002
⁴ D _{5/2}	54572	183	0.0005	0.2197	0.0000	0.0017	22560	5	0.033
² H _{9/2} ⁽²⁾	56804	176	0.0547	0.2591	0.0016	0.0000	42587	0	0.063
² D _{5/2} ⁽¹⁾	58398	171	0.0047	0.0359	0.0000	0.0099	5679	35	0.008
⁴ G _{7/2}	59212	169	0.0727	0.0883	0.0000	0.0044	30441	16	0.045

Table D.3: Radiative emission properties of Er:ZBLAN (*continued*)

final	k_{calc} cm ⁻¹	λ_{calc} nm	$ \mathbf{U}^{(2)} ^2$	$ \mathbf{U}^{(4)} ^2$	$ \mathbf{U}^{(6)} ^2$	$ \mathbf{M}/\beta_m ^2$	A_{ed} s ⁻¹	A_{md} s ⁻¹	β
⁴ G _{5/2}	59843	167	0.0019	0.0183	0.0000	0.0057	2993	22	0.004
² K _{13/2}	60220	166	0.0000	0.6943	0.0073	0.0000	96207	0	0.141
² P _{1/2}	60295	166	0.1196	0.0000	0.0000	0.0000	32852	0	0.048
² P _{3/2}	61715	162	0.0185	0.0122	0.0000	0.0001	7245	0	0.011
⁴ G _{7/2}	65182	153	0.0555	0.1604	0.0285	0.0002	51207	1	0.075
² K _{15/2}	65519	153	0.0000	0.0000	0.0024	0.0000	348	0	0.001
⁴ G _{9/2}	65785	152	0.0158	0.0193	0.0003	0.0000	9122	0	0.013
⁴ G _{11/2}	66845	150	0.0000	0.0132	0.0127	0.0000	4408	0	0.006
⁴ F _{9/2}	68703	146	0.0001	0.0000	0.0279	0.0000	4634	0	0.007
⁴ F _{3/2}	70699	141	0.0000	0.0122	0.0000	0.0000	2722	0	0.004
⁴ F _{5/2}	71088	141	0.0000	0.0077	0.0000	0.0004	1747	2	0.003
⁴ F _{7/2}	72778	137	0.0062	0.0097	0.0006	0.0000	5478	0	0.008
² H _{11/2} ⁽²⁾	74107	135	0.0000	0.0017	0.0147	0.0000	3478	0	0.005
⁴ S _{3/2}	74861	134	0.0032	0.0010	0.0000	0.0000	1963	0	0.003
⁴ F _{9/2}	78010	128	0.0037	0.0087	0.0015	0.0000	5160	0	0.008
⁴ I _{9/2}	80833	124	0.0018	0.0012	0.0110	0.0000	4536	0	0.007
⁴ I _{11/2}	83078	120	0.0000	0.0001	0.0061	0.0000	1831	0	0.003
⁴ I _{13/2}	86730	115	0.0000	0.0008	0.0002	0.0000	403	0	0.001
⁴ I _{15/2}	93265	107	0.0000	0.0000	0.0000	0.0000	9	0	0.000
	initial: ² G _{9/2} ⁽²⁾						$\tau = 0.01$ ms		
² G _{7/2} ⁽²⁾	3986	2509	0.0900	0.0536	0.1169	4.1851	7	2	0.000
² F _{5/2} ⁽²⁾	7103	1408	0.1495	0.0341	0.0731	0.0000	45	0	0.000
² D _{3/2} ⁽²⁾	15192	658	0.0000	0.0297	0.5535	0.0000	541	0	0.005
² F _{7/2} ⁽²⁾	15774	634	0.4067	0.2615	0.0029	0.0681	1363	2	0.013
² H _{11/2} ⁽¹⁾	19128	523	1.4599	0.0065	0.0137	0.1231	6671	8	0.066
² D _{5/2} ⁽²⁾	21306	469	0.0562	0.0158	0.0551	0.0000	546	0	0.005
² H _{9/2} ⁽¹⁾	22127	452	0.0468	0.0043	0.1159	0.2854	680	29	0.007
² L _{15/2}	22451	445	0.0000	0.0503	0.0127	0.0000	225	0	0.002
⁴ D _{1/2}	23226	431	0.0000	0.0078	0.0000	0.0000	32	0	0.000

Table D.3: Radiative emission properties of Er:ZBLAN (*continued*)

final	k_{calc} cm ⁻¹	λ_{calc} nm	$ \mathbf{U}^{(2)} ^2$	$ \mathbf{U}^{(4)} ^2$	$ \mathbf{U}^{(6)} ^2$	$ \mathbf{M}/\beta_m ^2$	A_{ed} s ⁻¹	A_{md} s ⁻¹	β
² I _{13/2}	26711	374	1.5970	0.0005	0.0014	0.0000	20211	0	0.199
² P _{3/2}	27420	365	0.0000	0.3156	0.2047	0.0000	3315	0	0.033
⁴ D _{3/2}	27967	358	0.0000	0.1483	0.0333	0.0000	1284	0	0.013
² L _{17/2}	28679	349	0.0000	1.0039	0.3633	0.0000	10278	0	0.101
² I _{11/2}	29143	343	0.1380	0.0844	0.0927	0.0577	3615	14	0.036
⁴ D _{7/2}	30988	323	0.0058	0.0015	0.0043	0.0036	168	1	0.002
⁴ D _{5/2}	31567	317	0.1378	0.0878	0.0953	0.0000	4694	0	0.046
² H _{9/2} ⁽²⁾	33799	296	0.0126	0.4785	0.0002	0.0000	6671	0	0.066
² D _{5/2} ⁽¹⁾	35393	283	0.0314	0.0855	0.0119	0.0000	2417	0	0.024
⁴ G _{7/2}	36207	276	0.0089	0.1324	0.0108	0.0033	2616	2	0.026
⁴ G _{5/2}	36838	271	0.0012	0.0142	0.0015	0.0000	311	0	0.003
² K _{13/2}	37216	269	0.0445	0.0082	0.0191	0.0000	2018	0	0.020
² P _{1/2}	37290	268	0.0000	0.0848	0.0000	0.0000	1533	0	0.015
² P _{3/2}	38710	258	0.0000	0.0438	0.0161	0.0000	1159	0	0.011
⁴ G _{7/2}	42177	237	0.0019	0.0625	0.0112	0.0048	2028	4	0.020
² K _{15/2}	42514	235	0.0000	0.0524	0.0675	0.0000	2952	0	0.029
⁴ G _{9/2}	42780	234	0.0001	0.0271	0.0001	0.0093	774	7	0.008
⁴ G _{11/2}	43840	228	0.0651	0.0527	0.0035	0.0144	5645	12	0.056
⁴ F _{9/2}	45698	219	0.0002	0.0870	0.0089	0.0061	3305	6	0.033
⁴ F _{3/2}	47694	210	0.0000	0.0133	0.0000	0.0000	538	0	0.005
⁴ F _{5/2}	48083	208	0.0075	0.0126	0.0000	0.0000	1141	0	0.011
⁴ F _{7/2}	49773	201	0.0005	0.0251	0.0015	0.0014	1268	2	0.012
² H _{11/2} ⁽²⁾	51103	196	0.0042	0.0860	0.0011	0.0011	4797	2	0.047
⁴ S _{3/2}	51856	193	0.0000	0.0215	0.0002	0.0000	1138	0	0.011
⁴ F _{9/2}	55005	182	0.0008	0.0679	0.0001	0.0031	4371	6	0.043
⁴ I _{9/2}	57828	173	0.0000	0.0150	0.0026	0.0007	1256	1	0.012
⁴ I _{11/2}	60074	166	0.0025	0.0129	0.0003	0.0000	1487	0	0.015
⁴ I _{13/2}	63725	157	0.0000	0.0028	0.0001	0.0000	278	0	0.003
⁴ I _{15/2}	70260	142	0.0000	0.0014	0.0000	0.0000	187	0	0.002

Table D.3: Radiative emission properties of Er:ZBLAN (*continued*)

final	k_{calc} cm ⁻¹	λ_{calc} nm	$ \mathbf{U}^{(2)} ^2$	$ \mathbf{U}^{(4)} ^2$	$ \mathbf{U}^{(6)} ^2$	$ \mathbf{M}/\beta_m ^2$	A_{ed} s ⁻¹	A_{md} s ⁻¹	β
	initial: ${}^2G_{7/2}^{(2)}$						$\tau = 0.01$ ms		
${}^2F_{5/2}^{(2)}$	3116	3209	0.5042	0.1678	0.0591	0.0399	14	0	0.000
${}^2D_{3/2}^{(2)}$	11206	892	0.0513	0.0026	0.0000	0.0000	59	0	0.001
${}^2F_{7/2}^{(2)}$	11788	848	0.0380	0.0592	0.0043	0.0873	91	2	0.001
${}^2H_{11/2}^{(1)}$	15142	660	0.1392	0.0018	0.0412	0.0000	438	0	0.004
${}^2D_{5/2}^{(2)}$	17320	577	0.1111	0.0183	0.4050	0.0049	1195	0	0.012
${}^2H_{9/2}^{(1)}$	18141	551	1.2511	0.0258	0.0596	0.1254	6224	9	0.064
${}^2L_{15/2}$	18465	542	0.0000	0.7242	0.1916	0.0000	2251	0	0.023
${}^4D_{1/2}$	19240	520	0.0000	0.0150	0.0000	0.0000	44	0	0.000
${}^2I_{13/2}$	22724	440	0.0000	0.0032	0.0183	0.0000	87	0	0.001
${}^2P_{3/2}$	23434	427	0.0841	0.0008	0.0000	0.0000	893	0	0.009
${}^4D_{3/2}$	23981	417	0.0163	0.0086	0.0000	0.0000	233	0	0.002
${}^2L_{17/2}$	24693	405	0.0000	0.0000	0.0353	0.0000	178	0	0.002
${}^2I_{11/2}$	25157	398	1.3949	0.0001	0.0032	0.0000	18348	0	0.189
${}^4D_{7/2}$	27002	370	0.0008	0.0000	0.0057	0.0053	51	1	0.001
${}^4D_{5/2}$	27581	363	0.0515	0.0124	0.2257	0.0000	2609	0	0.027
${}^2H_{9/2}^{(2)}$	29813	335	0.0249	0.0006	0.0041	0.0015	596	0	0.006
${}^2D_{5/2}^{(1)}$	31407	318	0.0069	0.0728	0.1103	0.0000	2310	0	0.024
${}^4G_{7/2}$	32221	310	0.0043	0.1992	0.0089	0.0017	3061	1	0.031
${}^4G_{5/2}$	32852	304	0.0326	0.0049	0.0112	0.0310	1194	13	0.012
${}^2K_{13/2}$	33229	301	0.0000	0.0804	0.0726	0.0000	2183	0	0.022
${}^2P_{1/2}$	33304	300	0.0000	0.1783	0.0000	0.0000	2818	0	0.029
${}^2P_{3/2}$	34724	288	0.0490	0.2485	0.0000	0.0000	6240	0	0.064
${}^4G_{7/2}$	38191	262	0.0001	0.2984	0.0160	0.0092	7602	6	0.078
${}^2K_{15/2}$	38527	260	0.0000	0.1193	0.0220	0.0000	3441	0	0.035
${}^4G_{9/2}$	38794	258	0.0011	0.0147	0.0000	0.0048	435	3	0.005
${}^4G_{11/2}$	39854	251	0.0072	0.0238	0.0040	0.0000	1156	0	0.012
${}^4F_{9/2}$	41712	240	0.0397	0.2060	0.0000	0.0000	9244	0	0.095
${}^4F_{3/2}$	43708	229	0.0172	0.0502	0.0000	0.0000	3185	0	0.033
${}^4F_{5/2}$	44097	227	0.0007	0.0233	0.0091	0.0022	1247	2	0.013

Table D.3: Radiative emission properties of Er:ZBLAN (*continued*)

final	k_{calc} cm ⁻¹	λ_{calc} nm	$ \mathbf{U}^{(2)} ^2$	$ \mathbf{U}^{(4)} ^2$	$ \mathbf{U}^{(6)} ^2$	$ \mathbf{M}/\beta_m ^2$	A_{ed} s ⁻¹	A_{md} s ⁻¹	β
⁴ F _{7/2}	45787	218	0.0003	0.0222	0.0009	0.0023	1037	3	0.011
² H _{11/2} ⁽²⁾	47116	212	0.0002	0.0437	0.0029	0.0000	2247	0	0.023
⁴ S _{3/2}	47870	209	0.0085	0.0882	0.0000	0.0000	5364	0	0.055
⁴ F _{9/2}	51019	196	0.0009	0.0131	0.0001	0.0010	940	2	0.010
⁴ I _{9/2}	53841	186	0.0123	0.0886	0.0001	0.0000	8340	0	0.086
⁴ I _{11/2}	56087	178	0.0000	0.0198	0.0015	0.0000	1756	0	0.018
⁴ I _{13/2}	59738	167	0.0000	0.0000	0.0003	0.0000	26	0	0.000
⁴ I _{15/2}	66274	151	0.0000	0.0008	0.0000	0.0000	110	0	0.001
	initial: ² F _{5/2} ⁽²⁾						$\tau = 0.01$ ms		
² D _{3/2} ⁽²⁾	8090	1236	0.7753	0.0765	0.0000	0.3906	456	3	0.007
² F _{7/2} ⁽²⁾	8671	1153	0.0721	0.0112	0.0764	3.1593	75	31	0.002
² H _{11/2} ⁽¹⁾	12025	832	0.0000	0.0346	0.4510	0.0000	371	0	0.005
² D _{5/2} ⁽²⁾	14204	704	0.0054	0.0001	0.0000	1.0807	17	47	0.001
² H _{9/2} ⁽¹⁾	15024	666	0.0006	0.1753	0.0823	0.0000	444	0	0.006
² L _{15/2}	15349	652	0.0000	0.0000	0.5445	0.0000	857	0	0.012
⁴ D _{1/2}	16123	620	0.0029	0.0000	0.0000	0.0000	13	0	0.000
² I _{13/2}	19608	510	0.0000	0.1292	0.2637	0.0000	1404	0	0.020
² P _{3/2}	20317	492	0.0916	0.0698	0.0000	0.0149	1152	2	0.017
⁴ D _{3/2}	20864	479	0.2407	0.0669	0.0000	0.1277	2707	18	0.039
² L _{17/2}	21576	463	0.0000	0.0000	0.0084	0.0000	38	0	0.001
² I _{11/2}	22041	454	0.0000	0.0411	0.0002	0.0000	242	0	0.003
⁴ D _{7/2}	23885	419	0.0016	0.0106	0.0000	0.0014	104	0	0.001
⁴ D _{5/2}	24464	409	0.0032	0.0045	0.0000	0.0359	88	8	0.001
² H _{9/2} ⁽²⁾	26696	375	0.7168	0.9648	0.0366	0.0000	25600	0	0.367
² D _{5/2} ⁽¹⁾	28290	353	0.0316	0.0038	0.0000	0.0019	844	1	0.012
⁴ G _{7/2}	29104	344	0.0082	0.0863	0.0045	0.1526	1469	60	0.022
⁴ G _{5/2}	29735	336	0.0001	0.0072	0.0000	0.0811	110	34	0.002
² K _{13/2}	30113	332	0.0000	0.0213	0.3277	0.0000	4398	0	0.063
² P _{1/2}	30187	331	0.0025	0.0000	0.0000	0.0000	76	0	0.001

Table D.3: Radiative emission properties of Er:ZBLAN (*continued*)

final	k_{calc} cm ⁻¹	λ_{calc} nm	$ \mathbf{U}^{(2)} ^2$	$ \mathbf{U}^{(4)} ^2$	$ \mathbf{U}^{(6)} ^2$	$ \mathbf{M}/\beta_m ^2$	A_{ed} s ⁻¹	A_{md} s ⁻¹	β
² P _{3/2}	31607	316	0.0054	0.0249	0.0000	0.0224	636	11	0.009
⁴ G _{7/2}	35074	285	0.0200	0.0080	0.0648	0.0269	2490	19	0.036
² K _{15/2}	35411	282	0.0000	0.0000	0.1127	0.0000	2331	0	0.033
⁴ G _{9/2}	35677	280	0.0507	0.1117	0.0000	0.0000	5568	0	0.080
⁴ G _{11/2}	36738	272	0.0000	0.0136	0.0107	0.0000	639	0	0.009
⁴ F _{9/2}	38595	259	0.0580	0.0110	0.0259	0.0000	4958	0	0.071
⁴ F _{3/2}	40591	246	0.0130	0.0028	0.0000	0.0084	1136	9	0.016
⁴ F _{5/2}	40980	244	0.0065	0.0001	0.0000	0.0063	536	7	0.008
⁴ F _{7/2}	42670	234	0.0011	0.0036	0.0002	0.0035	281	5	0.004
² H _{11/2} ⁽²⁾	44000	227	0.0000	0.0213	0.0080	0.0000	1432	0	0.021
⁴ S _{3/2}	44753	223	0.0050	0.0056	0.0000	0.0003	844	0	0.012
⁴ F _{9/2}	47902	209	0.0009	0.0054	0.0018	0.0000	596	0	0.009
⁴ I _{9/2}	50725	197	0.0198	0.0140	0.0113	0.0000	5134	0	0.074
⁴ I _{11/2}	52971	189	0.0000	0.0091	0.0060	0.0000	1304	0	0.019
⁴ I _{13/2}	56622	177	0.0000	0.0099	0.0000	0.0000	1134	0	0.016
⁴ I _{15/2}	63157	158	0.0000	0.0000	0.0000	0.0000	0	0	0.000
initial: ² D _{3/2} ⁽²⁾							$\tau = 0.03$ ms		
² F _{7/2} ⁽²⁾	582	—	0.0646	0.0004	0.0000	0.0000	0	0	0.000
² H _{11/2} ⁽¹⁾	3936	2541	0.0000	0.0275	0.3198	0.0000	14	0	0.000
² D _{5/2} ⁽²⁾	6114	1636	0.0317	0.0944	0.0000	2.9049	29	15	0.001
² H _{9/2} ⁽¹⁾	6935	1442	0.0000	0.0142	0.0318	0.0000	11	0	0.000
² L _{15/2}	7259	1378	0.0000	0.0000	0.5262	0.0000	129	0	0.004
⁴ D _{1/2}	8034	1245	0.0707	0.0000	0.0000	1.3093	58	15	0.002
² I _{13/2}	11518	868	0.0000	0.0000	0.0001	0.0000	0	0	0.000
² P _{3/2}	12228	818	0.1237	0.0000	0.0000	0.2613	362	11	0.012
⁴ D _{3/2}	12775	783	0.0008	0.0000	0.0000	0.2275	3	11	0.000
² L _{17/2}	13487	741	0.0000	0.0000	0.0000	0.0000	0	0	0.000
² I _{11/2}	13951	717	0.0000	0.0857	0.0033	0.0000	193	0	0.006
⁴ D _{7/2}	15796	633	0.0070	0.0428	0.0000	0.0000	181	0	0.006
⁴ D _{5/2}	16375	611	0.0124	0.0312	0.0000	0.2614	199	27	0.007

Table D.3: Radiative emission properties of Er:ZBLAN (*continued*)

final	k_{calc} cm ⁻¹	λ_{calc} nm	$ \mathbf{U}^{(2)} ^2$	$ \mathbf{U}^{(4)} ^2$	$ \mathbf{U}^{(6)} ^2$	$ \mathbf{M}/\beta_m ^2$	A_{ed} s ⁻¹	A_{md} s ⁻¹	β
² H _{9/2} ⁽²⁾	18607	537	0.0000	0.0002	0.0022	0.0000	10	0	0.000
² D _{5/2} ⁽¹⁾	20201	495	0.0003	0.1222	0.0000	0.1741	828	33	0.028
⁴ G _{7/2}	21015	476	0.3375	0.0192	0.0000	0.0000	5252	0	0.173
⁴ G _{5/2}	21646	462	0.0142	0.0001	0.0000	0.0049	237	1	0.008
² K _{13/2}	22023	454	0.0000	0.0000	0.0050	0.0000	35	0	0.001
² P _{1/2}	22098	453	0.0385	0.0000	0.0000	0.0237	680	6	0.023
² P _{3/2}	23518	425	0.1160	0.0000	0.0000	0.0357	2479	11	0.082
⁴ G _{7/2}	26985	371	0.0338	0.0303	0.0000	0.0000	1598	0	0.053
² K _{15/2}	27321	366	0.0000	0.0000	0.0027	0.0000	37	0	0.001
⁴ G _{9/2}	27588	362	0.0000	0.0079	0.0407	0.0000	715	0	0.024
⁴ G _{11/2}	28648	349	0.0000	0.0014	0.1204	0.0000	1949	0	0.064
⁴ F _{9/2}	30505	328	0.0000	0.1747	0.0026	0.0000	4243	0	0.140
⁴ F _{3/2}	32502	308	0.0009	0.0000	0.0000	0.0052	50	4	0.002
⁴ F _{5/2}	32890	304	0.0190	0.0122	0.0000	0.0081	1522	7	0.050
⁴ F _{7/2}	34581	289	0.0051	0.0000	0.0000	0.0000	361	0	0.012
² H _{11/2} ⁽²⁾	35910	278	0.0000	0.0112	0.0142	0.0000	911	0	0.030
⁴ S _{3/2}	36664	273	0.0033	0.0000	0.0000	0.0013	278	2	0.009
⁴ F _{9/2}	39813	251	0.0000	0.0004	0.0002	0.0000	30	0	0.001
⁴ I _{9/2}	42635	235	0.0000	0.0000	0.0005	0.0000	31	0	0.001
⁴ I _{11/2}	44881	223	0.0000	0.0916	0.0010	0.0000	7609	0	0.251
⁴ I _{13/2}	48532	206	0.0000	0.0000	0.0011	0.0000	93	0	0.003
⁴ I _{15/2}	55068	182	0.0000	0.0000	0.0008	0.0000	103	0	0.003
	initial: ² F _{7/2} ⁽²⁾						$\tau = 0.01$ ms		
² H _{11/2} ⁽¹⁾	3354	2982	0.0196	0.1165	0.1211	0.0000	4	0	0.000
² D _{5/2} ⁽²⁾	5532	1808	0.4004	0.0119	0.0298	0.1449	56	0	0.001
² H _{9/2} ⁽¹⁾	6353	1574	0.0001	0.0305	0.2454	0.0009	23	0	0.000
² L _{15/2}	6677	1498	0.0000	0.0007	0.0453	0.0000	4	0	0.000
⁴ D _{1/2}	7452	1342	0.0000	0.0202	0.0000	0.0000	3	0	0.000
² I _{13/2}	10936	914	0.0000	0.0005	0.1734	0.0000	74	0	0.001
² P _{3/2}	11646	859	0.0556	0.0602	0.0000	0.0000	108	0	0.001

Table D.3: Radiative emission properties of Er:ZBLAN (*continued*)

final	k_{calc} cm ⁻¹	λ_{calc} nm	$ \mathbf{U}^{(2)} ^2$	$ \mathbf{U}^{(4)} ^2$	$ \mathbf{U}^{(6)} ^2$	$ \mathbf{M}/\beta_m ^2$	A_{ed} s ⁻¹	A_{md} s ⁻¹	β
⁴ D _{3/2}	12193	820	0.0185	0.0062	0.0000	0.0000	31	0	0.000
² L _{17/2}	12905	775	0.0000	0.0000	0.5175	0.0000	361	0	0.004
² I _{11/2}	13369	748	0.0181	0.0070	0.4416	0.0000	385	0	0.004
⁴ D _{7/2}	15214	657	0.0145	0.0081	0.0018	0.4991	55	20	0.001
⁴ D _{5/2}	15793	633	0.0908	0.0003	0.0120	0.3261	304	15	0.004
² H _{9/2} ⁽²⁾	18025	555	0.0102	0.0245	0.0719	0.0059	245	0	0.003
² D _{5/2} ⁽¹⁾	19619	510	0.7892	0.0452	0.0113	0.1184	5008	10	0.056
⁴ G _{7/2}	20433	489	0.0115	0.0631	0.0493	0.0014	439	0	0.005
⁴ G _{5/2}	21064	475	0.0003	0.0142	0.0120	0.0175	94	2	0.001
² K _{13/2}	21441	466	0.0000	0.0369	0.4550	0.0000	1635	0	0.018
² P _{1/2}	21516	465	0.0000	0.0948	0.0000	0.0000	387	0	0.004
² P _{3/2}	22936	436	0.1538	0.1374	0.0000	0.0000	2204	0	0.025
⁴ G _{7/2}	26403	379	0.0173	0.0543	0.0483	0.0888	978	19	0.011
² K _{15/2}	26739	374	0.0000	0.1908	1.0787	0.0000	8469	0	0.094
⁴ G _{9/2}	27006	370	0.0011	0.1056	0.0102	0.4272	953	100	0.012
⁴ G _{11/2}	28066	356	0.6895	0.4525	0.0006	0.0000	16905	0	0.188
⁴ F _{9/2}	29924	334	0.2020	0.5707	0.0249	0.1785	11221	57	0.125
⁴ F _{3/2}	31920	313	0.0220	0.0036	0.0000	0.0000	655	0	0.007
⁴ F _{5/2}	32309	310	0.0427	0.0004	0.0027	0.0339	1259	14	0.014
⁴ F _{7/2}	33999	294	0.0002	0.0005	0.0110	0.0368	164	18	0.002
² H _{11/2} ⁽²⁾	35328	283	0.3923	0.5278	0.0042	0.0000	24987	0	0.278
⁴ S _{3/2}	36082	277	0.0079	0.0144	0.0000	0.0000	614	0	0.007
⁴ F _{9/2}	39231	255	0.0000	0.0120	0.0087	0.0116	506	9	0.006
⁴ I _{9/2}	42053	238	0.0144	0.1053	0.0001	0.0016	4465	2	0.050
⁴ I _{11/2}	44299	226	0.0483	0.0524	0.0002	0.0000	5866	0	0.065
⁴ I _{13/2}	47950	209	0.0000	0.0016	0.0013	0.0000	133	0	0.001
⁴ I _{15/2}	54486	184	0.0000	0.0141	0.0000	0.0000	1075	0	0.012
	initial: ² H _{11/2} ⁽¹⁾						$\tau = 0.07$ ms		
² D _{5/2} ⁽²⁾	2178	4591	0.0000	0.0163	0.0041	0.0000	0	0	0.000
² H _{9/2} ⁽¹⁾	2999	3334	0.0605	0.1664	0.4265	3.6162	4	1	0.000

Table D.3: Radiative emission properties of Er:ZBLAN (*continued*)

final	k_{calc} cm ⁻¹	λ_{calc} nm	$ \mathbf{U}^{(2)} ^2$	$ \mathbf{U}^{(4)} ^2$	$ \mathbf{U}^{(6)} ^2$	$ \mathbf{M}/\beta_m ^2$	A_{ed} s ⁻¹	A_{md} s ⁻¹	β
² L _{15/2}	3323	3009	0.7016	0.1533	0.0442	0.0000	15	0	0.001
⁴ D _{1/2}	4098	2440	0.0000	0.0000	0.0006	0.0000	0	0	0.000
² I _{13/2}	7582	1319	0.7129	0.5838	0.3189	1.8619	262	6	0.020
² P _{3/2}	8292	1206	0.0000	0.1135	0.1454	0.0000	35	0	0.003
⁴ D _{3/2}	8839	1131	0.0000	0.0038	0.2725	0.0000	41	0	0.003
² L _{17/2}	9551	1047	0.0000	0.2400	1.2104	0.0000	283	0	0.021
² I _{11/2}	10015	998	0.0471	0.1213	0.0561	2.7569	70	21	0.007
⁴ D _{7/2}	11860	843	0.0019	0.0006	0.0027	0.0000	3	0	0.000
⁴ D _{5/2}	12439	804	0.0000	0.1816	0.0205	0.0000	102	0	0.007
² H _{9/2} ⁽²⁾	14671	682	0.3009	0.5755	0.0508	0.0045	1032	0	0.075
² D _{5/2} ⁽¹⁾	16265	615	0.0000	0.1731	0.1239	0.0000	317	0	0.023
⁴ G _{7/2}	17079	586	0.0375	0.0000	0.1270	0.0000	239	0	0.017
⁴ G _{5/2}	17710	565	0.0000	0.0040	0.0242	0.0000	35	0	0.003
² K _{13/2}	18087	553	0.0239	0.0681	0.3386	0.1956	624	9	0.046
² P _{1/2}	18162	551	0.0000	0.0000	0.0795	0.0000	104	0	0.008
² P _{3/2}	19582	511	0.0000	0.0376	0.0004	0.0000	78	0	0.006
⁴ G _{7/2}	23049	434	0.0322	0.0008	0.1434	0.0000	608	0	0.044
² K _{15/2}	23385	428	0.5507	0.0552	0.1071	0.0000	4352	0	0.317
⁴ G _{9/2}	23652	423	0.0056	0.0277	0.0478	0.0797	282	8	0.021
⁴ G _{11/2}	24712	405	0.0066	0.0726	0.0196	0.1602	423	19	0.032
⁴ F _{9/2}	26570	376	0.0377	0.0109	0.0003	0.0058	449	1	0.033
⁴ F _{3/2}	28566	350	0.0000	0.0022	0.0714	0.0000	390	0	0.028
⁴ F _{5/2}	28955	345	0.0000	0.0321	0.0014	0.0000	226	0	0.016
⁴ F _{7/2}	30645	326	0.0004	0.0005	0.0576	0.0000	389	0	0.028
² H _{11/2} ⁽²⁾	31974	313	0.0002	0.0581	0.0012	0.0227	552	6	0.041
⁴ S _{3/2}	32728	306	0.0000	0.0064	0.0001	0.0000	64	0	0.005
⁴ F _{9/2}	35877	279	0.0123	0.0635	0.0138	0.0018	1322	1	0.097
⁴ I _{9/2}	38699	258	0.0003	0.0081	0.0017	0.0000	172	0	0.013
⁴ I _{11/2}	40945	244	0.0001	0.0085	0.0046	0.0021	252	1	0.018
⁴ I _{13/2}	44596	224	0.0003	0.0179	0.0021	0.0001	542	0	0.040

Table D.3: Radiative emission properties of Er:ZBLAN (*continued*)

final	k_{calc} cm ⁻¹	λ_{calc} nm	$ \mathbf{U}^{(2)} ^2$	$ \mathbf{U}^{(4)} ^2$	$ \mathbf{U}^{(6)} ^2$	$ \mathbf{M}/\beta_m ^2$	A_{ed} s ⁻¹	A_{md} s ⁻¹	β
⁴ I _{15/2}	51132	196	0.0001	0.0084	0.0000	0.0000	366	0	0.027
	initial: ² D _{5/2} ⁽²⁾						$\tau = 0.03$ ms		
² H _{9/2} ⁽¹⁾	821	—	0.0049	0.0555	0.2541	0.0000	0	0	0.000
² L _{15/2}	1145	—	0.0000	0.0000	0.0018	0.0000	0	0	0.000
⁴ D _{1/2}	1920	5209	0.1358	0.0000	0.0000	0.0000	1	0	0.000
² I _{13/2}	5404	1850	0.0000	0.1464	0.0390	0.0000	15	0	0.000
² P _{3/2}	6114	1636	0.1510	0.0021	0.0000	0.0833	37	0	0.001
⁴ D _{3/2}	6661	1501	0.0264	0.0001	0.0000	1.3753	8	6	0.000
² L _{17/2}	7373	1356	0.0000	0.0000	0.4260	0.0000	73	0	0.002
² I _{11/2}	7837	1276	0.0000	0.0090	0.0381	0.0000	10	0	0.000
⁴ D _{7/2}	9682	1033	0.0903	0.0481	0.0037	3.1977	112	44	0.004
⁴ D _{5/2}	10261	975	0.0119	0.0759	0.0000	0.4671	57	8	0.002
² H _{9/2} ⁽²⁾	12493	800	0.1008	0.0182	0.0236	0.0000	248	0	0.006
² D _{5/2} ⁽¹⁾	14086	710	0.2583	0.0330	0.0000	0.1020	822	4	0.022
⁴ G _{7/2}	14901	671	0.1394	0.1786	0.0296	0.0730	855	4	0.022
⁴ G _{5/2}	15532	644	0.0027	0.0008	0.0000	0.2069	13	12	0.001
² K _{13/2}	15909	629	0.0000	0.0435	0.0953	0.0000	262	0	0.007
² P _{1/2}	15984	626	0.0583	0.0000	0.0000	0.0000	256	0	0.007
² P _{3/2}	17404	575	0.1415	0.1476	0.0000	0.0349	1224	3	0.032
⁴ G _{7/2}	20871	479	0.0004	0.1014	0.0267	0.0279	614	4	0.016
² K _{15/2}	21207	472	0.0000	0.0000	0.0025	0.0000	10	0	0.000
⁴ G _{9/2}	21474	466	0.3357	0.0032	0.0735	0.0000	3957	0	0.103
⁴ G _{11/2}	22534	444	0.0000	0.1594	0.0726	0.0000	1368	0	0.036
⁴ F _{9/2}	24391	410	0.2669	0.1546	0.0946	0.0000	6101	0	0.159
⁴ F _{3/2}	26388	379	0.0641	0.0124	0.0000	0.0424	1427	12	0.038
⁴ F _{5/2}	26776	373	0.0202	0.0027	0.0000	0.0001	458	0	0.012
⁴ F _{7/2}	28466	351	0.0899	0.0151	0.0057	0.0186	2563	7	0.067
² H _{11/2} ⁽²⁾	29796	336	0.0000	0.2565	0.0002	0.0000	3816	0	0.100
⁴ S _{3/2}	30550	327	0.0096	0.0001	0.0000	0.0003	307	0	0.008
⁴ F _{9/2}	33698	297	0.0008	0.0411	0.0101	0.0000	1113	0	0.029

Table D.3: Radiative emission properties of Er:ZBLAN (*continued*)

final	k_{calc} cm ⁻¹	λ_{calc} nm	$ \mathbf{U}^{(2)} ^2$	$ \mathbf{U}^{(4)} ^2$	$ \mathbf{U}^{(6)} ^2$	$ \mathbf{M}/\beta_m ^2$	A_{ed} s ⁻¹	A_{md} s ⁻¹	β
⁴ I _{9/2}	36521	274	0.0133	0.0006	0.0012	0.0000	790	0	0.021
⁴ I _{11/2}	38767	258	0.0000	0.0168	0.0067	0.0000	759	0	0.020
⁴ I _{13/2}	42418	236	0.0000	0.2249	0.0031	0.0000	10383	0	0.271
⁴ I _{15/2}	48954	204	0.0000	0.0000	0.0098	0.0000	581	0	0.015
	initial: ² H _{9/2} ⁽¹⁾						$\tau = 0.07$ ms		
² L _{15/2}	324	—	0.0000	0.1547	1.1396	0.0000	0	0	0.000
⁴ D _{1/2}	1099	—	0.0000	0.0159	0.0000	0.0000	0	0	0.000
² I _{13/2}	4583	2182	0.0029	0.0948	0.1504	0.0000	7	0	0.000
² P _{3/2}	5293	1889	0.0000	0.0752	0.0062	0.0000	4	0	0.000
⁴ D _{3/2}	5840	1712	0.0000	0.0743	0.0738	0.0000	8	0	0.001
² L _{17/2}	6552	1526	0.0000	0.0130	0.1938	0.0000	15	0	0.001
² I _{11/2}	7016	1425	0.7608	0.4669	0.1539	1.6544	231	5	0.017
⁴ D _{7/2}	8861	1129	0.0021	0.0006	0.0062	0.0014	2	0	0.000
⁴ D _{5/2}	9440	1059	0.0175	0.1095	0.0100	0.0000	41	0	0.003
² H _{9/2} ⁽²⁾	11672	857	0.0067	0.0172	0.0422	0.0008	33	0	0.002
² D _{5/2} ⁽¹⁾	13266	754	0.0000	0.0697	0.4757	0.0000	341	0	0.024
⁴ G _{7/2}	14080	710	0.2108	0.0697	0.0246	0.0439	458	1	0.033
⁴ G _{5/2}	14711	680	0.0017	0.0112	0.0036	0.0000	18	0	0.001
² K _{13/2}	15088	663	1.3057	0.0108	0.0544	0.0000	2945	0	0.210
² P _{1/2}	15163	660	0.0000	0.1396	0.0000	0.0000	157	0	0.011
² P _{3/2}	16583	603	0.0000	0.0182	0.0610	0.0000	100	0	0.007
⁴ G _{7/2}	20050	499	0.1901	0.0374	0.1319	0.0935	1376	7	0.098
² K _{15/2}	20386	491	0.0000	0.0003	0.0659	0.0000	148	0	0.011
⁴ G _{9/2}	20653	484	0.0017	0.0316	0.0002	0.1262	101	10	0.008
⁴ G _{11/2}	21713	461	0.0013	0.0766	0.0042	0.0108	278	1	0.020
⁴ F _{9/2}	23571	424	0.0077	0.2173	0.0215	0.0201	1080	2	0.077
⁴ F _{3/2}	25567	391	0.0000	0.0311	0.0330	0.0000	320	0	0.023
⁴ F _{5/2}	25956	385	0.0025	0.0229	0.1047	0.0000	654	0	0.047
⁴ F _{7/2}	27646	362	0.0092	0.0105	0.0010	0.0009	209	0	0.015
² H _{11/2} ⁽²⁾	28975	345	0.0041	0.0621	0.0023	0.0582	590	14	0.043

Table D.3: Radiative emission properties of Er:ZBLAN (*continued*)

final	k_{calc} cm ⁻¹	λ_{calc} nm	$ \mathbf{U}^{(2)} ^2$	$ \mathbf{U}^{(4)} ^2$	$ \mathbf{U}^{(6)} ^2$	$ \mathbf{M}/\beta_m ^2$	A_{ed} s ⁻¹	A_{md} s ⁻¹	β
⁴ S _{3/2}	29729	336	0.0000	0.0142	0.0171	0.0000	248	0	0.018
⁴ F _{9/2}	32878	304	0.0000	0.0121	0.0226	0.0007	369	0	0.026
⁴ I _{9/2}	35700	280	0.0020	0.1573	0.0194	0.0120	2785	5	0.199
⁴ I _{11/2}	37946	264	0.0001	0.0639	0.0027	0.0000	1268	0	0.090
⁴ I _{13/2}	41597	240	0.0002	0.0016	0.0001	0.0000	56	0	0.004
⁴ I _{15/2}	48133	208	0.0000	0.0036	0.0001	0.0000	152	0	0.011
	initial: ² L _{15/2}						$\tau = 0.15$ ms		
⁴ D _{1/2}	775	–	0.0000	0.0000	0.0000	0.0000	0	0	0.000
² I _{13/2}	4259	2348	0.1204	0.8390	0.0212	0.0417	17	0	0.002
² P _{3/2}	4969	2013	0.0000	0.0000	0.0218	0.0000	0	0	0.000
⁴ D _{3/2}	5516	1813	0.0000	0.0000	0.1341	0.0000	4	0	0.001
² L _{17/2}	6228	1606	0.0621	0.1679	0.2059	7.9939	22	11	0.005
² I _{11/2}	6692	1494	0.5547	0.5983	0.4571	0.0000	123	0	0.018
⁴ D _{7/2}	8537	1171	0.0000	0.0000	0.0059	0.0000	1	0	0.000
⁴ D _{5/2}	9116	1097	0.0000	0.0000	0.0156	0.0000	2	0	0.000
² H _{9/2} ⁽²⁾	11348	881	0.0000	0.7422	0.4468	0.0000	323	0	0.048
² D _{5/2} ⁽¹⁾	12941	773	0.0000	0.0000	0.0129	0.0000	5	0	0.001
⁴ G _{7/2}	13756	727	0.0000	0.0048	0.2541	0.0000	110	0	0.017
⁴ G _{5/2}	14387	695	0.0000	0.0000	0.0290	0.0000	14	0	0.002
² K _{13/2}	14764	677	0.0339	1.4635	1.1608	0.3829	1603	7	0.241
² P _{1/2}	14839	674	0.0000	0.0000	0.0000	0.0000	0	0	0.000
² P _{3/2}	16259	615	0.0000	0.0000	0.0013	0.0000	1	0	0.000
⁴ G _{7/2}	19726	507	0.0000	0.0138	0.2058	0.0000	282	0	0.042
² K _{15/2}	20062	498	0.0301	0.0485	0.2541	0.8799	517	41	0.084
⁴ G _{9/2}	20329	492	0.0000	0.1336	0.1351	0.0000	417	0	0.062
⁴ G _{11/2}	21389	468	0.0011	0.0156	0.0033	0.0000	41	0	0.006
⁴ F _{9/2}	23246	430	0.0000	0.0829	0.0035	0.0000	222	0	0.033
⁴ F _{3/2}	25243	396	0.0000	0.0000	0.0262	0.0000	71	0	0.011
⁴ F _{5/2}	25631	390	0.0000	0.0000	0.0003	0.0000	1	0	0.000
⁴ F _{7/2}	27321	366	0.0000	0.0017	0.0497	0.0000	178	0	0.027

Table D.3: Radiative emission properties of Er:ZBLAN (*continued*)

final	k_{calc} cm ⁻¹	λ_{calc} nm	$ \mathbf{U}^{(2)} ^2$	$ \mathbf{U}^{(4)} ^2$	$ \mathbf{U}^{(6)} ^2$	$ \mathbf{M}/\beta_m ^2$	A_{ed} s ⁻¹	A_{md} s ⁻¹	β
² H _{11/2} ⁽²⁾	28651	349	0.0008	0.0170	0.0043	0.0000	109	0	0.016
⁴ S _{3/2}	29405	340	0.0000	0.0000	0.0025	0.0000	11	0	0.002
⁴ F _{9/2}	32554	307	0.0000	0.0315	0.0473	0.0000	513	0	0.077
⁴ I _{9/2}	35376	283	0.0000	0.1154	0.0383	0.0000	1399	0	0.210
⁴ I _{11/2}	37622	266	0.0003	0.0019	0.0031	0.0000	57	0	0.009
⁴ I _{13/2}	41273	242	0.0013	0.0179	0.0101	0.0021	450	1	0.068
⁴ I _{15/2}	47809	209	0.0002	0.0026	0.0021	0.0011	119	1	0.018
	initial: ⁴ D _{1/2}						$\tau = 0.02$ ms		
² I _{13/2}	3484	2870	0.0000	0.0000	0.0266	0.0000	1	0	0.000
² P _{3/2}	4194	2384	0.0011	0.0000	0.0000	1.6161	0	5	0.000
⁴ D _{3/2}	4741	2109	0.2465	0.0000	0.0000	2.6555	82	13	0.002
² L _{17/2}	5453	1834	0.0000	0.0000	0.0000	0.0000	0	0	0.000
² I _{11/2}	5917	1690	0.0000	0.0000	0.0279	0.0000	7	0	0.000
⁴ D _{7/2}	7762	1288	0.0000	0.1705	0.0000	0.0000	127	0	0.003
⁴ D _{5/2}	8341	1199	0.0003	0.0000	0.0000	0.0000	1	0	0.000
² H _{9/2} ⁽²⁾	10573	946	0.0000	0.0476	0.0000	0.0000	90	0	0.002
² D _{5/2} ⁽¹⁾	12167	822	0.0740	0.0000	0.0000	0.0000	426	0	0.010
⁴ G _{7/2}	12981	770	0.0000	0.0156	0.0000	0.0000	55	0	0.001
⁴ G _{5/2}	13612	735	0.2833	0.0000	0.0000	0.0000	2290	0	0.055
² K _{13/2}	13989	715	0.0000	0.0000	0.0024	0.0000	8	0	0.000
² P _{1/2}	14064	711	0.0000	0.0000	0.0000	0.0481	0	6	0.000
² P _{3/2}	15484	646	0.0027	0.0000	0.0000	0.0520	32	9	0.001
⁴ G _{7/2}	18951	528	0.0000	0.0105	0.0000	0.0000	117	0	0.003
² K _{15/2}	19287	518	0.0000	0.0000	0.0000	0.0000	0	0	0.000
⁴ G _{9/2}	19554	511	0.0000	0.0213	0.0000	0.0000	259	0	0.006
⁴ G _{11/2}	20614	485	0.0000	0.0000	0.1558	0.0000	1805	0	0.043
⁴ F _{9/2}	22472	445	0.0000	0.0105	0.0000	0.0000	196	0	0.005
⁴ F _{3/2}	24468	409	0.1132	0.0000	0.0000	0.0007	5461	1	0.131
⁴ F _{5/2}	24857	402	0.0850	0.0000	0.0000	0.0000	4305	0	0.103
⁴ F _{7/2}	26547	377	0.0000	0.1780	0.0000	0.0000	5548	0	0.133

Table D.3: Radiative emission properties of Er:ZBLAN (*continued*)

final	k_{calc} cm ⁻¹	λ_{calc} nm	$ \mathbf{U}^{(2)} ^2$	$ \mathbf{U}^{(4)} ^2$	$ \mathbf{U}^{(6)} ^2$	$ \mathbf{M}/\beta_m ^2$	A_{ed} s ⁻¹	A_{md} s ⁻¹	β
² H _{11/2} ⁽²⁾	27876	359	0.0000	0.0000	0.0470	0.0000	1379	0	0.033
⁴ S _{3/2}	28630	349	0.0308	0.0000	0.0000	0.0015	2413	2	0.058
⁴ F _{9/2}	31779	315	0.0000	0.1622	0.0000	0.0000	8852	0	0.213
⁴ I _{9/2}	34601	289	0.0000	0.0793	0.0000	0.0000	5656	0	0.136
⁴ I _{11/2}	36847	271	0.0000	0.0000	0.0151	0.0000	1061	0	0.025
⁴ I _{13/2}	40498	247	0.0000	0.0000	0.0149	0.0000	1420	0	0.034
⁴ I _{15/2}	47034	213	0.0000	0.0000	0.0000	0.0000	0	0	0.000
	initial: ² I _{13/2}						$\tau = 0.15$ ms		
² P _{3/2}	710	–	0.0000	0.0000	0.1586	0.0000	0	0	0.000
⁴ D _{3/2}	1257	7958	0.0000	0.0000	0.0201	0.0000	0	0	0.000
² L _{17/2}	1969	5079	1.2939	0.6938	0.5115	0.0000	6	0	0.001
² I _{11/2}	2433	4110	0.3787	0.3087	0.2007	3.9678	4	0	0.001
⁴ D _{7/2}	4278	2338	0.0000	0.0018	0.0169	0.0000	0	0	0.000
⁴ D _{5/2}	4857	2059	0.0000	0.2099	0.0893	0.0000	7	0	0.001
² H _{9/2} ⁽²⁾	7088	1411	0.1033	0.0002	0.6316	0.0000	58	0	0.009
² D _{5/2} ⁽¹⁾	8682	1152	0.0000	0.0106	0.1896	0.0000	24	0	0.004
⁴ G _{7/2}	9497	1053	0.0000	0.1200	0.0690	0.0000	34	0	0.005
⁴ G _{5/2}	10128	987	0.0000	0.0058	0.0407	0.0000	9	0	0.001
² K _{13/2}	10505	952	0.0367	0.0421	0.0735	1.1877	46	9	0.008
² P _{1/2}	10580	945	0.0000	0.0000	0.3401	0.0000	74	0	0.011
² P _{3/2}	12000	833	0.0000	0.0000	0.1841	0.0000	59	0	0.009
⁴ G _{7/2}	15467	647	0.0000	0.0930	0.0292	0.0000	100	0	0.015
² K _{15/2}	15803	633	0.1117	0.5610	0.6488	0.7153	1193	19	0.179
⁴ G _{9/2}	16070	622	0.0070	0.0087	0.1067	0.0000	104	0	0.015
⁴ G _{11/2}	17130	584	0.1217	0.3305	0.0173	0.0100	683	0	0.101
⁴ F _{9/2}	18987	527	0.0118	0.0626	0.0001	0.0000	137	0	0.020
⁴ F _{3/2}	20984	477	0.0000	0.0000	0.0109	0.0000	19	0	0.003
⁴ F _{5/2}	21372	468	0.0000	0.0125	0.0362	0.0000	95	0	0.014
⁴ F _{7/2}	23062	434	0.0000	0.0081	0.0162	0.0000	61	0	0.009
² H _{11/2} ⁽²⁾	24392	410	0.0326	0.1528	0.0979	0.0591	1018	6	0.151

Table D.3: Radiative emission properties of Er:ZBLAN (*continued*)

final	k_{calc} cm ⁻¹	λ_{calc} nm	$ \mathbf{U}^{(2)} ^2$	$ \mathbf{U}^{(4)} ^2$	$ \mathbf{U}^{(6)} ^2$	$ \mathbf{M}/\beta_m ^2$	A_{ed} s ⁻¹	A_{md} s ⁻¹	β
⁴ S _{3/2}	25146	398	0.0000	0.0000	0.1296	0.0000	395	0	0.058
⁴ F _{9/2}	28294	353	0.0106	0.0084	0.0909	0.0000	558	0	0.083
⁴ I _{9/2}	31117	321	0.0001	0.0399	0.0024	0.0000	308	0	0.045
⁴ I _{11/2}	33363	300	0.0187	0.0552	0.0092	0.0118	907	3	0.135
⁴ I _{13/2}	37014	270	0.0019	0.0025	0.0062	0.0215	144	8	0.022
⁴ I _{15/2}	43550	230	0.0053	0.0166	0.0049	0.0106	665	6	0.099
	initial: ² P _{3/2}						$\tau = 0.06$ ms		
⁴ D _{3/2}	547	—	0.0025	0.0000	0.0000	0.0295	0	0	0.000
² L _{17/2}	1259	7943	0.0000	0.0000	0.0000	0.0000	0	0	0.000
² I _{11/2}	1723	5803	0.0000	0.0857	0.1175	0.0000	1	0	0.000
⁴ D _{7/2}	3568	2803	0.0175	0.0333	0.0000	0.0000	2	0	0.000
⁴ D _{5/2}	4147	2411	0.0010	0.0052	0.0000	2.6639	0	4	0.000
² H _{9/2} ⁽²⁾	6379	1568	0.0000	0.0044	0.1498	0.0000	26	0	0.002
² D _{5/2} ⁽¹⁾	7973	1254	0.1497	0.0208	0.0000	0.0596	129	1	0.008
⁴ G _{7/2}	8787	1138	0.0004	0.0774	0.0000	0.0000	42	0	0.003
⁴ G _{5/2}	9418	1062	0.0947	0.0014	0.0000	0.0262	127	0	0.008
² K _{13/2}	9795	1021	0.0000	0.0000	0.0000	0.0000	0	0	0.000
² P _{1/2}	9870	1013	0.2095	0.0000	0.0000	0.1024	321	2	0.020
² P _{3/2}	11290	886	0.0029	0.0000	0.0000	0.8568	7	28	0.002
⁴ G _{7/2}	14757	678	0.1419	0.1139	0.0000	0.0000	1028	0	0.063
² K _{15/2}	15093	663	0.0000	0.0000	0.2197	0.0000	493	0	0.030
⁴ G _{9/2}	15360	651	0.0000	0.0158	0.0003	0.0000	47	0	0.003
⁴ G _{11/2}	16420	609	0.0000	0.1184	0.0992	0.0000	712	0	0.043
⁴ F _{9/2}	18278	547	0.0000	0.0075	0.0004	0.0000	39	0	0.002
⁴ F _{3/2}	20274	493	0.0173	0.0000	0.0000	0.0669	235	13	0.015
⁴ F _{5/2}	20663	484	0.0009	0.1107	0.0000	0.0508	812	10	0.050
⁴ F _{7/2}	22353	447	0.1082	0.0448	0.0000	0.0000	2389	0	0.145
² H _{11/2} ⁽²⁾	23682	422	0.0000	0.1130	0.0000	0.0000	1239	0	0.075
⁴ S _{3/2}	24436	409	0.1107	0.0000	0.0000	0.0218	2659	8	0.162
⁴ F _{9/2}	27585	363	0.0000	0.0108	0.0042	0.0000	249	0	0.015

Table D.3: Radiative emission properties of Er:ZBLAN (*continued*)

final	k_{calc} cm ⁻¹	λ_{calc} nm	$ \mathbf{U}^{(2)} ^2$	$ \mathbf{U}^{(4)} ^2$	$ \mathbf{U}^{(6)} ^2$	$ \mathbf{M}/\beta_m ^2$	A_{ed} s ⁻¹	A_{md} s ⁻¹	β
⁴ I _{9/2}	30407	329	0.0000	0.1532	0.0088	0.0000	3810	0	0.232
⁴ I _{11/2}	32653	306	0.0000	0.0273	0.0249	0.0000	1410	0	0.086
⁴ I _{13/2}	36304	275	0.0000	0.0000	0.0173	0.0000	580	0	0.035
⁴ I _{15/2}	42840	233	0.0000	0.0000	0.0004	0.0000	22	0	0.001
	initial: ⁴ D _{3/2}						$\tau = 0.05$ ms		
² L _{17/2}	712	—	0.0000	0.0000	0.0000	0.0000	0	0	0.000
² I _{11/2}	1176	—	0.0000	0.0206	0.0223	0.0000	0	0	0.000
⁴ D _{7/2}	3021	3310	0.1083	0.2093	0.0000	0.0000	9	0	0.000
⁴ D _{5/2}	3600	2778	0.2301	0.0397	0.0000	0.9461	18	1	0.001
² H _{9/2} ⁽²⁾	5832	1715	0.0000	0.0012	0.0073	0.0000	1	0	0.000
² D _{5/2} ⁽¹⁾	7426	1347	0.0230	0.0024	0.0000	3.3071	16	31	0.002
⁴ G _{7/2}	8240	1214	0.2207	0.0481	0.0000	0.0000	217	0	0.011
⁴ G _{5/2}	8871	1127	0.0503	0.0007	0.0000	0.0000	56	0	0.003
² K _{13/2}	9248	1081	0.0000	0.0000	0.0576	0.0000	29	0	0.001
² P _{1/2}	9323	1073	0.0007	0.0000	0.0000	0.6590	1	12	0.001
² P _{3/2}	10743	931	0.1307	0.0000	0.0000	0.7603	258	22	0.014
⁴ G _{7/2}	14210	704	0.1081	0.0186	0.0000	0.0000	541	0	0.027
² K _{15/2}	14547	687	0.0000	0.0000	0.0577	0.0000	116	0	0.006
⁴ G _{9/2}	14813	675	0.0000	0.0412	0.1426	0.0000	411	0	0.021
⁴ G _{11/2}	15873	630	0.0000	0.0054	0.0154	0.0000	58	0	0.003
⁴ F _{9/2}	17731	564	0.0000	0.2044	0.0392	0.0000	1068	0	0.054
⁴ F _{3/2}	19727	507	0.0103	0.0000	0.0000	0.0134	128	2	0.007
⁴ F _{5/2}	20116	497	0.0389	0.0910	0.0000	0.0722	1120	14	0.057
⁴ F _{7/2}	21806	459	0.1097	0.0275	0.0000	0.0000	2092	0	0.105
² H _{11/2} ⁽²⁾	23135	432	0.0000	0.0012	0.1739	0.0000	1447	0	0.073
⁴ S _{3/2}	23889	419	0.1173	0.0000	0.0000	0.0065	2628	2	0.132
⁴ F _{9/2}	27038	370	0.0000	0.0024	0.0001	0.0000	42	0	0.002
⁴ I _{9/2}	29861	335	0.0000	0.1613	0.0064	0.0000	3737	0	0.188
⁴ I _{11/2}	32107	311	0.0000	0.1506	0.0000	0.0000	4242	0	0.214
⁴ I _{13/2}	35758	280	0.0000	0.0000	0.0272	0.0000	869	0	0.044

Table D.3: Radiative emission properties of Er:ZBLAN (*continued*)

final	k_{calc} cm ⁻¹	λ_{calc} nm	$ \mathbf{U}^{(2)} ^2$	$ \mathbf{U}^{(4)} ^2$	$ \mathbf{U}^{(6)} ^2$	$ \mathbf{M}/\beta_m ^2$	A_{ed} s ⁻¹	A_{md} s ⁻¹	β
⁴ I _{15/2}	42293	236	0.0000	0.0000	0.0123	0.0000	672	0	0.034
	initial: ² L _{17/2}						$\tau = 0.12$ ms		
² I _{11/2}	464	—	0.0000	0.0156	0.1371	0.0000	0	0	0.000
⁴ D _{7/2}	2309	4331	0.0000	0.0000	0.0362	0.0000	0	0	0.000
⁴ D _{5/2}	2888	3463	0.0000	0.0000	0.0572	0.0000	0	0	0.000
² H _{9/2} ⁽²⁾	5120	1953	0.0000	0.0000	0.1342	0.0000	3	0	0.000
² D _{5/2} ⁽¹⁾	6714	1489	0.0000	0.0000	0.3949	0.0000	17	0	0.002
⁴ G _{7/2}	7528	1328	0.0000	0.0000	0.0261	0.0000	2	0	0.000
⁴ G _{5/2}	8159	1226	0.0000	0.0000	0.0126	0.0000	1	0	0.000
² K _{13/2}	8536	1171	0.1764	0.4877	0.0574	0.0000	98	0	0.012
² P _{1/2}	8611	1161	0.0000	0.0000	0.0000	0.0000	0	0	0.000
² P _{3/2}	10031	997	0.0000	0.0000	0.0000	0.0000	0	0	0.000
⁴ G _{7/2}	13498	741	0.0000	0.0000	0.1680	0.0000	60	0	0.007
² K _{15/2}	13834	723	0.1888	2.0767	0.9792	0.4743	1537	6	0.193
⁴ G _{9/2}	14101	709	0.0000	0.0011	0.0112	0.0000	5	0	0.001
⁴ G _{11/2}	15161	660	0.0000	0.4831	0.0768	0.0000	341	0	0.043
⁴ F _{9/2}	17019	588	0.0000	0.0776	0.3223	0.0000	300	0	0.037
⁴ F _{3/2}	19015	526	0.0000	0.0000	0.0000	0.0000	0	0	0.000
⁴ F _{5/2}	19404	515	0.0000	0.0000	0.0729	0.0000	78	0	0.010
⁴ F _{7/2}	21094	474	0.0000	0.0000	0.0008	0.0000	1	0	0.000
² H _{11/2} ⁽²⁾	22423	446	0.0000	0.4963	0.3520	0.0000	1608	0	0.201
⁴ S _{3/2}	23177	431	0.0000	0.0000	0.0000	0.0000	0	0	0.000
⁴ F _{9/2}	26326	380	0.0000	0.0026	0.0677	0.0000	194	0	0.024
⁴ I _{9/2}	29148	343	0.0000	0.0342	0.1792	0.0000	829	0	0.103
⁴ I _{11/2}	31394	319	0.0000	0.1799	0.0913	0.0000	1481	0	0.185
⁴ I _{13/2}	35045	285	0.0011	0.0000	0.0034	0.0000	41	0	0.005
⁴ I _{15/2}	41581	240	0.0046	0.0643	0.0318	0.0024	1413	1	0.176
	initial: ² I _{11/2}						$\tau = 0.12$ ms		
⁴ D _{7/2}	1845	5421	0.0041	0.0000	0.0198	0.0000	0	0	0.000
⁴ D _{5/2}	2424	4126	0.0000	0.0106	0.0604	0.0000	0	0	0.000

Table D.3: Radiative emission properties of Er:ZBLAN (*continued*)

final	k_{calc} cm ⁻¹	λ_{calc} nm	$ \mathbf{U}^{(2)} ^2$	$ \mathbf{U}^{(4)} ^2$	$ \mathbf{U}^{(6)} ^2$	$ \mathbf{M}/\beta_m ^2$	A_{ed} s ⁻¹	A_{md} s ⁻¹	β
² H _{9/2} ⁽²⁾	4656	2148	0.0002	0.0325	0.0288	0.0005	1	0	0.000
² D _{5/2} ⁽¹⁾	6250	1600	0.0000	0.0772	0.3065	0.0000	21	0	0.002
⁴ G _{7/2}	7064	1416	0.0075	0.0827	0.0129	0.0000	10	0	0.001
⁴ G _{5/2}	7695	1300	0.0000	0.0011	0.0001	0.0000	0	0	0.000
² K _{13/2}	8072	1239	0.2577	0.8230	0.4405	0.4072	236	2	0.028
² P _{1/2}	8147	1227	0.0000	0.0000	0.1675	0.0000	19	0	0.002
² P _{3/2}	9567	1045	0.0000	0.1894	0.1489	0.0000	72	0	0.008
⁴ G _{7/2}	13034	767	0.0201	0.0642	0.0624	0.0000	92	0	0.011
² K _{15/2}	13370	748	0.7601	0.2012	0.0896	0.0000	1146	0	0.133
⁴ G _{9/2}	13637	733	0.0074	0.0241	0.0052	0.1087	29	2	0.004
⁴ G _{11/2}	14697	680	0.0043	0.2449	0.0102	0.0591	223	1	0.026
⁴ F _{9/2}	16554	604	0.2703	0.1107	0.3041	0.0053	1096	0	0.128
⁴ F _{3/2}	18551	539	0.0000	0.0694	0.0002	0.0000	120	0	0.014
⁴ F _{5/2}	18939	528	0.0000	0.0143	0.0464	0.0000	95	0	0.011
⁴ F _{7/2}	20630	485	0.0057	0.0252	0.0016	0.0000	91	0	0.011
² H _{11/2} ⁽²⁾	21959	455	0.0151	0.1352	0.1208	0.1886	762	16	0.091
⁴ S _{3/2}	22713	440	0.0000	0.0295	0.0717	0.0000	281	0	0.033
⁴ F _{9/2}	25862	387	0.0016	0.0060	0.0682	0.0076	308	1	0.036
⁴ I _{9/2}	28684	349	0.0779	0.0801	0.1802	0.0457	2516	9	0.294
⁴ I _{11/2}	30930	323	0.0063	0.0536	0.0274	0.0228	737	5	0.086
⁴ I _{13/2}	34581	289	0.0023	0.0019	0.0000	0.0085	77	3	0.009
⁴ I _{15/2}	41117	243	0.0002	0.0269	0.0033	0.0000	617	0	0.072
	initial: ⁴ D _{7/2}						$\tau = 0.02$ ms		
⁴ D _{5/2}	579	–	0.1646	0.0856	0.0019	2.5413	0	0	0.000
² H _{9/2} ⁽²⁾	2811	3558	0.0032	0.0002	0.0069	0.0097	0	0	0.000
² D _{5/2} ⁽¹⁾	4405	2270	0.1605	0.1105	0.0045	0.8744	15	1	0.000
⁴ G _{7/2}	5219	1916	0.0008	0.0003	0.1422	0.0484	7	0	0.000
⁴ G _{5/2}	5850	1709	0.0018	0.0083	0.2766	0.1173	19	0	0.000
² K _{13/2}	6227	1606	0.0000	0.0002	0.0177	0.0000	1	0	0.000
² P _{1/2}	6302	1587	0.0000	0.0383	0.0000	0.0000	4	0	0.000

Table D.3: Radiative emission properties of Er:ZBLAN (*continued*)

final	k_{calc} cm ⁻¹	λ_{calc} nm	$ \mathbf{U}^{(2)} ^2$	$ \mathbf{U}^{(4)} ^2$	$ \mathbf{U}^{(6)} ^2$	$ \mathbf{M}/\beta_m ^2$	A_{ed} s ⁻¹	A_{md} s ⁻¹	β
² P _{3/2}	7722	1295	0.0481	0.0028	0.0000	0.0000	18	0	0.000
⁴ G _{7/2}	11189	894	0.0131	0.0092	0.1611	0.1527	93	2	0.002
² K _{15/2}	11526	868	0.0000	0.0008	0.0370	0.0000	19	0	0.000
⁴ G _{9/2}	11792	848	0.2280	0.0209	0.1805	0.1821	408	3	0.008
⁴ G _{11/2}	12852	778	0.4595	0.0190	0.0180	0.0000	809	0	0.016
⁴ F _{9/2}	14710	680	0.1566	0.0073	0.0118	0.0440	422	2	0.009
⁴ F _{3/2}	16706	599	0.0566	0.0789	0.0000	0.0000	362	0	0.007
⁴ F _{5/2}	17095	585	0.0419	0.2438	0.0004	0.0576	664	3	0.014
⁴ F _{7/2}	18785	532	0.2457	0.4282	0.0019	0.0014	2479	0	0.050
² H _{11/2} ⁽²⁾	20114	497	0.6851	0.0068	0.0343	0.0000	4649	0	0.094
⁴ S _{3/2}	20868	479	0.3391	0.0084	0.0000	0.0000	2542	0	0.052
⁴ F _{9/2}	24017	416	0.3553	0.1483	0.0002	0.0007	4897	0	0.099
⁴ I _{9/2}	26840	373	0.0929	0.0719	0.0026	0.0002	2089	0	0.042
⁴ I _{11/2}	29085	344	0.0107	0.0379	0.0228	0.0000	802	0	0.016
⁴ I _{13/2}	32737	305	0.0000	0.2684	0.0605	0.0000	4751	0	0.096
⁴ I _{15/2}	39272	255	0.0000	0.8856	0.0278	0.0000	24236	0	0.492
initial: ⁴ D _{5/2}							$\tau = 0.04$ ms		
² H _{9/2} ⁽²⁾	2232	4481	0.0012	0.1138	0.0684	0.0000	1	0	0.000
² D _{5/2} ⁽¹⁾	3826	2614	0.1969	0.0621	0.0000	0.1370	13	0	0.001
⁴ G _{7/2}	4640	2155	0.0258	0.1085	0.1396	0.2515	14	0	0.001
⁴ G _{5/2}	5271	1897	0.0165	0.0050	0.0000	0.3543	3	1	0.000
² K _{13/2}	5648	1770	0.0000	0.0475	0.0529	0.0000	9	0	0.000
² P _{1/2}	5723	1747	0.0892	0.0000	0.0000	0.0000	18	0	0.001
² P _{3/2}	7143	1400	0.0863	0.0067	0.0000	1.0200	34	6	0.002
⁴ G _{7/2}	10610	943	0.2133	0.0293	0.0005	0.1168	290	2	0.013
² K _{15/2}	10947	914	0.0000	0.0000	0.1200	0.0000	68	0	0.003
⁴ G _{9/2}	11213	892	0.1965	0.0035	0.0269	0.0000	314	0	0.014
⁴ G _{11/2}	12273	815	0.0000	0.1203	0.0731	0.0000	178	0	0.008
⁴ F _{9/2}	14131	708	0.1205	0.0053	0.0035	0.0000	376	0	0.016
⁴ F _{3/2}	16127	620	0.1313	0.1909	0.0000	0.0162	1023	1	0.044

Table D.3: Radiative emission properties of Er:ZBLAN (*continued*)

final	k_{calc} cm ⁻¹	λ_{calc} nm	$ \mathbf{U}^{(2)} ^2$	$ \mathbf{U}^{(4)} ^2$	$ \mathbf{U}^{(6)} ^2$	$ \mathbf{M}/\beta_m ^2$	A_{ed} s ⁻¹	A_{md} s ⁻¹	β
⁴ F _{5/2}	16516	605	0.1670	0.0149	0.0000	0.0053	845	0	0.037
⁴ F _{7/2}	18206	549	0.0904	0.0807	0.0074	0.1293	872	12	0.038
² H _{11/2} ⁽²⁾	19535	512	0.0000	0.0680	0.0296	0.0000	373	0	0.016
⁴ S _{3/2}	20289	493	0.2124	0.0101	0.0000	0.0675	1970	9	0.086
⁴ F _{9/2}	23438	427	0.2379	0.3573	0.0164	0.0000	5976	0	0.259
⁴ I _{9/2}	26261	381	0.0469	0.0097	0.0381	0.0000	1346	0	0.058
⁴ I _{11/2}	28507	351	0.0000	0.1719	0.0016	0.0000	2244	0	0.097
⁴ I _{13/2}	32158	311	0.0000	0.3341	0.0063	0.0000	6402	0	0.277
⁴ I _{15/2}	38693	258	0.0000	0.0000	0.0256	0.0000	703	0	0.030
	initial: ² H _{9/2} ⁽²⁾						$\tau = 0.18$ ms		
² D _{5/2} ⁽¹⁾	1594	6274	0.0078	0.1087	0.0519	0.0000	0	0	0.000
⁴ G _{7/2}	2408	4153	0.0198	0.0050	0.1759	4.2013	1	1	0.000
⁴ G _{5/2}	3039	3290	0.0042	0.0254	0.0221	0.0000	0	0	0.000
² K _{13/2}	3417	2927	0.0228	0.0267	0.3381	0.0000	4	0	0.001
² P _{1/2}	3491	2864	0.0000	0.0468	0.0000	0.0000	1	0	0.000
² P _{3/2}	4911	2036	0.0000	0.0078	0.0216	0.0000	1	0	0.000
⁴ G _{7/2}	8378	1194	0.0076	0.0239	0.0926	0.0071	21	0	0.004
² K _{15/2}	8715	1147	0.0000	0.4446	0.0839	0.0000	108	0	0.019
⁴ G _{9/2}	8981	1113	0.0015	0.0362	0.0004	1.6643	9	11	0.004
⁴ G _{11/2}	10041	996	0.0751	0.0010	0.5230	4.1724	186	39	0.040
⁴ F _{9/2}	11899	840	0.0820	0.0087	0.0242	2.6920	104	42	0.026
⁴ F _{3/2}	13895	720	0.0000	0.0182	0.0211	0.0000	30	0	0.005
⁴ F _{5/2}	14284	700	0.0144	0.0072	0.0075	0.0000	39	0	0.007
⁴ F _{7/2}	15974	626	0.0473	0.0009	0.0475	0.0750	176	3	0.032
² H _{11/2} ⁽²⁾	17304	578	0.0183	0.0627	0.2123	0.3183	455	15	0.085
⁴ S _{3/2}	18057	554	0.0000	0.0245	0.0012	0.0000	49	0	0.009
⁴ F _{9/2}	21206	472	0.0061	0.0037	0.0005	0.0099	51	1	0.009
⁴ I _{9/2}	24029	416	0.0044	0.0002	0.0155	0.0262	99	3	0.018
⁴ I _{11/2}	26275	381	0.0086	0.0226	0.0256	0.1104	365	19	0.069
⁴ I _{13/2}	29926	334	0.1445	0.0150	0.0175	0.0000	2866	0	0.516

Table D.3: Radiative emission properties of Er:ZBLAN (*continued*)

final	k_{calc} cm ⁻¹	λ_{calc} nm	$ \mathbf{U}^{(2)} ^2$	$ \mathbf{U}^{(4)} ^2$	$ \mathbf{U}^{(6)} ^2$	$ \mathbf{M}/\beta_m ^2$	A_{ed} s ⁻¹	A_{md} s ⁻¹	β
⁴ I _{15/2}	36461	274	0.0000	0.0510	0.0001	0.0000	860	0	0.155
	initial: ² D _{5/2} ⁽¹⁾						$\tau = 0.22$ ms		
⁴ G _{7/2}	814	—	0.0002	0.0102	0.0002	0.0522	0	0	0.000
⁴ G _{5/2}	1445	6920	0.0032	0.0047	0.0000	0.0130	0	0	0.000
² K _{13/2}	1823	5487	0.0000	0.0020	0.0204	0.0000	0	0	0.000
² P _{1/2}	1897	5271	0.0055	0.0000	0.0000	0.0000	0	0	0.000
² P _{3/2}	3317	3015	0.0334	0.0061	0.0000	0.5647	1	0	0.000
⁴ G _{7/2}	6784	1474	0.0556	0.0056	0.1982	0.0691	46	0	0.010
² K _{15/2}	7121	1404	0.0000	0.0000	0.3593	0.0000	56	0	0.012
⁴ G _{9/2}	7387	1354	0.2279	0.0001	0.1404	0.0000	121	0	0.026
⁴ G _{11/2}	8447	1184	0.0000	0.0222	0.0048	0.0000	8	0	0.002
⁴ F _{9/2}	10305	970	0.0260	0.0067	0.0098	0.0000	39	0	0.008
⁴ F _{3/2}	12301	813	0.0228	0.0150	0.0000	0.1413	60	4	0.014
⁴ F _{5/2}	12690	788	0.0628	0.0388	0.0000	0.1896	179	6	0.040
⁴ F _{7/2}	14380	695	0.0173	0.0000	0.0000	1.6349	55	75	0.028
² H _{11/2} ⁽²⁾	15710	637	0.0000	0.0723	0.0315	0.0000	204	0	0.044
⁴ S _{3/2}	16463	607	0.0472	0.0025	0.0000	0.0000	232	0	0.050
⁴ F _{9/2}	19612	510	0.0434	0.1184	0.0039	0.0000	853	0	0.185
⁴ I _{9/2}	22435	446	0.0212	0.0032	0.0019	0.0000	290	0	0.063
⁴ I _{11/2}	24681	405	0.0000	0.0726	0.0630	0.0000	1025	0	0.222
⁴ I _{13/2}	28332	353	0.0000	0.0159	0.0667	0.0000	887	0	0.192
⁴ I _{15/2}	34867	287	0.0000	0.0000	0.0244	0.0000	480	0	0.104
	initial: ⁴ G _{7/2}						$\tau = 0.09$ ms		
⁴ G _{5/2}	631	—	0.0015	0.1120	0.0386	6.5418	0	0	0.000
² K _{13/2}	1008	—	0.0000	0.5054	0.0223	0.0000	0	0	0.000
² P _{1/2}	1083	—	0.0000	0.0037	0.0000	0.0000	0	0	0.000
² P _{3/2}	2503	3995	0.0213	0.1101	0.0000	0.0000	1	0	0.000
⁴ G _{7/2}	5970	1675	0.0413	0.0018	0.0377	0.1941	10	0	0.001
² K _{15/2}	6307	1586	0.0000	0.0454	0.0308	0.0000	7	0	0.001
⁴ G _{9/2}	6573	1521	0.0004	0.2378	0.0237	6.8767	29	22	0.004

Table D.3: Radiative emission properties of Er:ZBLAN (*continued*)

final	k_{calc} cm ⁻¹	λ_{calc} nm	$ \mathbf{U}^{(2)} ^2$	$ \mathbf{U}^{(4)} ^2$	$ \mathbf{U}^{(6)} ^2$	$ \mathbf{M}/\beta_m ^2$	A_{ed} s ⁻¹	A_{md} s ⁻¹	β
⁴ G _{11/2}	7633	1310	0.0025	0.0167	0.5056	0.0000	76	0	0.007
⁴ F _{9/2}	9491	1054	0.0995	0.0210	0.4090	0.1347	188	1	0.016
⁴ F _{3/2}	11487	871	0.0437	0.0002	0.0000	0.0000	53	0	0.005
⁴ F _{5/2}	11876	842	0.2058	0.0059	0.1311	0.1814	351	3	0.031
⁴ F _{7/2}	13566	737	0.1383	0.0519	0.0038	0.3684	332	11	0.030
² H _{11/2} ⁽²⁾	14895	671	0.0492	0.0023	0.0009	0.0000	135	0	0.012
⁴ S _{3/2}	15649	639	0.0107	0.1451	0.0000	0.0000	258	0	0.022
⁴ F _{9/2}	18798	532	0.0001	0.0006	0.0279	0.0301	63	2	0.006
⁴ I _{9/2}	21621	463	0.0251	0.1178	0.0156	0.0751	748	9	0.065
⁴ I _{11/2}	23867	419	0.5284	0.0931	0.0521	0.0000	6663	0	0.575
⁴ I _{13/2}	27518	363	0.0000	0.1882	0.0512	0.0000	1999	0	0.173
⁴ I _{15/2}	34053	294	0.0000	0.0345	0.0031	0.0000	628	0	0.054
	initial: ⁴ G _{5/2}						$\tau = 0.07$ ms		
² K _{13/2}	377	—	0.0000	0.0143	0.0368	0.0000	0	0	0.000
² P _{1/2}	452	—	0.0820	0.0000	0.0000	0.0000	0	0	0.000
² P _{3/2}	1872	5341	0.1049	0.0003	0.0000	0.0043	1	0	0.000
⁴ G _{7/2}	5339	1873	0.0028	0.2299	0.1271	5.2418	27	12	0.003
² K _{15/2}	5676	1762	0.0000	0.0000	0.0002	0.0000	0	0	0.000
⁴ G _{9/2}	5942	1683	0.0177	0.0714	0.2727	0.0000	36	0	0.002
⁴ G _{11/2}	7002	1428	0.0000	0.0003	0.0359	0.0000	5	0	0.000
⁴ F _{9/2}	8860	1129	0.0241	0.0298	0.0243	0.0000	36	0	0.002
⁴ F _{3/2}	10856	921	0.3368	0.0805	0.0000	0.0241	513	0	0.034
⁴ F _{5/2}	11245	889	0.3154	0.1225	0.0000	0.0280	570	1	0.038
⁴ F _{7/2}	12935	773	0.0393	0.1276	0.1519	0.0352	381	1	0.025
² H _{11/2} ⁽²⁾	14264	701	0.0000	0.0000	0.1048	0.0000	132	0	0.009
⁴ S _{3/2}	15018	666	0.0384	0.1331	0.0000	0.0055	382	0	0.025
⁴ F _{9/2}	18167	550	0.2354	0.1814	0.1308	0.0000	2456	0	0.162
⁴ I _{9/2}	20990	476	0.6043	0.2206	0.0018	0.0000	7194	0	0.474
⁴ I _{11/2}	23236	430	0.0000	0.3406	0.0563	0.0000	2662	0	0.175
⁴ I _{13/2}	26887	372	0.0000	0.0270	0.0509	0.0000	737	0	0.049

Table D.3: Radiative emission properties of Er:ZBLAN (*continued*)

final	k_{calc} cm ⁻¹	λ_{calc} nm	$ \mathbf{U}^{(2)} ^2$	$ \mathbf{U}^{(4)} ^2$	$ \mathbf{U}^{(6)} ^2$	$ \mathbf{M}/\beta_m ^2$	A_{ed} s ⁻¹	A_{md} s ⁻¹	β
⁴ I _{15/2}	33422	299	0.0000	0.0000	0.0025	0.0000	43	0	0.003
	initial: ² K _{13/2}						$\tau = 0.56$ ms		
² P _{1/2}	75	—	0.0000	0.0000	0.0388	0.0000	0	0	0.000
² P _{3/2}	1495	6690	0.0000	0.0000	0.3965	0.0000	0	0	0.000
⁴ G _{7/2}	4962	2015	0.0000	0.4748	0.0039	0.0000	13	0	0.007
² K _{15/2}	5298	1887	0.1723	0.1101	0.0008	6.4116	15	6	0.012
⁴ G _{9/2}	5565	1797	0.0107	0.0000	0.1612	0.0000	6	0	0.003
⁴ G _{11/2}	6625	1509	0.0240	0.0078	0.2056	0.0017	15	0	0.008
⁴ F _{9/2}	8482	1179	0.0279	0.1828	0.4824	0.0000	87	0	0.049
⁴ F _{3/2}	10479	954	0.0000	0.0000	0.1078	0.0000	23	0	0.013
⁴ F _{5/2}	10867	920	0.0000	0.0008	0.0049	0.0000	1	0	0.001
⁴ F _{7/2}	12557	796	0.0000	0.0539	0.0074	0.0000	27	0	0.015
² H _{11/2} ⁽²⁾	13887	720	0.0078	0.0049	0.3156	0.0101	170	0	0.096
⁴ S _{3/2}	14641	683	0.0000	0.0000	0.1238	0.0000	72	0	0.041
⁴ F _{9/2}	17789	562	0.0009	0.0170	0.0019	0.0000	27	0	0.015
⁴ I _{9/2}	20612	485	0.0321	0.0720	0.2591	0.0000	707	0	0.397
⁴ I _{11/2}	22858	437	0.0011	0.0017	0.1455	0.1498	341	12	0.198
⁴ I _{13/2}	26509	377	0.0045	0.0018	0.0015	0.1378	53	17	0.040
⁴ I _{15/2}	33045	303	0.0031	0.0028	0.0148	0.0131	183	3	0.105
	initial: ² P _{1/2}						$\tau = 0.45$ ms		
² P _{3/2}	1420	7042	0.0036	0.0000	0.0000	0.6430	0	0	0.000
⁴ G _{7/2}	4887	2046	0.0000	0.0266	0.0000	0.0000	5	0	0.002
² K _{15/2}	5223	1914	0.0000	0.0000	0.0000	0.0000	0	0	0.000
⁴ G _{9/2}	5490	1822	0.0000	0.0084	0.0000	0.0000	2	0	0.001
⁴ G _{11/2}	6550	1527	0.0000	0.0000	0.0263	0.0000	9	0	0.004
⁴ F _{9/2}	8408	1189	0.0000	0.0001	0.0000	0.0000	0	0	0.000
⁴ F _{3/2}	10404	961	0.0339	0.0000	0.0000	0.0067	122	0	0.055
⁴ F _{5/2}	10793	927	0.0069	0.0000	0.0000	0.0000	28	0	0.013
⁴ F _{7/2}	12483	801	0.0000	0.0200	0.0000	0.0000	63	0	0.028
² H _{11/2} ⁽²⁾	13812	724	0.0000	0.0000	0.1678	0.0000	576	0	0.261

Table D.3: Radiative emission properties of Er:ZBLAN (*continued*)

final	k_{calc} cm ⁻¹	λ_{calc} nm	$ \mathbf{U}^{(2)} ^2$	$ \mathbf{U}^{(4)} ^2$	$ \mathbf{U}^{(6)} ^2$	$ \mathbf{M}/\beta_m ^2$	A_{ed} s ⁻¹	A_{md} s ⁻¹	β
⁴ S _{3/2}	14566	687	0.0060	0.0000	0.0000	0.2635	60	37	0.044
⁴ F _{9/2}	17715	565	0.0000	0.0465	0.0000	0.0000	420	0	0.191
⁴ I _{9/2}	20537	487	0.0000	0.0258	0.0000	0.0000	366	0	0.166
⁴ I _{11/2}	22783	439	0.0000	0.0000	0.0323	0.0000	509	0	0.231
⁴ I _{13/2}	26434	378	0.0000	0.0000	0.0003	0.0000	6	0	0.003
⁴ I _{15/2}	32970	303	0.0000	0.0000	0.0000	0.0000	0	0	0.000
	initial: ² P _{3/2}						$\tau = 0.24$ ms		
⁴ G _{7/2}	3467	2884	0.0122	0.0008	0.0000	0.0000	1	0	0.000
² K _{15/2}	3803	2629	0.0000	0.0000	0.0312	0.0000	1	0	0.000
⁴ G _{9/2}	4070	2457	0.0000	0.0080	0.0039	0.0000	1	0	0.000
⁴ G _{11/2}	5130	1949	0.0000	0.0314	0.0101	0.0000	4	0	0.001
⁴ F _{9/2}	6988	1431	0.0000	0.2047	0.2604	0.0000	113	0	0.027
⁴ F _{3/2}	8984	1113	0.0124	0.0000	0.0000	1.8208	14	30	0.011
⁴ F _{5/2}	9373	1067	0.0176	0.0427	0.0000	1.4665	51	28	0.019
⁴ F _{7/2}	11063	904	0.0201	0.0085	0.0000	0.0000	53	0	0.013
² H _{11/2} ⁽²⁾	12392	807	0.0000	0.0155	0.0288	0.0000	59	0	0.014
⁴ S _{3/2}	13146	761	0.0801	0.0000	0.0000	0.3928	291	20	0.075
⁴ F _{9/2}	16295	614	0.0000	0.0467	0.0058	0.0000	180	0	0.043
⁴ I _{9/2}	19117	523	0.0000	0.0419	0.0050	0.0000	261	0	0.063
⁴ I _{11/2}	21363	468	0.0000	0.1007	0.0383	0.0000	1053	0	0.254
⁴ I _{13/2}	25014	400	0.0000	0.0000	0.1518	0.0000	1592	0	0.384
⁴ I _{15/2}	31550	317	0.0000	0.0000	0.0184	0.0000	397	0	0.096
	initial: ⁴ G _{7/2}						$\tau = 0.15$ ms		
² K _{15/2}	337	—	0.0000	0.1198	0.0044	0.0000	0	0	0.000
⁴ G _{9/2}	603	—	0.0034	0.1886	0.1502	6.2518	0	0	0.000
⁴ G _{11/2}	1663	6012	0.0142	0.0553	0.0176	0.0000	0	0	0.000
⁴ F _{9/2}	3521	2840	0.0150	0.0051	0.0243	3.1545	1	2	0.000
⁴ F _{3/2}	5517	1813	0.0952	0.0339	0.0000	0.0000	15	0	0.002
⁴ F _{5/2}	5906	1693	0.3811	0.0016	0.0381	0.5558	65	1	0.010
⁴ F _{7/2}	7596	1317	0.1224	0.0410	0.0069	0.5744	51	3	0.008

Table D.3: Radiative emission properties of Er:ZBLAN (*continued*)

final	k_{calc} cm ⁻¹	λ_{calc} nm	$ \mathbf{U}^{(2)} ^2$	$ \mathbf{U}^{(4)} ^2$	$ \mathbf{U}^{(6)} ^2$	$ \mathbf{M}/\beta_m ^2$	A_{ed} s ⁻¹	A_{md} s ⁻¹	β
² H _{11/2} ⁽²⁾	8925	1120	0.0010	0.0377	0.2714	0.0000	74	0	0.011
⁴ S _{3/2}	9679	1033	0.0461	0.1595	0.0000	0.0000	91	0	0.014
⁴ F _{9/2}	12828	780	0.0000	0.0101	0.0143	0.0892	18	2	0.003
⁴ I _{9/2}	15651	639	0.1638	0.3675	0.2203	0.1180	1351	5	0.208
⁴ I _{11/2}	17896	559	0.5028	0.2752	0.1632	0.0000	3279	0	0.503
⁴ I _{13/2}	21548	464	0.0000	0.1001	0.0309	0.0000	513	0	0.079
⁴ I _{15/2}	28083	356	0.0000	0.0198	0.1157	0.0000	1051	0	0.161
	initial: ² K _{15/2}						$\tau = 0.76$ ms		
⁴ G _{9/2}	266	—	0.0000	0.0060	0.0560	0.0000	0	0	0.000
⁴ G _{11/2}	1327	7538	0.0992	0.0579	0.6707	0.0000	0	0	0.000
⁴ F _{9/2}	3184	3141	0.0000	0.7155	0.0816	0.0000	5	0	0.004
⁴ F _{3/2}	5180	1930	0.0000	0.0000	0.0000	0.0000	0	0	0.000
⁴ F _{5/2}	5569	1796	0.0000	0.0000	0.0461	0.0000	1	0	0.001
⁴ F _{7/2}	7259	1378	0.0000	0.0001	0.0001	0.0000	0	0	0.000
² H _{11/2} ⁽²⁾	8589	1164	0.1013	0.0000	1.1473	0.0000	143	0	0.108
⁴ S _{3/2}	9343	1070	0.0000	0.0000	0.0039	0.0000	1	0	0.000
⁴ F _{9/2}	12491	801	0.0000	0.0805	0.0128	0.0000	36	0	0.027
⁴ I _{9/2}	15314	653	0.0000	0.2146	0.0982	0.0000	213	0	0.162
⁴ I _{11/2}	17560	569	0.0469	0.0018	0.2474	0.0000	324	0	0.246
⁴ I _{13/2}	21211	471	0.0001	0.0016	0.0255	0.2480	44	14	0.044
⁴ I _{15/2}	27746	360	0.0213	0.0039	0.0733	0.5126	472	65	0.407
	initial: ⁴ G _{9/2}						$\tau = 0.09$ ms		
⁴ G _{11/2}	1060	—	0.0000	0.2118	0.1539	3.4405	0	0	0.000
⁴ F _{9/2}	2918	3427	0.0246	0.0003	0.0352	1.6269	1	0	0.000
⁴ F _{3/2}	4914	2035	0.0000	0.1714	0.1128	0.0000	10	0	0.001
⁴ F _{5/2}	5303	1886	0.1649	0.0841	0.0025	0.0000	20	0	0.002
⁴ F _{7/2}	6993	1430	0.6215	0.0071	0.1210	0.0020	146	0	0.012
² H _{11/2} ⁽²⁾	8322	1202	0.0236	0.3431	0.1555	8.5254	95	45	0.012
⁴ S _{3/2}	9076	1102	0.0000	0.1663	0.0101	0.0000	42	0	0.004
⁴ F _{9/2}	12225	818	0.2176	0.3174	0.3666	0.2976	614	5	0.053

Table D.3: Radiative emission properties of Er:ZBLAN (*continued*)

final	k_{calc} cm ⁻¹	λ_{calc} nm	$ \mathbf{U}^{(2)} ^2$	$ \mathbf{U}^{(4)} ^2$	$ \mathbf{U}^{(6)} ^2$	$ \mathbf{M}/\beta_m ^2$	A_{ed} s ⁻¹	A_{md} s ⁻¹	β
⁴ I _{9/2}	15048	665	0.0050	0.0049	0.0038	0.1687	20	5	0.002
⁴ I _{11/2}	17293	578	0.0931	0.1585	0.0165	0.0134	600	1	0.051
⁴ I _{13/2}	20945	477	1.1054	0.3654	0.0114	0.0000	7749	0	0.660
⁴ I _{15/2}	27480	364	0.0000	0.2349	0.1353	0.0000	2389	0	0.203
	initial: ⁴ G _{11/2}						$\tau = 0.07$ ms		
⁴ F _{9/2}	1857	5384	0.2920	0.1077	0.1391	2.4960	1	0	0.000
⁴ F _{3/2}	3854	2595	0.0000	0.0232	0.0921	0.0000	1	0	0.000
⁴ F _{5/2}	4242	2357	0.0000	0.0366	0.0817	0.0000	2	0	0.000
⁴ F _{7/2}	5933	1686	0.0877	0.1280	0.0174	0.0000	17	0	0.001
² H _{11/2} ⁽²⁾	7262	1377	0.0004	0.1507	0.0500	3.6527	19	11	0.002
⁴ S _{3/2}	8016	1248	0.0000	0.1284	0.0040	0.0000	18	0	0.001
⁴ F _{9/2}	11165	896	0.4305	0.0378	0.0126	0.2558	336	3	0.023
⁴ I _{9/2}	13987	715	0.0689	0.0131	0.0221	0.0333	124	1	0.008
⁴ I _{11/2}	16233	616	0.0002	0.0491	0.0134	0.0013	70	0	0.005
⁴ I _{13/2}	19884	503	0.1012	0.2666	0.2580	0.6383	1448	39	0.101
⁴ I _{15/2}	26420	379	0.9222	0.5300	0.1165	0.0000	12592	0	0.858
	initial: ⁴ F _{9/2}						$\tau = 0.43$ ms		
⁴ F _{3/2}	1996	5010	0.0000	0.0177	0.0064	0.0000	0	0	0.000
⁴ F _{5/2}	2385	4193	0.0092	0.0227	0.0060	0.0000	0	0	0.000
⁴ F _{7/2}	4075	2454	0.0913	0.0477	0.0274	1.2815	5	1	0.003
² H _{11/2} ⁽²⁾	5405	1850	0.0276	0.1651	0.0620	0.7449	13	1	0.006
⁴ S _{3/2}	6158	1624	0.0000	0.0033	0.0015	0.0000	0	0	0.000
⁴ F _{9/2}	9307	1074	0.0074	0.0261	0.0438	5.1823	20	38	0.025
⁴ I _{9/2}	12130	824	0.0141	0.0068	0.0036	0.0403	22	1	0.010
⁴ I _{11/2}	14376	696	0.0392	0.0761	0.1098	1.1401	233	31	0.115
⁴ I _{13/2}	18027	555	0.0613	0.1065	0.3523	0.0000	977	0	0.425
⁴ I _{15/2}	24562	407	0.0000	0.0229	0.2130	0.0000	957	0	0.416
	initial: ⁴ F _{3/2}						$\tau = 0.49$ ms		
⁴ F _{5/2}	389	—	0.0609	0.0361	0.0000	6.3039	0	0	0.000

Table D.3: Radiative emission properties of Er:ZBLAN (*continued*)

final	k_{calc} cm ⁻¹	λ_{calc} nm	$ \mathbf{U}^{(2)} ^2$	$ \mathbf{U}^{(4)} ^2$	$ \mathbf{U}^{(6)} ^2$	$ \mathbf{M}/\beta_m ^2$	A_{ed} s ⁻¹	A_{md} s ⁻¹	β
⁴ F _{7/2}	2079	4810	0.0029	0.0579	0.0000	0.0000	0	0	0.000
² H _{11/2} ⁽²⁾	3408	2934	0.0000	0.0002	0.0029	0.0000	0	0	0.000
⁴ S _{3/2}	4162	2403	0.0258	0.0000	0.0000	3.0351	3	5	0.004
⁴ F _{9/2}	7311	1368	0.0000	0.0033	0.0595	0.0000	16	0	0.008
⁴ I _{9/2}	10134	987	0.0000	0.2323	0.0573	0.0000	232	0	0.114
⁴ I _{11/2}	12380	808	0.0000	0.0919	0.4836	0.0000	736	0	0.361
⁴ I _{13/2}	16031	624	0.0000	0.0000	0.0364	0.0000	98	0	0.048
⁴ I _{15/2}	22566	443	0.0000	0.0000	0.1239	0.0000	947	0	0.465
	initial: ⁴ F _{5/2}						$\tau = 0.44$ ms		
⁴ F _{7/2}	1690	5917	0.0772	0.0505	0.1001	10.1114	1	1	0.001
² H _{11/2} ⁽²⁾	3020	3312	0.0000	0.0594	0.1838	0.0000	3	0	0.001
⁴ S _{3/2}	3773	2650	0.0077	0.0036	0.0000	0.5896	1	0	0.000
⁴ F _{9/2}	6922	1445	0.0005	0.2365	0.3545	0.0000	92	0	0.040
⁴ I _{9/2}	9745	1026	0.0106	0.0601	0.1076	0.0000	83	0	0.036
⁴ I _{11/2}	11991	834	0.0000	0.0976	0.0028	0.0000	92	0	0.040
⁴ I _{13/2}	15642	639	0.0000	0.1800	0.3431	0.0000	943	0	0.412
⁴ I _{15/2}	22177	451	0.0000	0.0000	0.2221	0.0000	1072	0	0.469
	initial: ⁴ F _{7/2}						$\tau = 0.34$ ms		
² H _{11/2} ⁽²⁾	1330	7521	0.1246	0.0158	0.3980	0.0000	0	0	0.000
⁴ S _{3/2}	2083	4800	0.0001	0.0052	0.0000	0.0000	0	0	0.000
⁴ F _{9/2}	5232	1911	0.0120	0.0360	0.0130	6.4133	4	10	0.005
⁴ I _{9/2}	8055	1242	0.0159	0.0959	0.4300	1.8014	99	11	0.037
⁴ I _{11/2}	10301	971	0.0034	0.2660	0.1541	0.0000	174	0	0.059
⁴ I _{13/2}	13952	717	0.0000	0.3383	0.0001	0.0000	370	0	0.125
⁴ I _{15/2}	20487	488	0.0000	0.1467	0.6283	0.0000	2301	0	0.775
	initial: ² H _{11/2} ⁽²⁾						$\tau = 0.26$ ms		
⁴ S _{3/2}	754	—	0.0000	0.2000	0.0096	0.0000	0	0	0.000
⁴ F _{9/2}	3902	2562	0.3683	0.0228	0.0017	0.2819	12	0	0.003
⁴ I _{9/2}	6725	1487	0.2021	0.0661	0.2844	0.2632	56	1	0.015

Table D.3: Radiative emission properties of Er:ZBLAN (*continued*)

final	k_{calc} cm ⁻¹	λ_{calc} nm	$ \mathbf{U}^{(2)} ^2$	$ \mathbf{U}^{(4)} ^2$	$ \mathbf{U}^{(6)} ^2$	$ \mathbf{M}/\beta_m ^2$	A_{ed} s ⁻¹	A_{md} s ⁻¹	β
⁴ I _{11/2}	8971	1115	0.0356	0.1383	0.0370	1.3507	46	7	0.014
⁴ I _{13/2}	12622	792	0.0230	0.0607	0.0523	3.7573	80	58	0.036
⁴ I _{15/2}	19158	522	0.7091	0.4106	0.0934	0.0000	3625	0	0.933
initial: ⁴ S _{3/2}							$\tau = 0.73$ ms		
⁴ F _{9/2}	3149	3176	0.0000	0.0002	0.0254	0.0000	1	0	0.000
⁴ I _{9/2}	5971	1675	0.0000	0.0756	0.2539	0.0000	47	0	0.035
⁴ I _{11/2}	8217	1217	0.0000	0.0049	0.0783	0.0000	30	0	0.022
⁴ I _{13/2}	11868	843	0.0000	0.0000	0.3403	0.0000	369	0	0.271
⁴ I _{15/2}	18404	543	0.0000	0.0000	0.2233	0.0000	915	0	0.672
initial: ⁴ F _{9/2}							$\tau = 0.86$ ms		
⁴ I _{9/2}	2823	3543	0.1256	0.0060	0.0249	11.5670	2	2	0.004
⁴ I _{11/2}	5069	1973	0.0709	0.0106	1.2752	4.8271	49	6	0.047
⁴ I _{13/2}	8720	1147	0.0105	0.1536	0.0775	0.0000	50	0	0.043
⁴ I _{15/2}	15255	656	0.0000	0.5431	0.4637	0.0000	1053	0	0.906
initial: ⁴ I _{9/2}							$\tau = 6.78$ ms		
⁴ I _{11/2}	2246	4452	0.0026	0.0681	0.1379	10.6725	1	1	0.011
⁴ I _{13/2}	5897	1696	0.0004	0.0099	0.7159	0.0000	38	0	0.260
⁴ I _{15/2}	12432	804	0.0000	0.1670	0.0090	0.0000	108	0	0.729
initial: ⁴ I _{11/2}							$\tau = 7.87$ ms		
⁴ I _{13/2}	3651	2739	0.0332	0.1705	1.0886	20.7669	14	8	0.171
⁴ I _{15/2}	10186	982	0.0279	0.0003	0.3937	0.0000	105	0	0.829
initial: ⁴ I _{13/2}							$\tau = 8.52$ ms		
⁴ I _{15/2}	6535	1530	0.0195	0.1173	1.4328	18.8413	83	34	1.000

Table D.4: Radiative absorption properties of Er:ZBLAN

final	k_{calc} cm ⁻¹	λ_{calc} nm	$ \mathbf{U}^{(2)} ^2$	$ \mathbf{U}^{(4)} ^2$	$ \mathbf{U}^{(6)} ^2$	$ \mathbf{M}/\beta_m ^2$	f_{ed} 10 ⁻⁸	f_{md} 10 ⁻⁸
initial: ⁴ I _{15/2}								
⁴ I _{13/2}	6535	1530	0.0195	0.1173	1.4328	18.8413	113.9	46.6

Table D.4: Radiative absorption properties of Er:ZBLAN (*continued*)

final	k_{calc} cm ⁻¹	λ_{calc} nm	$ \mathbf{U}^{(2)} ^2$	$ \mathbf{U}^{(4)} ^2$	$ \mathbf{U}^{(6)} ^2$	$ \mathbf{M}/\beta_m ^2$	f_{ed} 10 ⁻⁸	f_{md} 10 ⁻⁸
⁴ I _{11/2}	10186	982	0.0279	0.0003	0.3937	0.0000	50.7	0.0
⁴ I _{9/2}	12432	804	0.0000	0.1670	0.0090	0.0000	28.9	0.0
⁴ F _{9/2}	15255	656	0.0000	0.5431	0.4637	0.0000	186.9	0.0
⁴ S _{3/2}	18404	543	0.0000	0.0000	0.2233	0.0000	44.5	0.0
² H _{11/2} ⁽²⁾	19158	522	0.7091	0.4106	0.0934	0.0000	486.7	0.0
⁴ F _{7/2}	20487	488	0.0000	0.1467	0.6283	0.0000	179.7	0.0
⁴ F _{5/2}	22177	451	0.0000	0.0000	0.2221	0.0000	53.5	0.0
⁴ F _{3/2}	22566	443	0.0000	0.0000	0.1239	0.0000	30.4	0.0
⁴ F _{9/2}	24562	407	0.0000	0.0229	0.2130	0.0000	64.5	0.0
⁴ G _{11/2}	26420	379	0.9222	0.5300	0.1165	0.0000	876.9	0.0
⁴ G _{9/2}	27480	364	0.0000	0.2349	0.1353	0.0000	127.8	0.0
² K _{15/2}	27746	360	0.0213	0.0039	0.0733	0.5126	39.6	5.5
⁴ G _{7/2}	28083	356	0.0000	0.0198	0.1157	0.0000	43.0	0.0
² P _{3/2}	31550	317	0.0000	0.0000	0.0184	0.0000	6.4	0.0
² P _{1/2}	32970	303	0.0000	0.0000	0.0000	0.0000	0.0	0.0
² K _{13/2}	33045	303	0.0031	0.0028	0.0148	0.0131	9.4	0.2
⁴ G _{5/2}	33422	299	0.0000	0.0000	0.0025	0.0000	0.9	0.0
⁴ G _{7/2}	34053	294	0.0000	0.0345	0.0031	0.0000	17.2	0.0
² D _{5/2} ⁽¹⁾	34867	287	0.0000	0.0000	0.0244	0.0000	9.4	0.0
² H _{9/2} ⁽²⁾	36461	274	0.0000	0.0510	0.0001	0.0000	25.5	0.0
⁴ D _{5/2}	38693	258	0.0000	0.0000	0.0256	0.0000	11.0	0.0
⁴ D _{7/2}	39272	255	0.0000	0.8856	0.0278	0.0000	491.3	0.0
² I _{11/2}	41117	243	0.0002	0.0269	0.0033	0.0000	17.0	0.0
² L _{17/2}	41581	240	0.0046	0.0643	0.0318	0.0024	57.0	0.0
⁴ D _{3/2}	42293	236	0.0000	0.0000	0.0123	0.0000	5.8	0.0
² P _{3/2}	42840	233	0.0000	0.0000	0.0004	0.0000	0.2	0.0
² I _{13/2}	43550	230	0.0053	0.0166	0.0049	0.0106	18.9	0.2
⁴ D _{1/2}	47034	213	0.0000	0.0000	0.0000	0.0000	0.0	0.0
² L _{15/2}	47809	209	0.0002	0.0026	0.0021	0.0011	3.1	0.0
² H _{9/2} ⁽¹⁾	48133	208	0.0000	0.0036	0.0001	0.0000	2.5	0.0

Table D.4: Radiative absorption properties of Er:ZBLAN (*continued*)

final	k_{calc} cm ⁻¹	λ_{calc} nm	$ \mathbf{U}^{(2)} ^2$	$ \mathbf{U}^{(4)} ^2$	$ \mathbf{U}^{(6)} ^2$	$ \mathbf{M}/\beta_m ^2$	f_{ed} 10 ⁻⁸	f_{md} 10 ⁻⁸
² D _{5/2} ⁽²⁾	48954	204	0.0000	0.0000	0.0098	0.0000	5.5	0.0
² H _{11/2} ⁽¹⁾	51132	196	0.0001	0.0084	0.0000	0.0000	6.3	0.0
² F _{7/2} ⁽²⁾	54486	184	0.0000	0.0141	0.0000	0.0000	10.9	0.0
² D _{3/2} ⁽²⁾	55068	182	0.0000	0.0000	0.0008	0.0000	0.5	0.0
² F _{5/2} ⁽²⁾	63157	158	0.0000	0.0000	0.0000	0.0000	0.0	0.0
² G _{7/2} ⁽²⁾	66274	151	0.0000	0.0008	0.0000	0.0000	0.7	0.0
² G _{9/2} ⁽²⁾	70260	142	0.0000	0.0014	0.0000	0.0000	1.4	0.0
² F _{5/2} ⁽¹⁾	93265	107	0.0000	0.0000	0.0000	0.0000	0.0	0.0
² F _{7/2} ⁽¹⁾	97760	102	0.0000	0.0049	0.0000	0.0000	6.8	0.0
	initial: ⁴ I _{13/2}							
⁴ I _{11/2}	3651	2739	0.0332	0.1705	1.0886	20.7669	61.4	32.6
⁴ I _{9/2}	5897	1696	0.0004	0.0099	0.7159	0.0000	52.6	0.0
⁴ F _{9/2}	8720	1147	0.0105	0.1536	0.0775	0.0000	31.4	0.0
⁴ S _{3/2}	11868	843	0.0000	0.0000	0.3403	0.0000	49.7	0.0
² H _{11/2} ⁽²⁾	12622	792	0.0230	0.0607	0.0523	3.7573	28.6	20.6
⁴ F _{7/2}	13952	717	0.0000	0.3383	0.0001	0.0000	71.9	0.0
⁴ F _{5/2}	15642	639	0.0000	0.1800	0.3431	0.0000	109.2	0.0
⁴ F _{3/2}	16031	624	0.0000	0.0000	0.0364	0.0000	7.2	0.0
⁴ F _{9/2}	18027	555	0.0613	0.1065	0.3523	0.0000	141.4	0.0
⁴ G _{11/2}	19884	503	0.1012	0.2666	0.2580	0.6383	206.0	5.5
⁴ G _{9/2}	20945	477	1.1054	0.3654	0.0114	0.0000	826.6	0.0
² K _{15/2}	21211	471	0.0001	0.0016	0.0255	0.2480	7.3	2.3
⁴ G _{7/2}	21548	464	0.0000	0.1001	0.0309	0.0000	41.3	0.0
² P _{3/2}	25014	400	0.0000	0.0000	0.1518	0.0000	47.2	0.0
² P _{1/2}	26434	378	0.0000	0.0000	0.0003	0.0000	0.1	0.0
² K _{13/2}	26509	377	0.0045	0.0018	0.0015	0.1378	4.9	1.6
⁴ G _{5/2}	26887	372	0.0000	0.0270	0.0509	0.0000	28.3	0.0
⁴ G _{7/2}	27518	363	0.0000	0.1882	0.0512	0.0000	97.5	0.0
² D _{5/2} ⁽¹⁾	28332	353	0.0000	0.0159	0.0667	0.0000	30.6	0.0

Table D.4: Radiative absorption properties of Er:ZBLAN (*continued*)

final	k_{calc} cm ⁻¹	λ_{calc} nm	$ \mathbf{U}^{(2)} ^2$	$ \mathbf{U}^{(4)} ^2$	$ \mathbf{U}^{(6)} ^2$	$ \mathbf{M}/\beta_m ^2$	f_{ed} 10 ⁻⁸	f_{md} 10 ⁻⁸
² H _{9/2} ⁽²⁾	29926	334	0.1445	0.0150	0.0175	0.0000	146.9	0.0
⁴ D _{5/2}	32158	311	0.0000	0.3341	0.0063	0.0000	169.6	0.0
⁴ D _{7/2}	32737	305	0.0000	0.2684	0.0605	0.0000	161.6	0.0
² I _{11/2}	34581	289	0.0023	0.0019	0.0000	0.0085	3.5	0.1
² L _{17/2}	35045	285	0.0011	0.0000	0.0034	0.0000	2.7	0.0
⁴ D _{3/2}	35758	280	0.0000	0.0000	0.0272	0.0000	12.3	0.0
² P _{3/2}	36304	275	0.0000	0.0000	0.0173	0.0000	7.9	0.0
² I _{13/2}	37014	270	0.0019	0.0025	0.0062	0.0215	6.6	0.4
⁴ D _{1/2}	40498	247	0.0000	0.0000	0.0149	0.0000	7.7	0.0
² L _{15/2}	41273	242	0.0013	0.0179	0.0101	0.0021	18.7	0.0
² H _{9/2} ⁽¹⁾	41597	240	0.0002	0.0016	0.0001	0.0000	1.4	0.0
² D _{5/2} ⁽²⁾	42418	236	0.0000	0.2249	0.0031	0.0000	152.9	0.0
² H _{11/2} ⁽¹⁾	44596	224	0.0003	0.0179	0.0021	0.0001	14.3	0.0
² F _{7/2} ⁽²⁾	47950	209	0.0000	0.0016	0.0013	0.0000	2.0	0.0
² D _{3/2} ⁽²⁾	48532	206	0.0000	0.0000	0.0011	0.0000	0.7	0.0
² F _{5/2} ⁽²⁾	56622	177	0.0000	0.0099	0.0000	0.0000	9.1	0.0
² G _{7/2} ⁽²⁾	59738	167	0.0000	0.0000	0.0003	0.0000	0.3	0.0
² G _{9/2} ⁽²⁾	63725	157	0.0000	0.0028	0.0001	0.0000	2.9	0.0
² F _{5/2} ⁽¹⁾	86730	115	0.0000	0.0008	0.0002	0.0000	1.4	0.0
² F _{7/2} ⁽¹⁾	91224	110	0.0000	0.0006	0.0003	0.0000	1.2	0.0
	initial: ⁴ I _{11/2}							
⁴ I _{9/2}	2246	4452	0.0026	0.0681	0.1379	10.6725	7.2	11.9
⁴ F _{9/2}	5069	1973	0.0709	0.0106	1.2752	4.8271	105.8	12.3
⁴ S _{3/2}	8217	1217	0.0000	0.0049	0.0783	0.0000	9.9	0.0
² H _{11/2} ⁽²⁾	8971	1115	0.0356	0.1383	0.0370	1.3507	38.0	6.1
⁴ F _{7/2}	10301	971	0.0034	0.2660	0.1541	0.0000	72.6	0.0
⁴ F _{5/2}	11991	834	0.0000	0.0976	0.0028	0.0000	21.3	0.0
⁴ F _{3/2}	12380	808	0.0000	0.0919	0.4836	0.0000	106.1	0.0
⁴ F _{9/2}	14376	696	0.0392	0.0761	0.1098	1.1401	62.1	8.3

Table D.4: Radiative absorption properties of Er:ZBLAN (*continued*)

final	k_{calc} cm ⁻¹	λ_{calc} nm	$ \mathbf{U}^{(2)} ^2$	$ \mathbf{U}^{(4)} ^2$	$ \mathbf{U}^{(6)} ^2$	$ \mathbf{M}/\beta_m ^2$	f_{ed} 10 ⁻⁸	f_{md} 10 ⁻⁸
⁴ G _{11/2}	16233	616	0.0002	0.0491	0.0134	0.0013	17.5	0.0
⁴ G _{9/2}	17293	578	0.0931	0.1585	0.0165	0.0134	110.1	0.1
² K _{15/2}	17560	569	0.0469	0.0018	0.2474	0.0000	92.4	0.0
⁴ G _{7/2}	17896	559	0.5028	0.2752	0.1632	0.0000	449.3	0.0
² P _{3/2}	21363	468	0.0000	0.1007	0.0383	0.0000	50.3	0.0
² P _{1/2}	22783	439	0.0000	0.0000	0.0323	0.0000	10.7	0.0
² K _{13/2}	22858	437	0.0011	0.0017	0.1455	0.1498	49.7	1.7
⁴ G _{5/2}	23236	430	0.0000	0.3406	0.0563	0.0000	160.8	0.0
⁴ G _{7/2}	23867	419	0.5284	0.0931	0.0521	0.0000	508.1	0.0
² D _{5/2} ⁽¹⁾	24681	405	0.0000	0.0726	0.0630	0.0000	54.7	0.0
² H _{9/2} ⁽²⁾	26275	381	0.0086	0.0226	0.0256	0.1104	28.6	1.5
⁴ D _{5/2}	28507	351	0.0000	0.1719	0.0016	0.0000	89.1	0.0
⁴ D _{7/2}	29085	344	0.0107	0.0379	0.0228	0.0000	40.7	0.0
² I _{11/2}	30930	323	0.0063	0.0536	0.0274	0.0228	49.4	0.4
² L _{17/2}	31394	319	0.0000	0.1799	0.0913	0.0000	144.3	0.0
⁴ D _{3/2}	32107	311	0.0000	0.1506	0.0000	0.0000	87.7	0.0
² P _{3/2}	32653	306	0.0000	0.0273	0.0249	0.0000	28.1	0.0
² I _{13/2}	33363	300	0.0187	0.0552	0.0092	0.0118	60.5	0.2
⁴ D _{1/2}	36847	271	0.0000	0.0000	0.0151	0.0000	8.2	0.0
² L _{15/2}	37622	266	0.0003	0.0019	0.0031	0.0000	3.4	0.0
² H _{9/2} ⁽¹⁾	37946	264	0.0001	0.0639	0.0027	0.0000	46.1	0.0
² D _{5/2} ⁽²⁾	38767	258	0.0000	0.0168	0.0067	0.0000	15.8	0.0
² H _{11/2} ⁽¹⁾	40945	244	0.0001	0.0085	0.0046	0.0021	9.3	0.0
² F _{7/2} ⁽²⁾	44299	226	0.0483	0.0524	0.0002	0.0000	122.3	0.0
² D _{3/2} ⁽²⁾	44881	223	0.0000	0.0916	0.0010	0.0000	77.1	0.0
² F _{5/2} ⁽²⁾	52971	189	0.0000	0.0091	0.0060	0.0000	13.9	0.0
² G _{7/2} ⁽²⁾	56087	178	0.0000	0.0198	0.0015	0.0000	22.3	0.0
² G _{9/2} ⁽²⁾	60074	166	0.0025	0.0129	0.0003	0.0000	20.6	0.0
² F _{5/2} ⁽¹⁾	83078	120	0.0000	0.0001	0.0061	0.0000	7.9	0.0

Table D.4: Radiative absorption properties of Er:ZBLAN (*continued*)

final	k_{calc} cm ⁻¹	λ_{calc} nm	$ \mathbf{U}^{(2)} ^2$	$ \mathbf{U}^{(4)} ^2$	$ \mathbf{U}^{(6)} ^2$	$ \mathbf{M}/\beta_m ^2$	f_{ed} 10 ⁻⁸	f_{md} 10 ⁻⁸
² F _{7/2} ⁽¹⁾	87573	114	0.0061	0.0083	0.0014	0.0000	35.7	0.0
	initial: ⁴ I _{9/2}							
⁴ F _{9/2}	2823	3543	0.1256	0.0060	0.0249	11.5670	16.4	19.6
⁴ S _{3/2}	5971	1675	0.0000	0.0756	0.2539	0.0000	35.6	0.0
² H _{11/2} ⁽²⁾	6725	1487	0.2021	0.0661	0.2844	0.2632	99.7	1.1
⁴ F _{7/2}	8055	1242	0.0159	0.0959	0.4300	1.8014	81.3	8.8
⁴ F _{5/2}	9745	1026	0.0106	0.0601	0.1076	0.0000	34.8	0.0
⁴ F _{3/2}	10134	987	0.0000	0.2323	0.0573	0.0000	60.1	0.0
⁴ F _{9/2}	12130	824	0.0141	0.0068	0.0036	0.0403	9.8	0.3
⁴ G _{11/2}	13987	715	0.0689	0.0131	0.0221	0.0333	50.1	0.3
⁴ G _{9/2}	15048	665	0.0050	0.0049	0.0038	0.1687	5.8	1.5
² K _{15/2}	15314	653	0.0000	0.2146	0.0982	0.0000	96.1	0.0
⁴ G _{7/2}	15651	639	0.1638	0.3675	0.2203	0.1180	291.4	1.1
² P _{3/2}	19117	523	0.0000	0.0419	0.0050	0.0000	18.8	0.0
² P _{1/2}	20537	487	0.0000	0.0258	0.0000	0.0000	11.4	0.0
² K _{13/2}	20612	485	0.0321	0.0720	0.2591	0.0000	152.7	0.0
⁴ G _{5/2}	20990	476	0.6043	0.2206	0.0018	0.0000	641.8	0.0
⁴ G _{7/2}	21621	463	0.0251	0.1178	0.0156	0.0751	83.7	1.0
² D _{5/2} ⁽¹⁾	22435	446	0.0212	0.0032	0.0019	0.0000	22.6	0.0
² H _{9/2} ⁽²⁾	24029	416	0.0044	0.0002	0.0155	0.0262	11.1	0.4
⁴ D _{5/2}	26261	381	0.0469	0.0097	0.0381	0.0000	75.9	0.0
⁴ D _{7/2}	26840	373	0.0929	0.0719	0.0026	0.0002	150.2	0.0
² I _{11/2}	28684	349	0.0779	0.0801	0.1802	0.0457	236.6	0.8
² L _{17/2}	29148	343	0.0000	0.0342	0.1792	0.0000	113.1	0.0
⁴ D _{3/2}	29861	335	0.0000	0.1613	0.0064	0.0000	107.8	0.0
² P _{3/2}	30407	329	0.0000	0.1532	0.0088	0.0000	105.8	0.0
² I _{13/2}	31117	321	0.0001	0.0399	0.0024	0.0000	28.5	0.0
⁴ D _{1/2}	34601	289	0.0000	0.0793	0.0000	0.0000	60.0	0.0
² L _{15/2}	35376	283	0.0000	0.1154	0.0383	0.0000	113.2	0.0
² H _{9/2} ⁽¹⁾	35700	280	0.0020	0.1573	0.0194	0.0120	138.2	0.3

Table D.4: Radiative absorption properties of Er:ZBLAN (*continued*)

final	k_{calc} cm ⁻¹	λ_{calc} nm	$ \mathbf{U}^{(2)} ^2$	$ \mathbf{U}^{(4)} ^2$	$ \mathbf{U}^{(6)} ^2$	$ \mathbf{M}/\beta_m ^2$	f_{ed} 10 ⁻⁸	f_{md} 10 ⁻⁸
² D _{5/2} ⁽²⁾	36521	274	0.0133	0.0006	0.0012	0.0000	22.4	0.0
² H _{11/2} ⁽¹⁾	38699	258	0.0003	0.0081	0.0017	0.0000	8.6	0.0
² F _{7/2} ⁽²⁾	42053	238	0.0144	0.1053	0.0001	0.0016	125.0	0.0
² D _{3/2} ⁽²⁾	42635	235	0.0000	0.0000	0.0005	0.0000	0.4	0.0
² F _{5/2} ⁽²⁾	50725	197	0.0198	0.0140	0.0113	0.0000	71.7	0.0
² G _{7/2} ⁽²⁾	53841	186	0.0123	0.0886	0.0001	0.0000	137.9	0.0
² G _{9/2} ⁽²⁾	57828	173	0.0000	0.0150	0.0026	0.0007	22.5	0.0
² F _{5/2} ⁽¹⁾	80833	124	0.0018	0.0012	0.0110	0.0000	25.0	0.0
² F _{7/2} ⁽¹⁾	85327	117	0.0121	0.0296	0.0009	0.0000	105.0	0.0
initial: ⁴ F _{9/2}								
⁴ S _{3/2}	3149	3176	0.0000	0.0002	0.0254	0.0000	1.4	0.0
² H _{11/2} ⁽²⁾	3902	2562	0.3683	0.0228	0.0017	0.2819	62.4	0.7
⁴ F _{7/2}	5232	1911	0.0120	0.0360	0.0130	6.4133	7.8	20.3
⁴ F _{5/2}	6922	1445	0.0005	0.2365	0.3545	0.0000	77.0	0.0
⁴ F _{3/2}	7311	1368	0.0000	0.0033	0.0595	0.0000	8.0	0.0
⁴ F _{9/2}	9307	1074	0.0074	0.0261	0.0438	5.1823	15.1	29.3
⁴ G _{11/2}	11165	896	0.4305	0.0378	0.0126	0.2558	215.1	1.7
⁴ G _{9/2}	12225	818	0.2176	0.3174	0.3666	0.2976	272.7	2.2
² K _{15/2}	12491	801	0.0000	0.0805	0.0128	0.0000	24.2	0.0
⁴ G _{7/2}	12828	780	0.0000	0.0101	0.0143	0.0892	5.9	0.7
² P _{3/2}	16295	614	0.0000	0.0467	0.0058	0.0000	17.9	0.0
² P _{1/2}	17715	565	0.0000	0.0465	0.0000	0.0000	17.6	0.0
² K _{13/2}	17789	562	0.0009	0.0170	0.0019	0.0000	7.7	0.0
⁴ G _{5/2}	18167	550	0.2354	0.1814	0.1308	0.0000	293.8	0.0
⁴ G _{7/2}	18798	532	0.0001	0.0006	0.0279	0.0301	9.4	0.3
² D _{5/2} ⁽¹⁾	19612	510	0.0434	0.1184	0.0039	0.0000	87.4	0.0
² H _{9/2} ⁽²⁾	21206	472	0.0061	0.0037	0.0005	0.0099	7.4	0.1
⁴ D _{5/2}	23438	427	0.2379	0.3573	0.0164	0.0000	425.6	0.0
⁴ D _{7/2}	24017	416	0.3553	0.1483	0.0002	0.0007	442.4	0.0

Table D.4: Radiative absorption properties of Er:ZBLAN (*continued*)

final	k_{calc} cm ⁻¹	λ_{calc} nm	$ \mathbf{U}^{(2)} ^2$	$ \mathbf{U}^{(4)} ^2$	$ \mathbf{U}^{(6)} ^2$	$ \mathbf{M}/\beta_m ^2$	f_{ed} 10 ⁻⁸	f_{md} 10 ⁻⁸
² I _{11/2}	25862	387	0.0016	0.0060	0.0682	0.0076	35.8	0.1
² L _{17/2}	26326	380	0.0000	0.0026	0.0677	0.0000	32.6	0.0
⁴ D _{3/2}	27038	370	0.0000	0.0024	0.0001	0.0000	1.5	0.0
² P _{3/2}	27585	363	0.0000	0.0108	0.0042	0.0000	8.4	0.0
² I _{13/2}	28294	353	0.0106	0.0084	0.0909	0.0000	63.0	0.0
⁴ D _{1/2}	31779	315	0.0000	0.1622	0.0000	0.0000	112.1	0.0
² L _{15/2}	32554	307	0.0000	0.0315	0.0473	0.0000	49.4	0.0
² H _{9/2} ⁽¹⁾	32878	304	0.0000	0.0121	0.0226	0.0007	21.8	0.0
² D _{5/2} ⁽²⁾	33698	297	0.0008	0.0411	0.0101	0.0000	37.4	0.0
² H _{11/2} ⁽¹⁾	35877	279	0.0123	0.0635	0.0138	0.0018	77.9	0.0
² F _{7/2} ⁽²⁾	39231	255	0.0000	0.0120	0.0087	0.0116	16.5	0.3
² D _{3/2} ⁽²⁾	39813	251	0.0000	0.0004	0.0002	0.0000	0.5	0.0
² F _{5/2} ⁽²⁾	47902	209	0.0009	0.0054	0.0018	0.0000	9.4	0.0
² G _{7/2} ⁽²⁾	51019	196	0.0009	0.0131	0.0001	0.0010	17.3	0.0
² G _{9/2} ⁽²⁾	55005	182	0.0008	0.0679	0.0001	0.0031	86.6	0.1
² F _{5/2} ⁽¹⁾	78010	128	0.0037	0.0087	0.0015	0.0000	30.5	0.0
² F _{7/2} ⁽¹⁾	82505	121	0.0106	0.0141	0.0030	0.0000	70.2	0.0
	initial: ⁴ S _{3/2}							
² H _{11/2} ⁽²⁾	754	—	0.0000	0.2000	0.0096	0.0000	7.4	0.0
⁴ F _{7/2}	2083	4800	0.0001	0.0052	0.0000	0.0000	0.6	0.0
⁴ F _{5/2}	3773	2650	0.0077	0.0036	0.0000	0.5896	3.8	3.4
⁴ F _{3/2}	4162	2403	0.0258	0.0000	0.0000	3.0351	11.3	19.1
⁴ F _{9/2}	6158	1624	0.0000	0.0033	0.0015	0.0000	1.5	0.0
⁴ G _{11/2}	8016	1248	0.0000	0.1284	0.0040	0.0000	56.1	0.0
⁴ G _{9/2}	9076	1102	0.0000	0.1663	0.0101	0.0000	84.2	0.0
² K _{15/2}	9343	1070	0.0000	0.0000	0.0039	0.0000	1.6	0.0
⁴ G _{7/2}	9679	1033	0.0461	0.1595	0.0000	0.0000	129.3	0.0
² P _{3/2}	13146	761	0.0801	0.0000	0.0000	0.3928	111.7	7.9
² P _{1/2}	14566	687	0.0060	0.0000	0.0000	0.2635	9.3	5.8

Table D.4: Radiative absorption properties of Er:ZBLAN (*continued*)

final	k_{calc} cm ⁻¹	λ_{calc} nm	$ \mathbf{U}^{(2)} ^2$	$ \mathbf{U}^{(4)} ^2$	$ \mathbf{U}^{(6)} ^2$	$ \mathbf{M}/\beta_m ^2$	f_{ed} 10 ⁻⁸	f_{md} 10 ⁻⁸
² K _{13/2}	14641	683	0.0000	0.0000	0.1238	0.0000	78.2	0.0
⁴ G _{5/2}	15018	666	0.0384	0.1331	0.0000	0.0055	168.0	0.1
⁴ G _{7/2}	15649	639	0.0107	0.1451	0.0000	0.0000	139.0	0.0
² D _{5/2} ⁽¹⁾	16463	607	0.0472	0.0025	0.0000	0.0000	84.8	0.0
² H _{9/2} ⁽²⁾	18057	554	0.0000	0.0245	0.0012	0.0000	24.6	0.0
⁴ D _{5/2}	20289	493	0.2124	0.0101	0.0000	0.0675	470.8	2.1
⁴ D _{7/2}	20868	479	0.3391	0.0084	0.0000	0.0000	764.9	0.0
² I _{11/2}	22713	440	0.0000	0.0295	0.0717	0.0000	106.7	0.0
² L _{17/2}	23177	431	0.0000	0.0000	0.0000	0.0000	0.0	0.0
⁴ D _{3/2}	23889	419	0.1173	0.0000	0.0000	0.0065	300.1	0.2
² P _{3/2}	24436	409	0.1107	0.0000	0.0000	0.0218	289.9	0.8
² I _{13/2}	25146	398	0.0000	0.0000	0.1296	0.0000	141.9	0.0
⁴ D _{1/2}	28630	349	0.0308	0.0000	0.0000	0.0015	94.9	0.1
² L _{15/2}	29405	340	0.0000	0.0000	0.0025	0.0000	3.3	0.0
² H _{9/2} ⁽¹⁾	29729	336	0.0000	0.0142	0.0171	0.0000	45.2	0.0
² D _{5/2} ⁽²⁾	30550	327	0.0096	0.0001	0.0000	0.0003	31.7	0.0
² H _{11/2} ⁽¹⁾	32728	306	0.0000	0.0064	0.0001	0.0000	11.4	0.0
² F _{7/2} ⁽²⁾	36082	277	0.0079	0.0144	0.0000	0.0000	59.6	0.0
² D _{3/2} ⁽²⁾	36664	273	0.0033	0.0000	0.0000	0.0013	13.0	0.1
² F _{5/2} ⁽²⁾	44753	223	0.0050	0.0056	0.0000	0.0003	38.7	0.0
² G _{7/2} ⁽²⁾	47870	209	0.0085	0.0882	0.0000	0.0000	283.1	0.0
² G _{9/2} ⁽²⁾	51856	193	0.0000	0.0215	0.0002	0.0000	63.4	0.0
² F _{5/2} ⁽¹⁾	74861	134	0.0032	0.0010	0.0000	0.0000	31.5	0.0
² F _{7/2} ⁽¹⁾	79356	126	0.0175	0.0106	0.0000	0.0000	204.2	0.0
	initial: ² H _{11/2} ⁽²⁾							
⁴ F _{7/2}	1330	7521	0.1246	0.0158	0.3980	0.0000	13.0	0.0
⁴ F _{5/2}	3020	3312	0.0000	0.0594	0.1838	0.0000	11.0	0.0
⁴ F _{3/2}	3408	2934	0.0000	0.0002	0.0029	0.0000	0.2	0.0
⁴ F _{9/2}	5405	1850	0.0276	0.1651	0.0620	0.7449	25.8	2.0

Table D.4: Radiative absorption properties of Er:ZBLAN (*continued*)

final	k_{calc} cm ⁻¹	λ_{calc} nm	$ \mathbf{U}^{(2)} ^2$	$ \mathbf{U}^{(4)} ^2$	$ \mathbf{U}^{(6)} ^2$	$ \mathbf{M}/\beta_m ^2$	f_{ed} 10 ⁻⁸	f_{md} 10 ⁻⁸
⁴ G _{11/2}	7262	1377	0.0004	0.1507	0.0500	3.6527	24.7	13.4
⁴ G _{9/2}	8322	1202	0.0236	0.3431	0.1555	8.5254	76.0	35.9
² K _{15/2}	8589	1164	0.1013	0.0000	1.1473	0.0000	171.8	0.0
⁴ G _{7/2}	8925	1120	0.0010	0.0377	0.2714	0.0000	41.0	0.0
² P _{3/2}	12392	807	0.0000	0.0155	0.0288	0.0000	8.5	0.0
² P _{1/2}	13812	724	0.0000	0.0000	0.1678	0.0000	33.3	0.0
² K _{13/2}	13887	720	0.0078	0.0049	0.3156	0.0101	68.0	0.1
⁴ G _{5/2}	14264	701	0.0000	0.0000	0.1048	0.0000	21.5	0.0
⁴ G _{7/2}	14895	671	0.0492	0.0023	0.0009	0.0000	26.7	0.0
² D _{5/2} ⁽¹⁾	15710	637	0.0000	0.0723	0.0315	0.0000	27.3	0.0
² H _{9/2} ⁽²⁾	17304	578	0.0183	0.0627	0.2123	0.3183	83.5	2.8
⁴ D _{5/2}	19535	512	0.0000	0.0680	0.0296	0.0000	32.1	0.0
⁴ D _{7/2}	20114	497	0.6851	0.0068	0.0343	0.0000	502.6	0.0
² I _{11/2}	21959	455	0.0151	0.1352	0.1208	0.1886	103.3	2.1
² L _{17/2}	22423	446	0.0000	0.4963	0.3520	0.0000	313.5	0.0
⁴ D _{3/2}	23135	432	0.0000	0.0012	0.1739	0.0000	58.8	0.0
² P _{3/2}	23682	422	0.0000	0.1130	0.0000	0.0000	48.0	0.0
² I _{13/2}	24392	410	0.0326	0.1528	0.0979	0.0591	129.9	0.7
⁴ D _{1/2}	27876	359	0.0000	0.0000	0.0470	0.0000	19.1	0.0
² L _{15/2}	28651	349	0.0008	0.0170	0.0043	0.0000	11.4	0.0
² H _{9/2} ⁽¹⁾	28975	345	0.0041	0.0621	0.0023	0.0582	37.7	0.9
² D _{5/2} ⁽²⁾	29796	336	0.0000	0.2565	0.0002	0.0000	138.2	0.0
² H _{11/2} ⁽¹⁾	31974	313	0.0002	0.0581	0.0012	0.0227	34.5	0.4
² F _{7/2} ⁽²⁾	35328	283	0.3923	0.5278	0.0042	0.0000	845.2	0.0
² D _{3/2} ⁽²⁾	35910	278	0.0000	0.0112	0.0142	0.0000	14.9	0.0
² F _{5/2} ⁽²⁾	44000	227	0.0000	0.0213	0.0080	0.0000	22.7	0.0
² G _{7/2} ⁽²⁾	47116	212	0.0002	0.0437	0.0029	0.0000	40.9	0.0
² G _{9/2} ⁽²⁾	51103	196	0.0042	0.0860	0.0011	0.0011	91.7	0.0
² F _{5/2} ⁽¹⁾	74107	135	0.0000	0.0017	0.0147	0.0000	19.0	0.0

Table D.4: Radiative absorption properties of Er:ZBLAN (*continued*)

final	k_{calc} cm ⁻¹	λ_{calc} nm	$ \mathbf{U}^{(2)} ^2$	$ \mathbf{U}^{(4)} ^2$	$ \mathbf{U}^{(6)} ^2$	$ \mathbf{M}/\beta_m ^2$	f_{ed} 10 ⁻⁸	f_{md} 10 ⁻⁸
² F _{7/2} ⁽¹⁾	78602	127	0.0333	0.0209	0.0111	0.0000	142.5	0.0
	initial: ⁴ F _{7/2}							
⁴ F _{5/2}	1690	5917	0.0772	0.0505	0.1001	10.1114	12.3	12.5
⁴ F _{3/2}	2079	4810	0.0029	0.0579	0.0000	0.0000	3.4	0.0
⁴ F _{9/2}	4075	2454	0.0913	0.0477	0.0274	1.2815	27.1	3.9
⁴ G _{11/2}	5933	1686	0.0877	0.1280	0.0174	0.0000	49.8	0.0
⁴ G _{9/2}	6993	1430	0.6215	0.0071	0.1210	0.0020	249.1	0.0
² K _{15/2}	7259	1378	0.0000	0.0001	0.0001	0.0000	0.0	0.0
⁴ G _{7/2}	7596	1317	0.1224	0.0410	0.0069	0.5744	58.5	3.3
² P _{3/2}	11063	904	0.0201	0.0085	0.0000	0.0000	14.3	0.0
² P _{1/2}	12483	801	0.0000	0.0200	0.0000	0.0000	6.7	0.0
² K _{13/2}	12557	796	0.0000	0.0539	0.0074	0.0000	20.0	0.0
⁴ G _{5/2}	12935	773	0.0393	0.1276	0.1519	0.0352	113.3	0.3
⁴ G _{7/2}	13566	737	0.1383	0.0519	0.0038	0.3684	119.5	3.8
² D _{5/2} ⁽¹⁾	14380	695	0.0173	0.0000	0.0000	1.6349	13.2	17.9
² H _{9/2} ⁽²⁾	15974	626	0.0473	0.0009	0.0475	0.0750	56.9	0.9
⁴ D _{5/2}	18206	549	0.0904	0.0807	0.0074	0.1293	129.9	1.8
⁴ D _{7/2}	18785	532	0.2457	0.4282	0.0019	0.0014	461.9	0.0
² I _{11/2}	20630	485	0.0057	0.0252	0.0016	0.0000	21.0	0.0
² L _{17/2}	21094	474	0.0000	0.0000	0.0008	0.0000	0.4	0.0
⁴ D _{3/2}	21806	459	0.1097	0.0275	0.0000	0.0000	143.9	0.0
² P _{3/2}	22353	447	0.1082	0.0448	0.0000	0.0000	156.2	0.0
² I _{13/2}	23062	434	0.0000	0.0081	0.0162	0.0000	13.1	0.0
⁴ D _{1/2}	26547	377	0.0000	0.1780	0.0000	0.0000	127.5	0.0
² L _{15/2}	27321	366	0.0000	0.0017	0.0497	0.0000	30.9	0.0
² H _{9/2} ⁽¹⁾	27646	362	0.0092	0.0105	0.0010	0.0009	22.1	0.0
² D _{5/2} ⁽²⁾	28466	351	0.0899	0.0151	0.0057	0.0186	153.0	0.4
² H _{11/2} ⁽¹⁾	30645	326	0.0004	0.0005	0.0576	0.0000	39.8	0.0
² F _{7/2} ⁽²⁾	33999	294	0.0002	0.0005	0.0110	0.0368	9.0	1.0
² D _{3/2} ⁽²⁾	34581	289	0.0051	0.0000	0.0000	0.0000	9.6	0.0

Table D.4: Radiative absorption properties of Er:ZBLAN (*continued*)

final	k_{calc} cm ⁻¹	λ_{calc} nm	$ \mathbf{U}^{(2)} ^2$	$ \mathbf{U}^{(4)} ^2$	$ \mathbf{U}^{(6)} ^2$	$ \mathbf{M}/\beta_m ^2$	f_{ed} 10 ⁻⁸	f_{md} 10 ⁻⁸
$^2F_{5/2}^{(2)}$	42670	234	0.0011	0.0036	0.0002	0.0035	7.1	0.1
$^2G_{7/2}^{(2)}$	45787	218	0.0003	0.0222	0.0009	0.0023	30.2	0.1
$^2G_{9/2}^{(2)}$	49773	201	0.0005	0.0251	0.0015	0.0014	38.4	0.1
$^2F_{5/2}^{(1)}$	72778	137	0.0062	0.0097	0.0006	0.0000	46.5	0.0
$^2F_{7/2}^{(1)}$	77273	129	0.0018	0.0064	0.0034	0.0000	28.0	0.0
	initial: $^4F_{5/2}$							
$^4F_{3/2}$	389	—	0.0609	0.0361	0.0000	6.3039	1.9	2.2
$^4F_{9/2}$	2385	4193	0.0092	0.0227	0.0060	0.0000	3.8	0.0
$^4G_{11/2}$	4242	2357	0.0000	0.0366	0.0817	0.0000	15.3	0.0
$^4G_{9/2}$	5303	1886	0.1649	0.0841	0.0025	0.0000	77.6	0.0
$^2K_{15/2}$	5569	1796	0.0000	0.0000	0.0461	0.0000	7.3	0.0
$^4G_{7/2}$	5906	1693	0.3811	0.0016	0.0381	0.5558	165.1	3.3
$^2P_{3/2}$	9373	1067	0.0176	0.0427	0.0000	1.4665	25.8	13.9
$^2P_{1/2}$	10793	927	0.0069	0.0000	0.0000	0.0000	5.3	0.0
$^2K_{13/2}$	10867	920	0.0000	0.0008	0.0049	0.0000	1.8	0.0
$^4G_{5/2}$	11245	889	0.3154	0.1225	0.0000	0.0280	299.5	0.3
$^4G_{7/2}$	11876	842	0.2058	0.0059	0.1311	0.1814	219.9	2.2
$^2D_{5/2}^{(1)}$	12690	788	0.0628	0.0388	0.0000	0.1896	73.9	2.4
$^2H_{9/2}^{(2)}$	14284	700	0.0144	0.0072	0.0075	0.0000	21.3	0.0
$^4D_{5/2}$	16516	605	0.1670	0.0149	0.0000	0.0053	204.3	0.1
$^4D_{7/2}$	17095	585	0.0419	0.2438	0.0004	0.0576	199.5	1.0
$^2I_{11/2}$	18939	528	0.0000	0.0143	0.0464	0.0000	35.0	0.0
$^2L_{17/2}$	19404	515	0.0000	0.0000	0.0729	0.0000	40.8	0.0
$^4D_{3/2}$	20116	497	0.0389	0.0910	0.0000	0.0722	121.1	1.5
$^2P_{3/2}$	20663	484	0.0009	0.1107	0.0000	0.0508	83.1	1.1
$^2I_{13/2}$	21372	468	0.0000	0.0125	0.0362	0.0000	31.9	0.0
$^4D_{1/2}$	24857	402	0.0850	0.0000	0.0000	0.0000	151.0	0.0
$^2L_{15/2}$	25631	390	0.0000	0.0000	0.0003	0.0000	0.2	0.0
$^2H_{9/2}^{(1)}$	25956	385	0.0025	0.0229	0.1047	0.0000	105.0	0.0
$^2D_{5/2}^{(2)}$	26776	373	0.0202	0.0027	0.0000	0.0001	41.4	0.0

Table D.4: Radiative absorption properties of Er:ZBLAN (*continued*)

final	k_{calc} cm ⁻¹	λ_{calc} nm	$ \mathbf{U}^{(2)} ^2$	$ \mathbf{U}^{(4)} ^2$	$ \mathbf{U}^{(6)} ^2$	$ \mathbf{M}/\beta_m ^2$	f_{ed} 10 ⁻⁸	f_{md} 10 ⁻⁸
$^2\text{H}_{11/2}^{(1)}$	28955	345	0.0000	0.0321	0.0014	0.0000	34.7	0.0
$^2\text{F}_{7/2}^{(2)}$	32309	310	0.0427	0.0004	0.0027	0.0339	102.7	1.1
$^2\text{D}_{3/2}^{(2)}$	32890	304	0.0190	0.0122	0.0000	0.0081	59.8	0.3
$^2\text{F}_{5/2}^{(2)}$	40980	244	0.0065	0.0001	0.0000	0.0063	19.8	0.3
$^2\text{G}_{7/2}^{(2)}$	44097	227	0.0007	0.0233	0.0091	0.0022	52.5	0.1
$^2\text{G}_{9/2}^{(2)}$	48083	208	0.0075	0.0126	0.0000	0.0000	49.7	0.0
$^2\text{F}_{5/2}^{(1)}$	71088	141	0.0000	0.0077	0.0000	0.0004	20.7	0.0
$^2\text{F}_{7/2}^{(1)}$	75583	132	0.0021	0.0104	0.0014	0.0002	45.0	0.0
	initial: $^4\text{F}_{3/2}$							
$^4\text{F}_{9/2}$	1996	5010	0.0000	0.0177	0.0064	0.0000	2.4	0.0
$^4\text{G}_{11/2}$	3854	2595	0.0000	0.0232	0.0921	0.0000	19.9	0.0
$^4\text{G}_{9/2}$	4914	2035	0.0000	0.1714	0.1128	0.0000	68.3	0.0
$^2\text{K}_{15/2}$	5180	1930	0.0000	0.0000	0.0000	0.0000	0.0	0.0
$^4\text{G}_{7/2}$	5517	1813	0.0952	0.0339	0.0000	0.0000	65.3	0.0
$^2\text{P}_{3/2}$	8984	1113	0.0124	0.0000	0.0000	1.8208	11.8	24.8
$^2\text{P}_{1/2}$	10404	961	0.0339	0.0000	0.0000	0.0067	37.3	0.1
$^2\text{K}_{13/2}$	10479	954	0.0000	0.0000	0.1078	0.0000	48.6	0.0
$^4\text{G}_{5/2}$	10856	921	0.3368	0.0805	0.0000	0.0241	433.9	0.4
$^4\text{G}_{7/2}$	11487	871	0.0437	0.0002	0.0000	0.0000	53.3	0.0
$^2\text{D}_{5/2}^{(1)}$	12301	813	0.0228	0.0150	0.0000	0.1413	39.5	2.6
$^2\text{H}_{9/2}^{(2)}$	13895	720	0.0000	0.0182	0.0211	0.0000	26.1	0.0
$^4\text{D}_{5/2}$	16127	620	0.1313	0.1909	0.0000	0.0162	389.5	0.4
$^4\text{D}_{7/2}$	16706	599	0.0566	0.0789	0.0000	0.0000	171.1	0.0
$^2\text{I}_{11/2}$	18551	539	0.0000	0.0694	0.0002	0.0000	69.0	0.0
$^2\text{L}_{17/2}$	19015	526	0.0000	0.0000	0.0000	0.0000	0.0	0.0
$^4\text{D}_{3/2}$	19727	507	0.0103	0.0000	0.0000	0.0134	21.6	0.4
$^2\text{P}_{3/2}$	20274	493	0.0173	0.0000	0.0000	0.0669	37.5	2.1
$^2\text{I}_{13/2}$	20984	477	0.0000	0.0000	0.0109	0.0000	9.9	0.0
$^4\text{D}_{1/2}$	24468	409	0.1132	0.0000	0.0000	0.0007	296.8	0.0

Table D.4: Radiative absorption properties of Er:ZBLAN (*continued*)

final	k_{calc} cm ⁻¹	λ_{calc} nm	$ \mathbf{U}^{(2)} ^2$	$ \mathbf{U}^{(4)} ^2$	$ \mathbf{U}^{(6)} ^2$	$ \mathbf{M}/\beta_m ^2$	f_{ed} 10 ⁻⁸	f_{md} 10 ⁻⁸
² L _{15/2}	25243	396	0.0000	0.0000	0.0262	0.0000	28.8	0.0
² H _{9/2} ⁽¹⁾	25567	391	0.0000	0.0311	0.0330	0.0000	79.6	0.0
² D _{5/2} ⁽²⁾	26388	379	0.0641	0.0124	0.0000	0.0424	199.3	1.7
² H _{11/2} ⁽¹⁾	28566	350	0.0000	0.0022	0.0714	0.0000	92.6	0.0
² F _{7/2} ⁽²⁾	31920	313	0.0220	0.0036	0.0000	0.0000	82.3	0.0
² D _{3/2} ⁽²⁾	32502	308	0.0009	0.0000	0.0000	0.0052	3.0	0.3
² F _{5/2} ⁽²⁾	40591	246	0.0130	0.0028	0.0000	0.0084	64.4	0.5
² G _{7/2} ⁽²⁾	43708	229	0.0172	0.0502	0.0000	0.0000	205.1	0.0
² G _{9/2} ⁽²⁾	47694	210	0.0000	0.0133	0.0000	0.0000	35.8	0.0
² F _{5/2} ⁽¹⁾	70699	141	0.0000	0.0122	0.0000	0.0000	48.9	0.0
² F _{7/2} ⁽¹⁾	75194	133	0.0005	0.0214	0.0000	0.0000	95.5	0.0
	initial: ⁴ F _{9/2}							
⁴ G _{11/2}	1857	5384	0.2920	0.1077	0.1391	2.4960	30.7	2.7
⁴ G _{9/2}	2918	3427	0.0246	0.0003	0.0352	1.6269	4.8	2.8
² K _{15/2}	3184	3141	0.0000	0.7155	0.0816	0.0000	52.4	0.0
⁴ G _{7/2}	3521	2840	0.0150	0.0051	0.0243	3.1545	4.1	6.7
² P _{3/2}	6988	1431	0.0000	0.2047	0.2604	0.0000	61.6	0.0
² P _{1/2}	8408	1189	0.0000	0.0001	0.0000	0.0000	0.0	0.0
² K _{13/2}	8482	1179	0.0279	0.1828	0.4824	0.0000	113.3	0.0
⁴ G _{5/2}	8860	1129	0.0241	0.0298	0.0243	0.0000	18.3	0.0
⁴ G _{7/2}	9491	1054	0.0995	0.0210	0.4090	0.1347	110.9	0.8
² D _{5/2} ⁽¹⁾	10305	970	0.0260	0.0067	0.0098	0.0000	14.6	0.0
² H _{9/2} ⁽²⁾	11899	840	0.0820	0.0087	0.0242	2.6920	48.5	19.5
⁴ D _{5/2}	14131	708	0.1205	0.0053	0.0035	0.0000	74.8	0.0
⁴ D _{7/2}	14710	680	0.1566	0.0073	0.0118	0.0440	103.2	0.4
² I _{11/2}	16554	604	0.2703	0.1107	0.3041	0.0053	316.5	0.1
² L _{17/2}	17019	588	0.0000	0.0776	0.3223	0.0000	123.0	0.0
⁴ D _{3/2}	17731	564	0.0000	0.2044	0.0392	0.0000	89.5	0.0
² P _{3/2}	18278	547	0.0000	0.0075	0.0004	0.0000	3.0	0.0

Table D.4: Radiative absorption properties of Er:ZBLAN (*continued*)

final	k_{calc} cm ⁻¹	λ_{calc} nm	$ \mathbf{U}^{(2)} ^2$	$ \mathbf{U}^{(4)} ^2$	$ \mathbf{U}^{(6)} ^2$	$ \mathbf{M}/\beta_m ^2$	f_{ed} 10 ⁻⁸	f_{md} 10 ⁻⁸
² I _{13/2}	18987	527	0.0118	0.0626	0.0001	0.0000	35.0	0.0
⁴ D _{1/2}	22472	445	0.0000	0.0105	0.0000	0.0000	5.1	0.0
² L _{15/2}	23246	430	0.0000	0.0829	0.0035	0.0000	42.9	0.0
² H _{9/2} ⁽¹⁾	23571	424	0.0077	0.2173	0.0215	0.0201	126.7	0.3
² D _{5/2} ⁽²⁾	24391	410	0.2669	0.1546	0.0946	0.0000	400.5	0.0
² H _{11/2} ⁽¹⁾	26570	376	0.0377	0.0109	0.0003	0.0058	49.4	0.1
² F _{7/2} ⁽²⁾	29924	334	0.2020	0.5707	0.0249	0.1785	644.4	3.3
² D _{3/2} ⁽²⁾	30505	328	0.0000	0.1747	0.0026	0.0000	117.1	0.0
² F _{5/2} ⁽²⁾	38595	259	0.0580	0.0110	0.0259	0.0000	125.2	0.0
² G _{7/2} ⁽²⁾	41712	240	0.0397	0.2060	0.0000	0.0000	263.5	0.0
² G _{9/2} ⁽²⁾	45698	219	0.0002	0.0870	0.0089	0.0061	96.6	0.2
² F _{5/2} ⁽¹⁾	68703	146	0.0001	0.0000	0.0279	0.0000	35.3	0.0
² F _{7/2} ⁽¹⁾	73198	137	0.0340	0.1247	0.0002	0.0003	318.6	0.0
	initial: ⁴ G _{11/2}							
⁴ G _{9/2}	1060	—	0.0000	0.2118	0.1539	3.4405	5.7	1.7
² K _{15/2}	1327	7538	0.0992	0.0579	0.6707	0.0000	17.6	0.0
⁴ G _{7/2}	1663	6012	0.0142	0.0553	0.0176	0.0000	2.8	0.0
² P _{3/2}	5130	1949	0.0000	0.0314	0.0101	0.0000	3.6	0.0
² P _{1/2}	6550	1527	0.0000	0.0000	0.0263	0.0000	2.5	0.0
² K _{13/2}	6625	1509	0.0240	0.0078	0.2056	0.0017	26.0	0.0
⁴ G _{5/2}	7002	1428	0.0000	0.0003	0.0359	0.0000	3.6	0.0
⁴ G _{7/2}	7633	1310	0.0025	0.0167	0.5056	0.0000	58.2	0.0
² D _{5/2} ⁽¹⁾	8447	1184	0.0000	0.0222	0.0048	0.0000	3.9	0.0
² H _{9/2} ⁽²⁾	10041	996	0.0751	0.0010	0.5230	4.1724	102.1	21.2
⁴ D _{5/2}	12273	815	0.0000	0.1203	0.0731	0.0000	39.1	0.0
⁴ D _{7/2}	12852	778	0.4595	0.0190	0.0180	0.0000	216.5	0.0
² I _{11/2}	14697	680	0.0043	0.2449	0.0102	0.0591	68.4	0.4
² L _{17/2}	15161	660	0.0000	0.4831	0.0768	0.0000	147.1	0.0
⁴ D _{3/2}	15873	630	0.0000	0.0054	0.0154	0.0000	5.0	0.0

Table D.4: Radiative absorption properties of Er:ZBLAN (*continued*)

final	k_{calc} cm ⁻¹	λ_{calc} nm	$ \mathbf{U}^{(2)} ^2$	$ \mathbf{U}^{(4)} ^2$	$ \mathbf{U}^{(6)} ^2$	$ \mathbf{M}/\beta_m ^2$	f_{ed} 10 ⁻⁸	f_{md} 10 ⁻⁸
² P _{3/2}	16420	609	0.0000	0.1184	0.0992	0.0000	58.1	0.0
² I _{13/2}	17130	584	0.1217	0.3305	0.0173	0.0100	179.1	0.1
⁴ D _{1/2}	20614	485	0.0000	0.0000	0.1558	0.0000	46.4	0.0
² L _{15/2}	21389	468	0.0011	0.0156	0.0033	0.0000	7.8	0.0
² H _{9/2} ⁽¹⁾	21713	461	0.0013	0.0766	0.0042	0.0108	32.1	0.1
² D _{5/2} ⁽²⁾	22534	444	0.0000	0.1594	0.0726	0.0000	88.0	0.0
² H _{11/2} ⁽¹⁾	24712	405	0.0066	0.0726	0.0196	0.1602	45.1	2.0
² F _{7/2} ⁽²⁾	28066	356	0.6895	0.4525	0.0006	0.0000	923.8	0.0
² D _{3/2} ⁽²⁾	28648	349	0.0000	0.0014	0.1204	0.0000	51.0	0.0
² F _{5/2} ⁽²⁾	36738	272	0.0000	0.0136	0.0107	0.0000	14.9	0.0
² G _{7/2} ⁽²⁾	39854	251	0.0072	0.0238	0.0040	0.0000	30.3	0.0
² G _{9/2} ⁽²⁾	43840	228	0.0651	0.0527	0.0035	0.0144	150.5	0.3
² F _{5/2} ⁽¹⁾	66845	150	0.0000	0.0132	0.0127	0.0000	29.5	0.0
² F _{7/2} ⁽¹⁾	71340	140	0.0028	0.0655	0.0120	0.0000	108.5	0.0
	initial: ⁴ G _{9/2}							
² K _{15/2}	266	—	0.0000	0.0060	0.0560	0.0000	0.3	0.0
⁴ G _{7/2}	603	—	0.0034	0.1886	0.1502	6.2518	3.6	2.0
² P _{3/2}	4070	2457	0.0000	0.0080	0.0039	0.0000	1.0	0.0
² P _{1/2}	5490	1822	0.0000	0.0084	0.0000	0.0000	1.0	0.0
² K _{13/2}	5565	1797	0.0107	0.0000	0.1612	0.0000	17.9	0.0
⁴ G _{5/2}	5942	1683	0.0177	0.0714	0.2727	0.0000	41.2	0.0
⁴ G _{7/2}	6573	1521	0.0004	0.2378	0.0237	6.8767	36.0	27.4
² D _{5/2} ⁽¹⁾	7387	1354	0.2279	0.0001	0.1404	0.0000	89.0	0.0
² H _{9/2} ⁽²⁾	8981	1113	0.0015	0.0362	0.0004	1.6643	7.5	9.1
⁴ D _{5/2}	11213	892	0.1965	0.0035	0.0269	0.0000	99.4	0.0
⁴ D _{7/2}	11792	848	0.2280	0.0209	0.1805	0.1821	155.9	1.3
² I _{11/2}	13637	733	0.0074	0.0241	0.0052	0.1087	12.5	0.9
² L _{17/2}	14101	709	0.0000	0.0011	0.0112	0.0000	3.1	0.0
⁴ D _{3/2}	14813	675	0.0000	0.0412	0.1426	0.0000	49.5	0.0

Table D.4: Radiative absorption properties of Er:ZBLAN (*continued*)

final	k_{calc} cm ⁻¹	λ_{calc} nm	$ \mathbf{U}^{(2)} ^2$	$ \mathbf{U}^{(4)} ^2$	$ \mathbf{U}^{(6)} ^2$	$ \mathbf{M}/\beta_m ^2$	f_{ed} 10 ⁻⁸	f_{md} 10 ⁻⁸
² P _{3/2}	15360	651	0.0000	0.0158	0.0003	0.0000	5.3	0.0
² I _{13/2}	16070	622	0.0070	0.0087	0.1067	0.0000	37.4	0.0
⁴ D _{1/2}	19554	511	0.0000	0.0213	0.0000	0.0000	8.9	0.0
² L _{15/2}	20329	492	0.0000	0.1336	0.1351	0.0000	105.8	0.0
² H _{9/2} ⁽¹⁾	20653	484	0.0017	0.0316	0.0002	0.1262	15.6	1.6
² D _{5/2} ⁽²⁾	21474	466	0.3357	0.0032	0.0735	0.0000	337.0	0.0
² H _{11/2} ⁽¹⁾	23652	423	0.0056	0.0277	0.0478	0.0797	39.4	1.2
² F _{7/2} ⁽²⁾	27006	370	0.0011	0.1056	0.0102	0.4272	67.6	7.1
² D _{3/2} ⁽²⁾	27588	362	0.0000	0.0079	0.0407	0.0000	24.3	0.0
² F _{5/2} ⁽²⁾	35677	280	0.0507	0.1117	0.0000	0.0000	166.0	0.0
² G _{7/2} ⁽²⁾	38794	258	0.0011	0.0147	0.0000	0.0048	14.5	0.1
² G _{9/2} ⁽²⁾	42780	234	0.0001	0.0271	0.0001	0.0093	26.1	0.3
² F _{5/2} ⁽¹⁾	65785	152	0.0158	0.0193	0.0003	0.0000	75.8	0.0
² F _{7/2} ⁽¹⁾	70280	142	0.0003	0.0010	0.0107	0.0024	16.3	0.1
	initial: ² K _{15/2}							
⁴ G _{7/2}	337	—	0.0000	0.1198	0.0044	0.0000	0.5	0.0
² P _{3/2}	3803	2629	0.0000	0.0000	0.0312	0.0000	1.3	0.0
² P _{1/2}	5223	1914	0.0000	0.0000	0.0000	0.0000	0.0	0.0
² K _{13/2}	5298	1887	0.1723	0.1101	0.0008	6.4116	31.8	12.8
⁴ G _{5/2}	5676	1762	0.0000	0.0000	0.0002	0.0000	0.0	0.0
⁴ G _{7/2}	6307	1586	0.0000	0.0454	0.0308	0.0000	5.9	0.0
² D _{5/2} ⁽¹⁾	7121	1404	0.0000	0.0000	0.3593	0.0000	27.4	0.0
² H _{9/2} ⁽²⁾	8715	1147	0.0000	0.4446	0.0839	0.0000	59.3	0.0
⁴ D _{5/2}	10947	914	0.0000	0.0000	0.1200	0.0000	14.1	0.0
⁴ D _{7/2}	11526	868	0.0000	0.0008	0.0370	0.0000	4.7	0.0
² I _{11/2}	13370	748	0.7601	0.2012	0.0896	0.0000	318.4	0.0
² L _{17/2}	13834	723	0.1888	2.0767	0.9792	0.4743	598.3	2.5
⁴ D _{3/2}	14547	687	0.0000	0.0000	0.0577	0.0000	9.1	0.0
² P _{3/2}	15093	663	0.0000	0.0000	0.2197	0.0000	35.8	0.0

Table D.4: Radiative absorption properties of Er:ZBLAN (*continued*)

final	k_{calc} cm ⁻¹	λ_{calc} nm	$ \mathbf{U}^{(2)} ^2$	$ \mathbf{U}^{(4)} ^2$	$ \mathbf{U}^{(6)} ^2$	$ \mathbf{M}/\beta_m ^2$	f_{ed} 10 ⁻⁸	f_{md} 10 ⁻⁸
² I _{13/2}	15803	633	0.1117	0.5610	0.6488	0.7153	275.9	4.3
⁴ D _{1/2}	19287	518	0.0000	0.0000	0.0000	0.0000	0.0	0.0
² L _{15/2}	20062	498	0.0301	0.0485	0.2541	0.8799	84.3	6.7
² H _{9/2} ⁽¹⁾	20386	491	0.0000	0.0003	0.0659	0.0000	14.6	0.0
² D _{5/2} ⁽²⁾	21207	472	0.0000	0.0000	0.0025	0.0000	0.6	0.0
² H _{11/2} ⁽¹⁾	23385	428	0.5507	0.0552	0.1071	0.0000	389.2	0.0
² F _{7/2} ⁽²⁾	26739	374	0.0000	0.1908	1.0787	0.0000	383.6	0.0
² D _{3/2} ⁽²⁾	27321	366	0.0000	0.0000	0.0027	0.0000	0.8	0.0
² F _{5/2} ⁽²⁾	35411	282	0.0000	0.0000	0.1127	0.0000	44.1	0.0
² G _{7/2} ⁽²⁾	38527	260	0.0000	0.1193	0.0220	0.0000	72.7	0.0
² G _{9/2} ⁽²⁾	42514	235	0.0000	0.0524	0.0675	0.0000	63.1	0.0
² F _{5/2} ⁽¹⁾	65519	153	0.0000	0.0000	0.0024	0.0000	1.8	0.0
² F _{7/2} ⁽¹⁾	70013	143	0.0000	0.5794	0.0211	0.0000	590.3	0.0
	initial: ⁴ G _{7/2}							
² P _{3/2}	3467	2884	0.0122	0.0008	0.0000	0.0000	2.3	0.0
² P _{1/2}	4887	2046	0.0000	0.0266	0.0000	0.0000	3.4	0.0
² K _{13/2}	4962	2015	0.0000	0.4748	0.0039	0.0000	62.8	0.0
⁴ G _{5/2}	5339	1873	0.0028	0.2299	0.1271	5.2418	47.8	21.2
⁴ G _{7/2}	5970	1675	0.0413	0.0018	0.0377	0.1941	18.1	0.9
² D _{5/2} ⁽¹⁾	6784	1474	0.0556	0.0056	0.1982	0.0691	49.8	0.4
² H _{9/2} ⁽²⁾	8378	1194	0.0076	0.0239	0.0926	0.0071	25.4	0.0
⁴ D _{5/2}	10610	943	0.2133	0.0293	0.0005	0.1168	128.2	0.9
⁴ D _{7/2}	11189	894	0.0131	0.0092	0.1611	0.1527	49.3	1.3
² I _{11/2}	13034	767	0.0201	0.0642	0.0624	0.0000	53.7	0.0
² L _{17/2}	13498	741	0.0000	0.0000	0.1680	0.0000	48.9	0.0
⁴ D _{3/2}	14210	704	0.1081	0.0186	0.0000	0.0000	88.6	0.0
² P _{3/2}	14757	678	0.1419	0.1139	0.0000	0.0000	156.1	0.0
² I _{13/2}	15467	647	0.0000	0.0930	0.0292	0.0000	48.1	0.0
⁴ D _{1/2}	18951	528	0.0000	0.0105	0.0000	0.0000	5.3	0.0

Table D.4: Radiative absorption properties of Er:ZBLAN (*continued*)

final	k_{calc} cm ⁻¹	λ_{calc} nm	$ \mathbf{U}^{(2)} ^2$	$ \mathbf{U}^{(4)} ^2$	$ \mathbf{U}^{(6)} ^2$	$ \mathbf{M}/\beta_m ^2$	f_{ed} 10 ⁻⁸	f_{md} 10 ⁻⁸
² L _{15/2}	19726	507	0.0000	0.0138	0.2058	0.0000	95.2	0.0
² H _{9/2} ⁽¹⁾	20050	499	0.1901	0.0374	0.1319	0.0935	280.7	1.4
² D _{5/2} ⁽²⁾	20871	479	0.0004	0.1014	0.0267	0.0279	69.2	0.4
² H _{11/2} ⁽¹⁾	23049	434	0.0322	0.0008	0.1434	0.0000	112.0	0.0
² F _{7/2} ⁽²⁾	26403	379	0.0173	0.0543	0.0483	0.0888	91.0	1.8
² D _{3/2} ⁽²⁾	26985	371	0.0338	0.0303	0.0000	0.0000	71.0	0.0
² F _{5/2} ⁽²⁾	35074	285	0.0200	0.0080	0.0648	0.0269	96.2	0.7
² G _{7/2} ⁽²⁾	38191	262	0.0001	0.2984	0.0160	0.0092	327.1	0.3
² G _{9/2} ⁽²⁾	42177	237	0.0019	0.0625	0.0112	0.0048	88.2	0.2
² F _{5/2} ⁽¹⁾	65182	153	0.0555	0.1604	0.0285	0.0002	541.5	0.0
² F _{7/2} ⁽¹⁾	69677	144	0.0002	0.0632	0.0049	0.0005	133.0	0.0
initial: ² P _{3/2}								
² P _{1/2}	1420	7042	0.0036	0.0000	0.0000	0.6430	0.5	1.3
² K _{13/2}	1495	6690	0.0000	0.0000	0.3965	0.0000	24.3	0.0
⁴ G _{5/2}	1872	5341	0.1049	0.0003	0.0000	0.0043	20.2	0.0
⁴ G _{7/2}	2503	3995	0.0213	0.1101	0.0000	0.0000	19.9	0.0
² D _{5/2} ⁽¹⁾	3317	3015	0.0334	0.0061	0.0000	0.5647	12.7	2.8
² H _{9/2} ⁽²⁾	4911	2036	0.0000	0.0078	0.0216	0.0000	6.5	0.0
⁴ D _{5/2}	7143	1400	0.0863	0.0067	0.0000	1.0200	67.7	11.0
⁴ D _{7/2}	7722	1295	0.0481	0.0028	0.0000	0.0000	40.4	0.0
² I _{11/2}	9567	1045	0.0000	0.1894	0.1489	0.0000	157.6	0.0
² L _{17/2}	10031	997	0.0000	0.0000	0.0000	0.0000	0.0	0.0
⁴ D _{3/2}	10743	931	0.1307	0.0000	0.0000	0.7603	148.8	12.4
² P _{3/2}	11290	886	0.0029	0.0000	0.0000	0.8568	3.4	14.7
² I _{13/2}	12000	833	0.0000	0.0000	0.1841	0.0000	95.1	0.0
⁴ D _{1/2}	15484	646	0.0027	0.0000	0.0000	0.0520	4.5	1.2
² L _{15/2}	16259	615	0.0000	0.0000	0.0013	0.0000	0.9	0.0
² H _{9/2} ⁽¹⁾	16583	603	0.0000	0.0182	0.0610	0.0000	59.8	0.0
² D _{5/2} ⁽²⁾	17404	575	0.1415	0.1476	0.0000	0.0349	399.4	0.9

Table D.4: Radiative absorption properties of Er:ZBLAN (*continued*)

final	k_{calc} cm ⁻¹	λ_{calc} nm	$ \mathbf{U}^{(2)} ^2$	$ \mathbf{U}^{(4)} ^2$	$ \mathbf{U}^{(6)} ^2$	$ \mathbf{M}/\beta_m ^2$	f_{ed} 10 ⁻⁸	f_{md} 10 ⁻⁸
² H _{11/2} ⁽¹⁾	19582	511	0.0000	0.0376	0.0004	0.0000	39.8	0.0
² F _{7/2} ⁽²⁾	22936	436	0.1538	0.1374	0.0000	0.0000	546.9	0.0
² D _{3/2} ⁽²⁾	23518	425	0.1160	0.0000	0.0000	0.0357	292.2	1.3
² F _{5/2} ⁽²⁾	31607	316	0.0054	0.0249	0.0000	0.0224	61.1	1.1
² G _{7/2} ⁽²⁾	34724	288	0.0490	0.2485	0.0000	0.0000	656.6	0.0
² G _{9/2} ⁽²⁾	38710	258	0.0000	0.0438	0.0161	0.0000	121.1	0.0
² F _{5/2} ⁽¹⁾	61715	162	0.0185	0.0122	0.0000	0.0001	170.9	0.0
² F _{7/2} ⁽¹⁾	66210	151	0.0528	0.0659	0.0000	0.0000	640.5	0.0
	initial: ² P _{1/2}							
² K _{13/2}	75	—	0.0000	0.0000	0.0388	0.0000	0.2	0.0
⁴ G _{5/2}	452	—	0.0820	0.0000	0.0000	0.0000	7.0	0.0
⁴ G _{7/2}	1083	—	0.0000	0.0037	0.0000	0.0000	0.4	0.0
² D _{5/2} ⁽¹⁾	1897	5271	0.0055	0.0000	0.0000	0.0000	2.2	0.0
² H _{9/2} ⁽²⁾	3491	2864	0.0000	0.0468	0.0000	0.0000	17.2	0.0
⁴ D _{5/2}	5723	1747	0.0892	0.0000	0.0000	0.0000	107.7	0.0
⁴ D _{7/2}	6302	1587	0.0000	0.0383	0.0000	0.0000	25.6	0.0
² I _{11/2}	8147	1227	0.0000	0.0000	0.1675	0.0000	117.2	0.0
² L _{17/2}	8611	1161	0.0000	0.0000	0.0000	0.0000	0.0	0.0
⁴ D _{3/2}	9323	1073	0.0007	0.0000	0.0000	0.6590	1.4	18.6
² P _{3/2}	9870	1013	0.2095	0.0000	0.0000	0.1024	437.9	3.1
² I _{13/2}	10580	945	0.0000	0.0000	0.3401	0.0000	309.5	0.0
⁴ D _{1/2}	14064	711	0.0000	0.0000	0.0000	0.0481	0.0	2.1
² L _{15/2}	14839	674	0.0000	0.0000	0.0000	0.0000	0.0	0.0
² H _{9/2} ⁽¹⁾	15163	660	0.0000	0.1396	0.0000	0.0000	225.9	0.0
² D _{5/2} ⁽²⁾	15984	626	0.0583	0.0000	0.0000	0.0000	198.2	0.0
² H _{11/2} ⁽¹⁾	18162	551	0.0000	0.0000	0.0795	0.0000	124.9	0.0
² F _{7/2} ⁽²⁾	21516	465	0.0000	0.0948	0.0000	0.0000	219.0	0.0
² D _{3/2} ⁽²⁾	22098	453	0.0385	0.0000	0.0000	0.0237	182.0	1.6
² F _{5/2} ⁽²⁾	30187	331	0.0025	0.0000	0.0000	0.0000	16.1	0.0

Table D.4: Radiative absorption properties of Er:ZBLAN (*continued*)

final	k_{calc} cm ⁻¹	λ_{calc} nm	$ \mathbf{U}^{(2)} ^2$	$ \mathbf{U}^{(4)} ^2$	$ \mathbf{U}^{(6)} ^2$	$ \mathbf{M}/\beta_m ^2$	f_{ed} 10 ⁻⁸	f_{md} 10 ⁻⁸
$^2G_{7/2}^{(2)}$	33304	300	0.0000	0.1783	0.0000	0.0000	647.5	0.0
$^2G_{9/2}^{(2)}$	37290	268	0.0000	0.0848	0.0000	0.0000	347.0	0.0
$^2F_{5/2}^{(1)}$	60295	166	0.1196	0.0000	0.0000	0.0000	1624.0	0.0
$^2F_{7/2}^{(1)}$	64790	154	0.0000	0.0188	0.0000	0.0000	137.6	0.0
	initial: $^2K_{13/2}$							
$^4G_{5/2}$	377	—	0.0000	0.0143	0.0368	0.0000	0.2	0.0
$^4G_{7/2}$	1008	—	0.0000	0.5054	0.0223	0.0000	7.2	0.0
$^2D_{5/2}^{(1)}$	1823	5487	0.0000	0.0020	0.0204	0.0000	0.5	0.0
$^2H_{9/2}^{(2)}$	3417	2927	0.0228	0.0267	0.3381	0.0000	17.8	0.0
$^4D_{5/2}$	5648	1770	0.0000	0.0475	0.0529	0.0000	7.7	0.0
$^4D_{7/2}$	6227	1606	0.0000	0.0002	0.0177	0.0000	1.4	0.0
$^2I_{11/2}$	8072	1239	0.2577	0.8230	0.4405	0.4072	207.3	1.4
$^2L_{17/2}$	8536	1171	0.1764	0.4877	0.0574	0.0000	114.7	0.0
$^4D_{3/2}$	9248	1081	0.0000	0.0000	0.0576	0.0000	6.5	0.0
$^2P_{3/2}$	9795	1021	0.0000	0.0000	0.0000	0.0000	0.0	0.0
$^2I_{13/2}$	10505	952	0.0367	0.0421	0.0735	1.1877	27.9	5.4
$^4D_{1/2}$	13989	715	0.0000	0.0000	0.0024	0.0000	0.4	0.0
$^2L_{15/2}$	14764	677	0.0339	1.4635	1.1608	0.3829	555.8	2.5
$^2H_{9/2}^{(1)}$	15088	663	1.3057	0.0108	0.0544	0.0000	610.7	0.0
$^2D_{5/2}^{(2)}$	15909	629	0.0000	0.0435	0.0953	0.0000	29.3	0.0
$^2H_{11/2}^{(1)}$	18087	553	0.0239	0.0681	0.3386	0.1956	107.7	1.5
$^2F_{7/2}^{(2)}$	21441	466	0.0000	0.0369	0.4550	0.0000	133.0	0.0
$^2D_{3/2}^{(2)}$	22023	454	0.0000	0.0000	0.0050	0.0000	1.4	0.0
$^2F_{5/2}^{(2)}$	30113	332	0.0000	0.0213	0.3277	0.0000	133.6	0.0
$^2G_{7/2}^{(2)}$	33229	301	0.0000	0.0804	0.0726	0.0000	72.0	0.0
$^2G_{9/2}^{(2)}$	37216	269	0.0445	0.0082	0.0191	0.0000	65.5	0.0
$^2F_{5/2}^{(1)}$	60220	166	0.0000	0.6943	0.0073	0.0000	681.1	0.0
$^2F_{7/2}^{(1)}$	64715	155	0.0000	0.0002	0.0519	0.0000	44.2	0.0
	initial: $^4G_{5/2}$							

Table D.4: Radiative absorption properties of Er:ZBLAN (*continued*)

final	k_{calc} cm ⁻¹	λ_{calc} nm	$ \mathbf{U}^{(2)} ^2$	$ \mathbf{U}^{(4)} ^2$	$ \mathbf{U}^{(6)} ^2$	$ \mathbf{M}/\beta_m ^2$	f_{ed} 10 ⁻⁸	f_{md} 10 ⁻⁸
⁴ G _{7/2}	631	—	0.0015	0.1120	0.0386	6.5418	2.9	3.7
² D _{5/2} ⁽¹⁾	1445	6920	0.0032	0.0047	0.0000	0.0130	0.5	0.0
² H _{9/2} ⁽²⁾	3039	3290	0.0042	0.0254	0.0221	0.0000	5.5	0.0
⁴ D _{5/2}	5271	1897	0.0165	0.0050	0.0000	0.3543	7.1	1.9
⁴ D _{7/2}	5850	1709	0.0018	0.0083	0.2766	0.1173	48.7	0.7
² I _{11/2}	7695	1300	0.0000	0.0011	0.0001	0.0000	0.3	0.0
² L _{17/2}	8159	1226	0.0000	0.0000	0.0126	0.0000	2.9	0.0
⁴ D _{3/2}	8871	1127	0.0503	0.0007	0.0000	0.0000	31.7	0.0
² P _{3/2}	9418	1062	0.0947	0.0014	0.0000	0.0262	63.4	0.2
² I _{13/2}	10128	987	0.0000	0.0058	0.0407	0.0000	13.9	0.0
⁴ D _{1/2}	13612	735	0.2833	0.0000	0.0000	0.0000	272.8	0.0
² L _{15/2}	14387	695	0.0000	0.0000	0.0290	0.0000	12.0	0.0
² H _{9/2} ⁽¹⁾	14711	680	0.0017	0.0112	0.0036	0.0000	9.1	0.0
² D _{5/2} ⁽²⁾	15532	644	0.0027	0.0008	0.0000	0.2069	3.5	3.3
² H _{11/2} ⁽¹⁾	17710	565	0.0000	0.0040	0.0242	0.0000	14.9	0.0
² F _{7/2} ⁽²⁾	21064	475	0.0003	0.0142	0.0120	0.0175	18.5	0.4
² D _{3/2} ⁽²⁾	21646	462	0.0142	0.0001	0.0000	0.0049	22.0	0.1
² F _{5/2} ⁽²⁾	29735	336	0.0001	0.0072	0.0000	0.0811	8.0	2.5
² G _{7/2} ⁽²⁾	32852	304	0.0326	0.0049	0.0112	0.0310	94.1	1.1
² G _{9/2} ⁽²⁾	36838	271	0.0012	0.0142	0.0015	0.0000	24.1	0.0
² F _{5/2} ⁽¹⁾	59843	167	0.0019	0.0183	0.0000	0.0057	50.1	0.4
² F _{7/2} ⁽¹⁾	64338	155	0.0018	0.0019	0.0108	0.0006	34.3	0.0
	initial: ⁴ G _{7/2}							
² D _{5/2} ⁽¹⁾	814	—	0.0002	0.0102	0.0002	0.0522	0.2	0.0
² H _{9/2} ⁽²⁾	2408	4153	0.0198	0.0050	0.1759	4.2013	11.7	7.6
⁴ D _{5/2}	4640	2155	0.0258	0.1085	0.1396	0.2515	33.5	0.9
⁴ D _{7/2}	5219	1916	0.0008	0.0003	0.1422	0.0484	16.2	0.2
² I _{11/2}	7064	1416	0.0075	0.0827	0.0129	0.0000	20.3	0.0
² L _{17/2}	7528	1328	0.0000	0.0000	0.0261	0.0000	4.2	0.0

Table D.4: Radiative absorption properties of Er:ZBLAN (*continued*)

final	k_{calc} cm ⁻¹	λ_{calc} nm	$ \mathbf{U}^{(2)} ^2$	$ \mathbf{U}^{(4)} ^2$	$ \mathbf{U}^{(6)} ^2$	$ \mathbf{M}/\beta_m ^2$	f_{ed} 10 ⁻⁸	f_{md} 10 ⁻⁸
⁴ D _{3/2}	8240	1214	0.2207	0.0481	0.0000	0.0000	106.7	0.0
² P _{3/2}	8787	1138	0.0004	0.0774	0.0000	0.0000	18.3	0.0
² I _{13/2}	9497	1053	0.0000	0.1200	0.0690	0.0000	44.4	0.0
⁴ D _{1/2}	12981	770	0.0000	0.0156	0.0000	0.0000	5.4	0.0
² L _{15/2}	13756	727	0.0000	0.0048	0.2541	0.0000	77.1	0.0
² H _{9/2} ⁽¹⁾	14080	710	0.2108	0.0697	0.0246	0.0439	191.2	0.5
² D _{5/2} ⁽²⁾	14901	671	0.1394	0.1786	0.0296	0.0730	190.9	0.8
² H _{11/2} ⁽¹⁾	17079	586	0.0375	0.0000	0.1270	0.0000	80.9	0.0
² F _{7/2} ⁽²⁾	20433	489	0.0115	0.0631	0.0493	0.0014	68.9	0.0
² D _{3/2} ⁽²⁾	21015	476	0.3375	0.0192	0.0000	0.0000	389.5	0.0
² F _{5/2} ⁽²⁾	29104	344	0.0082	0.0863	0.0045	0.1526	83.8	3.4
² G _{7/2} ⁽²⁾	32221	310	0.0043	0.1992	0.0089	0.0017	188.4	0.0
² G _{9/2} ⁽²⁾	36207	276	0.0089	0.1324	0.0108	0.0033	157.5	0.1
² F _{5/2} ⁽¹⁾	59212	169	0.0727	0.0883	0.0000	0.0044	390.1	0.2
² F _{7/2} ⁽¹⁾	63707	157	0.0091	0.0751	0.0056	0.0002	176.0	0.0
initial: ² D _{5/2} ⁽¹⁾								
² H _{9/2} ⁽²⁾	1594	6274	0.0078	0.1087	0.0519	0.0000	9.0	0.0
⁴ D _{5/2}	3826	2614	0.1969	0.0621	0.0000	0.1370	61.1	0.5
⁴ D _{7/2}	4405	2270	0.1605	0.1105	0.0045	0.8744	67.3	3.9
² I _{11/2}	6250	1600	0.0000	0.0772	0.3065	0.0000	71.8	0.0
² L _{17/2}	6714	1489	0.0000	0.0000	0.3949	0.0000	75.8	0.0
⁴ D _{3/2}	7426	1347	0.0230	0.0024	0.0000	3.3071	12.7	24.8
² P _{3/2}	7973	1254	0.1497	0.0208	0.0000	0.0596	90.0	0.5
² I _{13/2}	8682	1152	0.0000	0.0106	0.1896	0.0000	50.4	0.0
⁴ D _{1/2}	12167	822	0.0740	0.0000	0.0000	0.0000	63.6	0.0
² L _{15/2}	12941	773	0.0000	0.0000	0.0129	0.0000	4.8	0.0
² H _{9/2} ⁽¹⁾	13266	754	0.0000	0.0697	0.4757	0.0000	214.2	0.0
² D _{5/2} ⁽²⁾	14086	710	0.2583	0.0330	0.0000	0.1020	274.1	1.5
² H _{11/2} ⁽¹⁾	16265	615	0.0000	0.1731	0.1239	0.0000	158.2	0.0

Table D.4: Radiative absorption properties of Er:ZBLAN (*continued*)

final	k_{calc} cm ⁻¹	λ_{calc} nm	$ \mathbf{U}^{(2)} ^2$	$ \mathbf{U}^{(4)} ^2$	$ \mathbf{U}^{(6)} ^2$	$ \mathbf{M}/\beta_m ^2$	f_{ed} 10 ⁻⁸	f_{md} 10 ⁻⁸
² F _{7/2} ⁽²⁾	19619	510	0.7892	0.0452	0.0113	0.1184	1139.0	2.4
² D _{3/2} ⁽²⁾	20201	495	0.0003	0.1222	0.0000	0.1741	88.7	3.6
² F _{5/2} ⁽²⁾	28290	353	0.0316	0.0038	0.0000	0.0019	68.0	0.1
² G _{7/2} ⁽²⁾	31407	318	0.0069	0.0728	0.1103	0.0000	200.0	0.0
² G _{9/2} ⁽²⁾	35393	283	0.0314	0.0855	0.0119	0.0000	203.6	0.0
² F _{5/2} ⁽¹⁾	58398	171	0.0047	0.0359	0.0000	0.0099	99.8	0.6
² F _{7/2} ⁽¹⁾	62893	159	0.0287	0.0414	0.0007	0.0000	234.9	0.0
	initial: ² H _{9/2} ⁽²⁾							
⁴ D _{5/2}	2232	4481	0.0012	0.1138	0.0684	0.0000	8.0	0.0
⁴ D _{7/2}	2811	3558	0.0032	0.0002	0.0069	0.0097	0.7	0.0
² I _{11/2}	4656	2148	0.0002	0.0325	0.0288	0.0005	5.5	0.0
² L _{17/2}	5120	1953	0.0000	0.0000	0.1342	0.0000	11.8	0.0
⁴ D _{3/2}	5832	1715	0.0000	0.0012	0.0073	0.0000	0.9	0.0
² P _{3/2}	6379	1568	0.0000	0.0044	0.1498	0.0000	17.0	0.0
² I _{13/2}	7088	1411	0.1033	0.0002	0.6316	0.0000	107.8	0.0
⁴ D _{1/2}	10573	946	0.0000	0.0476	0.0000	0.0000	10.7	0.0
² L _{15/2}	11348	881	0.0000	0.7422	0.4468	0.0000	266.6	0.0
² H _{9/2} ⁽¹⁾	11672	857	0.0067	0.0172	0.0422	0.0008	16.1	0.0
² D _{5/2} ⁽²⁾	12493	800	0.1008	0.0182	0.0236	0.0000	63.3	0.0
² H _{11/2} ⁽¹⁾	14671	682	0.3009	0.5755	0.0508	0.0045	380.6	0.0
² F _{7/2} ⁽²⁾	18025	555	0.0102	0.0245	0.0719	0.0059	39.7	0.1
² D _{3/2} ⁽²⁾	18607	537	0.0000	0.0002	0.0022	0.0000	0.8	0.0
² F _{5/2} ⁽²⁾	26696	375	0.7168	0.9648	0.0366	0.0000	1396.0	0.0
² G _{7/2} ⁽²⁾	29813	335	0.0249	0.0006	0.0041	0.0015	34.5	0.0
² G _{9/2} ⁽²⁾	33799	296	0.0126	0.4785	0.0002	0.0000	371.5	0.0
² F _{5/2} ⁽¹⁾	56804	176	0.0547	0.2591	0.0016	0.0000	474.4	0.0
² F _{7/2} ⁽¹⁾	61299	163	0.0634	0.0440	0.0444	0.0002	285.7	0.0
	initial: ⁴ D _{5/2}							
⁴ D _{7/2}	579	—	0.1646	0.0856	0.0019	2.5413	7.6	1.3

Table D.4: Radiative absorption properties of Er:ZBLAN (*continued*)

final	k_{calc} cm ⁻¹	λ_{calc} nm	$ \mathbf{U}^{(2)} ^2$	$ \mathbf{U}^{(4)} ^2$	$ \mathbf{U}^{(6)} ^2$	$ \mathbf{M}/\beta_m ^2$	f_{ed} 10 ⁻⁸	f_{md} 10 ⁻⁸
² I _{11/2}	2424	4126	0.0000	0.0106	0.0604	0.0000	5.0	0.0
² L _{17/2}	2888	3463	0.0000	0.0000	0.0572	0.0000	4.7	0.0
⁴ D _{3/2}	3600	2778	0.2301	0.0397	0.0000	0.9461	63.0	3.4
² P _{3/2}	4147	2411	0.0010	0.0052	0.0000	2.6639	1.0	11.1
² I _{13/2}	4857	2059	0.0000	0.2099	0.0893	0.0000	48.3	0.0
⁴ D _{1/2}	8341	1199	0.0003	0.0000	0.0000	0.0000	0.2	0.0
² L _{15/2}	9116	1097	0.0000	0.0000	0.0156	0.0000	4.1	0.0
² H _{9/2} ⁽¹⁾	9440	1059	0.0175	0.1095	0.0100	0.0000	51.0	0.0
² D _{5/2} ⁽²⁾	10261	975	0.0119	0.0759	0.0000	0.4671	36.2	4.9
² H _{11/2} ⁽¹⁾	12439	804	0.0000	0.1816	0.0205	0.0000	87.5	0.0
² F _{7/2} ⁽²⁾	15793	633	0.0908	0.0003	0.0120	0.3261	107.3	5.2
² D _{3/2} ⁽²⁾	16375	611	0.0124	0.0312	0.0000	0.2614	32.6	4.3
² F _{5/2} ⁽²⁾	24464	409	0.0032	0.0045	0.0000	0.0359	9.6	0.9
² G _{7/2} ⁽²⁾	27581	363	0.0515	0.0124	0.2257	0.0000	295.6	0.0
² G _{9/2} ⁽²⁾	31567	317	0.1378	0.0878	0.0953	0.0000	502.6	0.0
² F _{5/2} ⁽¹⁾	54572	183	0.0005	0.2197	0.0000	0.0017	453.8	0.1
² F _{7/2} ⁽¹⁾	59067	169	0.0237	0.2363	0.0001	0.0048	631.3	0.3
	initial: ⁴ D _{7/2}							
² I _{11/2}	1845	5421	0.0041	0.0000	0.0198	0.0000	1.1	0.0
² L _{17/2}	2309	4331	0.0000	0.0000	0.0362	0.0000	1.8	0.0
⁴ D _{3/2}	3021	3310	0.1083	0.2093	0.0000	0.0000	33.7	0.0
² P _{3/2}	3568	2803	0.0175	0.0333	0.0000	0.0000	6.4	0.0
² I _{13/2}	4278	2338	0.0000	0.0018	0.0169	0.0000	1.7	0.0
⁴ D _{1/2}	7762	1288	0.0000	0.1705	0.0000	0.0000	35.1	0.0
² L _{15/2}	8537	1171	0.0000	0.0000	0.0059	0.0000	1.1	0.0
² H _{9/2} ⁽¹⁾	8861	1129	0.0021	0.0006	0.0062	0.0014	2.3	0.0
² D _{5/2} ⁽²⁾	9682	1033	0.0903	0.0481	0.0037	3.1977	59.4	23.5
² H _{11/2} ⁽¹⁾	11860	843	0.0019	0.0006	0.0027	0.0000	2.1	0.0
² F _{7/2} ⁽²⁾	15214	657	0.0145	0.0081	0.0018	0.4991	15.6	5.8

Table D.4: Radiative absorption properties of Er:ZBLAN (*continued*)

final	k_{calc} cm ⁻¹	λ_{calc} nm	$ \mathbf{U}^{(2)} ^2$	$ \mathbf{U}^{(4)} ^2$	$ \mathbf{U}^{(6)} ^2$	$ \mathbf{M}/\beta_m ^2$	f_{ed} 10 ⁻⁸	f_{md} 10 ⁻⁸
² D _{3/2} ⁽²⁾	15796	633	0.0070	0.0428	0.0000	0.0000	23.9	0.0
² F _{5/2} ⁽²⁾	23885	419	0.0016	0.0106	0.0000	0.0014	8.9	0.0
² G _{7/2} ⁽²⁾	27002	370	0.0008	0.0000	0.0057	0.0053	4.6	0.1
² G _{9/2} ⁽²⁾	30988	323	0.0058	0.0015	0.0043	0.0036	14.0	0.1
² F _{5/2} ⁽¹⁾	53993	185	0.0004	0.0016	0.0106	0.0072	16.6	0.3
² F _{7/2} ⁽¹⁾	58488	171	0.0016	0.0055	0.0036	0.0408	19.3	1.9
	initial: ² I _{11/2}							
² L _{17/2}	464	—	0.0000	0.0156	0.1371	0.0000	0.9	0.0
⁴ D _{3/2}	1176	—	0.0000	0.0206	0.0223	0.0000	0.7	0.0
² P _{3/2}	1723	5803	0.0000	0.0857	0.1175	0.0000	5.3	0.0
² I _{13/2}	2433	4110	0.3787	0.3087	0.2007	3.9678	51.9	4.8
⁴ D _{1/2}	5917	1690	0.0000	0.0000	0.0279	0.0000	2.4	0.0
² L _{15/2}	6692	1494	0.5547	0.5983	0.4571	0.0000	245.3	0.0
² H _{9/2} ⁽¹⁾	7016	1425	0.7608	0.4669	0.1539	1.6544	261.4	5.9
² D _{5/2} ⁽²⁾	7837	1276	0.0000	0.0090	0.0381	0.0000	5.5	0.0
² H _{11/2} ⁽¹⁾	10015	998	0.0471	0.1213	0.0561	2.7569	46.2	14.0
² F _{7/2} ⁽²⁾	13369	748	0.0181	0.0070	0.4416	0.0000	95.0	0.0
² D _{3/2} ⁽²⁾	13951	717	0.0000	0.0857	0.0033	0.0000	21.9	0.0
² F _{5/2} ⁽²⁾	22041	454	0.0000	0.0411	0.0002	0.0000	16.3	0.0
² G _{7/2} ⁽²⁾	25157	398	1.3949	0.0001	0.0032	0.0000	1256.1	0.0
² G _{9/2} ⁽²⁾	29143	343	0.1380	0.0844	0.0927	0.0577	228.4	0.9
² F _{5/2} ⁽¹⁾	52148	192	0.0000	0.5822	0.0496	0.0000	611.7	0.0
² F _{7/2} ⁽¹⁾	56643	177	0.1491	0.0103	0.1592	0.0000	465.4	0.0
	initial: ² L _{17/2}							
⁴ D _{3/2}	712	—	0.0000	0.0000	0.0000	0.0000	0.0	0.0
² P _{3/2}	1259	7943	0.0000	0.0000	0.0000	0.0000	0.0	0.0
² I _{13/2}	1969	5079	1.2939	0.6938	0.5115	0.0000	83.4	0.0
⁴ D _{1/2}	5453	1834	0.0000	0.0000	0.0000	0.0000	0.0	0.0
² L _{15/2}	6228	1606	0.0621	0.1679	0.2059	7.9939	33.6	16.7

Table D.4: Radiative absorption properties of Er:ZBLAN (*continued*)

final	k_{calc} cm ⁻¹	λ_{calc} nm	$ \mathbf{U}^{(2)} ^2$	$ \mathbf{U}^{(4)} ^2$	$ \mathbf{U}^{(6)} ^2$	$ \mathbf{M}/\beta_m ^2$	f_{ed} 10 ⁻⁸	f_{md} 10 ⁻⁸
$^2\text{H}_{9/2}^{(1)}$	6552	1526	0.0000	0.0130	0.1938	0.0000	13.1	0.0
$^2\text{D}_{5/2}^{(2)}$	7373	1356	0.0000	0.0000	0.4260	0.0000	30.0	0.0
$^2\text{H}_{11/2}^{(1)}$	9551	1047	0.0000	0.2400	1.2104	0.0000	137.5	0.0
$^2\text{F}_{7/2}^{(2)}$	12905	775	0.0000	0.0000	0.5175	0.0000	63.9	0.0
$^2\text{D}_{3/2}^{(2)}$	13487	741	0.0000	0.0000	0.0000	0.0000	0.0	0.0
$^2\text{F}_{5/2}^{(2)}$	21576	463	0.0000	0.0000	0.0084	0.0000	1.8	0.0
$^2\text{G}_{7/2}^{(2)}$	24693	405	0.0000	0.0000	0.0353	0.0000	8.4	0.0
$^2\text{G}_{9/2}^{(2)}$	28679	349	0.0000	1.0039	0.3633	0.0000	447.6	0.0
$^2\text{F}_{5/2}^{(1)}$	51684	193	0.0000	0.0000	0.0829	0.0000	43.5	0.0
$^2\text{F}_{7/2}^{(1)}$	56179	178	0.0000	0.0000	0.6325	0.0000	360.9	0.0
	initial: $^4\text{D}_{3/2}$							
$^2\text{P}_{3/2}$	547	—	0.0025	0.0000	0.0000	0.0295	0.1	0.0
$^2\text{I}_{13/2}$	1257	7958	0.0000	0.0000	0.0201	0.0000	1.0	0.0
$^4\text{D}_{1/2}$	4741	2109	0.2465	0.0000	0.0000	2.6555	123.1	19.0
$^2\text{L}_{15/2}$	5516	1813	0.0000	0.0000	0.1341	0.0000	31.7	0.0
$^2\text{H}_{9/2}^{(1)}$	5840	1712	0.0000	0.0743	0.0738	0.0000	41.5	0.0
$^2\text{D}_{5/2}^{(2)}$	6661	1501	0.0264	0.0001	0.0000	1.3753	18.6	13.9
$^2\text{H}_{11/2}^{(1)}$	8839	1131	0.0000	0.0038	0.2725	0.0000	105.3	0.0
$^2\text{F}_{7/2}^{(2)}$	12193	820	0.0185	0.0062	0.0000	0.0000	28.0	0.0
$^2\text{D}_{3/2}^{(2)}$	12775	783	0.0008	0.0000	0.0000	0.2275	1.1	4.4
$^2\text{F}_{5/2}^{(2)}$	20864	479	0.2407	0.0669	0.0000	0.1277	611.1	4.1
$^2\text{G}_{7/2}^{(2)}$	23981	417	0.0163	0.0086	0.0000	0.0000	52.9	0.0
$^2\text{G}_{9/2}^{(2)}$	27967	358	0.0000	0.1483	0.0333	0.0000	265.1	0.0
$^2\text{F}_{5/2}^{(1)}$	50972	196	0.0288	0.0327	0.0000	0.0125	259.5	1.0
$^2\text{F}_{7/2}^{(1)}$	55467	180	0.0164	0.0244	0.0000	0.0000	178.8	0.0
	initial: $^2\text{P}_{3/2}$							
$^2\text{I}_{13/2}$	710	—	0.0000	0.0000	0.1586	0.0000	4.3	0.0
$^4\text{D}_{1/2}$	4194	2384	0.0011	0.0000	0.0000	1.6161	0.5	10.2
$^2\text{L}_{15/2}$	4969	2013	0.0000	0.0000	0.0218	0.0000	4.6	0.0

Table D.4: Radiative absorption properties of Er:ZBLAN (*continued*)

final	k_{calc} cm ⁻¹	λ_{calc} nm	$ \mathbf{U}^{(2)} ^2$	$ \mathbf{U}^{(4)} ^2$	$ \mathbf{U}^{(6)} ^2$	$ \mathbf{M}/\beta_m ^2$	f_{ed} 10 ⁻⁸	f_{md} 10 ⁻⁸
² H _{9/2} ⁽¹⁾	5293	1889	0.0000	0.0752	0.0062	0.0000	22.5	0.0
² D _{5/2} ⁽²⁾	6114	1636	0.1510	0.0021	0.0000	0.0833	98.1	0.8
² H _{11/2} ⁽¹⁾	8292	1206	0.0000	0.1135	0.1454	0.0000	101.8	0.0
² F _{7/2} ⁽²⁾	11646	859	0.0556	0.0602	0.0000	0.0000	105.9	0.0
² D _{3/2} ⁽²⁾	12228	818	0.1237	0.0000	0.0000	0.2613	160.4	4.9
² F _{5/2} ⁽²⁾	20317	492	0.0916	0.0698	0.0000	0.0149	274.6	0.5
² G _{7/2} ⁽²⁾	23434	427	0.0841	0.0008	0.0000	0.0000	212.1	0.0
² G _{9/2} ⁽²⁾	27420	365	0.0000	0.3156	0.2047	0.0000	712.8	0.0
² F _{5/2} ⁽¹⁾	50425	198	0.0002	0.1728	0.0000	0.0008	493.9	0.1
² F _{7/2} ⁽¹⁾	54920	182	0.1300	0.1192	0.0000	0.0000	1174.1	0.0
	initial: ² I _{13/2}							
⁴ D _{1/2}	3484	2870	0.0000	0.0000	0.0266	0.0000	1.1	0.0
² L _{15/2}	4259	2348	0.1204	0.8390	0.0212	0.0417	70.5	0.1
² H _{9/2} ⁽¹⁾	4583	2182	0.0029	0.0948	0.1504	0.0000	15.4	0.0
² D _{5/2} ⁽²⁾	5404	1850	0.0000	0.1464	0.0390	0.0000	14.6	0.0
² H _{11/2} ⁽¹⁾	7582	1319	0.7129	0.5838	0.3189	1.8619	260.1	6.1
² F _{7/2} ⁽²⁾	10936	914	0.0000	0.0005	0.1734	0.0000	23.4	0.0
² D _{3/2} ⁽²⁾	11518	868	0.0000	0.0000	0.0001	0.0000	0.0	0.0
² F _{5/2} ⁽²⁾	19608	510	0.0000	0.1292	0.2637	0.0000	102.8	0.0
² G _{7/2} ⁽²⁾	22724	440	0.0000	0.0032	0.0183	0.0000	6.3	0.0
² G _{9/2} ⁽²⁾	26711	374	1.5970	0.0005	0.0014	0.0000	1310.6	0.0
² F _{5/2} ⁽¹⁾	49715	201	0.0000	0.0006	0.1580	0.0000	103.0	0.0
² F _{7/2} ⁽¹⁾	54210	184	0.0000	0.7919	0.1580	0.0000	805.4	0.0
	initial: ⁴ D _{1/2}							
² L _{15/2}	775	—	0.0000	0.0000	0.0000	0.0000	0.0	0.0
² H _{9/2} ⁽¹⁾	1099	—	0.0000	0.0159	0.0000	0.0000	1.7	0.0
² D _{5/2} ⁽²⁾	1920	5209	0.1358	0.0000	0.0000	0.0000	53.7	0.0
² H _{11/2} ⁽¹⁾	4098	2440	0.0000	0.0000	0.0006	0.0000	0.2	0.0
² F _{7/2} ⁽²⁾	7452	1342	0.0000	0.0202	0.0000	0.0000	16.0	0.0

Table D.4: Radiative absorption properties of Er:ZBLAN (*continued*)

final	k_{calc} cm ⁻¹	λ_{calc} nm	$ \mathbf{U}^{(2)} ^2$	$ \mathbf{U}^{(4)} ^2$	$ \mathbf{U}^{(6)} ^2$	$ \mathbf{M}/\beta_m ^2$	f_{ed} 10 ⁻⁸	f_{md} 10 ⁻⁸
$^2D_{3/2}^{(2)}$	8034	1245	0.0707	0.0000	0.0000	1.3093	120.1	31.9
$^2F_{5/2}^{(2)}$	16123	620	0.0029	0.0000	0.0000	0.0000	9.8	0.0
$^2G_{7/2}^{(2)}$	19240	520	0.0000	0.0150	0.0000	0.0000	30.9	0.0
$^2G_{9/2}^{(2)}$	23226	431	0.0000	0.0078	0.0000	0.0000	19.4	0.0
$^2F_{5/2}^{(1)}$	46231	216	0.0118	0.0000	0.0000	0.0000	121.9	0.0
$^2F_{7/2}^{(1)}$	50726	197	0.0000	0.0051	0.0000	0.0000	29.0	0.0
	initial: $^2L_{15/2}$							
$^2H_{9/2}^{(1)}$	324	—	0.0000	0.1547	1.1396	0.0000	4.1	0.0
$^2D_{5/2}^{(2)}$	1145	—	0.0000	0.0000	0.0018	0.0000	0.0	0.0
$^2H_{11/2}^{(1)}$	3323	3009	0.7016	0.1533	0.0442	0.0000	69.4	0.0
$^2F_{7/2}^{(2)}$	6677	1498	0.0000	0.0007	0.0453	0.0000	3.3	0.0
$^2D_{3/2}^{(2)}$	7259	1378	0.0000	0.0000	0.5262	0.0000	41.0	0.0
$^2F_{5/2}^{(2)}$	15349	652	0.0000	0.0000	0.5445	0.0000	90.2	0.0
$^2G_{7/2}^{(2)}$	18465	542	0.0000	0.7242	0.1916	0.0000	217.2	0.0
$^2G_{9/2}^{(2)}$	22451	445	0.0000	0.0503	0.0127	0.0000	18.2	0.0
$^2F_{5/2}^{(1)}$	45456	220	0.0000	0.0000	0.6402	0.0000	328.6	0.0
$^2F_{7/2}^{(1)}$	49951	200	0.0000	0.1019	0.0610	0.0000	106.8	0.0
	initial: $^2H_{9/2}^{(1)}$							
$^2D_{5/2}^{(2)}$	821	—	0.0049	0.0555	0.2541	0.0000	4.2	0.0
$^2H_{11/2}^{(1)}$	2999	3334	0.0605	0.1664	0.4265	3.6162	39.8	6.5
$^2F_{7/2}^{(2)}$	6353	1574	0.0001	0.0305	0.2454	0.0009	30.9	0.0
$^2D_{3/2}^{(2)}$	6935	1442	0.0000	0.0142	0.0318	0.0000	5.9	0.0
$^2F_{5/2}^{(2)}$	15024	666	0.0006	0.1753	0.0823	0.0000	78.0	0.0
$^2G_{7/2}^{(2)}$	18141	551	1.2511	0.0258	0.0596	0.1254	995.7	1.4
$^2G_{9/2}^{(2)}$	22127	452	0.0468	0.0043	0.1159	0.2854	90.8	3.9
$^2F_{5/2}^{(1)}$	45132	222	0.9041	0.3173	0.0171	0.0000	2147.7	0.0
$^2F_{7/2}^{(1)}$	49627	202	0.0168	0.0172	0.0959	0.0031	143.6	0.1
	initial: $^2D_{5/2}^{(2)}$							
$^2H_{11/2}^{(1)}$	2178	4591	0.0000	0.0163	0.0041	0.0000	1.5	0.0

Table D.4: Radiative absorption properties of Er:ZBLAN (*continued*)

final	k_{calc} cm ⁻¹	λ_{calc} nm	$ \mathbf{U}^{(2)} ^2$	$ \mathbf{U}^{(4)} ^2$	$ \mathbf{U}^{(6)} ^2$	$ \mathbf{M}/\beta_m ^2$	f_{ed} 10 ⁻⁸	f_{md} 10 ⁻⁸
$^2F_{7/2}^{(2)}$	5532	1808	0.4004	0.0119	0.0298	0.1449	162.8	0.8
$^2D_{3/2}^{(2)}$	6114	1636	0.0317	0.0944	0.0000	2.9049	34.1	17.9
$^2F_{5/2}^{(2)}$	14204	704	0.0054	0.0001	0.0000	1.0807	5.5	15.6
$^2G_{7/2}^{(2)}$	17320	577	0.1111	0.0183	0.4050	0.0049	350.0	0.1
$^2G_{9/2}^{(2)}$	21306	469	0.0562	0.0158	0.0551	0.0000	131.3	0.0
$^2F_{5/2}^{(1)}$	44311	226	0.0000	0.1689	0.0000	0.0173	278.0	0.8
$^2F_{7/2}^{(1)}$	48806	205	0.1004	0.0886	0.0224	0.0216	561.9	1.1
	initial: $^2H_{11/2}^{(1)}$							
$^2F_{7/2}^{(2)}$	3354	2982	0.0196	0.1165	0.1211	0.0000	14.9	0.0
$^2D_{3/2}^{(2)}$	3936	2541	0.0000	0.0275	0.3198	0.0000	19.8	0.0
$^2F_{5/2}^{(2)}$	12025	832	0.0000	0.0346	0.4510	0.0000	85.2	0.0
$^2G_{7/2}^{(2)}$	15142	660	0.1392	0.0018	0.0412	0.0000	84.1	0.0
$^2G_{9/2}^{(2)}$	19128	523	1.4599	0.0065	0.0137	0.1231	998.3	1.2
$^2F_{5/2}^{(1)}$	42133	237	0.0000	0.0523	0.2248	0.0000	182.2	0.0
$^2F_{7/2}^{(1)}$	46628	214	0.7869	0.5181	0.0017	0.0000	1816.9	0.0
	initial: $^2F_{7/2}^{(2)}$							
$^2D_{3/2}^{(2)}$	582	—	0.0646	0.0004	0.0000	0.0000	1.8	0.0
$^2F_{5/2}^{(2)}$	8671	1153	0.0721	0.0112	0.0764	3.1593	49.9	20.8
$^2G_{7/2}^{(2)}$	11788	848	0.0380	0.0592	0.0043	0.0873	43.4	0.8
$^2G_{9/2}^{(2)}$	15774	634	0.4067	0.2615	0.0029	0.0681	452.1	0.8
$^2F_{5/2}^{(1)}$	38779	258	0.0014	0.0501	0.5088	0.0958	495.4	2.9
$^2F_{7/2}^{(1)}$	43274	231	0.1953	0.0499	0.1060	0.0067	630.7	0.2
	initial: $^2D_{3/2}^{(2)}$							
$^2F_{5/2}^{(2)}$	8090	1236	0.7753	0.0765	0.0000	0.3906	696.2	4.8
$^2G_{7/2}^{(2)}$	11206	892	0.0513	0.0026	0.0000	0.0000	62.5	0.0
$^2G_{9/2}^{(2)}$	15192	658	0.0000	0.0297	0.5535	0.0000	386.9	0.0
$^2F_{5/2}^{(1)}$	38197	262	0.1944	0.0226	0.0000	0.0033	860.4	0.2
$^2F_{7/2}^{(1)}$	42692	234	0.0065	0.0792	0.0000	0.0000	218.2	0.0
	initial: $^2F_{5/2}^{(2)}$							

Table D.4: Radiative absorption properties of Er:ZBLAN (*continued*)

final	k_{calc} cm ⁻¹	λ_{calc} nm	$ \mathbf{U}^{(2)} ^2$	$ \mathbf{U}^{(4)} ^2$	$ \mathbf{U}^{(6)} ^2$	$ \mathbf{M}/\beta_m ^2$	f_{ed} 10 ⁻⁸	f_{md} 10 ⁻⁸
$^2G_{7/2}^{(2)}$	3116	3209	0.5042	0.1678	0.0591	0.0399	133.2	0.1
$^2G_{9/2}^{(2)}$	7103	1408	0.1495	0.0341	0.0731	0.0000	98.2	0.0
$^2F_{5/2}^{(1)}$	30108	332	0.2855	0.0052	0.0000	0.0005	624.6	0.0
$^2F_{7/2}^{(1)}$	34603	289	0.0017	0.1630	0.4579	0.0609	676.2	2.2
initial: $^2G_{7/2}^{(2)}$								
$^2G_{9/2}^{(2)}$	3986	2509	0.0900	0.0536	0.1169	4.1851	34.4	12.6
$^2F_{5/2}^{(1)}$	26991	370	1.5392	0.3735	0.0527	0.0507	2536.7	1.1
$^2F_{7/2}^{(1)}$	31486	318	0.0590	0.1874	0.4580	0.1519	577.7	3.7
initial: $^2G_{9/2}^{(2)}$								
$^2F_{5/2}^{(1)}$	23005	435	0.0227	0.1143	0.4126	0.0000	243.8	0.0
$^2F_{7/2}^{(1)}$	27500	364	2.1349	0.6503	0.1815	0.0815	3000.5	1.4
initial: $^2F_{5/2}^{(1)}$								
$^2F_{7/2}^{(1)}$	4495	2225	0.1498	0.1273	0.0732	3.2904	76.8	14.9

D.3 Tm:ZBLAN

Table D.5: Radiative emission properties of Tm:ZBLAN

final	k_{calc} cm ⁻¹	λ_{calc} nm	$ \mathbf{U}^{(2)} ^2$	$ \mathbf{U}^{(4)} ^2$	$ \mathbf{U}^{(6)} ^2$	$ \mathbf{M}/\beta_m ^2$	A_{ed} s ⁻¹	A_{md} s ⁻¹	β
initial: 1S_0							$\tau = 0.00$ ms		
3P_2	36664	273	0.3019	0.0000	0.0000	0.0000	103195	0	0.114
3P_1	38428	260	0.0000	0.0000	0.0000	0.1144	0	647	0.001
3P_0	39363	254	0.0000	0.0000	0.0000	0.0000	0	0	0.000
1I_6	40014	250	0.0000	0.0000	0.5428	0.0000	56350	0	0.062
1D_2	46938	213	0.2200	0.0000	0.0000	0.0000	167595	0	0.184
1G_4	53610	187	0.0000	0.4161	0.0000	0.0000	306823	0	0.338
3F_2	59918	167	0.0454	0.0000	0.0000	0.0000	73520	0	0.081
3F_3	60423	165	0.0000	0.0000	0.0000	0.0000	0	0	0.000
3H_4	62306	160	0.0000	0.0552	0.0000	0.0000	63944	0	0.070
3H_5	66695	150	0.0000	0.0000	0.0000	0.0000	0	0	0.000

Table D.5: Radiative emission properties of Tm:ZBLAN (*continued*)

final	k_{calc} cm ⁻¹	λ_{calc} nm	$ \mathbf{U}^{(2)} ^2$	$ \mathbf{U}^{(4)} ^2$	$ \mathbf{U}^{(6)} ^2$	$ \mathbf{M}/\beta_m ^2$	A_{ed} s ⁻¹	A_{md} s ⁻¹	β
³ F ₄	69144	145	0.0000	0.0864	0.0000	0.0000	136721	0	0.150
³ H ₆	74856	134	0.0000	0.0000	0.0000	0.0000	17	0	0.000
	initial: ³ P ₂						$\tau = 0.02$ ms		
³ P ₁	1765	5666	0.1903	0.0000	0.0000	1.5131	1	0	0.000
³ P ₀	2699	3705	0.1174	0.0000	0.0000	0.0000	3	0	0.000
¹ I ₆	3350	2985	0.0000	0.0958	0.6581	0.0000	10	0	0.000
¹ D ₂	10274	973	0.0006	0.1628	0.0000	2.1422	144	42	0.004
¹ G ₄	16947	590	0.5967	0.0013	0.1048	0.0000	3913	0	0.085
³ F ₂	23254	430	0.0049	0.0472	0.0000	0.0004	578	0	0.013
³ F ₃	23760	421	0.1489	0.2381	0.0000	0.2525	5303	64	0.116
³ H ₄	25642	390	0.2773	0.0097	0.0083	0.0000	6375	0	0.138
³ H ₅	30032	333	0.0000	0.1987	0.1883	0.0000	6183	0	0.134
³ F ₄	32481	308	0.1431	0.0879	0.0000	0.0000	9273	0	0.201
³ H ₆	38192	262	0.0000	0.2798	0.0239	0.0000	14277	0	0.309
	initial: ³ P ₁						$\tau = 0.02$ ms		
³ P ₀	934	—	0.0000	0.0000	0.0000	1.8856	0	0	0.000
¹ I ₆	1585	6308	0.0000	0.0000	0.0011	0.0000	0	0	0.000
¹ D ₂	8509	1175	0.4385	0.0000	0.0000	0.9400	573	18	0.013
¹ G ₄	15182	659	0.0000	0.0039	0.0000	0.0000	19	0	0.000
³ F ₂	21489	465	0.1391	0.0000	0.0000	0.0468	3009	14	0.067
³ F ₃	21995	455	0.5714	0.1964	0.0000	0.0000	16175	0	0.357
³ H ₄	23878	419	0.0000	0.4101	0.0000	0.0000	7791	0	0.172
³ H ₅	28267	354	0.0000	0.2857	0.0893	0.0000	10173	0	0.225
³ F ₄	30716	326	0.0000	0.1039	0.0000	0.0000	4307	0	0.095
³ H ₆	36428	275	0.0000	0.0000	0.1239	0.0000	3175	0	0.070
	initial: ³ P ₀						$\tau = 0.02$ ms		
¹ I ₆	651	—	0.0000	0.0000	0.0243	0.0000	0	0	0.000
¹ D ₂	7575	1320	0.0270	0.0000	0.0000	0.0000	75	0	0.001
¹ G ₄	14248	702	0.0000	0.0440	0.0000	0.0000	520	0	0.009
³ F ₂	20555	486	0.3596	0.0000	0.0000	0.0000	20376	0	0.344
³ F ₃	21061	475	0.0000	0.0000	0.0000	0.0000	0	0	0.000
³ H ₄	22943	436	0.0000	0.0218	0.0000	0.0000	1099	0	0.019

Table D.5: Radiative emission properties of Tm:ZBLAN (*continued*)

final	k_{calc} cm ⁻¹	λ_{calc} nm	$ \mathbf{U}^{(2)} ^2$	$ \mathbf{U}^{(4)} ^2$	$ \mathbf{U}^{(6)} ^2$	$ \mathbf{M}/\beta_m ^2$	A_{ed} s ⁻¹	A_{md} s ⁻¹	β
³ H ₅	27333	366	0.0000	0.0000	0.0000	0.0000	0	0	0.000
³ F ₄	29782	336	0.0000	0.2812	0.0000	0.0000	31746	0	0.536
³ H ₆	35493	282	0.0000	0.0000	0.0758	0.0000	5362	0	0.091
	initial: ¹ I ₆						$\tau = 0.10$ ms		
¹ D ₂	6924	1444	0.0000	0.0544	0.8708	0.0000	38	0	0.004
¹ G ₄	13597	735	0.2170	1.2723	0.6409	0.0000	1456	0	0.140
³ F ₂	19904	502	0.0000	0.0408	0.3517	0.0000	421	0	0.041
³ F ₃	20410	490	0.0000	0.0028	0.0074	0.0000	15	0	0.001
³ H ₄	22292	449	0.0624	0.2869	0.0891	0.0000	1481	0	0.143
³ H ₅	26682	375	0.0009	0.0020	0.0056	0.0945	34	13	0.005
³ F ₄	29131	343	0.0625	0.5026	0.3916	0.0000	6019	0	0.580
³ H ₆	34842	287	0.0106	0.0390	0.0135	0.1311	861	42	0.087
	initial: ¹ D ₂						$\tau = 0.06$ ms		
¹ G ₄	6673	1499	0.1999	0.1708	0.0003	0.0000	116	0	0.007
³ F ₂	12980	770	0.0634	0.3038	0.0000	0.8776	720	35	0.043
³ F ₃	13485	742	0.1568	0.0642	0.0000	1.3042	622	59	0.039
³ H ₄	15368	651	0.1283	0.0129	0.2261	0.0000	881	0	0.050
³ H ₅	19758	506	0.0000	0.0007	0.0208	0.0000	52	0	0.003
³ F ₄	22206	450	0.5495	0.0928	0.0237	0.0000	8813	0	0.505
³ H ₆	27918	358	0.0000	0.3004	0.0923	0.0000	6164	0	0.353
	initial: ¹ G ₄						$\tau = 0.73$ ms		
³ F ₂	6307	1585	0.0047	0.0689	0.0405	0.0000	10	0	0.007
³ F ₃	6813	1468	0.0096	0.0687	0.2955	0.6924	27	2	0.021
³ H ₄	8696	1150	0.1560	0.0032	0.3512	3.0140	111	20	0.095
³ H ₅	13085	764	0.0723	0.0046	0.5355	3.4173	316	78	0.287
³ F ₄	15534	644	0.0034	0.0207	0.0777	0.1632	92	6	0.072
³ H ₆	21246	471	0.0502	0.0766	0.0140	0.0000	711	0	0.517
	initial: ³ F ₂						$\tau = 1.35$ ms		
³ F ₃	505	–	0.0038	0.0735	0.0000	5.1100	0	0	0.000
³ H ₄	2388	4187	0.2915	0.1707	0.0799	0.0000	7	0	0.009
³ H ₅	6778	1475	0.0000	0.2891	0.5825	0.0000	125	0	0.169
³ F ₄	9226	1084	0.3090	0.0597	0.0423	0.0000	357	0	0.481

Table D.5: Radiative emission properties of Tm:ZBLAN (*continued*)

final	k_{calc} cm ⁻¹	λ_{calc} nm	$ \mathbf{U}^{(2)} ^2$	$ \mathbf{U}^{(4)} ^2$	$ \mathbf{U}^{(6)} ^2$	$ \mathbf{M}/\beta_m ^2$	A_{ed} s ⁻¹	A_{md} s ⁻¹	β
³ H ₆	14938	669	0.0000	0.0000	0.2570	0.0000	253	0	0.341
	initial: ³ F ₃						$\tau = 0.75$ ms		
³ H ₄	1883	5311	0.0828	0.3564	0.2850	1.8894	2	0	0.002
³ H ₅	6272	1594	0.6286	0.3468	0.0000	0.0000	189	0	0.141
³ F ₄	8721	1147	0.0022	0.0002	0.1751	4.1682	26	36	0.046
³ H ₆	14433	693	0.0000	0.3164	0.8411	0.0000	1089	0	0.811
	initial: ³ H ₄						$\tau = 1.36$ ms		
³ H ₅	4389	2278	0.0129	0.4846	0.0085	6.4643	19	5	0.033
³ F ₄	6838	1462	0.1334	0.1275	0.1917	3.9994	58	13	0.097
³ H ₆	12550	797	0.2431	0.1135	0.6013	0.0000	638	0	0.870
	initial: ³ H ₅						$\tau = 5.64$ ms		
³ F ₄	2449	4084	0.0919	0.1228	0.9287	0.9184	3	0	0.018
³ H ₆	8161	1225	0.1074	0.2314	0.6383	10.7389	126	48	0.982
	initial: ³ F ₄						$\tau = 7.35$ ms		
³ H ₆	5712	1751	0.5297	0.7200	0.2301	0.0000	136	0	1.000

Table D.6: Radiative absorption properties of Tm:ZBLAN

final	k_{calc} cm ⁻¹	λ_{calc} nm	$ \mathbf{U}^{(2)} ^2$	$ \mathbf{U}^{(4)} ^2$	$ \mathbf{U}^{(6)} ^2$	$ \mathbf{M}/\beta_m ^2$	f_{ed} 10 ⁻⁸	f_{md} 10 ⁻⁸
	initial: ³ H ₆							
³ F ₄	5712	1751	0.5297	0.7200	0.2301	0.0000	193.2	0.0
³ H ₅	8161	1225	0.1074	0.2314	0.6383	10.7389	106.7	40.9
³ H ₄	12550	797	0.2431	0.1135	0.6013	0.0000	185.9	0.0
³ F ₃	14433	693	0.0000	0.3164	0.8411	0.0000	186.2	0.0
³ F ₂	14938	669	0.0000	0.0000	0.2570	0.0000	28.9	0.0
¹ G ₄	21246	471	0.0502	0.0766	0.0140	0.0000	71.4	0.0
¹ D ₂	27918	358	0.0000	0.3004	0.0923	0.0000	196.5	0.0
¹ I ₆	34842	287	0.0106	0.0390	0.0135	0.1311	45.0	2.2
³ P ₀	35493	282	0.0000	0.0000	0.0758	0.0000	20.7	0.0
³ P ₁	36428	275	0.0000	0.0000	0.1239	0.0000	34.8	0.0
³ P ₂	38192	262	0.0000	0.2798	0.0239	0.0000	236.2	0.0

Table D.6: Radiative absorption properties of Tm:ZBLAN (*continued*)

final	k_{calc} cm ⁻¹	λ_{calc} nm	$ \mathbf{U}^{(2)} ^2$	$ \mathbf{U}^{(4)} ^2$	$ \mathbf{U}^{(6)} ^2$	$ \mathbf{M}/\beta_m ^2$	f_{ed} 10 ⁻⁸	f_{md} 10 ⁻⁸
¹ S ₀	74856	134	0.0000	0.0000	0.0000	0.0000	0.0	0.0
	initial: ³ F ₄							
³ H ₅	2449	4084	0.0919	0.1228	0.9287	0.9184	43.4	1.5
³ H ₄	6838	1462	0.1334	0.1275	0.1917	3.9994	83.1	18.4
³ F ₃	8721	1147	0.0022	0.0002	0.1751	4.1682	17.5	24.5
³ F ₂	9226	1084	0.3090	0.0597	0.0423	0.0000	155.1	0.0
¹ G ₄	15534	644	0.0034	0.0207	0.0777	0.1632	25.3	1.7
¹ D ₂	22206	450	0.5495	0.0928	0.0237	0.0000	649.0	0.0
¹ I ₆	29131	343	0.0625	0.5026	0.3916	0.0000	659.8	0.0
³ P ₀	29782	336	0.0000	0.2812	0.0000	0.0000	255.7	0.0
³ P ₁	30716	326	0.0000	0.1039	0.0000	0.0000	97.6	0.0
³ P ₂	32481	308	0.1431	0.0879	0.0000	0.0000	311.8	0.0
¹ S ₀	69144	145	0.0000	0.0864	0.0000	0.0000	190.3	0.0
	initial: ³ H ₅							
³ H ₄	4389	2278	0.0129	0.4846	0.0085	6.4643	54.3	15.6
³ F ₃	6272	1594	0.6286	0.3468	0.0000	0.0000	204.8	0.0
³ F ₂	6778	1475	0.0000	0.2891	0.5825	0.0000	82.8	0.0
¹ G ₄	13085	764	0.0723	0.0046	0.5355	3.4173	100.2	24.7
¹ D ₂	19758	506	0.0000	0.0007	0.0208	0.0000	4.0	0.0
¹ I ₆	26682	375	0.0009	0.0020	0.0056	0.0945	3.7	1.4
³ P ₀	27333	366	0.0000	0.0000	0.0000	0.0000	0.0	0.0
³ P ₁	28267	354	0.0000	0.2857	0.0893	0.0000	224.1	0.0
³ P ₂	30032	333	0.0000	0.1987	0.1883	0.0000	200.2	0.0
¹ S ₀	66695	150	0.0000	0.0000	0.0000	0.0000	0.0	0.0
	initial: ³ H ₄							
³ F ₃	1883	5311	0.0828	0.3564	0.2850	1.8894	32.3	2.3
³ F ₂	2388	4187	0.2915	0.1707	0.0799	0.0000	46.2	0.0
¹ G ₄	8696	1150	0.1560	0.0032	0.3512	3.0140	97.8	17.7
¹ D ₂	15368	651	0.1283	0.0129	0.2261	0.0000	137.0	0.0
¹ I ₆	22292	449	0.0624	0.2869	0.0891	0.0000	281.4	0.0
³ P ₀	22943	436	0.0000	0.0218	0.0000	0.0000	15.1	0.0
³ P ₁	23878	419	0.0000	0.4101	0.0000	0.0000	296.8	0.0

Table D.6: Radiative absorption properties of Tm:ZBLAN (*continued*)

final	k_{calc} cm ⁻¹	λ_{calc} nm	$ \mathbf{U}^{(2)} ^2$	$ \mathbf{U}^{(4)} ^2$	$ \mathbf{U}^{(6)} ^2$	$ \mathbf{M}/\beta_m ^2$	f_{ed} 10 ⁻⁸	f_{md} 10 ⁻⁸
³ P ₂	25642	390	0.2773	0.0097	0.0083	0.0000	349.7	0.0
¹ S ₀	62306	160	0.0000	0.0552	0.0000	0.0000	109.6	0.0
	initial: ³ F ₃							
³ F ₂	505	—	0.0038	0.0735	0.0000	5.1100	1.4	2.0
¹ G ₄	6813	1468	0.0096	0.0687	0.2955	0.6924	49.9	4.1
¹ D ₂	13485	742	0.1568	0.0642	0.0000	1.3042	161.9	15.3
¹ I ₆	20410	490	0.0000	0.0028	0.0074	0.0000	4.3	0.0
³ P ₀	21061	475	0.0000	0.0000	0.0000	0.0000	0.0	0.0
³ P ₁	21995	455	0.5714	0.1964	0.0000	0.0000	937.0	0.0
³ P ₂	23760	421	0.1489	0.2381	0.0000	0.2525	437.3	5.3
¹ S ₀	60423	165	0.0000	0.0000	0.0000	0.0000	0.0	0.0
	initial: ³ F ₂							
¹ G ₄	6307	1585	0.0047	0.0689	0.0405	0.0000	30.8	0.0
¹ D ₂	12980	770	0.0634	0.3038	0.0000	0.8776	283.1	13.9
¹ I ₆	19904	502	0.0000	0.0408	0.3517	0.0000	181.5	0.0
³ P ₀	20555	486	0.3596	0.0000	0.0000	0.0000	632.3	0.0
³ P ₁	21489	465	0.1391	0.0000	0.0000	0.0468	255.9	1.2
³ P ₂	23254	430	0.0049	0.0472	0.0000	0.0004	69.7	0.0
¹ S ₀	59918	167	0.0454	0.0000	0.0000	0.0000	245.4	0.0
	initial: ¹ G ₄							
¹ D ₂	6673	1499	0.1999	0.1708	0.0003	0.0000	96.8	0.0
¹ I ₆	13597	735	0.2170	1.2723	0.6409	0.0000	753.5	0.0
³ P ₀	14248	702	0.0000	0.0440	0.0000	0.0000	18.8	0.0
³ P ₁	15182	659	0.0000	0.0039	0.0000	0.0000	1.8	0.0
³ P ₂	16947	590	0.5967	0.0013	0.1048	0.0000	499.0	0.0
¹ S ₀	53610	187	0.0000	0.4161	0.0000	0.0000	710.6	0.0
	initial: ¹ D ₂							
¹ I ₆	6924	1444	0.0000	0.0544	0.8708	0.0000	137.5	0.0
³ P ₀	7575	1320	0.0270	0.0000	0.0000	0.0000	17.3	0.0
³ P ₁	8509	1175	0.4385	0.0000	0.0000	0.9400	316.3	9.7
³ P ₂	10274	973	0.0006	0.1628	0.0000	2.1422	90.7	26.7

Table D.6: Radiative absorption properties of Tm:ZBLAN (*continued*)

final	k_{calc} cm ⁻¹	λ_{calc} nm	$ \mathbf{U}^{(2)} ^2$	$ \mathbf{U}^{(4)} ^2$	$ \mathbf{U}^{(6)} ^2$	$ \mathbf{M}/\beta_m ^2$	f_{ed} 10 ⁻⁸	f_{md} 10 ⁻⁸
¹ S ₀	46938	213	0.2200	0.0000	0.0000	0.0000	923.8	0.0
	initial: ¹ I ₆							
³ P ₀	651	–	0.0000	0.0000	0.0243	0.0000	0.1	0.0
³ P ₁	1585	6308	0.0000	0.0000	0.0011	0.0000	0.0	0.0
³ P ₂	3350	2985	0.0000	0.0958	0.6581	0.0000	22.9	0.0
¹ S ₀	40014	250	0.0000	0.0000	0.5428	0.0000	168.8	0.0
	initial: ³ P ₀							
³ P ₁	934	–	0.0000	0.0000	0.0000	1.8856	0.0	9.5
³ P ₂	2699	3705	0.1174	0.0000	0.0000	0.0000	132.5	0.0
¹ S ₀	39363	254	0.0000	0.0000	0.0000	0.0000	0.0	0.0
	initial: ³ P ₁							
³ P ₂	1765	5666	0.1903	0.0000	0.0000	1.5131	45.9	5.2
¹ S ₀	38428	260	0.0000	0.0000	0.0000	0.1144	0.0	9.2
	initial: ³ P ₂							
¹ S ₀	36664	273	0.3019	0.0000	0.0000	0.0000	968.3	0.0

Appendix E

Setup of the fluorescence spectrometer

To measure the emission spectrum of a rare earth doped glass, it is first of all necessary to excite the rare earth ions with a suitable pump source. What is measured is the spectrum emitted due to relaxation to lower energy levels. An excited ion may undergo spontaneous transitions to all lower lying energy levels and therefore the emission spectrum in principle contains the emission lines from all pairs of energy levels between the pump level and the ground state. Under certain circumstances even transitions from levels above the pump level can occur if the wavelength of the pump source matches an excited state absorption. This up-conversion effect is indeed effective especially for low phonon energy glasses like ZBLAN because in such glasses the energy levels of the rare earth ions have relatively long lifetimes. Nevertheless, to measure weak lines at high intensity it is usually best to pump directly the upper level of the transition. This is of special importance for transitions in the mid-infrared, which are always in competition to parallel multiphonon relaxations and thus relatively weak.

In general, to build a fluorescence spectrometer it is possible to use the same setup as for absorption measurements inserting the pumped sample instead of the light source. But the emission spectra of rare earth ions are relatively sharp line spectra which must be filtered from the background noise in contrast to an absorption measurement where the sharp lines are written into the strong temperature spectrum of the light source. By use of a monochromator it acts as a bandpass filter suppressing large parts of the background noise. To raise the signal to noise ratio to higher levels, a lock-in amplifier may be used in such a setup. In case of an interferometer setup the detector always receives the full noise spectrum, which makes the measurement of weak emission lines very difficult. Furthermore applying noise suppression methods such as a lock-in amplifier is very troublesome for such a setup.

Therefore, a setup of a monochromator spectrometer was developed so that the weak emission lines of rare earth ions could be measured especially in the mid-infrared. The main goal was high power efficiency, i.e. as much emitted radiation as possible should reach the detector. Furthermore, the existing monochromator and InSb/Si detectors had to be used.

E.1 General considerations

Figure E.1 shows the principles of the spectrometer setup with the definitions of some parameters in the following calculations. The source of the fluorescence light is a glass sample pumped by a laser focussed into the sample. Therefore, the source is a cylinder with Gaussian intensity distribution across the diameter. The diameter of the cylinder is considered to be constant on the full length, which is a good approximation if the pump laser is only moderately focussed. Besides, we neglect the reduction of fluorescence intensity along the cylinder due to absorption because this would not change the results. For the same reason

the refraction of the fluorescence radiation at the glass surface is neglected in the calculations.

In figure E.1 the monochromator is reduced to a slit because the lightpath inside is of no importance here. Only two parameters are needed: focal length and diameter of the collimating mirrors inside the monochromator, in our case $f_m = 200$ mm and $d_m = 50$ mm respectively. These values fix the maximum beam angle ϕ . Furthermore d_m serves as a hint for useful sizes of the imaging optics, depicted as lenses L_1 and L_2 , the diameter of which in principle may be chosen freely by varying the corresponding distances b_1 and b_2 . The diameter of the lenses on the one hand should be as large as possible, compared with the fluorescence source and the monochromator slit, to keep imaging errors small. Using diameters much larger than d_m , on the other hand, cannot increase the overall imaging quality of the whole optical system significantly. Therefore the lens diameter is more or less fixed and was chosen as 60 mm in our case. A monochromator distance of $b_1 = b_2 = 220$ mm leaves about 5 mm of the lens diameter for mounting. For measurements in the mid infrared the lens material is of importance, since usual glasses strongly absorb in this wavelength range. Therefore, in addition to lenses made from IRGN6 glass, mainly CaF_2 lenses were used.

As we will see from the calculations in the following, lens L_1 should deliver an image magnification as large as possible, whereas L_2 should reduce the image as much as possible. Therefore, instead of single lenses, on both sides of the monochromator double lenses were placed, symmetrically to each other. Figure E.2 gives the definition of the parameters needed to calculate the magnification $V = f_2/f_1$ of such a double lens system. The focal length f_2 is fixed by the monochromator to $f_2/d = 4$, as explained above, and f_1 is limited by the maximum curvature of the lens surface. In case of the CaF_2 lenses used, the manufacturer specified a limit of $f_1/d \geq 1.25$. The magnification of the double lens system is thus fixed to $V \leq 3.2$, regardless of the lens diameter. As in our case the free diameter of each lens is 55 mm, the magnification is 2.9 using $f_1 = 75$ mm and $f_2 = 220$ mm. An analogous analysis shows that a single lens would allow a maximum magnification of 2.2 reduced to 2.0 due to the space needed for mounting the lens.

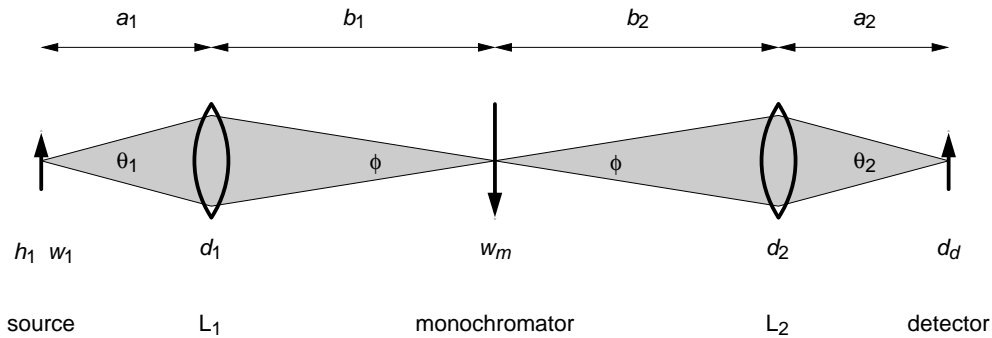


Figure E.1: Sketch of the light path in the fluorescence spectrometer

E.2 Calculations

In the following we will develop an approximate equation for the optimum setup maximizing the fraction of the fluorescence radiation reaching the detector area. It is favourable to start calculating along the beam path in backward direction, virtually imaging the detector area and the monochromator slit onto the fluorescence cylinder. The effective height of the fluorescence cylinder is then given by the diameter d_d of the detector area, whereas in our case $d_d = 0.25 - 5$ mm holds

$$h_1 = \frac{d_d}{V_1 V_2} \quad (\text{E.1})$$

with the imaging factors $V_1 = b_1/a_1$ and $V_2 = a_2/b_2$ of the lens systems L_1 and L_2 respectively. The modification in case of a narrow slit limiting the effective fluorescence height would be straightforward. The effective width of the fluorescence cylinder, on the other hand, is fixed by the width w_m of the monochromator slit:

$$w_1 = \frac{w_m}{V_1} . \quad (\text{E.2})$$

In addition to the effective dimensions of the fluorescence cylinder the solid acceptance angle $\Omega_1 = 2\pi(1 - \cos\theta_1)$ is of importance. With the beam diameter d_1 on L_1 , the angle $\theta = 2 \arctan(d_1/2a_1)$, and $V_1 = b_1/a_1$, we get

$$\Omega_1 = 2\pi \left(1 - \cos \left(2 \arctan \frac{V_1 d_1}{2b_1} \right) \right) . \quad (\text{E.3})$$

The radiation power emitted by the full fluorescence cylinder of height h_0 shall be P_0 . If we take into account the Gaussian intensity profile of the fluorescence with the $1/e^2$ -width 2σ , we get as the efficiency, i.e. the detected fraction of the total fluorescence power P_0 :

$$\frac{P}{P_0} = \frac{\Omega_1}{4\pi} \frac{2}{\pi\sigma^2 h_0} \int_{-\frac{w_1}{2}}^{\frac{w_1}{2}} dx \int_0^{h_1} dy \int_{-\infty}^{\infty} dz e^{-\frac{2(x^2+z^2)}{\sigma^2}} . \quad (\text{E.4})$$

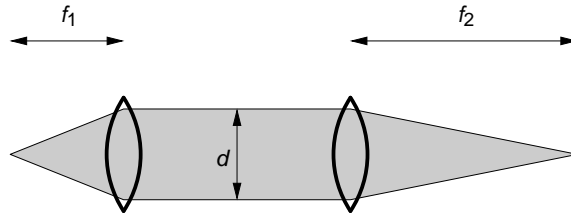


Figure E.2: Parameters of the double lens

The integrals over y and z may be carried out immediately and for x we choose the substitution $t = \sqrt{2}x/\sigma$:

$$\frac{P}{P_0} = \frac{\Omega_1}{4\pi} \frac{2h_1}{\sqrt{\pi}h_0} \int_0^{\frac{w_1}{\sqrt{2}\sigma}} e^{-t^2} dt \quad (\text{E.5})$$

and inserting the equations (E.1)–(E.3) we receive

$$\frac{P}{P_0} = \frac{d_d}{\sqrt{\pi}V_1V_2h_0} \left(1 - \cos \left(2 \arctan \frac{V_1d_1}{2b_1} \right) \right) \int_0^{\frac{w_m}{\sqrt{2}\sigma V_1}} e^{-t^2} dt . \quad (\text{E.6})$$

Finally we introduce the dimensionless quantities $H = d_d/h_0$, $F = b_1/d_1$, and $B = w_m/2\sigma$ and the error function $\text{erf}(x) = \frac{2}{\sqrt{\pi}} \int_0^x e^{-t^2} dt$ and get as the end result:

$$\frac{P}{P_0} = \frac{H}{2V_1V_2} \left(1 - \cos \left(2 \arctan \frac{V_1}{2F} \right) \right) \text{erf} \left(\frac{\sqrt{2}B}{V_1} \right) . \quad (\text{E.7})$$

E.3 Conclusions

From equation (E.7) we can deduce the preliminations for the optimum design of the fluorescence setup:

- (a) The power efficiency is proportional to H , therefore, the detector area should be as large as possible. The noise level also increases with an increasing detector area, of course, which is not taken into account here, however.
- (b) The trigonometric functions in the parantheses are monotonous decreasing functions of F , which should therefore be as small as possible, in other words the acceptance angle of the monochromator should be as large as possible, which is not surprising.
- (c) The error function is a monotonous increasing function of B . The slit width of the monochromator therefore should be large compared with the diameter of the fluorescence cylinder. But $\text{erf}(x)$ for $x = 2.3$, corresponding to $B = 1.6 V_1$, already reaches 98 % of its maximum value. Increasing B further increases the efficiency only insignificantly. Apart from that, we should remember that the fluorescence cylinder has the intensity profile of a Gaussian beam. In case of too small beam diameters the fluorescence therefore is not cylindric any more and we must take σ as a function of y . For values of $2\sigma = 50 - 100 \mu\text{m}$ the cylinder approximation stays valid and the usable range $w_m = 0.1 - 6 \text{ mm}$ of our monochomator leads to $B = 1 - 120$.
- (d) Figure E.3 shows the dependence of the efficiency on the imaging factor V_1 . With increasing values of B the maximum efficiency is increasing and shifted to larger values of V_1 . For the value $V_1 = 2.9$ derived above, values of $B > 5$ do not increase the efficiency significantly any more.

- (e) Since P/P_0 is proportional to $1/V_2$, the lens system L_2 should reduce the image spot as much as possible. Therefore the best choice is $V_2 = 1/V_1$ as already mentioned. The optimum setup is symmetric to the monochromator and the fluorescence cylinder is imaged in the ratio 1:1 onto the detector area.

Compared with the analogous setup with single lenses and $V_1 = 1/V_2 = 2.0$, the double lens design with $V_1 = 1/V_2 = 2.9$ according to equation (E.7) leads to a nearly doubled efficiency. Obviously, this is significantly more than the additional losses due to fresnel reflections at two more lenses. Unfortunately it is impossible to use lenses with anti-reflection coating in a broadband spectrometer.

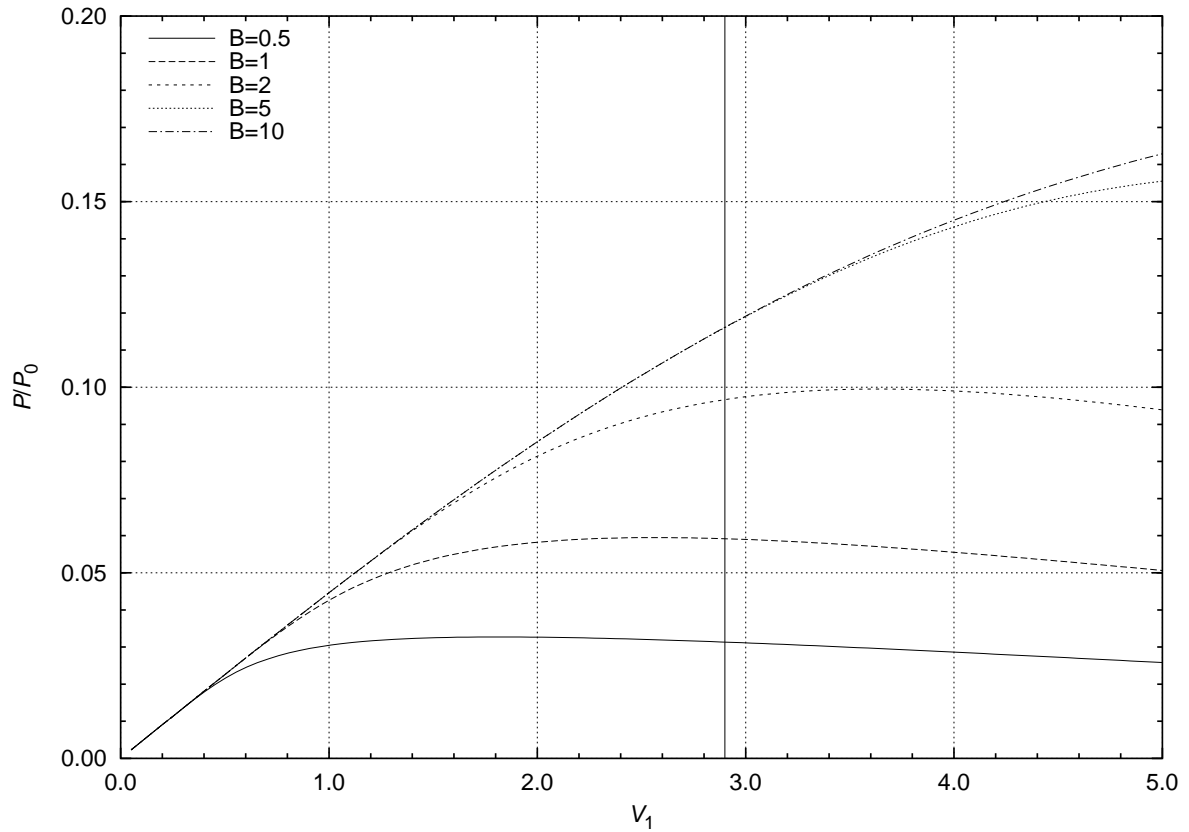


Figure E.3: Efficiency of the fluorescence spectrometer according to equation (E.7) with $H = 1$, $V_1 = 1/2.9$, and $F = 4$

E.4 The Setup

Figure E.4 shows the final setup of the fluorescence spectrometer built according to the calculations and discussions above. The beam of the pump laser is focussed into the glass sample by a lens with a focussed beam diameter of $50 - 100 \mu\text{m}$. A spherical silver mirror with a focal length of 37.5 mm is reflecting the backward radiation back to its origin. In fact it turned out that use of this mirror nearly doubles the measured intensities. The lens system L_1 images the fluorescence cylinder onto the entrance slit of the monochromator. The first lens is a symmetric bi-convex lens with a focal length of 75 mm , the second a plano-convex lens with a focal length of 220 mm , both with a diameter of 60 mm . The chopper, together with a lock-in amplifier, is used for noise reduction. The monochromator *PTI 01-001* from Photon Technology International (PTI) is of the Czerny-Turner type with one grating. As already mentioned, the collimating mirrors in the monochromator have a diameter of 50 mm and a focal length of 200 mm . The bandwidth $\Delta\lambda$ of the monochromator is proportional to the slit width w_m and proportional to the inverse focal length f_m of the monochromator mirror and the inverse grating number g (inverse line distance):

$$\Delta\lambda = \frac{w_m}{ngf_m} \quad (\text{E.8})$$

where n is the diffraction order of the beam reflected by the grating. The manufacturer of the monochromator specifies the instrument limit to be reached at a slit width of 0.125 mm . Below this value equation (E.8) is not valid any more. Behind the monochromator a long-pass filter may be placed to block the higher diffraction orders. The double lens system L_2 is imaging the exit slit onto the detector and is symmetric to L_1 . The used detectors are InSb/Si two-color detectors with diameters of the detecting areas in the range $0.25 - 5 \text{ mm}$.

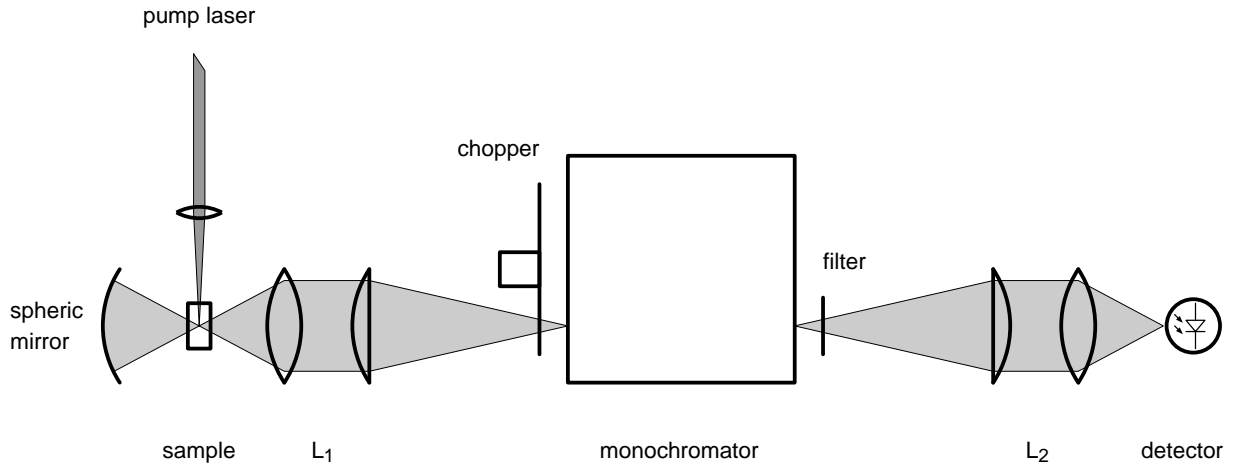


Figure E.4: Full setup of the optimized fluorescence spectrometer

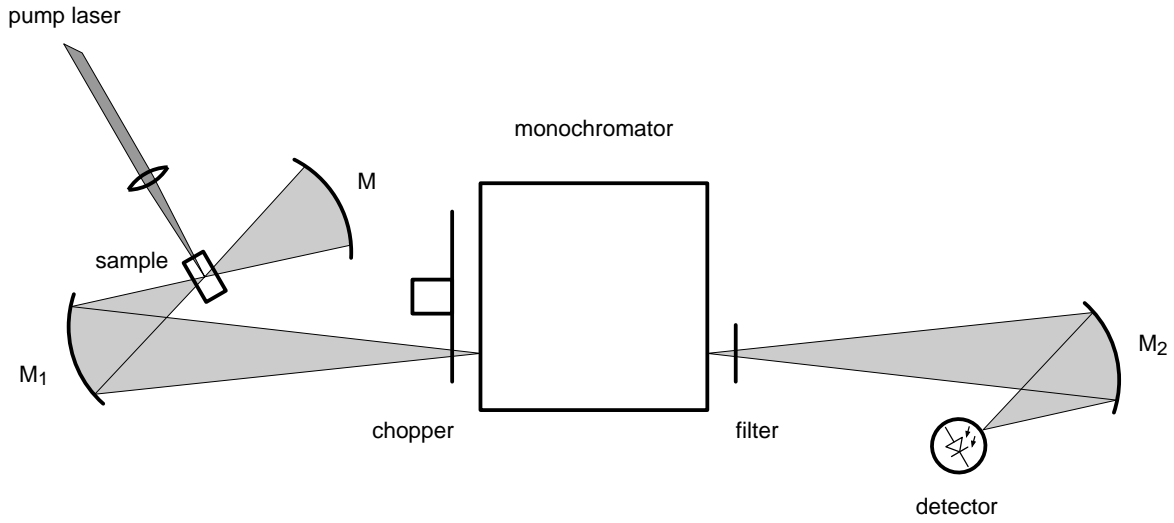


Figure E.5: Alternative setup of a fluorescence spectrometer using mirrors instead of lenses

The same setup may be used to measure the fluorescence from fibers. Due to the above calculations the radiation emerging lateral from a doped fiber core is detected efficiently because of the small core diameter of a fiber. The radiation from the fiber end can be used as well. In that case the acceptance angle of the lens optics corresponds to a numerical aperture $NA = 0.34$ of the fiber. The image of the fiber core on the monochromator slit is enlarged by a factor of 2.9.

Some preliminary tests were performed with an alternative setup of a fluorescence spectrometer according to figure E.5. In this design the lens systems L_1 and L_2 are replaced by spherical mirrors M_1 and M_2 . The advantage of the setup lies in the fact that mirrors do not show material dispersion. This facilitates the alignment of the setup, which is always necessary when the glass sample or pump laser is changed. Even more important is the fact that for this spectrometer the optimum alignment does not depend on the wavelength. Unfortunately, it turned out that the image of the fluorescence cylinder on the monochromator slit even for small elevation angles was so strongly bent that the power efficiency was too low for this setup to be a reasonable alternative to the lens setup. Using two parabolic mirrors instead of one spheric mirror should avoid this drawback but this was not tested.